

Published in Journals: Sustainability, Materials,
Sensors, Applied Sciences and Processes

Topic Reprint

Sustainability in Buildings

New Trends in the Management
of Construction and Demolition Waste
Volume II

Edited by
Carlos Morón Fernández and Daniel Ferrández Vega

mdpi.com/topics



**Sustainability in Buildings:
New Trends in the Management
of Construction and Demolition
Waste—Volume II**

Sustainability in Buildings: New Trends in the Management of Construction and Demolition Waste—Volume II

Editors

Carlos Morón Fernández

Daniel Ferrández Vega



Basel • Beijing • Wuhan • Barcelona • Belgrade • Novi Sad • Cluj • Manchester

Editors

Carlos Morón Fernández
Universidad Politécnica de Madrid
Spain

Daniel Ferrández Vega
Universidad Politécnica de Madrid
Spain

Editorial Office

MDPI
St. Alban-Anlage 66
4052 Basel, Switzerland

This is a reprint of articles from the Topic published online in the open access journals *Sustainability* (ISSN 2071-1050), *Materials* (ISSN 1996-1944), *Sensors* (ISSN 1424-8220), *Applied Sciences* (ISSN 2076-3417), and *Processes* (ISSN 2227-9717) (available at: https://www.mdpi.com/topics/sustainability_buildings).

For citation purposes, cite each article independently as indicated on the article page online and as indicated below:

| |
|--|
| Lastname, A.A.; Lastname, B.B. Article Title. <i>Journal Name</i> Year , <i>Volume Number</i> , Page Range. |
|--|

Volume II

ISBN 978-3-0365-8304-4 (Hbk)

ISBN 978-3-0365-8305-1 (PDF)

doi.org/10.3390/books978-3-0365-8305-1

Set

ISBN 978-3-0365-8300-6 (Hbk)

ISBN 978-3-0365-8301-3 (PDF)

Contents

| | |
|--|-----|
| About the Editors | ix |
| Preface | xi |
| Koki Nakao, Shinya Inazumi, Toshiaki Takaue, Shigeaki Tanaka and Takayuki Shinoi Evaluation of Discharging Surplus Soils for Relative Stirred Deep Mixing Methods by MPS-CAE Analysis Reprinted from: <i>Sustainability</i> 2022 , <i>14</i> , 58, doi:10.3390/su14010058 | 1 |
| Jiangang Yang, Luhua Luo, Jie Gao, Jing Xu and Chengping He Study on the Effect of Regeneration Agent on the Viscosity Properties of Aged Asphalt Reprinted from: <i>Materials</i> 2022 , <i>15</i> , 380, doi:10.3390/ma15010380 | 19 |
| Adrian AlexandruȘerbănoiu, Cătălina Mihaela Grădinaru, Radu Muntean, Nicanor Cimpoeșu and Bogdan Vasile Șerbănoiu Corn Cob Ash versus Sunflower Stalk Ash, Two Sustainable Raw Materials in an Analysis of Their Effects on the Concrete Properties Reprinted from: <i>Materials</i> 2022 , <i>15</i> , 868, doi:10.3390/ma15030868 | 37 |
| Daniel Ferrández, Manuel Álvarez, Pablo Saiz and Alicia Zaragoza Experimental Study with Plaster Mortars Made with Recycled Aggregate and Thermal Insulation Residues for Application in Building Reprinted from: <i>Sustainability</i> 2022 , <i>14</i> , 2386, doi:10.3390/su14042386 | 55 |
| Petros Petrounias, Aikaterini Rogkala, Panagiota P. Giannakopoulou, Angeliki Christogerou, Paraskevi Lampropoulou, Spyridon Liogris, et al. Utilization of Industrial Ferronickel Slags as Recycled Concrete Aggregates Reprinted from: <i>Appl. Sci.</i> 2022 , <i>12</i> , 2231, doi:10.3390/app12042231 | 73 |
| Wanchai Yodsudjai and Kirati Nitichote Chloride Penetration Behavior of Concrete Made from Various Types of Recycled Concrete Aggregate Reprinted from: <i>Sustainability</i> 2022 , <i>14</i> , 2768, doi:10.3390/su14052768 | 93 |
| Robert B. Ataria and Yong C. Wang Mechanical Properties and Durability Performance of Recycled Aggregate Concrete Containing Crumb Rubber Reprinted from: <i>Materials</i> 2022 , <i>15</i> , 1776, doi:10.3390/ma15051776 | 107 |
| Anton Mazur, Peter Tolstoy and Konstantinos Sotiriadis ¹³ C, ²⁷ Al and ²⁹ Si NMR Investigation of the Hydration Kinetics of Portland-Limestone Cement Pastes Containing CH ₃ -COO ⁻ -R ⁺ (R=H or Na) Additives Reprinted from: <i>Materials</i> 2022 , <i>15</i> , 2004, doi:10.3390/ma15062004 | 119 |
| An Wang, Ren Togo, Takahiro Ogawa and Miki Haseyama Defect Detection of Subway Tunnels Using Advanced U-Net Network Reprinted from: <i>Sensors</i> 2022 , <i>22</i> , 2330, doi:10.3390/s22062330 | 133 |
| Ying Sun, and Zhaolin Gu Implementation of Construction Waste Recycling under Construction Sustainability Incentives: A Multi-Agent Stochastic Evolutionary Game Approach Reprinted from: <i>Sustainability</i> 2022 , <i>14</i> , 3702, doi:10.3390/su14063702 | 151 |

| | |
|---|-----|
| Xiaoyan Zhang, Yuehao Cao, Mingfang Tang, Enyi Yu, Yiqun Zhang and Gang Wu Evaluation of a Chongqing Industrial Zone Transformation Based on Sustainable Development Reprinted from: <i>Sustainability</i> 2022 , <i>14</i> , 5122, doi:10.3390/su14095122 | 173 |
| Maria Spanou, Sokrates Ioannou, Konstantina Oikonomopoulou, Pericles Savva, Konstantinos Sakkas, Michael F. Petrou and Demetris Nicolaidis Investigation of the Geopolymerization Potential of a Waste Silica-Rich Diabase Mud Reprinted from: <i>Materials</i> 2022 , <i>15</i> , 3189, doi:10.3390/ma15093189 | 187 |
| Ming-Qiang Huang and Rui-Juan Lin Evolutionary Game Analysis of Energy-Saving Renovations of Existing Rural Residential Buildings from the Perspective of Stakeholders Reprinted from: <i>Sustainability</i> 2022 , <i>14</i> , 5723, doi:10.3390/su14095723 | 201 |
| Sérgio Roberto da Silva and Jairo José de Oliveira Andrade A Review on the Effect of Mechanical Properties and Durability of Concrete with Construction and Demolition Waste (CDW) and Fly Ash in the Production of New Cement Concrete Reprinted from: <i>Sustainability</i> 2022 , <i>14</i> , 6740, doi:10.3390/su14116740 | 221 |
| Ali Al-Otaibi, Patrick Aaniamenga Bowan, Mahmoud M. Abdel daiem, Noha Said, John Obas Ebohon, Aasem Alabdullatief, et al. Identifying the Barriers to Sustainable Management of Construction and Demolition Waste in Developed and Developing Countries Reprinted from: <i>Sustainability</i> 2022 , <i>14</i> , 7532, doi:10.3390/su14137532 | 249 |
| David Suescum-Morales, José Ramón Jiménez and José María Fernández-Rodríguez Use of Carbonated Water as Kneading in Mortars Made with Recycled Aggregates Reprinted from: <i>Materials</i> 2022 , <i>15</i> , 4876, doi:10.3390/ma15144876 | 267 |
| Kun Tu, Jin Wu, Yiyuan Wang, Huachao Deng and Rui Zhang Uniaxial Compressive Stress–Strain Relation of Recycled Coarse Aggregate Concrete with Different Carbonation Depths Reprinted from: <i>Materials</i> 2022 , <i>15</i> , 5429, doi:10.3390/ma15155429 | 291 |
| Yu-Zhang Bi, Jia-Ming Wen, Hao-Liang Wu and Yan-Jun Du Evaluation of Performance of Polyacrylamide-Modified Compacted Clay as a Gas Barrier: Water Retention and Gas Permeability and Diffusion Characteristics Reprinted from: <i>Appl. Sci.</i> 2022 , <i>12</i> , 8379, doi:10.3390/app12168379 | 309 |
| María Paz Sáez-Pérez, Jorge A. Durán-Suárez, Amparo Verdú-Vázquez and Tomás Gil-López Study and Characterization of Special Gypsum-Based Pastes for Their Use as a Replacement Material in Architectural Restoration and Construction Reprinted from: <i>Materials</i> 2022 , <i>15</i> , 5877, doi:10.3390/ma15175877 | 325 |
| Mais Abdulrazzaq Ibrahim, Nihat Atmaca, Ahmed Assim Abdullah and Adem Atmaca Mechanical Properties of Concrete Produced by Light Cement-Based Aggregates Reprinted from: <i>Sustainability</i> 2022 , <i>14</i> , 15991, doi:10.3390/su142315991 | 345 |
| Qinghui Zhou, Haoshi Liu, Yuhang Qiu and Wuchao Zheng Object Detection for Construction Waste Based on an Improved YOLOv5 Model Reprinted from: <i>Sustainability</i> 2023 , <i>15</i> , 681, doi:10.3390/su15010681 | 363 |
| Piotr Sobierajewicz, Janusz Adamczyk and Robert Dylewski Ecological and Economic Assessment of the Reuse of Steel Halls in Terms of LCA Reprinted from: <i>Appl. Sci.</i> 2023 , <i>13</i> , 1597, doi:10.3390/app13031597 | 379 |

| | |
|---|------------|
| Li Wang, Yanhong Lv, Siyu Huang, Yu Liu and Xinrong Li The Evolution of Research on C&D Waste and Sustainable Development of Resources: A Bibliometric Study Reprinted from: <i>Sustainability</i> 2023 , <i>15</i> , 9141, doi:10.3390/su15129141 | 399 |
| Chongshi Gu, Xinran Cui, Hao Gu and Meng Yang A New Hybrid Monitoring Model for Displacement of the Concrete Dam Reprinted from: <i>Sustainability</i> 2023 , <i>15</i> , 9609, doi:10.3390/su15129609 | 419 |

About the Editors

Carlos Morón Fernández

Carlos Morón Fernández, PhD. He is a full professor at the Universidad Politécnica de Madrid and is currently the director of the research group on “Monitoring and Technological Innovation in Building”. He is currently the director of the Department of Building Technology at the E.T.S. de Edificación de Madrid, has numerous scientific publications in high-impact-factor journals, and has supervised 10 doctoral theses.

Daniel Ferrández Vega

Daniel Ferrández Vega, PhD. He is an associate professor at the Universidad Politécnica de Madrid and is an internationally recognized researcher in the field of building engineering. He is currently developing his research in the field of new materials for sustainable construction and the application of new measurement techniques to buildings. He has nearly 50 publications in JCR- and SJR-indexed journals, and has supervised three doctoral theses.

Preface

The building sector is evolving towards a more efficient management of natural resources and the incorporation of circular economy criteria. In this way, the recovery and revaluation of construction and demolition waste (CDW), energy efficiency or the development of new composite materials are some of the lines that define research in building engineering in this decade. This work compiles some of the most cutting-edge research on sustainability in building, showing advances in the development of new materials, more efficient construction systems, the recycling of construction waste and other topics of interest to construction professionals.

In this sense, the Guest Editors and the research group "Monitorización e Innovación Tecnológica en Edificación (MITE)" would like to thank all the researchers for their collaboration, and for their confidence in this MDPI Topic. We sincerely hope that the work will be useful for other professors, professionals, and researchers, and that future editions will receive the same level of participation. For all these reasons, we can only say thank you.

Carlos Morón Fernández and Daniel Ferrández Vega

Editors

Article

Evaluation of Discharging Surplus Soils for Relative Stirred Deep Mixing Methods by MPS-CAE Analysis

Koki Nakao¹, Shinya Inazumi^{2,*}, Toshiaki Takaue³, Shigeaki Tanaka⁴ and Takayuki Shinoi⁵

¹ Graduate School of Engineering and Science, Shibaura Institute of Technology Toyosu Campus, Tokyo 135-8548, Japan; na21105@shibaura-it.ac.jp

² Department of Civil Engineering, Shibaura Institute of Technology Toyosu Campus, Tokyo 135-8548, Japan

³ Aoyama Kiko Co., Ltd., 2-18-4 Kita-ueno, Taito-ku, Tokyo 110-0014, Japan; takaue@aoyamakiko.co.jp

⁴ Ibuki Industry Co., Ltd., 1-17-5 Higashi-Nakashima, Yodogawa-ku, Osaka 533-0033, Japan; tanaka@ibukisangyo.co.jp

⁵ Nihon Kaiko Co., Ltd., 119 Ito-cho, Chuo-ku, Kobe 650-0032, Japan; t_shinoin@nipponkaiko.co.jp

* Correspondence: inazumi@shibaura-it.ac.jp

Abstract: Most of the ground in Japan is soft, leading to great damage in the event of liquefaction. Various ground-improvement measures are being taken to suppress such damage. However, it is difficult to carry out ground-improvement work while checking the internal conditions of the ground during the construction. Therefore, a visible and measurable evaluation of the performance of the ground-improvement work was conducted in this study. The authors performed a simulation analysis of the relative stirred deep mixing method (RS-DMM), a kind of ground-improvement method, using a computer-aided engineering (CAE) analysis based on particle-based methods (PBM). In the RS-DMM, the “displacement reduction type (DRT)” suppresses displacement during construction. Both the DRT and the normal type (NT) were simulated, and a visible and measurable evaluation was performed on the internal conditions during each construction, the quality of the improved body, and the displacement reduction performance. As an example of these results, it was possible to visually evaluate the discharge of surplus soil by the spiral rod attached to the stirring wing of the DRT. In addition, the authors succeeded in quantitatively showing that more surplus soil was discharged when the stirring wing of the DRT was used than when the stirring wing of the NT was used.

Keywords: excavation and stirring; ground improvement; MPS-CAE analysis; relative stirred deep mixing method; visualization

Citation: Nakao, K.; Inazumi, S.; Takaue, T.; Tanaka, S.; Shinoi, T. Evaluation of Discharging Surplus Soils for Relative Stirred Deep Mixing Methods by MPS-CAE Analysis.

Sustainability **2022**, *14*, 58. <https://doi.org/10.3390/su14010058>

Academic Editors: Carlos Morón Fernández, Castorina Silva Vieira and Daniel Ferrández Vega

Received: 17 October 2021

Accepted: 12 December 2021

Published: 22 December 2021

Publisher’s Note: MDPI stays neutral with regard to jurisdictional claims in published maps and institutional affiliations.



Copyright: © 2021 by the authors. Licensee MDPI, Basel, Switzerland. This article is an open access article distributed under the terms and conditions of the Creative Commons Attribution (CC BY) license (<https://creativecommons.org/licenses/by/4.0/>).

1. Introduction

Japan is a disaster-prone country that is exposed to the threat of various disasters, such as earthquakes, tsunamis, and floods caused by heavy rains. In addition, there are many soft grounds mainly composed of fine particles, such as clay, silt, and sand, especially in urban waterfront areas, which are the cause of great damage due to liquefaction. The phenomenon of liquefaction was first noticed in the 1964 Niigata Earthquake, and more recently in the Great East Japan Earthquake that occurred on 11 March 2011 and caused substantial damage, especially in Urayasu City, Chiba Prefecture [1–3]. There is great concern about damage caused by liquefaction in the event of an earthquake directly beneath the Tokyo metropolitan area or a huge Nankai Trough earthquake that is expected to occur in the future. In modern times, the world must protect its land from various disasters, such as earthquakes, tsunamis, and floods caused by heavy rains. For that purpose, it is necessary to improve the land, that is, the ground, so that it is sustainable against disasters. This concept will directly contribute to the achievement of Goal 11 (Sustainable Cities and Communities) in the Sustainable Development Goals (SDGs).

Various ground-improvement measures are being taken to suppress damage associated with various disaster [4,5]. Ground-improvement measures are indispensable measures for forming sustainable ground in the future. By performing ground-improvement

work, it is possible to prevent the liquefaction phenomenon and suppress its damage. However, it is difficult to perform ground-improvement work while checking the internal conditions of the ground during the construction, and the design and evaluation are based on empirical rules [6–8]. Therefore, the purpose of the present study was to conduct a visible and measurable evaluation of the quality and performance of ground-improvement work by computer simulation.

A simulation analysis of the relative stirred deep mixing method (RS-DMM) [9], a kind of ground-improvement method, was performed in this study using a computer-aided engineering (CAE) analysis based on the moving particle semi-implicit (MPS) method, which is one of the particle-based methods (PBMs) [10,11]. The RS-DMM is a method of penetrating and stirring while rotating the inner and outer wings of the stirring wing in opposite directions and discharging the solidifying material from the tip of the stirring wing [9,12]. In addition, the “displacement reduction type (DRT)” of RS-DMM suppresses displacement during the construction. A series of operations, such as penetration, stirring, and extraction, performed by the DRT and the normal-type (NT) RS-DMM, was reproduced with a 3D model. Then, a visible and measurable evaluation was conducted on the conditions of the inside of the ground during each construction, the quality of the improved body, and the displacement reduction performance.

2. Deep Mixing and Relative Stirred Deep Mixing Methods

2.1. Construction Methods

Ground improvement has various sustainable effects on soft grounds, such as the prevention of liquefaction, increase in bearing capacity, and promotion of consolidation. Currently, there are many ground-improvement methods, such as the replacement method, accelerated consolidation method, compaction method, solidifying method, reinforcement method, and injection method. They are selected for use according to the characteristics of the targeted soft ground and the purpose of the improvement. Deep mixing methods (DMMs) comprise one of the solidifying methods among ground-improvement methods. In DMMs, while the stirring wing penetrates the targeted soft ground, slurry-like or powder-like solidifying material and the soft ground are forcibly stirred and mixed to construct a columnar improved body in the targeted soft ground. One of the DMMs, the relative stirred deep mixing method (RS-DMM), is a method of rotating the inner and outer wings of the stirring wing in opposite directions at different speeds while discharging a slurry-like solidifying material from the tip of the stirring wing [9,12,13]. By rotating the inner and outer wings in opposite directions, it is possible to add the effects of “kneading” and “mixing” to the mixing of the targeted soft ground and the solidifying material. One of the issues that can occur when a DMM is applied to a soft ground is “co-rotation”. Co-rotation is the phenomenon in which the unimproved parts remain due to their rotating together with the cohesive soil that becomes attached to the stirring wing during stirring and mixing. It occurs especially in cohesive soil and causes variations in the quality of the improved bodies. Cohesive soil adheres to the stirring wing due to the cohesion force of the cohesive soil, further cohesive soil adheres due to the cohesion force of the adhered cohesive soil, and cohesive soil also adheres to the outside. In this way, the mass of cohesive soil becomes larger and larger and results in the stirring capacity of the stirring wing becoming significantly reduced. The RS-DMM prevents such co-rotation by “kneading” and “mixing” and makes it possible to construct a high-quality, high-strength improved body without variation.

DMMs are used not only as liquefaction countermeasures but also as measures against the subsidence of embankments, the prevention of the slip destruction of grounds including embankments, the stabilization of foundation structures, and so on, and they can be applied under a wide range of ground conditions. The construction flow of DMMs is shown in Figure 1 and is described in the following:

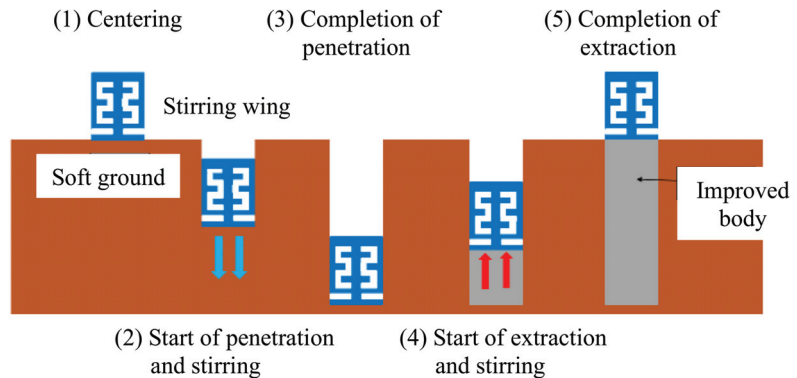


Figure 1. Outline of construction process of DMMs.

- (1) Axial core set of the stirring wing: The construction position is determined, and the axial core of the stirring wing is set.
- (2) Penetration and stirring of the stirring wing: Penetration and stirring are performed while solidifying material is discharged from the tip of the stirring wing.
- (3) Bottoming and tip treatment: After the specified construction depth has been reached, stirring is performed with the stirring wing for 1 min.
- (4) Extraction and stirring of the stirring wing: Extraction and stirring is performed while the solidifying material is discharged from the tip of the stirring wing. The stirring wing rotates in the opposite direction to that during the penetration.

2.2. Occurrence of Displacement and Displacement Reduction Type of Stirring Wing

One of the situations that may arise when performing ground improvement using the relative stirred deep mixing method (RS-DMM) is the effect of “displacement”. When applying the RS-DMM, it is necessary to penetrate the stirring wing into the targeted soft ground and inject a slurry-like solidifying material. When this solidifying material is injected, the material pushes the surrounding soft ground out, increasing the pressure inside the soft ground and causing “displacement” [14,15].

If there are railroads or buildings around the construction site, the construction must be executed while giving due consideration to the impact of displacement. Especially in construction works near railways, there must be strict control of track displacement, and the construction must be handled with the utmost of care.

The stirring wing of the displacement reduction type (DRT) is used in the above situations. The stirring wing of the DRT uses the stirring wing rod as a spiral rod. In order to suppress the displacement, it is necessary to prevent the solidifying material from pushing out the ground, but the effect of the spiral rod promotes the discharge of excess soil equivalent to the solidifying material injection, as shown in Figure 2, and the displacement can be suppressed by releasing the internal pressure in the soft ground. By using the stirring wing of the DRT, it is possible to reduce the displacement as well as its influence on the surrounding structures.

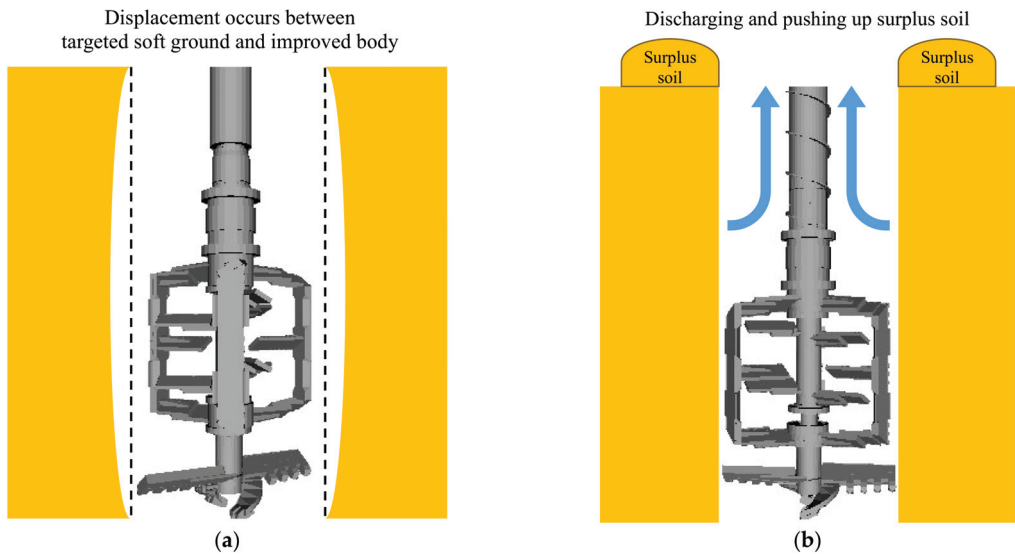


Figure 2. Stirring wing of NT and stirring wing of DRT: (a) Stirring wing of NT; (b) Stirring wing of DRT.

3. Computer-Aided Engineering Analysis with Particle-Based Methods

3.1. Computer-Aided Engineering (CAE)

Computer-aided engineering (CAE) is an alternative technology for large-scale experiments, conducted in a room or in situ, using prototypes that have been prepared in a study as part of the development process of “manufacturing”. In other words, CAE is a general term for technology that simulates and analyzes prototypes on a computer created by a computer-aided design (CAD) and so on, considering the site conditions [16–19]. At the same time, CAE may refer to computer-aided engineering work or its tools for the prior examination, design, manufacturing, and process design of construction methods and products. In the field of geotechnical engineering, CAE can be used not only to visualize the inside of the ground and the stress loading on the inside of the ground but also to estimate the results of experiments that would entail very high costs and/or phenomena that would be difficult to reproduce. In addition, by performing appropriate post-processing, it is possible to communicate with other people in a visually easy-to-understand manner.

In this study, a simulation using a CAE analysis, based on the moving particle semi-implicit (MPS) method as one of the typical particle-based methods (PBMs), that is an “MPS-CAE analysis”, for the RS-DMM, is performed as a kind of ground-improvement method, and the visible and measurable performance in the targeted soft ground is evaluated.

The possibility and validity of applying the MPS-CAE analysis to the ground and ground-improvement methods has been clarified by Inazumi et al. [13,18,20–22] and Nakao et al. [23].

3.2. Particle-Based Methods (PBMs) and Moving Particle Semi-Implicit (MPS) Method

A major feature of particle-based methods (PBMs) is that, unlike the finite element method (FEM) and the finite difference method (FDM), they do not use a lattice, but instead discretize the continuum as particles that move each calculation point with a physical quantity. However, this causes a large difference in the governing equation. When describing the behavior of a continuum, the Euler method (with lattice: FEM, FDM, and so on) and the Lagrange method (non-grid: PBM) are available. In the Lagrange method, the calculation point moves as the object moves and deforms, so the convection term

disappears from the governing equation. Equations (1) and (2) show the Navier–Stokes equations by the Euler method and the Lagrange method, respectively [13,21,24–26]:

$$\frac{\partial u(x,t)}{\partial t} + (u(x,t) \cdot \nabla)u(x,t) = -\frac{1}{\rho} \nabla P(x,t) + \nu \nabla^2 u(x,t) + g(x,t) \quad (1)$$

$$\frac{Du(X,t)}{Dt} = \frac{1}{\rho} \nabla P(x,t) + \nu \nabla^2 u(X,t) + g(X,t) \quad (2)$$

where u is the velocity, P is the pressure, g is the external force, ρ is the density, and ν is the kinematic viscosity coefficient.

The moving particle semi-implicit (MPS) method, one of the typical PBMs, is an incompressible flow analysis method that discretizes a continuum with particles, and the basic governing equations are the continuity equation shown in Equation (3) and the Navier–Stokes equation shown in Equation (4):

$$\frac{D\rho}{Dt} = 0 \quad (3)$$

$$\frac{D\vec{u}}{Dt} = -\frac{\nabla P}{\rho} + \nu \nabla^2 \vec{u} + \vec{g} \quad (4)$$

where D/Dt represents the Lagrange derivative, ρ is the density, \vec{u} is the velocity, P is the pressure, ν is the coefficient of kinematic viscosity, and \vec{g} is the gravity. In PBMs, the Navier–Stokes equation is divided into two stages, namely, the pressure term is calculated explicitly from Equation (5) and the pressure gradient term is implicitly calculated from Equations (6) and (7):

$$\frac{\vec{u}^* - \vec{u}^k}{\Delta t} = \nu \nabla^2 \vec{u}^k + \vec{g} \quad (5)$$

$$\nabla^2 p^{k+1} = \frac{\rho}{\Delta t^2} \frac{n^* - n^0}{n^0} \quad (6)$$

$$\frac{\vec{u}^{k+1} - \vec{u}^*}{\Delta t} = -\frac{\nabla p^{k+1}}{\rho} \quad (7)$$

where n is the particle number density (dimensionless quantity representing the density of the particle arrangement), n_0 is the standard particle number density, and k is the time step. The * indicates the physical quantity at the stage when the explicit calculation is completed. Figure 3 shows the calculation algorithm of the MPS.

3.3. Visualization in Ground by MPS-CAE Analysis

Conventionally, when performing ground-improvement work, the construction management is carried out by repeating measures based on the empirical rules of the site. This is because the target of the construction is the ground, and it is impossible to directly and visually check the ground and its internal conditions during the construction. Therefore, what is required is the visualization of the ground. By simulating the ground improvement in advance and visualizing the construction status, it is possible to carry out surveys, designs, and construction management based on scientific methods. In addition, ground improvement situations can be simulated by applying various conditions, such as physical property values and the movements of the stirring wing, which can be useful for improving the economic efficiency and quality of the ground-improvement work.

Nakao et al. (2021) used an MPS-CAE analysis to three-dimensionally model the process of penetration and stirring by the RS-DMM on a computer, and examined the behavior inside a targeted soft ground and the effect of the RS-DMM on the surrounding ground. They succeeded in visually capturing the process of penetration and stirring by the RS-DMM and the inside of the targeted soft ground in the MPS-CAE analysis. It has

also been confirmed that the simulation results by the MPS-CAE analysis are in good agreement with the results of the mixture model experiment. However, a quantitative evaluation based on the results of an MPS-CAE analysis has not been achieved, and the inside of the targeted soft ground must be measurably reproduced and evaluated. After that, if various external factors inside the ground can be incorporated into the MPS-CAE analysis, it is expected that the co-rotation mechanism can be successfully investigated and that an effective ground-improvement method can be designed and developed.

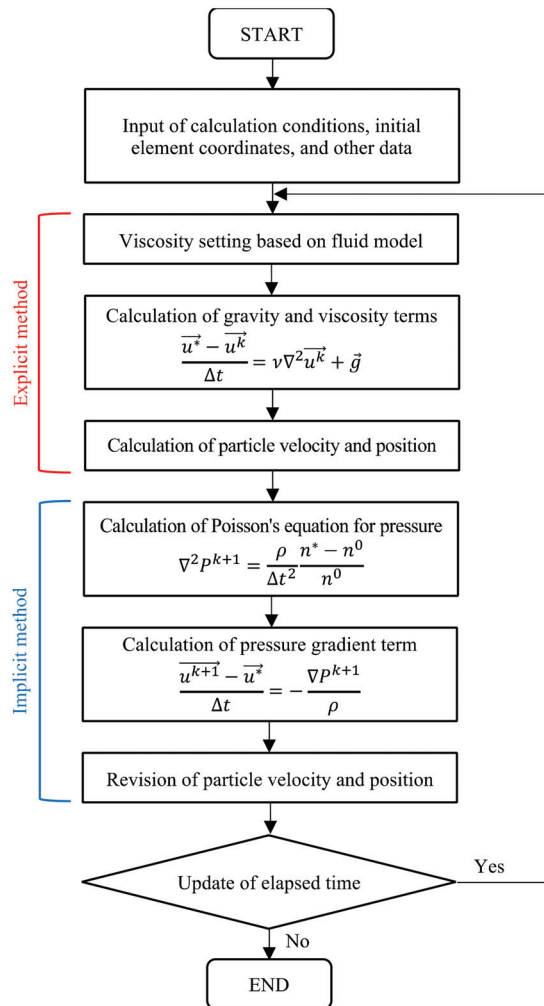


Figure 3. Calculation algorithm for MPS.

In this study, the visualization of the RS-DMM, a kind of ground-improvement method, was attempted using an MPS-CAE analysis, which is one of the numerical analysis methods. By expressing the targeted soft ground and the solidifying material as collections of particles, the purpose is to evaluate how they are stirred and the quality of the improved body in the MPS-CAE analysis. In addition, the performance of the displacement reduction and the quality of the improved body when the stirring wing of the DRT was used were compared with those when the stirring wing of the normal type (NT) was used, and the performances were evaluated.

4. Parameter Setting and Analysis Model

4.1. Bingham Fluid Model

The MPS-CAE analysis requires the determination of the rheological parameters for each fluid. In this analysis, the rheological properties of the cement slurry and targeted soft ground are assumed as Bingham fluid models, which are non-Newtonian fluids because they are mixtures of various substances.

The Bingham fluid model is a fluid in which the strain ratio remains 0 until the shear stress exceeds the yield value. The authors adopted the bi-viscosity model, which behaves as a viscoelastic fluid when flowing and as a highly viscous fluid when immobile (see Figure 4). The apparent viscosity when flowing is shown in Equation (8), and the apparent viscosity when immobile is shown in Equation (9):

$$\eta = \eta_p + \frac{\tau_y}{\dot{\gamma}} \quad \dot{\gamma} \geq \dot{\gamma}_c \quad (8)$$

$$\eta = \eta_p + \frac{\tau_y}{\dot{\gamma}_c} \quad \dot{\gamma} < \dot{\gamma}_c \quad (9)$$

where τ_y is the yield value, η_p is the plastic viscosity, $\dot{\gamma}$ is the average shear velocity, and $\dot{\gamma}_c$ is the yield reference value at the boundary between the fluid state and the immobility state. A preliminary analysis was performed in this analysis, and the result was $\dot{\gamma}_c = 1$. In the preliminary analysis, the value of $\dot{\gamma}_c$ was constantly changed and set in terms of flow time, solution stability, and calculation time.

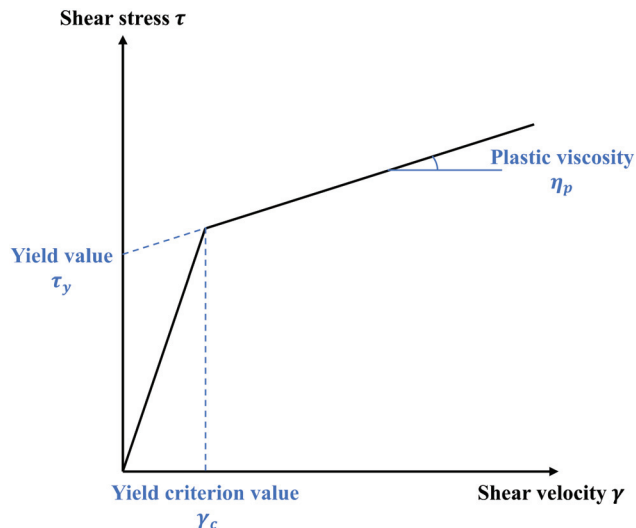


Figure 4. Concept of bi-viscosity model.

4.2. Parameter Setting

The parameters required for this analysis are density, yield value, and plastic viscosity. Table 1 shows the parameters used in this analysis.

Regarding the analysis parameters of the cement slurry, the density was determined by measuring the mass using a quantitative container with a known volume, and the plastic viscosity was determined using a rotary viscometer. The rotary viscometer employs a B-type viscometer (DV2T), which is relatively easy to handle. The yield value was set to 10 Pa in this analysis by referring to the yield stress of an unconfined compression test on fresh concrete as the yield value of the Bingham fluid.

Regarding the analysis parameters of the ground, the targeted soft ground was determined by assuming a soft ground that needs improvement, referring to the results of tests on soil collected from the field site of the soft ground [21,22]. For the yield value, the authors referred to half of the unconfined compressive strength.

Table 1. MPS-CAE analysis parameters.

| | Density ρ (kg/m ³) | Yield Value τ_y (Pa) | Plastic Viscosity η_p (Pa s) |
|---------------|--|------------------------------|--------------------------------------|
| Cement slurry | 1500 | 10 | 0.28 |
| Soft ground | 1600 | 1,000,000 | 1000 |

4.3. Analysis Model

In this study, the RS-DMM, which is a kind of ground-improvement method, is reproduced by an MPS-CAE analysis, and the behavior of each particle assumed as cement slurry and the behavior of the targeted soft ground are evaluated. In order to perform the analysis, two types of stirring wing, NT and DRT, as well as one ground model, were modeled on a computer using CAE.

The stirring wing used in the RS-DMM is composed of an inner wing and an outer wing, which are rotated in opposite directions to penetrate and stir. The rod part of the stirring wing of the NT is columnar, while that of the stirring wing of the DRT is spiral. Figure 5 shows the stirring wing model used in this analysis. In addition, when performing the analysis, it is necessary to set the parameters related to the rotation, penetration, and volume of the cement slurry being injected into the stirring wing. The parameters shown in Table 2 were set by referring to the construction results of the RS-DMM, which is the analysis target of this study.

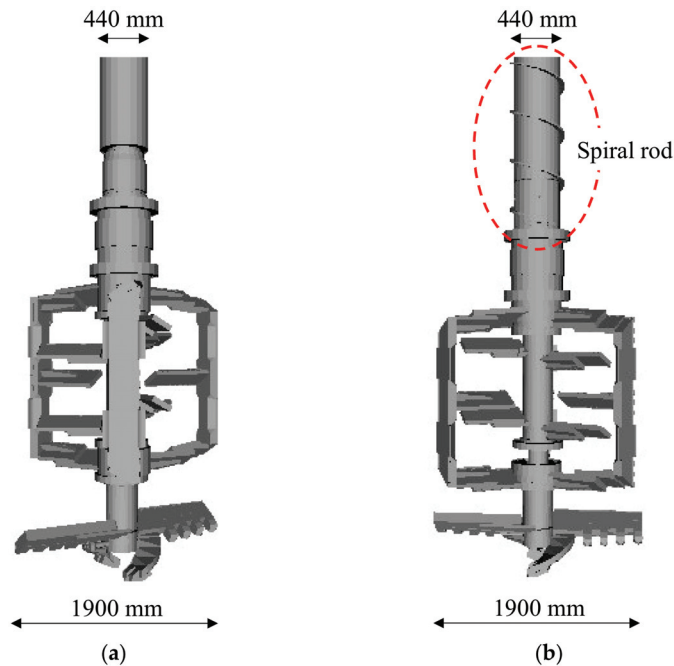
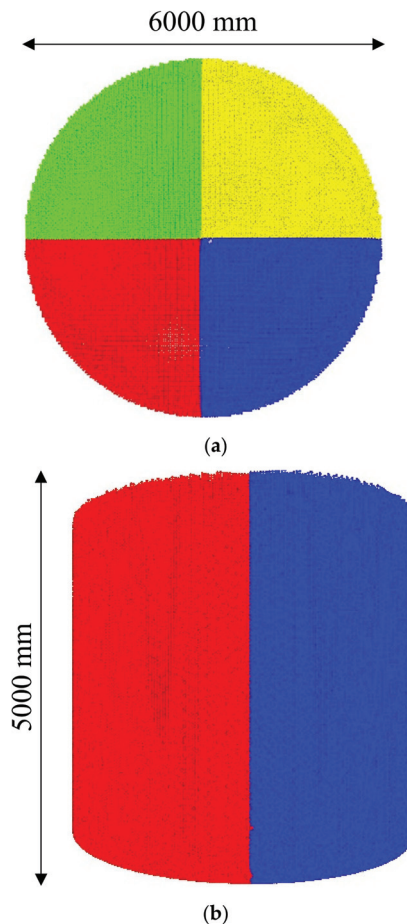


Figure 5. Stirring wing model used for MPS-CAE analysis: (a) Stirring wing of NT; (b) Stirring wing of DRT.

Table 2. MPS-CAE analysis parameters related to stirring wing behavior.

| Elapsed Time Classification (s) | Rotational Speed of Inner Wing (rpm) | Rotational Speed of Outer Wing (rpm) | Penetration Speed (m/s) | Injected Volume of Solidifying Material (m ³ /s) |
|---------------------------------|--------------------------------------|--------------------------------------|-------------------------|---|
| 0~10 | -10 | 20 | -0.1 | 0 |
| 10~50 | -10 | 20 | -0.1 | 0.03 |
| 50~110 | -10 | 20 | 0 | 0 |
| 110~150 | 10 | -20 | 0.1 | 0.03 |
| 150~160 | 10 | -20 | 0.1 | 0 |

A columnar ground model, with a diameter of 6000 mm and a height of 5000 mm, was used as the targeted soft ground. In the PBMs, the inter-particle distance, which corresponds to the size of the particles, was set to 40 mm in consideration of the calculation load. In addition, the targeted soft ground was divided into four parts in advance and color-coded so that it would be easier to evaluate the state of the stirring and mixing of the targeted soft ground and the cement slurry to be injected during excavation and the state of stirring by the stirring wing (see Figure 6). The particles of the solidifying material injected from the stirring wing are displayed in gray.

**Figure 6.** Targeted soft ground model used for MPS-CAE analysis: (a) Plan (top) view; (b) Side view.

4.4. Analysis Case and Evaluation Method

In order to conduct a visible and measurable evaluation of the displacement reduction performance when the stirring wing of the DRT is used, the results are compared with the results when the stirring wing of the NT is used.

In the evaluation of the displacement reduction performance, attention was paid to the moving velocity of the particles assuming the targeted soft ground. In order to suppress the occurrence of displacement due to the construction, it is important to discharge the surplus soil generated when the solidifying material is injected. For the particles inside the targeted soft ground during the analysis, the velocity components in the Z-axis direction were color-coded, and the mechanism of the discharging surplus soil and its performance were evaluated. In order to quantitatively evaluate the performance of the discharging surplus soil, the volume of discharging surplus soil was estimated by measuring the Z-axis velocity of the particles existing in the specified region and calculating the flow ratio. The volumes of discharging surplus soil in the two cases of the stirring wing of the NT and the stirring wing of the DRT were estimated, and the results were compared.

In addition, in order to compare the construction process of the improved body when the stirring wing of the NT is used and when the stirring wing of the DRT is used, the cross section during the analysis is cut out, and the behavior of the particles, assuming the cement slurry and the targeted soft ground, were visually evaluated. Specifically, the difference in the quality of the improved body due to the difference in the stirring wing, the effect of the stirring wing of the DRT on the improved body, and the distribution of the solidifying material were evaluated.

5. Analysis Results and Discussion

5.1. Visualization for Performance of Discharging Surplus Soil by Velocity Display

The conditions during the discharge of surplus soil in the RS-DMM construction were evaluated by the distribution of the moving velocity of the particles. Figure 7 shows the analysis cross section at the stage (at 70 s) when the penetration and stirring are completed and the static stirring is performed at the bottom. Focusing on the moving velocity of the particles around the rod in the figure (the area surrounded by the black rectangle), in the case of using the stirring wing of the NT, many particles with a moving velocity close to 0 m/s are distributed. On the other hand, in the case of using the stirring wing of the DRT, there are many particles with a moving velocity of 0.3 m/s or more. Due to the effect of the spiral rod attached to the stirring wing of the DRT, particles are forcibly moved upward, and the surplus soil is discharged. Therefore, construction using the stirring wing of the DRT in the RS-DMM is found to be effective for suppressing displacement.

5.2. Quantitative Evaluation of Discharge of Surplus Soil

In order to quantitatively evaluate the performance of the discharge of the surplus soil, the volume of the discharging surplus was estimated. The volume of the discharging surplus soil was estimated at the stage of static stirring at the bottom (40 s from 70 to 110 s) after the completion of the penetration and stirring.

The volume of the discharging surplus soil was calculated using the following equation, Equation (10), assuming the flow ratio of the particles that had passed through the cross section:

$$Q = A \cdot v \quad (10)$$

where Q is the unit volume, A is the cross-sectional area, and v is the moving velocity of the particles. Regarding the cross-sectional area, the cross-sectional area through which the particles pass was calculated by subtracting the cross-sectional area of the rod ($\phi = 440$ mm) from the cross-sectional area around the rod (500 mm \times 500 mm) and was set to 0.1 m². For the moving velocity of the particles, the average moving velocity of the particles around the rod (the area surrounded by the black rectangle), shown in Figure 7, was adopted. The average moving velocity of the particles was calculated every 0.1 s, and the unit volume

was calculated every 0.1 s in the same way to estimate the volume of discharging surplus soil for 40 s.

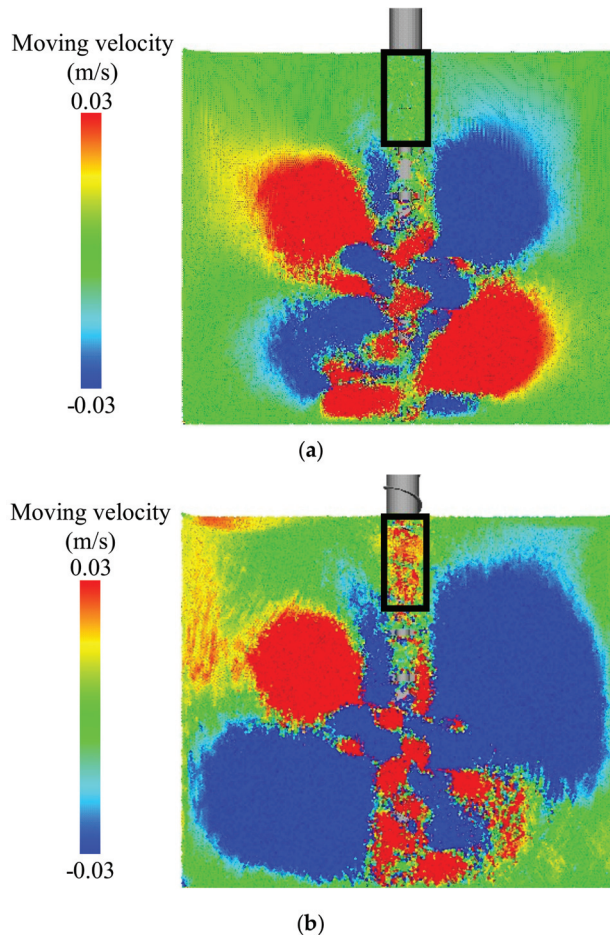


Figure 7. Analysis cross section (velocity component in Z-axis direction) at stage of static stirring at bottom: (a) Stirring wing of NT; (b) Stirring wing of DRT.

Table 3 shows the results of calculating the volume of discharging surplus soil. When the stirring wing of the NT was used, the average moving velocity of the particles was very slow, namely, 0.007 m/s. As a result, the total volume of discharging surplus soil over 40 s was 0.026 m³. It can be confirmed that the discharge of surplus soil is rarely performed. On the other hand, when using the stirring wing of the DRT, the average moving velocity of the particles was 0.152 m/s. More particles continued to be discharged when using the stirring wing of the DRT than when using that of the NT, namely, the total volume of discharging surplus soil was 0.609 m³ over 40 s. With the stirring wing of the DRT, about 23 times more surplus soil was discharged than with that of the NT. In this study, the volume of discharging surplus soil was calculated within a limited range and time, so it is possible that the value was smaller than the actual volume of discharging surplus soil. However, because there was a large difference in the volumes of the discharging surplus soil, even under these measurement conditions, it can be said that the stirring wing of the DRT provides an excellent performance in discharging surplus soil.

Table 3. Calculation results of volume of discharging surplus soil.

| | Average Moving Velocity for 40 s (m/s) | Total Volume of Discharging Surplus Soil for 40 s (m ³) |
|----------------------|---|--|
| Stirring wing of NT | 0.007 | 0.026 |
| Stirring wing of DRT | 0.152 | 0.609 |

5.3. Comparison of Improved Body due to Different Stirring Wing

The construction process and quality of the improved body constructed using the stirring wing of the NT and the improved body constructed using the stirring wing of the DRT are compared. Figures 8 and 9 show the analysis cross sections using the stirring wings of the NT and the DRT, respectively. The construction process is described every 20 s in order to compare the construction process of the improved body. It can be seen in these figures that there are no major differences in each construction process. In both cases, penetration and stirring are performed in a columnar shape while injecting the solidifying material at the beginning. After that, stirring is conducted so that the lower part swells from 60 to 100 s. This is thought to be due to the fact that static stirring is performed for 1 min at the bottom and that the surrounding ground is also stirred at the same time due to the viscosity of the ground. Then, from around 120 s, extraction and stirring are started while injecting the solidifying material again. As the solidifying material is injected from the lower part of the stirring wing, in accordance with the rotation of the stirring wing, there are some parts that do not exist in the cross-sectional display, but they are present in the columns as a whole. Therefore, it is unlikely that the quality will vary. In addition, the stirring wing is pulled out of the ground to the ground surface from 140 s to 160 s. At that time, the particles near the ground surface are stirred over a wider area than the particles per 1 m underground. Compared to the inside of the ground, the particles on the ground surface have a higher degree of freedom of movement, and it is thought that the range has expanded due to the large wavy effect.

From the above results, it is thought that the difference the in stirring wings does not affect the construction process of the improved body. However, construction using the stirring wing of the DRT can suppress the discharge of surplus soil and displacement while maintaining the quality of the improved body, but it exists near the ground surface due to the discharge of surplus soil. As the surplus soil contains solidifying material, it is necessary to dispose of it as industrial waste instead of disposing it as residual soil in the usual manner.

5.4. Depth Distribution of Injected Cement Slurry

In order to compare the distribution of injected cement slurry in the depth direction, the ground at the end of the analysis was divided into depths of 1 m, and the number of cement slurry particles existing in each range was measured. The results are shown in Figure 10. In both cases of the NT and DRT stirring wings, the number of particles present at a depth of 3 to 4 m was the largest, followed by 0 to 1 m, 2 to 3 m, 1 to 2 m, and 4 to 5 m. The reason why many cement slurry particles exist at the depths of 3 to 4 m and 0 to 1 m is considered to be that the operation of the stirring wing is changed (started/stopped). It is thought that this is because the cement slurry particles moved together with the soil particles pushed by the movement of the stirring wing, and the particles stayed due to the stoppage of the stirring wing. In addition, the number of cement slurry particles is extremely small at a depth of 4 to 5 m, but this result is inevitable because only the tip of the stirring wing can reach this region.

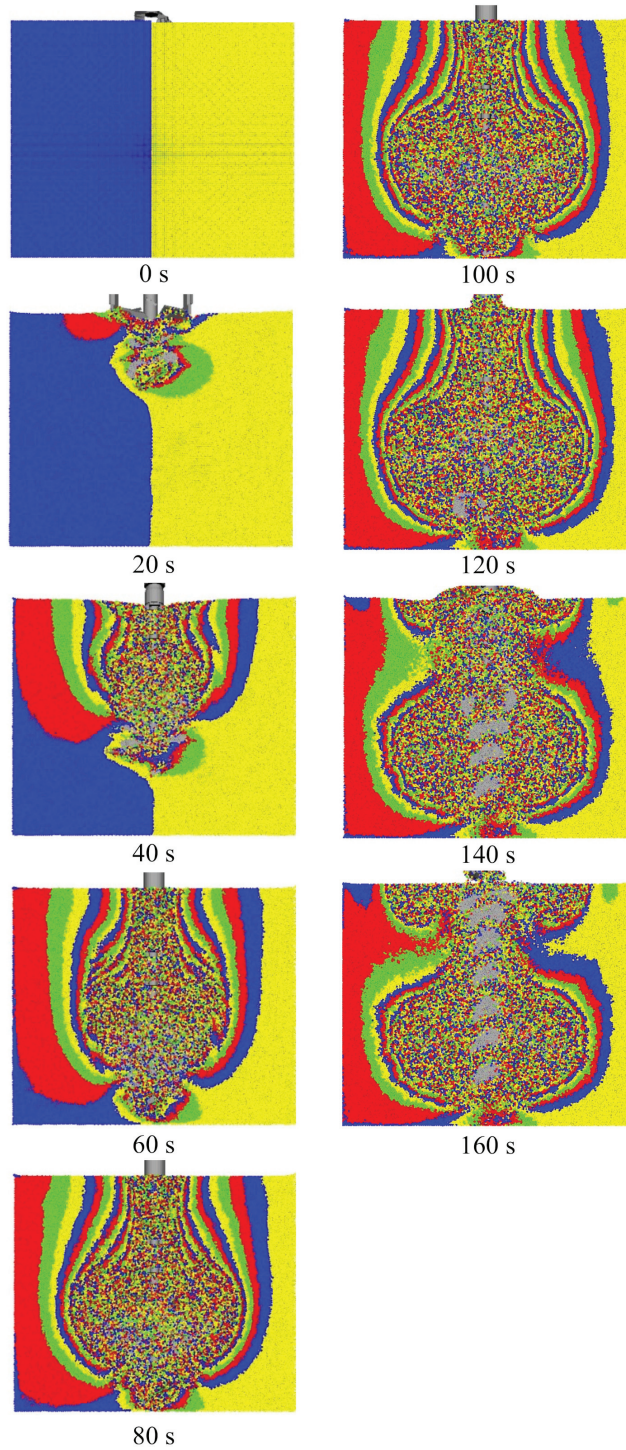


Figure 8. Analysis cross section of construction using stirring wing of NT.

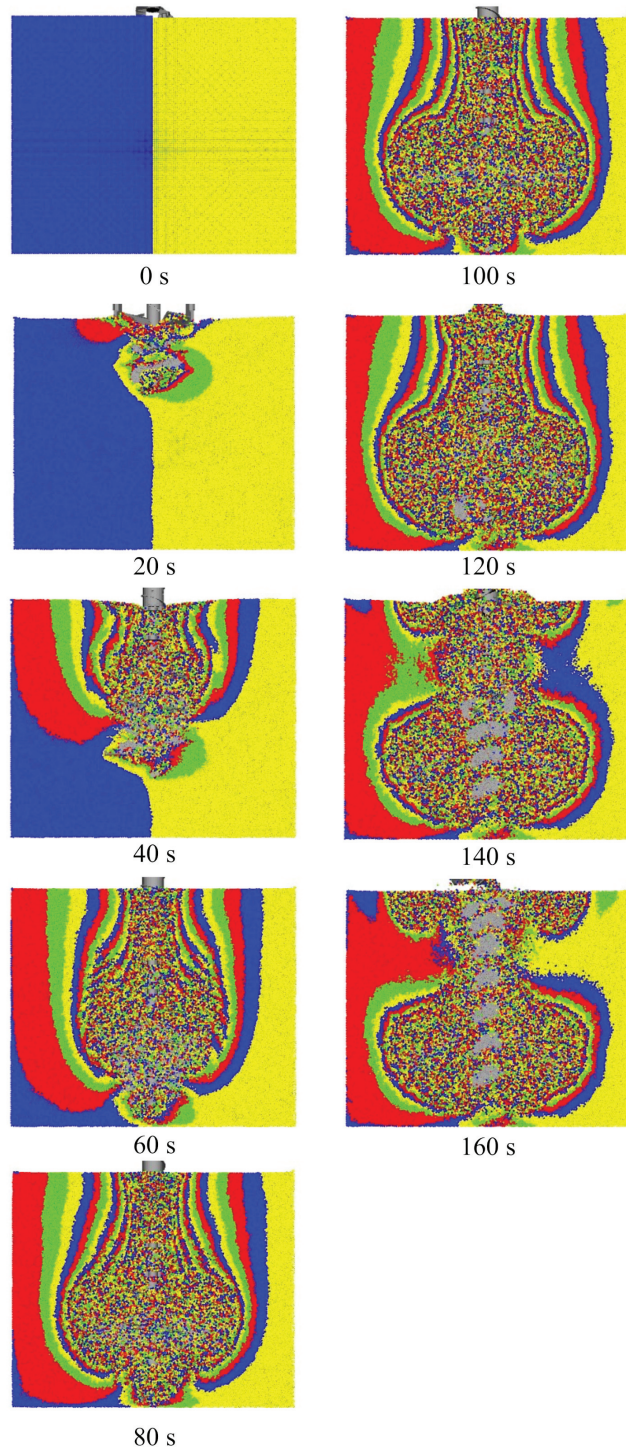


Figure 9. Analysis cross section of construction using stirring wing of DRT.

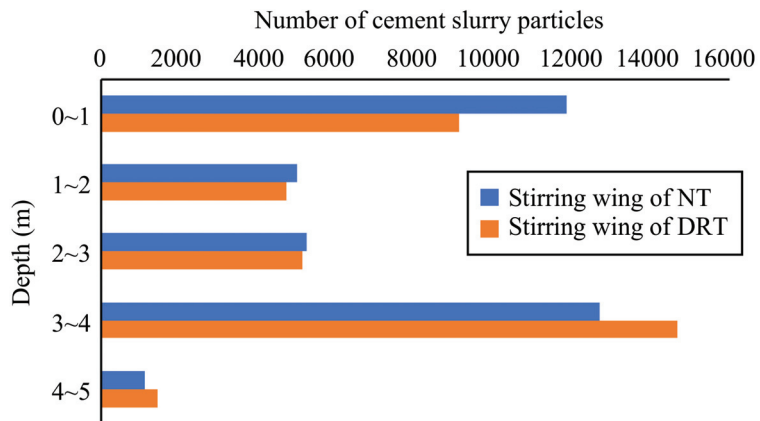


Figure 10. Depth distribution of injected cement slurry particles.

The big difference between the two cases was at the depths of 0 to 1 m and 3 to 4 m. At 0 to 1 m, the number of cement slurry particles increased in the case of the stirring wing of the NT, but at 3 to 4 m, the number of cement slurry particles increased. The reason for this is thought to be an increase in the pressure inside the ground due to the injection of the solidifying material. The cause of the displacement is an increase in pressure inside the ground due to the injection of the solidifying material, and the discharge of surplus soil is performed to release this pressure. In the NT, without the discharge of surplus soil, it is considered that many soil particles and cement slurry particles adhered to the stirring wing due to the increase in pressure and were carried to the ground surface at the same time as the stirring wing was being pulled out. On the other hand, in the DRT, it is considered that the amount of soil particles and cement slurry particles adhering to the stirring wing decreased due to the release of pressure.

The effect of the improved body on the strength characteristics cannot be evaluated by the MPS-CAE analysis used in this study; thus, other treatments, such as curing, are also required. However, it was confirmed that the presence or absence of discharged surplus soil may affect the distribution of the solidifying material. In the future, it will be necessary to clarify this point by conducting strength tests.

5.5. Applicability and Validity of Analysis in Real Fields

As the subject of this study, the displacement reduction performance of just one improved body was evaluated in this analysis. Therefore, it will be necessary to increase the number of improved bodies and bring them closer to the site construction. The targeted soft ground was expressed here as an aggregate of the same particles, but grounds are originally non-uniform and contain impurities, such as stones and dust. By bringing the ground model settings closer to those of the site ground, it will be possible to perform more practical simulations. The targeted soft ground was set as a columnar region in this study, but site grounds originally exist semi-permanently, and it will be necessary to consider the effects of earth pressure and groundwater in the future. In addition, the validity of these analysis results must be evaluated by conducting an indoor model experiment. When conducting a model experiment, it will be necessary to carry out the experiment under conditions and an environment that imitate those of the targeted soft ground in situ.

Considering the above points, an analysis and model experiment must be carried out in the future that can more closely reflect the conditions of the construction site.

6. Conclusions

In this study, the performance of a visible and measurable evaluation of the relative stirred deep mixing method was conducted using an MPS-CAE analysis. By visualizing the

case using the stirring wing of the NT and the case using the stirring wing of the DRT, the evaluation was performed by comparing the two cases. The results and findings obtained in this study are shown in the following.

- (1) It was possible to visually evaluate the discharge of surplus soil by the spiral rod attached to the stirring wing of the DRT.
- (2) It was quantitatively shown that more surplus soil was discharged when the stirring wing of the DRT was used than when the stirring wing of the NT was used.
- (3) No significant difference was found between the improved body using the stirring wing of the NT and the improved body using the stirring wing of the DRT. Therefore, it was confirmed that the construction could be executed without affecting the improved body even if the surplus soil was discharged.
- (4) Comparing the analysis results, it was found that the construction using the stirring wing of the DRT had a better displacement reduction effect than the stirring wing of the NT.
- (5) A simulation of the relative stirred deep mixing method using an MPS-CAE analysis was achieved. By changing the conditions, such as the ground and solidifying material parameters, the rotation speed of the stirring wing, the penetration speed, and the injection volume of the solidifying material, it was possible to perform simulations according to more construction conditions. The visualization of the ground improvement by an MPS-CAE analysis is thought to have contributed to an improvement in construction efficiency, quality, and economy, as well as the development of new research on construction technology and displacement. Thus, further studies will be required in the future.

Author Contributions: Conceptualization, S.I.; methodology, K.N., S.I. and T.T.; software, K.N. and S.I.; validation, S.T. and T.S.; formal analysis, K.N. and S.I.; investigation, T.T., S.T. and T.S.; resources, T.T., S.T. and T.S.; data curation, S.I. and T.S.; writing—original draft preparation, K.N. and S.I.; writing—review and editing, S.I.; visualization, S.I.; supervision, S.I.; project administration, S.I. All authors have read and agreed to the published version of the manuscript.

Funding: This research received no external funding.

Institutional Review Board Statement: Not applicable.

Informed Consent Statement: Not applicable.

Data Availability Statement: Data sharing is applicable to this article.

Conflicts of Interest: The authors declare no conflict of interest.

References

1. Ishihara, K.; Araki, K.; Toshiyuki, K. Liquefaction in Tokyo Bay and Kanto Regions in the 2011 Great East Japan Earthquake. *1755 Lisbon Earthq. Revisit.* **2013**, *28*, 93–140. [[CrossRef](#)]
2. Kazama, M.; Kawai, T.; Mori, T.; Kim, J.; Yamazaki, T. Subjects of the liquefaction research seen to the liquefaction damage of the great east japan earthquake disaster. *J. Jpn. Assoc. Earthq. Eng.* **2018**, *18*, 26–39. [[CrossRef](#)]
3. Yasuda, S.; Harada, K.; Ishikawa, K.; Kanemaru, Y. Characteristics of liquefaction in Tokyo Bay area by the 2011 Great East Japan Earthquake. *Soils Found.* **2012**, *52*, 793–810. [[CrossRef](#)]
4. Ma, B.; Cai, K.; Zeng, X.; Li, Z.; Hu, Z.; Chen, Q.; He, C.; Chen, B.; Huang, X. Experimental Study on Physical-Mechanical Properties of Expansive Soil Improved by Multiple Admixtures. *Adv. Civ. Eng.* **2021**, *2021*, 1–15. [[CrossRef](#)]
5. Ma, B.; Li, Z.; Cai, K.; Liu, M.; Zhao, M.; Chen, B.; Chen, Q.; Hu, Z. Pile-Soil Stress Ratio and Settlement of Composite Foundation Bidirectionally Reinforced by Piles and Geosynthetics under Embankment Load. *Adv. Civ. Eng.* **2021**, *2021*, 1–10. [[CrossRef](#)]
6. Adachi, Y.; Kizuki, T.; Tsuchiya, J.; Inazumi, S. Visualization of pile and ground improvement work by introducing ICT construction. *Geotech. Eng. J.* **2018**, *66*, 24–25.
7. Inazumi, S.; Adachi, Y.; Nguyen, H.S.; Takaue, T. Ground improvement work with N-value estimation by measurement of current value. *Innov. Infrastruct. Solut.* **2021**, *6*, 1–14. [[CrossRef](#)]
8. Nguyen, H.-S. Integration of information and communication technology (ict) into cement deep mixing method. *Int. J. GEOMATE* **2020**, *19*, 194–200. [[CrossRef](#)]
9. The Society of Materials Science Japan (JSMS). *DCS Method, 2nd Version*; Technical Evaluation Certificate, No. 1006; The Society of Materials Science Japan (JSMS): Kyoto, Japan, 2015.

10. Koshizuka, S.; Oka, Y. Moving-Particle Semi-Implicit Method for Fragmentation of Incompressible Fluid. *Nucl. Sci. Eng.* **1996**, *123*, 421–434. [[CrossRef](#)]
11. Yamanoi, M.; Kasahara, T. Basics of particle based CFD software, “Particleworks” and our approach into casting engineering. *J. Jpn Foundry Eng. Soc.* **2014**, *86*, 965–969.
12. Yokoi, T.; Okuno, R.; Ookori, K. Construction case of large diameter relative mixing method. *Found. Eng. Equip.* **2017**, *45*, 41–43.
13. Inazumi, S.; Jotisankasa, A.; Nakao, K.; Chaiprakaikeow, S. Performance of mechanical agitation type of ground-improvement by CAE system using 3-D DEM. *Results Eng.* **2020**, *6*, 100108. [[CrossRef](#)]
14. Gigwon, H. Experimental study on soft ground with DCM column. *J. Korean Geosynth. Soc.* **2020**, *19*, 35–44. [[CrossRef](#)]
15. Shen, S.-L.; Wang, Z.F.; Cheng, W.C. Estimation of lateral displacement induced by jet grouting in clayey soils. *Géotechnique* **2017**, *67*, 621–630. [[CrossRef](#)]
16. Adeli, H.; Kumar, S. *Distributed Computer-Aided Engineering for Analysis, Design, and Visualization*; CRC Press: Boca Raton, FL, USA, 2020.
17. Chang, K.H. *Product Design Modeling Using CAD/CAE: The Computer Aided Engineering Design Series*; Elsevier: Amsterdam, The Netherlands, 2014.
18. Inazumi, S.; Tanaka, S.; Komaki, T.; Kuwahara, S. Evaluation of effect of insertion of casing by rotation on existing piles. *Geotech. Res.* **2021**, *8*, 25–37. [[CrossRef](#)]
19. Pan, Z.; Wang, X.; Teng, R.; Cao, X. Computer-aided design-while-engineering technology in top-down modeling of mechanical product. *Comput. Ind.* **2016**, *75*, 151–161. [[CrossRef](#)]
20. Inazumi, S.; Kaneko, M.; Shigematsu, Y.; Shishido, K.-I. Fluidity evaluation of fluidisation treated soils based on the moving particle semi-implicit method. *Int. J. Geotech. Eng.* **2017**, *12*, 325–336. [[CrossRef](#)]
21. Inazumi, S. Mps-Cae simulation on dynamic interaction between steel casing and existing pile when pulling out existing piles. *Int. J. Geomate* **2020**, *18*, 68–73. [[CrossRef](#)]
22. Inazumi, S.; Kuwahara, S.; Ogura, T.; Hamada, S.; Nakao, K. Visualization and performance evaluation of existing pile pulling method with pile tip chucking by MPS-CAE. *Jiban Kogaku Janaru (Jpn. Geotech. J.)* **2020**, *15*, 383–393. [[CrossRef](#)]
23. Nakao, K.; Inazumi, S.; Takaue, T.; Tanaka, S.; Shinoi, T. Visual evaluation of relative deep mixing method type of ground-improvement method. *Results Eng.* **2021**, *10*, 100233. [[CrossRef](#)]
24. Sanyal, J.; Goldin, G.M.; Zhu, H.; Kee, R.J. A particle-based model for predicting the effective conductivities of composite electrodes. *J. Power Sources* **2010**, *195*, 6671–6679. [[CrossRef](#)]
25. Zhu, C.; Chen, Z.; Huang, Y. Coupled Moving Particle Simulation–Finite-Element Method Analysis of Fluid–Structure Interaction in Geodisasters. *Int. J. Géoméch.* **2021**, *21*, 04021081. [[CrossRef](#)]
26. Nohara, S.; Suenaga, H.; Nakamura, K. Large deformation simulations of geomaterials using moving particle semi-implicit method. *J. Rock Mech. Geotech. Eng.* **2018**, *10*, 1122–1132. [[CrossRef](#)]

Article

Study on the Effect of Regeneration Agent on the Viscosity Properties of Aged Asphalt

Jiangang Yang^{1,2}, Luhua Luo³, Jie Gao^{1,2,*}, Jing Xu^{1,2} and Chengping He⁴

¹ School of Civil Engineering and Architecture, East China Jiaotong University, Nanchang 330013, China; jekong@ecjtu.edu.cn (J.Y.); jingxu@ecjtu.edu.cn (J.X.)

² Institute of Road Engineering, East China Jiaotong University, Nanchang 330013, China

³ School of Transportation and Logistics, East China Jiaotong University, Nanchang 330013, China; luoluhua@163.com

⁴ Fujian Expressway Maintenance Engineering Co., Ltd., Fuzhou 350001, China; hechengping@163.com

* Correspondence: gaojie@ecjtu.edu.cn

Abstract: China's highway asphalt pavement has entered the stage of major repair, and improving the utilization rate of recycled asphalt pavement (RAP) is the main issue. The key link affecting the performance of recycled asphalt mixtures is the regeneration of aged asphalt, and the effect of the regenerant dosing on the high-temperature performance and viscosity of aged asphalt is the main content to be studied in this research. The aging behavior of asphalt seriously affects the roadworthiness of asphalt mixtures. In this study, we investigated the effect of changes in the microscopic properties of the aged asphalt on its viscosity properties during regeneration using gel permeation chromatography (GPC), Fourier-transform infrared spectroscopy (FTIR), and atomic force microscopy (AFM) as well as Brinell viscosity tests. This study simulated asphalt aging by the RTFOT test, and then we obtained an aged asphalt with a needle penetration of 30. We prepared different regenerated asphalts by adding regeneration agent with doses of 2%, 4%, and 6% to the aged asphalt. The results showed that the regeneration agent could effectively reduce the viscosity of the aged asphalt, which can play a positive role in improving the construction and ease of the aged asphalt. Rejuvenation agents affected the aging asphalt sulfoxide and carbon group indices. Moreover, rejuvenation agents can also significantly reduce the intensities of their characteristic functional group indices. The results of the AFM test showed that the increase in the dose of regeneration agent increased the number of the asphalt bee-like structures and decreased the area of individual bee-like structures. The results of the GPC test were consistent with the results of the AFM test, and the increase in the dose of regeneration agent reduced the asphalt macromolecule content. The viscosity properties and microstructure of the aged asphalt changed positively after the addition of the regeneration agent, indicating that the regeneration agent had a degrading and diluting effect on macromolecules.

Citation: Yang, J.; Luo, L.; Gao, J.; Xu, J.; He, C. Study on the Effect of Regeneration Agent on the Viscosity Properties of Aged Asphalt. *Materials* **2022**, *15*, 380. <https://doi.org/10.3390/ma15010380>

Academic Editor: Simon Hesp

Received: 26 November 2021

Accepted: 2 January 2022

Published: 5 January 2022

Publisher's Note: MDPI stays neutral with regard to jurisdictional claims in published maps and institutional affiliations.



Copyright: © 2022 by the authors. Licensee MDPI, Basel, Switzerland. This article is an open access article distributed under the terms and conditions of the Creative Commons Attribution (CC BY) license (<https://creativecommons.org/licenses/by/4.0/>).

Keywords: road engineering; viscosity properties; gel permeation chromatography; atomic force microscope; aged asphalt

1. Introduction

Asphalt pavements are subject to deterioration by light, heat, and oxygen during service, resulting in the deterioration of pavement performance [1,2]. The critical factor in the regeneration of asphalt pavements is the regeneration of aged asphalt. Springback agents are generally used to restore the performance of aged asphalt during the reuse of asphalt pavements. The literature shows [3] that the main types of regeneration agents include vegetable oils, waste-derived oils, engineering products, and various refinery base oils. Previous studies on asphalt regeneration have focused more on the effects of regeneration agents on asphalt and the macroscopic properties of asphalt mixtures [4]. Still,

in recent years, scholars at home and abroad have turned their attention to studying the mechanism of asphalt regeneration and have achieved specific results.

Huang et al. [5] explored the interaction between new asphalt, old asphalt, and regeneration agent by Fourier-transform infrared spectroscopy (FTIR) and gel permeation chromatography (GPC). Moreover, the results showed that the changes of the functional group index and the molecular weight distribution could explain the regeneration effect of the regeneration agent. The parameters of the sulfoxide index and the GPC of qFTIR can be used as reliable indicators to predict the macroscopic properties of asphalt. Lin et al. [6] studied the changes of the characteristic functional group content of asphalt before and after regeneration using FTIR. The results showed that the addition of the regeneration agent made the characteristic functional group content of regenerated asphalt decrease. Zhao et al. [7] studied regeneration agent changes on asphalt's relative molecular weight distribution using gel permeation chromatography. The results showed that the regeneration agent reduced the macromolecular content of the aged asphalt, which effectively reduced the viscosity of the asphalt. Cui et al. [8] used atomic force microscopy (AFM) tests to obtain Young's modulus (DMT) and adhesion indexes and explored the changes of regeneration agents on asphalt viscoelastic properties. From the study results, we can see that the DMT of the regenerated asphalt was reduced after the addition of the recycler. As a result, the viscoelastic properties were well recovered, and the adhesion properties of the asphalt-aggregate interface were enhanced. Li et al. [9] analyzed the effect of regeneration agents on the microstructure of aged asphalt using FTIR and AFM. The results showed that the regeneration agents made the absorption intensity of some specific functional groups decrease, enhanced the asphalt molecular motility and decreased the asphalt viscosity. He et al. [10] used infrared spectroscopy to explore the mechanism of reagents on SBS-modified asphalt. The results showed that a layer of interfacial film was formed between asphaltene and a soft pitch due to the addition of reagents, which further played a role in lubricating the asphalt, thereby reducing the viscosity of the aging asphalt. Yao [11] studied the mechanism of the effect of regeneration agents on aged asphalt, and the results showed that the regeneration agent could regulate the molecular weight distribution of the aged asphalt.

In summary, the current research on asphalt regeneration mainly focuses on the mechanism of asphalt regeneration and the prediction of post-regeneration performance, and fewer studies combined microscopic morphology and macroscopic performance on the change law of the viscosity performance of aged asphalt after regeneration. In this study, indoor simulated aging tests were conducted on the matrix asphalt, from which aged asphalt with a needle penetration of 30 was obtained, and the doses of a springback agent were 2%, 4%, and 6%. GPC, FTIR, and AFM tests, as well as activation energy, were used to analyze the changes of the relative molecular weight, chemical components, microstructure, and viscosity properties of asphalt before and after regeneration and to explore the change law of the microscopic properties of the regenerated asphalt and its influence on the viscosity properties.

2. Experimental Methods

2.1. Raw Materials

Asphalt's primary performance test results are shown in Table 1, and its main indexes met the specification requirements [12]. The test materials included 70# matrix asphalt and a regeneration agent. Figure 1 illustrates a sample of rejuvenators, and Table 2 describes specific technical properties.

Table 1. Basic properties of 70# base asphalt.

| Projects | Test Values |
|-----------------------------|-------------|
| Penetration (25 °C, 0.1 mm) | 60.4 |
| Softening point (°C) | 49.7 |
| Ductility (15 °C, cm) | >100 |
| Viscosity at 135 °C (Pa·s) | 0.475 |

**Figure 1.** Regeneration agent.**Table 2.** Basic properties of the regeneration agent.

| Physical Form | Density at 25 °C (g·cm ⁻³) | Specific Gravity | Flash Point (°C) |
|---------------|--|------------------|------------------|
| Brown liquid | 0.946 | 0.95 | 209 |

2.2. Test method

2.2.1. Aging Asphalt

The rotating film oven (RTFOT; Figure 2) was used to age the 70# matrix asphalt into the asphalt with a needle penetration (0.1 mm) of 30. The aging time required for the asphalt was determined by relating the aging time to the degree of aging [13], and the results are shown in Figure 3. One hundred and thirty-five minutes were the aging time required for the 70# matrix asphalt to meet the performance index of 30# asphalt after aging.

**Figure 2.** Rotating film oven.

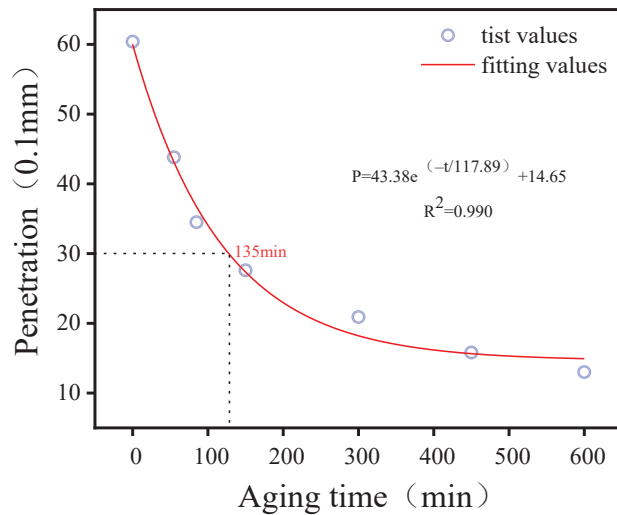


Figure 3. Needle penetration depths at different aging times in the RTFOT.

2.2.2. Asphalt Regeneration

The regeneration agent was similar to asphalt in chemical properties, and they had good compatibility. The aged asphalt was heated to the flowing state, and the regeneration agent with doses of 0%, 2%, 4%, and 6% were added and stirred for 30 min at 140 °C and 1000 rad/min using a high-speed shear to produce the regenerated asphalt. The preparation process referred to the literature [14]. For the convenience of presentation, the regenerated asphalts with the regeneration agent doping of 0%, 2%, 4%, and 6% was recorded as RA0, RA2, RA4, and RA6, respectively, and the 70# matrix asphalt was recorded as MA, as shown in Table 3.

Table 3. Sample descriptions.

| Specimen Number | Aged Asphalt Ratio (%) | Rejuvenation Agent Content (%) | Remarks |
|-----------------|------------------------|--------------------------------|---------------------|
| MA | 0 | 0 | Matrix asphalt |
| RA0 | 100 | 0 | Aging asphalt |
| RA2 | 100 | 2 | Regenerated asphalt |
| RA4 | 100 | 4 | Regenerated asphalt |
| RA6 | 100 | 6 | Regenerated asphalt |

2.2.3. Physical Properties Test

JTG E20-2011 “Highway Engineering Asphalt and Asphalt Mixture Experimental Procedure” [15] was used to determine the physical properties of the regenerated asphalt, including the softening point (T0606-2011), the ductility at 15 °C (T0605-2011), and needle penetration at 25 °C (T0604-2011).

2.2.4. Viscosity Test

A Brookfield viscometer with a temperature control device was selected to determine the viscosities of various asphalts. Due to the low viscosity of the target asphalt, we measured the viscosities of 120 °C, 135 °C, and 150 °C at 20 rad/min according to T0625-2011. To further analyze the change of the asphalt viscosity, we chose activation energy to analyze the change of the viscosity of the regenerated asphalt. Activation energy is the minimum energy required for molecules to reach the activation molecule to do work [16]. Activation

energy can reflect the difficulty of the asphalt material to reach the flow state; the lower the activation energy, the better the construction and ease. The Arrhenius equation was described as:

$$\ln \eta = \frac{E_{\eta}}{RT} + \ln A \quad (1)$$

where η is the viscosity of asphalt (Pa·s); T is the absolute temperature (K); A is a constant; E_{η} is the activation energy of asphalt when it undergoes change ($\text{kJ}\cdot\text{mol}^{-1}$); R is the universal gas constant with a magnitude of $8.314 \text{ J}\cdot\text{mol}^{-1} \text{ K}^{-1}$. The study used the Brinell viscosity to derive the activation energy of the regenerated asphalt, which was utilized to analyze the construction and ease of regenerated asphalt [17].

2.2.5. GPC Test

An Agilent PL-GPC220 gel permeation chromatography was used to dissolve the asphalt specimens in a tetrahydrofuran (THF) solvent to form a solution at a specific concentration, with a specimen volume of $100 \mu\text{L}$ and a flow rate of $1 \text{ mL}\cdot\text{mL}^{-1}$. The column used to separate the asphalt specimens was maintained at $35 \text{ }^{\circ}\text{C}$. The molecular weight and molecular weight size distribution of the asphalt were determined experimentally. Figure 4 shows the principle of GPC. In the GPC test, the separation mode was not based on the molecular weight, but molecules' apparent size and molecular aggregation in a specific solution. After the asphalt sample was adequately dissolved, it was introduced into a group of columns through the injection mechanism as a molecular filtration system. The chromatographic column was filled with a cross-linked gel containing surface pores, which were different in size and played the role of molecular filters. Therefore, larger-size molecules (LMSs) were not able to enter smaller pores, and smaller molecules (MMSs) fit most pores and remained for a longer time.

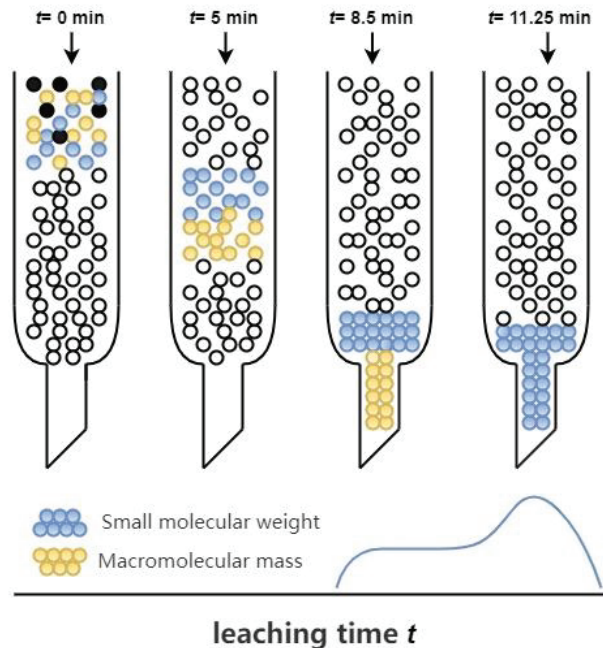


Figure 4. Gel permeation chromatography (GPC) schematic diagram.

GPC research results can show the differences of asphalt in molecular size distribution. In other words, GPC provided the “fingerprint” of each asphalt and provided a reasonable explanation for the changes of its macro-properties in combination with the knowledge

of the relative molecular weight of asphalt components. Equations (2) and (3) show the formulae for the calculation of M_n (number average molecular weight) and M_w (heavy average molecular weight), respectively [18]:

$$M_n = \frac{\sum H_i}{\sum (H_i/M_i)}, \quad (2)$$

$$M_w = \frac{\sum M_i H_i}{\sum H_i}, \quad (3)$$

where H_i is the peak height, M_i is the molecular weight, M_n is the number average molecular weight, and M_w is the heavy average molecular weight.

2.2.6. FTIR Spectroscopy Test

FTIR can be used to detect chemical functional groups in solids, gases, and liquids. Many researchers have now used FTIR spectroscopy to characterize the aging and regeneration behavior of asphalt and the content of polymers [19]. In this study, a Breaker Alpha FTIR spectrometer with a spectral acquisition range of 500–4000 cm^{-1} was used to determine the functional groups of each asphalt specimen. OMNIC software was used for the baseline correction and smoothing of the IR curves to evaluate the regenerative effect of the regenerator on the aging asphalt with the use of the characteristic functional group (C=O and S=O) indices and the equation method [20] to calculate the sulfoxide group index (IS=O) and the carbonyl group index (IC=O) with the equations as in Equations (4) and (5):

$$I_{S=O} = \frac{A_{1032}}{A_{2923} + A_{2852}}, \quad (4)$$

$$I_{C=O} = \frac{A_{1700}}{A_{2923} + A_{2852}}. \quad (5)$$

2.2.7. AFM Test

A Bruker Dimension Icon AFM was used to observe the surface morphologies of the asphalt specimens to obtain the asphalt morphology map. The test was performed in the tap mode with a scanning area of 20 $\mu\text{m} \times 20 \mu\text{m}$. Figure 5 shows the schematic diagram of the AFM working principle. Figure 6 shows the asphalt AFM specimens, and the asphalt specimens were hot-cast. Firstly, the asphalt was heated to the flowing state, and then, a small amount of asphalt was dropped on the center of a slide and heated to make it flow freely on the slide. Finally, it was tested after natural cooling.

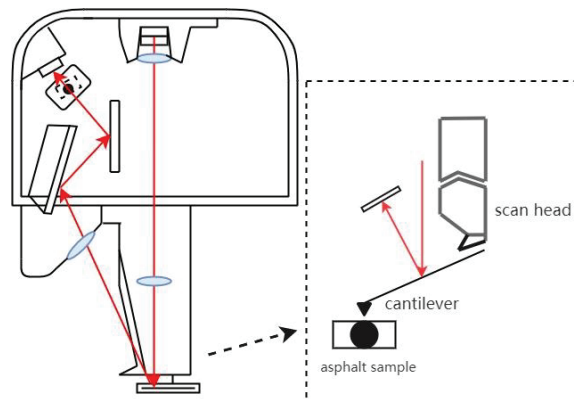


Figure 5. Schematic diagram of the atomic force microscopy (AFM) working principle.

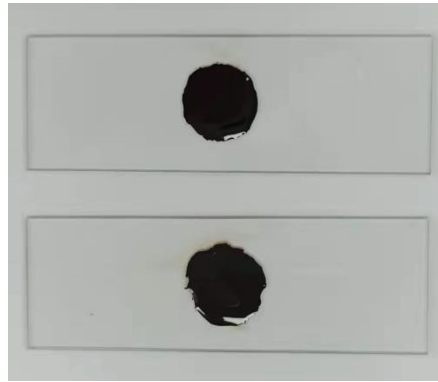


Figure 6. AFM specimens.

R_q and R_a could characterize the roughness in the asphalt microscopic appearance and were described as Equations (6) and (7), respectively [21]:

$$R_q = \sqrt{\frac{\sum_{i=1}^N Z_i^2}{N}}, \quad (6)$$

$$R_a = \frac{1}{N} \sum_{j=1}^N |Z_j|, \quad (7)$$

where R_q is the average root mean square of the planar adhesion deviation, R_a is the arithmetic mean of the absolute values of the adhesion deviation measured in the average plane, and Z_i denotes the corresponding adhesion deviation. In order to further quantitatively investigate the microscopic property change of the regenerated asphalt, in this paper, the AFM morphological images were pre-processed and quantitatively calculated. Figure 7 shows the image processing and calculation process.

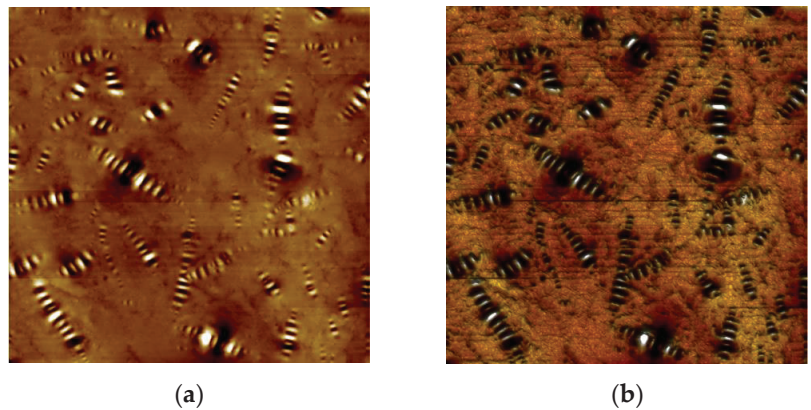


Figure 7. Cont.

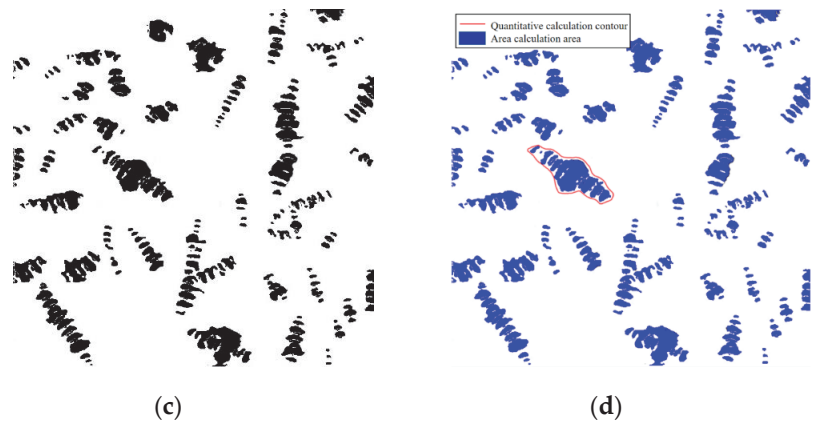


Figure 7. Quantitative analysis process of the asphalt micromorphological map processing: (a) original morphology; (b) pre-processing; (c) identification; (d) calculation.

3. Analysis of Test Results

3.1. Analysis of Physical Properties Test Results

As shown in Figure 8, the performance of the regenerated asphalt improved with the increase of the regenerator dose during the aging asphalt regeneration process. The needle penetration and the ductility increased significantly. In contrast, the softening point showed a decreasing trend. When the regenerator dose was 6%, the indicators of RA6 and MA tended to be close to each other, which indicated that the three primary indicators of the regenerated asphalt met the technical requirements of 70# base asphalt.

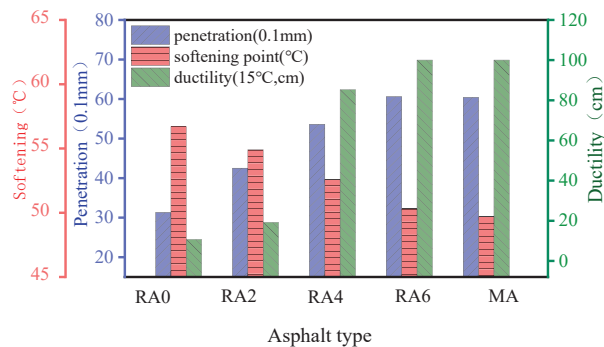


Figure 8. Physical properties of the regenerated asphalt at different doses.

3.2. Viscosity and Activation Energy Analysis

The asphalt viscosity was closely related to the construction and ease. As seen in Figure 9, the asphalt viscosity tended to decrease, as the dosage of the regenerator increased. The viscosities difference between RA6 and MA was slight, indicating that the viscosity of the regenerated asphalt with a dose of 6% was close to the base asphalt. It indicated that the regenerator had the effect of reducing the viscosity of aging asphalt. The viscosity activation energy reflected the energy required for the regenerated asphalt to reach the flow state, in order to characterize the construction and ease of the regenerated asphalt. The smaller the viscosity activation energy, the better the construction and ease. Figure 10 shows that the viscosity activation energy of asphalt increased after aging. In addition, the activation energy of RA2, RA4, and RA6 decreased by 1.1%, 3.2%, and 4.6%, respectively,

compared with that of RA0, indicating that the regeneration agent can reduce the viscosity of the aged asphalt and improve the construction. In addition, the activation energy of the viscosity of aged asphalt was similar to that of the base asphalt, when the dose of the rejuvenator was 6%.

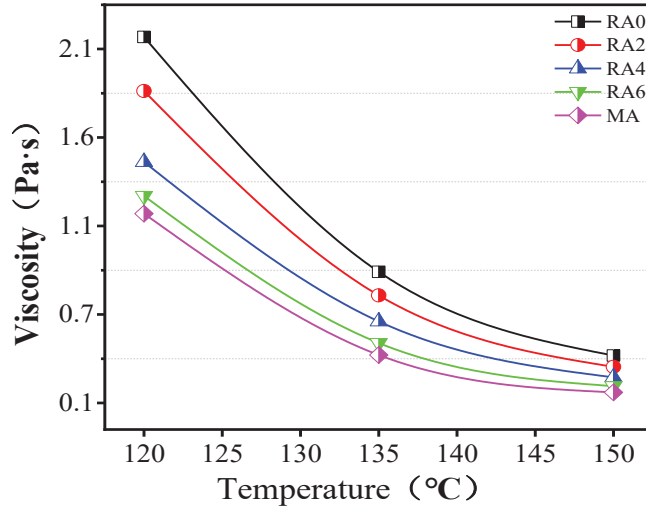


Figure 9. Viscosities of different asphalts.

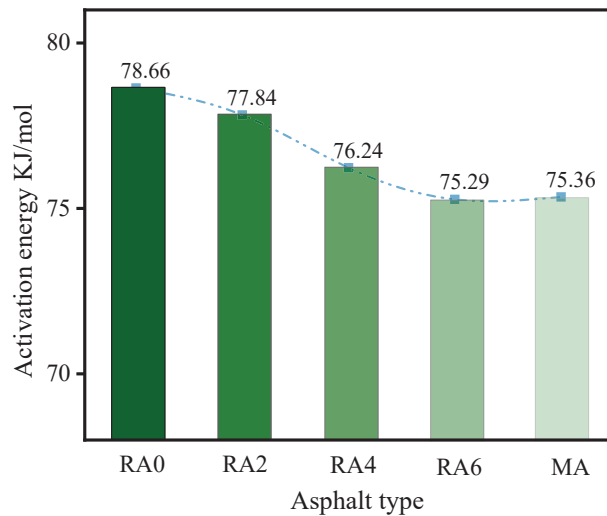


Figure 10. Activation energies of different asphalt viscosities.

3.3. Analysis of GPC Test Results

3.3.1. Molecular Weight and Polydispersity

GPC provided valuable data about molecular weight distribution. Table 4 gives the GPC parameters of each asphalt specimen, including M_n (number average molecular weight), M_w (heavy average molecular weight), and polydispersity coefficient ($PD = M_w/M_n$). Generally, the larger the polydispersity index is, the wider the molecular weight distribution is. In addition, polydispersity represents the degree of component migration [22]. As shown in Table 4, the M_n value decreased with the increasing dose of the rejuvenator, which means

that the asphalt formed smaller molecules through physical or chemical reactions during the regeneration process. By observing changes in the M_w and PD values of various asphalts, we can see that the M_w and PD of RA6 were lower than those of other asphalts, indicating that the regeneration agent led to lower M_w and PD values and had a degrading and diluting effect on the aged asphalt macromolecules.

Table 4. GPC parameters of different asphalt specimens.

| Asphalt Type | M_n (g·mol ⁻¹) | M_w (g·mol ⁻¹) | PD |
|--------------|------------------------------|------------------------------|------|
| MA | 593 | 1600 | 2.69 |
| RA0 | 595 | 1895 | 3.18 |
| RA2 | 569 | 2009 | 3.53 |
| RA4 | 563 | 2060 | 3.65 |
| RA6 | 522 | 1694 | 3.24 |

3.3.2. Molecular Weight Distribution

Figure 11 shows the relative molecular mass (M_n) distribution structure of the 70# matrix asphalt and the regenerated asphalt. The horizontal coordinate is the logarithm of the heavy average molecular weight, and the vertical coordinate is the relative content of asphalt. From Figure 11, we can see that the molecular weight of asphalt was mainly in the range of 10^2 – 10^4 and the molecular weight distribution of asphalt after aging showed a shoulder peak in the range of $10^{3.5}$ – $10^{4.5}$. The relative content increased, which indicated that the aging of asphalt promoted the increase of the macromolecular content. At the same time, the macromolecular content of asphalt decreased after the addition of the regeneration agent. The shoulder in the range of $10^{3.5}$ – $10^{4.5}$ slowly became slower with the increase of the regeneration agent dose. The correlation study concluded a correlation between the molecular weight size of asphalt and asphalt properties. The more the macromolecular size in asphalt, the worse the asphalt performance [23]. The results of Jenning [23] and Kim [24] averaged the GPC data into 13 intervals with a sizeable molecular size (LMSs; intervals 1–5), a medium molecular size (MMSs; intervals 6–9), and a small molecular size (SMSs; intervals 10–13). Figure 11 shows the molecular size distributions of the asphalt specimens. As seen in Figure 12, the increase in the rejuvenation agent admixture and the regenerated asphalt exhibited higher MMSs and reduced LMSs. This is consistent with the GPC results, where adding a rejuvenation agent resulted in lower M_w and PD values. The LMSs of asphalt showed a better correlation with the asphalt properties than other dimensions [23]. Therefore, the study on the regeneration agent effect focused on LMSs, showing that LMSs significantly decreased when the regeneration agent dose was 6%, which coincided with the lower M_w and PD values found in the GPC test. It indicated that the regenerating agent could significantly reduce the asphalt macromolecular size. Although rejuvenation agents could replenish the components lost by asphalt due to aging, it was not easy to rebalance the distribution of regulated molecules. The GPC test results showed that the rejuvenator could reduce the size of large and medium molecules and increase the size of small molecules; the rejuvenator had the effect of decomposing the large and medium molecules in asphalt. At the same time, the proportion of heavy components in the asphalt was reduced, and the proportion of light components was increased after the incorporation of regenerants. This inevitably weakened the high temperature performance and the Brinell viscosity of the aged asphalt. However, whether the ratio of each component in the recycled asphalt is the same as that of the original asphalt needs further study and analysis.

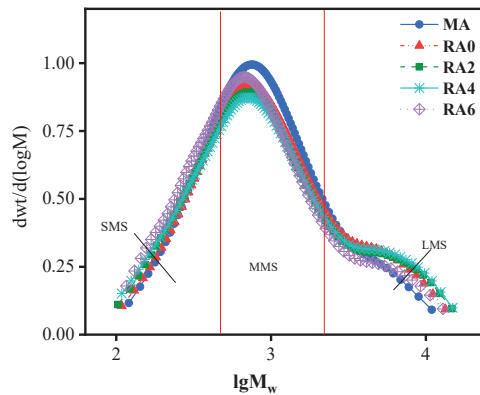


Figure 11. Chromatograms of the original asphalt and the regenerated asphalt.

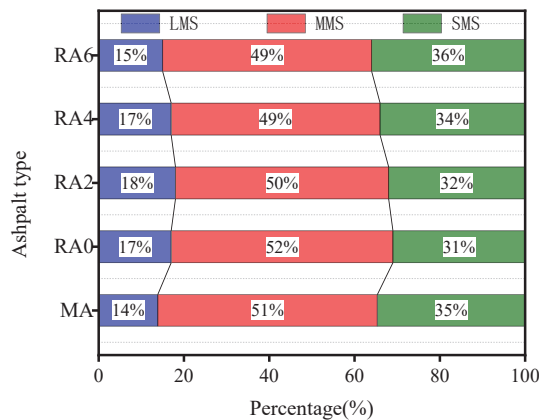


Figure 12. Molecular size distributions of the asphalt specimens.

3.4. FTIR Analysis

Figure 13 shows the infrared spectra of the asphalts in the wavenumber range of 4000 cm^{-1} to 500 cm^{-1} . As shown from Figure 13, the infrared spectrum of the aged asphalt after the addition of the regenerating agent remained the same as that of the aged asphalt, and no apparent new absorption peaks appeared; the difference lied in the change of the transmittance size. The spectral difference between the aged asphalt and the regenerated asphalt was related to the functional group index. The functional groups that changed in the IR spectra were located at 1700 cm^{-1} and 1032 cm^{-1} , representing the absorption peaks of carbonyl (C=O) and sulfoxide (S=O), respectively. Figure 14 shows the carbonyl and sulfoxide group indices for each asphalt specimen. We can see from Figure 14 that the sulfoxide index did not change significantly when the regeneration agent dose increased. When the regeneration agent dose was 2%, the carbonyl index also did not change. However, when the regeneration agent dose was 6%, the carbonyl index of the regenerated asphalt decreased by 50% compared with the aged asphalt, and the carbonyl functional group transmission rate of the regenerated asphalt increased significantly. The index of the carbonyl group showed a decreasing trend, when the doses of rejuvenator were 4% and 6%; it showed that the dose of rejuvenator that was greater than the dose of 2% was beneficial to reduce the content of heavy components in asphalts, so as to achieve the purpose of reducing the viscosity of the aged asphalt.

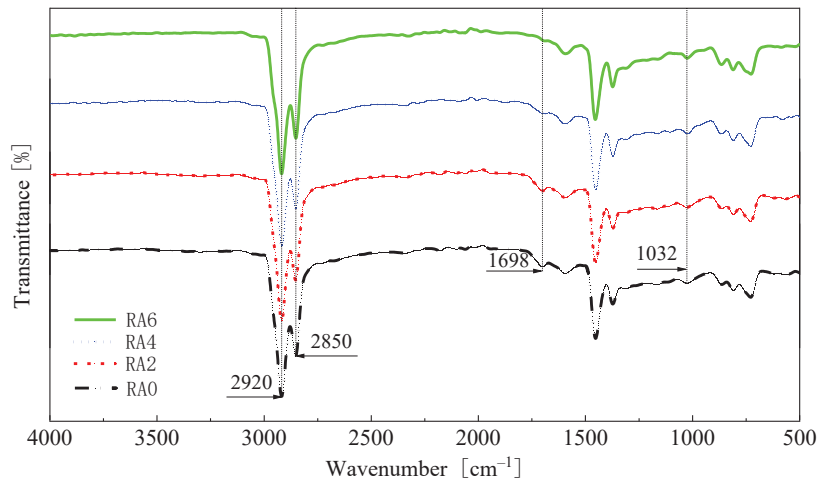


Figure 13. Infrared spectra of the asphalts.

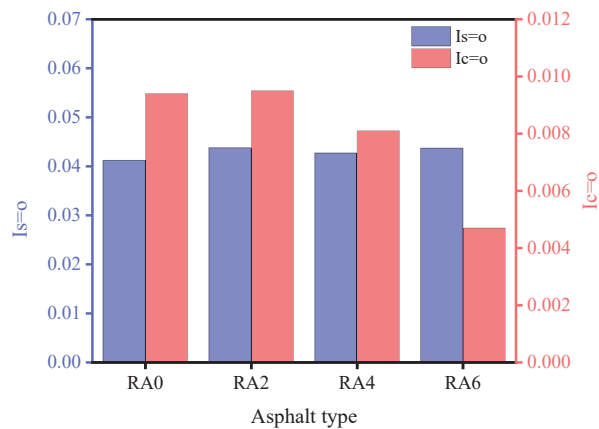


Figure 14. Sulfinyl and carbonyl index diagrams.

3.5. AFM Analysis

Figure 15 shows the two-dimensional and three-dimensional morphology maps of the matrix asphalt. As seen in Figure 15, the microscopic surface of the asphalt was widely distributed with a bee-like structure, which was called a “bee-like structure” in the current study [25]. The colors in the asphalt morphology diagram only represent the height of the microscopic morphology and do not represent the actual color of the asphalt sample. A bee-like structure in the matrix asphalt was randomly selected using NanoScope analysis software to extract its height profile information. As shown in Figure 16, the height of this bee-like structure had a “wavy” shape along the horizontal axis. The peaks correspond to lighter areas of the morphology, while the valleys correspond to the darker areas of the morphology. Numerous studies have shown that the bee-like structures on the microscopic surface of asphalt are wax crystals formed by the eutectic of wax molecules and long-chain alkyl groups of polar macromolecules, and the molecular motility of asphalt significantly affects its aggregation state [26–28].

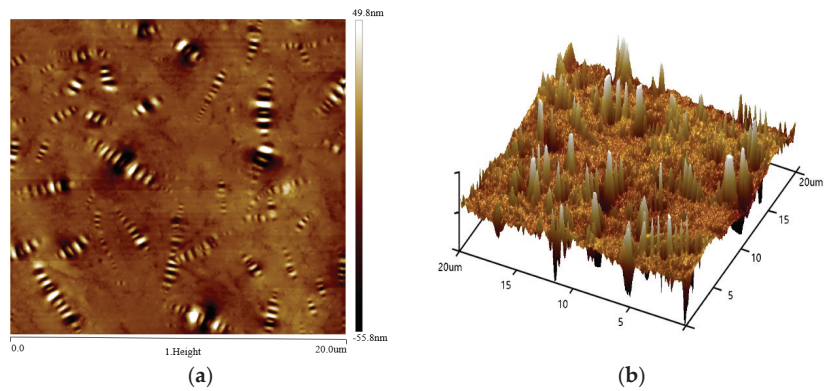


Figure 15. Two-dimensional (a) and three-dimensional (b) maps of the substrate asphalt morphology.

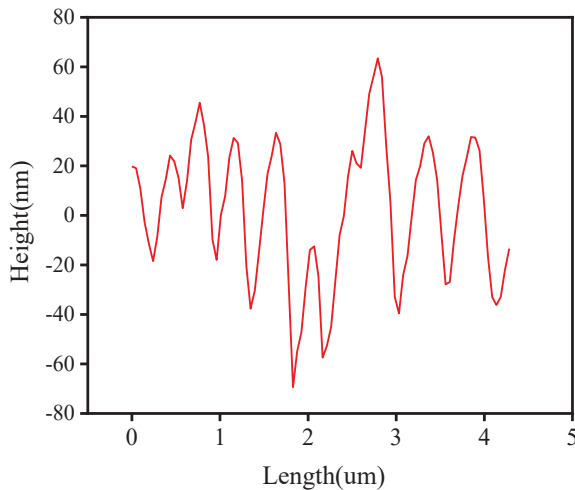


Figure 16. Bee-type structure cross-section.

Figure 17 shows the 2D morphologies of the different asphalts. We can see that all asphalts showed a bee-like structure. There was no essential difference between the microstructures of the matrix asphalt, aged asphalt, and regenerated asphalt; the main difference was the size and number of the bee-like structures. The aged asphalt had a smaller number of bee-like structures and a larger size compared to the matrix asphalt. The addition of the regenerating agent increased the number of bee-like structures and decreased the size of bee-like structures, which was an improvement compared to those of the aged asphalt. The presence of macromolecules was the main reason for the formation of bee-like structures. The addition of regenerating agent regulated the asphalt components and reduced the content of macromolecules in the aged asphalt, which is consistent with the results of GPC analysis. Table 5 and Figure 16 show the number of bee-like structures, the area of individual bee-like structures, and the roughness parameters.

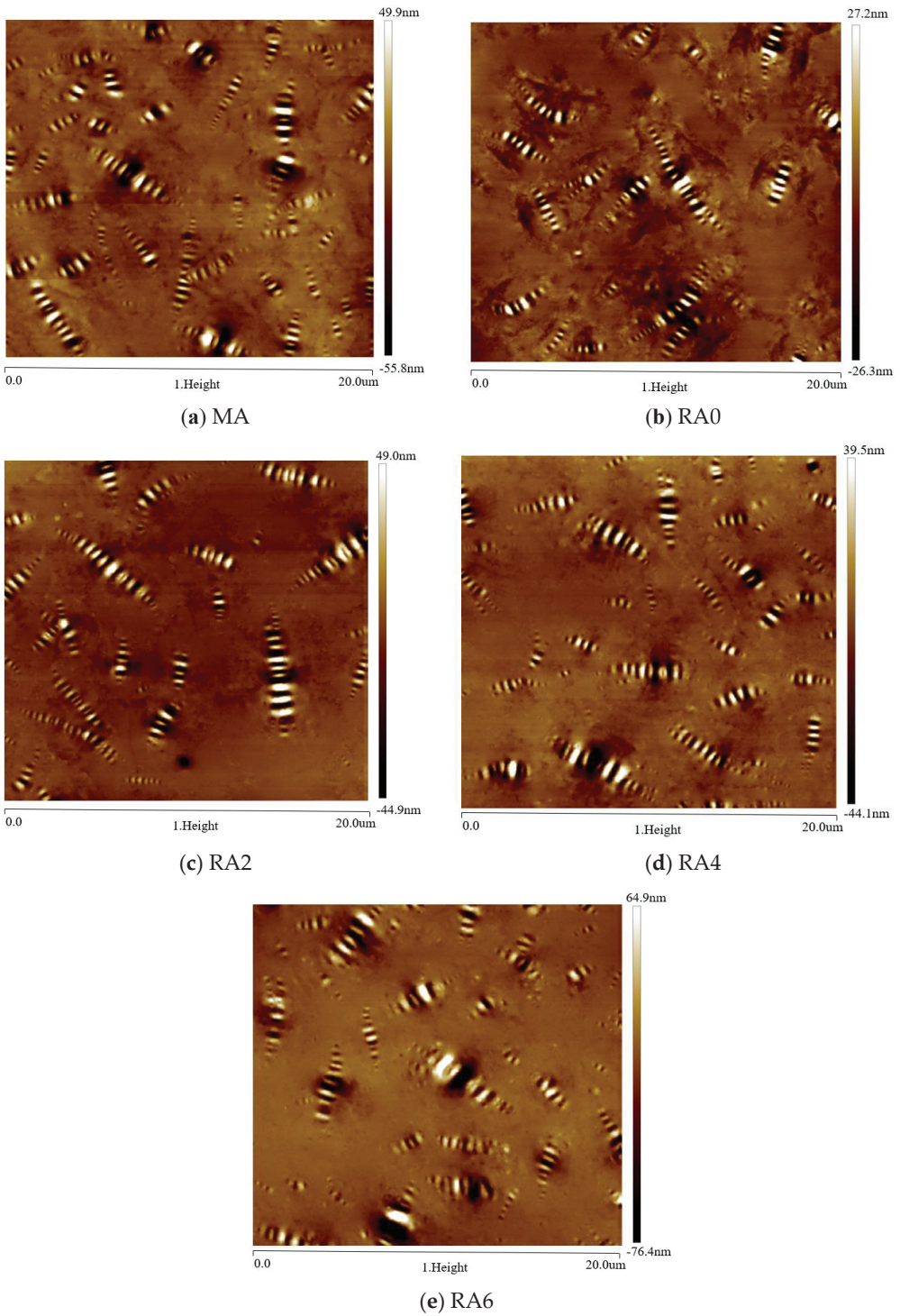
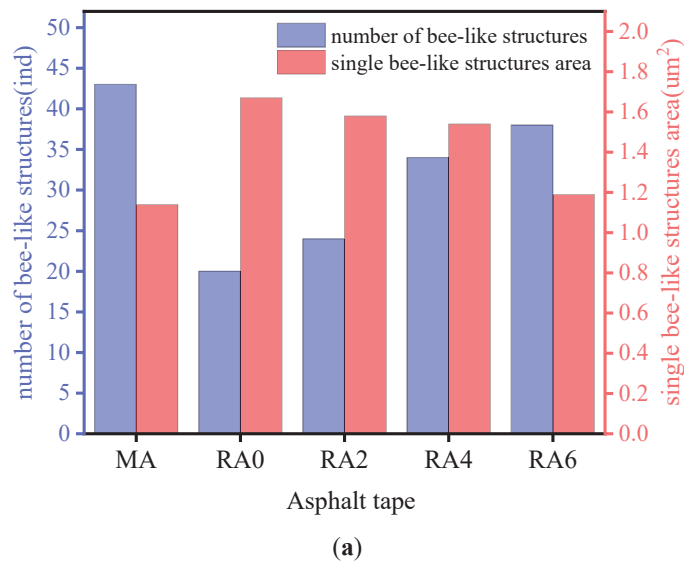


Figure 17. AFM morphologies of different asphalts.

Table 5. Results of parameters for different asphalts.

| Parameters | MA | RA0 | RA2 | RA4 | RA6 |
|---------------------------------|-------|------|------|-------|-------|
| N (number) | 43 | 21 | 27 | 35 | 38 |
| Single area (μm^2) | 1.14 | 1.57 | 1.40 | 1.39 | 1.18 |
| R_q (nm) | 10.60 | 5.59 | 9.28 | 10.36 | 14.30 |
| R_a (nm) | 6.36 | 3.39 | 5.44 | 7.00 | 7.89 |

As seen in Figure 18, the number of bee-like structures of the matrix asphalt decreased by 50% after short-term aging. The number of bee-like structures increased with the dose of the revertant. The aging process increased the area of the individual bee-like structures of the matrix asphalt. The area of the individual bee-like structures of the asphalt decreased after the addition of the rejuvenation agent. The more the dose of the rejuvenation agent, the more the area of the individual bee-like structures of the asphalt decreased. The asphalt surface roughness R_q and R_a increased gradually with the increase of the rejuvenation agent dose. The results showed that aging led to the increased asphaltene content, providing a crystalline core for wax molecules, which helped reduce the number of bee-like structures and increase their area. The addition of a regenerating agent had a degrading and diluting effect on the internal macromolecules of the asphalt, thus reducing the viscosity of the asphalt. Consistent with the results of the GPC and FTIR tests described above, the rejuvenator helped to reduce the proportion of heavy components in the aged asphalt and to convert the heavy components to light components by physical or chemical action, thus reducing the asphalt viscosity and softening the aged asphalt. The microscopic level analysis of the rejuvenation agent can improve the construction and ease of the aged asphalt.

**Figure 18.** Cont.

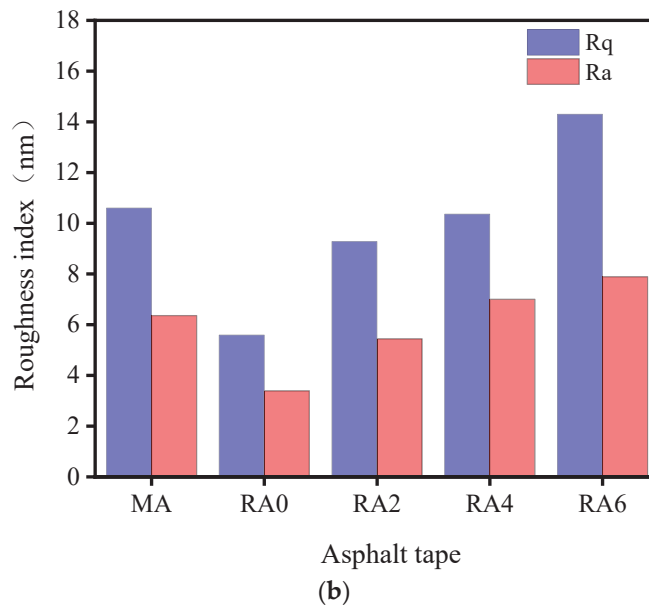


Figure 18. Variations of different asphalt parameters. (a) Trends of different asphalt bee-like structure indicators. (b) Trends of different asphalt roughness indices.

4. Conclusions

The significance of this study was to analyze the effect of the recycler dosing on the high-temperature performance and viscosity of recycled asphalt at the macroscopic and microscopic levels, to provide a scientific basis for the dosing of the recycled asphalt pavement, the mixing temperature of the recycled asphalt mixture, and the recycler dosing, to maximize the reuse rate of recycled asphalt pavement and to optimize the overall performance of the recycled asphalt mixture. In this paper, the changes of the relative molecular weight, the chemical composition, the microstructure, and the viscosity properties of asphalt before and after regeneration were analyzed by GPC, FTIR, AFM tests, and the asphalt activation energy. This paper also explored the microscopic change mechanism of the regenerated asphalt. The following main conclusions were obtained in this paper.

1. The addition of a regenerating agent significantly improved the flexibility and viscosity of aged asphalt but harmed the softening point. The regenerating agent could effectively reduce the viscosity of the aged asphalt, positively improving the construction and ease of the aging asphalt.
2. The FTIR results showed that the regenerating agent did not chemically react with the asphalt to produce new substances and the regenerating agent with a dose of 6% could significantly adjust the ratio of asphalt components. The regenerating agent could affect the contents of the sulfoxide group and carbon group in the regeneration process of aging asphalt and reduce the strength of its functional group index.
3. The GPC and AFM results showed that the content of macromolecules and the area of individual bee-like structures decreased with the rejuvenation agent dose. In addition, the number of bee-like structures on the microscopic surface of asphalt increased with the rejuvenation agent. We can also see that the rejuvenation agent had a degrading and diluting effect on the aging asphalt macromolecules, leading to a decreased asphalt viscosity.

Author Contributions: Conceptualization, J.G. and J.Y.; methodology, J.X.; investigation, C.H. and L.L.; writing—original draft preparation, L.L.; writing—review and editing, J.G.; funding acquisition, J.G. and J.Y. All authors have read and agreed to the published version of the manuscript.

Funding: Natural Science Foundation of Jiangxi Province (Grant No. 20202BABL214046); Youth fund of Jiangxi Provincial Department of Education (Grant No. GJJ190361); Central University Basic Scientific Research Fund (Grant No. 300102210501); Key R & D projects of Xinjiang Uygur Autonomous Region (Grant No. 2021B01005).

Institutional Review Board Statement: Not applicable.

Informed Consent Statement: Not applicable.

Data Availability Statement: The experimental and modeling data used to support the findings of this study are available from the corresponding author upon request.

Conflicts of Interest: The authors declare no conflict of interest.

References

- Geng, J.G. Study on the Aging Mechanism and Recycling Technique of Asphalt. Master's Thesis, ChangAn University, Xi'an, China, 2009.
- Chen, H.X.; Chen, S.F.; Wang, B.G. The aging behavior and mechanism of base asphalts. *J. Shandong Univ.* **2009**, *39*, 125–130.
- Moghaddam, T.B.; Baaj, H. The use of rejuvenating agents in production of regenerated hot mix asphalt: A systematic review. *Constr. Build. Mater.* **2016**, *114*, 805–816. [[CrossRef](#)]
- Idham, M.K.; Hainin, M.R.; Warid, M.N.M.; Raman, N.A.A.; Mamat, R. Evaluation on the performance of aged asphalt binder and mixture under various aging methods. *J. Teknol.* **2015**, *77*. [[CrossRef](#)]
- Huang, W.; Guo, Y.; Zheng, Y.; Ding, Q.; Sun, C.; Yu, J.; Zhu, M.; Yu, H. Chemical and rheological characteristics of rejuvenated bitumen with typical regeneration agents. *Constr. Build. Mater.* **2021**, *273*, 121525. [[CrossRef](#)]
- Lin, M.; Li, P.; Nian, T.; Wei, X. Effect of microstructure of regenerated asphalt on rheological properties. *J. Huazhong Univ. Sci. Technol.* **2019**, *47*, 121–126.
- Zhao, K.; Wang, Y.; Chen, Y.; Huang, K. Effect of Regeneration agents on Relative Molecular Mass and Size Distribution of Asphalt Binders. *J. Build. Mater.* **2020**, *23*, 1130–1136.
- Cui, Y.; Cui, S.; Guo, L. Research on Performance and Mechanism of Regenerated SBS Modified Asphalt. *J. Build. Mater.* **2021**, 1–13.
- Li, X.; Wei, D.; Yao, Z.; Li, B. Effect of Regeneration agents on Rheological Properties and Microstructure of Aged Asphalt. *J. Build. Mater.* **2018**, *21*, 992–999.
- He, Z.; Ran, L.; Cao, Q. Mechanism Study of Recycle of SBS Modified Asphalt Based on Spectrum Analysis. *J. Build. Mater.* **2015**, *18*, 900–904.
- Yao, Z. *Study on Microscopic Mechanism Action of Regeneration Agent and Aged Asphalt*; Lanzhou Jiaotong University: Lanzhou, China, 2018.
- Research Institute of Highway Ministry of Transport. *Technical Specification for Construction of Highway Asphalt Pavements*; JTG F40-201; Research Institute of Highway Ministry of Transport: Beijing, China, 2004.
- Ying, X. *Research on Warm-Mixed Recycling Mechanism and Pavement Performance of Regenerated Asphalt Mixture*; Harbin Institute of Technology: Harbin, China, 2017.
- Wu, X. *Study on Performance of Warm Regenerated SBS Modified Asphalt Mixture*; South China University of Technology: Guangzhou, China, 2019.
- Research Institute of Highway Ministry of Transport. *Standard Test Methods of Bitumen and Bituminous Mixture for Highway Engineering*; JTG E20-2011; Research Institute of Highway Ministry of Transport: Beijing, China, 2011. Available online: <https://www.chinesestandard.net/PDF/English.aspx/JTGE20-2011> (accessed on 1 January 2022).
- Zhang, J. *Investigation on Aging Properties of Bio-Rejuvenated Asphalt Binded*; Southeast University: Nanjing, China, 2018.
- Ren, W. Study on Rheological Properties of Regenerated Asphalt with Biological Regenerator. *J. Highway Transp. Technol.* **2020**, *16*, 70–75.
- Yang, Z. *Study on Multi-Scale Behavioral Characteristics of Asphalt before and after Aging*; South China University of Technology: Guangzhou, China, 2018.
- Yu, H.; Leng, Z.; Zhang, Z.; Li, D.; Zhang, J. Selective absorption of swelling rubber in hot and warm asphalt binder fractions. *Constr. Build. Mater.* **2020**, *238*, 117727. [[CrossRef](#)]
- Zhang, B. *Characterization of Bitumen Structure Based on Fourier Transform Infrared*; Wuhan University of Technology: Wuhan, China, 2014.
- Ding, L.; Wang, X.; Zhang, M.; Chen, Z.; Meng, J.; Shao, X. Morphology and properties changes of virgin and aged asphalt after fusion. *Constr. Build. Mater.* **2021**, *291*, 123284. [[CrossRef](#)]

22. Ye, W.; Jiang, W.; Li, P.; Yuan, D.; Shan, J.; Xiao, J. Analysis of mechanism and time-temperature equivalent effects of asphalt binder in short-term aging. *Constr. Build. Mater.* **2019**, *215*, 823–838. [[CrossRef](#)]
23. Jennings, P.; Pribanic, P.; Campbell, W.; Dawson, K.; Shane, S.; Taylor, R. *High Pressure Liquid Chromatography as a Method of Measuring Asphalt Composition*; Federal Highway Administration: Washington, DC, USA, 1980.
24. Kwang, W.K. Methodology for Defining LMS Portion in Asphalt Chromatogram. *J. Mater. Civ. Eng.* **1995**, *7*, 31–40.
25. Tan, Y.; Li, G.; Shan, L.; Lv, H. Research progress of bitumen microstructures and components. *J. Transp. Eng.* **2020**, *20*, 1–17.
26. Nciri, N.; Cho, N. A Thorough Study on the Molecular Weight Distribution in Natural Asphalts by Gel Permeation Chromatography (GPC): The Case of Trinidad Lake Asphalt and Asphalt Ridge Bitumen. *Mater. Today: Proc.* **2018**, *5*, 23656–23663. [[CrossRef](#)]
27. Zhang, H.; Wang, Y.; Yu, T.; Liu, Z. Microstructural characteristics of differently aged asphalt samples based on atomic force microscopy (AFM). *Constr. Build. Mater.* **2020**, *255*, 119388. [[CrossRef](#)]
28. Xu, M.; Yi, J.; Pei, Z.; Feng, D.; Huang, Y.; Yang, Y. Generation and evolution mechanisms of pavement asphalt aging based on variations in surface structure and micromechanical characteristics with AFM. *Mater. Today Commun.* **2017**, *12*, 106–118.

Article

Corn Cob Ash versus Sunflower Stalk Ash, Two Sustainable Raw Materials in an Analysis of Their Effects on the Concrete Properties

Adrian Alexandru Șerbănoiu ¹, Cătălina Mihaela Grădinaru ^{1,*}, Radu Muntean ², Nicanor Cimpoșu ³ and Bogdan Vasile Șerbănoiu ⁴

- ¹ Faculty of Civil Engineering and Building Services, “Gheorghe Asachi” Technical University of Iași, 700050 Iași, Romania; serbanoiu.adrian@tuiasi.ro
- ² Faculty of Civil Engineering, Transilvania University of Brașov, 500152 Brașov, Romania; radu.m@unitbv.ro
- ³ Faculty of Material Science and Engineering, “Gheorghe Asachi” Technical University of Iași, 700050 Iași, Romania; nicanor.cimposu@academic.tuiasi.ro
- ⁴ Faculty of Architecture “G.M. Cantacuzino”, “Gheorghe Asachi” Technical University of Iași, 700050 Iași, Romania; bogdan-vasile.serbanoiu@academic.tuiasi.ro
- * Correspondence: catalina.gradinaru@tuiasi.ro

Abstract: The increased CO₂ emissions determined by the cement industry led to continuous and intensive research on the discovery of sustainable raw materials with cementitious properties. One such raw material category is agricultural waste. This study involved research on the effects of corn cob ash and sunflower stalk ash, respectively, on compressive strength measured after 28 days and 3 months, the flexural and splitting tensile strengths, the resistance to repeated freeze–thaw cycles, and on the resistance to chemical attack of hydrochloric acid of the concrete. A 2.5% and 5% replacement of the cement volume with corn cob ash (CCA) of A and B quality was applied, and with sunflower stalk ash (SSA) at A and B quality, respectively. The obtained results revealed that CCA and SSA decreased the compressive and tensile strength, but led to higher resistance of the concrete on repeated freeze–thaw cycles and to hydrochloric acid. The mixes with 2.5% SSA at A quality obtained the best results regarding splitting the tensile strength and resistance to repeated freeze–thaw cycles, the mixes with 2.5% SSA at B quality led to the highest resistance to hydrochloric acid, and those with 2.5% CCA at A quality led to the best values of compressive strength and flexural tensile strength.

Citation: Șerbănoiu, A.A.; Grădinaru, C.M.; Muntean, R.; Cimpoșu, N.; Șerbănoiu, B.V. Corn Cob Ash versus Sunflower Stalk Ash, Two Sustainable Raw Materials in an Analysis of Their Effects on the Concrete Properties. *Materials* **2022**, *15*, 868. <https://doi.org/10.3390/ma15030868>

Academic Editors: Carlos Morón Fernández and Daniel Ferrández Vega

Received: 20 December 2021

Accepted: 18 January 2022

Published: 24 January 2022

Publisher’s Note: MDPI stays neutral with regard to jurisdictional claims in published maps and institutional affiliations.



Copyright: © 2022 by the authors. Licensee MDPI, Basel, Switzerland. This article is an open access article distributed under the terms and conditions of the Creative Commons Attribution (CC BY) license (<https://creativecommons.org/licenses/by/4.0/>).

Keywords: agro-waste; eco-friendly material; sustainable building materials; ecological concrete

1. Introduction

The world’s cement production has been estimated to around 4.1 billion metric tons [1]; it emitted around 2.3 gigatons of CO₂ in 2019, this value being around 7% of total CO₂ emissions [2], and it is expected to reach 4.83 billion metric tons in 2030 [3]. A solution for decreasing the CO₂ emissions determined by the cement industry is its replacement by supplementary cementitious materials (SCMs). These SCMs can contribute to reduce the environmental impact and costs related to the cement and concrete industry, since they need less process heating and emit smaller CO₂ levels [4], enhance sustainability, and improve some of the concrete’s properties [5]. The SCMs category includes, among many others, the vegetal ashes obtained from the burning of different plants. A few examples of such vegetal ashes that were studied as SCMs in concrete composition are: rice husk ash [6–8], sugarcane bagasse ash [9,10], corn cobs [5,11,12], wheat [13,14], and many others. Previous studies showed that lignocellulosic ash containing significant rates of silica and alumina can develop pozzolanic activity in the presence of calcium hydroxide, leading to improved properties of concrete [15,16]. Maize and sunflower, important crops that have an annual

global cultivated area of around 178×10^6 ha [17], and 26.03×10^6 ha [18], respectively, represent significant and widely spread sources of lignocellulosic materials. Maize crops are cultivated mainly in China, USA, South Africa, and Eastern Europe, whereas sunflower crops are grown in southern South America, Southern Europe, South Africa, and South and European Russia [19].

Corn cob ash is a SCM studied quite intensively lately, as it has proven pozzolanic properties in various studies that have been conducted on the use of corn cobs as a cement partial replacement in concrete, but the results have been mixed. Adesanya, 1996 [20], and Binici et al., 2008 [21], showed that corn cob ash (CCA) determined less water absorption and improved resistance to sulfate attack. The studies led by Adesanya, 1996 [20], Adesanya and Raheem, 2009 [12], Kamau et al., 2017 [22], and Memon and Khan, 2018 [23], concluded that CCA determined a significant decrease in concrete compressive strength. Adesanya and Raheem, 2009 [12], found that CCA decreases the concrete slump, whereas Kamau et al., 2016 [5], found that it increases it. In 2012, Olafusi and Olutoge [24] studied the strength characteristics of corn cob ash concrete and concluded that the concrete did not reach its design strength after 28 days, and this depends on the pozzolanic activity of the corn cob ash. From the results of the various tests carried out by Mujedu et al., 2014 [25], it can be concluded that the combination of corn cob ash (CCA) and sawdust ash (SDA) is a suitable material for pozzolana, because it has a combination of more than 70% ($\text{SiO}_2 + \text{Al}_2\text{O}_3 + \text{Fe}_2\text{O}_3$) to meet the requirements of this material. The compressive strength of concrete increases with curing time and decreases as the percentage combination of CCA and SDA increases up to 10% of ordinary Portland cement in concrete to obtain the greatest strength gain. Although the strength of CCA-SDA concrete is lower than that used as reference, it can still be used for general concrete projects where strength is not important, such as floors, mortars, and mass concrete [25]. According to Ahangba and Tiza, 2016 [26], when 10% CCA is used instead of cement, the cement setting time increases from 258 min to 277 min). Substitution beyond this range will reduce the strength of concrete and cannot be controlled. This kind of substitution can also be used in building walls and beam units to reduce the use of cement and its high cost. Analyzing the research of Owolabi et al., 2015 [27], it can be pointed out that the workability of fresh corn cob ash concrete decreases with the increases in corn cob ash content, its compressive strength of concrete decreases with increasing CCA replacement rate, but increases with increasing age of cure, and to obtain the best compressive strength of the concrete, it is recommended to replace 5% of the cement with corn cob ash. The studies developed on CCA concrete focused mainly on the mechanical properties of fresh and hardened material, and on the resistance to sulphate attack. Fewer studies were conducted on the hydration process and chloride resistance of this type of concrete. Shakouri et al., 2020 [28], studied the effects of CCA as a cement replacement between 3% and 20% in concrete, and they found that it negatively affects the cement hydration and decreases the compressive strength and the chloride ion permeability of the concrete. The durability of CCA concrete to chloride corrosion represents an important problem that can reduce infrastructure service life worldwide [28].

Sunflower stalk ash (SSA) is a SCM much less studied than CCA, to our knowledge. Aksoğan et al. (2016) [14] studied the compressive strength, abrasive resistance, and linear absorption coefficient of concrete made with barite, colemanite, and SSA as a cement replacement and they found that the optimum replacement rate was 2.5% of SSA. A higher rate of 5% of SSA increased the concrete resistance to 5% sodium sulfate solution during an 180 days test. They also found that SSA improved the concrete behavior during the freeze–thaw process [14]. Darweesh (2020) [29] studied the physical, chemical, and mechanical properties of cement pastes with SSA, and found that SSA increases the compressive strength, the CSH amount, and decreases the free lime content, and that 24 wt% was the optimum rate of cement replacement with SSA, with higher rates as 30 wt% having negative effects on the cement paste properties.

The aim of this study was to study the effects of corn cob ash and sunflower stalk ash obtained by two methods on the mechanical and some durability properties of the

normal concrete. The study novelty consists of the comparative analysis of these two types of vegetal ashes, since to our knowledge very few studies were carried out on concrete with sunflower stalks, and we did not find any with which to compare directly their performances. For obtaining the CCA and SSA, the same methods were applied in order to have a clear view of the differences given by the two plants. The research implied the development of eight mixes with 2.5 vol.% and 5 vol.% cement replacement with CCA at A and B quality, and with SSA at A and B quality. The objective was to obtain a type of concrete with comparable performance to ordinary concrete, but adapted to the new requirements of cost, energy efficiency, and sustainability. The tests performed included compressive strength at 28 days and 3 months, flexural tensile strength, splitting tensile strength, and the resistance to the action of repeated freeze–thaw cycles and to the action of hydrochloric acid.

2. Materials and Methods

2.1. Materials

The vegetal materials used in this research were: ash from corn cobs of quality A and quality B, and ash from sunflower stalks of quality A and quality B. The developed and analyzed compositions were as follows:

- A reference composition of micro concrete, RC, with cement, sand and river gravel aggregates up to 8 mm in diameter, with a water/cement ratio of 0.5;
- Eight concrete compositions with vegetal ash developed on the basis of RC:
 - With corn cob ash of A quality, as 2.5% and 5% replacement of cement volume (CCA1A, CCA2A),
 - With corn cob ash of B quality, as 2.5% and 5% replacement of cement volume (CCA1B, CCA2B),
 - With sunflower stalk ash of A quality, as 2.5% and 5% replacement of cement volume (SSA1A, SSA2A),
 - With sunflower stalks ash of B quality, as 2.5% and 5% replacement of cement volume (SSA1B, SSA2B).

The reference composition, RC, of 30/37 strength class, was realized for river gravel (sort 4–8 mm), sand (sort 0–4mm), cement Portland CEM II/A-LL42.5R type (notations according to EN 197-1:2011) [30] (HeidelbergCement Romania, Bucharest, Romania), super-plasticizer additive based on polycarboxylateter (2% of binder), and water, according to NE 012/1-2007 [31].

2.2. Methods

2.2.1. Vegetal Ash Preparation

Sunflower stalks (SS) were broken manually into pieces of around 0.5 m in length, and corn cobs (CC) were mechanically shredded with a mill for grinding animal feed in granules smaller than 6 mm in diameter. SS and CC were free burned in a brick kiln, after they were left to dry in outside natural conditions of the environment. The burning temperature was not controlled; it was measured, and it achieved around 700 °C in the case of SS case and 570 °C in the case of CC.

The raw ash obtained after free burning was sifted for 5 min through sieves of 20 mm, 10 mm, 2 mm, and 300 µm, using an automatic sieving equipment (Endocotts Powermatic Test Sieve Shaker). The 300 µm sieve was chosen as Bahuradeen et al., 2015 [10], stated that the pozzolanic properties of ash can be improved if the particles are smaller than this dimension.

The sieved ash was then ground for 120 min in a ball dust crusher to obtain even smaller dimensions of the ash particles. The ground ash (Figure 1) was noted as A quality ash and it was used as cement partial replacement in CCA1A, CCA2A, SSA1A, and SSA2A concrete mixes.



Figure 1. The SSA of A and B quality and CCA of A and B quality, compared with the cement aspect.

The vegetal material that did not pass through the 300 μm sieve was subjected to supplementary thermal treatment at around 550 $^{\circ}\text{C}$ for 120 min. After this treatment, the vegetal material was sieved again through 20 mm, 10 mm, 2 mm, and 300 μm sieves for 5 min, with the same sieving equipment, and then ground for 120 min in the ball dust crusher. This ground ash (Figure 1) was noted as B quality ash and it was used as cement partial replacement in CCA1B, CCA2B, SSA1B, and SSA2B concrete mixes.

The ashes' bulk density and specific gravity are presented in Table 1.

Table 1. The bulk density and specific gravity of CCA and SSA.

| Ash Type | Bulk Density (g/L) | Specific Gravity (N/m^3) |
|------------------|--------------------|-------------------------------------|
| CCA of A quality | 725 | 2.102 |
| CCA of B quality | 699 | 2.027 |
| SSA of A quality | 805 | 2.334 |
| SSA of B quality | 799 | 2.317 |

2.2.2. Sunflower Stalk Ash Analysis

CCA and SSA were analyzed using Scanning Electron Microscopy (SEM, Vega Tescan LMH II, SE detector, 30 kV, Tescan Orsay Holding, Brno—Kohoutovice, Czech Republic) coupled with Energy Dispersive X-Ray Spectrometer detector (EDS, Bruker XFlash 6I30, Automatic mode, Bruker, Billerica, MA, USA) from composition and aspect point of view.

2.2.3. Composite Mixes Preparation

In this study, concrete with 2.5 vol.% and 5.0 vol.% corn cob ash and sunflower stalk ash, of two qualities each, as a cement substitute were developed. The 9 mixes were prepared according to NE 012/1-2007 [31]. A portable electric concrete mixer was used for fresh mixes preparation. The concrete specimens were unmolded after 24 h from pouring

in molds, and cured in ambient conditions for 28 days. The ambient conditions were: temperature of 20 ± 3 °C, and relative humidity of $55 \pm 10\%$.

2.2.4. Concrete Specimens Properties

Composition Analysis

The chemical elements and aspect of the developed concretes were analyzed through Scanning Electron Microscopy (SEM, VegaTescan LMH II, SE detector, 30 kV) coupled with Energy Dispersive X-Ray Spectrometer detector (EDS, Bruker XFlash 6I30, Automatic mode). A low vacuum mode was necessary to analyze the samples due to the fact that all samples gassed quite hard. Cubes samples (1 cm³ volume) were mechanically cut and used for analyses.

Mechanical and Durability Properties Analysis

In Table 2, the essential elements for the applied methods in performing tests are presented regarding the compressive strength, flexural tensile strength, splitting tensile strength, resistance to repeated freeze–thaw cycles, and resistance to hydrochloric acid action.



Figure 2. Resistance to the action of hydrochloric acid: (a) Specimens immersed in 18% HCl solution; (b) Specimens' aspect after 10 days of immersion in 18% HCl solution.

Table 2. Mechanical and durability test details.

| Test | Specimens' Type | Specimens' Dimensions | Specimens Number Tested for Each Mix | Standard Applied |
|--|-----------------|---|--------------------------------------|---|
| Compressive strength | Cylinder | 100 mm diameter 200 mm length | 3 | EN 12390-3: 2019 [32] |
| Flexural tensile strength | Prism | 100 × 100 mm ² transversal section 550 mm length | 3 | EN 12390-5: 2019 [33] |
| Splitting tensile strength | Cylinder | 100 mm diameter 200 mm length | 3 | EN 12390-6: 2010 [34] |
| Resistance to freeze–thaw | Cube | sides of 100 mm | 6 | SR 3518: 2009 [35] EN 12390-3: 2019 [32] |
| Resistance to hydrochloric acid action | Cube | sides of 50 mm | 3 | Figure 2 |

The specimens were prepared by casting in metal molds: cylinders with 100 mm diameter and 200 mm length, prisms of 100 × 100 × 550 mm, cubes with sides of 100 mm and 50 mm. The tests were performed at 28 days. In all tests, 3 specimens were used for each mixture and each test, according to the standards mentioned in Table 2, and the average value was calculated. Only for the freeze–thaw resistance test were six specimens used for

each mix, as three specimens were the control samples, not subjected to the freeze–thaw cycles, and three specimens were subjected to the action of the freeze–thaw process.

Resistance to Repeated Freeze–Thaw Cycles

For the freeze–thaw test, cube specimens with sides of 100 mm were used, according to the SR 3518:2009 [35] standard. Before the start of the 50 freeze–thaw cycles, 6 specimens for each composition were immersed in water. The water had a temperature of 20 ± 5 °C. The immersion was prepared gradually, the water level being raised every 24 h, first up to $\frac{1}{4}$ of their height, then up to $\frac{1}{2}$, then up to $\frac{3}{4}$, and finally to the total immersion. After the water immersion, three of the six specimens were kept in a water bath, whereas the other three were tested in 50 freeze–thaw cycles. During the freeze–thaw cycle of 8 h, for the first 4 h, the specimens were frozen in a cold room at the temperature of -17 ± 2 °C, and then for next 4 h, they were introduced in water with a temperature of 20 ± 5 °C.

After 50 cycles, the specimens subjected to freeze–thaw and those kept only in water were tested for compressive strength, in accordance with EN 12390-3:2019 [32] stipulations. The evaluation was conducted through the difference between the average compressive strength of the three specimens kept in water and the average compressive strength of the three specimens tested in 50 freeze–thaw cycles.

Resistance to Chemical Attack of Hydrochloric Acid (HCl)

Three cubes with side of 50 mm were used for each mix in performing the test for resistance to chemical attack of hydrochloric acid. The cubes were first dried in an oven at 90 °C until constant mass was reached, and then they were weighed. Afterwards, they were introduced in a HCl solution of 18% concentration (Figure 2a) for 10 days. This concentration level has been chosen in order to perform the test in a shorten period and to subject the mixes to an aggressive action of this acid. After a period of 10 days, the cubes were washed with clean water and brushed for the removal all loose particles (Figure 2b) and dried out in the oven at 90 °C till the constant mass was attained. Finally, the specimens were weighed. The resistance evaluation was performed by determining the average relative mass loss.

3. Results and Discussions

3.1. Vegetal Ashes and Cement

EDS analysis led to the quantitative elementary chemical composition of CCA and SSA presented in Table 3. As it can be seen in the cement composition, Si, Al, Ca and Fe are the predominant chemical elements. Compared with cement, if we look at the composition of the vegetal ashes, it can be observed that Si lacks the B quality of SSA, Al and Fe are present only in the B quality of CCA, and Ca content is a little smaller in the SSA at A and B quality and in a much smaller rate in the CCA at A and B quality. If we look to the other two elements present in cement, namely K and S, it can be observed that the K content is much higher (around 20–23 times), whereas the S content is quite similar or a little smaller in CCA and it lacks in SSA. In contrast to the cement, in both vegetal ashes supplementary elements appear, namely small rates of C, Mg, and Cl, and in CCA, S and P.

In a comparative analysis between CCA and SSA compositions, the following observations can be drawn:

- Si content in CCA is quite significant compared with SSA, being 10 times higher for A quality, whereas it is lacking in SSA at B quality;
- Only CCA at B quality has a small rate of Al and Fe;
- Ca content is around six times higher in SSA than in CCA;
- K quantities are very high in all ashes, around 21–23% in CCA and around 23–25% in SSA; the B quality of SSA has the bigger K content;
- S and P are present only in CCA;
- C content is much higher in CCA than in SSA, with 1.8 times higher for A-quality ash, and with 2.5 times higher for B quality;

- Mg content is almost double in SSA than in CCA, whereas the Cl rates does not differ significantly between them.

Table 3. CCA, SSA and cement elementary chemical composition, quantitative identification.

| Element | CCA | | | | SSA | | | | Cement | |
|----------------|----------------|----------|----------------|----------|----------------|----------|----------------|----------|----------------|----------|
| | A | | B | | A | | B | | Mass Norm. (%) | Atom (%) |
| | Mass Norm. (%) | Atom (%) | Mass Norm. (%) | Atom (%) | Mass Norm. (%) | Atom (%) | Mass Norm. (%) | Atom (%) | | |
| Oxygen (O) | 47.58 | 56.28 | 39.56 | 45.81 | 50.81 | 63.76 | 52.85 | 65.29 | 47.65 | 64.17 |
| Silicon (Si) | 7.14 | 4.81 | 5.42 | 3.58 | 0.68 | 0.49 | - | - | 20.97 | 16.09 |
| Aluminum (Al) | - | - | 1.76 | 1.21 | - | - | - | - | 12.89 | 10.29 |
| Calcium (Ca) | 1.63 | 0.77 | 1.41 | 0.65 | 10.18 | 5.10 | 8.94 | 4.41 | 12.12 | 6.51 |
| Iron (Fe) | - | - | 1.14 | 0.38 | - | - | - | - | 4.25 | 1.64 |
| Potassium (K) | 21.22 | 10.27 | 22.75 | 10.78 | 22.85 | 11.73 | 25.00 | 12.64 | 1.07 | 0.59 |
| Sulfur (S) | 1.18 | 0.70 | 0.69 | 0.40 | - | - | - | - | 1.05 | 0.70 |
| Carbon (C) | 14.62 | 23.64 | 22.13 | 34.13 | 7.91 | 13.23 | 8.97 | 14.77 | - | - |
| Magnesium (Mg) | 1.83 | 1.43 | 1.13 | 0.86 | 5.41 | 4.47 | 2.06 | 1.68 | - | - |
| Chlorine (Cl) | 3.03 | 1.62 | 2.50 | 1.31 | 2.16 | 1.22 | 2.18 | 1.21 | - | - |
| Phosphorus (P) | 1.77 | 1.08 | 1.51 | 0.90 | - | - | - | - | - | - |
| SUM | 100 | 100 | 100 | 100 | 100 | 100 | 100 | 100 | 100 | 100 |

Scanning electron microscopy (SEM) images of A- and B-quality ashes of corn cobs and sunflower stalks are presented in Figure 3, at the 50 μm scale. SSA and CCA particles are bigger and less compact than the cement ones and present an agglomerated aspect (in Figure 3, some examples are marked). The aspect of SSA at B quality is more compacted than that of SSA at A quality. In the case of CCA, the aspect of the two variants has no big differences. The agglomeration of particles can be due to the high content of K, and it is in agreement with the results observed by Shakouri et al., 2020 [28], and Kamau et al., 2016 [5]. According to Shakouri et al., 2020 [28], the K content depends on the plant species and on the fertilizers used in crops.

In Figure 4 are presented the distributions of the main identified elements through EDS analysis from Table 3, on a 0.01 mm^2 area, highlighting the main components of the A- and B-quality ashes of corn cobs and sunflower stalks and their distribution on the conglomerate. Beside the general oxide mass, a few small compounds based on Si or Cl can be observed.

3.2. Composite Specimens Properties

3.2.1. Chemical Composition Analysis

In Table 4, the chemical composition of the studied concretes, according to EDS analysis, is presented from the mass and atomic percentage points of view.

Table 4. Chemical composition of the studied concretes, according to EDS analysis.

| Element | RC | | CCA1A | | CCA2A | | CCA1B | | CCA2B | | SSA1A | | SSA2A | | SSA1B | | SSA2B | |
|-----------|----------|----------|----------|----------|----------|----------|----------|----------|----------|----------|----------|----------|----------|----------|----------|----------|----------|----------|
| | Mass [%] | Atom [%] | Mass [%] | Atom [%] | Mass [%] | Atom [%] | Mass [%] | Atom [%] | Mass [%] | Atom [%] | Mass [%] | Atom [%] | Mass [%] | Atom [%] | Mass [%] | Atom [%] | Mass [%] | Atom [%] |
| Oxygen | 53.96 | 61.22 | 53.33 | 64.29 | 53.62 | 64.10 | 53.01 | 63.51 | 53.69 | 64.01 | 52.34 | 60.75 | 51.54 | 62.22 | 51.92 | 62.15 | 52.07 | 59.86 |
| Silicon | 20.69 | 13.38 | 26.63 | 18.29 | 20.80 | 14.17 | 25.79 | 17.60 | 21.24 | 14.42 | 20.94 | 13.84 | 24.86 | 17.10 | 35.58 | 24.26 | 20.15 | 13.20 |
| Carbon | 13.02 | 19.68 | 6.74 | 10.82 | 8.27 | 13.16 | 7.71 | 12.30 | 8.40 | 13.33 | 11.80 | 18.24 | 7.22 | 11.61 | 6.09 | 9.71 | 13.05 | 19.98 |
| Calcium | 10.39 | 4.71 | 10.26 | 4.94 | 13.75 | 6.56 | 10.25 | 4.90 | 13.34 | 6.35 | 12.13 | 5.62 | 7.74 | 3.73 | - | - | 11.26 | 5.17 |
| Aluminum | 1.13 | 0.76 | 1.67 | 1.20 | 1.89 | 1.34 | 1.58 | 1.12 | 1.82 | 1.29 | 1.75 | 1.20 | 4.04 | 2.89 | 4.04 | 2.87 | 1.49 | 1.02 |
| Iron | 0.81 | 0.26 | 1.37 | 0.47 | 1.03 | 0.35 | 1.66 | 0.57 | 0.91 | 0.31 | 1.04 | 0.35 | 2.02 | 0.70 | 1.01 | 0.35 | 1.13 | 0.37 |
| Sodium | - | - | - | - | - | - | - | - | - | - | - | - | 1.39 | 1.17 | - | - | - | - |
| Potassium | - | - | - | - | 0.63 | 0.31 | - | - | 0.61 | 0.30 | - | - | 1.19 | 0.59 | 1.36 | 0.67 | 0.85 | 0.40 |
| SUM | 100 | 100 | 100 | 100 | 100 | 100 | 100 | 100 | 100 | 100 | 100 | 100 | 100 | 100 | 100 | 100 | 100 | 100 |

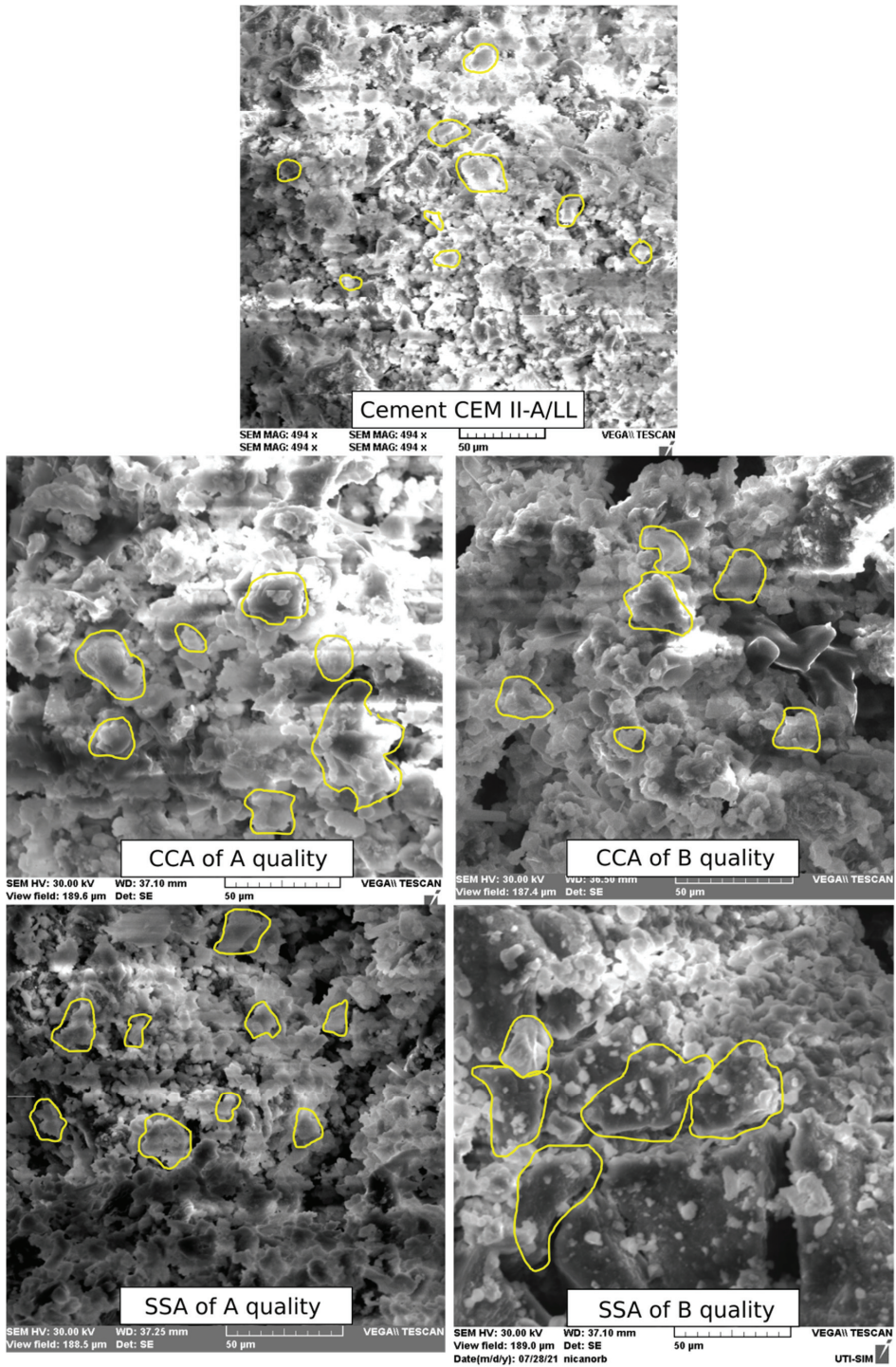


Figure 3. SEM images of CCA, SSA and cement at the magnification rate of 50 µm.

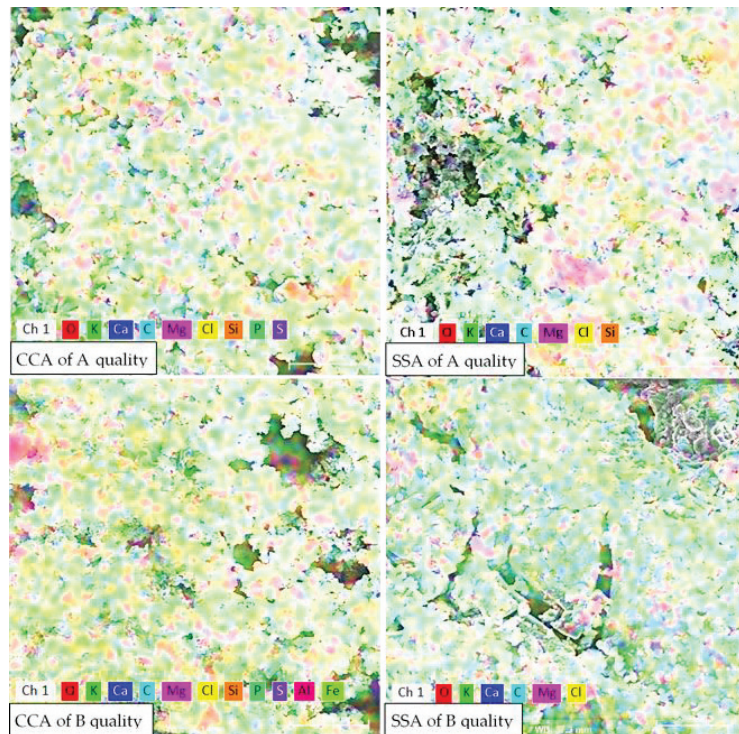


Figure 4. The distribution of the main identified elements in CCA and SSA, identified by EDS analysis, at the magnification rate of 80 μm .

The silicon content can be observed to be increased in almost all concretes with vegetal ashes than in the RC; only in SSA2B is it very insignificantly decreased. The carbon level is significantly decreased (up to 50%) in all mixes with vegetal ashes, except for SSA1A and SSA2B, which have very close values to RCs. The Calcium content is quite similar in CCA1A and CCA1B to that in RCs, being around 2–3% higher in CCA2A, CCA2B, and SSA1A, being almost 3% smaller in SSA2A, and it lacks in SSA1B. Aluminum levels are very close to that of RC in almost all mixes with vegetal ashes, except SSA2A and SSA1B, where they are almost four times higher. Regarding the Iron, there are no significant differences between the mixes. SSA2A contains a very small rate of Sodium, and in CCA2A, CCA2B, SSA2A, SSA1B, and SSA2B there exists small amounts of Potassium that are directly related to the strength performances of the concrete, even if its rate is very small [36].

In Figure 5, the distribution of the main identified elements in the studied concretes is presented at a magnification rate of 400 μm . In SSA1A and CCA1A, the O, Si, Ca, C, Al, and Fe elements are visible, and the greener zones containing more Si (from the aggregates composition), and the bluer ones (given by the Ca element color from the legend of each image) are correspondent to calcium-silicate-hydrate (CSH) resulting from the pozzolanic reaction within the matrix. The C content contributes to the decreasing strength of the concrete. In SSA2A and CCA2A, the distribution of O, Si, Al, Ca, Fe, C, and K elements can be seen, according to the attached legend of attributed colors to each element, the bluer zones corresponding to the CSH content. The difference between those two mixes is the Na element present in SSA2A. In SSA1B, the Si, Al, and Fe content is more pronounced than the other elements, O, C, and K. In SSA2B, Al, Si and Ca are predominant. Additionally, the K element is quite visible. In CCA1A and CCA2B, the CSH zones are visible in the left half and bottom half of the images, respectively.

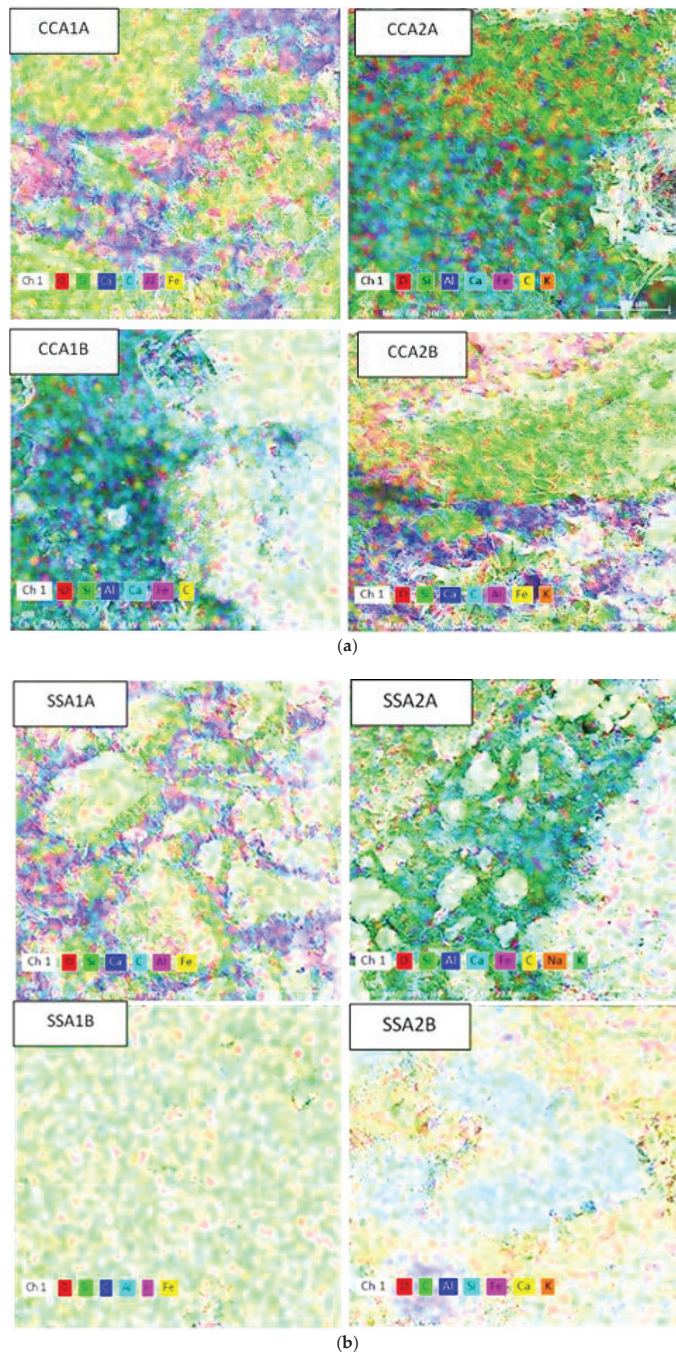


Figure 5. The distribution of the main identified elements in the studied concretes, at the magnification rate of 400 μm : (a) CCA concretes, (b) SSA concretes.

3.2.2. Compressive Strength

The compressive strength determined at 28 days is presented in Figure 6. As it can be seen in the graph, CCA1A, CCA1B, and SSA1A registered similar values for compressive strength, being around 14.7 ± 0.3% smaller than RC. Therefore, in the case of CCA, the qualities of the two types of ash led to almost the same result, and between CCA and SSA at A quality there are no big differences. CCA1A and CCA2A registered the best results between the ash mixes due to the Si content. SSA1A good result can be attributed to the smaller content of C in SSA than in CCA. Instead, B quality of SSA determined the biggest decrease in compressive strength than RC, with 42% in the case of concrete compositions with 2.5% ash. From the mixes with 5% vegetal ash, the best result was registered by SSA2A, followed by CCA2B and CCA2A, with 25.30%, 27.80%, and 30.00% smaller values than RC.

In conclusion, regarding the compressive strength measured at 28 days, for the 2.5% replacement rate of cement, the best result was given by the A quality of CCA, and for the 5% replacement rate, by the A quality of SSA.

Regarding the compressive strength evolution from 28 days to 3 months, according to Figure 6, it can be observed that the biggest increase was achieved by SSA2B, namely 14.74%, with around 12.5% bigger than that of RCs. SSA1A also had a good evolution, with a 11.40% increase, but with around 1% under the RCs. SSA2A, SSA1B, and CCA2A also registered good results, scoring 9.40%, 8.30%, and 8.10% more than the initial compressive strength. CCA at B quality instead determined a decrease in the time of this parameter, with around 3.5%.

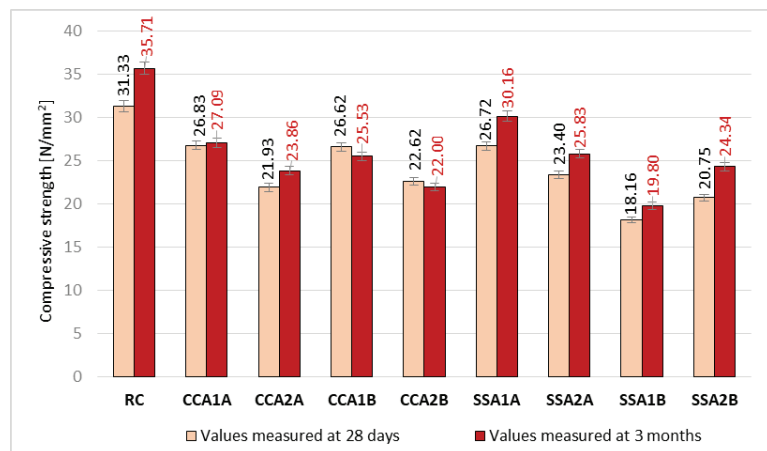


Figure 6. Compressive strength values at 28 days and 3 months age (N/mm²).

If the value obtained at 28 days and evolution in time are considered together, the best result was obtained by SSA1A, which had a decrease in compressive strength of 14.70% than RC and a strength gain in time very close to that of RC's, being only 0.9% smaller.

3.2.3. Flexural Tensile Strength

The vegetal ash used in the concrete composition led to a decrease in the flexural tensile strength (Figure 7). CCA1A and SSA2B registered the best results regarding this parameter, being only 0.95% and 1.30% smaller than RC. This can be attributed to the Si presence in CCA, and the higher content of Ca plus a much smaller C content in SSA, respectively. In CCA group, the ash at B quality led to smaller values than that at A quality, at around 12%. The SSA group registered more inferior results than the CCA one, especially in the case of using A-quality ash. SSA1A and SSA2A achieved a smaller flexural tensile strength with 29.5% and 33%, respectively, than RC. SSA at B quality obtained better results for this parameter than that of A quality, especially in the case of the 5% replacement rate.

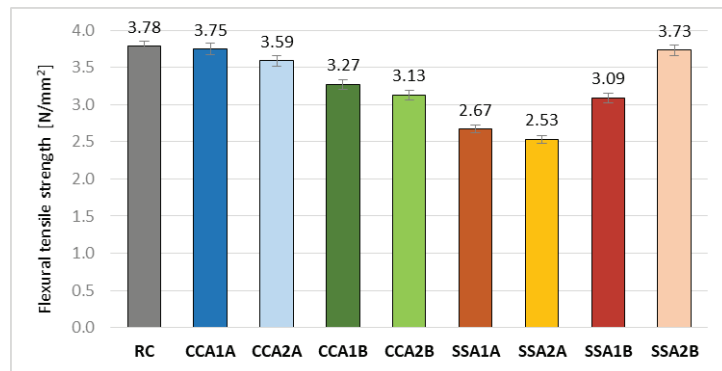


Figure 7. Flexural tensile strength values [N/mm²].

In conclusion, the A-quality ash from corn cobs led to the best values among the studied mixes with vegetal ash, regarding the flexural tensile strength.

3.2.4. Splitting Tensile Strength

The corn cob and sunflower stalk ash had significant negative effects on the splitting tensile strength of the RC (Figure 8). The best result among the mixes with vegetal ash was obtained by SSA1A, being around 31% smaller than the RC's results, followed by CCA2A, with a decrease of 39.4%. The best result for SSA1A can be attributed to a combination of elements: the higher Ca content in SSA at A quality for all ashes, its smallest C content, and Si presence. CCA1A, CCA1B, and SSA2A registered smaller values, with 43%, 44%, and 46.6%, respectively, than the reference. CCA2B obtained the biggest decrease, at around 54%.

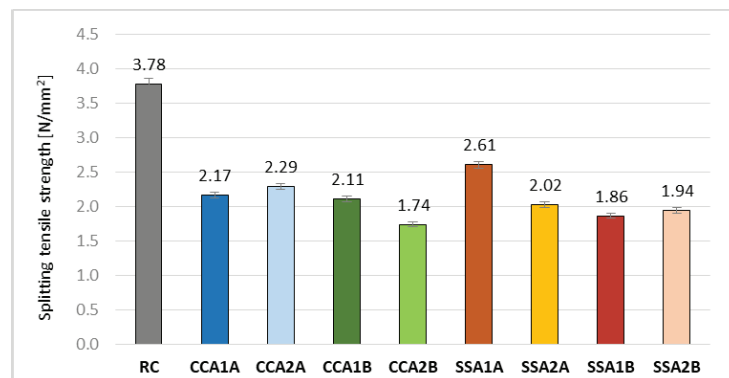


Figure 8. Splitting tensile strength values [N/mm²].

3.2.5. Resistance to Repeated Freeze–Thaw Cycles

After 50 freeze–thaw cycles, RC registered a 34.80% decrease in compressive strength (Figure 9). A 2.5% replacement rate of cement with SSA of A quality led to a significant improvement of this parameter, this composition obtaining a 11.90% decrease only compared with control samples. The SSA1A performance can be attributed to a combination of chemical elements of SSA of A quality than the other ashes, namely the highest Ca rate, the smallest C content, and Si presence. The 5% B-quality ash of CCA and SSA also had positive effects, these mixes registering a 13.3 ± 0.2% decrease. CCA1B also obtained better freeze–thaw resistance than RC, but in a smaller rate than CCA2B and SSA2B, respectively;

therefore, the conclusion can be drawn that a higher replacement rate of cement with B-quality ash for both plant cases led to improved freeze–thaw resistance. The good results obtained by CCA1B and CCA2B can be due to the Al and Fe content in the CCA at B quality. Regarding the A-quality ash, a higher replacement rate in the case of CCA led to an improvement of about 9%, but in the case of SSA led to a significant decrease from 11.9% up to 32%. Only CCA1A registered a smaller resistance, at around 2% (Figure 9).

3.2.6. Resistance to HCl Chemical Attack

All compositions with vegetal ash registered an improved resistance to chemical attack of 18% HCl solution, with more than 29.50% (Figure 10). The best results were obtained by SSA1B, CCA1A, SSA2B, and SSA1A, registering higher values with $45.5 \pm 1.5\%$ than RC. The good results obtained by CCA1A can be attributed to the highest Si content of CCA at A quality, whereas those of SSA1B and SSA2B to the combination of high content of Ca and small C content of the SSA at B quality. CCA2A and CCA2B registered a $40 \pm 1\%$ improvement than RC, whereas the results for CCA1B and SSA2B were 33% and 29.50%, respectively.

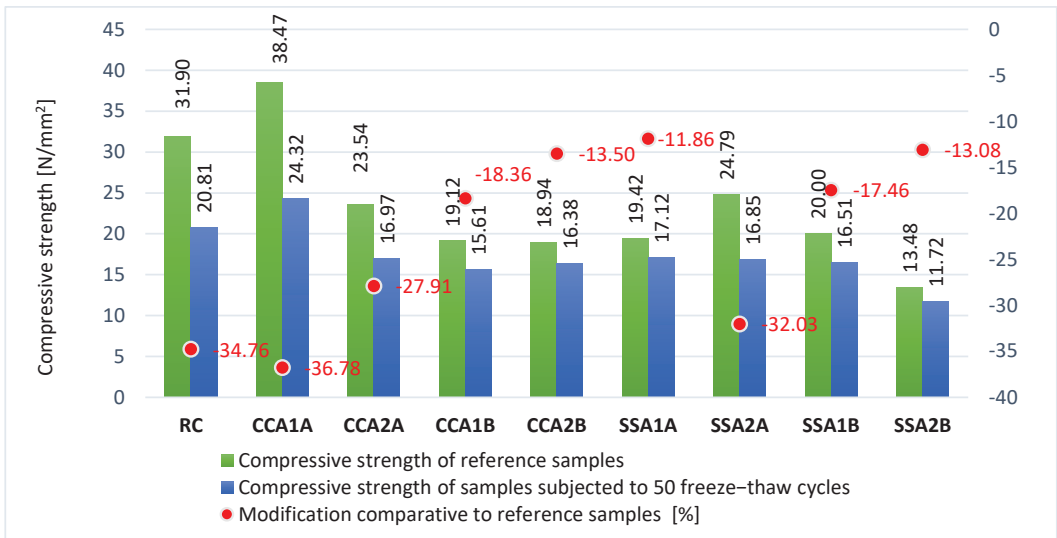


Figure 9. Compressive strength variation after 50 freeze–thaw cycles [%].

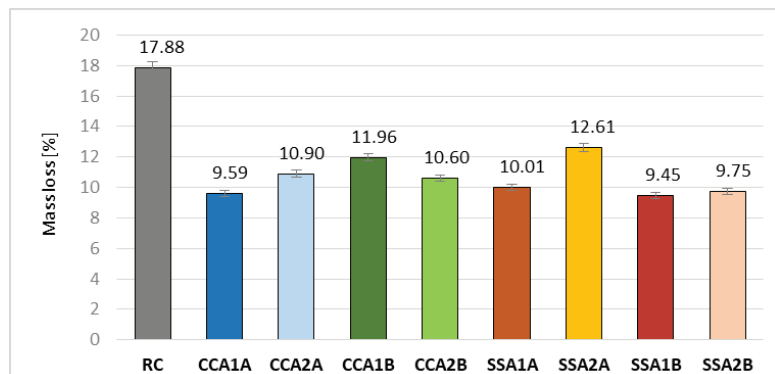


Figure 10. Mass loss due in case of chemical attack of 18% HCl solution [%].

In CCA group, A quality ash led to better results than the B one, and an increased replacement rate of this ash type led also to improved resistance. In SSA group, B quality ash registered better values for resistance to the action of 18% HCl solution than the A one, but the improvement decreased as the replacement rate increased (Figure 10).

In conclusion, 2.5% of A quality of CCA and B quality of SSA led to the best values of resistance to 18% HCl solution (Figure 10).

4. Conclusions

This study aimed to analyze the effects of two different qualities of ashes obtained by corn cobs and sunflower stalks free burning, on some properties of a micro concrete, by applying 2.5 vol.% and 5 vol.% replacement of the cement. The analyzed properties were compressive strength, flexural tensile strength, splitting tensile strength, freeze–thaw resistance, and resistance to chemical attack of hydrochloric acid solution:

- The best results for compressive strength between all mixes with vegetal ash were obtained by CCA1A, SSA1A, and CCA1B, with very close values between them. Therefore, the 2.5% of CCA, no matter its quality, and 2.5% of SSA of A quality led to similar compressive strength values. Between these three variants of mixes with vegetal ashes, only SSA1A obtained a very good gain in compressive strength during a period of 3 months, very close to that of RC.
- Regarding flexural tensile strength, CCA1A and SSA2B registered the best results, with a more insignificant decrease than RC of only about 1%.
- CCA and SSA, no matter of the quality used, determined decreases in splitting tensile strength of RC, between 31% and 54%. The smallest decreases were registered by SSA1A and CCA2A, with 31% and 39%, respectively, smaller than the reference.
- All vegetal ashes used in this study led to very significant improvement of resistance to freeze–thaw and to the chemical attack of HCl. Regarding resistance to repeated freeze–thaw cycles, the biggest improvements were obtained by SSA1A, followed very closely by SSA2B and CCA2B, with 23–23% smaller losses in compressive strength than RC. Regarding resistance to chemical attack of 18% HCl solution, all studied mixes with vegetal ash obtained improvements of this parameter, between 30% and 47% more than the reference.
- CCA1A led to the smallest decreases in compressive strength at 28 days and flexural tensile strength, and it registered one of the biggest values regarding resistance to HCl action.
- SSA1A was the optimum mix regarding compressive strength at 28 days and 3 months, splitting tensile strength and freeze–thaw resistance, and it obtained a very significant improvement of resistance to HCl, at 44%.
- SSA1B obtained the biggest improvement of the resistance from the HCl action point of view, and one of the best results from the freeze–thaw resistance point of view.
- CCA2B and SSA2B obtained very significant increases as resistance to freeze–thaw cycles and to HCl action.
- SSA2B registered the biggest compressive strength gain in time, bigger than RC, and one of the smallest decreases in flexural tensile strength.

Most concrete and reinforced concrete applications are based on the idea of improving the strength properties. However, the role of using corn cob and sunflower stalk ash as partial substitutes for cement is not to improve the mechanical strength, but to improve other properties of concrete, such as resistance to repeated freeze–thaw cycles or resistance to various chemical agents, properties that make them more economical in terms of production costs and more environmentally friendly by reducing the amount of energy incorporated in their production. If engineers stop thinking about strength, it will not be difficult to find many other areas of application for these new materials, as well as improving them at the same time.

Regarding applications for concrete with the studied vegetal ashes, the chloride content of CCA and SSA limits their use to unreinforced concrete applications or to applications with non-corrosive reinforcement or non-structural ones.

As future directions to be researched, the effects of bigger rates of CCA and SSA as cement replacement or as additive material on the freeze–thaw resistance can be studied; in general, in this study, bigger improvements were observed as the vegetal ash content increased.

Author Contributions: Conceptualization, C.M.G., A.A.Ş., R.M., N.C. and B.V.Ş.; formal analysis, C.M.G.; resources, A.A.Ş., R.M. and B.V.Ş.; investigation, C.M.G., N.C. and A.A.Ş.; methodology, C.M.G. and N.C.; writing original draft, C.M.G., N.C.; writing review, C.M.G. and R.M. All authors have read and agreed to the published version of the manuscript.

Funding: This research received no external funding.

Institutional Review Board Statement: Not applicable.

Informed Consent Statement: Not applicable.

Data Availability Statement: Data is contained within the article.

Acknowledgments: Special thanks to the Sika Romania representatives for their technical support and for providing the necessary additives in order to accomplish this research.

Conflicts of Interest: The authors declare no conflict of interest.

References

- Rui Guo, R.; Wang, J.; Bing, L.; Dan Tong, D.; Ciaisi, P.; Davis, S.J.; Andrew, R.M.; Xi, F.; Liu, Z. Global CO₂ uptake of cement in 1930–2019. *Earth Syst. Sci. Data* **2020**, *13*, 1791–1805. [CrossRef]
- Hasanbeigi, A. Global Cement Industry’s GHG Emissions. 2021. Available online: <https://www.globalefficiencyintel.com/new-blog/2021/global-cement-industry-ghg-emissions> (accessed on 15 October 2021).
- Garside, M. Major Countries in Worldwide Cement Production 2010–2020. 2021. Available online: <https://www.statista.com/statistics/267364/world-cement-production-by-country> (accessed on 15 October 2021).
- Gambhir. *Concrete Technology 4e*; Tata McGraw-Hill Education: New York, NY, USA, 2009.
- Kamau, J.; Ahmed, A.; Hirst, P.; Kangwa, J. Suitability of Corn cob Ash as a supplementary Cementitious Material. *Int. J. Mater. Sci. Eng.* **2016**, *4*, 215–228. [CrossRef]
- Bie, R.S.; Song, X.F.; Liu, Q.Q.; Ji, X.Y.; Chen, P. Studies on effects of burning conditions and rice husk ash (RHA) blending amount on the mechanical behavior of cement. *Cem. Concr. Compos.* **2015**, *55*, 162–168. [CrossRef]
- Antiohos, S.K.; Tapali, J.G.; Zervaki, M.; Sousa-Coutinho, J.; Tsimas, S.; Papadakis, V.G. Low embodied energy cement containing untreated RHA: A strength development and durability study. *Constr. Build. Mat.* **2013**, *49*, 455–463. [CrossRef]
- Chindaprasirt, P.; Rukzon, S.; Sirivivatnanon, V. Resistance to Chloride Penetration of Blended Portland cement Mortar Containing Palm Oil Fuel Ash, Rice Husk Ash and Fly Ash. *Constr. Build. Mat.* **2008**, *22*, 932–938. [CrossRef]
- Amin, M.N.; Khan, K.; Aslam, F.; Shah, M.I.; Javed, M.F.; Musarat, M.A.; Usanova, K. Multigene Expression Programming Based Forecasting the Hardened Properties of Sustainable Bagasse Ash Concrete. *Materials* **2021**, *14*, 5659. [CrossRef]
- Bahurudeen, A.; Kanraj, D.; Gokul Dev, V.; Santhanam, M. Performance evaluation of sugarcane bagasse ash blended cement in concrete. *Cem. Concr. Compos.* **2015**, *59*, 77–88. [CrossRef]
- Bheel, N.; Adesina, A. Influence of Binary Blend of Corn Cob Ash and Glass Powder as Partial Replacement of Cement in Concrete. *Silicon* **2021**, *13*, 1647–1654. [CrossRef]
- Adesanya, D.A.; Raheem, A.A. Development of corn cob ash blended cement. *Constr. Build. Mater.* **2009**, *23*, 347–352. [CrossRef]
- Memon, S.A.; Javed, U.; Haris, M.; Khushnood, R.A.; Kim, J. Incorporation of Wheat Straw Ash as Partial Sand Replacement for Production of Eco-Friendly Concrete. *Materials* **2021**, *14*, 2078. [CrossRef] [PubMed]
- Aksoğan, O.; Binici, H.; Ortlek, E. Durability of concrete made by partial replacement of fine aggregate by colemanite and barite and cement by ashes of corn stalk, wheat straw and sunflower stalk ashes. *Constr. Build. Mater.* **2016**, *106*, 253–263. [CrossRef]
- Martirena, F.; Monzó, J. Vegetable ashes as supplementary cementitious materials. *Cem. Concr. Res.* **2018**, *114*, 57–64. [CrossRef]
- Shafiq, P.; Mahmud, H.B.; Jumaat, M.Z.; Zargar, M. Agricultural wastes as aggregate in concrete mixtures—A review. *Constr. Build. Mater.* **2014**, *53*, 110–117. [CrossRef]
- OECD (Organisation for Economic Cooperation and Development). Crop Production (Indicator). Available online: https://www.oecd-ilibrary.org/agriculture-and-food/crop-production/indicator/english_49a4e677-en (accessed on 20 September 2021).
- USDA (United States Department of Agriculture). World Agricultural Production. Circular Series WAP 10-21 2021, 38. Available online: <https://apps.fas.usda.gov/psdonline/circulars/production.pdf> (accessed on 20 September 2021).

19. Leff, B.; Ramankutty, N.; Foley, J.A. Geographic distribution of major crops across the world. *Glob. Biogeochem. Cycles* **2004**, *18*, 33. [[CrossRef](#)]
20. Adesanya, D. Evaluation of blended cement mortar, concrete and stabilized earth made from ordinary Portland cement and corn cob ash. *Constr. Build. Mater.* **1996**, *10*, 451–456. [[CrossRef](#)]
21. Binici, H.; Yucegok, F.; Aksogan, O.; Kaplan, H. Effect of corncob, wheat straw, and plane leaf ashes as mineral admixtures on concrete durability. *J. Mater. Civ. Eng.* **2008**, *20*, 478–483. [[CrossRef](#)]
22. Kamau, J.; Ahmed, A.; Hirst, P.; Kangwa, J. Permeability of corncob ash, anthill soils and rice husk replaced concrete. *Int. J. Sci. Environ. Technol.* **2017**, *6*, 1299–1308.
23. Memon, S.A.; Khan, M.K. Ash blended cement composites: Eco-friendly and sustainable option for utilization of corncob ash. *J. Clean. Prod.* **2018**, *175*, 442–455. [[CrossRef](#)]
24. Oladipupo, O.S.; Olutoge, F.A. Strength Properties of Corn Cob Ash Concrete. *J. Emerg. Trends Eng. Appl. Sci.* **2012**, *3*, 297–301.
25. Mujedu, K.A.; Adebara, S.A.; Lamidi, I.O. The Use of Corn Cob Ash and Saw Dust Ash as Cement. *Int. J. Eng. Sci.* **2014**, *3*, 22–28.
26. Ahangba, A.; Michael, T. Partial replacement of cement with corn cob ash. *Int. J. Innov. Res. Multidiscip. Field* **2016**, *2*, 158–169.
27. Owolabi, T.A.; Oladipo, I.O.; Popoola, O.O. Effect of corncob ash as partial substitute for cement in concrete. *N. Y. Sci. J.* **2015**, *8*, 1–4.
28. Shakouri, M.; Exstrom, C.L.; Ramanathan, S.; Suraneni, P. Hydration, strength, and durability of cementitious materials incorporating untreated corn cob ash. *Constr. Build. Mater.* **2020**, *243*, 118171. [[CrossRef](#)]
29. Darweesh, H.H.M. Influence of sun flower stalk ash (SFSA) on the behavior of Portland cement pastes. *Results Eng.* **2020**, *8*, 100171. [[CrossRef](#)]
30. EN 197-1:2011. *Cement. Composition, Specifications and Conformity Criteria for Common Cements*; European Committee for Standardization: Brussels, Belgium, 2011.
31. NE 012/1-2007. *Normativ Pentru Producerea Betonului Si Executarea Lucrarilor Din. Beton, Beton Armat Si Beton Precomprimat—Partea 1: Producerea Betonului (Regulations for the Production of Concrete and the Execution of Concrete, Reinforced Concrete and Prestressed Concrete)*; ASRO—Romanian Standardization Association: Bucharest, Romania, 2007.
32. EN 12390-3:2019. *Testing Hardened Concrete Part. 3: Compressive Strength of Test. Specimens*; European Committee for Standardization: Brussels, Belgium, 2019.
33. EN 12390-5:2019. *Testing Hardened Concrete Part. 3: Flexural Tensile Strength of Test. Specimens*; European Committee for Standardization: Brussels, Belgium, 2019.
34. EN 12390-6:2010. *Testing Hardened Concrete; Part. 6: Split Tensile Strength of Test. Specimens*; European Committee for Standardization: Brussels, Belgium, 2010.
35. SR 3518:2009. *Încercări Pe Betoane. Determinarea Rezistenței La Îngheț-Dezghet Prin Masurarea Variației Rezistenței La Compresiune, Si/Sau Modulului de Elasticitate Dinamic Relativ (Tests Hard-Ened Concrete. Determination of Freeze-Thaw Resistance by Measuring the Variation of the Com-Pressive Strength and/or the Relatively Dynamic Modulus of Elasticity)*; ASRO—Romanian Standardization Association: Bucharest, Romania, 2009.
36. Neville, A.M. *Properties of Concrete*, 5th ed.; Trans-Atlantic Publications, Inc.: Philadelphia, PA, USA, 2012.

Article

Experimental Study with Plaster Mortars Made with Recycled Aggregate and Thermal Insulation Residues for Application in Building

Daniel Ferrández ^{1,*}, Manuel Álvarez ¹, Pablo Saiz ² and Alicia Zaragoza ¹

¹ Department of Building Technology, Polytechnic University of Madrid, Avenida Juan de Herrera, 6, 28040 Madrid, Spain; manuel.alvarezd@upm.es (M.Á.); alicia.zaragoza@alumnos.upm.es (A.Z.)

² Department of Financial Economics, Accounting and Modern Language, Rey Juan Carlos University, Vicalvaro Campus, Paseo de los Artilleros, s/n, 28032 Madrid, Spain; pablo.saiz@urjc.es

* Correspondence: daniel.fvega@upm.es

Abstract: The high demand for natural resources and increased industrial activity is driving the construction sector to search for new, more environmentally friendly materials. This research aims to analyse plaster mortars with the incorporation of construction and demolition waste (CDW) to move towards a more sustainable building sector. Three types of aggregates (natural, recycled concrete and recycled from ceramic walls) and two types of insulation waste (expanded polystyrene with graphite and mineral wool) have been added to the plaster matrix to evaluate its mechanical and physical properties and its suitability in the elaboration of prefabricated materials. The results show how plaster mortars made with recycled aggregates have higher mechanical resistance than conventional plaster without incorporating sand. The incorporation of crushed mineral wool residues improves the flexural strength of plaster mortars and their application in the execution of prefabricated panels. Likewise, the expanded polystyrene residues reduce the final density of mortars, improving their behaviour against water absorption and reducing the final thermal conductivity of plaster material.

Keywords: plaster mortar; recycled aggregates; thermal insulation; building

Citation: Ferrández, D.; Álvarez, M.; Saiz, P.; Zaragoza, A. Experimental Study with Plaster Mortars Made with Recycled Aggregate and Thermal Insulation Residues for Application in Building. *Sustainability* **2022**, *14*, 2386. <https://doi.org/10.3390/su14042386>

Academic Editor: Jorge de Brito

Received: 31 January 2022

Accepted: 16 February 2022

Published: 19 February 2022

Publisher's Note: MDPI stays neutral with regard to jurisdictional claims in published maps and institutional affiliations.



Copyright: © 2022 by the authors. Licensee MDPI, Basel, Switzerland. This article is an open access article distributed under the terms and conditions of the Creative Commons Attribution (CC BY) license (<https://creativecommons.org/licenses/by/4.0/>).

1. Introduction

The construction sector is included in the six factors (cropland, grazing land, fishing grounds, forest products, carbon and built-up land) that make up the ecological footprint of humanity [1]. For this reason, it is necessary to involve efforts to develop new construction materials based on circular economy criteria [2]. To this end, the European Union has defined a firm line of action that is included in the “European Green Deal” presented by the Commission Communication of 11 December 2019 [3]. This document includes as a main element the efficient use of resources in construction, as well as ensuring that less waste is produced. For this reason, more and more researchers are channelling their studies towards the scope of sustainable construction and the use of raw materials from construction and demolition waste (CDW) management [4,5].

These CDW are the main source of waste generation in modern society [6]. Thus, the application of the 3Rs principle (reduce-reuse-recycle) avoids the generation of waste and converts it back into resources, thus closing the circle in industrial ecosystems [7]. With regard to the composition of these CDW, according to reports published by the European Commission [8], most of the waste comes from the demolition of concrete structures (12–40%) and factory works made with ceramic materials (8–54%), and the main recycling process of these residues is the generation of aggregates for construction [9]. Additionally, the volume of waste from insulating materials is growing due to European initiatives to improve the energy efficiency of buildings and their rehabilitation [10].

Concrete and ceramic material waste are generally inert and low polluters; however, they occupy a large volume in landfills and have a strong impact on waste management in cities [11]. The crushing, treatment, and preparation of the waste to produce recycled aggregates is currently widespread [12]. In general, aggregates from CDW have a wide field of application in the production of masonry mortars, totally or partially replacing the natural aggregate [13]. Regarding its properties for use in building, it should be highlighted that recycled aggregates have a lower density and a higher coefficient of friability than natural aggregates. This has repercussions in a lower resistance to compression of mortars that incorporate them [14]. The recycled ceramic aggregate has a higher water absorption coefficient compared to recycled concrete aggregate and natural aggregate [15]. This means that the recycled aggregates also have a high water content in fines and other impurities derived from the manufacture [16]. Recycled ceramic aggregate from brick waste and factory works has been proven to have good properties for improving the mechanical resistance of plaster mortars for use in rehabilitation and restoration works of architectural heritage [17]. On the other hand, recycled concrete aggregates have also been used by several authors to increase the density of gypsum compounds, expanding their field of application towards the production of prefabricated building materials [18].

Furthermore, residues from thermal insulation have also been frequently used to improve the physical and mechanical properties of mortars [19]. In the case of expanded polystyrene (EPS), this has been used in various investigations as a substitute for aggregates for the manufacture of mortars with the intention of reducing the final density of the materials and lowering their thermal conductivity [20,21]. It is a material that can be added to the manufacturing process of plaster plates and panels, improving its thermal performance to produce prefabricated elements, although reducing its mechanical resistance to bending [22]. On the contrary, resistance to bending is implemented if insulating mineral wool fibre residues are incorporated [23]. Piña et al. demonstrated the possibility of incorporating this type of crushed waste as a partial replacement for aggregates, presenting good mechanical behaviour and good stability against fire [24,25].

The use of gypsum or plaster mortars to produce prefabricated elements is well known since the incorporation of aggregates improves the mechanical rigidity of the material and increases its resistance [26]. In this sense, Santa Cruz-Astorqui et al. analysed the behaviour of some original $40 \times 20 \times 10$ cm blocks composed of a sandwich panel with two plasterboards and a core of plaster and EPS, showing that this type of prefabricated material has good deformation capacity under external stresses [27]. To improve this deformation capacity, studies have been carried out by various authors in which they have opted for the incorporation of fibres into plaster matrix, together with the incorporation of insulation residues to reduce the final thermal conductivity of the panels produced [28]. Finally, it is worth highlighting the study by Dolezelova et al., where the importance of the shape of aggregates for the manufacture of plaster mortars has been demonstrated, where sands with a rougher particle surface are the ones with a higher quality for the manufacturing of mortars, facilitating the adherence of the conglomerate to its surface and improving resistance to compression [29].

In short, these studies seek to reduce the environmental impact exerted by the construction sector during the process of execution, rehabilitation, and demolition of buildings, seeking ways to prevent and recover CDW in line with the objective established by Directive 2009/98/EC [30]. The main objective of this paper is to study the technical feasibility of plaster mortars made with recycled aggregate and thermal insulation residues, as no study has been found that shows the possible effect of combining these two types of CDW in plaster mortars for the elaboration of precast concrete products. To do this, an experimental campaign is developed in which, on the one hand, a mechanical and physical characterization is carried out of the material to produce mortars, and, on the other hand, the possible application of these materials for their use in panels and prefabricated building blocks is studied.

2. Methodology

This section presents the materials used to manufacture mortars, as well as dosages and a description of the experimental program carried out.

2.1. Materials Used

To carry out the experimental campaign of this research, the following raw materials have been used in the preparation of mortars: plaster, water, natural sand, recycled aggregates, and thermal insulation residues (Figure 1).

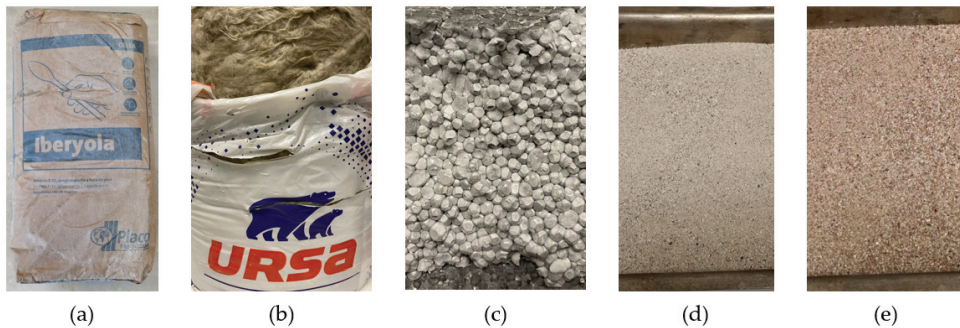
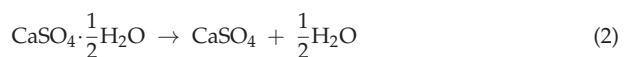
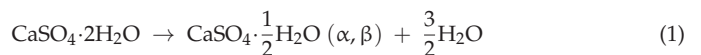


Figure 1. (a) Plaster E-35; (b) mineral wool insulation; (c) insulation of expanded polystyrene with graphite; (d) recycled concrete aggregate; (e) mixed ceramic recycled aggregate.

2.1.1. Binder

E-35 construction plaster was used as a conglomerating material for mixing mortars [31]. It is a material commonly used in construction for wall coverings, the production of prefabricated panels, and the execution of plates for false ceilings [32]. Equations (1) and (2) show the basic scheme of reactions to obtain this raw material [33]:



More specifically, Table 1 shows the characteristics of E-35 plaster used in accordance with the UNE-EN 13279-1:2009 standard [34], which has been supplied by Placo Saint Gobain, S.A. (Madrid Spain). Additionally, X-ray fluorescence analysis revealed that the composition of this raw material is as follows: CaSO_4 (99.7%), Al (0.022%), Fe (0.035%), Si (0.068%), Sr (0.157%), and P (0.01%).

Table 1. Physical properties of plaster E-35.

| Fire Resistance | Thermal Conductivity | pH | Granulometry | Water Vapor Diffusion Factor | Flexural Strength | Purity Index |
|-----------------|-------------------------------|----|--------------|------------------------------|------------------------|--------------|
| Euro class AY | $\lambda = 0.34 \text{ W/mK}$ | >6 | 0–0.2 mm | $\mu = 6$ | >3.5 N/mm ² | >92% |

2.1.2. Thermal Insulation Waste

To improve the thermal behaviour of plaster mortars produced in this research, residues of two types of thermal insulation were used: expanded polystyrene with the addition of graphite and insulating mineral wool. The physical characteristics of these materials provided by URSA Ibérica Aislantes, S.A. (Madrid, Spain), are shown in Table 2.

Table 2. Physical properties of the different types of thermal insulation used.

| Insulation | Thermal Conductivity | Density | Water Vapor Diffusion Factor | Geometric Characteristics |
|------------------------------------|------------------------|-------------------------|------------------------------|---------------------------|
| Expanded Polystyrene with Graphite | $\lambda = 0.031$ W/mK | 28–30 kg/m ³ | $\mu = 20$ –100 | $\phi = 4$ mm |
| Insulating Mineral Wool | $\lambda = 0.037$ W/mK | 40 kg/m ³ | $\mu = 1$ | L = 12 mm |

Before being used in the mortar mix, both types of insulators had to be prepared, as can be seen in Table 2. In the case of expanded polystyrene with graphite, this was separated manually until individual spheres with a mean diameter of four millimetres were obtained, as has been done previously by other researchers [35]. Likewise, mineral wool fibre also had to be crushed and separated manually to a length of 12 mm, following the recommendations of other researchers [36].

2.1.3. Aggregates

Three different types of aggregates have been used in this research: natural aggregate (NA), recycled aggregate from concrete waste (RAcon) and recycled mixed ceramic aggregate from the demolition of masonry walls (RAmix). A physical characterization of these sands for the manufacture of mortars is shown in Table 3.

Table 3. Physical characterization of aggregates.

| Test | Fine Content (%) | Particle Form | Fineness Modulus (%) | Friability (%) | Bulk Dens. (kg/m ³) | Dry Dens. (kg/m ³) | Water Absorption (%) |
|-------|-------------------|-------------------|----------------------|--------------------|---------------------------------|--------------------------------|----------------------|
| Norma | UNE-EN 933-1 [37] | UNE-EN 13139 [38] | UNE-EN 13139 [38] | UNE-EN 146404 [39] | UNE-EN 1097-3 [40] | UNE-EN 1097-6 [41] | UNE-EN 1097-6 [41] |
| NA | 1.63 | - | 4.47 | 20.43 | 1562 | 2479 | 0.84 |
| RAcon | 3.89 | Not relevant | 4.08 | 23.17 | 1328 | 2246 | 6.43 |
| RAmix | 4.21 | Not relevant | 3.96 | 25.12 | 1297 | 2188 | 7.12 |

A comparison between densities of recycled and natural aggregates can be seen in the analysis in Table 3. Density in recycled aggregates is lower than in natural aggregates. This allows the elaboration of lighter prefabricated elements for use in construction, although it also results in lower mechanical performance [42]. It is also worth noting the high content of fines in these recycled sands, although for the specific case of this investigation, aggregates were sieved and particles retained in the sieves with diameters of 1 mm (60%) and 0.5 mm (40%) were used in order to obtain a homogeneous mixture. Finally, the greater water absorption of these recycled sands is also highlighted, this has its repercussion in a lower workability of mortars during the kneading process, the absorption of the RAmix being greater compared to the RAcon in accordance with other previous studies [43].

Regarding the chemical composition, this was obtained by X-ray fluorescence using Bruker S2 Puma equipment and is shown in Table 4.

Table 4. X-Ray fluorescence assay.

| Samples | Al ₂ O ₃ | CaO | Fe ₂ O ₃ | K ₂ O | MgO | SiO ₂ | MnO | TiO ₂ | SO ₃ | P ₂ O ₅ | NaO ₂ | L.Loss (%) |
|---------|--------------------------------|-------|--------------------------------|------------------|------|------------------|-------|------------------|-----------------|-------------------------------|------------------|------------|
| RAcon | 6.03 | 11.21 | 1.34 | 2.22 | 0.61 | 68.32 | 0.029 | 0.11 | - | 0.12 | 0.35 | 9.66 |
| RAmix | 10.45 | 18.32 | 2.14 | 1.98 | 1.71 | 47.70 | - | 0.34 | 5.37 | 0.12 | 0.63 | 11.24 |

Table 4 shows the higher SiO₂ content of RAcon with respect to RAmix, which in turn has a higher CaO and SO₃ content because of gypsum impurities derived from the masonry wall cladding [44]. A higher Al₂O₃ content is also observed in the RAmix because of the ceramic origin of the bricks used in the execution of masonry works [45].

Finally, Table 5 shows the analysis performed by X-ray diffraction with the help of a Siemens D5000 diffractometer with a graphite monochromator Cu-K α ($\lambda = 1.540598 \text{ \AA}$). The results obtained are shown in Table 5 where it is observed that the predominant crystalline phases for the two types of recycled aggregates used are quartz and calcite [46].

Table 5. Analysis by X-ray diffraction, where each (*) shows the relative abundance of each type of mineral crystalline phase.

| Mineral Phase | Calcite | Quartz | Gypsum | Sanidine | Phlogopite |
|---------------|---------|--------|--------|----------|------------|
| RAcon | **** | ***** | * | * | * |
| RAmix | **** | ***** | ** | ** | ** |

2.1.4. Water

For the mixing of different dosages, drinking water from Canal de Isabell II (Madrid, Spain) has been used, which has been used successfully in other previous works [47]. The main characteristics of this type of water are its softness (25 mg CaCO₃/l) and neutral pH between 7 and 8 [48]. In addition, the following elements can be found in its chemical composition, as listed in Table 6.

Table 6. Composition of drinking water in the community of Madrid.

| Nitrate | Nitrite | Free Chlorine | Calcium | Sulphates | Fluorides | Iron | Aluminium |
|-----------|------------|---------------|------------|-----------|------------|-----------|-----------|
| 0.60 mg/L | <0.05 mg/L | 0.50 mg/L | 17.80 mg/L | 5.30 mg/L | <0.10 mg/L | 0.01 mg/L | 0.03 mg/L |

2.2. Experimental Program

2.2.1. Dosages Used

Throughout this investigation, the following notation presented in Equation (3) has been used to refer to the different types of mortars:

$$E0.8 - \text{Aggregate} - \text{Isolation} \quad (3)$$

where E0.8 refers to the water/plaster ratio used to prepare the different dosages, Aggregate refers to the type of sand used, which can be of three types: NA (natural sand), RAcon (recycled concrete aggregate) and RAmix (mixed recycled aggregate), and, finally, Isolation refers to the type of thermal insulation waste incorporated: graphite-incorporated expanded polystyrene (EPS) or insulating mineral wool (MW).

For the elaboration of the different types of mortars used in this investigation, the dosages collected in Table 7 have been used. In all cases, the mixtures were carried out following the same techniques and methods that are collected in the UNE-EN standard 12379-2:2014 [49].

Table 7. Proportions of each material used in dosages.



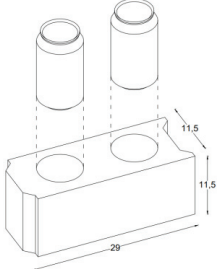
| Name | Plaster (g) | Water (g) | Aggregates (g) | EPS (g) | MW (g) |
|----------------|-------------|-----------|----------------|---------|--------|
| E0.8 | 1000 | 800 | | | |
| E0.8-NA | 1000 | 800 | 600 | | |
| E0.8-NA-EPS | 1000 | 800 | 600 | 10 | |
| E0.8-NA-MW | 1000 | 800 | 600 | | 7.5 |
| E0.8-RAcon | 1000 | 800 | 600 | | |
| E0.8-RAcon-EPS | 1000 | 800 | 600 | 10 | |
| E0.8-RAcon-MW | 1000 | 800 | 600 | | 7.5 |
| E0.8-RAmix | 1000 | 800 | 600 | | |
| E0.8-RAmix-EPS | 1000 | 800 | 600 | 10 | |
| E0.8-RAmix-MW | 1000 | 800 | 600 | | 7.5 |

It should be noted that in all the mixtures listed in Table 7, residues were manually mixed with plaster powder and then gradually poured into the water to start the mixing process. In addition, samples were kept at a temperature of 22 ± 2 °C and a relative humidity of $60 \pm 5\%$. After seven days of storage under laboratory conditions, samples were dried in an oven at a constant temperature of 40 ± 2 °C for 24 h, as recommended in the UNE-EN 12379-2:2014 standard [49].

2.2.2. Instruments and Experimental Plan

In this research, an experimental campaign has been carried out that can be divided into three phases: (1) mechanical characterization, (2) physical characterization of plaster mortars produced, and, later, (3) study of the suitability of these materials for the manufacture of panels and prefabricated blocks. A diagram of the tests carried out is shown in Table 8.

Table 8. Planning of the tests carried out in the laboratory.

| Samples | Tests |
|---|---|
|  <p data-bbox="126 838 372 861">Dimensions: $4 \times 4 \times 16$ cm</p> | <p data-bbox="448 676 739 698">Mechanical characterization tests</p> <ul data-bbox="448 707 1212 925" style="list-style-type: none"> <li data-bbox="448 707 1212 753">• Flexural and compressive strength tests based on UNE-EN-13279-2: 2014 [49], using an AUTOTEST 200-10SW hydraulic press. <li data-bbox="448 755 757 778">• Physical characterization tests <li data-bbox="448 779 1212 826">• Shore C surface hardness and bulk density according to the recommendations of the UNE 102042: 2014 [50]. <li data-bbox="448 827 1212 874">• Longitudinal modulus of elasticity by ultrasound, using an Ultrasonic Tester E46 equipment with 55 kHz receiver–transmitter contact probes. <li data-bbox="448 875 1212 898">• Water absorption by capillarity according to the UNE-EN 459-2:2011 standard [51]. <li data-bbox="448 899 1212 925">• Thermal conductivity coefficient with the help of a Hot Disk 5501 Kapton Sensor. |
|  <p data-bbox="123 1042 374 1064">Dimensions: $50 \times 30 \times 2$ cm</p> | <p data-bbox="448 968 703 990">Tests on prefabricated panels</p> <ul data-bbox="448 999 1212 1045" style="list-style-type: none"> <li data-bbox="448 999 1212 1045">• Determination of the resistance to bending in panels and plates using Proeti, S.A. equipment, following the recommendations of the UNE-EN 12859: 2012 [52] standard. |
|  <p data-bbox="104 1378 394 1400">Dimensions: $29 \times 11.5 \times 11.5$ cm</p> | <p data-bbox="448 1129 703 1151">Tests on prefabricated blocks</p> <ul data-bbox="448 1160 1212 1354" style="list-style-type: none"> <li data-bbox="448 1160 1212 1258">• Preparation of prefabricated blocks of plaster mortar with recycled aggregate and thermal insulation waste for which some original moulds have been designed, and recycled beverage cans have been used to make the alveoli of the precast and lighten the final weight. <li data-bbox="448 1260 1212 1306">• Suction or initial rate of water absorption by capillarity according to the guidelines of the UNE-EN 722-1: 2011 standard [53]. <li data-bbox="448 1308 1212 1354">• Compressive strength of the blocks using an IBERTEST model MIB-60/AM universal press. |

On the other hand, to determine the effect of the incorporation of sands of a different nature and the different types of thermal insulation residues incorporated in plaster mortars, a study on the analysis of variance (ANOVA) has been carried out. Table 9 shows the factors and levels that have been taken into consideration in the design of experiments.

All the tests performed for statistical analysis have been carried out for a significance level of 5%. For the diagnosis of the model, it has been verified that the residuals of each response variable meet the conditions of normality, homoscedasticity, and independence [54]. A multiple range test has also been included to observe the existence or not of homogeneous groups between the different types of mortars included.

Table 9. Factors and levels used for the analysis of variance (ANOVA).

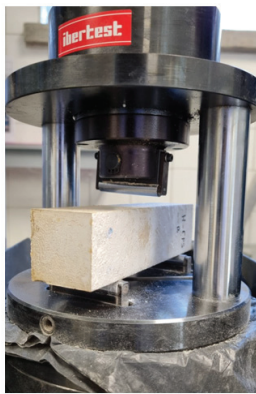
| Factor | Level |
|------------|--|
| Aggregate | Natural (NA); Concrete Recycling (RAcon); Mixed Recycling (RAmix) |
| Insulating | Non-Insulating (NI); Expanded Polystyrene (EPS); Mineral Wool (MW) |

3. Results and Discussion

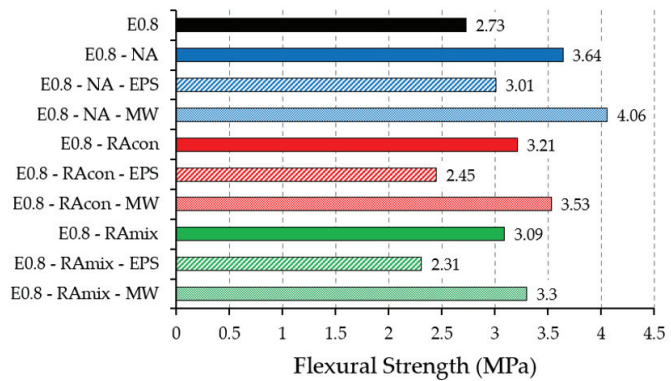
This section presents the results derived from the experimental campaign proposed for this study and their discussion.

3.1. Mechanical Characterization Tests

Next, Figures 2 and 3 show the results of flexural and compressive strength tests carried out on the $4 \times 4 \times 16$ cm prismatic specimens of plaster mortar.



(a)

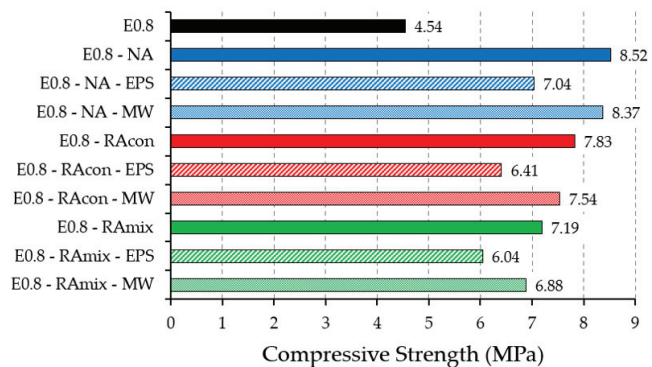


(b)

Figure 2. (a) Flexural strength test according to UNE-EN-13279-2: 2014; (b) results derived from flexural strength test on the prepared mortars.



(a)



(b)

Figure 3. (a) Compressive strength test according to UNE-EN-13279-2: 2014; (b) results derived from compressive strength test on the prepared mortars.

Figure 2 shows the improvement in flexural strength of plaster materials by incorporating sand into their constitution. All mortars with the incorporation of aggregate without insulation exceeded the E0.8 plaster reference, with mortars made with natural

sand showing the highest values. On the other hand, it can be seen how the incorporation of expanded polystyrene residue with graphite in the manufacture of mortars reduces flexural strength. This is because preferential breakage points occur between EPS spheres and plaster mortar matrix, thus generating greater heterogeneity that negatively affects the mechanical behaviour of the material [55]. On the other hand, the incorporation of mineral wool residue improves the flexural strength of the hardened plaster mortar. This is in line with other studies that highlight the beneficial effect of the incorporation of fibres in the mortar matrix to improve its ductility and deformation capacity [56,57]. Regarding recycled aggregates, mortars that incorporate sand from concrete waste have better performance than mortars with aggregates from mixed ceramic waste.

Furthermore, Figure 3 shows how the incorporation of aggregates improves the compressive strength of plaster material, where mortars made with natural aggregates are the ones that presented the best results. Among mortars with recycled aggregate, the ones that incorporated RAcon obtained the greatest resistance. Finally, it can be seen how the incorporation of EPS residue also decreases the compressive strength of mortars, while the incorporation of mineral wool residue is not decisive in improving this mechanical property [58].

Table 10 shows the results derived from the analysis of variance (ANOVA) carried out to determine the effect of the factors included in the study on the mechanical behaviour of plaster mortars.

Table 10. Analysis of variance (ANOVA) for flexural and compressive strength.

| Property | Source | Sum of Squares | Df | Mean Square | F-Ratio | <i>p</i> -Value |
|----------------------------|-------------------|----------------|----|-------------|---------|-----------------|
| Flexural Strength (MPa) | A: Aggregate | 2.22279 | 2 | 1.11139 | 47.27 | 0.0000 |
| | B: Insulating | 5.12703 | 2 | 2.56351 | 109.03 | 0.0000 |
| | AB: Interactions | 0.03833 | 4 | 0.00958 | 0.41 | 0.8008 |
| | Residual | 0.42320 | 18 | 0.02351 | | |
| | Total (Corrected) | 7.81134 | 26 | | | |
| Compression Strength (MPa) | A: Aggregate | 7.32241 | 2 | 3.66120 | 36.89 | 0.0000 |
| | B: Insulating | 9.31770 | 2 | 4.65885 | 46.94 | 0.0000 |
| | AB: Interactions | 0.19813 | 4 | 0.04953 | 0.50 | 0.7367 |
| | Residual | 1.78640 | 18 | 0.09924 | | |
| | Total (Corrected) | 18.62460 | 26 | | | |

As can be seen in Table 10, both in mechanical resistance to bending and in compressive strength of mortars, the two factors included in this study (type of aggregate and thermal insulation residue) are statistically significant, having *p*-values lower than the level of significance ($\alpha = 0.05$).

Finally, Table 11 includes the results obtained for the multiple range test performed for the mechanical properties of mortars.

Table 11. Multiple range test for mechanical properties.

| Property | Aggregate | LS Mean | Homogeneous Group | Insulating | LS Mean | Homogeneous Group |
|-------------------------|-----------|---------|-------------------|------------|---------|-------------------|
| Flexural Strength (MPa) | RAmix | 2.900 | X | EPS | 2.590 | X |
| | RAcon | 3.062 | X | NI | 3.314 | X |
| | NA | 3.573 | X | MW | 3.631 | X |
| Comp. Strength (MPa) | RAmix | 6.704 | X | EPS | 6.495 | X |
| | RAcon | 7.260 | X | NI | 7.598 | X |
| | NA | 7.976 | X | MW | 7.847 | X |

In the multiple range test shown in Table 11, it can be seen how there are significant differences for mechanical resistance to bending at all levels for the two factors analysed in

this study. On the other hand, for mechanical compressive resistance, there are significant differences at all levels when we refer to the aggregate type of factor. However, in the case of the incorporation of thermal insulation residues, it cannot be affirmed that there are significant differences between plaster mortars without thermal insulation and those that incorporate mineral wool fibre, both types of mortars presenting greater resistance to statistically significant compression compared to plaster mortars with EPS.

3.2. Physical Characterization Tests

This section includes the tests for the physical properties of plaster mortars carried out in this work. These tests have also been carried out on $4 \times 4 \times 16$ cm specimens, and include the following measurements: bulk density, Shore C surface hardness, longitudinal Young's modulus determined by ultrasound, and thermal conductivity coefficient. These are parameters that allow a characterization of the material to later define its possible uses and applications in the building sector.

Figure 4 shows the method used to perform physical characterization tests, and, in Table 12, the results obtained for each of the properties are presented.

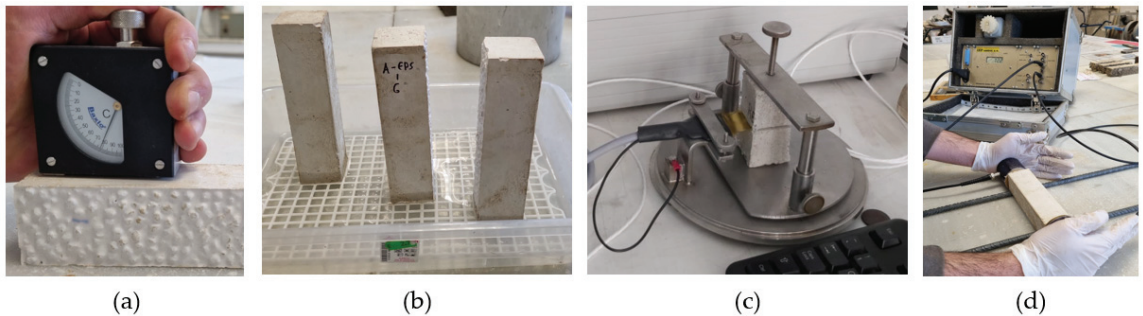


Figure 4. (a) Shore C hardness test; (b) water absorption by capillarity test; (c) determination of the coefficient of thermal conductivity; (d) ultrasound test.

Table 12. Physical characterization tests of plaster mortars.

| Mortar | Density (kg/m ³) | Water Absorption (cm) | Superficial Hardness (Ud. Shore C) | Young Modulus (MPa) | Thermal Conductivity (W/mK) |
|----------------|------------------------------|-----------------------|------------------------------------|---------------------|-----------------------------|
| E0.8 | 951.7 | 8.8 | 60.7 | 5753.4 | 0.26 |
| E0.8-NA | 1280.0 | 7.4 | 81.3 | 7134.2 | 0.42 |
| E0.8-NA-EPS | 1216.6 | 6.7 | 75.7 | 5599.6 | 0.33 |
| E0.8-NA-MW | 1277.3 | 6.0 | 79.3 | 6044.1 | 0.38 |
| E0.8-RAcon | 1241.7 | 7.8 | 80.7 | 6379.4 | 0.38 |
| E0.8-RAcon-EPS | 1174.0 | 7.1 | 72.7 | 4756.6 | 0.32 |
| E0.8-RAcon-MW | 1233.4 | 7.5 | 77.7 | 5121.3 | 0.36 |
| E0.8-RAmix | 1176.7 | 8.1 | 77.7 | 6117.0 | 0.36 |
| E0.8-RAmix-EPS | 1108.0 | 7.6 | 71.3 | 4491.2 | 0.27 |
| E0.8-RAmix-MW | 1168.7 | 7.7 | 73.7 | 5101.3 | 0.31 |

From the results presented in Table 12, it can be seen how all plaster mortars have a higher density than reference plaster E0.8 due to the incorporation of aggregates in their dosage. In addition, among the elaborated mortars, it can be observed how those that incorporate recycled ceramic aggregate are lighter and how density is reduced when EPS residues are added to the composition of mixtures [59]. On the other hand, absorption of water by capillarity is reduced in plaster mortars. Absorption is lower when mortars are made with natural aggregate compared to those made with recycled aggregate [43]. In addition, in this case, the incorporation of EPS in plaster mortars makes it difficult for the water to rise by capillarity in the materials studied.

In addition, the surface hardness is also increased with the incorporation of sand in plaster mixes, with mortars made with natural aggregate having greater hardness and density being lower in mortars that incorporate EPS. On the other hand, longitudinal Young's modulus determined by ultrasound is also increased in mortars. This is in accordance with the greater mechanical resistance to bending obtained by plaster mortars compared to the reference sample E0.8 [60]. This Young's modulus is greater in mortars made with natural aggregate compared to mortars that incorporate recycled aggregate, furthermore, it decreases when EPS is incorporated in the mortar manufacturing process, while when MW is incorporated, a significant decrease it is noticed. Finally, and in accordance with the results obtained for density, plaster mortars have a higher thermal conductivity than reference E0.8 plaster [61]. However, this thermal conductivity is reduced with the incorporation of thermal insulation residues in mortar mixtures, obtaining lower conductivity values for plaster mortars with EPS than those incorporating MW.

Table 13 shows the results obtained for the analysis of variance (ANOVA) performed for the physical characterization tests, while Table 14 shows the results obtained after performing the multiple range test.

As can be seen in Table 13, all the *p*-values were lower than the level of significance ($\alpha = 0.05$), which implies that both factors included in the design of experiments, type of aggregate and type of insulation, are statistically significant for all the response variables analysed in physical properties of plaster mortars.

Table 13. Analysis of variance (ANOVA) for flexural and compressive strength.

| Property | Source | Sum of Squares | Df | Mean Square | F-Ratio | <i>p</i> -Value |
|-----------------------------------|-------------------|----------------------|----|----------------------|---------|-----------------|
| Density (kg/m ³) | A: Aggregate | 52,245.9 | 2 | 26,122.9 | 106.72 | 0.0000 |
| | B: Insulating | 24,289.4 | 2 | 12,144.7 | 49.62 | 0.0000 |
| | AB: Interactions | 37,481.5 | 4 | 9,370.4 | 0.04 | 0.9969 |
| | Residual | 4406.0 | 18 | 244.778 | | |
| | Total (Corrected) | 80,978.7 | 26 | | | |
| Capillarity water absorption (cm) | A: Aggregate | 2.59556 | 2 | 1.29778 | 16.45 | 0.0001 |
| | B: Insulating | 1.72222 | 2 | 0.86111 | 10.92 | 0.0008 |
| | AB: Interactions | 0.04889 | 4 | 0.01222 | 0.15 | 0.9583 |
| | Residual | 1.42000 | 18 | 0.07889 | | |
| | Total (Corrected) | 5.78667 | 26 | | | |
| Superficial hardness(Shore C) | A: Aggregate | 94.889 | 2 | 47.444 | 19.41 | 0.0000 |
| | B: Insulating | 200.667 | 2 | 100.333 | 41.05 | 0.0000 |
| | AB: Interactions | 8.444 | 4 | 2.111 | 0.86 | 0.5044 |
| | Residual | 44.0 | 18 | 2.444 | | |
| | Total (Corrected) | 348.0 | 26 | | | |
| Young modulus (MPa) | A: Aggregate | 5.3566×10^6 | 2 | 2.6783×10^6 | 166.64 | 0.0000 |
| | B: Insulating | 1.2071×10^7 | 2 | 6.0356×10^6 | 375.53 | 0.0000 |
| | AB: Interactions | 67,449.1 | 4 | 16,862.3 | 1.05 | 0.4097 |
| | Residual | 289,302 | 18 | 16,072.4 | | |
| | Total (Corrected) | 1.7784×10^7 | 26 | | | |
| Thermal conductivity (W/mK) | A: Aggregate | 0.017785 | 2 | 0.008892 | 18.19 | 0.0000 |
| | B: Insulating | 0.028052 | 2 | 0.014026 | 28.69 | 0.0000 |
| | AB: Interactions | 0.001948 | 4 | 0.000487 | 1.00 | 0.4350 |
| | Residual | 0.008800 | 18 | 0.000489 | | |
| | Total (Corrected) | 0.056585 | 26 | | | |

Table 14. Multiple range test for physical properties.

| Property | Aggregate | LS Mean | Homogeneous Group | Insulating | LS Mean | Homogeneous Group |
|---------------------------------|-----------|---------|-------------------|------------|---------|-------------------|
| Density (kg/m ³) | RAmix | 1151.11 | X | EPS | 1166.22 | X |
| | RAcon | 1216.22 | X | MW | 1226.44 | X |
| | NA | 1258.00 | X | NI | 1232.78 | X |
| Water absorption (cm) | NA | 7.022 | X | EPS | 7.144 | X |
| | RAcon | 7.367 | X | MW | 7.367 | X |
| | RAmix | 7.778 | X | NI | 7.756 | X |
| Hardness Shore C | RAmix | 74.2 | X | EPS | 73.2 | X |
| | RAcon | 77.0 | X | MW | 76.9 | X |
| | NA | 78.8 | X | NI | 79.9 | X |
| Young modulus (MPa) | RAmix | 5236.48 | X | EPS | 4948.97 | X |
| | RAcon | 5418.96 | X | MW | 5422.24 | X |
| | NA | 6259.28 | X | NI | 6543.50 | X |
| Thermal Conduct. (W/mK) | RAmix | 0.3156 | X | EPS | 0.3089 | X |
| | RAcon | 0.3544 | X | MW | 0.3511 | X |
| | NA | 0.3778 | X | NI | 0.3878 | X |

Table 14 shows the composition of homogeneous groups after the multiple range test. This table shows how mortars with natural aggregate have a higher surface hardness and a higher Young's modulus, in accordance with Table 12, and how the incorporation of thermal insulation residues decreases the values obtained in these physical properties. In regard to thermal conductivity, mortars with recycled aggregate have better performance for this property, reducing this conductivity with the incorporation of thermal insulation waste and especially EPS [62]. Finally, with respect to apparent density, it can be seen how mortars with recycled aggregate are lighter. This affects the results of the compressive strength test, but it can also be seen that there are no differences between homogeneous groups in mortars with mineral wool insulation and without insulation. Likewise, in the absorption of water by capillarity, mortars with a natural aggregate present the best behaviour. It can also be observed how the incorporation of thermal insulation residues reduces the height reached by the water in this test with respect to mortars without insulation.

3.3. Tests on Prefabricated Plates and Blocks

3.3.1. Prefabricated Blocks

A possible use of these plaster mortars is the production of prefabricated blocks for construction. This section presents the results obtained after the tests carried out on blocks of $29 \times 11.5 \times 11.5$ cm, where the alveoli to lighten weight have been made by incorporating two recycled soft drink cans with a diameter of 6.5 cm and a height of 11.5 cm. The template and test blocks used are shown in Figure 5.

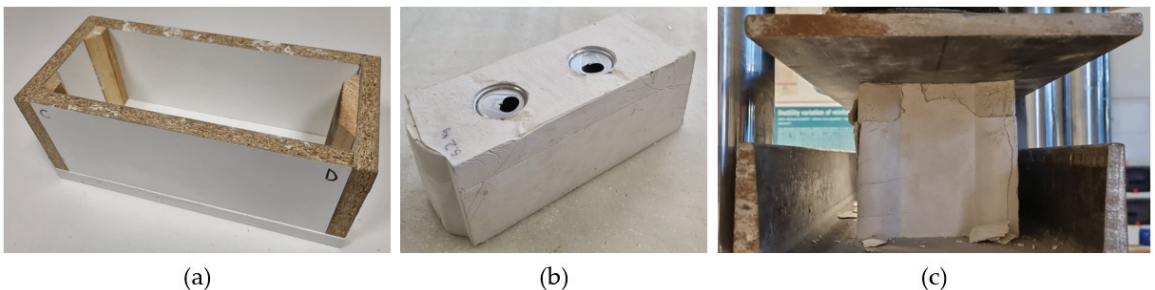


Figure 5. (a) Mould for the elaboration of prefabricated blocks; (b) type prefabricated block; (c) test of resistance to compression of the blocks.

The capillarity water absorption tests are shown in Table 15 for the different blocks produced.

Table 15. Initial rate of water absorption by capillarity according to the guidelines of the UNE-EN 722-1: 2011 standard.

| Aggregates Insulation Absorption (kg/mm ² min) | NA | | | RAcon | | | RAmix | | | E0.8 |
|---|------|------|------|-------|------|------|-------|------|------|------|
| | NI | EPS | MW | NI | EPS | MW | NI | EPS | MW | |
| | 4.89 | 4.53 | 4.68 | 5.17 | 4.95 | 5.12 | 5.36 | 5.14 | 5.31 | 7.03 |

As can be seen in Table 15, the incorporation of sand in plaster material reduces the water absorption coefficient compared to the reference material E.08. Mortars with the incorporation of RAMix presented the highest absorption coefficient [63], and, in all cases, the incorporation of thermal insulation residues has reduced this absorption coefficient.

Figure 6 shows the results obtained after the compressive strength test on mortar blocks.

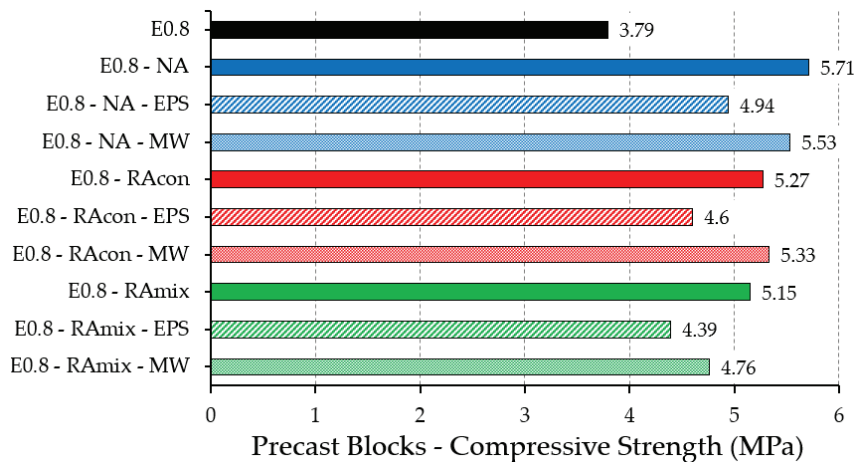


Figure 6. Results of compressive strength test on prefabricated blocks.

As can be seen in Figure 6, all plaster mortar blocks exceeded in their mechanical capacity the compressive strength of the reference block E0.8. The results are in accordance with those presented in Figure 3, where mortars made with natural aggregate have higher resistance than mortars made with RAcon, and these in turn have higher resistance than those made with RAMix. It is also observed how the incorporation of thermal insulation residues reduces compressive strength, especially in the case of expanded polystyrene with graphite. Finally, it should be noted that in all the cases tested, plaster mortar presented good adherence to the cans used to make the alveoli, even so, in all the blocks the effect of the breakage in the core of the precast was observed, coinciding with these alveoli that are the most fragile areas and therefore the preferred points of breakage.

3.3.2. Prefabricated Plates

This section includes the results derived from the tests on 50 × 30 × 2 cm mortar plates. Figure 7 shows the test method used.

These tests on plates and panels are of special importance to study the behaviour of plaster mortars made in prefabricated pieces with dimensions close to the real ones used in the study, as well as to evaluate their deformation capacity under possible alterations of the structure [64]. The results obtained for the different types of plates made in this study are shown in Figure 8.

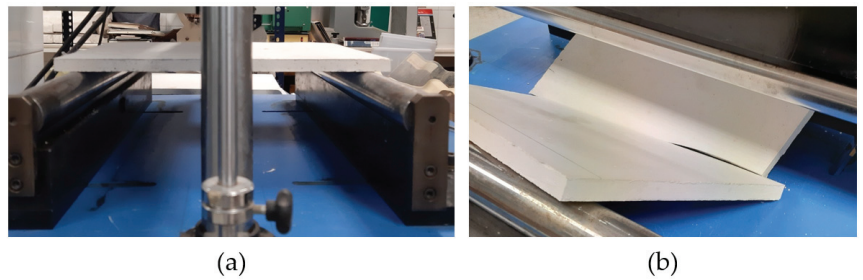


Figure 7. Flexural strength test on prefabricated panels. (a) Plate before the test; (b) plate after assay.

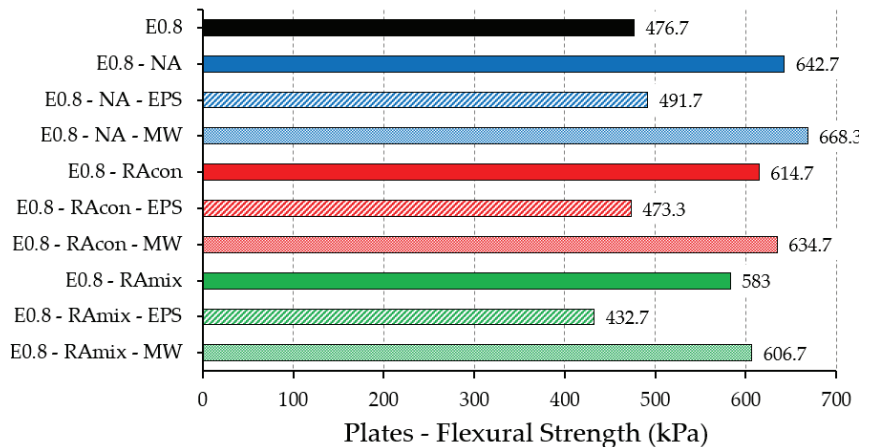


Figure 8. Results of flexural strength test on prefabricated plates.

Figure 8 shows how flexural strength is reduced in plates and panels with dimensions close to reality, in comparison with standardized RILEM $4 \times 4 \times 16$ cm specimens studied in Section 3.1. Likewise, it is observed how flexural strength is increased by incorporating aggregates in the matrix of plaster material. In addition, and as expected, mortars that incorporate mineral wool fibres have a greater resistance to bending and are more suitable for the manufacture of prefabricated panels and plates. On the other hand, mortars with the incorporation of expanded polystyrene residue with graphite showed lower flexural strengths, and mortars made with RAMix-EPS show strengths below the reference E0.8 plaster.

The results obtained in this research should be understood as a characterization of materials tested. If these materials were to be used in real on-site prefabricated elements, mechanical tests should be carried out on pieces with the specific geometry of the slabs and panels in order to consider the size effect. In addition, it is recommended to use these materials in interiors and not as cladding mortars on external facades. However, it would be advisable in future studies to carry out research that considers the durability of these materials, such as: humidity and drying cycles, total water absorption, thermal shock, etc. Thus, a future line of research to improve the technical performance of these materials involves the incorporation of reinforcement fibres in plaster matrix.

4. Conclusions

From the results obtained in this work, it can be concluded that recycled aggregates and thermal insulation residues for the elaboration of plaster mortars can be applied in building and are more respectful to the environment. In particular, the following conclusions were reached:

- With regard to the mechanical properties, these are implemented in plaster mortars with respect to the reference material E0.8. Mortars with natural aggregate offer better mechanical behaviour than mortars with recycled aggregate, where mortars with RAMix obtained the lowest compressive and flexural strength. In the specific case of flexural strength, it has been possible to observe the positive effect offered by the incorporation of mineral wool insulation fibre, increasing the flexural strength of mortars. In turn, compressive strength is reduced when EPS residues are incorporated into the plaster mortar matrix.
- The density of plaster mortars is much higher than that obtained by the reference plaster E0.8, although the incorporation of EPS waste manages to lighten the weight of these construction materials.
- The incorporation of EPS residues in the manufacture of mortars reduces the height reached by the water in the capillary absorption test in plaster mortars. Mortars that presented the greatest absorption were those made with RAMix. Any of them exceeded the reference E0.8 plaster values.
- In turn, mortars with the incorporation of EPS residue presented the lowest coefficient of thermal conductivity. Additionally, in all cases, it was possible to observe the beneficial effects of incorporating thermal insulation residues to improve this property of mortars.
- In terms of surface hardness and Young's modulus, plaster mortars made with natural aggregate obtained the best results. In addition, in all cases, the incorporation of thermal insulation residues reduces the values obtained for these physical properties.
- Regarding the viability of plaster mortars to make plates and panels, it has been possible to verify how the incorporation of mineral wool fibre in its composition improves the final resistance to bending of the precast.
- Finally, some prefabricated blocks of plaster mortar of our own design have been made. These presented a good resistance to compression and the best results were obtained for mortars with natural sand and without thermal insulation residues.

In general, it can be seen how plaster mortars have good technical performance for their application in building, and how the incorporation of recycled aggregates and thermal insulation residues improves the mechanical and physical properties of traditional plasters. The performance of this type of study is in line with the Sustainable Development Goals set by the United Nations Organization, supporting a more efficient use of natural resources and a decrease in the consumption of raw materials.

Author Contributions: Conceptualization, D.F. and M.Á.; methodology, D.F.; software, D.F. and P.S.; validation, P.S., D.F. and A.Z.; formal analysis, D.F. and P.S.; investigation, D.F. and M.Á.; resources, D.F.; data curation, D.F. and P.S.; writing—original draft preparation, D.F. and A.Z.; writing—review and editing, M.Á.; visualization, A.Z.; supervision, D.F.; project administration, D.F.; funding acquisition, D.F. All authors have read and agreed to the published version of the manuscript.

Funding: This research was funded by URSA Ibérica Aislantes, S.A., grant number P2054090068.

Institutional Review Board Statement: Not applicable.

Informed Consent Statement: Not applicable.

Data Availability Statement: Not applicable.

Acknowledgments: The authors would like to acknowledge the collaboration of the company URSA Ibérica Aislantes, SA, through the project P2054090068 "Thermo-acoustic solutions in housing renovation, simulation, and monitoring", which has served as a support and initiative framework for the realization of this research.

Conflicts of Interest: The authors declare no conflict of interest.

References

1. McLellan, R.; Iyengar, L.; Jeffries, B.; Oerlemans, N. *Living Planet. Report 2014: Species and Spaces, People and Places*; WWF International: Gland, Switzerland, 2014.
2. Vidales, A.; del Rio, M.; Atanes-Sánchez, E.; Piña, C.; Viñas, C. Analysis of the feasibility of the use of CDW as a low-environmental impact aggregate in conglomerates. *Constr. Build. Mater.* **2018**, *178*, 83–91. [[CrossRef](#)]
3. Lozano-Cutanda, B.; Turrillas, A.; Juan-Cruz, C. *Administración y Legislación Ambiental*, 11th ed.; Dykinson: Madrid, Spain, 2020.
4. Hossain, U.; Antwi-Afari, P.; Thomas, S.; Amor, B. Circular economy and the construction industry: Existing trends, challenges, and prospective framework for sustainable construction. *Renew. Sustain. Energy Rev.* **2020**, *130*, 109948. [[CrossRef](#)]
5. Shahzad Aslam, M.; Huang, B.; Cui, L. Review of construction and demolition waste management in China and USA. *J. Environ. Manag.* **2020**, *264*, 110445. [[CrossRef](#)] [[PubMed](#)]
6. Zhang, C.; Hu, M.; Di Maio, F.; Sprecher, B.; Yang, X.; Tukker, A. An overview of the waste hierarchy framework for analyzing the circularity in construction and demolition waste management in Europe. *Sci. Total Environ.* **2022**, *803*, 149892. [[CrossRef](#)] [[PubMed](#)]
7. Kabirifar, K.; Mojtahedi, M.; Changxin Wang, C.; Tam, V.W.Y. A conceptual foundation for effective construction and demolition waste management. *Clean. Eng. Technol.* **2020**, *1*, 100019. [[CrossRef](#)]
8. Monier, V.; Hestin, M.; Trarieux, M.; Mimid, S.; Domröse, L.; Van Acoleyen, M.; Hjerp, P.; Mudgal, S. *Study on the Management of Construction and Demolition Waste in the EU*; Final Report for the European Commission; European Commission: Brussels, Belgium, 2011.
9. Sáiz Martínez, P.; González Cortina, M.; Fernández Martínez, F.; Rodríguez Sánchez, A. Comparative study of three types of fine recycled aggregates from construction and demolition waste (CDW), and their use in masonry mortar fabrication. *J. Clean. Prod.* **2016**, *118*, 162–169. [[CrossRef](#)]
10. Bicer, A. Investigation of waste EPS foams modified by heat treatment method as concrete aggregate. *J. Build. Eng.* **2021**, *42*, 102472. [[CrossRef](#)]
11. Shooshtarian, S.; Maqsood, T.; Caldera, S.; Ryley, T. Transformation towards a circular economy in the Australian construction and demolition waste management system. *Sustain. Prod. Consum.* **2022**, *30*, 89–106. [[CrossRef](#)]
12. Waskow, R.; Gonçalves Maciel, V.; Tubino, R.; Passuello, A. Environmental performance of construction and demolition waste management strategies for valorization of recycled coarse aggregate. *J. Environ. Manag.* **2021**, *295*, 113094. [[CrossRef](#)]
13. Bentchikou, M.; Bouriah, S.; Hamdane, N.; Debieb, F.; Boukendakdji, O. Comparative study of the properties of mortars with recycled glass aggregates incorporated by addition and substitution. *Energy Procedia* **2017**, *139*, 499–504. [[CrossRef](#)]
14. Saiz, P.; Ferrández, D.; Morón, C.; Payan, A. Comparative study of the influence of three types of fibre in the shrinkage of recycled mortar. *Mater. Construcción* **2018**, *68*, e168. [[CrossRef](#)]
15. Liang, K.; Hou, Y.; Sun, J.; Li, X.; Bai, J.; Tian, W.; Liu, Y. Theoretical analysis of water absorption kinetics of recycled aggregates immersed in water. *Constr. Build. Mater.* **2021**, *302*, 124156. [[CrossRef](#)]
16. Rosca, B. Comparative aspects regarding concrete of structural grade made with recycled brick aggregate with / without fine particles from crushing. *Mater. Today Proc.* **2022**, in press. [[CrossRef](#)]
17. Santos Jiménez, M.R. *Reciclaje de Residuos de Construcción y Demolición (RCD) de Tipocerámico Para Nuevos materiales de Construccionsostenibles*. Ph.D. Thesis, E.T.S. de Edificación, Universidad Politécnica de Madrid, Madrid, Spain, 2018.
18. Del Rio, M.; Vidales, A.; Piña, C.; Vitiello, V.; Santa-Cruz, J.; Castelluccio, R. A review of the research about gypsum mortars with waste aggregate. *J. Build. Eng.* **2022**, *45*, 103338. [[CrossRef](#)]
19. Del Rio, M.; Santa-Cruz, J.; Villoria, P.; Santos, R.; González, M. Eco plaster mortars with addition of waste for high hardness coatings. *Constr. Build. Mater.* **2018**, *158*, 649–656. [[CrossRef](#)]
20. Ferrándiz-Mas, V.; García-Alcoel, E. Physical and mechanical characterization of Portland cement mortars made with expanded polystyrene particles addition (EPS). *Mater. Construcción* **2012**, *62*, 547–566. [[CrossRef](#)]
21. Herrero, S.; Mayor, P.; Hernández-Olivares, F. Influence of proportion and particle size gradation of rubber from end-of-life tires on mechanical, thermal and acoustic properties of plaster-rubber mortars. *Mater. Des.* **2013**, *47*, 633–642. [[CrossRef](#)]
22. San Antonio, A.; Del Rio, M.; Viñas, C.; Villoria, P. Lightweight material made with gypsum and extruded polystyrene waste with enhanced thermal behaviour. *Constr. Build. Mater.* **2015**, *93*, 57–63. [[CrossRef](#)]
23. Fantilli, A.P.; Sicardi, S.; Dotti, F. The use of wool as fiber-reinforcement in cement-based mortar. *Constr. Build. Mater.* **2017**, *139*, 562–569. [[CrossRef](#)]
24. Piña, C.; Del Rio, M.; Viñas, C.; Vidales, A.; Kosior-Kazberuk, M. Analysis of the mechanical behaviour of the cement mortars with additives of mineral wool fibres from recycling of CDW. *Constr. Build. Mater.* **2019**, *210*, 56–62. [[CrossRef](#)]
25. Piña, C.; Vidales, A.; Serrano, R.; del Rio, M.; Atanes-Sánchez, E. Analysis of fire resistance of cement mortars with mineral wool from recycling. *Constr. Build. Mater.* **2020**, *265*, 120349. [[CrossRef](#)]
26. Santamaría, I.; Alameda, L.; Gutiérrez, S.; Calderón, V.; Rodríguez, A. Design and Characterization of Gypsum Mortars Dosed with Polyurethane Foam Waste PFW. *Materials* **2020**, *13*, 1497. [[CrossRef](#)] [[PubMed](#)]
27. Santa-Cruz-Astorqui, J.; Del-Río-Merino, M.; Villoria-Sáez, P.; Porrás-Amores, C. Analysis of the viability of prefabricated elements for partitions manufactured with plaster and EPS from waste recycling. *DYNA* **2019**, *94*, 415–420.
28. Alameda, L.; Calderón, V.; Junco, C.; Rodríguez, A.; Gadea, J.; Gutiérrez-González, S. Characterization of gypsum plasterboard with polyurethane foam waste reinforced with polypropylene fibers. *Mater. Constr.* **2016**, *66*, 100. [[CrossRef](#)]

29. Dolezelova, M.; Krejsova, J.; Scheinherrova, L.; Vimmrova, A. Comparison of structure and properties of gypsum mortars with different types of aggregates. *IOP Conf. Series Mater. Sci. Eng.* **2021**, *1039*, 012009. [[CrossRef](#)]
30. Commission, E. (Ed.) Directive 2008/98/EC of the European Parliament and of the Council on Waste. *Off. J. Eur. Union* **2008**, *312*, 3–30.
31. Boquera, L.; Olacia, E.; Fabiani, C.; Pisello, A.L.; D'Alessandro, A.; Ubertini, F.; Cabeza, L.F. Thermo-acoustic and mechanical characterization of novel bio-based plasters: The valorisation of lignin as by-product from biomass extraction for green building applications. *Constr. Build. Mater.* **2021**, *278*, 122373. [[CrossRef](#)]
32. San Antonio González, A.; del Río Merino, M.; ViñasArrebola, C.; VilloriaSaez, P. *Procedimiento Para la Obtención de un Material de Construcción a Base de Yeso*; REF: ES 2 515 640 A1; Oficina Española de Patentes y Marcas: Madrid, Spain, 2014.
33. Strydom, C.A.; Potgieter, J.H. Dehydration behaviour of a natural gypsum and a phosphogypsum during milling. *Thermochim. Acta* **1999**, *332*, 89–96. [[CrossRef](#)]
34. UNE-EN 13279-1:2009; Gypsum Binders and Gypsum Plasters—Part 1: Definitions and Requirements. Spanish Association for Standardization: Madrid, Spain, 2009.
35. San-Antonio-González, A.; Merino, M.D.R.; Arrebola, C.V.; Villoria-Sáez, P. Lightweight material made with gypsum and EPS waste with enhanced mechanical strength. *J. Mater. Civ. Eng.* **2015**, *28*. [[CrossRef](#)]
36. Piña, C.; Atanes-Sánchez, E.; del Río Merino, M.; ViñasArrebola, C.; Vidales, A. Feasibility of the use of mineral wool fibres recovered from CDW for the reinforcement of conglomerates by study of their porosity. *Constr. Build. Mater.* **2018**, *191*, 460–468. [[CrossRef](#)]
37. UNE-EN 13139:2003; Aggregates for Mortar. Spanish Association for Standardization: Madrid, Spain, 2003.
38. UNE-EN 933-1:2012; Tests for Geometrical Properties of Aggregates—Part 1: Determination of Particle Size Distribution—Sieving Method. Spanish Association for Standardization: Madrid, Spain, 2012.
39. UNE-EN 146404:2018; Aggregates for Concrete. Determination of the Coefficient of Friability of the Sands. Spanish Association for Standardization: Madrid, Spain, 2018.
40. UNE-EN 1097-3:1999; Tests for Mechanical and Physical Properties of Aggregates—Part 3: Determination of Loose Bulk Density and Voids. Spanish Association for Standardization: Madrid, Spain, 1999.
41. UNE-EN 1097-6:2014; Tests for Mechanical and Physical Properties of Aggregates—Part 6: Determination of Particle Density and Water Absorption. Spanish Association for Standardization: Madrid, Spain, 2014.
42. Martínez, I.; Etxeberria, M.; Pavón, E.; Díaz, N. A comparative analysis of the properties of recycled and natural aggregate in masonry mortars. *Constr. Build. Mater.* **2013**, *49*, 384–392. [[CrossRef](#)]
43. Yedra, E.; Ferrández, D.; Morón, C.; Saiz, P. New test methods to determine water absorption by capillarity. Experimental study in masonry mortars. *Constr. Build. Mater.* **2022**, *319*, 125988. [[CrossRef](#)]
44. Morón, A.; Ferrández, D.; Saiz, P.; Morón, C. Experimental Study with Cement Mortars Made with Recycled Concrete Aggregate and Reinforced with Aramid Fibers. *Appl. Sci.* **2021**, *11*, 7791. [[CrossRef](#)]
45. Jiménez, J.R.; Ayuso, J.; López, M.; Fernández, J.M.; de Brito, J. Use of fine recycled aggregates from ceramic waste in masonry mortar manufacturing. *Constr. Build. Mater.* **2013**, *40*, 679–690. [[CrossRef](#)]
46. Saiz Martínez, P. Utilización de Arenas Procedentes de Residuos de Construcción y Demolición, RCD, en la Fabricación de Morteros de Albañilería. Ph.D. Thesis, E.T.S. de Edificación, Universidad Politécnica de Madrid, Madrid, Spain, 2015.
47. Bustos García, A. Morteros con Propiedadesmejoradas de Ductilidad por Adición de Fibras de Vidrio, Carbono y Basalto. Ph.D. Thesis, E.T.S. de Edificación, Universidad Politécnica de Madrid, Madrid, Spain, 2018. [[CrossRef](#)]
48. Canal de Isabel II. *Informe Anual Sobre la Calidad del Agua en Madrid*; Canal de Isabel II: Madrid, Spain, 2012.
49. UNE-EN 12379-2:2014; Gypsum Binders and Gypsum Plasters—Part 2: Test Methods. Spanish Association for Standardization: Madrid, Spain, 2014.
50. UNE 102042: 2014; Gypsum Plasters. Other Test Methods. Spanish Association for Standardization: Madrid, Spain, 2014.
51. UNE-EN 459-2:2011; Building Lime—Part 2: Test Methods. Spanish Association for Standardization: Madrid, Spain, 2011.
52. UNE-EN 12859:2012; Gypsum Blocks—Definitions, Requirements, and Test Methods. Spanish Association for Standardization: Madrid, Spain, 2012.
53. UNE-EN 772-11:2011; Methods of Test for Masonry Units—Part 11: Determination of Water Absorption of Aggregate Concrete, Autoclaved Aerated Concrete, Manufactured Stone, and Natural Stone Masonry Units due to Capillary Action and the Initial Rate of Water Absorption of Clay Masonry Units. Spanish Association for Standardization: Madrid, Spain, 2011.
54. Peña, D. *Regresión y Diseño de Experimentos*; Alianza Editorial: Madrid, Spain, 2010; ISBN 9788420693897.
55. Aocharoen, Y.; Chotickai, P. Compressive mechanical properties of cement mortar containing recycled high-density polyethylene aggregates: Stress-strain relationship. *Case Stud. Constr. Mater.* **2021**, *15*, e00752. [[CrossRef](#)]
56. Pedergnana, M.; Elias-Ozkan, S.T. Impact of various sands and fibres on the physical and mechanical properties of earth mortars for plasters and renders. *Constr. Build. Mater.* **2021**, *308*, 125013. [[CrossRef](#)]
57. Cardinale, T.; Arleo, G.; Bernardo, F.; Feo, A.; De Fazio, P. Thermal and mechanical characterization of panels made by cement mortar and sheep's wool fibres. *Energy Procedia* **2017**, *140*, 159–169. [[CrossRef](#)]
58. Ferrández, D.; Saiz, P.; Morón, C.; Atanes-Sánchez, E. Comparative analysis of fibre-reinforced plasters for the production of precast elements. *DYNA* **2020**, *95*, 333–338. [[CrossRef](#)]

59. González-Madariaga, F.J.; Lloveras-Macia, J. EPS (expanded polystyrene) recycled bends mixed with plaster or stucco, some applications in building industry. *Inf. Construcción* **2008**, *60*, 34–43. [[CrossRef](#)]
60. Rosell, J.R.; Cantalapiedra, I.R. Simple method of dynamic young's modulus determination in lime and cement mortars. *Mater. Construcción* **2011**, *61*, 39–48. [[CrossRef](#)]
61. VilloriaSáez, P.; del Río Merino, M.; Sorrentino, M.; Porras Amores, C.; Santa Cruz Astorqui, J.; ViñasArrebola, C. Mechanical Characterization of Gypsum Composites Containing Inert and Insulation Materials from Construction and Demolition Waste and Further Application as A Gypsum Block. *Materials* **2020**, *13*, 193. [[CrossRef](#)] [[PubMed](#)]
62. Guna, V.; Yadav, C.; Maithri, B.R.; Ilangovan, M.; Touchaleaume, F.; Saulnier, B.; Grohens, Y.; Reddy, N. Wool and coir fiber reinforced gypsum ceiling tiles with enhanced stability and acoustic and thermal resistance. *J. Build. Eng.* **2021**, *41*, 102433. [[CrossRef](#)]
63. Morón, C.; Ferrández, D.; Saiz, P.; Yedra, E. Measuring system of capillary rising damp in cement mortars. *Measurement* **2019**, *135*, 252–259. [[CrossRef](#)]
64. Santa Cruz Astorqui, J. Estudio Tipológico, Constructivo y Estructural de las Casas de Corredor en Madrid. Ph.D. Thesis, E.T.S. de Edificación, Universidad Politécnica de Madrid, Madrid, Spain, 2012.

Article

Utilization of Industrial Ferronickel Slags as Recycled Concrete Aggregates

Petros Petrounias ^{1,2,*}, Aikaterini Rogkala ¹, Panagiota P. Giannakopoulou ¹, Angeliki Christogerou ³, Paraskevi Lampropoulou ¹, Spyridon Liogris ⁴, Petros Koutsovitis ¹ and Nikolaos Koukouzas ²

¹ Section of Earth Materials, Department of Geology, University of Patras, 26504 Patras, Greece; krogkala@upatras.gr (A.R.); peny_giannakopoulou@windowslive.com (P.P.G.); p.lampropoulou@upatras.gr (P.L.); pkoutsovitis@upatras.gr (P.K.)

² Chemical Process & Energy Resources Institute, Centre for Research & Technology Hellas (CERTH), 6th km Charilaou-Thermi Rd, 60361 Maroussi, Greece; koukouzas@certh.gr

³ Department of Chemical Engineering, University of Patras, Caratheodori 1, 26504 Patras, Greece; angiechristo@upatras.gr

⁴ Wasco Coatings Europe BV, Vi.Pe. Thisvis, Domvrainia, 32010 Viotia, Greece; spyridon.liogris@wascoenergy.com

* Correspondence: geo.plan@outlook.com

Abstract: The scope of this study focuses on the use of two different types of industrial byproducts such as slags (FeNi and Electric Arc Furnace slag) combined with natural sand as concrete aggregates as well as the evaluation of their suitability on the final physicochemical behavior of the produced concrete specimens. For this reason, twelve concrete specimens were prepared using variable concentrations of these slags which were compared to concrete specimens made by natural rocks as aggregates (limestones). The mineralogical, petrographic, chemical and morphological characteristics of these raw materials were related to the physicochemical characteristics of the produced concrete specimens. Those concrete specimens containing aggregates of higher amount of Electric Arc Furnace slags seems to present better mechanical strength both in 7 and in 28 days of curing regarding the other mixtures and regarding the specimens made by natural rocks as aggregates (limestones). This is due to the mineralogical, textural and morphological characteristics of the tested slags, which lead to a better bonding between them and the cement paste making them at the same time a promising alternative in the production of green concrete for construction applications. The compact texture of slags is responsible for the stronger bonding with the aggregates in relation to the unevenly distributed porosity of the natural aggregates. Wüstite presents negative effect on the final mechanical strength of concrete specimens which is documented both by the microscope images and by the three-dimensional study of the produced concretes.

Keywords: industrial by products; slags; recycled concrete; recycled aggregates

Citation: Petrounias, P.; Rogkala, A.; Giannakopoulou, P.P.; Christogerou, A.; Lampropoulou, P.; Liogris, S.; Koutsovitis, P.; Koukouzas, N. Utilization of Industrial Ferronickel Slags as Recycled Concrete Aggregates. *Appl. Sci.* **2022**, *12*, 2231. <https://doi.org/10.3390/app12042231>

Academic Editors: Laurent Daudeville, Carlos Morón Fernández and Daniel Ferrández Vega

Received: 16 January 2022

Accepted: 17 February 2022

Published: 21 February 2022

Publisher's Note: MDPI stays neutral with regard to jurisdictional claims in published maps and institutional affiliations.



Copyright: © 2022 by the authors. Licensee MDPI, Basel, Switzerland. This article is an open access article distributed under the terms and conditions of the Creative Commons Attribution (CC BY) license (<https://creativecommons.org/licenses/by/4.0/>).

1. Introduction

Concrete is the most used and cost-effective construction material in the world with an annual production of about 33 billion tons [1], and in view of the global population growth [2], the usage trend for building new infrastructures is estimated to increase up to 6% [3]. The basic components of concrete are made up of cement—a mixture of clinker and gypsum, aggregates and water, all of whom significantly affect the workability, durability and mechanical performance of the final product. From the environmental point of view, the cement production technology has a strong impact on energy consumption and increased CO₂ levels, ~8% of the global anthropogenic emissions [4], mainly associated with the high calcination temperature (~1450 °C) of raw materials (limestone and clay minerals) necessary for the cement clinker formation. The latter has the role of the hydraulic binder and is by far the most important ingredient in concrete, constituting about 7% to 15% of

its total volume. Aggregates, on the other hand, also raise environmental concerns related with their extraction and processing as they make up more than the half of the concrete's volume, approximately 60–75% [5]. Moreover, the quality of the hardened concrete depends upon the suitable use of both fine and coarse aggregates, usually consisting of natural sand and gravel or crushed stone and their efficient bond with the surrounding cement paste. Bearing all this in mind, it is obvious that for the huge concrete volumes produced every year, vast amounts of natural resources are required both for aggregates and cement leading to severe environmental problems.

Based on the ecological footprint caused by the unsustainable linear production model—take, make and dispose—which is clearly impacting climate change, waste management and natural resource depletion, a worldwide challenge have become even more apparent in driving change. Accordingly, a new legally binding agreement was adopted in December 2015 by the United Nations known as the Paris Climate Change Agreement aiming to reduce the greenhouse gas emissions on a global base [6]. The objective of the net-zero CO₂ emissions by 2050–2070 applying to heavy industry as well, including the steel, cement, chemicals and other materials sectors. Under this prism, the circular economy initiatives published by the European Commission in March 2020 [7] can certainly offer successful and realistic decarbonization pathways not only in overcoming strict legislation and financial burden, but also in the development of a sustainable future with considerable social and economic benefits in the upcoming years.

One of the targets of the circular economy action plan is waste recycling and industrial by-products utilization, a practice that cement manufacturing industries has already made progress on either through the implementation of different production processes or as well through the adoption of synergy practices.

A great example of the industrial symbiosis is the steel slags valorization that have attracted the construction sector during the last decades as they have the potential to be used as partial replacement of cement clinker due to their pozzolanic characteristics, but as well as aggregates replacement in the formation of concrete. The latter application field though is more favorable as little, or no processing of the aggregates is required against the use as a binder material where grinding of these by-products is prerequisite and associated with high energy consumptions [3]. Thereafter, different types of coarse and/or fine slag aggregates have been investigated for the manufacturing of eco-friendly concrete which may find use in various construction applications such as asphaltic pavement structures, road bases and surfaces or in other concrete shaped applications, e.g., breakwater blocks and dams.

Moreover, the European Waste Framework Directive [8,9] makes clear the importance of industrial by-products valorization such as iron and steel slag aggregates that contributes to waste minimization and resource conservations. Ferrous containing slags, are silicate melts that are formed during the manufacturing of crude steel and crude iron, mainly due to the combination of slagging agents and fluxes used to remove impurities from iron ore and other metal feeds of the smelting furnaces [10]. The hot slags are tapped from the liquid metal and transported to a slag damp where they are stockpiled, after cooling (open-air or water spraying) and processed to solid material. In Europe, ~45 Mt of blast furnace slags and steel slags were produced in 2018 [11], whereas in the U.S., steel slag production is estimated in the range of 8 to 12 Mt [10]. The most common produced metallurgical slags are steel, ferronickel, copper, lead, zinc, phosphorous and stainless steel slags. An important parameter affecting the physical and chemical properties of the slag by-products is by far the source ore and the metal processing method used by each country. Greece for example is the one of the largest ferronickel (FeNi) producer in Europe utilizing the domestic laterite ore deposits [12]. The pyrometallurgical process comprises of two main stages: (a) preheating of the feeding materials in rotary kilns and (b) reduction and smelting (1600–1700 °C) of output calcine in electric arc furnaces (EAFs). This process leads to the production of two co-existing materials: the ferronickel product and the slag. Given the

fact that the EAF slag produced make up about 80–90% of the feeds material's mass [13], it is apparent that large quantities are generated, which concerns steel production industries.

During the past decades, extensive work has been published on the utilization of steel slags as alternative aggregates in Portland concretes. Depending on the physical characteristics of the slag aggregates, e.g., density, granulometric size and shape, and the application field of the final product interesting findings are reported by scientists with emphasis on mechanical, physico-chemical and environmental properties of slag-containing concrete. Durability studies of concrete mixes containing electric arc furnace (EAF) slag aggregates include systematic tests of compressive strength, water penetration, freeze–thaw cycles, leaching tests and chemical reactivity of the slag with the surrounding cement components [3,14–17]. For example, Manso et al. [18] found that the high porosity of EAF slag used in this work reveals a low-quality concrete in terms of freezing resistance, thus suggesting the additional use of specific admixtures. Leaching tests, on the other hand, showed a beneficial cloistering effect of fluorides and chromium in the concrete mix. In a recent study, conducted by Chatzopoulos et al. [19], conventional sand and gravel were replaced by EAF and ladle furnace (LD) slags, individually or in combination, resulting in the production of a durable concrete. From the 14 test samples prepared, all quality indexes investigated remained either stable or improved in comparison to the reference concrete. The most efficient mixture was achieved when sand was replaced with 30% by volume of EAF and LD slag sand, respectively, and gravel by 50% of EAF gravel aggregates leading to concretes with reduced carbonate and chloride penetration. However, granulated blast furnace slags (GBFS) attract also special scientific interest as due to their finer grain size they can be utilized instead of natural fine aggregates (e.g., river sand). Patra et al. [20] for examples state that incorporation of GBFS (<5 mm) up to 40% was feasible, whereas higher percentages (up to 60%) lead to reduced workability of the concrete mixes attributed to the higher water absorption of GBFS. Nevertheless, the authors suggest the use of superplasticizers to achieve the appropriate workability as compressive strength shows increased values (up to 45 MPa) in case of 60% replacement most probably due to the pozzolanic effect of the steel slag used. An interesting experimental approach on the production of an eco-friendly concrete was done by Anastasiou et al. [21] aiming on the maximum valorization of alternative raw materials. Fly ash was incorporated as cement replacement, EAF slag and recycled aggregates from construction demolition wastes (CDW) as coarse and fine aggregates, respectively. They found that the use of CDW increases the porosity of concrete with subsequent decrease in strength and durability compared to a reference mix, while the synergy of CDW with EAF slag partly overcomes these drawbacks reaching compressive strength values of about 30 MPa at 28 days. In spite the poor bonding between aggregate-binder, the formed concrete might be used in lower-demand applications. Blended concretes have been also studied using FeNi slag aggregates in different grain sizes and by substituting ordinary binding materials as presented for example by Kim et al. [22]. They found that early strength of the test samples was affected, but with time hydration reaction can overcome this issue. According to Sun et al. [23], natural aggregates can feasibly be replaced by FeNi slag as the final concrete mix conforms with type C50 due to the obtained mechanical strength reaching 55 MPa at 28 days of curing. However, best engineering results are observed with the use of blast furnace slag as well. Lately, Nuruzzaman et al. [24] investigated the combined use of FeNi slag and ground FeNi slag as supplementary binder for enhancing the sustainability of self-compacting concrete. After assessing strength, permeability and microstructure of the produced concrete samples, they came to the conclusion that a replacement of cement up to 30% by ground FeNi slag and, respectively, of sand by 50% replacement of FeNi slag is feasible as they presented high durability.

There is still room for further research on the production of eco-friendly concretes from different types of slags and/or other industrial by-products in relation to the technical properties of the new concrete mixes as for sure environmental benefits are anticipated. As the economy and the smelting industry developed rapidly, the quantity of smelter slag has

been increasing for a long time. Common smelting furnace slag includes steel smelting slag, red mud, copper smelting slag, lead slag, ferronickel slag, sulfuric acid slag, etc. Approximately 30 million tons of ferronickel slag are emitted each year, accounting for more than a fifth of the global production [3,25,26]. The large stockpiles of nickel slag not only occupy land and pollute the environment, but also bring about severe challenges to the sustainable development of the nickel smelting industry [27,28]. Furthermore, it is essential to develop and utilize smelter slag through environmental-friendly technologies [29,30]. Different types of industrial by-products were studied in the past few decades in order to find suitable alternatives of natural sand in concrete. Blast furnace slag, steel slag, copper slag, foundry slag and ferronickel slag are the most common types of by-product slags that can be used as fine aggregate in concrete. Rashad et al. [31] showed that the use of blast furnace slag as a replacement of natural sand improved the compressive strength of mortar. The physical and chemical properties of the by-product slag can vary significantly depending on the type of the ore, the smelting process and temperature, and the cooling method. The amount of literature available on the use of ferronickel slag in concrete is very limited. Sato et al. [32] pointed out that freeze–thaw resistance of concrete decreased with the use of 50% ferronickel slag replacing natural coarse aggregate. The reason was attributed to the increase of bleeding and the resulting reduction in air content of concrete with the increase of ferronickel slag. Tomosawa et al. [33] pointed out a deleterious expansion due to the alkali-silica reaction of concrete containing 50% ferronickel slag aggregate and recommended to use low alkali cement to mitigate this expansion. Improved frost resistance of concrete was reported by the partial or full replacement of sand by ferronickel slag aggregate [34,35] showed that ferronickel slag could be used as a suitable replacement of natural aggregates in hot mix asphalt and in base and sub-base layers of roads. It was also reported that ferronickel slag could be used to make composites with waste glass. These composites were described as safe to use as any toxic elements in the slag were chemically locked in the composite [36].

It can be observed from the above literature review that utilization of ferronickel slags from different sources was attempted in different applications. The aim of this study is double. From the one hand is the significant improvement of the sustainability of concrete production by reducing the use of natural aggregates and simultaneously by the increase of use of industrial by-products (i.e., slags) enhances the green policy of industries as well as their financial benefits. On the other hand, by the prediction of the concrete behavior through the tools of petrography and mineralogy the human footprint on the environment reduces. A comprehensive study is necessary in order to understand the properties of concrete using these aggregates. The workability of fresh concrete, physic-mechanical properties of hardened concrete using these aggregates as a supplementary cementing material are evaluated in this study. Thus, this work presents an innovative study on a green concrete using two industrial by-products evaluating the engineering properties.

2. Materials and Methods

The present study emerged after the constructive cooperation of research institutions with industrial companies having as main goal their interconnection and in order to bring significant results both in constructions and in the wider society through the reuse of slags as high-quality aggregates.

2.1. Materials

In this study, the morphological and mechanical characteristics of alternative aggregates (slags) of variable concentrations were evaluated for their use as concrete aggregates and linked with the performance of the resultant produced high-strength concrete specimens. More specifically, the alternative aggregates were FeNi and Electric Arc Furnace slags. Furthermore, micritic limestone was used as concrete aggregate in order to produce specimens containing only natural aggregates (standard concrete). Moreover, cement of Type II ASTM C 150 (Lafarge) [37] was used as well as potable tap water, free of impurities

such as salt, silt, clay and organic matter, was also used for mixing and curing the concrete. The pH value of water was 7.0. Natural washed sand was also used for the concrete production whose concentration varies from 5.5 to 7.5%. The water/cement ratio was 0.33.

2.2. Methods

2.2.1. Methods for Raw Materials

The mineralogical and textural characteristics of the used raw materials were examined in polished thin sections with a polarizing microscope according to EN-932-3 [38] standard for petrographic description of aggregates. Thin sections were prepared to study the mineralogical composition and textural characteristics of the studied materials. The thin sections were examined under a petrographic microscope (Leitz Ortholux II POL-BK Ltd., Midland, ON, Canada) for mean grain size and grain shape. The bulk mineral composition of the studied samples was also determined by X-ray Diffraction (XRD), using a Bruker D8 advance diffractometer, with Ni-filtered $\text{CuK}\alpha$ radiation. Random powder mounts were prepared by gently pressing the powder into the cavity holder. The scanning area for bulk mineralogy of specimens covered the 2θ interval $2\text{--}70^\circ$, with a scanning angle step size of 0.015° and a time step of 0.1 s. The mineral phases were determined using the DIFFRACplus EVA 12[®] software (Bruker-AXS, GmbH, Karlsruhe, Germany) based on the ICDD Powder Diffraction File of PDF-2 2006. Furthermore, loss on ignition (LOI) of the studied samples was determined according to the ASTM D7348-13 standard [39]. Additionally, an XRF (X-ray Fluorescence) spectrometer and a sequential spectrometer cited at the Laboratory of Electron Microscopy and Microanalysis (University of Patras, Greece) were used for the determination of the major and trace elements of the studied zeolite. An amount of 0.8 g of dried ground sample was mixed with 0.2 g of wax (acting as binder) and was pressed to a pellet under 15 tones. Pressed pellets were analyzed with a RIGAKU ZSX PRIMUS II spectrometer, which is equipped with Rh-anode. In order to examine the mineralogical and textural characteristics of the tested slags, a scanning electron microscope (JEOL JSM-6300 SEM) equipped with energy dispersive (EDS: Model: 6699, Det. Area: 10 mm^2 , Resol.: 138 eV) using the INCA software was used. The scanning electron microscope used is located in the Laboratory of Electron Microscopy and Microanalysis (University of Patras, Greece). Operating conditions were accelerating voltage 25 kV and beam current 3.3 nA, with a $4\text{ }\mu\text{m}$ beam diameter. The total counting time was 60 s and dead-time 40%. Synthetic oxides and natural minerals were used as standards for the analyses, where the detection limits are $\sim 0.1\%$ and accuracy better than 5% was obtained. Moreover, the specific gravity of the raw materials (slags) used as aggregates were calculated according to ASTM C1567 standard [40].

2.2.2. Methods for the Produced Concrete

Twelve concrete cylindrical specimens were made from two different types of slags and three standard concretes were made containing natural aggregates (limestones) according to ACI-211.1-91 [41]. The aggregates were crushed through standard sieves a separated into the size classes of 2.00–4.75, 4.45–9.5 and 9.5–19.1 mm. After 24 h, the samples were removed from the mold and were cured in water for 28 days. Curing temperature was $20 \pm 3^\circ\text{C}$. In the present study, concrete mixtures were prepared with variations in the quantitative proportions of the different types of slags as shown in Figure 1 and Table 1.

These specimens were tested in a compression testing machine. The compressive strength of concrete is calculated by the division of the value of the load at the moment of failure over the area of specimen both at 7 and 28 days. In this work, our aim was to study the process of hydration of cement at 7 and 28 days because they are the key days to come up to a reliable conclusion on a micro scale regarding the relationship of cement paste with aggregates in concrete, especially comparing different mixtures of raw materials. The compression test was elaborated according to ASTM C42/C42M-12 [42] in a compressive strength Pilot machine-Controls (Model C13C02) with maximum load 1500 kN (Figure 2a). The cylindrical specimens used for this test had 50 mm diameter and

55 mm high (Figure 2b). After the compressive strength test, the textural characteristics of concretes were examined. Polished thin sections were studied in a polarizing microscope according to ASTM C856–17 [43]. The surface texture of aggregate samples was studied by using Secondary Electron Images (SEI) according to BS 812 Part 1 [44] which outlines six qualitative categories, e.g., glassy, smooth, granular, rough, crystalline, honeycomb and porous. Furthermore, two physical properties of the produced concrete specimens were calculated, the water absorption as well as the density according to ASTM Standard C642 [45].

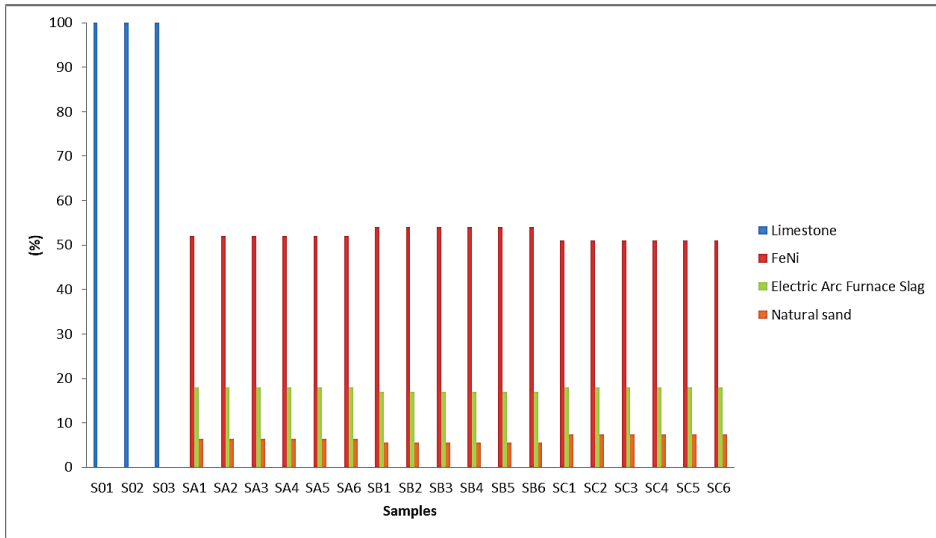


Figure 1. Results of the aggregates’ concentration of concrete samples.

Table 1. Aggregates’ concentration of concrete samples.

| Samples | Limestone (%) | FeNi (%) | Electric Arc Furnace Slag (%) | Natural Sand (%) |
|---------|---------------|----------|-------------------------------|------------------|
| S01 | 100 | - | - | - |
| S02 | 100 | - | - | - |
| S03 | 100 | - | - | - |
| SA1 | - | 52 | 18 | 6.5 |
| SA2 | - | 52 | 18 | 6.5 |
| SA3 | - | 52 | 18 | 6.5 |
| SA4 | - | 52 | 18 | 6.5 |
| SA5 | - | 52 | 18 | 6.5 |
| SA6 | - | 52 | 18 | 6.5 |
| SB1 | - | 54 | 17 | 5.5 |
| SB2 | - | 54 | 17 | 5.5 |
| SB3 | - | 54 | 17 | 5.5 |
| SB4 | - | 54 | 17 | 5.5 |
| SB5 | - | 54 | 17 | 5.5 |
| SB6 | - | 54 | 17 | 5.5 |
| SC1 | - | 51 | 18 | 7.5 |
| SC2 | - | 51 | 18 | 7.5 |
| SC3 | - | 51 | 18 | 7.5 |
| SC4 | - | 51 | 18 | 7.5 |
| SC5 | - | 51 | 18 | 7.5 |
| SC6 | - | 51 | 18 | 7.5 |



(a)

(b)

Figure 2. (a) The compressive strength test machine. (b) Cylindrical concrete specimen.

In this stage, the examination of the concrete textural features was carried out when using polished thin sections in a petrographic microscope (ASTM C856–17) [43]. A 3D depiction of the petrographic characteristics of the concrete as well as of the studied slags was carried out by the 3D Builder software using thin sections.

3. Results

3.1. Raw Materials Characterization

The microscopic observation of the studied slags under polarizing microscope is in accordance with the results of the X-ray diffraction analysis. In general, the studied slags present heterogeneous texture due to uneven aggregate of minerals or usually multi organic fragments. Slags are rich in opaque minerals, mainly wustite and spinels, while microcrystalline to cryptocrystalline, mainly anisotropic calcium-alumino silicate phases, as well as silica minerals complete the overall mineral composition (Figure 3a–c). Alternations of isotropics with anisotropic minerals that form banded structures are also observed. Some grains display different composition around their margins and more specifically they present microcrystalline material possibly alumina-calcium-silicate (anisotropic) in coexistence with an amorphous mass (isotropic). The shape of the opaque minerals and of those of the spinel group usually appears polygonal to spherical with peculiar-sub-dominated plains. The spinel group minerals appear more with dark brown or red to black color and less amber, which indicate their more ferritic-chromit character and less aluminum (Figure 3d). The anisotropic minerals predominate in a prismatic shape, euhedral or subhedral with the exception of silicon dioxide ores which are usually unehedral. Anisotropic minerals usually appear with gray, white and yellow colors, while olivine crystals were observed less frequently (Figure 3a).

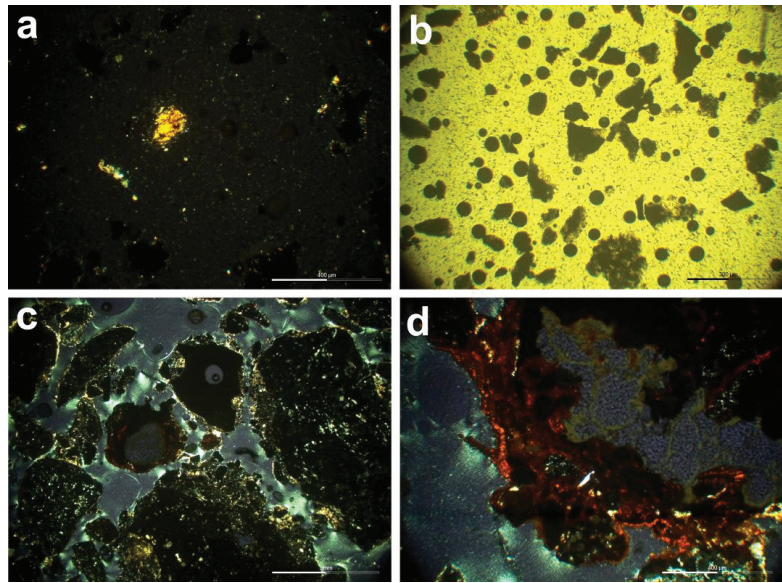


Figure 3. Representative photomicrographs of the studied slags showing: (a,b) anhedral olivine, spherical crystals of wüstite, spinels and microcrystalline opaque minerals in FeNi slag (XPL and PPL Nicols, respectively); (c) grains of spinels, wüstite, calc-aluminosilicate and silicon dioxide phases in Electric Arc Furnace slag (XPL Nicols); and (d) elongated and curved ferritchromit in Electric Arc Furnace slag (XPL Nicols).

The carbonate aggregates (limestones) used as components of the produced concrete specimens do not present many cracks or impurities in their structure as can be seen from the petrographic study. More specifically, limestones used display micritic texture with numerous of fossils and veinlets of microcrystalline calcite and stylolitic porosity filled with clay minerals and Fe-oxides (Figure 4a,b).

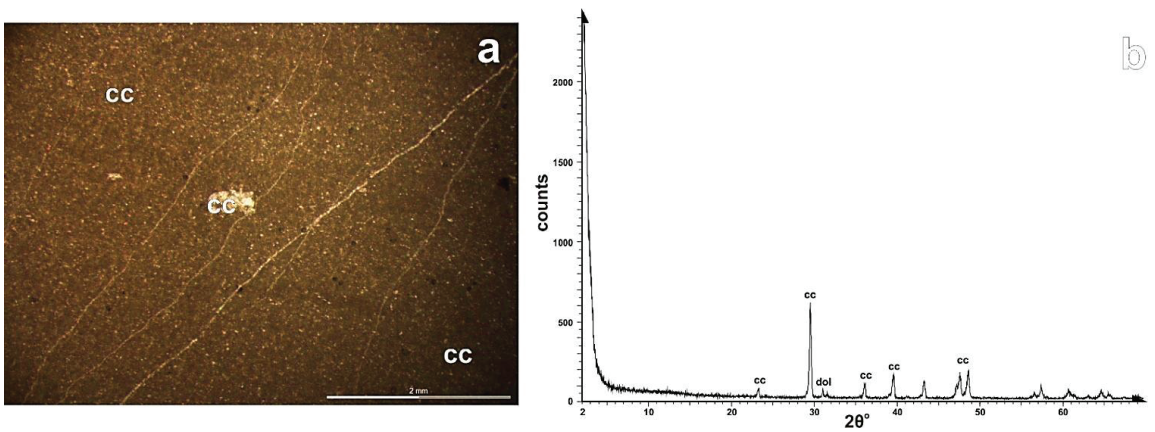


Figure 4. (a) Stylolitic porosity filled with clay minerals and Fe-oxides, fossils and dense network of veins in a micritic limestone; (b) XRD pattern of micritic limestone. Abbreviations: cc: calcite, dol: dolomite.

The results of the qualitative and semi-quantitative analysis of the tested slags are presented in Tables 2 and 3 and Figure 5a,b. Similar qualitative phase composition was detected in the studied samples with mainly quantitative variations. In general, wüstite, spinel group minerals and lime-alumino silicate phases constitute their modal composition. The highest percentages of the wüstite-spinel phases occur in FeNi slag, which reflects to the geochemical effects, as it contains the lowest percentages of calcium, silicon and higher levels of Fe. Indications derived from the mineralogical analysis of the samples for participation of amorphous phase in their mass in percentages up to ~20–30%.

Table 2. *** Mineral composition % of the studied FeNi slag.

| Name | Chemical Formula | Percentages (%) |
|-------------------------|---|-----------------|
| Spinel group | (Mg, Fe, Mn, Ni)(Cr, Al, Fe, V)O ₄ | 35 |
| Wustite | FeO | 45 |
| Merwinite | C ₃ MS ₂ | 7 |
| Beta dicalcium silicate | C ₂ S | 11 |
| Gehlenite | C ₂ AS | <3 |

*** In the semi-quantitative analysis, the amorphous phases are not included. It was calculated <30%.

Table 3. *** Mineral composition % of the studied Electric Arc Furnace slag.

| Name | Chemical Formula | Percentages (%) |
|--------------------------------|---|-----------------|
| Spinel group | (Mg, Fe, Mn, Ni)(Cr, Al, Fe, V)O ₄ | 27 |
| Wustite | FeO | 30 |
| Merwinite | C ₃ MS ₂ | 5 |
| Beta, gamma dicalcium silicate | C ₂ S | 18 |
| Gehlenite | C ₂ AS | 17 |
| Quartz | SiO ₂ | <2 |
| periclase | MgO | <2 |

*** In the semi-quantitative analysis, the amorphous phases are not included. It was calculated <30%.

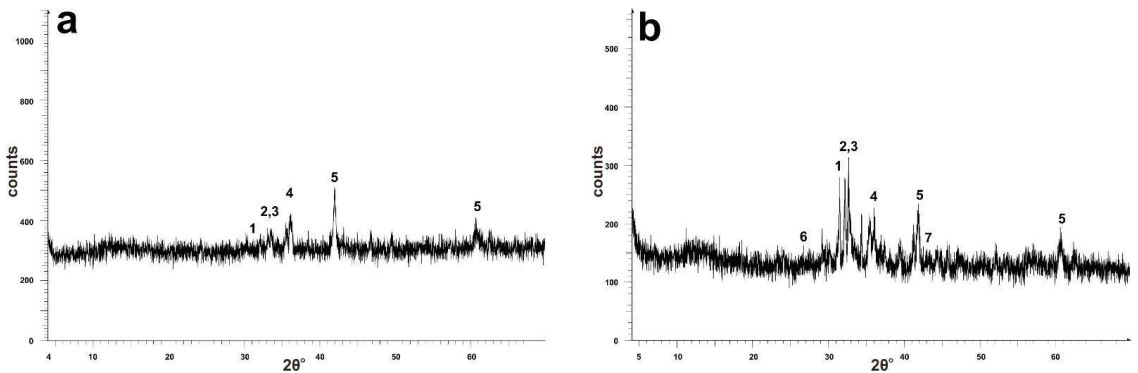


Figure 5. (a) XRD pattern of FeNi slag; (b) XRD pattern of Electric Arc Furnace slag (1: Gehlenite, 2: C₃MS₂, 3: C₂S, 4: Spinel, 5: Wüstite, 6: Quartz, 7: Periclase).

Results of the chemical composition analyses of the studied slag samples were performed by X-ray Fluorescence (XRF) are presented in Table 4. The results of XRF analyses shows that the FeNi slag contains higher amount of Fe₂O₃ (37.25 wt.% compared to the ELECTRIC ARC FURNACE SLAG slag (10.41 wt.%). The ELECTRIC ARC FURNACE SLAG slag displays higher amounts of SiO₂, Al₂O₃ and CaO (11.81 wt.%, 7.29 wt.% and 26.85 wt.%, respectively) in contrast to FeNi slag which contains significantly lower amounts (3.77 wt.%, 0.43 wt.% and 10.21 wt.%, respectively). Regarding the alkalis, they are not significant differences between the two types of slags (Table 3). ELECTRIC ARC FURNACE

SLAG slag presents LOI (loss on ignition) 1.21, while the FeNi slag does not present any value of LOI. As for the trace elements, FeNi slag is more enriched in Ni, while ELECTRIC ARC FURNACE SLAG slag is more enriched in Cr, Sr, Ba and V (Table 4).

Table 4. Results of the chemical composition of the tested samples (<DL: <below detection limit).

| Oxides | FeNi | ELECTRIC ARC FURNACE SLAG |
|---|-------|---------------------------|
| SiO ₂ | 3.77 | 11.81 |
| TiO ₂ | 0.02 | 0.57 |
| Al ₂ O ₃ | 0.43 | 7.29 |
| Fe ₂ O ₃ ^t | 37.25 | 10.41 |
| MnO | <DL | 1.74 |
| MgO | 2.30 | 1.74 |
| CaO | 10.21 | 26.85 |
| Na ₂ O | 0.04 | 0.10 |
| K ₂ O | 0.04 | 0.03 |
| P ₂ O ₅ | 0.33 | 0.39 |
| LOI | 0 | 1.21 |
| ppm | | |
| Cr | 2561 | 4537 |
| Co | 379 | 31 |
| Ni | 1327 | 20 |
| Cu | 27 | 156 |
| Zn | 12 | 115 |
| Rb | <DL | <DL |
| Sr | 39 | 486 |
| Y | 15 | 34 |
| Zr | <DL | 86 |
| Nb | <DL | <DL |
| Pb | <DL | <DL |
| Ba | 171 | 1203 |
| V | 31 | 207 |
| W | 37 | 28 |
| La | 1 | 12 |
| Ce | 58 | 94 |
| Th | <DL | <DL |
| Sc | <DL | <DL |

The slags have basicity value which range from 2.42 (ELECTRIC ARC FURNACE SLAG) to 3.31 (FeNi) which as calculated according to the following equation:

$$\text{Basicity} = (\% \text{CaO} + \% \text{MgO}) / \% \text{SiO}_2$$

where %CaO, %MgO and %SiO₂ are the contents of those mentioned oxides (wt%) in the studied slags.

Analyses with Scanning Electron Microscope (SEM) and Energy Dispersive X-ray mapping were conducted to determine the distributions of several major elements (Si, Al, Ca, Mg, Fe, Cr, K and Na) in the studied slags. SEM observations are in accordance with the petrographic features and XRD analyses as indicated in Figure 5 where spherical crystals of wüstite and curved subhedral spinels are shown. These minerals are surrounded by microcrystalline calc-silicate phases (C₂S). FeNi slag presents uniformly distributed porosity of brick type (Figure 6). Regarding ELECTRIC ARC FURNACE SLAG slag, in Figure 7 it is proved that it consists of spherical crystals of wüstite, elongated spinels, calc-silicate phase (C₂S) and microcrystalline gehlenite (Figure 7a).

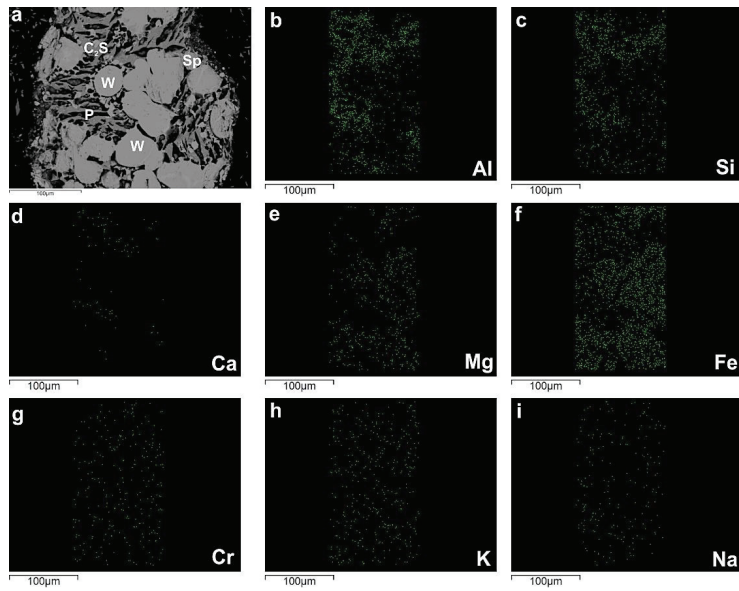


Figure 6. Back-scattered electron image of spherical crystals of wüstite (W), spinels (Sp) and microcrystalline calc-silicate phase (C₂S), as well as pores (P, distinguished as black) in FeNi slag (a) and mapping of major elements (Al, Si, Ca, Mg, Fe, Cr, K and Na, respectively) (b–i).

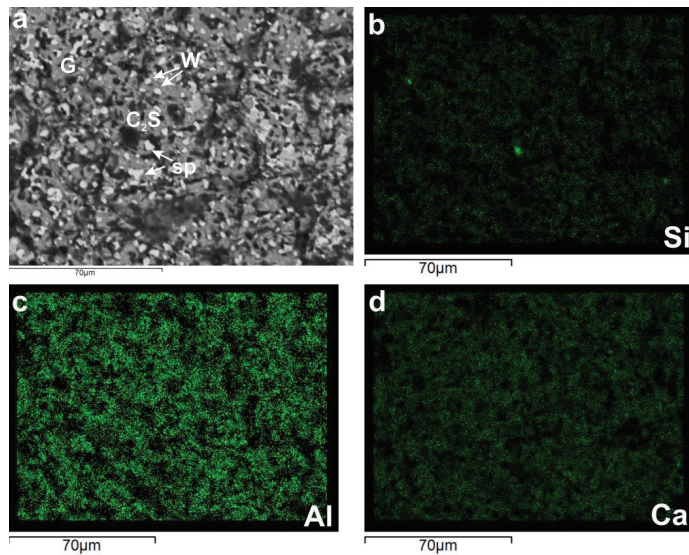


Figure 7. Back-scattered electron image of spherical crystals of wüstite (W), spinels (sp), calc-silicate phase (C₂S) and microcrystalline gehlenite (G) in ELECTRIC ARC FURNACE SLAG slag (a) and mapping of major elements (Si, Al and Ca, respectively) (b–d).

The results of SEM-X-ray mapping are presented in Figures 6 and 7. The SEM-X-ray mapping analysis result in FeNi slag indicates that Fe is uniformly distributed on the entire surface of the slag (Figure 6f). In addition to Mg, components in the slag that are in lower amounts are Si, Cr, Ca, K and Na (Figure 6b–e,g–i). Regarding ELECTRIC ARC FURNACE SLAG slag, the mapping results are in accordance with the chemical compositions and the

petrographic results. More specifically, slag composition is relatively uniform, in which Ca and Al are present as the major component of the slag, while Si is in smaller amounts (Figure 7b–d).

The specific gravity of the tested slags (both of two types) and of the natural aggregates (limestone) is identified. As can be seen from Table 5, the specific gravity of FeNi slags presents higher values than of those of ELECTRIC ARC FURNACE SLAG slags in all tested samples. More specifically, as for the SA group, its specific gravity values range from 4.51 to 4.61 T/m³ regarding FeNi slags while from 3.59 to 3.61 T/m³ regarding ELECTRIC ARC FURNACE SLAG slags. Similarly, the values range of SB group is from 4.54 to 4.59 and from 3.52 to 3.70 in FeNi and ELECTRIC ARC FURNACE SLAG slags respectively. As for the SC group, the range of specific gravity values is from 4.59 to 4.72 and from 3.45 to 3.70 in FeNi and ELECTRIC ARC FURNACE SLAG slags, respectively. The lowest value of this property is found in a FeNi slag of SC group, while the highest value in ELECTRIC ARC FURNACE SLAG slags of SB and SC groups. Regarding the measured specific gravity of the tested limestones used as concrete aggregates is 2.70 T/m³, intensively lower than that of the investigated slags.

Table 5. Results of the specific gravity test of the tested slags.

| Samples | Specific Gravity (T/m ³) of FeNi | Specific Gravity (T/m ³) of Electric Arc Furnace Slag |
|---------|--|---|
| S01 | 2.70 (limestone) | |
| S02 | 2.70 (limestone) | |
| S03 | 2.70 (limestone) | |
| SA1 | 4.51 | 3.61 |
| SA2 | 4.51 | 3.61 |
| SA3 | 4.61 | 3.59 |
| SA4 | 4.51 | 3.61 |
| SA5 | 4.51 | 3.61 |
| SA6 | 4.61 | 3.59 |
| SB1 | 4.59 | 3.52 |
| SB2 | 4.54 | 3.70 |
| SB3 | 4.56 | 3.60 |
| SB4 | 4.59 | 3.52 |
| SB5 | 4.54 | 3.70 |
| SB6 | 4.56 | 3.60 |
| SC1 | 4.59 | 3.45 |
| SC2 | 4.62 | 3.51 |
| SC3 | 4.70 | 3.56 |
| SC4 | 4.72 | 3.61 |
| SC5 | 4.71 | 3.70 |
| SC6 | 4.69 | 3.70 |

3.2. Results of Concrete Specimens

Regarding the physical properties of investigated concrete specimens such as density, concrete specimens produced by natural aggregates (limestones) show density from 2621 to 2709 kg/m³ (Figure 8a, Table 6). As for the specimens made from various percentages of two different slags (FeNi and ELECTRIC ARC FURNACE SLAG), samples of SA group present values of density range from 3093 to 3125 kg/m³, samples of SB group values from 3095 to 3181 kg/m³ and these of SC group from 3060 to 3169 kg/m³ (Figure 8a). Samples of SA group display water absorption, which ranges from 0.68 to 1.08%, samples of SB group from 1.01 to 1.59% and these of SC group from 1.09 to 1.48% (Figure 8b, Table 6). Furthermore, the uniaxial compressive strength (UCS) of the produced concrete specimens was measured. The compressive strength of the standard concrete specimens (produced by natural aggregates) ranges from 36.00 to 38.00 MPa in 7 days and from 47.00 to 48.50 MPa in 28 days (Figure 8c). In 7 days, the UCS of SA group ranges from 62.24 to 66.35 MPa, while in 28 days ranges from 75.80 to 83.42 MPa simultaneously indicating these samples as those presenting the highest concrete strength (Figure 8c,d, Table 6). As for the SB group, the UCS in 7 days it ranges from 50.02 to 56.91 MPa and from 57.12 to 61.74 MPa in 28 days (Figure 8c,d). The UCS of SC group in 7 days ranges from 45.53 to 55.18 MPa and in 28 days from 52.84 to 66.85 MPa (Figure 8c,d, Table 6).

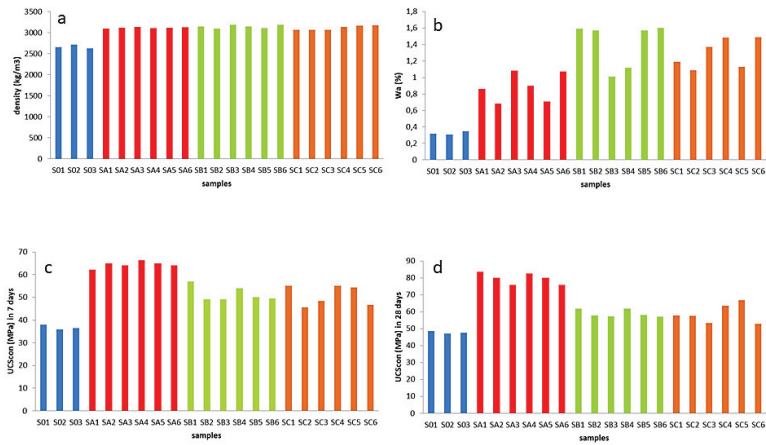


Figure 8. Results of the physical and mechanical properties of the produced concrete specimens. (a) density (kg/m^3); (b) Water absorption (%); (c) Uniaxial compressive strength of 7 days (MPa); (d) Uniaxial compressive strength of 28 days (MPa).

Table 6. Results of the physical and mechanical tests of the produced concrete specimens.

| Samples | Density (kg/m^3) | Water Absorption (%) | Uniaxial Compressive Strength of 7 Days (MPa) | Uniaxial Compressive Strength of 28 Days (MPa) |
|---------|------------------------------------|----------------------|---|--|
| S01 | 2650 | 0.32 | 38.00 | 48.50 |
| S02 | 2709 | 0.31 | 36.00 | 47.00 |
| S03 | 2621 | 0.35 | 36.55 | 47.50 |
| SA1 | 3093 | 0.86 | 62.24 | 83.42 |
| SA2 | 3113 | 0.68 | 64.94 | 80.02 |
| SA3 | 3129 | 1.08 | 64.13 | 75.88 |
| SA4 | 3098 | 0.90 | 66.35 | 82.48 |
| SA5 | 3112 | 0.71 | 64.94 | 80.06 |
| SA6 | 3125 | 1.07 | 64.15 | 75.80 |
| SB1 | 3140 | 1.59 | 56.91 | 61.74 |
| SB2 | 3095 | 1.57 | 49.15 | 57.85 |
| SB3 | 3179 | 1.01 | 49.14 | 57.43 |
| SB4 | 3141 | 1.12 | 53.90 | 61.70 |
| SB5 | 3098 | 1.57 | 50.02 | 58.02 |
| SB6 | 3181 | 1.60 | 49.53 | 57.12 |
| SC1 | 3065 | 1.19 | 55.17 | 57.84 |
| SC2 | 3064 | 1.09 | 45.53 | 57.50 |
| SC3 | 3060 | 1.37 | 48.35 | 53.26 |
| SC4 | 3129 | 1.48 | 55.18 | 63.59 |
| SC5 | 3166 | 1.13 | 54.37 | 66.85 |
| SC6 | 3169 | 1.49 | 46.80 | 52.84 |

As for the concrete specimens made by slags, the presence of fractures between the slags and the cement paste is partially observed (Figure 8). Moreover, samples SA1-SA6 and SC1-SC6 are characterized by satisfactory bonding with the cement paste (Figure 9a–d,f,h). On the contrary, samples SB1-SB6 presents lower microroughness and unsatisfactory bonding with the cement paste, which indicated from the zone around wüstite grains which acts as detachment zone during the load (Figure 9e,g). During the petrographic study of the concrete specimens, a large number of wüstite and spinel crystals were found to have been detached from the cement paste on a large scale after loading, while in none of the studied slags crystalline microcracks were found penetrating their mass. The general microroughness of the mineral components of the slags does not show any increase which is likely to work adversely within the concrete.

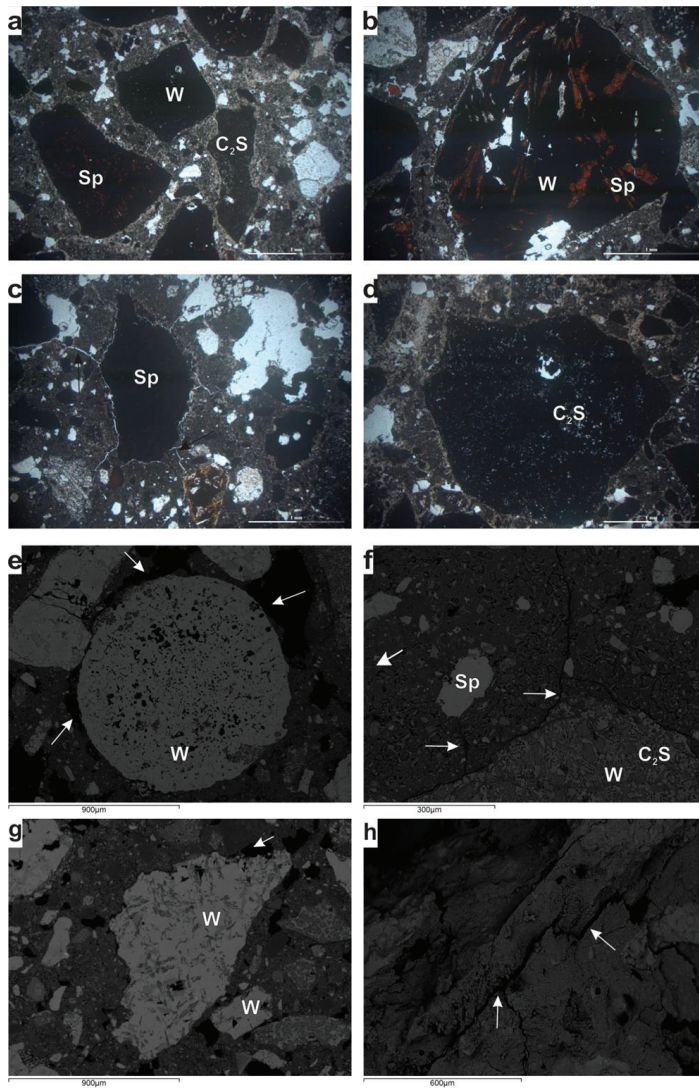


Figure 9. Textural characteristics of the studied concrete specimens: (a) Photomicrograph of sub-hedral spinel (Sp), wüstite (W) and anhedral calc-silicate phase (C₂S) (PPL Nicols, sample SA1). (b) Photomicrograph of elongated grain of slag consisting of spinel (Sp) and wüstite (W) (PPL Nicols, sample SC2). (c) Photomicrograph of subhedral and elongated spinel (Sp) in which scattered cracks are observed which do not penetrate it (PPL Nicols, sample SC5). (d) Photomicrograph of an elongated grain of ELECTRIC ARC FURNACE SLAG, which contains calc-silicate phase (C₂S) and has a good cohesion with the cement paste (PPL Nicols, sample SA4). (e) Back-scattered electron image of a spherical grain of wüstite (W) which does not have good cohesion with the cement paste and detachments are observed around it (sample SB6). (f) Back-scattered electron image of cracks in the cement paste and around a grain of an ELECTRIC ARC FURNACE SLAG that contains calc-silicate phase (C₂S) and spherical wüstite (W) (sample SA6). (g) Back-scattered electron image of subhedral wüstite (W) around which detachments are observed (sample SB2). (h) Back-scattered electron image of cracks and detachments between the cement paste and the FeNi slag (sample SC6).

All the above are enhanced either through the processing of microscopic images after the 3D depiction or through the study of the transition zone between the aggregate and the cement paste as it is shown in Figure 10a–d. The grains of C_2S phases and spinels (Figure 10 a,c,d) seem to present good cohesion with the cement paste. In addition, it is observed that the grains of wüstite have lower microroughness compared to that of the cement paste, where this alternation of the concrete components leads to the better cohesion among them (Figure 10b).

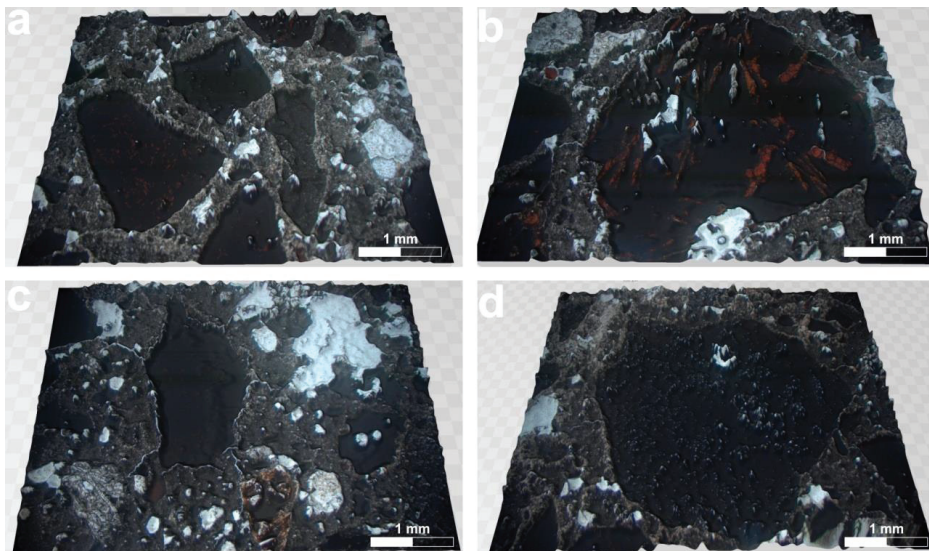


Figure 10. 3D depictions of the investigated concrete specimens: (a) spinel, wüstite and calc-silicate phase (sample SA1); (b) spinel and wüstite (sample SC2); (c) spinel (sample SC5); and (d) calc-silicate phase paste (sample SA4).

4. Discussion

Different types of industrial byproducts have been studied in the past few decades in order to find suitable alternatives of natural aggregates in concrete. Blast furnace slag, steel slag, copper slag and foundry slag can be used as concrete aggregates. In this study, different types of slags have been evaluated in various mixtures in order to identify the optimum combination of recycled raw materials such as slags for their use in several construction applications of high demands. For this reason, at the same time, a standard concrete of the same category was prepared containing only natural carbonate aggregates in order to carry out a direct comparative study between these types of concrete specimens so that a wider application of such type of by products could be established. At first, when studying the aggregate properties, significant differences regarding their physical and mechanical properties are identified. More specifically, slags used as aggregates display better properties in terms of their mechanical strength, while limestones present advantages in terms of water absorption and physical properties in order to be used as concrete aggregates. The density of slags used as aggregates appears significantly increased compared to natural aggregates that lead to the characterization of slags as heavy weight aggregates, while the same applies to their density. The water absorption of slags is particularly high compared to that of common limestones used as aggregates. This parameter must be taken into account when studying the composition of concrete, so that no reduced workability can be observed from the absorption of water by the aggregates. Several researchers have studied the influence of the aggregate type on the final concrete strength which is directly depends on their properties [46–48]. During the microscopic study of the raw materials where they

were studied as aggregates, significant differences are identified both between the natural aggregates and the slags as well as between slags of different origins. More specifically, natural aggregates are less compact and contain numerous microcracks, and thus they penetrate their entire mass compared to slags where they are more compact, and they display less intragranular microcracks. However, the porosity in the micro-scale seems to be increased in the whole of the studied slags in relation to the carbonate rocks in which the porosity is more uniformly distributed, something that probably affects in all the properties but also in their final relationship with the cement paste. However, there are significant differences between the slags during their microscopic observation where the FeNi slags show significantly higher percentage of wüstite and spinel than those of ELECTRIC ARC FURNACE SLAG, while at the same time, the FeNi slags show lower percentage of calc silicate phases than those of the ELECTRIC ARC FURNACE SLAG significantly affecting to the properties of aggregates. Moreover, a significant difference during the microscopic study is found in the porosity which seems to be greater in the FeNi slags in contrast to the corresponding ones of ELECTRIC ARC FURNACE SLAG, something that is mainly attributed to their special mineral characteristics.

Test results of the compressive strength from different concrete mixtures in 7 and 28 days are plotted in Figure 8c,d. The replacement of limestone aggregates with slags in concrete seems to significantly increase their compressive strength both in 7 and 28 days in all cases. The 28-day compressive strength levels of concrete specimens made by slags as aggregates present range of values from 52 MPa to 83 MPa compared to the corresponding concretes produced only by natural aggregates which do not exceed 40 MPa, i.e., much lower than expected, which is initially attributed to the higher hardness of slags as shown in the comparative table with the properties of the aggregates (natural and recycled).

In general, it seems that when slag is used regardless its source in all the aggregate grain sizes, then the density of the mixture can exceed 3000 kg/m^3 in relation to the corresponding concrete specimens which have been produced only by natural raw materials (density values up to 2650 kg/m^3). In most cases, however, the use of aggregate slag implies the production of concrete with density greater than 2700 kg/m^3 , which must be taken into account when designing such type of constructions. The uniaxial compressive strength of concrete specimens produced by slags is better than of those produced by natural aggregates with an increase of 20% in concrete with lower percentage of ELECTRIC ARC FURNACE SLAG slag and with higher percentage of FeNi slag. This increase reaches the percentage of 30% in the cases where it participates in a higher percentage of ELECTRIC ARC FURNACE SLAG slags and a lower percentage of FeNi slags. This is due to all the special characteristics of the slags in relation to their physical and especially to their mechanical characteristics directly dependent on their microscopic characteristics where slags present a compact texture without microcracks and uniformly distributed porosity which seems to affect the smooth crystallization process of the cement and therefore on its stronger bonding with the aggregates in relation to the unevenly distributed porosity of the natural aggregates. During the petrographic study of concrete, when studying the micro scale where the failures are born, significant differences in the microcracks' process are identified after the breaking of the concrete specimens. During the microscopic study of the oriented thin sections during the uniaxial compressive strength test of concrete specimens produced by natural aggregates microcracks are shown to break the carbonate aggregates transgranularly and intragranularly, something that in concrete specimens made by slags was not found in any of the examined mixtures. This fact is attributed to both mechanical of aggregate materials as well as in their mineralogical characteristics. Among the mixtures produced by different types of slags, significant differences in their mechanical strength were observed. The differences in the final compressive strength of the produced concretes are observed as significant even with small variations in the percentage participation of the different types of slag, something that reveals the strong influence of the special mineralogical characteristics on the final quality of the produced concrete specimens.

The superiority of mixtures of SA group in contrast to that of SB group (higher percentage of ELECTRIC ARC FURNACE SLAG slag) and that of SC group (lower percentage of natural sand) is evident both in 7 days and in 28 days of curing. This difference on the final concrete strength where different types of slags are participated is precisely related to their different weights and their different densities as the slag aggregates which are characterized as heavy weight aggregates produce heavy weight type concretes and as their weight increases it seems their durability to be reduced linearly.

The differences in all properties of the produced concretes which are identified between the groups SA, SB, SC can be interpreted by studying and evaluating the particular microscopic characteristics of both raw materials (slags and natural rocks) and the produced concrete specimens. The hydration of ladle slags with a content of hydraulically active mineral and the glass phase is taking place after adding water, without having to supply an alkali-activator. The hydraulic properties of slags are incommensurable compared to Portland cement however hydrating abilities are affected by the chemical composition. Samples SB do not present high compressive strength, while the other samples present better compressive strength after 28 days of hydration. Samples in which compressive strength values are higher than those of SB group contain mineral dicalcium silicate in this group. This mineral occurs in Portland clinker [1] and due to its hydration there are the so [32] called C-S-H phases formed. These phases are bearers of strength in the hydrated cement. Additionally, it is evident that mixtures containing higher amount of ELECTRIC ARC FURNACE SLAG slag and lower amount of FeNi slag (SA and SC group) yield increased mechanical concrete properties compared to the SB group, which seems to be related to the increased concentration of wüstite and merwinite in FeNi slags (Tables 1 and 2). The presence of wüstite in the concrete as it was detected through the microscopic study seems to act as a surface of weakness within the structure of the cement paste as the cubic system to which it belongs creates some plan surfaces capable of acting as levels of failure during uniaxial loads. The fact of the negative effect mainly of wüstite on the final mechanical strength of concrete specimens is documented both by the microscope images and by the three-dimensional study of the produced concretes. More specifically, as shown in Figure 9b, an extensive zone of detachment from the adhesive cement is located around the wüstite, which is found throughout the range of concrete. This fact indicates the existence of a point of weakness inside the concrete where during the uniaxial loading they act exactly as detachment points resulting in faster breaking. In addition, as shown in the three-dimensional study, the wüstite crystals do not show a particularly significant microtopography in relation to the rest of the mortar, while at the same time it presents extensive flat areas which may also function as slip levels during loading. The spinel shows similar behavior to wüstite as shown in Figures 8a and 9a. In contrast to wüstite and spinel, the presence of C_2S phases seems to have a significant positive effect on the mechanical concrete strength as no significant detachment zones are found perimetrically during the fracture while the three-dimensional microtopography seems to be satisfactory and evenly distributed throughout the surface (Figure 9d) creating formations which seem to mechanically trap the cement mortar. An extra significant parameter for uniaxial compressive strength of concrete with the increased percentage of FeNi slags seems to be the existence of merwinite when is regarded as a low hydraulically active mineral [49,50]. It seems to significantly affect the hydraulic properties of the cement and its smooth hydration reaction, resulting in a significant reduction in its mechanical strength and around these crystals to identify areas of reaction and weakness.

As it is shown through the study of the X-ray diffraction patterns of raw materials it seems that the compressive strength of samples prepared from the slags Electric Arc Furnace Slag were secured primarily by the presence of $b-C_2S$ phase. The $b-C_2S$ phase is considered the most important for ensuring the strength of products with water activated ladle slags. The Electric Arc Furnace Slag slags which after adding water have sufficient strength are in accordance with condition C/S. The low ratio C/S shows these slags which is hydraulically inactive. The other type of slags has a satisfactory C/S ratio but its hydraulicity is low.

Additionally, in contrast to mervinite and wüstite, the presence of gellenite in an increased percentage in the ELECTRIC ARC FURNACE SLAG slag seems to have a significant effect on both the properties of slags and on the behavior of the produced concrete. As can be seen through the microscopic study of the microstructure of concrete, strong adhesion with the cement paste is detected, which is probably due to the partial hydration reaction of these mineral phases and its special morphological characteristics. Additionally, the difference between FeNi and ELECTRIC ARC FURNACE SLAG slag can be observed not only in their mineralogical composition but also in their chemical composition and thus even the study of their chemical composition could potentially be used as a predictor of slag behavior in concrete. More specifically, FeNi slags show intensively lower percentage of free CaO compared to their respective ELECTRIC ARC FURNACE SLAG slag participation and the diversity in their composition confirms the strong heterogeneity of these slags and imbalances in their solidification the hardening of the hydrated slags is also involved in the presence of the amorphous phase, especially in the case of slags containing free CaO as Calcium hydroxide is the activator of the latent hydraulicity for the amorphous phase [51].

5. Conclusions

This paper examines industrial byproducts (ferronickel slags) to evaluate their suitability as concrete aggregates, with the ultimate goal of the production of environmentally friendly concrete from now on. The main conclusions of this study are given in the remarks below:

- The determinant factor for the final mechanical behavior of concrete seems to be the mineralogical and microstructural characteristics of slags used as aggregates. In contrast to wüstite and spinel, the presence of C₂S phases seems to have a significant positive effect on the concrete strength as no significant detachment zones are found perimetrically during the fracture.
- Natural aggregates are less compact as they contain numerous microcracks and hence they penetrate their entire mass compared to slags where they are more compact and they display less intargranular microcracks, making them suitable for concrete aggregates.
- The participation of slags in concrete mixtures improves their mechanical strength as the replacement of limestone aggregates with slags in concrete seems to significantly increase their compressive strength both in 7 and 28 days in all mixtures.
- Mixtures containing higher amount of ELECTRIC ARC FURNACE SLAG slag due to their lower concentration of wüstite and mervinite present increased mechanical concrete properties.

Author Contributions: Conceptualization, P.P.; methodology, P.P., A.R., P.P.G. and P.L.; software, P.P., A.R. and A.C.; investigation, P.P., A.R., P.P.G., A.C., S.L. and P.L.; resources, P.P., P.P.G., A.C. and P.L.; data curation, P.P., A.R., P.P.G., A.C. and P.L.; writing—original draft preparation, P.P. and P.P.G.; writing—review and editing, P.P., A.R., P.P.G. and N.K.; visualization, P.P. and P.K.; supervision, P.P. All authors have read and agreed to the published version of the manuscript.

Funding: This research received no external funding.

Institutional Review Board Statement: Not applicable.

Informed Consent Statement: Not applicable.

Conflicts of Interest: The authors declare no conflict of interest.

References

1. *ISO/TC 071*; Strategic Business Plan. ISO: Tokyo, Japan, 2016.
2. World Population Clock: 7.9 Billion People (2021)—Worldometer. Available online: <https://www.worldometers.info/world-population/> (accessed on 7 December 2021).
3. Saha, A.K.; Khan, M.N.N.; Sarker, P.K. Value added utilization of by-product electric furnace ferronickel slag as construction materials: A review. *Resour. Conserv. Recycl.* **2018**, *134*, 10–24. [[CrossRef](#)]

4. Andrew, R.M. Global CO₂ emissions from cement production. *Earth Syst. Sci. Data* **2018**, *10*, 195–217. [CrossRef]
5. Kosmatka, S.K.; Kerkhoff, B.; Panarese, W.C. *Design and Control of Concrete Mixtures*, 14th ed.; Portland Association: Skokie, IL, USA, 2002; ISBN 0-89312-217-3.
6. Paris Agreement. Available online: https://ec.europa.eu/clima/eu-action/international-action-climate-change/climate-negotiations/paris-agreement_el (accessed on 14 December 2021).
7. Circular Economy Action Plan. Available online: https://ec.europa.eu/environment/strategy/circular-economy-action-plan_en (accessed on 14 December 2021).
8. Directive, E.C. Directive 2008/98/EC of the European Parliament and of the Council of 19 November 2008 on waste and repealing certain Directives (Text with EEA relevance). *Off. J. Eur. Union* **2008**, *312*, 3–30.
9. Directive (Eu) 2018/851 of the European Parliament and of the Council of 30 May 2018 amending Directive 2008/98/EC on waste (Text with EEA relevance). *Off. J. Eur. Union* **2018**, *150*, 109–140.
10. Van Oss, H.G. *Slag-Iron and Steel, U.S. Geological Survey, Minerals Yearbook 2017*; USGS: Reston, VA, USA, 2017.
11. Statistics 2018—Euroslag. Available online: <https://www.euroslag.com/products/statistics/statistics-2018/> (accessed on 16 December 2021).
12. Bartzas, G.; Komnitsas, K. Life cycle assessment of ferronickel production in Greece. *Resour. Conserv. Recycl.* **2015**, *105*, 113–122. [CrossRef]
13. Criado, M.; Ke, X.; Provis, J.L.; Bernal, S.A. *Alternative Inorganic Binders Based on Alkali-Activated Metallurgical Slags*; Woodhead Publishing: Sawston, UK, 2017; ISBN 9780081020029.
14. Saha, A.K.; Sarker, P.K. Sustainable use of ferronickel slag fine aggregate and fly ash in structural concrete: Mechanical properties and leaching study. *J. Clean. Prod.* **2017**, *162*, 438–448. [CrossRef]
15. Dong, Q.; Wang, G.; Chen, X.; Tan, J.; Gu, X. Recycling of steel slag aggregate in Portland cement concrete: An overview. *J. Clean. Prod.* **2021**, *282*, 124447. [CrossRef]
16. Malek, M.; Jackowski, M.; Łasica, W.; Dydek, K.; Boczkowska, A. An Experimental Study of Possible Post-War Ferronickel Slag Waste Disposal in Szklary (Lower Silesian, Poland) as Partial Aggregate Substitute in Concrete: Characterization of Physical, Mechanical, and Thermal Properties. *Materials* **2021**, *14*, 2552. [CrossRef]
17. Palankar, N.; Ravi Shankar, A.U.; Mithun, B.M. Durability studies on eco-friendly concrete mixes incorporating steel slag as coarse aggregates. *J. Clean. Prod.* **2016**, *129*, 437–448. [CrossRef]
18. Manso, J.M.; Polanco, J.A.; Losañez, M.; González, J.J. Durability of concrete made with EAF slag as aggregate. *Cem. Concr. Compos.* **2006**, *28*, 528–534. [CrossRef]
19. Chatzopoulos, A.; Sideris, K.K.; Tassos, C. Production of concretes using slag aggregates: Contribution of increasing the durability and sustainability of constructions. *Case Stud. Constr. Mater.* **2021**, *15*, e00711. [CrossRef]
20. Patra, R.K.; Mukharjee, B.B. Influence of incorporation of granulated blast furnace slag as replacement of fine aggregate on properties of concrete. *J. Clean. Prod.* **2017**, *165*, 468–476. [CrossRef]
21. Anastasiou, E.; Georgiadis Filikas, K.; Stefanidou, M. Utilization of fine recycled aggregates in concrete with fly ash and steel slag. *Constr. Build. Mater.* **2014**, *50*, 154–161. [CrossRef]
22. Kim, H.; Lee, C.H.; Ann, K.Y. Feasibility of ferronickel slag powder for cementitious binder in concrete mix. *Constr. Build. Mater.* **2019**, *207*, 693–705. [CrossRef]
23. Sun, J.; Feng, J.; Chen, Z. Effect of ferronickel slag as fine aggregate on properties of concrete. *Constr. Build. Mater.* **2019**, *206*, 201–209. [CrossRef]
24. Nuruzzaman, M.; Kuri, J.C.; Sarker, P.K. Strength, permeability and microstructure of self-compacting concrete with the dual use of ferronickel slag as fine aggregate and supplementary binder. *Constr. Build. Mater.* **2022**, *318*, 125927. [CrossRef]
25. Yuan, S.; Liu, X.; Gao, P.; Han, Y.X. A semi-industrial experiment of suspension magnetization roasting technology for separation of iron minerals from red mud. *J. Hazard. Mater.* **2020**, *394*, 122579. [CrossRef]
26. Wu, Q.; Chen, Q.; Huang, Z.; Gu, B.; Zhu, H.; Tian, L. Preparation and characterization of porous ceramics from nickel smelter slag and metakaolin. *Ceram. Int.* **2020**, *46*, 4581–4586. [CrossRef]
27. Xi, B.; Li, R.; Zhao, X.; Dang, Q.; Zhang, D.; Tan, W. Constraints and opportunities for the recycling of growing ferronickel slag in China. *Resour. Conserv. Recycl.* **2018**, *139*, 15–16. [CrossRef]
28. Pan, J.; Zheng, G.; Zhu, D.; Zhou, X. Utilization of nickel slag using selective reduction followed by magnetic separation. *Trans. Nonferrous Met. Soc. China* **2013**, *23*, 3421–3427. [CrossRef]
29. Liu, X.; Feng, Y.; Li, H.; Yang, Z.; Cai, Z. Recovery of valuable metals from a low-grade nickel ore using an ammonium sulfate roasting-leaching process. *Int. J. Miner. Metall. Mater.* **2012**, *19*, 377–383. [CrossRef]
30. Yang, H.; Jing, L.; Zhang, B. Recovery of iron from vanadium tailings with coal-based direct reduction followed by magnetic separation. *J. Hazard. Mater.* **2011**, *185*, 1405–1411. [CrossRef]
31. Rashad, A.M.; Sadek, D.M.; Hassan, H.A. An investigation on blast-furnace slag as fine aggregate in alkali-activated slag mortars subjected to elevated temperatures. *J. Clean. Prod.* **2016**, *112*, 1086–1096. [CrossRef]
32. Sato, T.; Watanabe, K.; Ota, A.; Aba, M.; Sakoi, Y. Influence of Excessive Bleeding on Frost Susceptibility of Concrete Incorporating Ferronickel Slag as Aggregates. In Proceedings of the 36th Conference on Our World in Concrete and Structures, Singapore, 25–27 August 2011; Available online: www.cipremier.com/e107_files/downloads/Papers/100/36/100036049.pdf (accessed on 10 May 2015).

33. Tomosawa, F.; Nagataki, S.; Kajiwara, T.; Yokoyama, M. Alkali-aggregate Reactivity of Ferronickel-slag Aggregate Concrete. *Spec. Publ.* **1997**, *170*, 1591–1602.
34. Shoya, M.; Aba, M.; Tsukinaga, Y.; Tokuhashi, K. Frost resistance and air void system of self-compacting concrete incorporating slag as a fine aggregate. *Spec. Publ.* **2003**, *212*, 1093–1108.
35. Wang, G.; Thompson, R.; Wang, Y. Hot-mix asphalt that contains nickel slag aggregate: Laboratory evaluation of use in highway construction. *Transp. Res. Rec. J. Transp. Res. Board* **2011**, *2208*, 1–8. [[CrossRef](#)]
36. Fidancevska, E.; Vassilev, V.; Milosevski, M.; Parvanov, S.; Milosevski, D.; Aljihmani, L. Composites based on industrial wastes III. Production of composites of Fe-ni slag and waste glass. *J. Univ. Chem. Technol. Metal* **2007**, *42*, 285–290.
37. *ASTM C 150*; Standard Specification for Portland Cement. ASTM International: West Conshohocken, PA, USA, 2017.
38. *EN 932*; Part 3: Procedure and Terminology for Simplified Petrographic Description. European Standard: Warsaw, Poland, 1996.
39. *ASTM D 7348*; Standard Test. Methods for Loss on Ignition (LOI) of Solid Combustion. Residues. ASTM International: West Conshohocken, PA, USA, 2013.
40. *ASTM C1567*; Standard Test Method for Determining the Potential Alkali-Silica Reactivity of Combinations of Cementitious Materials and Aggregate (Accelerated Mortar-Bar Method). ASTM International: West Conshohocken, PA, USA, 2013.
41. *ACI-211.1-91*; Standard for Selecting Proportions for Normal, Heavyweight and Mass Concrete. American Concrete Institute: Farmington Hills, MI, USA, 2002.
42. *ASTM C42/C42M-12*; Standard Test. Method for Obtaining and Testing Drilled Cores and Sawed Beams of Concrete. ASTM International: West Conshohocken, PA, USA, 2013.
43. *ASTM C856*; Standard Practice for Petrographic Examination of Hardened Concrete. American Society for Testing and Materials: West Conshohocken, PA, USA, 2017.
44. *BS 812*; Methods for Sampling and Testing of Mineral. Aggregates, Sands and Fillers, Part. 1: Methods for Determination of Particle Size and Shape. British Standard Institution: London, UK, 1975.
45. *ASTM Standard C642*; Standard Test Method for Density, Absorption, and Voids in Hardened Concrete. ASTM International: West Conshohocken, PA, USA, 2006. [[CrossRef](#)]
46. Petrounias, P.; Giannakopoulou, P.P.; Rogkala, A.; Stamatis, P.M.; Tsikouras, B.; Papoulis, D.; Lampropoulou, P.; Hatzipanagiotou, K. The Influence of Alteration of Aggregates on the Quality of the Concrete: A Case Study from Serpentinities and Andesites from Central Macedonia (North Greece). *Geosciences* **2018**, *8*, 115. [[CrossRef](#)]
47. Petrounias, P.; Giannakopoulou, P.P.; Rogkala, A.; Lampropoulou, P.; Tsikouras, B.; Rigopoulos, I.; Hatzipanagiotou, K. Petrographic and Mechanical Characteristics of Concrete Produced by Different Type of Recycled Materials. *Geosciences* **2019**, *9*, 264. [[CrossRef](#)]
48. Petrounias, P.; Rogkala, A.; Giannakopoulou, P.P.; Lampropoulou, P.; Xanthopoulou, V.; Koutsovitis, P.; Koukouzas, N.; Lagogiannis, I.; Lykokanellos, G.; Golfopoulos, A. An Innovative Experimental Petrographic Study of Concrete Produced by Animal Bones and Human Hair Fibers. *Sustainability* **2021**, *13*, 8107. [[CrossRef](#)]
49. Muhmood, L.; Vitta, S.; Venkateswaran, D. Cementitious and pozzolanic of electric arc furnace steel slags. *Cem. Concr. Res.* **2009**, *39*, 102–109. [[CrossRef](#)]
50. Adolfsson, D.; Robinson, R.; Engström, F.; Björkman, B. Influence of mineralogy on the hydraulic properties of ladle slag. *Cem. Concr. Res.* **2011**, *41*, 865–871. [[CrossRef](#)]
51. Arnout, L.; Beersaerts, G.; Liard, M.; Lootens, D.; Pontikes, Y. Valorising Slags from Non-ferrous Metallurgy into Hybrid Cementitious Binders: Mix Design and Performance. *Waste Biomass Valor.* **2021**, *12*, 4679–4694. [[CrossRef](#)]

Article

Chloride Penetration Behavior of Concrete Made from Various Types of Recycled Concrete Aggregate

Wanchai Yodsudjai and Kirati Nitichote *

Department of Civil Engineering, Kasetsart University, Bangkok 10900, Thailand; fengwcy@ku.ac.th

* Correspondence: kirati.ni@ku.th

Abstract: This research aimed to identify the link between the chloride penetration behavior of concrete made from various types of recycled aggregate from three main sources—building demolition waste (B-RCA), laboratory waste (L-RCA), and precast concrete waste (P-RCA)—and the 28-days compressive strength of natural aggregate concrete with the replacement ratio 30%, 60% and 100% respectively. The results of the study revealed that the quality of recycled aggregate waste significantly impacted concrete behavior. To elaborate, finer aggregate potentially increased the inter-facial transition zone (ITZ), which is the weakness part of concrete, resulting in the concrete having less compressive strength as well as increasing amount of chloride ion penetration thought rapid test. In this research, an image processing technique, which is a simple method, was used to quantify the ITZ area of concrete. It was found that concrete with low compressive strength and high permeability values had an ITZ area significantly more than other types of concrete.

Keywords: construction demolition waste; recycle concrete aggregate; sustainable construction

Citation: Yodsudjai, W.; Nitichote, K. Chloride Penetration Behavior of Concrete Made from Various Types of Recycled Concrete Aggregate. *Sustainability* **2022**, *14*, 2768. <https://doi.org/10.3390/su14052768>

Academic Editors: Carlos Morón Fernández and Daniel Ferrández Vega

Received: 27 January 2022

Accepted: 22 February 2022

Published: 26 February 2022

Publisher's Note: MDPI stays neutral with regard to jurisdictional claims in published maps and institutional affiliations.



Copyright: © 2022 by the authors. Licensee MDPI, Basel, Switzerland. This article is an open access article distributed under the terms and conditions of the Creative Commons Attribution (CC BY) license (<https://creativecommons.org/licenses/by/4.0/>).

1. Introduction

The urban expansion leads to the rise of building construction, especially in developing countries. Therefore, the use of concrete which is the primary material in such construction is also increasing [1]. This results in an increase in the use of natural crushed stone which constitutes two-thirds of the total weight of concrete. Moreover, 5–10 percent of the concrete used in construction has turned into waste [2]. However, the inappropriate disposal of leftover concrete such as dumping it at a landfill and using it in the landfilling process has been widely practiced. This leads to more problems in the future. To tackle the problem, the concept of turning the leftover into aggregate used in concrete is developed.

The sources of aggregate waste from the construction industry come from three main sources: building demolition waste, laboratory waste, and precast concrete waste. [3] The behavior of recycled aggregate concrete differs from that of natural aggregate concrete [4,5] in terms of compressive strength, the efficiency of fresh concrete, chloride penetration, etc. The concrete properties have been tested over and over; however, there has been no explanation of how concrete behavior from various sources is linked to its actual behavior.

This research aimed to analyze the behavior of concrete made from various types of recycled aggregate from different sources in terms of compressive strength and chloride penetration through an image processing technique.

1.1. Chloride Penetration Behavior

The longer the concrete is in use, the higher the probability of water and air penetrating it becomes. Ref. [6] The presence of water and air is the cause of other undesirable compounds [7,8]. For example, chloride in the water might be found in the concrete. The most undesirable effect of chloride is that it can react with passive film covering the reinforcement, resulting in the passive film deteriorating. As a result, the reinforcement without the passive film will react with the penetrating water and air and will eventually rust. This

in turn makes the reinforcement occupy a greater volume of the concrete, allowing more air and water to penetrate the concrete. This process, as a chain reaction, accelerates the deterioration of the concrete and reinforcement. [9–11]

According to the EN 1744-1 [12] Test for Chemical Properties of Aggregate, ASTM C33 [13] Standard Specification for Concrete Aggregate, the amount of chloride in natural aggregate must be less than 0.01 percent and can be up to 0.03–0.15 percent in recycled aggregate by wet chemistry method. This is because chloride content might be present in mortar waste in recycled aggregate or the recycled aggregate itself was previously used where chloride content was present [14]. This results in the increase in water absorption of the concrete corresponding with the amount of the recycled aggregate. This also applies to the chloride penetration ratio of the concrete. According to previous studies, [15] the problem of chloride penetration behavior could be solved by decreasing the water over cement ratio. This would help the concrete yield the desirable strength. Moreover, the research conducted by [16] found that the type of recycled aggregate also plays a role in the chloride penetration behavior of concrete, with the chloride penetration of fine aggregate higher than that of coarse aggregate.

1.2. Sources of Recycled Aggregate

There have been studies on recycled aggregate in concrete for some time. Reliable studies mentioned the properties of concrete and the behavior of the construction from recycled aggregate concrete. They found that recycled aggregate concrete plays a significant role in water absorption in aggregate, leading to lowered permeability resistance [17]. The water absorption capacity of recycled aggregate concrete is considered high (>7 percent) according to the standardized measure provided by [18] JIS A5002. Moreover, recycled aggregate concrete has a lower compressive strength compared to natural aggregate concrete by 21 percent [19]. However, if the amount of recycled aggregate in the concrete is restricted to not more than 20–30 percent of the total concrete, there is a negligible difference between the properties of recycled aggregate concrete and those of natural aggregate concrete. [20] In 2014, [21] Duan and Poon conducted research on the properties of concrete with mortar on the stone surface and from different sources. The result was that recycled aggregate with a little amount of mortar on the stone surface had low water absorption capacity and therefore can be a substitute for natural aggregate. Likewise, the research by [22] Pedro et al., 2014 also found that the water absorption capacity of recycled aggregate was medium as represented by 3.9–7.6 percent. As a result, a recycled aggregate could be used in concrete with high compressive strength.

Still, the aforementioned research did not analyze the cause of different behaviors of three different types of aggregate concrete. Also, it is worth mentioning that the research did not take the recycled aggregate which came from different sources into account. More importantly, the area of ITZ which significantly affects the properties of the concrete was not considered.

2. Materials and Methods

The recycled aggregate made from 3 sources was investigated (Figure 1). The first was the leftover cube concrete specimens from laboratory testing, with an existing strength ranging from 40–45 MPa. The second was the waste from the rejected product from the precast hollow core slab industry with an average strength of 35 MPa. The last one was the building demolition waste, especially the building demolition concrete from the building of which the location interposes the new underground MRT Orange line in the capital city of Thailand. This example emphasizes the increasing demand for infrastructure renovation from the fast-growing city. The coring sample of concrete structure from the building was tested to verify its existing compressive strength which turned out to be 16 MPa on average. B-RA, P-RA, and L-RA represent recycled aggregate from building demolition, aggregate from precast concrete waste, and aggregate from laboratory waste respectively. The concrete waste was crushed and graded according to ACI 555 [23]. Then,

the natural aggregate concrete was replaced by L-RCA, P-RCA, B-RCA with the proportion of 30 percent, 60 percent, and 100 percent respectively as indicated in Table 1. Short-Term properties of concrete from recycled aggregate were verified in terms of strength and elastic modulus in the period of 7, 14, and 28 days. The durability of the concrete was represented by a rapid chloride penetration test (ASTM C 1202) [24] at 28 day-age concrete.



Figure 1. Recycled aggregate from various sources.

Table 1. Mixed proportions of concrete mixture.

| Mix | Mix Proportion (kg/m ³) | | | | |
|----------|-------------------------------------|-------|------|-------|------|
| | Cement | Water | Sand | Stone | RA |
| NCA | 411 | 206 | 827 | 1028 | - |
| L-RA 30 | 411 | 206 | 827 | 719 | 309 |
| L-RA 60 | 411 | 206 | 827 | 616 | 412 |
| L-RA 100 | 411 | 206 | 827 | - | 1028 |
| P-RA 30 | 411 | 206 | 827 | 719 | 309 |
| P-RA 60 | 411 | 206 | 827 | 616 | 412 |
| P-RA 100 | 411 | 206 | 827 | - | 1028 |
| B-RA 30 | 411 | 206 | 827 | 719 | 309 |
| B-RA 60 | 411 | 206 | 827 | 616 | 412 |
| B-RA 100 | 411 | 206 | 827 | - | 1028 |

The standard controlled concrete mix ratio for comparison with recycled aggregate concrete was Natural Concrete Aggregate (NCA). The mixing ratio was calculated to obtain the required tensile strength of approximately 25 Mpa. Then in the experiment, different proportions of the aggregates from natural stone were substituted. By using aggregate from the recycling as mentioned above. Table 1 shows the proportion of concrete mix used in the sample for this test.

2.1. Aggregate

The aggregate used in the concrete mixture was from three sources. From Figure 2, the particles of L-RCA and B-RCA were larger than that of P-RCA due to the smaller size of natural crushed stone used in precast concrete. Another point was that L-RCA possessed less cement paste on the aggregate's surface because of its higher parent strength compared to that of B-RA. The shape of L-RA aggregates is angular, similar to those obtained from natural stone. The B-RA is also angular, but from a comparative physical appearance, it appears to have more porosity from old-adhered mortar. The final aggregates that make up the fraction of Precast Hollow Core Slab are round but small and very porous as well.

According to the test, the distribution of different particle sizes of the coarse aggregate corresponded to ASTM C135 [25] Standard Test Method for Sieve Analysis of Fine and Coarse Aggregates as shown in Figure 3. However, it could be observed that the distribution of precast concrete waste of different sizes with mostly fine aggregate was higher than that of other types of aggregate.

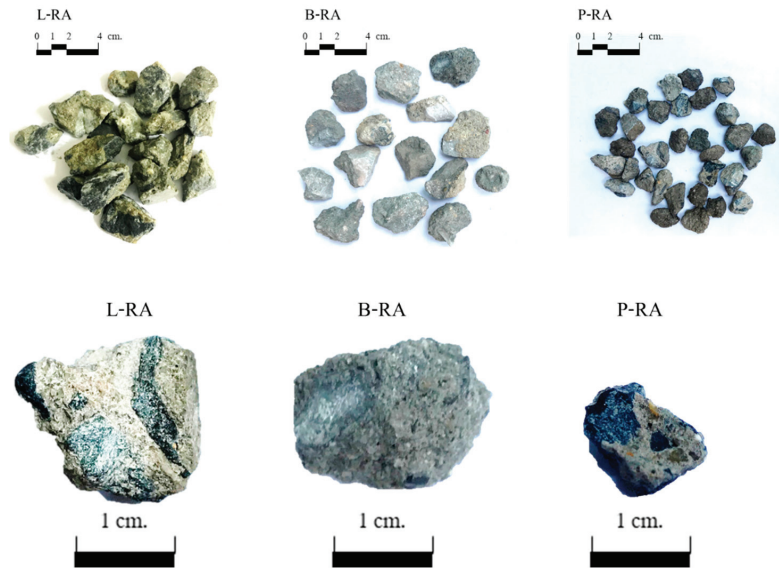
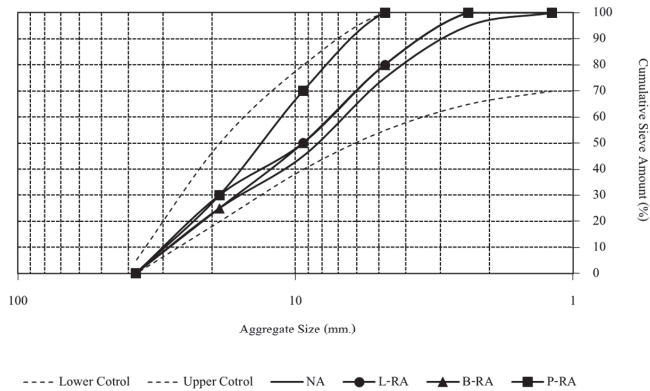


Figure 2. Recycled aggregate from laboratory waste (L-RA), building demolition waste (B-RA) and precast concrete waste (P-RA).



| | Cumulative Sieve Amount (%) | | | | | |
|---------|-----------------------------|--------------|-----|------|------|------|
| | Lower Cotrol | Upper Cotrol | NA | L-RA | P-RA | B-RA |
| No.16 | 70 | 100 | 100 | 100 | 100 | 100 |
| No.8 | 65 | 100 | 95 | 100 | 100 | 100 |
| No.4 | 55 | 100 | 75 | 80 | 100 | 80 |
| 3/8" | 40 | 80 | 45 | 50 | 70 | 50 |
| 3/4" | 20 | 50 | 25 | 30 | 30 | 25 |
| 1 1/2 " | 0 | 5 | 0 | 0 | 0 | 0 |

Figure 3. Aggregate particle size distribution.

2.2. Unit Weight and Absorption Rate of Aggregate

The unit weight of natural aggregate is a little bit higher than that of recycled aggregate, as represented by 14–19%. From Figure 4, the unit weight of natural aggregate was higher

than that of every type of recycled aggregate. This was because there was mortar waste on the surface and the crushing process might leave the shape of the surface distorted. Moreover, the particle size of recycled aggregate was mostly at the same size range, resulting in more rooms in concrete and eventually in lower unit weight. Considering the water absorption rate, it was obvious that the unit weight of natural aggregate was lower than that of recycled aggregate. From Figure 5, the water absorption percentage of recycled aggregate was 6.65, 8.72, and 6.78 times higher than that of natural aggregate. This was because there was mortar present on the outer surface of recycled aggregate, resulting in higher porosity, lower specific gravity, and higher water absorption when compared to natural aggregate.

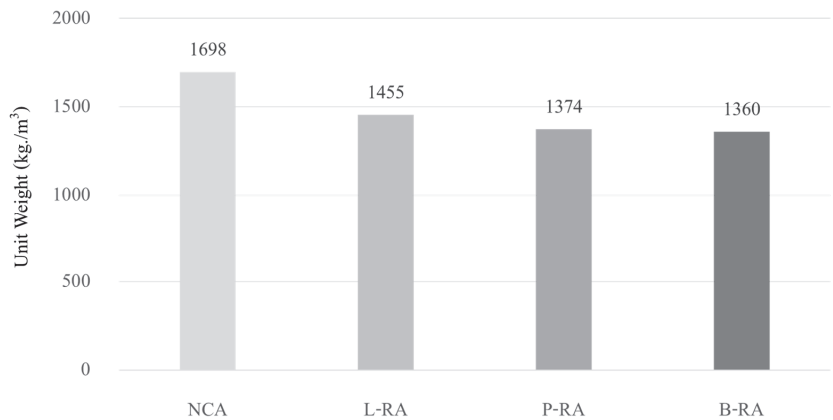


Figure 4. The unit weight of aggregate.

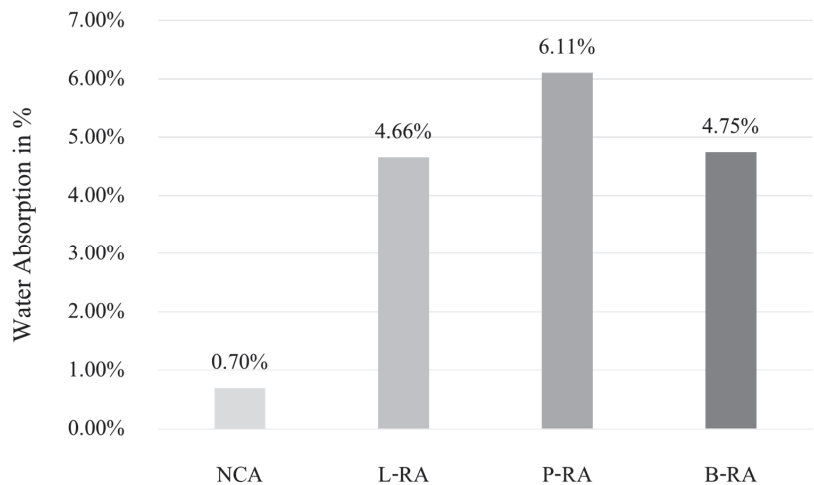


Figure 5. Percentage of Water Absorption for each type of Aggregates.

2.3. Rapid Chloride Penetration

The chloride penetration concrete test according to ASTM C 1202 was conducted using a rapid chloride permeability test after a 28-day period of curing. From Figure 6, the test consisted of a clamp tab, a concrete cube containing a 3 percent concentration of sodium chloride (NaCl) solution on the cathode side and a 0.3M concentration of sodium

hydroxide (NaOH) on the anode side. Then, it is connected to a 60-volt DC power supply and data logger.

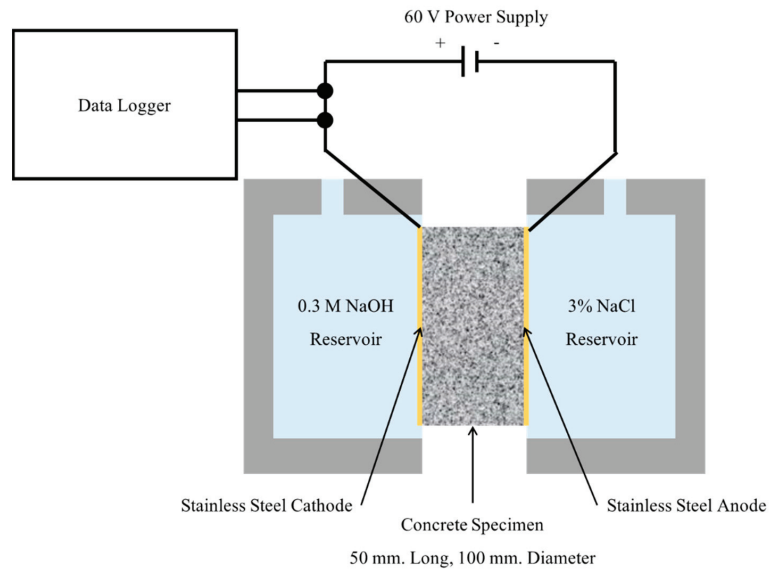


Figure 6. Test setup of the Rapid Chloride Penetration Test.

According to the experiment, although the chloride ion permeability, which is an indicator of concrete durability, could not be measured, the total amount of chloride ion permeating through the concrete was measured. Still, the result might not be easily applicable in real-life situations. However, ASTM C1202 presented a table to determine the concrete quality with different chloride ion permeabilities as shown in Table 2.

Table 2. Chloride permeability based on the total charge passed.

| Total Charge Passed (Coulombs) | Chloride Permeability |
|--------------------------------|-----------------------|
| >4000 | High |
| 2000–4000 | Moderate |
| 1000–2000 | Low |
| 100–1000 | Very low |
| <100 | Negligible |

2.4. Image Processing

Figure 7 shown vertical cross section of concrete sample so that the properties of the concrete could be carefully examined. Then, the concrete was captured with a digital camera with at least 5 MB resolution. The image was then analyzed by the MATLAB program, in which the process involved converting the image to greyscale so that the color intensity of each element in the concrete could be clearly seen. After this process, the image was denoised. Subsequently, the area of ITZ of each element was processed. The result was the differences in color intensity, with the void being the highest, followed by mortar and aggregate respectively. In order to analyze the area of ITZ, the perimeter needed to be identified. Then, the area of ITZ could be determined by multiplying the perimeter by an average ITZ thickness.

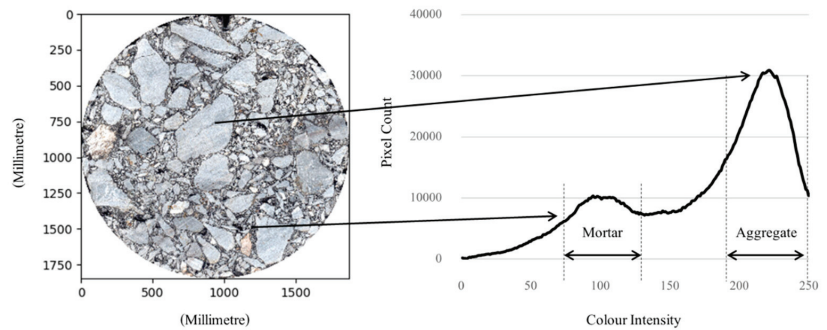


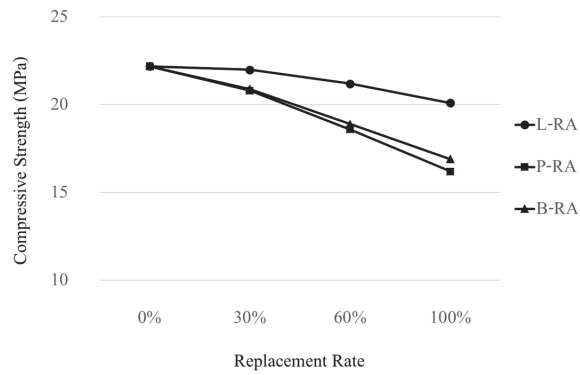
Figure 7. Color pixel population from image processing.

3. Results

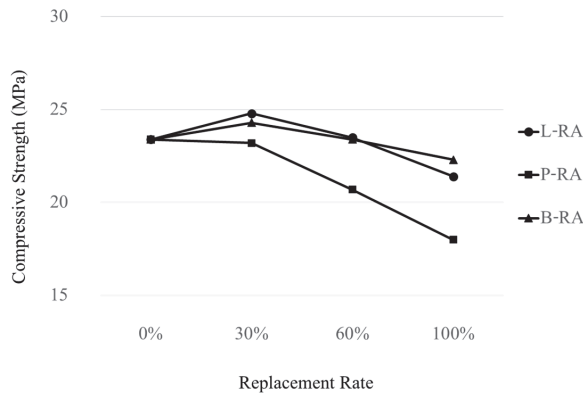
3.1. Compressive Strength

The compressive strength of concrete was tested by using a block of concrete with a compressive strength of 28 MPa. Then, each new concrete block was cast from standard cylinder-shaped concrete formworks with a 10 cm. diameter and a 20 cm. in height. After 24 h, the concrete formworks were removed and the concrete blocks were aged in clean water for 7 days, 14 days, and 28 days respectively. The concrete blocks were subsequently tested for compressive strength. Concrete samples with four different coarse aggregates were collected: natural aggregate concrete, laboratory waste concrete (L-RCA), precast concrete waste (P-RCA), and building demolition waste (B-RCA). The natural aggregate concrete was replaced by L-RCA, P-RCA, B-RCA with the proportion of 30 percent, 60 percent, and 100 percent respectively.

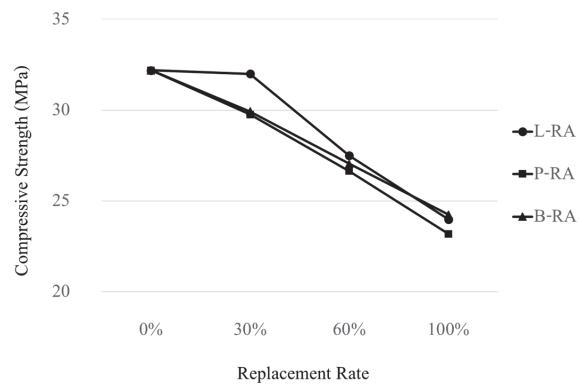
From Figure 8a–c the decreasing trend in compressive strength corresponded with the increasing amount of recycled aggregate mixed in the concrete. Three types of recycled aggregate concrete with a 30 percent replacement rate showed negligible differences in terms of compressive strength compared to the other two replacement rates. As for the recycled aggregate concrete blocks with a 30 percent replacement rate, the vertical crack propagation occurred, and the cracks split apart into two pieces. This stemmed from the fact that the mortar waste could handle less compressive strength than the coarse aggregate. On the other hand, the coarse aggregate and recycled aggregate themselves did not suffer any damages or cracks. As for the 60 percent replacement rate, the vertical crack propagation occurred and reached half of the concrete's height at a 70-degree angle. The crack resulted from the shear force coming from the bond strength of composite and internal friction. As for the 100 percent replacement rate, the vertical crack propagation occurred and reached one-thirds of the concrete's height, but the crack did not cover all the cross-section concrete areas. Moreover, some of the cracks split into tiny pieces due to the dramatic differences in compressive strength of each recycled aggregate, shear force coming from the bond strength of composite and internal friction. However, their failure tended to be the lowest and could handle the least compressive strength compared to the other two.



(a) Compressive strength at 7 days.



(b) Compressive strength at 14 days



(c) Compressive strength at 28 days

Figure 8. Compressive strength of concrete at 0%, 30%, 60% and 100% replacement rate at: (a) 7 days, (b) 14 days, and (c) 21 days.

3.2. Chloride Penetration Resistance

From Figure 9, the result showed total charge passed at 28 days of natural coarse aggregate and various types of recycled aggregate by rapid chloride test. It obviously seen that natural aggregate concrete (NCA) was the only type that had a moderate chloride ion permeability rate (2000–4000 coulombs) in accordance with ASTM C1202. On the other hand, all the proportions of recycled aggregate concrete were considered to have a high chloride ion permeability. Concrete made from laboratory and building demolition aggregate are slightly higher than NCA based value about 25% at any replacement ratio. There is also an increase in the recycled aggregate to natural aggregate ratio of these two types of samples do not increase the chloride permeability much. It is worth noting that concrete made from scraps of prefabricated concrete slabs. Instead, the permeability value of the chloride is very high. In one way it could be said that at 30% displacement, the permeability rate is close to that of natural aggregate concrete. But increasing the percentage of renewable aggregates to 60% or 100% increased the permeability significantly, over 71% and 106% compared to the 30% recycle aggregate samples, respectively.

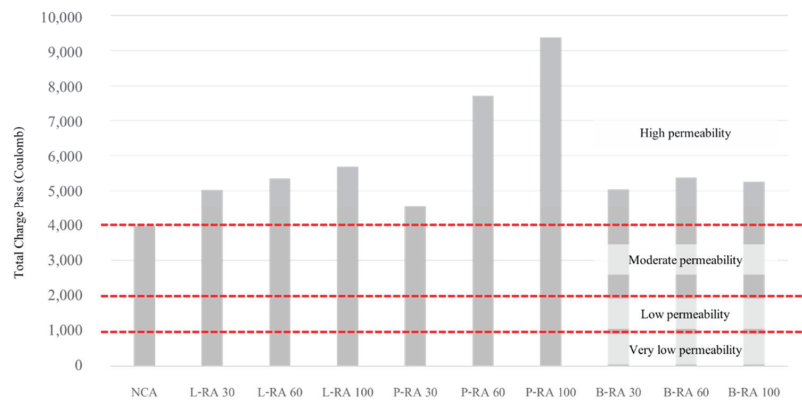


Figure 9. The total charge passed at 28 days of natural coarse aggregate and various types of recycled aggregate.

3.3. Chloride Penetration and Compressive Strength

The relationship between chloride penetration and compressive strength of 28-day recycled aggregate concrete is shown in Figure 10. The decreasing penetration rate of L-RCA (Circle), P-RCA (Square), and B-RCA RCA (Triangle) corresponded with their increasing compressive strength. The effect of replacement percentage, it has a high effect on the concrete mixed with P-RCA aggregate when the ratio is increased it will increase the compressive strength and chloride permeability as well. However, for the L-RCA and B-RCA samples, it was found that the increase in the aggregate's substitution ratio had a large effect on the compressive strength and chloride permeability. The two relationships between L-RCA and P-RCA could be explained by R^2 which was well fit up to 95 percent and 99 percent respectively. Based on this result, it can be confirmed that linear regression relationship between compressive strength and chloride penetration. However, as for aggregate from the precast slab waste, the chloride penetration rate tended to be very high, which was indirectly proportional to the compressive strength. On the other hand, when considering the water absorption of P-RCA aggregates, it is found that higher water absorption rates than other aggregates have a reliable effect on the absorption values. The passivity of chloride was also higher. This highlighted the sensitivity to a change of compressive strength which significantly affected the porosity of this type of recycled aggregate.

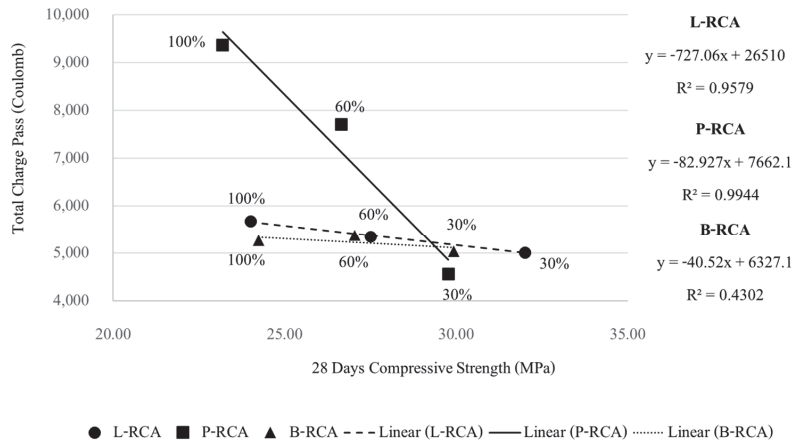


Figure 10. The relationship between the total charge passed and compressive strength.

4. Discussion

4.1. Failure Mode

The aggregate porosity played a vital role in how the crack occurred, which also directly affected the compressive strength of the concrete. Ref. [26] Normally, the crack path advances through aggregate, mortar, and ITZ, depending on the ability to handle the strength of each part as shown in Figure 11. In natural aggregate concrete (NCA), the crack path went through the mortar and ITZ around the aggregate. In contrast, in laboratory waste (L-RA) and building demolition waste aggregate concrete (B-CA), it was possible for some crack paths to go through the previously existing ITZ, which occurred between some of the previously existing mortar and aggregate, while other crack paths might go through the new ITZ, depending on which ITZ could bear higher strength. This result is explained by research from Li et al. [27] which found that old mortar is the weakest of Recycle Concrete Aggregate. If the parent strength of recycled aggregate is high, the ITZ might be able to handle more strength. Lastly, in precast slab waste aggregate (P-RA), due to high porosity in this type of aggregate, which resulted from the use of small-sized stones and in turn leading to a larger area of ITZ. Thus, the crack path could go through its ITZ much more easily compared to the other two.

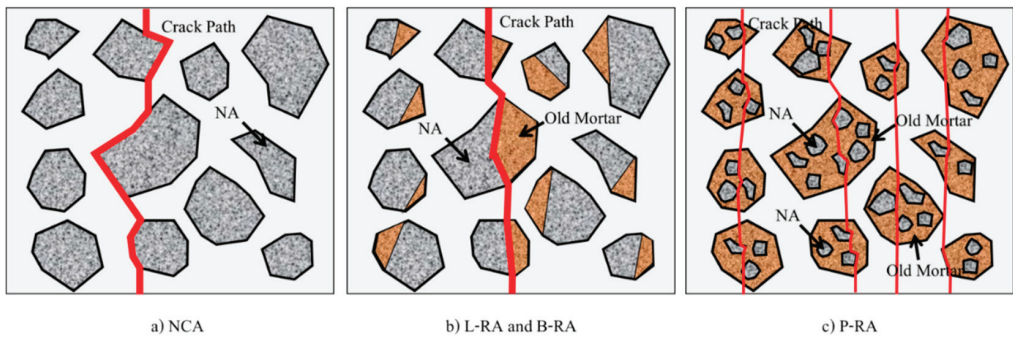


Figure 11. Crack propagation in composition containing: (a) concrete containing NCA, (b) concrete containing L-RA and B-RA, and (c) concrete containing P-RA.

4.2. Durability Mode

Photos from an image processing technique showed the area of each phase as shown in Figure 12. In the first row are raw photos which were denoised. The photos in the second row show the phase distribution in the cross-section area of the concrete after using an image processing technique. Finally, in the last row are the percentages of each phase of NCA, B-RA and P-RA. The phase of NCA and B-RA showed a similar distribution, unlike that of P-RA. To elaborate, the phase area of P-RA aggregate was nearly twice that of NCA and B-RA. The larger phase area of P-RA resulted in the increase in ITZ. The length of ITZ was determined by drawing a line in the CAD program as shown in Figure 13. Then, the area of ITZ of concrete cross-section was identified by multiplying the length of ITZ by its thickness 40 µm on average based on the research by Zouaoui et al. [28] which proposed that the ITZ thickness ranged from 30–50 µm.

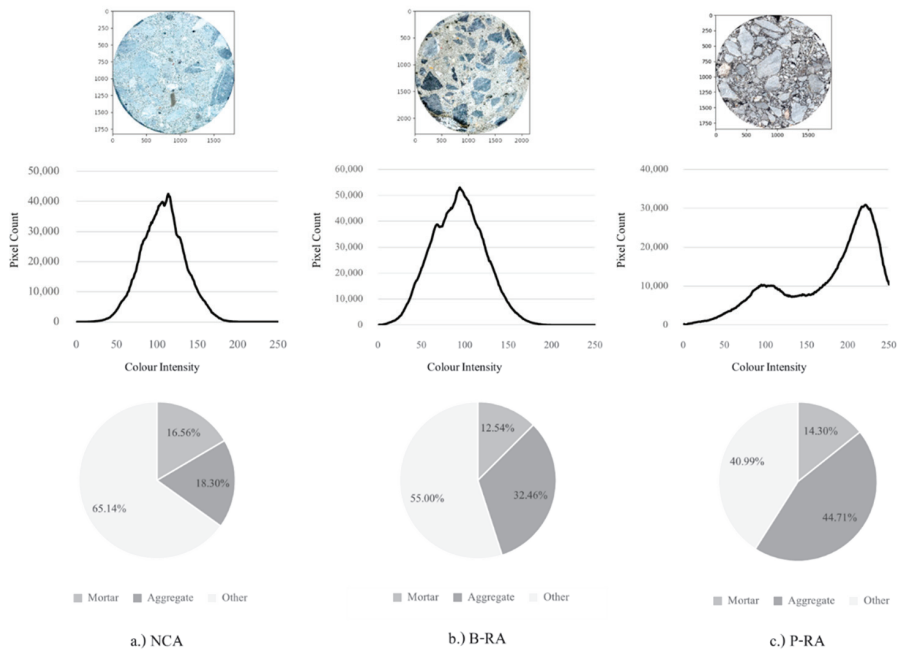


Figure 12. Phase distribution of (a) NCA and (b) B-RA and (c) P-RA using an image processing method from picture (top) to pixel distribution (middle) and pixel distribution (bottom).

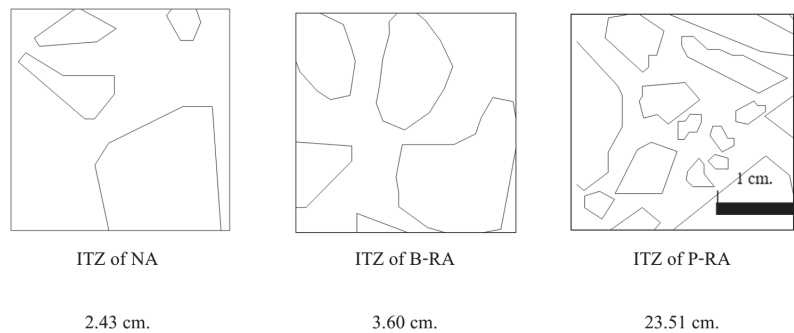


Figure 13. The length of Inter-Facial Transition Zone in concrete.

Figure 14 demonstrates the schematic of chloride penetration through the cross-section of concrete. Chloride could penetrate the mortar to certain extent, but could penetrate the ITZ area better, while chloride could barely penetrate or could not penetrate the stone area at all. According to the research by Silva et al. which investigated the relationship between the total charge passed and chloride migration coefficient based on 120 studies, the relationship between these two is linear as presented in the equation below

$$y = 0.0034x$$

If

$$y = \text{Chloride migration coefficient (De), } \times 10^{-12} \text{ m}^2/\text{s}$$

$$x = \text{Total charge passed, Coulombs}$$

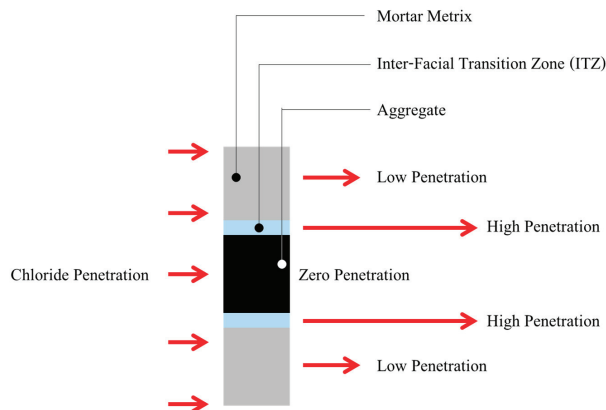


Figure 14. The schematic of chloride penetration through concrete.

The relationship between the ITZ area determined by the calculation above and the total charge passed was exponential. To illustrate, the area of ITZ obtained by an image processing technique played a crucial role in the amount of chloride penetration in exponential relationship which $R^2 = 0.9994$ (Figure 15). This also directly affects the concrete durability in accordance with the research by Azarsa and Gupta [29].

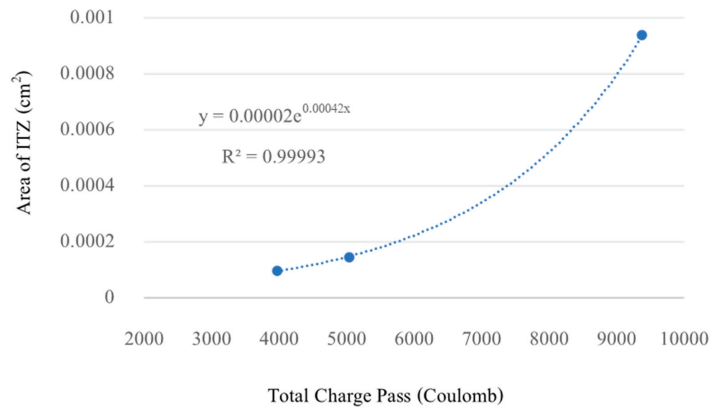


Figure 15. The relationship between the area of Inter-facial Transition Zone and the total charge passed.

5. Conclusions

This research analyzed the chloride penetration behavior of natural aggregate concrete and that of recycled aggregate from three different sources. An image processing technique was used to explain the results which could be summarized as follows:

- (a) Although the unit weight was similar to that of NA, the % Water Absorption difference was 6–8 times more on average. In this respect, the pre-formed RCA concrete has been used from different sources, including from old buildings (B-RCA), from precast concrete slab specimens (P-RCA), and from laboratory test specimens (L-RCA) has lower chloride permeability properties than NA based concrete, but its penetration rate also depends on the shape of the aggregate which the aggregates are small and the quantity of old-adhered mortar. It will make the permeability a lot. Otherwise, the compressive strength was not significantly different between the ages of 7, 14 and 28 days.
- (b) Increasing of percent replacement is added, higher the compressive strength and chloride penetration resistance, the better from the Rapid Chloride Penetration Test at all 30%, 60% and 100% Replacement Ratios. It is worth noting that P-RCA has the highest chloride permeability. When considering the % Water Absorption that P-RCA has the most and considering the mixed part of the aggregate which is somewhat more detailed than other types of aggregate, it can be determined that the chloride permeability properties and the strength is linked to the physical nature of the aggregates. In this experiment, the area of the ITZ was taken into account, which has a significant effect in the case of Recycle Aggregate concrete, since the aggregate is attached to the old ITZ from old-adhered Mortar.
- (c) Using the Image Processing method for considering ITZ in this experiment, it was found that a highly consistent relationship between the size of the imaging ITZ area was identified and the amount of chloride permeation. An image processing technique could be used to explain the characteristics of each element in the cross-section of the concrete. The method yielded the results in accordance with the concrete behaviors. In the future, it would be possible to predict the properties of concrete if there are ample information archives of the cross-section of concrete.

Author Contributions: Conceptualization, W.Y.; methodology, W.Y.; software, K.N.; validation, W.Y. and K.N.; formal analysis, K.N.; investigation, K.N.; resources, K.N.; data curation, K.N.; writing—original draft preparation, K.N.; writing—review and editing, K.N.; visualization, K.N.; supervision, W.Y. project administration, K.N.; funding acquisition, K.N. All authors have read and agreed to the published version of the manuscript.

Funding: This research received no external funding.

Institutional Review Board Statement: Not applicable.

Informed Consent Statement: Not applicable.

Data Availability Statement: Not applicable.

Conflicts of Interest: The authors declare no conflict of interest.

References

1. Opon, J.; Henty, M. An indicator framework for quantifying the sustainability of concrete materials from the perspectives of global sustainable development. *J. Clean. Prod.* **2019**, *218*, 718–737. [[CrossRef](#)]
2. Dhir, R.K.; Dyer, T.D.; Newman, M.D. Ultimate Concrete Opportunities: Achieving Sustainability in Construction. In Proceedings of the International Conference on Global construction, London, UK, 5–6 July 2005.
3. Saez, P.V.; del Rio Merino, M.; Gonzalez, A.S.A.; Porras-Amores, C. Best Practice measure assessment for construction and demolition waste management in building constructions. *Resour. Conserv. Recycl.* **2013**, *75*, 52–62. [[CrossRef](#)]
4. Otsuki, N.; Miyasato, S.; Yodsudjai, W. Influence of Recycled Concrete on Interfacial Transition Zone, Strength, Chloride Penetration and Carbonation of Concrete. *J. Mater. Civ. Eng.* **2004**, *15*, 443–451. [[CrossRef](#)]
5. Rao, A.; Jha, K.N.; Misra, S. Use of Aggregate from Recycled Construction and Demolition Waste in Concrete. *Resour. Conserv. Recycl.* **2007**, *50*, 71–81. [[CrossRef](#)]

6. Yu, Y.; Wang, P.; Yu, Z.; Yue, G.; Wang, L.; Guo, Y.; Li, Q. Study on the Effect of Recycled Coarse Aggregate on the Shrinkage Performance of Green Recycled Concrete. *Sustainability* **2021**, *13*, 13200. [[CrossRef](#)]
7. Malecot, Y.; Zingg, L.; Briffaut, M.; Baroth, J. Influence of free water on concrete triaxial behavior: The effect of porosity. *Cem. Concr. Res.* **2019**, *120*, 207–216. [[CrossRef](#)]
8. Accary, A.; Malecot, Y.; Daudeville, L. Design and Evaluation of a Deformable Sensor for Interstitial Pore Pressure Measurement in Concrete under Very High Stress Level. *Appl. Sci.* **2019**, *9*, 2610. [[CrossRef](#)]
9. Lu, B.; Shi, C.; Cao, Z.; Guo, M.; Zheng, J. Effect of carbonated coarse recycled concrete aggregate on the properties and micro-structure of recycled concrete. *J. Clean. Prod.* **2019**, *233*, 421–428. [[CrossRef](#)]
10. Kim, H.; Goulias, D.G. Shrinkage Behavior of Sustainable Concrete with Crushed Returned Concrete Aggregate. *J. Mater. Civ. Eng.* **2015**, *27*, 4014204. [[CrossRef](#)]
11. Knaack, A.M.; Kurama, C.Y. Behavior of Reinforced Concrete Beams with Recycled Concrete Coarse Aggregates. *J. Struct. Eng.* **2015**, *141*, B4014009. [[CrossRef](#)]
12. EN 1744-1; Tests for chemical properties of aggregates Chemical analysis. BSI: Pilsen, Czech Republic, 2012.
13. ASTM C33; Standard Specification for Concrete Aggregates. ASTM: West Conshohocken, PA, USA, 2016.
14. Vázquez, E.; Marilda Barra Bizinotto, M.B.; Aponte, D.; Jiménez, C. Improvement of the durability of concrete with recycled aggregates in chloride exposed environment. *Constr. Build. Mater.* **2014**, *67*, 61–67. [[CrossRef](#)]
15. Nakhi, A.B.; Alhumoud, J.M. Effects of Recycled Aggregate on Concrete Mix and Exposure to Chloride. *Adv. Mater. Sci. Eng.* **2019**, *2019*, 7605098. [[CrossRef](#)]
16. Silva, R.V.; de Brito, J.; Neves, R.; Dhir, R.K. Prediction of Chloride Ion Penetration of Recycled Aggregate Concrete. *Mater. Res.* **2015**, *18*, 427–440. [[CrossRef](#)]
17. Mehta, P.K. Greening of the Concrete Industry for Sustainable Development. *Concr. Int.* **2002**, *24*, 23–28.
18. Etxeberria, M.; Konoiko, M.; Garcia, C.; Perez, M.Á. Water-Washed Fine and Coarse Recycled Aggregates for Real Scale Concrete Production in Barcelona. *Sustainability* **2022**, *14*, 708. [[CrossRef](#)]
19. JIS A5002; Lightweight aggregates for structural concrete. JIS: Tokyo, Japan, 2003.
20. McNeil, K.; Kang, T. Recycled Concrete Aggregates: A Review. *Int. J. Concr. Struct. Mater.* **2012**, *7*, 61–69. [[CrossRef](#)]
21. Duan, Z.; Poon, C.S. Properties of recycled aggregate concrete made with recycled aggregates with different amounts of old adhered mortars. *Mater. Des.* **2014**, *58*, 19–29. [[CrossRef](#)]
22. Pedro, D.; de Brito, J.; Evangelista, L. Influence of the use of recycled concrete aggregates from different sources on structural concrete. *Constr. Build. Mater.* **2014**, *71*, 141–151. [[CrossRef](#)]
23. ACI 555; Concrete with Recycled Materials. ACI: Pflugerville, TX, USA, 2001.
24. ASTM C1202; Standard Test Method for Electrical Indication of Concrete's Ability to Resist Chloride Ion Penetration. ASTM: West Conshohocken, PA, USA, 2019.
25. ASTM C135; Standard Test Method for True Specific Gravity of Refractory Materials by Water Immersion. ASTM: West Conshohocken, PA, USA, 2015.
26. Yue, G.; Ma, Z.; Liu, M.; Liang, C.; Ba, G. Damage behavior of the multiple ITZs in recycled aggregate concrete subjected to aggressive ion environment. *Constr. Build. Mater.* **2020**, *245*, 118419. [[CrossRef](#)]
27. Li, W.; Xiao, J.; Sun, Z.; Shah, S. Failure processes of modeled recycled aggregate concrete under uniaxial compression. *Cem. Concr. Compos.* **2012**, *34*, 1149–1158. [[CrossRef](#)]
28. Azarsa, P.; Gupta, R. Electrical Resistivity of Concrete for Durability Evaluation: A Review. *Adv. Mater. Sci. Eng.* **2017**, *2017*, 8453095. [[CrossRef](#)]
29. Zouaoui, R.; Miled, K.; Limam, O.; Beddey, A. Analytical prediction of aggregates' effects on the ITZ volume fraction and Young's modulus of concrete. *Int. J. Numer. Anal. Methods Geomech.* **2017**, *41*, 976–993. [[CrossRef](#)]

Article

Mechanical Properties and Durability Performance of Recycled Aggregate Concrete Containing Crumb Rubber

Robert B. Ataria* and Yong C. Wang

School of Mechanical, Aerospace and Civil Engineering, University of Manchester, Manchester M1 7JR, UK; yong.wang@manchester.ac.uk

* Correspondence: robertataria@yahoo.com

Abstract: Despite extensive research studies, recycled aggregates and worn-out tyres of motor vehicles are still not fully reused and are hence disposed of in ways that are damaging to the environment. Several studies have been carried out on recycled aggregate and rubberized concrete, but very limited studies are conducted on rubber recycled aggregate concrete. This study focuses on the workability, mechanical properties and durability performance of concrete made with 100% recycled aggregates and crumb rubber at different replacement level (5%, 10%, 15% and 20%). The first stage of the study covers the effect of incorporating crumb rubber at different concentration on the workability and mechanical properties of recycled aggregate concrete. The results revealed that the workability and mechanical properties of the recycled aggregate concrete can be used for structural applications when 5% of crumb rubber are used to replace recycled aggregates. The 28-days compressive strength of the rubberized recycled aggregate concrete with 5% crumb rubber concentration is reduced by 21.1% and 32.8% when compared to recycled aggregate concrete and control concrete, respectively. The second stage of the study assesses the durability performance of the recycled aggregate concrete with 5% crumb rubber concentration. The 5% crumb rubber content for durability tests was considered because the ultrasonic pulse velocity tests revealed that the quality of the recycled aggregate concrete is questionable if the concentration of crumb rubber particles is beyond 5%. The durability performance using the surface resistivity test also shows that the chloride ion penetration of recycled aggregates concrete with 5% crumb rubber replacement is moderate using air dried curing technique and high using the water bath curing method. Hence the study suggests the use of rubber recycled aggregate concrete for applications where the exposure condition is not extreme.

Keywords: recycled aggregates; crumb rubber; recycled concrete; compressive strength; tensile strength; durability

Citation: Ataria, R.B.; Wang, Y.C. Mechanical Properties and Durability Performance of Recycled Aggregate Concrete Containing Crumb Rubber. *Materials* **2022**, *15*, 1776. <https://doi.org/10.3390/ma15051776>

Academic Editors: Daniel Ferrández Vega and Carlos Morón Fernández

Received: 18 December 2021

Accepted: 17 January 2022

Published: 26 February 2022

Publisher's Note: MDPI stays neutral with regard to jurisdictional claims in published maps and institutional affiliations.



Copyright: © 2022 by the authors. Licensee MDPI, Basel, Switzerland. This article is an open access article distributed under the terms and conditions of the Creative Commons Attribution (CC BY) license (<https://creativecommons.org/licenses/by/4.0/>).

1. Introduction

Waste tyre disposal is currently causing serious environmental issues all over the world. Every year, approximately 1 billion waste tyres are generated globally, with 1.6 billion new tyres being produced [1]. Likewise, the amount of construction and demolition (C&D) wastes generated as a result of the increasing demolition of existing infrastructures is a thing of concern. It also is estimated that the UK generated 67.8 million tonnes of non-hazardous C&D waste, of which 62.6 million tonnes (92.3%) was recovered [2]. Studies have tried to utilize recycled aggregates and crumb rubber particles in making new concrete for structural applications [3–5], however a limited number of the studies combine both recycled materials to produce concrete [6–8]. To tackle the twin challenges of improving properties of recycled aggregate concrete, with or without crumb rubber, and replacing concrete using natural aggregates with recycled aggregate, it is necessary to understand the properties of recycled aggregate concrete with and without crumb rubber for structural applications.

The performance of recycled aggregate concrete generally decreases [9–12] and the reduction depends on many factors such as the quality of recycled aggregates [13], replacement level in concrete [9,12], water cement (w/c) ratio [14,15], etc. The strength

reduction was also attributed to the amount of attached cement matrix on the recycled aggregates [10,12,16], which causes a weak interfacial bond between the attached old cement matrix and the surrounding concrete matrix. Different methods have been devised by authors to enhance the performance of the recycled concrete. Some of these techniques include the addition of extra amounts of cement, use of super plasticizers, incorporation of fly ash, silica fume [9,16–18] and the two stage mixing approach [19].

The research results so far also indicate that incorporating crumb rubber in concrete decreases the resulting concretes' compressive and tensile strengths. This is attributed to the lower strength of rubber particles, and their weak bonding with cement paste [20–24]. However, some researchers have demonstrated that if a small amount of crumb rubber (not more than 5% in volume according to [21,25] and not more than 3% according to [26]) is used to replace mineral aggregates in concrete, then the rubberized concrete could maintain the same mechanical properties as concrete without crumb rubber. It is also possible to enhance the mechanical properties of rubberized concrete as suggested in [27–29] by using silica fume. The ultrafine silica fume is believed to create a good bonding between the rubber particles and the surrounding cement paste matrix. Pre-treatment of the rubber particles by soaking in sodium hydroxide NaOH solution before incorporating them into concrete is another method of enhancing the mechanical properties of rubberised concrete, as demonstrated by [6,30]. This was attributed to the benefit of the NaOH solution dislodging the zinc stearate on the rubber surface thereby enhancing the bonding between the rubber powder and the concrete substrate. It was also reported by [23,25,31,32] that rubber particles with small sizes gave higher strength than coarse rubber particles. This was attributed to the formation of larger air voids in the concrete when coarse crumb rubber particles were used [31]. Reference [32] investigated the durability properties of rubberized concrete with up to 30% rubber content. The carbonation depth of rubberized concrete was also greater than that of conventional concrete, and it increased with the rubber content, indicating greater corrosion susceptibility. The study's findings suggest that rubberized concrete with a rubber content of up to 15% can be used for structural components with sufficient strength and service life. Rubberized concrete is frequently used in low-value applications such as road barriers, concrete paving blocks and playground concrete works. However, using rubberized concrete in structural members is an effective way to improve ductility, which is critical for structural members, particularly in seismic areas. When compared to conventional concrete, the use of crumb rubber in precast concrete panels is also beneficial in terms of sound absorption [33].

The current study assesses the performance of concrete made with recycled aggregate and crumb rubbers at different replacement levels. Different studies have been conducted on concrete performance either made with recycled aggregates or crumb rubber, but very limited studies utilize both recycled materials to make concrete [6–8]. Furthermore, there is a lack of information on the durability performance of rubber recycled aggregate concrete; thus, this study aims to fill these knowledge gaps.

2. Materials

2.1. Material Used

CEM 11/B-V 32.5N Portland fly ash cement complying with [34] was used for this study. Uncrushed natural aggregates of 10 mm size and recycled aggregates with composition shown in Table 1 were used in this work. The recycled aggregates used for this work sourced from Offerton Sand and Gravel (Manchester, UK). The recycled aggregates contain other impurities as detailed in Table 1. According to [35], the classification of recycled aggregates used in this study are low quality RC₈₀ (recycled aggregates obtained from concrete products with 20% impurities). The water absorption rates and the densities of both the recycled and natural aggregates are shown in Table 2.

The grading of the natural aggregates, recycled aggregates are shown in Figure 1. Crumb rubber of 8 mm length and 2mm thickness with an aspect ratio of 4 from worn out vehicle tyres as shown in Figure 2 were supplied by SRC Products Ltd. (Stockport, UK).

Table 1. Composition of natural and recycled aggregates.

| Composition | Proportion |
|---------------------|------------|
| Natural aggregates | |
| Quartzite | 79% |
| Sandstone | 6% |
| Basalt | 5% |
| Others | 10% |
| Recycled Aggregates | |
| Recycled Aggregates | 81% |
| Bricks | 13% |
| Dust | 6% |

Table 2. Water absorption rates and densities of natural and recycled aggregates.

| Type | Apparent Particle Density | Particle Density on Oven Dry Bases | Particle Density on Saturated and Oven Dry Bases | Water Absorption (%) |
|--------------------------|---------------------------|------------------------------------|--|----------------------|
| Natural aggregate | 2.69 | 2.62 | 2.65 | 1.05 |
| Recycled aggregates (RA) | 2.61 | 2.27 | 2.40 | 5.77 |

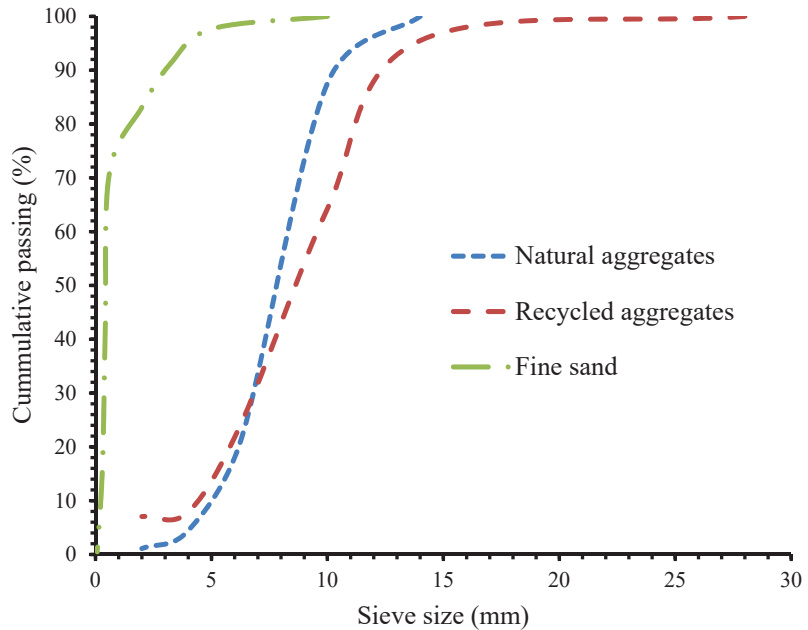


Figure 1. Grading of natural aggregates, recycled aggregates and fine sand [36].

2.2. Concrete Mix and Specimen Preparation

This study designed a reference concrete of 40 MPa cylindrical compressive strength as shown in Table 3. Crumb rubber was used to replace the coarse aggregates in different concentrations (5%, 10%, 15% and 20%). The experimental programme in Table 4 allows for the systematic investigation and comparison of the effects of different proportions of crumb rubber in recycled aggregate concrete to those of natural aggregate concrete (NAC). The percentages of replacement of recycled aggregates by crumb rubber were carefully

selected based on the recommendations made by [22,37,38] for the rubberised recycled aggregate concrete to achieve a substantial proportion of the mechanical properties of the reference concrete. In order to achieve a workable concrete, superplasticizer (1% of cement weight) was added to the recycled aggregate concrete with and without crumb rubber.



Figure 2. Crumb rubber (8 mm length) particles from worn out tyres.

Table 3. Concrete mix composition of the reference concrete.

| Mix Type | Cement (kg) | Water (kg) | w/c | Sand (kg) | Coarse Aggregates (kg) |
|----------|-------------|------------|-----|-----------|------------------------|
| NAC | 550 | 220 | 0.4 | 626 | 939 |

Table 4. Experimental programme.

| Specimen | Natural Aggregates | Recycled Aggregates (RA) | Crumb Rubber | Sand |
|-------------|--------------------|--------------------------|------------------|---------------|
| Designation | (% by Weight) | (% by Weight) | (% by RA Weight) | (% by Weight) |
| NAC | 100 | - | - | 100 |
| RAC | - | 100 | - | 100 |
| RRAC5 | - | 100 | 5 | 100 |
| RRAC10 | - | 100 | 10 | 100 |
| RRAC 15 | - | 100 | 15 | 100 |
| RRAC 20 | - | 100 | 20 | 100 |

NAC- Natural aggregate concrete; RAC- Recycled aggregate concrete; RA- Recycled aggregate; RRAC5, RRAC10, RRAC15 and RRAC20- Rubber recycled aggregate concrete with 5, 10, 15 and 20 percent of crumb rubber content respectively of recycled aggregate weight.

The recycled aggregates and fine sand were incorporated into the concrete mixer and mixed for 60 s followed by crumb rubber and 50% of water for another 60 s. Cement was then added for another 30 s and finally the remaining quantity of water was added in 120 s to attain a uniform concrete mix.

2.3. Concrete Resistivity of Specimens

For regular reinforced concrete structures using recycled aggregate concrete, durability is a particular concern [9,11,39] because recycled aggregates in their natural crushed state

have higher porosity and permeability than natural aggregates and are therefore more susceptible to corrosion of the reinforcement.

In this study, the concentration of crumb rubber particles in recycled aggregate concrete is limited to 5% in order to preserve its mechanical properties. Hence, the durability assessment of the recycled aggregate concrete with 5% of crumb rubber concentration will be conducted.

The surface resistivity test was used in this study to measure the durability performance (chloride ion penetration) of the recycled aggregate concrete with crumb rubber. The resistivity tests were conducted on cylindrical specimen of size $\phi 100 \times 200$ mm based on the specifications presented in [40]. The four probes are placed on the surface of the cylindrical specimen to produce electrical contact as shown in Figure 3. The two external probes generate pulse of alternating current through the concrete sample and the inner probes measure the electrical potential created. The surface resistivity measurements were taken with a fixed probe spacing of 38 mm with an alternating current frequency of 13 Hz [41,42].

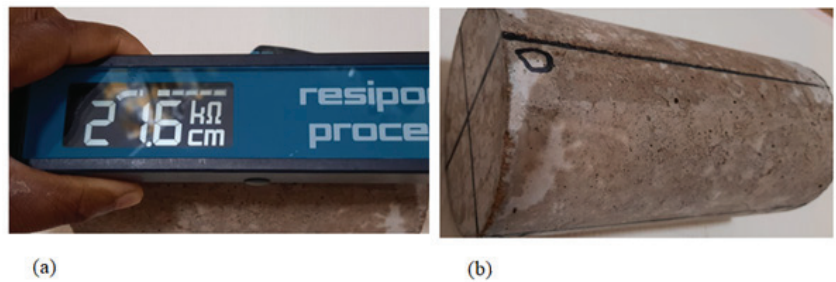


Figure 3. Surface resistivity measurements of cylindrical concrete samples. (a) Resistivity measurement on cylinders. (b) Sample markings.

3. Experimental Results

3.1. Fresh Properties

For each mix, slump tests were carried out and results presented to ascertain the workability of the concrete. The workability of all mixes was assessed by means of slump test according to [43]. The concrete was placed in a cone of 300 mm in three layers. At each layer, the concrete is compacted with 25 strokes of a tamping rod. After filling and compacting the top layer, the surface of the concrete is struck off by means of sawing and the rolling action of the compacting rod. The mould is then carefully lifted within a time interval of 2 to 5 s. Figure 4 shows the effect of the crumb rubber and recycled aggregates on the workability of concrete.

The workability of the recycled aggregate concrete was enhanced to level comparable to the reference concrete (165 mm) by adding superplasticizer (1% of the cement weight). The added superplasticizer compensates for the water absorbed by the recycled aggregates during mixing process [18,44,45]. However, adding crumb rubber reduces the workability of the recycled aggregate concrete. This can be attributed to the crumb rubber surface texture and water absorbability of the crumb rubber particles. The observed results are similar to those reported by [23,42,46]. There is no significant difference in workability when 5% of the recycled aggregates were replaced with crumb rubber particles in recycled aggregate concrete. This is due to the crumb rubber's slightly higher water absorption than the replaced recycled aggregates. According to [47], the water absorption of crumb rubber less than 50mm is 6.7%, while recycled aggregates, as shown in Table 2, have a water absorption of 5.77%. Hence, 5% crumb rubber replacement level did not have influence on workability. However, a sharp reduction in workability was observed for rubber recycled aggregate concrete when more than 5% crumb rubber particles were incorporated into the recycled aggregate concrete.

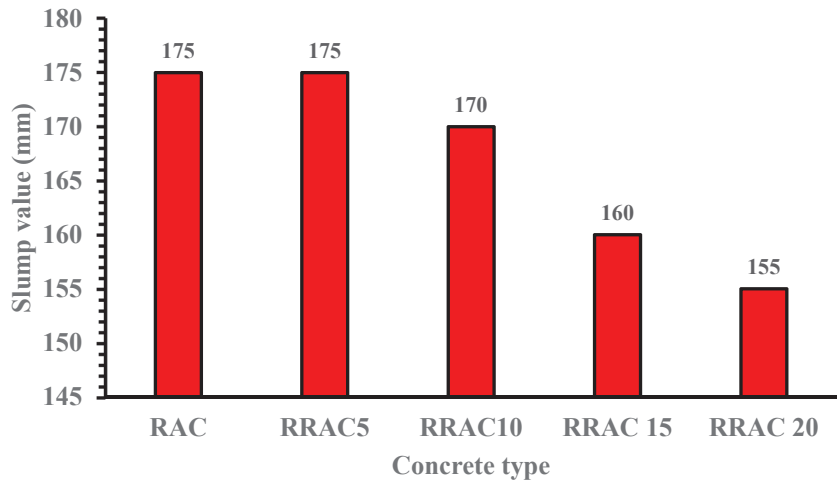


Figure 4. Influence of crumb rubber concentration on the workability of recycled aggregate concrete.

3.2. Hardened Properties

3.2.1. Compressive Strength

For each mix, three concrete cubes were tested as per specifications made in [48] and the results presented are the average values for 7, 28 and 90 days of curing. As expected, the results in Table 5 and Figure 5 reveals that addition of crumb rubber particles in the recycled aggregate concrete reduces its compressive strength. The reduction of the compressive strength was attributed to the low elastic modulus and high poisons ratio of the crumb rubber capable of initiating premature cracking under loading condition [23,49,50]. Weak bonding between the rubber particles and cement paste could also lead to reduction in compressive strength [51]. However, the recycled aggregate concrete maintains most of its properties when the crumb rubber concentration is limited to 5%.

Table 5. Experimental results of the concrete hardened properties.

| Specimen Type | Compressive Strength (MPa) | | | Tensile Strength MPa | Ultrasonic Pulse Velocity (KM/s) |
|---------------|----------------------------|---------|---------|----------------------|----------------------------------|
| | 7 days | 28 days | 90 days | | |
| NAC | 34.6 | 47.8 | 60.4 | 4.11 | 4.19 |
| RAC | 30 | 40.7 | 56.9 | 3.50 | 3.90 |
| RRAC5 | 23.7 | 32.1 | 44.3 | 2.72 | 3.72 |
| RRAC10 | 18.69 | 25.3 | 37.6 | 2.82 | 3.61 |
| RRAC15 | 15.28 | 21.9 | 29.4 | 2.33 | 3.54 |
| RRAC20 | 13.24 | 17.5 | 22.5 | 1.91 | 3.41 |

The results of the ultrasonic pulse velocity in Table 5 were used to ascertain the quality of already cast concrete. The ultrasonic pulse velocity tests were based on the specifications made in [52]. The pulse velocity of the recycled aggregate concrete drop by 6.9% compared to reference concrete mainly due to the micro cracks sustained by the recycled aggregates during extraction. Addition of crumb rubber to the recycled aggregate concrete further drop the pulse velocity in Table 5 and is attributed to the entrapped air by the crumb rubber particles, as well as the low ultrasonic wave velocity in crumb rubber. However, based on the criteria made in Table 6, the quality of the rubber recycled aggregate concrete in Table 5 is questionable if the rubber content is more than 5%.

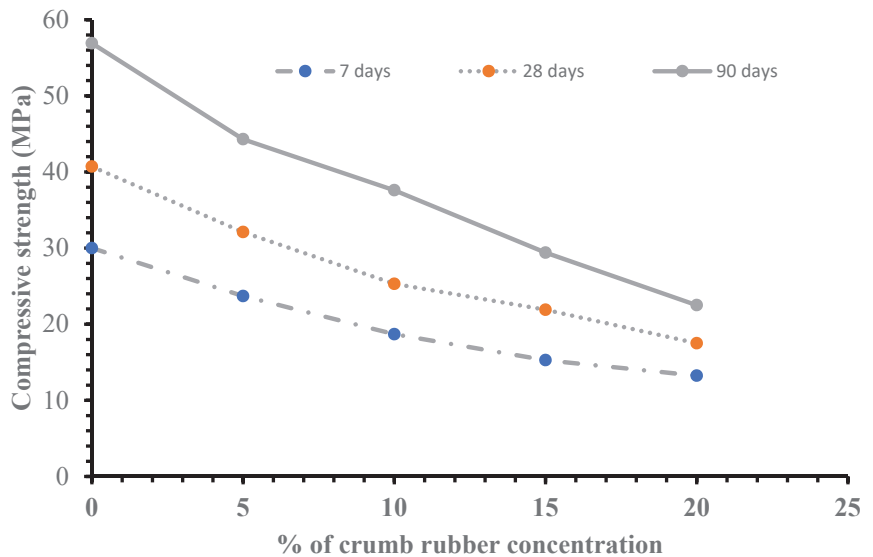


Figure 5. Influence of crumb rubber content on the compressive strength of recycled aggregate concrete.

Table 6. Concrete classification based on Ultrasonic pulse velocity [52].

| Ultrasonic Pulse Velocity (m/s) | Concrete Classification |
|---------------------------------|-------------------------|
| $V > 4575$ | Excellent |
| $4575 > V > 3660$ | Good |
| $3660 > V > 3050$ | Questionable |
| $3050 > V > 2135$ | Poor |
| $V < 2135$ | Very poor |

Figure 6 shows the compressive strength of the concrete mixes subject to axial monolithic loading. The stress strain results in Figure 6 shows higher ductility of the concrete with crumb rubber particles compared to the conventional concrete.

The failure mode of the concrete mixes without crumb rubber is brittle. However, addition of crumb rubber enhances the ductility of the recycled concrete mixes. This due to the higher deformability of the crumb rubber particles used in the replacing the recycled aggregates.

3.2.2. Tensile Strength

Three split tensile strength tests were carried out for each mix based on the specifications in [53] and the average results are presented in Figure 7, which shows how the amount of crumb rubber influenced the splitting tensile strength of rubber recycled aggregate concrete. A linear reduction is the best fit, ranging from 14.3% at 5% crumb rubber to reductions of 21.4%, 35.7% and 45.4% at 10%, 15% and 20% of crumb rubber, respectively, for rubber recycled aggregate concretes.

3.3. Durability of the Recycled Aggregate Concrete with Crumb Rubber

The samples for the concrete resistivity tests were cured for 28 days prior to testing. Two curing techniques were adopted in this study; some samples are fully submerged in tap water at a temperature of $(20 \pm 2) ^\circ\text{C}$ and relative humidity $\geq 95\%$ while others are wrapped with damp cloth at a temperature of $(20 \pm 5) ^\circ\text{C}$. The samples cured in tap water were tested under surface saturation condition. All the samples are marked at four locations

equally spaced at 90 degrees as shown in Figure 3 prior to curing process. The surface resistivity tests for surface saturated samples and air-dried samples were carried out after 28 days curing. Excess water on the samples surface cured in water were wiped off with damped cloth. The probes of the resistivity equipment are dipped in water prior to tests for air dried samples to ensure proper surface contact. Resistivity measurements of all samples were repeatedly taken at four different locations (total of eight readings on each sample) to ensure quality control applications as specified in [40].

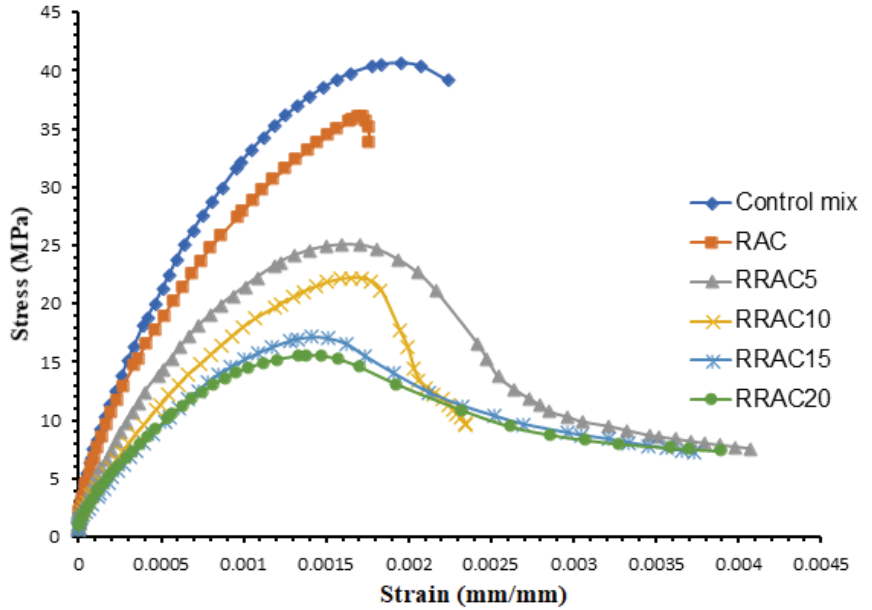


Figure 6. Compressive stress strain relationships of recycled aggregate concrete with different amounts of rubber particles.

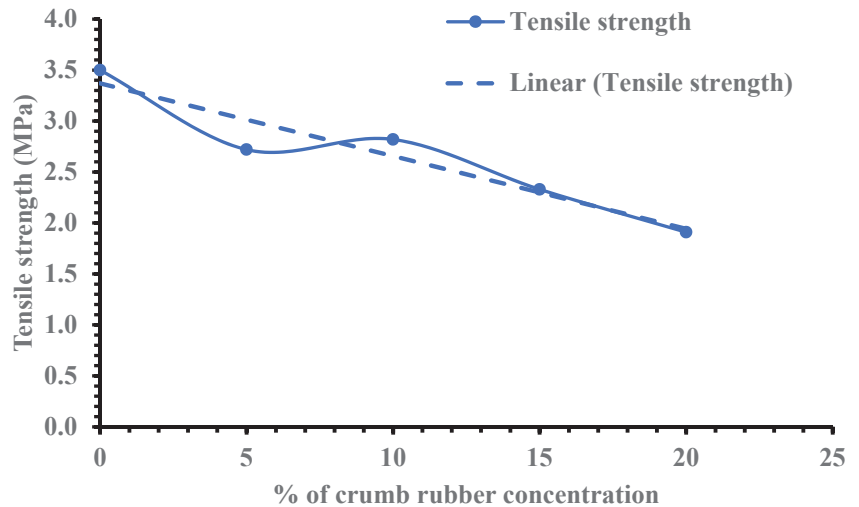


Figure 7. Influence of crumb rubber content on the tensile strength of recycled aggregate concrete.

The surface resistivity of concrete mixes cured for 7 and 28 days are shown in Figures 8 and 9. The chloride ion penetration of concrete mixes for rubber recycled aggregate

gate concrete under saturated surface dried state is high based on the specifications made in Table 7. This may be attributed to the voids in recycled concrete due to the presence of crumb rubber particles, hence creating a path for ingress of fluids into the concrete. This can also be illustrated with the ultrasonic pulse velocity tests in Table 5. The ultrasonic pulse velocity of the recycled aggregate concrete reduces with the increase in crumb rubber concentration, indicating the presence of voids in the concrete.

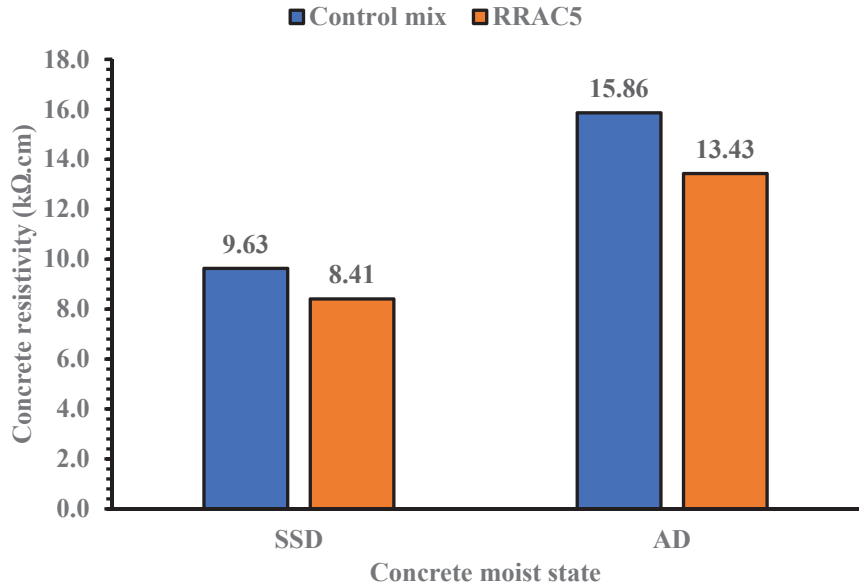


Figure 8. Surface resistivity of concrete mixes at saturated surface dried and air-dried state for 7 days curing.

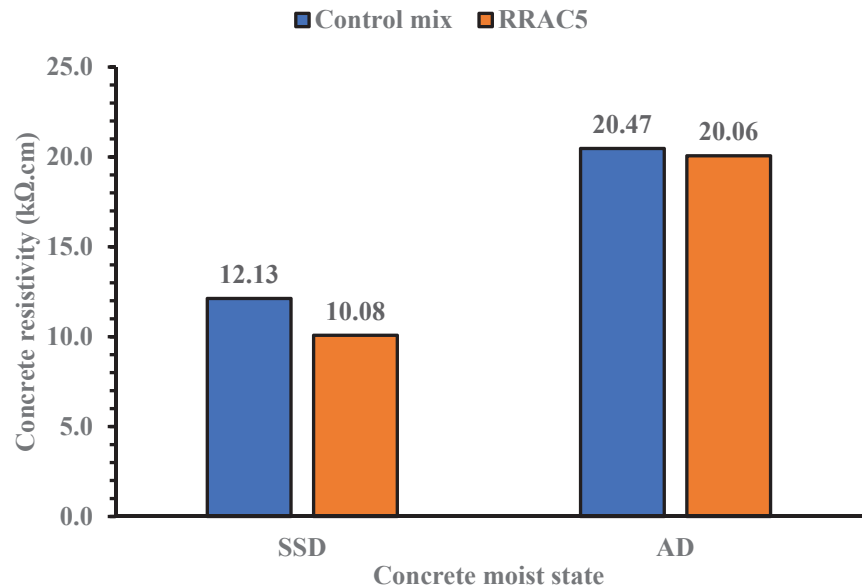


Figure 9. Surface resistivity of concrete mixes at saturated surface dried and air-dried state for 28 days curing.

Table 7. Comparison of chloride penetrability levels established for standards based on electrical resistivity (AASHTO TP 95) and charged passed (ASTM C1202) [40].

| Chloride Ion Penetrability | AASHTO TP 95, k Ω .cm | ASTM C1202, Coulombs |
|----------------------------|------------------------------|----------------------|
| High | <12 | >4000 |
| Moderate | 12 to 21 | 2000 to 4000 |
| Low | 21 to 37 | 1000 to 2000 |
| Very Low | 37 to 254 | 100 to 1000 |
| Negligible | >254 | <100 |

However, under air dried state the durability performance of the recycled concrete with 5% crumb rubber concentration is moderate based on the Table 7 specifications. The result of the recycled concrete is also comparable to the control mix under the air-dried curing method. Hence, the use of recycled concrete containing rubber content of limited amount (5%) could be useful for construction applications, especially where exposure condition is not extreme or critical.

4. Conclusions

The effect of crumb rubber on the strength and penetration of chloride ion in recycled aggregate concrete was investigated using the surface resistivity test method. Different concentrations (5%, 10%, 15% and 20%) of crumb rubber in recycled aggregate concrete were considered in the study. The results clearly shown that addition of crumb rubber reduces the compressive strength of the recycled aggregate concrete moderately when its concentration is limited to 5%. The study also observes the resistivity of chloride ions for recycled aggregate concrete with 5% crumb rubber concentration. Based on the ultrasonic pulse velocity results, the use of recycled aggregate concrete with crumb rubber content beyond 5% is questionable.

The results of the surface resistivity tests shows that the resistivity of the recycled aggregate concrete to chloride ion penetration is moderate under the air dried curing technique. However, using the water bath technique, the resistivity was found to be low based on the specifications listed in Table 7. Hence, the study suggests the application of recycled aggregate concrete with crumb rubber in the construction industry where the exposure conditions are not extreme. The rubber recycled aggregate concrete could be useful, for example, in making concrete wall panels, concrete lintels and road kerbs where the criteria for exposure conditions for durability are not so critical.

Furthermore, the ductility of recycled concrete with crumb rubber is found to be greater than that of recycled concrete without crumb rubber. As a result, using rubberized concrete for structural members subject to seismic loads is a promising potential application. Rubberized recycled concrete is an alternative solution for meeting sustainability targets and reducing embodied carbon in the construction industry. However, its limitations are the reduction in strength and the willingness of contractors to use the concrete product on new projects due to the previously mentioned associated drawbacks.

Further Research

Further research on the durability performance of the recycled concrete with crumb rubber concentration using different mix ratios is needed. Pre-treatment of the crumb rubber particles could also be considered when assessing the durability of the recycled concrete.

Author Contributions: R.B.A. and Y.C.W. proposed the study concept and designed the experiments. R.B.A. conducted the tests and analyzed the data. The first draught was authored by R.B.A. and Y.C.W. helped with the proofreading. All authors have read and agreed to the published version of the manuscript.

Funding: This research received no external funding.

Acknowledgments: The authors would like to convey their heartfelt gratitude and appreciation to Paul Nedwell and John Mason for their assistance with the laboratory experiments.

Conflicts of Interest: The authors declare no conflict of interest.

References

1. WBCSD. *Tire Industry Project, “End-of-Life Tires: A Framework for Effective Management Systems”*; World Business Council for Sustainable Development: Geneva, Switzerland, 2010.
2. Department for Environment, Food and Rural Affairs. *UK Statistics on Waste*; Government Statistical Service: London, UK, 2021.
3. Arezoumandi, M.; Smith, A.; Volz, J.S.; Khayat, K.H. An experimental study on shear strength of reinforced concrete beams with 100% recycled concrete aggregate. *Constr. Build. Mater.* **2014**, *53*, 612–620. [[CrossRef](#)]
4. Ismail, K.M.; Hassan, A.A.A.; Hussein, A.A. Structural behaviour of reinforced concrete beams containing crumb rubber and steel fibres. *Mag. Concr. Res.* **2017**, *69*, 939–953. [[CrossRef](#)]
5. Xiao, J.; Xie, H.; Yang, Z. Shear transfer across a crack in recycled aggregate concrete. *Cem. Concr. Res.* **2012**, *42*, 700–709. [[CrossRef](#)]
6. Tamanna, K.; Tiznobaik, M.; Banthia, N.; Alam, M.S. Mechanical Properties of Rubberized Concrete Containing Recycled Concrete Aggregate. *ACI Mater. J.* **2020**, *117*, 169–180.
7. Henry, M.; Yamashita, H.; Nishimura, T.; Kato, Y. Properties and mechanical–environmental efficiency of concrete combining recycled rubber with waste materials. *Int. J. Sustain. Eng.* **2011**, *5*, 66–75. [[CrossRef](#)]
8. Aslani, F.; Ma, G.; Wan, D.L.Y.; Muselin, G. Development of high-performance self-compacting concrete using waste recycled concrete aggregates and rubber granules. *J. Clean. Prod.* **2018**, *182*, 553–566. [[CrossRef](#)]
9. Kou, S.C.; Poon, C.S. Enhancing the durability properties of concrete prepared with coarse recycled aggregate. *Constr. Build. Mater.* **2012**, *35*, 69–76. [[CrossRef](#)]
10. Duan, Z.H.; Poon, C.S. Properties of recycled aggregate concrete made with recycled aggregates with different amounts of old adhered mortars. *Mater. Des.* **2014**, *58*, 19–29. [[CrossRef](#)]
11. Manzi, S.; Mazzotti, C.; Bignozzi, M.C. Short and long-term behavior of structural concrete with recycled concrete aggregate. *Cem. Concr. Compos.* **2013**, *37*, 312–318. [[CrossRef](#)]
12. Kwan, W.H.; Ramli, M.; Kam, K.J.; Sulieman, M.Z. Influence of the amount of recycled coarse aggregate in concrete design and durability properties. *Constr. Build. Mater.* **2012**, *26*, 565–573. [[CrossRef](#)]
13. Bolouri Bazaz, J.; Khayati, M. Properties and Performance of Concrete Made with Recycled Low-Quality Crushed Brick. *J. Mater. Civ. Eng.* **2012**, *24*, 330–338. [[CrossRef](#)]
14. Beltran, M.G.; Barbudo, A.; Agrela, F.; Galvín, A.P.; Jiménez, J.R. Effect of cement addition on the properties of recycled concretes to reach control concretes strengths. *J. Clean. Prod.* **2014**, *79*, 124–133. [[CrossRef](#)]
15. Etxeberria, M.; Vázquez, E.; Mari, A.; Barra, M. Influence of amount of recycled coarse aggregates and production process on properties of recycled aggregate concrete. *Cem. Concr. Res.* **2007**, *37*, 735–742. [[CrossRef](#)]
16. de Juan, M.S.; Gutiérrez, P.A. Study on the influence of attached mortar content on the properties of recycled concrete aggregate. *Constr. Build. Mater.* **2009**, *23*, 872–877. [[CrossRef](#)]
17. Dilbas, H.; Şimşek, M.; Çakır, Ö. An investigation on mechanical and physical properties of recycled aggregate concrete (RAC) with and without silica fume. *Constr. Build. Mater.* **2014**, *61*, 50–59. [[CrossRef](#)]
18. Barbudo, A.; De Brito, J.; Evangelista, L.; Bravo, M.; Agrela, F. Influence of water-reducing admixtures on the mechanical performance of recycled concrete. *J. Clean. Prod.* **2013**, *59*, 93–98. [[CrossRef](#)]
19. Ignjatović, I.S.; Marinković, S.B.; Mišković, Z.M.; Savić, A.R. Flexural behavior of reinforced recycled aggregate concrete beams under short-term loading. *Mater. Struct.* **2012**, *46*, 1045–1059. [[CrossRef](#)]
20. Tam, V.W.Y.; Gao, X.F.; Tam, C.M. Microstructural analysis of recycled aggregate concrete produced from two-stage mixing approach. *Cem. Concr. Res.* **2005**, *35*, 1195–1203. [[CrossRef](#)]
21. Toutanji, H.A. The Use of Rubber Tire Particles in Concrete to replace mineral aggregates. *Cem. Concr. Compos.* **1995**, *18*, 135–139. [[CrossRef](#)]
22. Ganjian, E.; Khorami, M.; Maghsoudi, A.A. Scrap-tyre-rubber replacement for aggregate and filler in concrete. *Constr. Build. Mater.* **2009**, *23*, 1828–1836. [[CrossRef](#)]
23. Khaloo, A.R.; Dehestani, M.; Rahmatabadi, P. Mechanical properties of concrete containing a high volume of tire-rubber particles. *Waste Manag.* **2008**, *28*, 2472–2482. [[CrossRef](#)] [[PubMed](#)]
24. Moustafa, A.; ElGawady, M.A. Mechanical properties of high strength concrete with scrap tire rubber. *Constr. Build. Mater.* **2015**, *93*, 249–256. [[CrossRef](#)]
25. Eldin, N.N.; Senouci, A.B. Measurement and Prediction of the Strength of Rubberized Concrete. *Cem. Concr. Compos.* **1994**, *16*, 287–298. [[CrossRef](#)]
26. Shah, S.F.A.; Naseer, A.; Shah, A.A.; Ashraf, M. Evaluation of Thermal and Structural Behavior of Concrete Containing Rubber Aggregate. *Arab. J. Sci. Eng.* **2014**, *39*, 6919–6926. [[CrossRef](#)]
27. Hernández-Olivares, F.; Barluenga, G. Fire performance of recycled rubber-filled high-strength concrete. *Cem. Concr. Res.* **2004**, *34*, 109–117. [[CrossRef](#)]

28. Gesoğlu, M.; Güneyisi, E. Strength development and chloride penetration in rubberized concretes with and without silica fume. *Mater. Struct.* **2007**, *40*, 953–964. [[CrossRef](#)]
29. Onuaguluchi, O.; Panesar, D.K. Hardened properties of concrete mixtures containing pre-coated crumb rubber and silica fume. *J. Clean. Prod.* **2014**, *82*, 125–131. [[CrossRef](#)]
30. Yilmaz, A.; Degirmenci, N. Possibility of using waste tire rubber and fly ash with Portland cement as construction materials. *Waste Manag.* **2009**, *29*, 1541–1546. [[CrossRef](#)]
31. Ma, Q.W.; Yue, J.C. Effect on Mechanical Properties of Rubberized Concrete due to Pretreatment of Waste Tire Rubber with NaOH. *Appl. Mech. Mater.* **2013**, *357*, 897–904. [[CrossRef](#)]
32. Su, H.; Yang, J.; Ling, T.C.; Ghataora, G.S.; Dirar, S. Properties of concrete prepared with waste tyre rubber particles of uniform and varying sizes. *J. Clean. Prod.* **2015**, *91*, 288–296. [[CrossRef](#)]
33. Najim, K.B.; Hall, M.R. Workability and mechanical properties of crumb-rubber concrete. *Proc. ICE—Constr. Mater.* **2013**, *166*, 7–17. [[CrossRef](#)]
34. Pham, T.M.; Elchalakani, M.; Hao, H.; Lai, J.; Ameduri, S.; Tran, T.M. Durability characteristics of lightweight rubberized concrete. *Constr. Build. Mater.* **2019**, *224*, 584–599. [[CrossRef](#)]
35. Sukontasukkul, P. Use of crumb rubber to improve thermal and sound properties of pre-cast concrete panel. *Constr. Build. Mater.* **2009**, *23*, 1084–1092. [[CrossRef](#)]
36. *BS EN 197-1:2011*; Composition, Specifications and Conformity Criteria for Common Cements. BSI Standards Publication: London, UK, 2011.
37. *BS EN 12620*; Aggregates for Concrete. BSI Standards Publication: London, UK, 2013.
38. Ling, T.C.; Nor, H.M.; Lim, S.K. Using recycled waste tyres in concrete paving blocks. In *Proceedings of the ICE—Waste and Resource Management*; ICE Virtual Library: London, UK, 2010; Volume 163, pp. 37–45.
39. Yadav, S.; Pathak, S. Durability Aspects of Recycled Aggregate Concrete: An Experimental Study. *Int. J. Civ. Environ. Eng.* **2018**, *12*, 313–323.
40. *AASHTO-TP95*; Surface Resistivity Indication of Concrete’s Ability to Resist Chloride Ion Penetration. American Association of State Highway and Transportation Officials: Washington, DC, USA, 2014.
41. *ACI228-2R*; Report on Nondestructive Test Methods for Evaluation of Concrete in Structures. ACI: Farmington Hills, MI, USA, 2013.
42. Layssi, H.; Ghods, P.; Alizadeh, A.R.; Salehi, M. Electrical Resistivity of Concrete: Concepts, applications, and measurement techniques. *Concr. Int.* **2015**, *37*, 41–46.
43. *BS-EN12350-2-2009*; Testing Fresh Concrete—Part 2: Slump-Test. British Standard Publications: London, UK, 2009.
44. Mefteh, H.; Kebaïli, O.; Oucief, H.; Berredjem, L.; Arabi, N. Influence of moisture conditioning of recycled aggregates on the properties of fresh and hardened concrete. *J. Clean. Prod.* **2013**, *54*, 282–288. [[CrossRef](#)]
45. Matias, D.; De Brito, J.; Rosa, A.; Pedro, D. Mechanical properties of concrete produced with recycled coarse aggregates—Influence of the use of superplasticizers. *Constr. Build. Mater.* **2013**, *44*, 101–109. [[CrossRef](#)]
46. Aiello, M.A.; Leuzzi, F. Waste tyre rubberized concrete: Properties at fresh and hardened state. *Waste Manag.* **2010**, *30*, 1696–1704. [[CrossRef](#)]
47. Moo-Young, H.; Sellasie, K.; Zeroka, D.; Sabnis, G. Physical and Chemical Properties of Recycled Tire Shreds for Use in Construction. *J. Environ. Eng.* **2003**, *129*. [[CrossRef](#)]
48. *BS-EN12390-3-2009*; Testing Hardened Concrete—Part 3: Compressive Strength of Test Specimens. British standard publications: London, UK, 2009.
49. Najim, K.B.; Hall, M.R. Mechanical and dynamic properties of self-compacting crumb rubber modified concrete. *Constr. Build. Mater.* **2012**, *27*, 521–530. [[CrossRef](#)]
50. Bignozzi, M.C.; Sandrolini, F. Tyre rubber waste recycling in self-compacting concrete. *Cem. Concr. Res.* **2006**, *36*, 735–739. [[CrossRef](#)]
51. Emiroglu, M.; Kelestemur, M.H.; Yildiz, S. An investigation on ITZ microstructure of the concrete containing waste vehicles tire. In *Proceedings of the 8th International Fracture Conference, Istanbul, Turkey, 8 November 2007*.
52. *BS1881-203:1986*; Testing Concrete—Part 203: Recommendations for Measurement of Velocity of Ultrasonic Pulses in Concrete. British Standard Publications: London, UK, 1986.
53. *BS-EN12390-6-2000*; Testing Hardened Concrete—Part 6: Tensile Splitting Strength of Test Specimens. British Standard Publications: London, UK, 2000.

Article

^{13}C , ^{27}Al and ^{29}Si NMR Investigation of the Hydration Kinetics of Portland-Limestone Cement Pastes Containing $\text{CH}_3\text{-COO}^- \text{-R}^+$ (R=H or Na) Additives

Anton Mazur ^{1,*}, Peter Tolstoy ¹ and Konstantinos Sotiriadis ^{2,3}

¹ Physical Chemistry Department, Institute of Chemistry, Saint Petersburg State University, Universitetsky pr. 26, 198504 Saint Petersburg, Russia; peter.tolstoy@spbu.ru

² Department of Theoretical and Applied Mechanics, Institute of Theoretical and Applied Mechanics of the Czech Academy of Sciences, Prosecká 809/76, 19000 Prague, Czech Republic; sotiriadis@itam.cas.cz

³ Department of Building Materials and Products, South Ural State University, pr. Lenina 76, 454080 Chelyabinsk, Russia

* Correspondence: a.mazur@spbu.ru

Abstract: The hydration kinetics of Portland-limestone cement pastes with organic additives in the form of acetic acid and sodium acetate were studied by using solid-state ^{13}C , ^{27}Al and ^{29}Si NMR spectroscopy. The evolution of the relative content of various phases was monitored over the period of one month: amorphous and crystalline calcite (in ^{13}C spectra), ettringite, aluminum in C-S-H gel, calcium aluminates and calcium hydroaluminates (in ^{27}Al spectra), as well as alite, belite and silicon in C-S-H gel (in ^{29}Si spectra). The retarding effect of the additives on cement hydration at early age was demonstrated. We show that the kinetics of phase assemblage formation is influenced by the acetate ion adsorption on the surface of the anhydrous cement components and hydrated phases. The kinetics of formation of ettringite in the cement paste, depending on the addition of acetic and/or sodium acetate, is discussed in the context of potential thaumasite sulfate attack.

Keywords: Portland-limestone cement; organic additives; hydration kinetics; NMR spectroscopy

Citation: Mazur, A.; Tolstoy, P.; Sotiriadis, K. ^{13}C , ^{27}Al and ^{29}Si NMR Investigation of the Hydration Kinetics of Portland-Limestone Cement Pastes Containing $\text{CH}_3\text{-COO}^- \text{-R}^+$ (R=H or Na) Additives. *Materials* **2022**, *15*, 2004. <https://doi.org/10.3390/ma15062004>

Academic Editors: Carlos Morón Fernández, Daniel Ferrández Vega and Jeong Gook Jang

Received: 16 December 2021

Accepted: 11 February 2022

Published: 8 March 2022

Publisher's Note: MDPI stays neutral with regard to jurisdictional claims in published maps and institutional affiliations.



Copyright: © 2022 by the authors. Licensee MDPI, Basel, Switzerland. This article is an open access article distributed under the terms and conditions of the Creative Commons Attribution (CC BY) license (<https://creativecommons.org/licenses/by/4.0/>).

1. Introduction

Cement-based building materials are among the most used in modern construction. Despite their widespread application and the large amount of information regarding the chemistry of cement pastes [1,2], several issues regarding their properties during the hydration process and the effect of various environmental factors on the hardened material are still not clear. One of these factors is the chemical sulfate attack, which might occur in the form of conventional (ettringite or gypsum formation) or thaumasite sulfate attack (TSA) [3,4]. The former process is associated with the active formation and growth of expansive ettringite and gypsum crystals in the cement paste matrix, while the latter involves the formation of thaumasite microcrystals, occurring readily in the presence of carbonate ions and at temperatures close to the freezing point of water, about 0–5 °C. The amount and volume occupied by these minerals increase during the attack, developing internal stresses that induce cracks in the hardened cement paste. Moreover, as more silicon is available for the formation of thaumasite during TSA, which is derived from the continuously deteriorating calcium silicate hydrate phase, cement paste gradually transforms into a non-cohesive mass, further contributing to the destruction of building structures. TSA is particularly dangerous for Portland-limestone cement materials, because the presence of calcium carbonate facilitates this type of chemical attack.

To reduce the effect of deleterious external factors and optimize the hydration process and the properties of the obtained cement pastes, various additives based on mineral, organic or multicomponent substances are actively used [5–8]. However, although complex

multicomponent additives are widely used, the hydration process in the presence of simple organic substances has not been fully investigated. In this work, we decided to study the effect of commonly used additives, such as sodium acetate and its parent acid, on the hydration kinetics of Portland-limestone cement. Sodium acetate is used as anti-freeze additive [9], as well as for reducing the permeability of concrete to water and sulfate ions [10]. Acetic acid, in turn, is used to control the hardening time of cement [11]. Moreover, an amount of additive about 3% by cement mass was observed as optimal for achieving the maximum strength of the cement stone.

^{13}C , ^{27}Al and ^{29}Si NMR spectroscopy was selected as the main research tool. The technique allows for obtaining information about the local environment of the investigated nuclei [12]. The advantage of the applied method, in comparison with X-ray diffraction research methods, is that NMR spectroscopy allows for recording signals from both the amorphous and crystalline parts of the investigated samples. In hydrated cements, the amorphous part mainly consists of the calcium silicate hydrate phase, which provides most of the strength of the hardened cement paste.

The main aim of this work was to study the kinetics of the phase assemblage formation in Portland-limestone cement pastes in the presence of acetic acid and its sodium salt, as well as to elucidate the mechanism behind the observed hardening rate and appraise the changes of its strength properties, based on the data obtained. Research on cement hydration that assesses a large number of nuclei with NMR spectroscopy is scarce in the literature. The applied method is supposed to provide detailed structural and quantitative information about the occurring phase changes.

2. Materials and Methods

Cement pastes were prepared with a type CEM II/A-L 42.5N Portland-limestone cement (SLK Cement–Sukhoy Log, Sverdlovsk Region, Russia), distilled water and p.a. organic additives (acetic acid and sodium acetate). A water-to-cement ratio of 0.45 was used. Organic additives amounted to 3% by cement mass each, both added to the mixing water. Cement pastes were cast in cylindrical plastic molds (12 mm in diameter; 30 mm in height), where they remained sealed for 24 h. After demolding, the specimens were immersed in distilled water and kept throughout the investigated hydration periods. To study the kinetics of the changes in the phase composition of the pastes at certain ages (after 1, 2, 3, 5, 7, 14 and 34 days), about 150 mg of hardened material was scraped off the specimens' end and placed in paper bags to prevent any further hydration. Such quantity was sufficient for conducting the NMR experiment. In this work, the following nomenclature was used to label the samples: C (cement paste without additives), CAA (cement paste with acetic acid) and CSA (cement paste with sodium acetate). The stage of hydration was indicated by the age of the cement paste, which was added to the sample marker.

Prior to hydration, the mineralogical composition of the employed cement was determined with X-ray powder diffraction (XRPD) analysis; the results are summarized in Table 1. XRPD analysis was performed at room temperature, using $\text{CuK}\alpha$ radiation 2-theta range $5\text{--}80^\circ$, step 0.0203° , voltage 30 kV and current 10 mA. Qualitative X-ray phase analysis was carried out with the software PDXL 2.8.4.0 (Rigaku, Tokyo, Japan), with connection of PDF-2 database (International Diffraction Data Center, ICDD). Quantitative phase analysis (wt.%) was carried out by applying the Rietveld method [13] on the obtained full-profile data with the software TOPAS 4.2 (Bruker, Billerica, MA, USA).

NMR experiments were performed by using an Avance III 400 WB spectrometer (Bruker, Billerica, MA, USA) at constant magnetic field of 9.4 T. ^{13}C , ^{27}Al and ^{29}Si nuclei were studied and characterized by the respective resonance frequencies of 100, 104 and 86 MHz. A probe that is able to rotate the samples at the magic angle to the direction of the constant magnetic field (stabilization accuracy of the rotation frequency ± 4 Hz) and stabilize their temperature (temperature stabilization accuracy ± 1 °C) was used. Powder samples were loaded on a 4 mm zircon oxide rotor and rotated at a frequency of 12.5 KHz

at 20 °C. Tetramethylsilane, for ^{13}C and ^{29}Si nuclei, and 1 M·D₂O AlCl₃ solution, for ^{27}Al nuclei, were used as external references.

Table 1. Quantitative phase analysis of Portland-limestone cement derived from Rietveld refinements of X-ray powder diffraction data (Bragg R factor −5.2%).

| Mineral Phase | Formula * | wt.% |
|----------------------|--|------|
| Alite | 3CaO·SiO ₂ (C ₃ S) | 56.2 |
| Belite | 2CaO·SiO ₂ (C ₂ S) | 4.7 |
| Tricalcium aluminate | 3CaO·Al ₂ O ₃ (C ₃ A) | 5.8 |
| Brownmillerite | 4CaO·Al ₂ O ₃ ·Fe ₂ O ₃ (C ₄ AF) | 10.6 |
| Gypsum | CaO·SO ₃ ·2H ₂ O (C $\bar{\text{S}}$ H ₂) | 1.2 |
| Basanite | 2CaO·2SO ₃ ·H ₂ O (C ₂ $\bar{\text{S}}$ ₂ H) | <1.0 |
| Anhydrite | CaO·SO ₃ (C $\bar{\text{S}}$) | 2.8 |
| Periclase | MgO (M) | 1.6 |
| Calcite | CaO·CO ₂ (C $\bar{\text{C}}$) | 9.3 |
| Dolomite | CaO·MgO·2CO ₂ (CM $\bar{\text{C}}$ ₂) | 7.2 |

* The formulas in brackets correspond to cement chemist notation.

All the spectra were recorded by using a single-pulse sequence. The duration of the exciting impulses was 2.5, 4.5 and 2.5 μs ; the relaxation delay was 4, 2 and 4 s; the number of scans was 1024, 512 and 1024 for ^{13}C , ^{27}Al and ^{29}Si nuclei, respectively.

Deconvolution of spectra into Gaussian-shape individual components was performed by the least squares method, using the software Origin 9.0. (OriginLab Corporation, Northampton, MA, USA) For all the spectra, the results of approximation were obtained with a coefficient of determination R^2 higher than 0.8. Since single-pulse sequence was used to record the NMR spectra, the relative integrated intensities of the signals can be interpreted as mole fractions of the corresponding phase components.

3. Results

3.1. ^{13}C

The ^{13}C NMR spectrum of the anhydrated cement (Figure 1 (top)) shows a single broad asymmetric line at a chemical shift of about 168.7 ppm. Most likely, this line originates from amorphous calcium carbonate and, possibly, small amounts of calcite and dolomite, which are contained in cement, according to the phase composition obtained from the XRPD analysis (Table 1). An effort to perform component deconvolution in this spectrum was not attempted, because its line shape is quite broad and the ^{13}C chemical shifts of the carbonate compounds fall close to each other [14]. The ^{13}C NMR spectra obtained at different ages of cement hydration show two (except for CAA and CSA at 1 d) clearly distinguished peaks (Figure 1 (bottom) is an example of the ^{13}C NMR spectrum of the sample C07; the other spectra are provided in Supplementary Figures S1a–S3a). Moreover, the peak at about 168.5 ppm consists of unresolved narrow and broad signals; the deconvolution into two peaks is justified in Supplementary Figure S1c,d. We note, however, that the precision of the deconvolution of unresolved signals might suffer from larger errors and a certain degree of caution should be exercised when analyzing these results. The position of the signal at about 171 ppm remains virtually unchanged over time. However, the narrow component of the signal at 168.5 ppm was slightly shifted to the weak field at the initial stage of hydration, and the broad component was shifted to the strong field throughout the entire hydration period, with the exception of the CSA sample, for which this component was shifted, on the contrary, to the weak field. The signals mentioned are contributed also by the presence of calcium monocarboaluminate hydrate, forming during the hydration process. The time dependences of the ^{13}C chemical shift values are shown in Supplementary Figures S1b–S3b in Supporting Information.

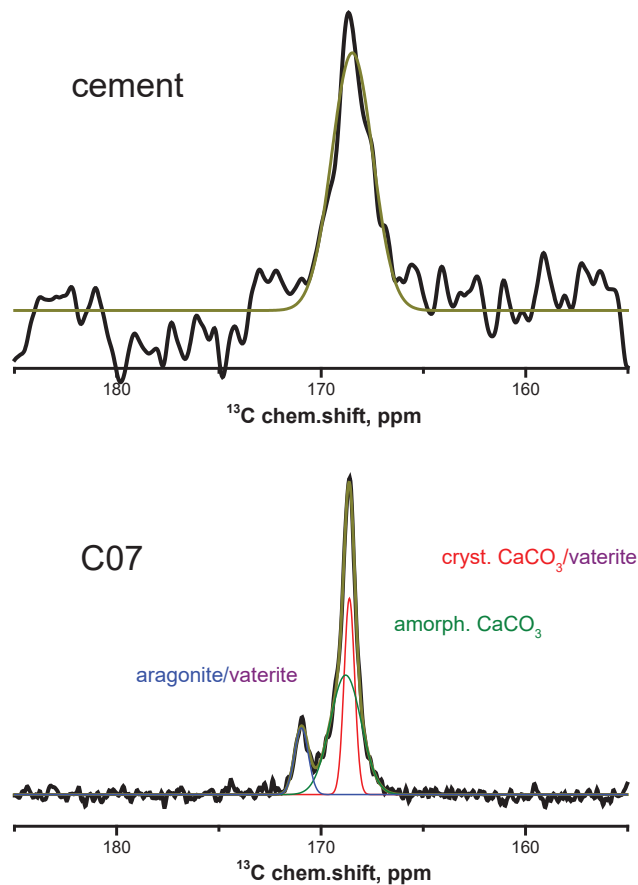


Figure 1. ^{13}C NMR spectra of the (top) anhydrated Portland-limestone cement, and (bottom) cement paste sample without additives on the 7th day of hydration.

According to the literature, all the observed signals correspond to CO_3^{2-} structural units of various amorphous and crystalline modifications of calcium carbonate and dolomite [14–16]: the broad signal at about 168.5 ppm corresponds to amorphous calcium carbonate and to metastable ikaite, which is possibly contained in the samples; the narrow signal corresponds to calcite, dolomite and vaterite; and the signal at about 171 ppm corresponds to carbon atoms in aragonite and vaterite. According to Reference [17], the two narrow signals from carbon nuclei in the structure of vaterite correspond to its two most probable crystal structures.

3.2. ^{27}Al

The ^{27}Al NMR spectrum of the anhydrated cement (Figure 2 (top)) shows two isotropic signals. The signal at 85 ppm corresponds to aluminum atoms in tetrahedral environment of oxygen atoms $\text{Al}^{\text{(IV)}}$, which are in the form of impurities in alite and belite [18]. The signal at about 10 ppm corresponds to aluminum atoms in octahedral environment of oxygen atoms $\text{Al}^{\text{(VI)}}$. This signal consists of two spectral components: the narrow component at about 15 ppm corresponds to aluminum atoms in $\text{Ca}_3\text{Al}_2\text{O}_6$ (C_3A), and the broad one at about 10 ppm to C_4AF [18].

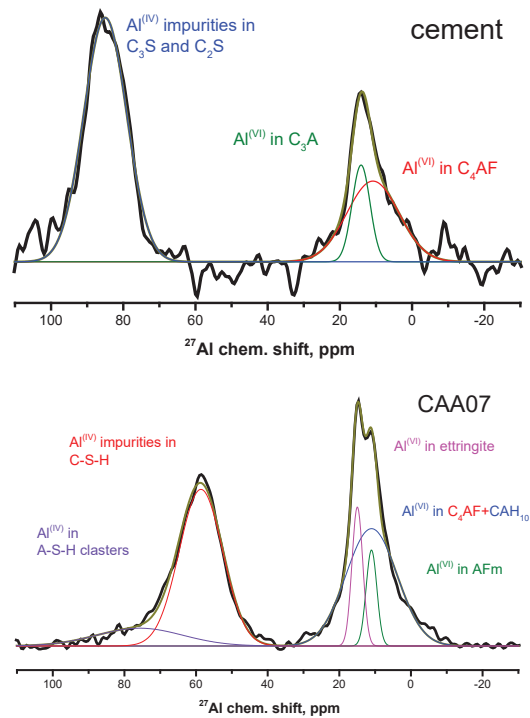


Figure 2. ^{27}Al NMR spectra of the (top) anhydrous Portland-limestone cement, and (bottom) cement paste sample with acetic acid addition at the 7th day of hydration.

In the ^{27}Al NMR spectra of all studied hydrated samples (Figure 2 (bottom)) shows the ^{27}Al NMR spectrum from the CAA07 sample; the rest of the spectra are shown in Supplementary Figures S4a–S6a), it can be seen that the signal from the aluminum atoms $\text{Al}^{(\text{IV})}$ in anhydrous alite and belite practically disappears already on the first day of hydration; there is only a weak signal at this age for the CAA and CSA samples. At the same time, a broad asymmetric signal appears at about 65 ppm that can be described as the sum of the two components at 60 and 75 ppm. Both correspond to aluminum atoms $\text{Al}^{(\text{IV})}$ in the amorphous cement hydration gel. In fact, the line at about 75 ppm is typical for aluminum incorporation in the C–S–H gel, while the line at around 60 ppm for aluminum atoms in an unstable aluminum silicate hydrate (A–S–H) gel, forming near the surface of clinker grains at conditions of calcium shortage and excess aluminum [19]. In this case, the total relative integrated intensity of the signals in the given spectral region decreased with increasing the hydration time.

For the C and CSA samples, a broad asymmetric signal in the region of $\text{Al}^{(\text{VI})}$ chemical shifts can be described also by two components: a narrow one at 15 ppm and a broad component, whose chemical shift decreased from 14 to 10.5 ppm from the 1st to the 7th day, and then increased to 14.5 ppm by the end of the investigated time interval. For the CAA sample, there is another narrow component, in this region of the spectrum, at about 11 ppm (see the example in Figure 2, bottom). The narrow intense line at about 15 ppm corresponds to aluminum atoms in ettringite [12]. The narrow line of weak intensity at about 11 ppm corresponds to calcium monocarboaluminate hydrate (AFm) [19]. The broad line, whose position varies in the range of about 10.5–14.5 ppm, corresponds to signals from several aluminum hydrates and calcium hydroaluminates of different compositions. According to the behavior of the chemical shift of the broad line under consideration, it can be assumed that redistribution of coexisting phases occurs, from aluminate hydrate (AH_3) through

mono-(CAH_{10}) and dicalcium hydroaluminat (C_2AH_8) to tricalcium hydroaluminat (C_3AH_6) [12].

3.3. ^{29}Si

The ^{29}Si NMR spectrum of the anhydrated cement (Figure 3 (top)) shows a single signal, which is superposition of a narrow line at about -70.6 ppm from silicon atoms in the structure of belite and a broad asymmetric line in the range from -65 to -75 ppm, which corresponds to silicon atoms in the structure of alite [20] that are located in various local environments.

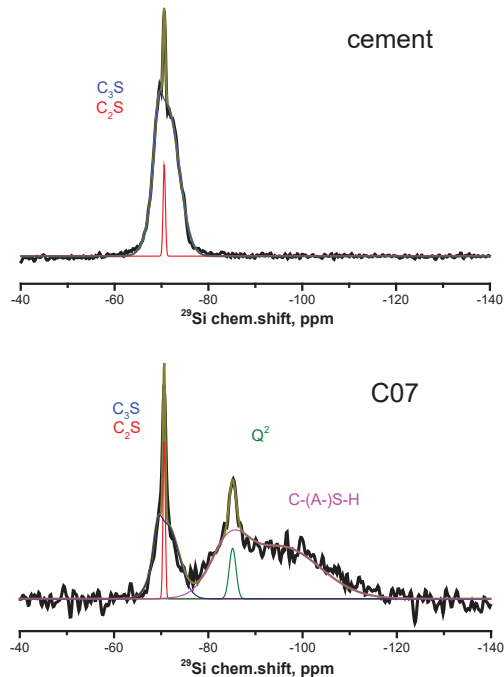


Figure 3. ^{29}Si NMR spectra of the (top) anhydrated Portland-limestone cement, and (bottom) cement paste sample without additives at the 7th day of hydration.

During the initial stage of hydration of all three cement mixtures, broad unresolved lines appear in the spectrum initially in the range from -75 to -95 ppm, and then the specified range expands to chemical shift values of about -120 ppm (Figure 3 (bottom)) shows the ^{29}Si NMR spectrum from the sample C07; the rest of the spectra are shown in Supplementary Figures S7–S9). This behavior corresponds to the appearance of an inhomogeneous phase, containing silicon atoms in tetrahedral environment of oxygen atoms, which are characterized by the presence of one to two linked silicon tetrahedra (Q^1 and Q^2 structural elements, from -75 to -90 ppm) or of three to four linked silicon tetrahedra (Q^3 and Q^4 structural elements, from -90 to -120 ppm) [12]. The presence of the former two structural elements in the cement paste characterizes the formation of the mostly amorphous C-(A-)S-H gel, while the latter two point to the formation of crosslinked silicate chains (C-(A-S-H of low Ca/Si ratio)) and amorphous hydrous silica [21].

At the later stages of hydration, a narrow line at about -86 ppm appeared in the spectra. This line corresponds to silicon atoms in Q^2 structural elements of the cement paste, in paired (Q^2_{P}) and/or bridged (Q^2_{b}) silicon tetrahedra in silicate chains, which form the bulk structure of the resulting cement paste [22].

4. Discussion

Figure 4 shows the time dependences of the relative integrated intensities of the ^{13}C NMR signals for all three studied samples. It can be seen that the intensities of the lines corresponding to amorphous calcium carbonate sharply decrease at the initial stage of the hydration process for C and CAA samples, and then a slight increase is observed. For the CSA sample, a gradual decrease in the relative proportion of amorphous calcium carbonate is observed. The proportion of calcite increases for all the samples, while that of aragonite decreases, as is especially noticeable for C sample. However, at the end of the studied hydration period (15–34 days), the relative content of calcite and aragonite essentially stabilizes and for CAA sample even slightly reverses. It should be noted that a significant amount of aragonite is observed on the first day of hydration only for C sample.

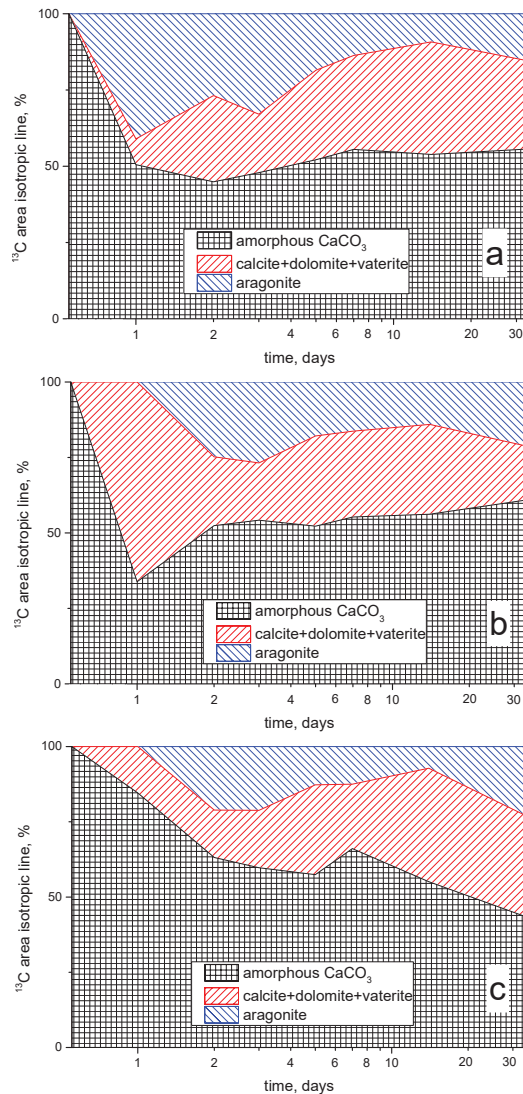


Figure 4. Time-evolution (in logarithmic scale) of the relative integrated areas of the isotropic components recognized in the ^{13}C NMR spectra of the samples: C (a), CAA (b) and CSA (c).

The increase in the content of the poorly soluble calcium carbonate polymorphs (calcite and aragonite), as noted for all samples, leads to their precipitation in the pores of the hardening cement paste, and this might cause an increase in its strength and a decrease in porosity [1,2]. The smallest amount of these calcium carbonate polymorphs is observed for the sample CAA.

Evidently, the formation of aragonite in the samples containing organic additives begins only on the second day of hydration, while the fraction of the initial amorphous CaCO_3 in the CSA sample, on the first day, is much lower than for the other samples. This observation can be attributed to the fact that the acetate ion (CH_3COO^-) can be adsorbed on the surface of the anhydrated cement microparticles and prevent their hydration [10,23], and also the crystallization of new phases [24]. However, in the case of acetic acid addition, the acidity of the pore solution increases, and this increase, at the initial stage of hydration, contributes to the dissolution of the fine particles of the anhydrated cement. At the same time, the presence of sodium cations hinders this process, forming a weakly alkaline medium in CSA mixture.

It is worth noting that it is not possible to quantify the amount of calcium monocarboaluminate hydrate (AFm) in CAA sample from ^{13}C NMR spectra, although this compound is resolved in the corresponding ^{27}Al NMR spectra. This is because of the negligible ^{13}C NMR chemical shift difference between AFm phase and other calcium carbonates (calcite and vaterite) that prevents a reliable deconvolution of the overlapped signals [14].

Figure 5 illustrates the time dependences of the relative integrated intensities of the ^{27}Al NMR signals for all three studied samples. Considering the observed changes in the intensities of the aforementioned spectral components, it can be concluded that, after the initial dissolution of the aluminate phases of the cement used, a large amount of aluminate hydrate forms, whose quantity gradually decreases. Then the amount of various compounds in the form of C–S–H, A–S–H or C–(A)–S–H gels grows in volume, further gradually decreasing. Finally, a gradual increase in the amount of various calcium hydroaluminates and ettringite is observed.

It should be noted that, for the CAA and CSA samples, on the first day, there is an insignificant amount of residual aluminum impurity in C_2S and C_3S . This can be associated with incomplete hydration of the anhydrous cement particles, due to the adsorption of the acetate ions on their surface.

The diagrams of Figure 5 show that, for all samples, the amount of ettringite initially increased and then decreased, and, at later stages, it again increased [2]. According to the generally accepted theory of hydration of aluminum-containing cements, ettringite crystallizes in two stages. In the initial stage, long narrow crystals form, which contribute to the initial binding of the hydrated cement grains. Later, during the deceleration of the hydration process, the initially formed ettringite recrystallizes in the form of large crystals in the voids of the matrix. Moreover, for the C sample, recrystallization of ettringite practically did not occur, while, in the CAA sample, the amount of the primary and secondary ettringite is noticeably larger than for all the other samples. The presence of acetate groups in the CAA and CSA samples can partially replace the sulfate groups [24]. Hence, the excess of the latter facilitates the formation of primary ettringite, whose content is larger than that in the C sample, resulting in the kinetics observed.

Since the surface of the aluminum-containing clinker phases is more electronegative than that of C_3S and C_2S [11], their dissolution occurs faster and, in parallel, a deficiency of calcium arises. Thus, in the CAA and CSA samples, at the early stages of hydration, an increased amount of aluminate hydrate is observed, which subsequently, with an increase in the calcium content, gradually transforms into the more stable C_3AH_6 phase.

Moreover, aluminum actively passes into the crystalline phases of ettringite and calcium hydroaluminate; hence, its content in the amorphous C–(A)–S–H phase decreases. It should be noted that the increased ettringite content observed in the CAA sample may act as a risk factor for sulfate corrosion.

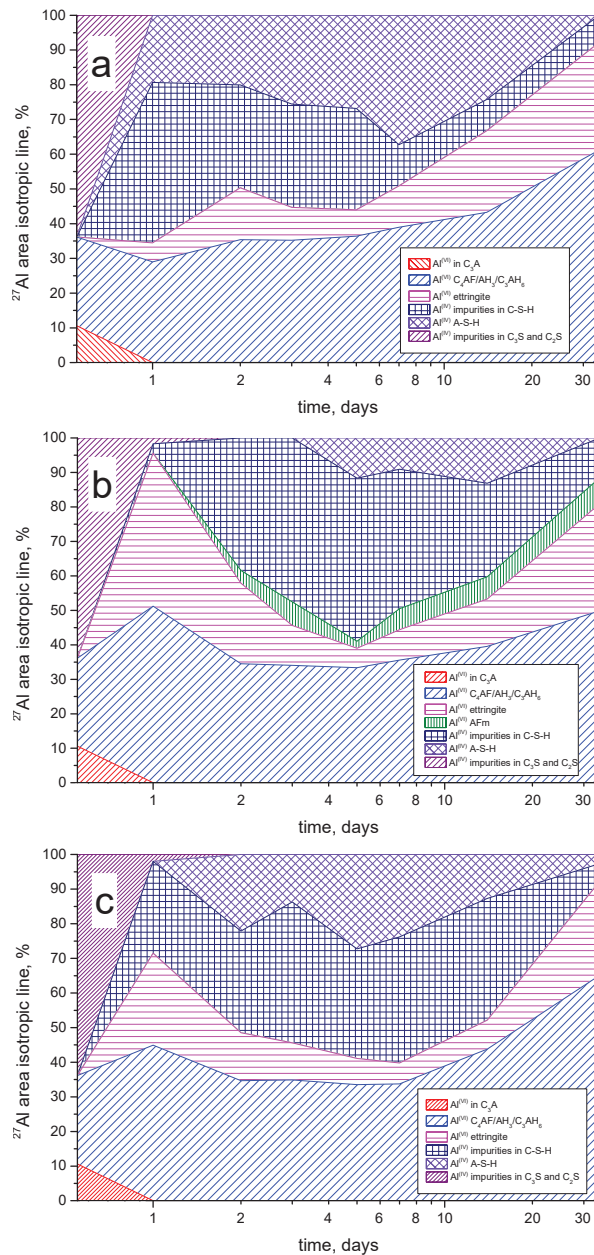


Figure 5. Time-evolution (in logarithmic scale) of the relative integrated areas of the isotropic components recognized in the ^{27}Al NMR spectra of the samples: C (a), CAA (b) and CSA (c).

Figure 6 illustrates the time dependences of the relative integrated intensities of the ^{29}Si NMR signals for all the three studied samples. When analyzing the change in the relative integrated intensities of the observed spectral components during hydration, we observed that the mass fraction of the silicate-containing clinker phases gradually decreases for all samples, while the mass fraction of the C-(A)-S-H phase increases proportionally, as well as the fraction of paired Q^2 tetrahedra. It should be noted that the Q^2 tetrahedra

resolved in the spectrum appear on the first day for the **CSA** sample, on the second day for the **C** sample, and only on the third day for the **CAA** sample. Moreover, for the **CAA** sample, the spectral component, which is visually distinguishable from the baseline and is characteristic for Q^3 and Q^4 structural elements, also appears only on the second day of hydration.

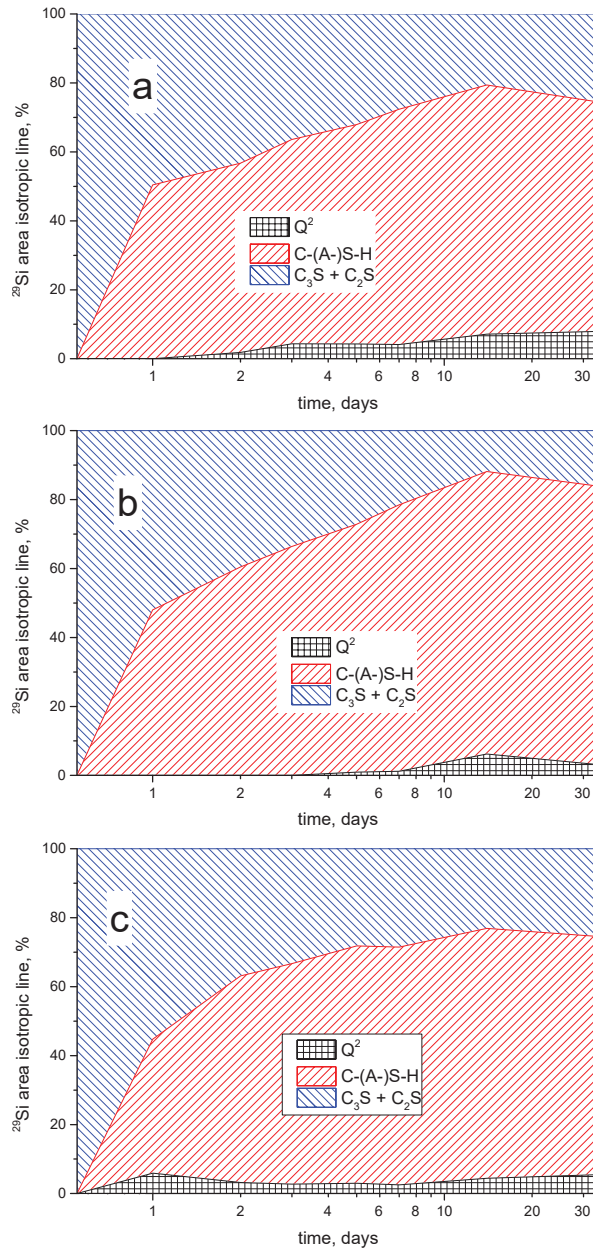


Figure 6. Time-evolution (in logarithmic scale) of the relative integrated areas of the isotropic components recognized in the ^{29}Si NMR spectra of the samples: C (a), CAA (b) and CSA (c).

These observations, along with the fact that no resolved peaks arise from other characteristic Q^1 , Q^2 and Q^3 structural elements [22], may indicate that such a characteristic layered structure of hydrated cements remains mainly amorphous; however, the number of paired Q^2 tetrahedra increases, and this increase can correspond to an increase in the length of silicate chains, consisting of paired silicate tetrahedra. The presence of such phase corresponds to an increase in strength of the cement matrix. The formation of this phase for the **CAA** sample is observed at later stages of hydration.

It should be noted that, during cement hydration, a relative redistribution of the amounts of alite and belite occurs (Figure 7). For all the pastes, an increase in the relative content of belite is observed that is much larger for the **CAA** sample as compared to the other two.

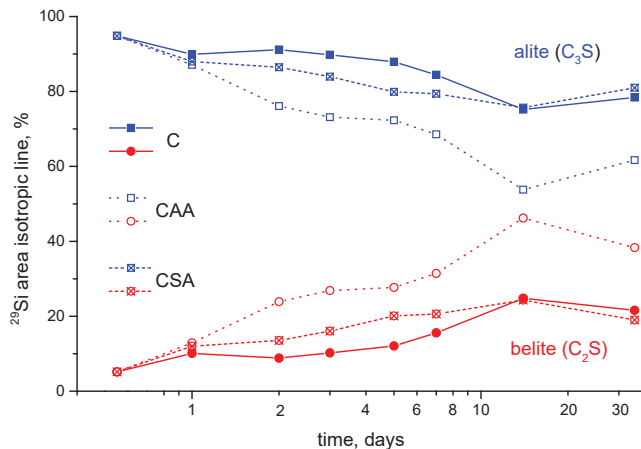


Figure 7. Time-evolution (in logarithmic scale) of the relative integrated areas of the isotropic component of calcium silicates (belite (C_2S , blue markers) and alite (C_3S , red markers)) recognized in the ^{29}Si NMR spectra of the studied samples (**C** (filled points), **CAA** (empty points) and **CSA** (crossed points)).

Over the entire investigated time interval, the silicon-containing anhydrous phases did not completely hydrate. It should be noted that, in the **CAA** sample, the remaining amount of such phases is slightly less than for the other two samples; the addition of acetic acid leads to the involvement of a larger amount of alite in the formation of the **C-(A)-S-H** gel. That is, at the later stages of the hydration process of the **CAA** paste a smaller amount of alite remains anhydrous, and, thus, it is more effectively transformed to amorphous hydrate phase, affecting the strength properties of the hardened material.

5. Conclusions

In contrast to X-ray studies, one of the advantages of the NMR method is the ability to directly observe the signals of the nuclei both in the crystalline and amorphous local environments. As a result, in this work, it was possible to trace the time dependences of a set of chemical phases in the studied cement pastes. Despite the natural difficulty in obtaining unambiguous deconvolution of strongly overlapped signals of some cases, it was possible to identify the main components the presence of which is assumed in the chemistry of cementitious materials, including the amorphous phases, especially the crucial ones containing ^{29}Si nuclei.

Considering all the above, it can be deduced that the addition of acetic acid and sodium acetate changes the kinetics of the cement paste phase composition during the hydration process. Adsorption of the acetate ion on the surface of the anhydrous and hydrated phases has a significant effect on the hydration process when the studied organic substances are

added in the mixtures. Moreover, the presence of sodium ions slightly increases the alkalinity of the pore solution, partially reducing the efficiency of such adsorption.

It can be concluded that the addition of 3% acetic acid or sodium acetate, by cement mass, to the cement paste hindered the initial stages of the hydration process. The addition of sodium acetate led to the formation of a large amount of poorly soluble forms of calcium carbonate and a significant increase in the amount of polymerized silicon-containing phases.

Concerning the sulfate degradation of the cement paste, we see that the addition of acetic acid led to the development of favorable conditions for the formation of ettringite; in contrast, the addition of sodium acetate slightly slowed down this process. Thus, in the future studies, it would be interesting to investigate whether sodium acetate is a useful additive for improving the durability of hardened cementitious materials against sulfate attack. As only cement pastes were investigated in this work, further applied studies in this field are needed.

Supplementary Materials: The following are available online at <https://www.mdpi.com/article/10.3390/ma15062004/s1>. Figure S1: ^{13}C NMR spectra of the anhydrated Portland-limestone cement and cement paste samples without additives (C) (a) and the chemical shift of spectra components (b) at the different hydration times. Deconvolution of C07 spectra per three (c) and two (d) components. Figure S2: ^{13}C NMR spectra of the anhydrated Portland-limestone cement and cement paste samples with acetic acid (CAA) (a) and the chemical shift of spectra components (b) at the different hydration times. Figure S3: ^{13}C NMR spectra of the anhydrated Portland-limestone cement and cement paste samples with sodium acetate (CSA) (a) and the chemical shift of spectra components (b) at the different hydration time. Figure S4: ^{27}Al NMR spectra of the anhydrated Portland-limestone cement and cement paste sample without additives (C) (a) and the chemical shift of spectra components (b) at the different hydration time. Figure S5: ^{27}Al NMR spectra of the anhydrated Portland-limestone cement and cement paste samples with acetic acid (CAA) (a) and the chemical shift of spectra components (b) at the different hydration time. Figure S6: ^{27}Al NMR spectra of the anhydrated Portland-limestone cement and cement paste samples with sodium acetate (CSA) (a) and the chemical shift of spectra components (b) at the different hydration time. Figure S7: ^{29}Si NMR spectra of the anhydrated Portland-limestone cement and cement paste sample without additives (C). Figure S8: ^{29}Si NMR spectra of the anhydrated Portland-limestone cement and cement paste samples with acetic acid (CAA). Figure S9: ^{29}Si NMR spectra of the anhydrated Portland-limestone cement and cement paste samples with sodium acetate (CSA).

Author Contributions: Conceptualization, P.T. and A.M.; formal analysis, P.T.; investigation, A.M.; funding acquisition, P.T. and K.S.; writing—original draft preparation, A.M.; writing—review and editing, P.T. and K.S. All authors have read and agreed to the published version of the manuscript.

Funding: This research was funded by the Russian Foundation for Basic Research (grant number: RFBR 20-52-26021) and the Czech Science Foundation (grant number: GAČR 21-35772J).

Institutional Review Board Statement: Not applicable.

Informed Consent Statement: Not applicable.

Data Availability Statement: Data available upon request to the authors.

Acknowledgments: The work was performed by using the equipment of the Saint Petersburg State University Research Park at the Resource Centers for Magnetic Resonance Research and X-ray Diffraction Studies.

Conflicts of Interest: The authors declare no conflict of interest.

References

- Hewlett, P. (Ed.) *Lea's Chemistry of Cement and Concrete*, 4th ed.; Elsevier Science & Technology Books: Burlington, MA, USA, 2004.
- Kurdowski, W. *Cement and Concrete Chemistry*; Springer: Berlin/Heidelberg, Germany, 2014.
- Whittaker, M.; Black, L. Current knowledge of external sulfate attack. *Adv. Cem. Res.* **2015**, *27*, 532–545. [[CrossRef](#)]
- Shi, C.; Wang, D.; Benhood, A. Review of thaumasite sulfate attack on cement mortar and concrete. *J. Mater. Civ. Eng.* **2012**, *24*, 1450–1460. [[CrossRef](#)]
- Khudhair, M.; El Hilal, B.; Elharfi, A. Review on chemical (organic) admixtures in the cementitious materials. *J. Mater. Environ. Sci.* **2018**, *9*, 1722–1734.

6. Plank, J.; Sakai, E.; Miao, C.; Yu, C.; Hong, J. Chemical admixtures—Chemistry, applications and their impact on concrete microstructure and durability. *Cem. Concr. Res.* **2015**, *78A*, 81–99. [[CrossRef](#)]
7. Young, J. A review of the mechanisms of set-retardation in portland cement pastes containing organic admixtures. *Cem. Concr. Res.* **1972**, *2*, 415–433. [[CrossRef](#)]
8. Chen, X.; Shi, X.; Zhou, J.; Chen, Q.; Li, E.; Du, X. Compressive behavior and microstructural properties of tailings polypropylene fibre-reinforced cemented paste backfill. *Constr. Build. Mater.* **2018**, *190*, 211–221. [[CrossRef](#)]
9. Al-Kheetan, M.; Hamidreza Ghaffar, S.; Abo Madyan, O.; Rahman, M. Development of low absorption and high-resistant sodium acetate concrete for severe environmental conditions. *Constr. Build. Mater.* **2020**, *230*, 117057. [[CrossRef](#)]
10. Kushartomo, W.; Prabowo, A. The Application of Sodium Acetate as Concrete Permeability-Reducing Admixtures. *IOP Conf. Ser. Mater. Sci. Eng.* **2019**, *508*, 012009. [[CrossRef](#)]
11. Smith, A.; El Hafiane, Y.; Bonnet, J.; Quintard, P.; Tanouti, B. Role of a Small Addition of Acetic Acid on the Setting Behavior and on the Microstructure of a Calcium Aluminate Cement. *J. Am. Ceram. Soc.* **2005**, *88*, 2079–2084. [[CrossRef](#)]
12. Walkley, B.; Provis, J. Solid-state nuclear magnetic resonance spectroscopy of cements. *Mater. Today Adv.* **2019**, *1*, 100007. [[CrossRef](#)]
13. Le Saout, G.; Kocaba, V.; Scrivener, K. Application of the Rietveld method to the analysis of anhydrous cement. *Cem. Concr. Res.* **2011**, *41*, 133–148. [[CrossRef](#)]
14. Sevelsted, T.; Herfort, H.; Skibsted, J. ^{13}C chemical shift anisotropies for carbonate ions in cement minerals and the use of ^{13}C , ^{27}Al and ^{29}Si MAS NMR in studies of Portland cement including limestone additions. *Cem. Concr. Res.* **2013**, *52*, 100–111. [[CrossRef](#)]
15. Marc Michel, F.; MacDonald, J.; Feng, J.; Phillips, B.; Ehm, L.; Tarabrella, C.; Parise, J.; Reeder, R. Structural Characteristics of Synthetic Amorphous Calcium Carbonate. *Chem. Mater.* **2008**, *20*, 4720–4728. [[CrossRef](#)]
16. Nebel, H.; Neumann, M.; Mayer, C.; Epple, M. On the Structure of Amorphous Calcium Carbonates. A Detailed Study by Solid-State NMR Spectroscopy. *Inorg. Chem.* **2008**, *47*, 7874–7879. [[CrossRef](#)] [[PubMed](#)]
17. Christy, A. A Review of the Structures of Vaterite: The Impossible, the Possible, and the Likely. *Cryst. Growth Des.* **2017**, *17*, 3567–3578. [[CrossRef](#)]
18. Skibsted, J.; Jakobsen, H. Direct Observation of Aluminium Guest Ions in the Silicate Phases of Cement Minerals by ^{27}Al MAS NMR Spectroscopy. *J. Chem. Soc. Faraday Trans.* **1994**, *90*, 2095–2098. [[CrossRef](#)]
19. Brykov, A.; Vasil'ev, A.; Mokeev, M. Hydration of Portland Cement in the Presence of High Activity Aluminum Hydroxides. *Russ. J. Appl. Chem.* **2012**, *85*, 1793–1799. [[CrossRef](#)]
20. Skibsted, J.; Jakobsen, H.; Hall, C. Quantification of Calcium Silicate Phases in Portland Cements by ^{29}Si MAS NMR Spectroscopy. *J. Chem. Soc. Faraday Trans.* **1995**, *91*, 4423–4430. [[CrossRef](#)]
21. MacLaren, D.; White, M. Cement: Its Chemistry and Properties. *J. Chem. Educ.* **2003**, *80*, 623–635. [[CrossRef](#)]
22. L'Hôpital, E.; Lothenbach, B.; Le Saout, G.; Kulik, D.; Scrivener, K. Incorporation of aluminium in calcium-silicate-hydrates. *Cem. Concr. Res.* **2015**, *75*, 91–103. [[CrossRef](#)]
23. Zhang, Y. *Study on Microstructure and Rheological Properties of Cement-Chemical Admixtures-Water Dispersion System at Early Stage*; Springer: Singapore, 2018.
24. Nguyen, D.; Devlin, L.; Koshy, P.; Sorrell, C. Effects of acetic acid on early hydration of Portland cement. *J. Therm. Anal. Calorim.* **2016**, *123*, 489–499. [[CrossRef](#)]

Article

Defect Detection of Subway Tunnels Using Advanced U-Net Network

An Wang ^{1,*}, Ren Togo ², Takahiro Ogawa ² and Miki Haseyama ²

¹ Graduate School of Information Science and Technology, Hokkaido University, N-14, W-9, Kita-ku, Sapporo 060-0814, Japan

² Faculty of Information Science and Technology, Hokkaido University, N-14, W-9, Kita-ku, Sapporo 060-0814, Japan; togo@lmd.ist.hokudai.ac.jp (R.T.); ogawa@lmd.ist.hokudai.ac.jp (T.O.); miki@ist.hokudai.ac.jp (M.H.)

* Correspondence: wang@lmd.ist.hokudai.ac.jp

Abstract: In this paper, we present a novel defect detection model based on an improved U-Net architecture. As a semantic segmentation task, the defect detection task has the problems of background–foreground imbalance, multi-scale targets, and feature similarity between the background and defects in the real-world data. Conventionally, general convolutional neural network (CNN)-based networks mainly focus on natural image tasks, which are insensitive to the problems in our task. The proposed method has a network design for multi-scale segmentation based on the U-Net architecture including an atrous spatial pyramid pooling (ASPP) module and an inception module, and can detect various types of defects compared to conventional simple CNN-based methods. Through the experiments using a real-world subway tunnel image dataset, the proposed method showed a better performance than that of general semantic segmentation including state-of-the-art methods. Additionally, we showed that our method can achieve excellent detection balance among multi-scale defects.

Keywords: deep learning; semantic segmentation; U-Net; defect detection; subway tunnel

Citation: Wang, A.; Togo, R.; Ogawa, T.; Haseyama, M. Defect Detection of Subway Tunnels Using Advanced U-Net Network. *Sensors* **2022**, *22*, 2330. <https://doi.org/10.3390/s22062330>

Academic Editors: Carlos Morón Fernández and Daniel Ferrández Vega

Received: 7 February 2022

Accepted: 13 March 2022

Published: 17 March 2022

Publisher's Note: MDPI stays neutral with regard to jurisdictional claims in published maps and institutional affiliations.



Copyright: © 2022 by the authors. Licensee MDPI, Basel, Switzerland. This article is an open access article distributed under the terms and conditions of the Creative Commons Attribution (CC BY) license (<https://creativecommons.org/licenses/by/4.0/>).

1. Introduction

With the growth of economies worldwide, various infrastructures such as tunnels, bridges, and viaducts have been constructed [1], which are indispensable for our daily life and are used by a large number of people in their daily lives [2]. However, infrastructures built more than five decades ago are experiencing aging problems, and the number of dilapidated infrastructures will significantly increase in the near future [1], and their maintenance cost will also increase exponentially [3,4]. Under these circumstances, a more efficient maintenance and management of infrastructures have become an urgent issue. Recently, much interest has been shown in smart maintenance and management technologies, including artificial intelligence (AI), Internet of Things (IoT), and big data analysis. These techniques have already been applied to real-world problems in various fields [5–9]. These techniques are required in the field of infrastructure to improve the efficiency and accuracy of infrastructure maintenance [10,11].

As an important infrastructure, urban railway systems have been mainly constructed during the high-speed economic growth period. In urban areas, the overground transportation network is already dense and its expansion potential is limited. On the other hand, the subway transportation environment, such as subway tunnels, is expected to expand further in the future. However, through the high frequency of use, tunnels that were built decades ago inevitably decay and suffer from a number of defects. Without repairs, these defects lead to significant economic losses and threaten safety.

In order to maintain a high level of security and economic growth, the daily maintenance and inspection of tunnels is necessary. Traditional inspection methods mainly rely on tunnel wall images taken by inspection vehicles or inspectors [12]. Inspectors look

for deterioration such as cracks and leaks when taking images and the deterioration of tunnel walls is evaluated and repaired according to their conditions. This process is performed manually, and it takes much time and labor. Technologies that enable the automatic detection of defects are required to facilitate this process [13,14].

The standard strategy for supporting the inspection of subway tunnels is to construct a detector for the estimation of defects from tunnel wall images. Among all kinds of defects, automated crack detection has been studied for a long time, and various methods based on image processing have been proposed [15–19]. Recently, in the field of computer vision, the performance of image recognition has been significantly improved with the emergence of deep learning, which has been useful for various tasks [20–24]. Therefore, it is expected that image recognition technology will enable the development of a detector that can automatically identify defects in infrastructures.

Deep learning-based methods have achieved higher performances in detecting defect in infrastructures than traditional methods that use handcrafted image features [25–27]. However, when applying deep learning methods to real-world problems, various characteristics and situations have to be considered. Since there are various kinds of defects in subway tunnels such as cracks, cold joints, and leakages, existing deep learning methods cannot be directly applied to this task. Specifically, the following problems need to be addressed to improve detection performance:

Problem 1:

Subway tunnel images have a high resolution and limited areas of defects. Hence, the problem of imbalance between the background and foreground in semantic segmentation is prominent.

Problem 2:

Defects in subway tunnels have multi-scale variations. It is necessary to distinguish between these types since the repair action differs depending on the type of defect.

Problem 3:

Subway tunnel image contains a complex background. Although there are no defects in the background area, it often contains structures similar to the defects due to the construction conditions.

Hence, it is desirable to devise more effective network architectures that can recover the details of defects in subway tunnel images and improve the detection accuracy of multi-scale defects.

To solve the above problems, we focus on the U-Net architecture [28], one of the most widely used methods in biomedical image segmentation tasks. The U-Net's skip connection method, which can concatenate up-sampled feature maps with feature maps skipped from an encoder, makes it possible to effectively capture details and location information about objects. U-Net and its variants have achieved impressive segmentation results in computer vision tasks, especially in detecting multi-scale targets [29–32]. Because the cracks feature in our task is long and thin, we require the network to have the capacity to maintain the feature in high resolution; U-Net is a suitable choice for this. Specifically, the feature of cracks (small targets) is mainly captured by the high-resolution layer, and the water leakage feature is mostly captured by the low-resolution layer. Because of the succinct architecture, it is easy to add extra modules or change the architecture to improve the detection capacity for different kinds of segmentation targets in our task. The U-Net architecture is, therefore, suitable for our task.

In this paper, we propose an improved version of the U-Net architecture to solve the above problems. As a network design for the multi-scale target segmentation of a particular image dataset, the U-Net architecture is a suitable foundation network for our task. To solve Problem 1, we adjust the image dataset to balance background and foreground images to overcome the problem of background examples dominating gradients. To solve Problems 2 and 3, we optimize the network architecture using the following strategies: First, we

replace all convolution blocks of the U-Net architecture with inception blocks [33]. Since the inception module consists of four different branches with different kernel sizes and enlarges the network's receptive field, we can improve the network adaption to different scales of features. For our task, this improvement increases the capacity to detect multi-scale defects. In addition, for the same purpose, we replace the first convolution layer of the bridge layer with an atrous spatial pyramid pooling (ASPP) module from Deeplab-v2 [34]. Combining these two kinds of structures results in more precise detection and mitigates the over-fitting problem.

Our contributions are summarized as follows:

- We propose a novel advanced U-Net for defect detection using subway tunnel images.
- We design an architecture that can grasp the characteristics of a variety of defects. The experimental results show the effectiveness of our new architecture.

This paper is organized as follows: Summaries of related works on defect detection and classification are presented in Section 2. Next, Section 3 shows the data characteristics, and Section 4 shows the proposed method and the adopted network architectures. The experimental results are shown in Section 5. Finally, our conclusion is presented in Section 6.

2. Related Works

In this section, we discuss related works of computer vision tasks for application, U-Net family, and defect detection, respectively. Recent application tasks in computer vision are mentioned in Section 2.1, more specific architectures based on U-Net are explained in Section 2.2, and methods for defect detection are presented in Section 2.3.

2.1. Computer Vision Task for Application

Computer vision tasks have made great progress with the rise of deep learning technologies [35]. In the past, computer vision tasks have been studied mainly with the aim of recognizing objects in images; however, with the rise of deep learning, the level of accuracy close to real-world applications has been achieved [25,36]. The recognition level of general objects exceeded human accuracy in a competition held in 2015, and various methods for more advanced tasks such as object detection and pixel-level segmentation have been proposed [37,38]. In parallel, this technology has been applied not only in the field of computer science but also in various other fields. Transfer learning has shown that feature representations acquired by general image recognition can be useful for tasks in other domains [39,40]. In addition, a number of studies have been proposed for tasks where the amount of data is not sufficient [41].

Following general images, medical images are the next area where the technology is expected to be applied to society [42–44]. Medical images are highly specialized due to the clarification of imaging standards, but the quality of the captured images is high. Therefore, supervised learning, which is the speciality of deep learning, has succeeded in building relatively accurate models [45].

2.2. Deep Learning with U-Net and Its Variants

As a well-known biomedical image segmentation network, U-Net architecture in 2015 has a completely symmetric encoder–decoder structure, where features extracted from the same size convolutional layers are concatenated with corresponding up-sampling layers; thus, high- or low-level feature maps can be preserved and inherited by the decoder to obtain more precise segmentation. After that, its variants were proposed in the following years and are still applied to real-world segmentation tasks nowadays.

The common improved variants of U-Net are committed to redesigning convolutional modules and modifying down- and up-sampling. Namely, many varying methods such as TerausNet [46], Res-UNet [47], Dense U-Net [48], and R2U-Net [31] have been proposed. For example, TenausNet replaces the encoder part with VGG11, Res-UNet and Dense U-Net replace all submodules with res-connection and dense-connection, and R2U-Net combines recurrent convolution and res-connection as a submodule. U-Net++ [29] and U-Net 3+ [30]

hope to increase multi-scale target detection capacity. The main advantage of these variants is that they can capture features of different levels and integrate them through feature superposition.

2.3. Defect Detection in Infrastructures

Before the high development age of deep learning techniques, the defect detection methods were mainly developed by using image processing method. In [10,11], the authors conducted surveys of newly developed robotic tunnel inspection systems and showed that they overcome these disadvantages and achieve high-quality inspection results. Additionally, Huang et al. reported a method for analyzing the morphological characteristics and distribution characteristics of structural damage based on an intelligent analysis method from visible images of tunnel images [13]. Furthermore, Koch et al. reported computer vision-based distress detection and condition assessment approaches related to concrete and asphalt civil infrastructure [49]. In addition, several methods for automatic detection based on computer vision techniques have been proposed [21,22]. Khoa et al. proposed automatic crack detection and classification methods by using morphological image processing techniques and feature extraction based on distance histogram-based shape descriptors [21]. Furthermore, Zhang et al. proposed a method called online CP-ALS to incrementally update tensor component matrices, followed by self-tuning a one-class support vector machine [24] for online damage identification [22].

In recent years, deep learning techniques have been successfully applied to defect detection tasks based on real-world datasets. For instance, Kim et al. [50] used Mask R-CNN to detect and segment defects in multiple kinds of civil infrastructure. Bai et al. [51] used Robust Mask R-CNN for the task of crack detection. Specifically, they proposed a two-step method, called cascaded network, in which ResNet is used to classify defects and then some state-of-art segmentation networks are used. Huang et al. [52] proposed an integrated method, which combines a deep learning algorithm and Mobile Laser Scanning (MLS) technology, achieving an automated three-dimensional inspection of water leakages in shield tunnel linings. Choi et al. [53] proposed a semantic damage detecting network (SDDNet) for crack segmentation, which achieves real-time segmentation effectively negating a wide range of various complex backgrounds and crack-like features. Chen et al. [54] present a switch module to improve the efficiency of the encoder-decoder model, demonstrating it with U-Net and DeepCrack as examples. In this way, deep learning-based defect detection methods have shown promising results for the classification and segmentation tasks with the benefit of high representation ability.

3. Dataset

In this section, we explain the inspection data used in our study. Figure 1 shows examples of the subway tunnel image data. We can see that the tunnel image data have different characteristics of natural image data. The size of the images is approximately $12,088 \times 10,000$ pixels or $12,588 \times 10,000$ pixels and the resolution is 1 mm/pixel, and so they can be considered high-resolution images. Typically, analyzing high-resolution images requires enormous computer resources and such image sizes are not used in the input of deep learning models. On the other hand, the resizing process results in the loss of fine-scale defects. We solve this problem by the patch division processing.

The subway tunnel image data consist of defect and background images. Figure 2 shows defect patch examples divided from original images shown in Figure 2 (a) cracks, (b) cold joint, (c) construction repair (d) deposition (e) peeling, and (f) trace of water leakage. As shown in Figure 2, we can see that each type of defect has its characteristics such as different texture edges and color features. As for a two-class segmentation task, this intra-class variance will cause false alarms. For instance, the size and color of cracks (Figure 2a) are different from those of traces of water leakage (Figure 2f).

Next, we show divided patch examples of background images that have no defects in Figure 3 (a) cable, (b) concrete joint, (c) connection component of overhead conductor rail,

(d) passage tunnels (e) overhead conductor rail, and (f) lighter. In Figure 3, some of them have characteristics similar to those of defect images, which can also cause a serious false alarm problem.

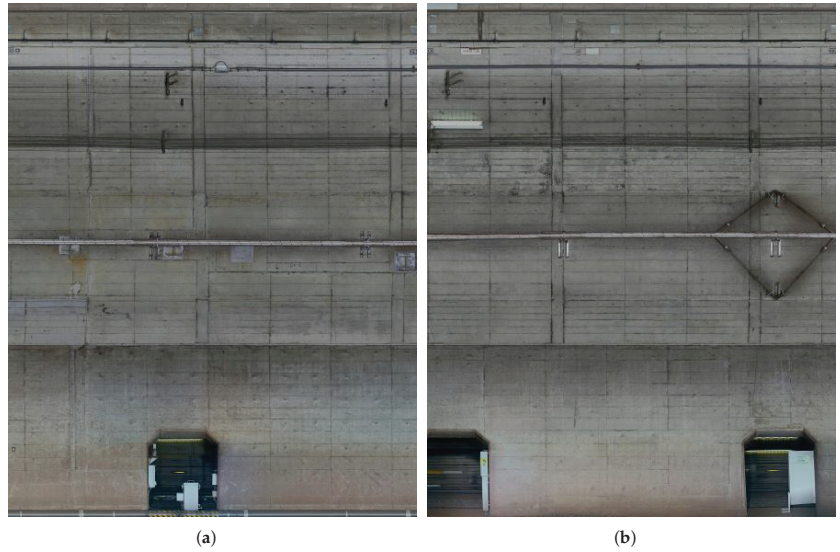


Figure 1. Examples of subway tunnel images used in this study. (a,b) are sample images taken from a visible camera for inspection. (Resolution: 1 mm/pixel, Image size: 12,088 × 10,000 pixels).

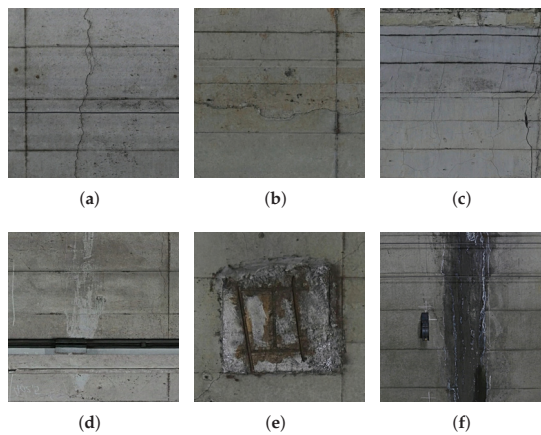


Figure 2. Example of defect images. (a–f) represent cracks, cold joint, construction repair, deposition, peeling, and trace of water leakage, respectively. (Resolution: 1 mm/pixel, Image size: 256 × 256 pixels).

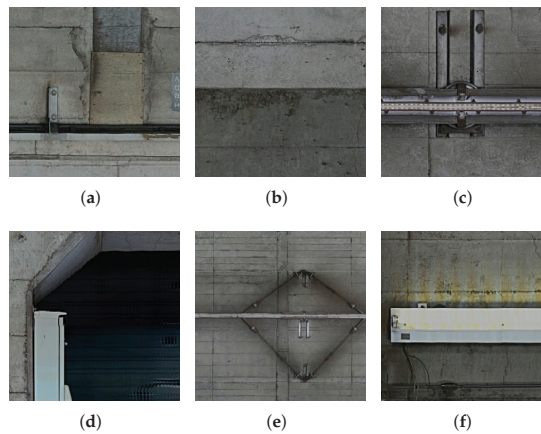


Figure 3. Example of background images. (a–f) show cable, concrete joint, connection component of overhead conductor rail, passage tunnels, overhead conductor rail, and lighter, respectively. (Resolution: 1 mm/pixel, Image size: 256×256 pixels).

4. Methodology

Inspired by Inception-v4, ASPP module, and U-Net, we propose a new model for defect detection. The proposed network combines the advantages of all three existing models. We explain data augmentation in Section 4.1 and introduce the architecture of our network in Section 4.2.

4.1. Data Augmentation

In this subsection, we propose our data augmentation strategy and patch selection method. First, we divide high-resolution subway tunnel images into multiple patches as shown in Figures 2 and 3. Let $P_i (i = 1, 2, 3, \dots, I)$ denote divided patches derived from the original images shown in Figure 1, where I represents the number of patches. Because of the imbalance distribution and multi-scale defects, we used an overlap strategy to ensure exhaustive defect patches, which extend the patch dataset. In addition, to construct the dataset via patch selection, we experimentally obtained a large-scale dataset containing background $B_n (n = 1, 2, \dots, N)$ and defect patches $D_m (m = 1, 2, \dots, M)$. Note that the ratio between M and N is approximately 7:3 and $N + M = I$.

For the training phase, since the dataset includes superfluous patches and a approximately half of them are background patches, it can cause a data imbalance problem. Under this condition, we randomly excluded some background patches to balance the number of patch samples. It should be noted that this strategy does not influence the detection accuracy. Finally, the ratio between defect and background patches can reach 1:1.

The advantage of data augmentation is that features between distributions of data can be resolved by pseudo-data generation. The model acquires a high degree of generality by learning to identify the transformed images as input. In recent years, this idea has been incorporated into self-supervised learning. In self-supervised learning, a transformation similar to data augmentation is performed, and learning is performed without labels. It has been reported that this method can dramatically improve the representational capability of the model itself. In this paper, we focus on data augmentation because we are interested in supervised learning.

4.2. Network Architecture

In this subsection, we explain the network architecture used in our method. Figure 4 depicts a model architecture of the proposed method, and Table 1 represents the details of our network. We chose U-Net as our backbone model to achieve a high performance in

the special data segmentation task. To increase the rate of detection of multi-scale defects in subway tunnel data, first, we replaced the convolution blocks of the U-Net architecture with inception blocks modified from Inception-v3 as shown in Table 1. Inception blocks extend the feature capture area to increase accuracy and mitigate the over-fitting problem. Second, we added the ASPP module to our model, and we imitated the usage of the ASPP in Deeplab-v3+ to set it after the last layer of the encoder (the bridge layer, middle of the network) shown in Figure 5a. In shallow architectures, the size of the encoder's last layer is no less than 16×16 . We adjusted the parameter settings of multiple parallel atrous convolutions in the ASPP module for adaptation to our task. In the following, we explain the details of our model.

Table 1. Architecture of the proposed model.

| Type | Size/Stride | Output Size | Depth |
|------------------|----------------|-----------------------------|-------|
| Inception Module | $3 \times 3/1$ | $256 \times 256 \times 64$ | 3 |
| Inception Module | $3 \times 3/1$ | $256 \times 256 \times 64$ | 3 |
| Inception Module | $3 \times 3/1$ | $256 \times 256 \times 64$ | 3 |
| Max Pooling | $3 \times 3/2$ | $128 \times 128 \times 64$ | 1 |
| Inception Module | $3 \times 3/1$ | $128 \times 128 \times 128$ | 3 |
| Inception Module | $3 \times 3/1$ | $128 \times 128 \times 128$ | 3 |
| Inception Module | $3 \times 3/1$ | $128 \times 128 \times 128$ | 3 |
| Max Pooling | $3 \times 3/2$ | $64 \times 64 \times 128$ | 1 |
| Inception Module | $3 \times 3/1$ | $64 \times 64 \times 256$ | 3 |
| Inception Module | $3 \times 3/1$ | $64 \times 64 \times 256$ | 3 |
| Inception Module | $3 \times 3/1$ | $64 \times 64 \times 256$ | 3 |
| Max Pooling | $3 \times 3/2$ | $32 \times 32 \times 256$ | 1 |
| Inception Module | $3 \times 3/1$ | $32 \times 32 \times 512$ | 3 |
| Inception Module | $3 \times 3/1$ | $32 \times 32 \times 512$ | 3 |
| Inception Module | $3 \times 3/1$ | $32 \times 32 \times 512$ | 3 |
| Max Pooling | $3 \times 3/2$ | $16 \times 16 \times 512$ | 1 |
| The ASPP module | – | $16 \times 16 \times 1024$ | 2 |
| Inception Module | $3 \times 3/1$ | $16 \times 16 \times 1024$ | 3 |
| Deconvolution | $3 \times 3/2$ | $32 \times 32 \times 512$ | 3 |
| Cat | – | $32 \times 32 \times 512$ | 1 |
| Inception Module | $3 \times 3/1$ | $32 \times 32 \times 512$ | 3 |
| Inception Module | $3 \times 3/1$ | $32 \times 32 \times 512$ | 3 |
| Deconvolution | $3 \times 3/2$ | $64 \times 64 \times 256$ | 1 |
| Cat | – | $64 \times 64 \times 512$ | 1 |
| Inception Module | $3 \times 3/1$ | $64 \times 64 \times 256$ | 3 |
| Inception Module | $3 \times 3/1$ | $64 \times 64 \times 256$ | 3 |
| Deconvolution | $3 \times 3/2$ | $128 \times 128 \times 128$ | 1 |
| Cat | – | $128 \times 128 \times 256$ | 1 |
| Inception Module | $3 \times 3/1$ | $128 \times 128 \times 128$ | 3 |
| Inception Module | $3 \times 3/1$ | $128 \times 128 \times 128$ | 3 |
| Deconvolution | $3 \times 3/2$ | $256 \times 256 \times 64$ | 1 |
| Cat | – | $256 \times 256 \times 128$ | 1 |
| Inception Module | $3 \times 3/1$ | $256 \times 256 \times 64$ | 3 |
| Inception Module | $3 \times 3/1$ | $256 \times 256 \times 64$ | 3 |
| Sigmoid | $1 \times 1/1$ | $256 \times 256 \times 1$ | 1 |

Our network consists of stacked layers of modified inception blocks shown in Figure 5b in the U-Net-based encoder–decoder network. The inception blocks consist of four parallel branches. Three of them have convolution layers with different kernel sizes, and the last one has one max-pooling layer. We replaced the 5×5 convolution layer with 5×1 and 1×5 convolution layers to decrease the training parameters. In the original U-Net architecture, the encoder part contains 8 convolution blocks. In addition, the output of every 2 convolution blocks is down-sampled by a max-pooling layer, and to construct a

deeper network, we add one inception block before each max-pooling layer, increasing the total number of convolution operations in the encoder from 8 to 12.

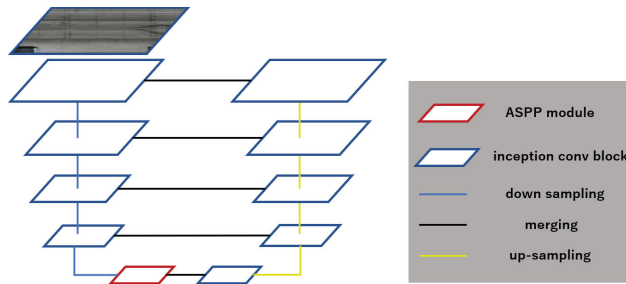


Figure 4. Overview of our defect detection network architecture.

At the end of the encoder part, we replaced the bridge's first convolution layer with the ASPP module, which is shown in Figure 5a; the input was split into 5 equal partitions. In the original ASPP module, the atrous rates of three 3×3 convolutions were set to 6, 12, and 18 (with 256 filters and batch normalization) to adapt to the input size, which is over 37×37 . When the rate value is close to the feature map size, the 3×3 filter degenerates to a 1×1 filter, and the atrous convolution loses its effectiveness. In our task, the input size was limited to 256×256 pixels, and after 4 max-pooling operations, the final input size of the ASPP module became 16×16 , which is less than the required 37×37 . Therefore, we changed the atrous rates from 4, 8, and 16 to 2, 4, and 6 to adapt to the input size. After the ASPP module, a 1×1 convolution operation (with 1024 channels) was added to merge the bridge layer.

In the decoder part, we used a convolution transpose layer (with a kernel size of 3×3 and a stride size of 2) to perform the up-sampling operation. Instead of using the deeper architecture as the encoder, we replaced all basic convolution layers with inception blocks.

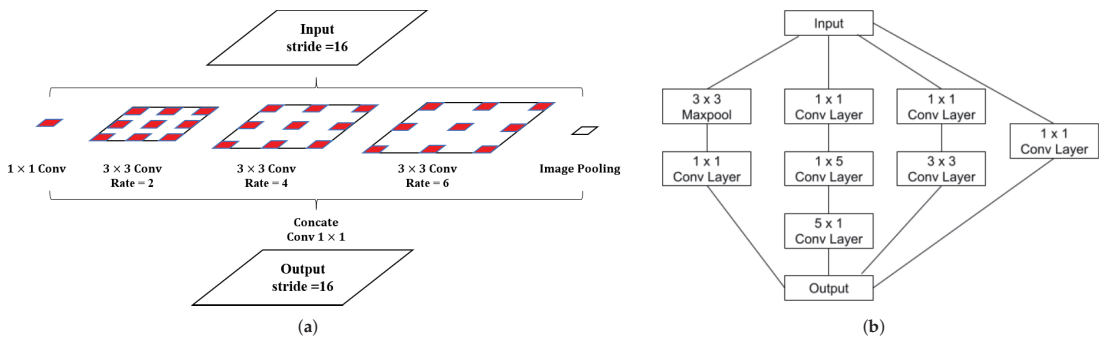


Figure 5. Modules introduced in our method. (a) represents the architecture of ASPP module and (b) represents the inception module.

5. Experiments and Results

This section shows quantitative and qualitative evaluations to confirm our network's effectiveness for detecting defects in subway tunnel images. The experimental settings are explained in Section 5.1, and the results and discussion are presented in Sections 5.2 and 5.3, respectively. Experimental data were provided by Tokyo Metro Co., Ltd, a Japanese subway company.

5.1. Settings

In our experiments, 47 images made up the subway tunnel image dataset. The images were obtained from visible cameras with high resolutions (e.g., $12,088 \times 10,000$ pixels or $12,588 \times 10,000$ pixels), and we divided the images into multiple patches of 256×256 pixels with a sliding interval of 64 pixels.

In the training phase, we filtered the patches using the strategy introduced in Section 4.1. The pixel-ground truth of defects was determined by inspectors. We selected 280,000 patches from 29 images as our training dataset. In this dataset, the ratio between the background and defect patches was set to 1:1. Then, in the validation phase, seven images were divided by the same strategy, as in the training phase, and finally, 71,818 patches were selected. The last 11 images were used in the test phase. We only used the same dividing strategy without abandoning background patches. Therefore, the number of patches used in the test phase was 326,172, which is significantly larger than that in the training phase. After the test phase, we generated estimation images by recombining the estimation results and the average probability of each pixel.

For the semantic segmentation task, Recall, Precision, F-measure, and Intersection over Union (IoU) were used to evaluate the binary classification performance as our estimation metrics. They can be calculated as follows:

$$\text{Recall} = \frac{TP}{TP + FN}, \quad (1)$$

$$\text{Precision} = \frac{TP}{TP + FP}, \quad (2)$$

$$\text{F-measure} = \frac{2 \times \text{Recall} \times \text{Precision}}{\text{Recall} + \text{Precision}}, \quad (3)$$

$$\text{IoU} = \frac{TP}{TP + FP + FN}, \quad (4)$$

where TP, TN, FP, and FN represent the number of true-positive, true-negative, false-positive, and false-negative samples, respectively.

We compared our method with classic segmentation methods including Deeplab-v3+ (CM1) [55], FCN (CM2) [56], and SegNet (CM3) [57]. Since the input of the network was set to 256×256 , the output size of the encoder in Deeplab-v3+ was 16×16 . According to our method, we adjusted the parameter settings of multiple parallel atrous convolutions in the ASPP module using the same strategy as introduced in Section 4.2. In addition, since our network is based on the U-Net architecture, we added several previous U-Net versions as comparative methods (CM4-CM7). The design of each method is shown in Table 2. Among them, CM5 [58] added additional down-sampling blocks to both the encoder and decoder of the network, changing the down-sampling stride from 16 to 32.

Table 2. Differences in the proposed method (PM) and U-Net-based comparative methods (CM4-CM7) used in the experiment.

| Method | Inception | ASPP | Layer Extend |
|----------------|-----------|------|--------------|
| PM | ✓ | ✓ | - |
| CM4 | - | ✓ | - |
| CM5 | - | - | ✓ |
| CM6 | ✓ | - | - |
| CM7 (Baseline) | - | - | - |

5.2. Results

In this subsection, we show the evaluation results and discuss some important details of the proposed model.

5.2.1. Quantitative Analysis

Table 3 shows the detection rate of all defects. From Table 3, we can compare the defect detection performance of our method and comparative methods (CM1-CM7). In these metrics, IoU, which is the standard metric of the semantic segmentation field, is the most important value to evaluate the total performance. We can see that PM obviously outperformed all CMs in this metric.

Next, Table 4 shows the recall rate of detection of each defect. From Table 4, we can observe the specific defect detection performance of our method and comparative methods (CM1-CM7). It should be noted that the metric Recall was used for the evaluation of each defect detection performance since the small crack defects were directly included. For the evaluation of the detection performance of cracks, IoU is not the best evaluation metric because of the difficulty of pixel-level matching. Moreover, considering the application situation, over-detection is considered preferable to miss-detection for the detection of defects. From the above reasons, we selected the evaluation metric Recall in this evaluation.

Table 3. Defect detection performance of the proposed method (PM) and the comparative methods (CMs).

| Method | Recall | Precision | F-Measure | IoU |
|----------|--------|-----------|-----------|-------|
| PM | 0.660 | 0.436 | 0.525 | 0.356 |
| CM1 [55] | 0.564 | 0.375 | 0.451 | 0.291 |
| CM2 [56] | 0.494 | 0.315 | 0.385 | 0.238 |
| CM3 [57] | 0.410 | 0.136 | 0.204 | 0.158 |
| CM4 | 0.493 | 0.405 | 0.444 | 0.286 |
| CM5 | 0.532 | 0.463 | 0.495 | 0.329 |
| CM6 | 0.617 | 0.346 | 0.443 | 0.285 |
| CM7 | 0.588 | 0.336 | 0.428 | 0.272 |

Table 4. Recall of all kinds of defects in each method.

| Defect | Recall | | | | | | | |
|------------------------------|--------|-------|-------|-------|-------|-------|-------|-------|
| | PM | CM1 | CM2 | CM3 | CM4 | CM5 | CM6 | CM7 |
| Peeling | 0.921 | 0.866 | 0.729 | 0.191 | 0.795 | 0.905 | 0.711 | 0.655 |
| Floating | 0.802 | 0.711 | 0.568 | 0.199 | 0.708 | 0.782 | 0.651 | 0.533 |
| Crack (0.3 mm–0.5 mm) | 0.173 | 0.230 | 0.163 | 0.209 | 0.159 | 0.140 | 0.125 | 0.110 |
| Crack (0.5 mm–1 mm) | 0.358 | 0.385 | 0.430 | 0.334 | 0.407 | 0.382 | 0.361 | 0.326 |
| Crack (1 mm–2 mm) | 0.402 | 0.463 | 0.384 | 0.422 | 0.455 | 0.434 | 0.409 | 0.388 |
| Crack(2mm+) | 0.414 | 0.409 | 0.394 | 0.431 | 0.467 | 0.444 | 0.426 | 0.389 |
| Cold joint | 0.013 | 0.017 | 0.016 | 0.014 | 0.016 | 0.016 | 0.007 | 0.005 |
| Honeycomb | 0.084 | 0.251 | 0.230 | 0.010 | 0.030 | 0.210 | 0.090 | 0.080 |
| Patching (intermediate pile) | 0.819 | 0.734 | 0.616 | 0.159 | 0.721 | 0.816 | 0.656 | 0.591 |
| Alligator crack | 0.362 | 0.308 | 0.216 | 0.063 | 0.317 | 0.368 | 0.306 | 0.244 |
| Early construction repair | 0.423 | 0.375 | 0.271 | 0.061 | 0.394 | 0.504 | 0.306 | 0.297 |
| Deposition | 0.054 | 0.049 | 0.015 | 0.001 | 0.080 | 0.012 | 0.005 | 0.010 |
| Construction repair | 0.591 | 0.307 | 0.167 | 0.078 | 0.413 | 0.556 | 0.364 | 0.375 |

The proposed method outperforms all comparative methods. According to Table 3 and Table 4, we can further discuss the importance of each component.

Limitation of Deeplab-v3+ (CM1):

Deeplab-v3+ used atrous convolution, ASPP module, and a simplified decoder branch, achieving great improvement compared with the baseline. There was a slight difference in the detection accuracy for various kinds of defect. Although Deeplab-v3+ applied multiple kinds of modules to improve detection performance

for multi-scale defects, it still lacks detection accuracy for large-scale defects as shown in Table 3.

FCN and SegNet (CM2, CM3):

FCN and SegNet, as classic segmentation networks, show a certain degree of incompatibility in our subway tunnel dataset, not only with a low accuracy but also with a large number of false detection instances as shown in Table 3. Especially, the performance of SegNet is extremely poor. Although the detection accuracy of small targets such as cracks can be maintained, it is almost impossible to detect large defects as shown in Table 4. These result in the low overall detection accuracy and precision of the network. Unlike U-Net, the SegNet decoder uses the max-pooling indices received from the corresponding encoder to perform nonlinear upsampling of the input feature map as a typical symmetric encoder–decoder architecture. It is considered that this function did not work well in the subway tunnel dataset.

Effectiveness of ASPP module (CM4):

In CM4, this module increases F-measure from 0.428 to 0.444 and IoU from 0.272 to 0.286 compared with the baseline module (CM7) in Table 3. Additionally, the obtained results from Table 4 suggest that the addition of the ASPP module significantly improved the detection performance of small-, medium-, and large-scale defects. The obtained results show the effectiveness of the ASPP module.

Effectiveness of layer extend operation (CM5):

In CM5, compared with the baseline (CM7), this module increases F-measure from 0.428 to 0.495 and IoU from 0.272 to 0.329 as shown in Table 3. Additionally, Table 4 suggests that CM5 is superior to CM4, CM6, and the baseline (CM7). These results suggest that deeper networks improve the detection of all scales of defects. However, this operation could not be applied to networks with the ASPP module due to patch size limitations in the experimental setting.

Effectiveness of Inception module (CM6):

In CM6, we only replaced all convolution blocks with the inception module. This operation increased F-measure from 0.428 to 0.443 and IoU from 0.272 to 0.285 compared with the baseline (CM7) in Table 3. Additionally, Table 4 shows that the detection rate of each scale significantly improved compared with the baseline. This indicates that the addition of the inception module can contribute to the representation ability of low- and high-level information.

Analysis of the proposed method:

As shown in Table 3, PM outperformed all other methods. Furthermore, from Table 4, we can see that PM achieves better accuracy in detecting large-scale defects but has some limitations in detecting small-scale defects. The limitation of small-scale defects may influence the detection performance of the inspection task. Thus, qualitative analysis is also required.

5.2.2. Qualitative Analysis

In this part, we discuss the visual quality of the results. The estimation results are shown in Figures 6–9. Figure 6 shows detection result samples of all regions of the test image. Figures 7 and 8 show the detection results of peeling and cracks. From Figures 6–8, we can see that PM achieves a high detection quality when detecting various defects compared to CMs. On the other hand, we show the over-fitting result sample in Figure 9. In some cases, we observed that vertical cracks tend to over-fit in our model. The quantitative analyses show that the proposed method has some limitations in detecting small-scale defects, and according to Figure 8, these limitations may not influence the actual inspection works. Compared with all CMs, the result of PM achieves fewer instances of false detection, which would lead to less unnecessary work for inspectors.

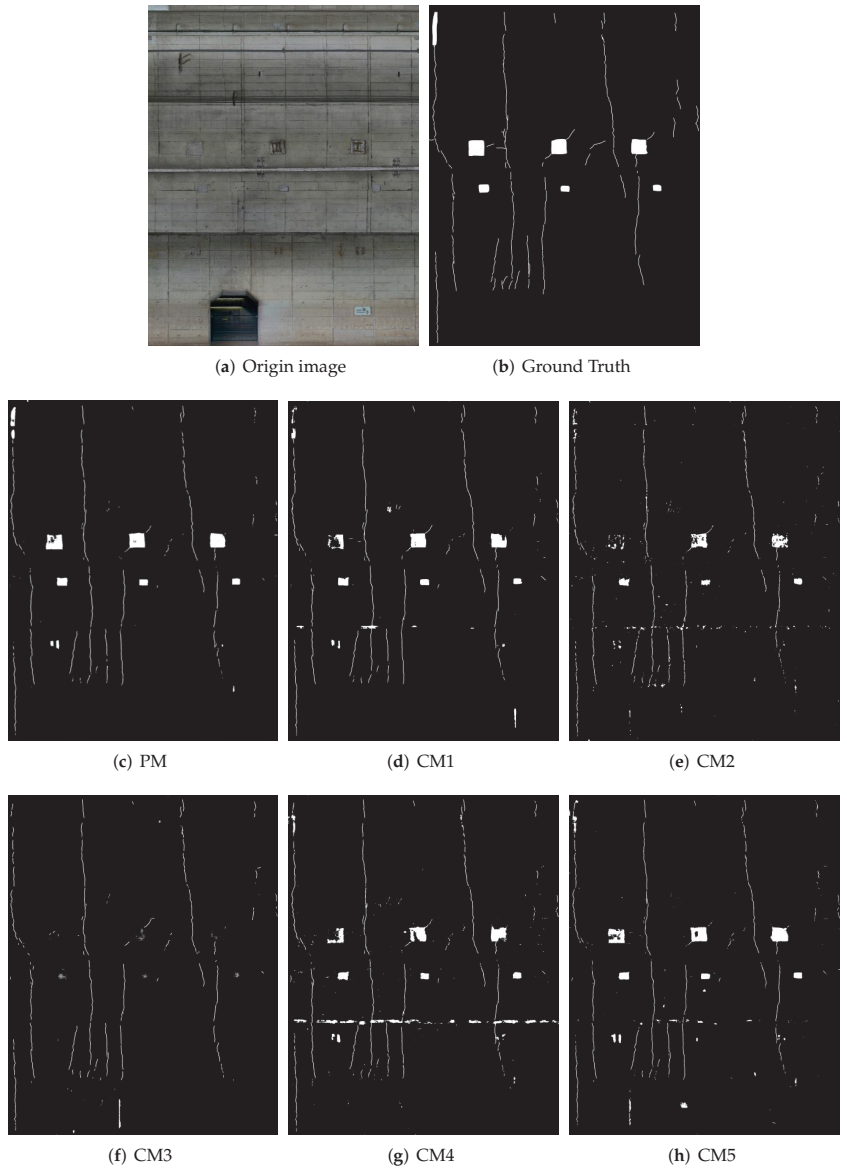


Figure 6. Cont.

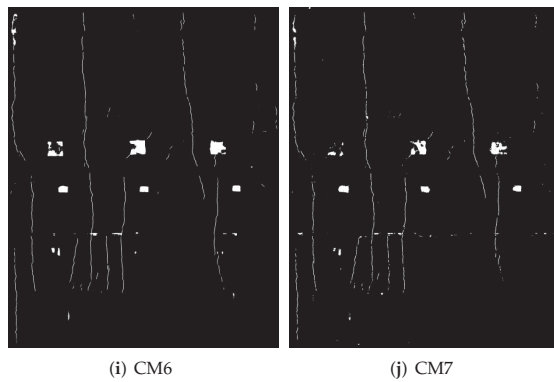


Figure 6. Results of proposed method and comparative methods. (From left to right: (a): original image; (b): ground truth; (c): results obtained by the proposed method; and (d–j): results obtained by the comparative methods.)

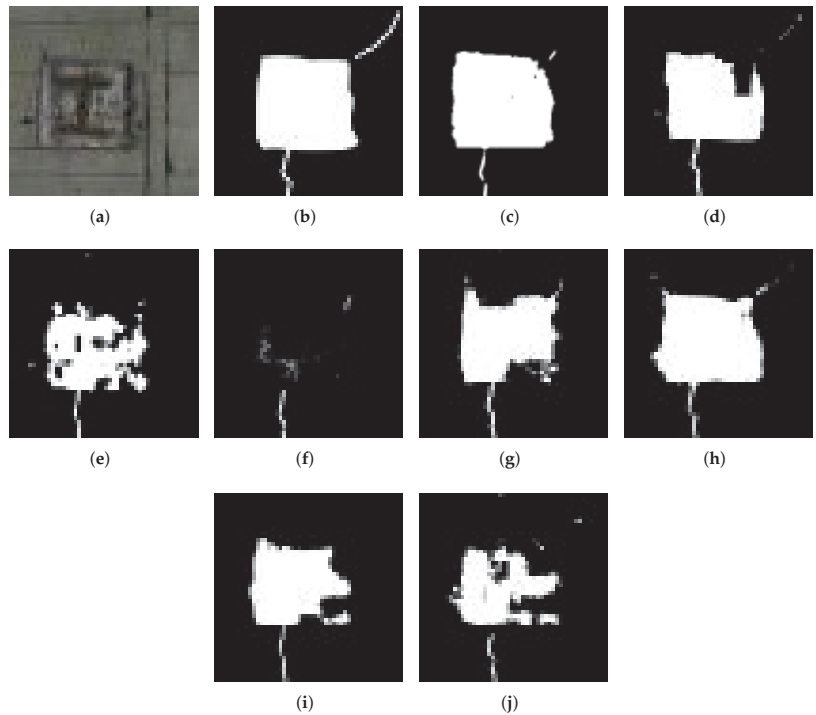


Figure 7. Example of the result in peeling detection. (a) Original image. (b) Ground Truth. (c) PM. (d) CM1. (e) CM2. (f) CM3. (g) CM4. (h) CM5. (i) CM6. (j) CM7.

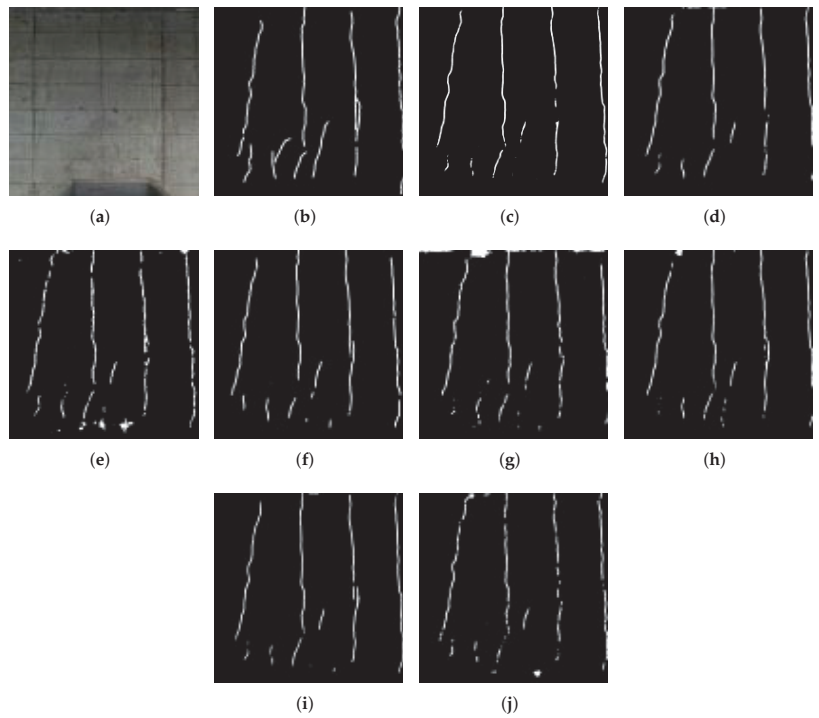


Figure 8. Example of the result for crack detection. (a) Original image. (b) Ground truth. (c) PM. (d) CM1. (e) CM2. (f) CM3. (g) CM4. (h) CM5. (i) CM6. (j) CM7.

5.3. Discussion

In the field of image recognition, various models have been proposed consistently owing to the AI boom. In the models for general object recognition, the error rate of recognition now exceeds that of humans, and there is a glimpse of a direction to target more advanced tasks. Applications of AI are beginning to be explored in all areas, one of which is infrastructure maintenance. In this paper, we have proposed a method for detecting defects in subway tunnel images. By constructing a model that takes into account the characteristics of the data, the proposed method achieved a higher accuracy in detecting defects compared to conventional methods.

What we should consider here is how much the system should achieve to reach the accuracy that can be applied in the real world. The quantitative evaluation results obtained from this experiment showed that the IoU was around 0.3–0.4. This value may not be sufficient when compared to the accuracy of general image recognition. However, as shown in the results of the qualitative evaluation, cracks and other defects in the image can be detected even if there is some deviation. For example, if we consider the practical applications of the proposed method, such as supporting the registration of defects in CAD systems or identifying dense regions of defects, we can say that the proposed method has reached a system that can be applied in practice.

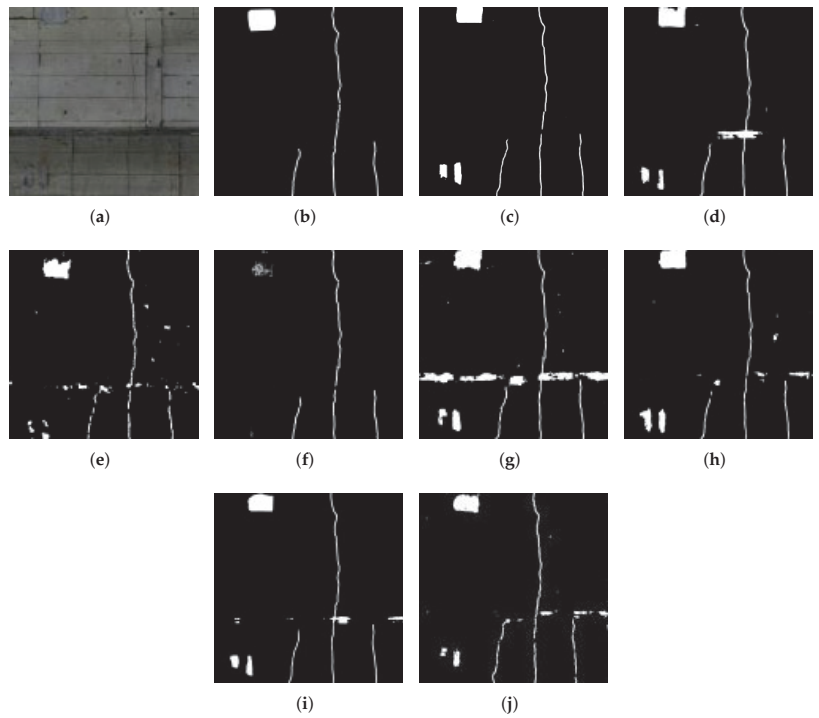


Figure 9. Example of the results of over-fitting parts. (a) Origin image. (b) Ground truth. (c) PM. (d) CM1. (e) CM2. (f) CM3. (g) CM4. (h) CM5. (i) CM6. (j) CM7.

There are some limitations in this study. This study was conducted using data from a certain subway line in Japan, and there is still room for future studies on the general applicability to a wide variety of data. In this study, 47 high-resolution subway tunnel images were divided into patches to enable the network training; however, it would be desirable to have a larger number of images to verify the robustness of our method. In addition, since the accuracy is considered to vary depending on the year of construction of tunnels, verification using a wide variety of data is necessary. Specifically, the condition of the wall depends on the construction method of the subway tunnel, and furthermore, the new construction method may be completely different from the conventional construction method. When considering the versatility of the model, it will be necessary to verify the versatility of the model for various types of data.

6. Conclusions

In this study, we present a new version of the U-Net architecture to improve the detection performance of defects in subway tunnel images. By introducing ASPP and inception modules in the U-Net-based network architecture, we improved the capacity of the network for defect detection. The experimental results on a real-world subway tunnel image dataset showed that our method outperformed other segmentation methods quantitatively and qualitatively. Different from conventional crack detection methods, our model can detect various types of defects in a single model, which enhances the practicality for supporting tunnel inspections. In future works, we will investigate a new strategy for enhancing detection accuracy and discuss its application to other real-world tasks.

Author Contributions: Conceptualization, A.W., R.T., T.O. and M.H.; methodology, A.W., R.T., T.O. and M.H.; software, A.W.; validation, A.W., R.T., T.O. and M.H.; data creation, A.W.; writing—original draft preparation, A.W.; writing—review and editing, R.T., T.O. and M.H.; visualization, A.W.; funding acquisition, T.O. and M.H. All authors read and agreed to the published version of the manuscript.

Funding: This work was supported by KAKENHI Grant Number JP17H01744.

Institutional Review Board Statement: Not applicable.

Informed Consent Statement: Not applicable.

Data Availability Statement: Not applicable.

Acknowledgments: The authors thank Tokyo Metro Co., Ltd, for providing the research data used in this study.

Conflicts of Interest: The authors declare no conflict of interest.

References

1. Ministry of Land, Infrastructure, Transport and Tourism; White Paper on Land, Infrastructure, Transport and Tourism in Japan. 2019. Available online: <https://www.mlit.go.jp/en/statistics/white-paper-mlit-index.html> (accessed on 26 June 2019).
2. Merenda, M.; Porcaro, C.; Iero, D. Edge machine learning for AI-enabled IoT devices: A review. *Sensors* **2020**, *20*, 2533. [CrossRef] [PubMed]
3. Underwood, B.S.; Guido, Z.; Gudipudi, P.; Feinberg, Y. Increased costs to US pavement infrastructure from future temperature rise. *Nat. Clim. Chang.* **2017**, *7*, 704–707. [CrossRef]
4. Onuma, A.; Tsuge, T. Comparing green infrastructure as ecosystem-based disaster risk reduction with gray infrastructure in terms of costs and benefits under uncertainty: A theoretical approach. *Int. J. Disaster Risk Reduct.* **2018**, *32*, 22–28. [CrossRef]
5. Lee, J.; Park, G.L.; Han, Y.; Yoo, S. Big data analysis for an electric vehicle charging infrastructure using open data and software. In Proceedings of the Eighth International Conference on Future Energy Systems, Hong Kong, China, 16–19 May 2017; pp. 252–253.
6. Lv, Z.; Hu, B.; Lv, H. Infrastructure monitoring and operation for smart cities based on IoT system. *IEEE Trans. Ind. Informatics* **2019**, *16*, 1957–1962. [CrossRef]
7. Wang, J.; Yang, Y.; Wang, T.; Sherratt, R.S.; Zhang, J. Big data service architecture: A survey. *J. Internet Technol.* **2020**, *21*, 393–405.
8. Arfat, Y.; Usman, S.; Mehmood, R.; Katib, I. Big data tools, technologies, and applications: A survey. In *Smart Infrastructure and Applications*; Springer: Berlin/Heidelberg, Germany, 2020; pp. 453–490.
9. Zhu, L.; Yu, F.R.; Wang, Y.; Ning, B.; Tang, T. Big data analytics in intelligent transportation systems: A survey. *IEEE Trans. Intell. Transp. Syst.* **2018**, *20*, 383–398. [CrossRef]
10. Montero, R.; Vicores, J.G.; Martinez, S.; Jardón, A.; Balaguer, C. Past, present and future of robotic tunnel inspection. *Autom. Constr.* **2015**, *59*, 99–112. [CrossRef]
11. Pouliot, N.; Richard, P.L.; Montambault, S. LineScout Technology Opens the Way to Robotic Inspection and Maintenance of High-Voltage Power Lines. *IEEE Power Energy Technol. Syst. J.* **2015**, *2*, 1–11. [CrossRef]
12. Dung, C.V. Autonomous concrete crack detection using deep fully convolutional neural network. *Autom. Constr.* **2019**, *99*, 52–58. [CrossRef]
13. Huang, Z.; Fu, H.; Chen, W.; Zhang, J.; Huang, H. Damage detection and quantitative analysis of shield tunnel structure. *Autom. Constr.* **2018**, *94*, 303–316. [CrossRef]
14. Hastak, M.; Baim, E.J. Risk factors affecting management and maintenance cost of urban infrastructure. *J. Infrastruct. Syst.* **2001**, *7*, 67–76. [CrossRef]
15. Mohan, A.; Poobal, S. Crack detection using image processing: A critical review and analysis. *Alex. Eng. J.* **2018**, *57*, 787–798. [CrossRef]
16. Yamaguchi, T.; Hashimoto, S. Fast crack detection method for large-size concrete surface images using percolation-based image processing. *Mach. Vis. Appl.* **2010**, *21*, 797–809. [CrossRef]
17. Liu, Z.; Suandi, S.A.; Ohashi, T.; Ejima, T. Tunnel crack detection and classification system based on image processing. In Proceedings of the Machine Vision Applications in Industrial Inspection X, San Jose, CA, USA, 21–22 January 2002; Volume 4664, pp. 145–152.
18. Yiyang, Z. The design of glass crack detection system based on image preprocessing technology. In Proceedings of the 2014 IEEE 7th Joint International Information Technology and Artificial Intelligence Conference, Chongqing, China, 20–21 December 2014; pp. 39–42.
19. Nishikawa, T.; Yoshida, J.; Sugiyama, T.; Fujino, Y. Concrete crack detection by multiple sequential image filtering. *Comput.-Aided Civ. Infrastruct. Eng.* **2012**, *27*, 29–47. [CrossRef]
20. Zhang, L.; Yang, F.; Zhang, Y.D.; Zhu, Y.J. Road crack detection using deep convolutional neural network. In Proceedings of the International Conference on Image Processing (ICIP), Phoenix, AZ, USA, 25–28 September 2016; pp. 3708–3712.

21. Khoa, N.L.D.; Anaissi, A.; Wang, Y. Smart infrastructure maintenance using incremental tensor analysis. In Proceedings of the 2017 ACM on Conference on Information and Knowledge Management, Singapore, 6–10 November 2017; pp. 959–967.
22. Zhang, W.; Zhang, Z.; Qi, D.; Liu, Y. Automatic crack detection and classification method for subway tunnel safety monitoring. *Sensors* **2014**, *14*, 19307–19328. [[CrossRef](#)]
23. Yang, X.; Li, H.; Yu, Y.; Luo, X.; Huang, T.; Yang, X. Automatic pixel-level crack detection and measurement using fully convolutional network. *Comput.-Aided Civ. Infrastruct. Eng.* **2018**, *33*, 1090–1109. [[CrossRef](#)]
24. Suykens, J.A.; Vandewalle, J. Least squares support vector machine classifiers. *Neural Process. Lett.* **1999**, *9*, 293–300. [[CrossRef](#)]
25. Krizhevsky, A.; Sutskever, I.; Hinton, G.E. Imagenet classification with deep convolutional neural networks. *Adv. Neural Inf. Process. Syst.* **2012**, *25*, 1097–1105. [[CrossRef](#)]
26. Deng, L.; Yu, D. Deep Learning: Methods and Applications. Foundations and Trends® in Signal Processing. *Signal Process* **2014**, *7*, 197–387.
27. Shin, H.C.; Roth, H.R.; Gao, M.; Lu, L.; Xu, Z.; Nogues, I.; Yao, J.; Mollura, D.; Summers, R.M.; Gao, M.; et al. Deep convolutional neural networks for computer-aided detection: CNN architectures, dataset characteristics and transfer learning. *IEEE Trans. Med. Imaging* **2016**, *35*, 1285–1298. [[CrossRef](#)]
28. Ronneberger, O.; Fischer, P.; Brox, T. U-net: Convolutional networks for biomedical image segmentation. In Proceedings of the International Conference on Medical Image Computing and Computer-Assisted Intervention (MICCAI), Munich, Germany, 5–9 October 2015; pp. 234–241.
29. Zhou, Z.; Siddiquee, M.M.R.; Tajbakhsh, N.; Liang, J. U-net++: A nested u-net architecture for medical image segmentation. In *Deep Learning in Medical Image Analysis and Multimodal Learning for Clinical Decision Support*; Springer: Cham, Switzerland, 2018; pp. 3–11.
30. Huang, H.; Lin, L.; Tong, R.; Hu, H.; Zhang, Q.; Iwamoto, Y.; Han, X.; Chen, Y.W.; Wu, J. UNet 3+: A Full-Scale Connected UNet for Medical Image Segmentation. In Proceedings of the IEEE International Conference on Acoustics, Speech and Signal Processing (ICASSP), Barcelona, Spain, 4–8 May 2020; pp. 1055–1059.
31. Alom, M.Z.; Hasan, M.; Yakopcic, C.; Taha, T.M.; Asari, V.K. Recurrent residual convolutional neural network based on u-net (r2u-net) for medical image segmentation. *arXiv* **2018**, arXiv:1802.06955.
32. Diakogiannis, F.I.; Waldner, F.; Caccetta, P.; Wu, C. Resunet-a: A deep learning framework for semantic segmentation of remotely sensed data. *ISPRS J. Photogramm. Remote. Sens.* **2020**, *162*, 94–114. [[CrossRef](#)]
33. Szegedy, C.; Ioffe, S.; Vanhoucke, V.; Alemi, A. Inception-v4, inception-resnet and the impact of residual connections on learning. In Proceedings of the AAAI Conference on Artificial Intelligence, San Francisco, CA, USA, 4–9 February 2017; Volume 31.
34. Chen, L.C.; Papandreou, G.; Kokkinos, I.; Murphy, K.; Yuille, A.L. Deeplab: Semantic image segmentation with deep convolutional nets, atrous convolution, and fully connected crfs. *IEEE Trans. Pattern Anal. Mach. Intell.* **2017**, *40*, 834–848. [[CrossRef](#)]
35. Schmidhuber, J. Deep learning in neural networks: An overview. *Neural Netw.* **2015**, *61*, 85–117. [[CrossRef](#)] [[PubMed](#)]
36. LeCun, Y.; Bengio, Y.; Hinton, G. Deep learning. *Nature* **2015**, *521*, 436–444. [[CrossRef](#)] [[PubMed](#)]
37. Girshick, R. Fast r-cnn. In Proceedings of the IEEE International Conference on Computer Vision (ICCV), Santiago, Chile, 7–13 December 2015; pp. 1440–1448.
38. Redmon, J.; Farhadi, A. YOLO9000: Better, faster, stronger. In Proceedings of the IEEE International Conference on Computer Vision (ICCV), Venice, Italy, 22–29 October 2017; pp. 7263–7271.
39. Weiss, K.; Khoshgoftaar, T.M.; Wang, D. A survey of transfer learning. *J. Big Data* **2016**, *3*, 1–40. [[CrossRef](#)]
40. Samala, R.K.; Chan, H.P.; Hadjiiski, L.; Helvie, M.A.; Richter, C.D.; Cha, K.H. Breast Cancer Diagnosis in Digital Breast Tomosynthesis: Effects of Training Sample Size on Multi-Stage Transfer Learning Using Deep Neural Nets. *IEEE Trans. Med. Imaging* **2019**, *38*, 686–696. [[CrossRef](#)]
41. Togo, R.; Watanabe, H.; Ogawa, T.; Haseyama, M. Deep convolutional neural network-based anomaly detection for organ classification in gastric X-ray examination. *Comput. Biol. Med.* **2020**, *123*, 103903. [[CrossRef](#)]
42. Togo, R.; Yamamichi, N.; Mabe, K.; Takahashi, Y.; Takeuchi, C.; Kato, M.; Sakamoto, N.; Ishihara, K.; Ogawa, T.; Haseyama, M. Detection of gastritis by a deep convolutional neural network from double-contrast upper gastrointestinal barium X-ray radiography. *J. Gastroenterol.* **2019**, *54*, 321–329. [[CrossRef](#)]
43. Togo, R.; Hirata, K.; Manabe, O.; Ohira, H.; Tsujino, I.; Magota, K.; Ogawa, T.; Haseyama, M.; Shiga, T. Cardiac sarcoidosis classification with deep convolutional neural network-based features using polar maps. *Comput. Biol. Med.* **2019**, *104*, 81–86. [[CrossRef](#)]
44. Litjens, G.; Kooi, T.; Bejnordi, B.E.; Setio, A.A.A.; Ciompi, F.; Ghafoorian, M.; Van Der Laak, J.A.; Van Ginneken, B.; Sánchez, C.I. A survey on deep learning in medical image analysis. *Med Image Anal.* **2017**, *42*, 60–88. [[CrossRef](#)] [[PubMed](#)]
45. Togo, R.; Ogawa, T.; Haseyama, M. Synthetic Gastritis Image Generation via Loss Function-Based Conditional PGGAN. *IEEE Access* **2019**, *7*, 87448–87457. [[CrossRef](#)]
46. Iglavikov, V.; Shvets, A. TeraNet: U-Net with VGG11 Encoder Pre-Trained on ImageNet for Image Segmentation. *arXiv* **2018**, arXiv:1801.05746.
47. Xiao, X.; Lian, S.; Luo, Z.; Li, S. Weighted Res-UNet for High-Quality Retina Vessel Segmentation. In Proceedings of the 2018 9th International Conference on Information Technology in Medicine and Education (ITME), Hangzhou, China, 19–21 October 2018; pp. 327–331. [[CrossRef](#)]

48. Guan, S.; Khan, A.A.; Sikdar, S.; Chitnis, P.V. Fully Dense UNet for 2D Sparse Photoacoustic Tomography Artifact Removal. *arXiv* **2018**, arXiv:1808.10848.
49. Koch, C.; Georgieva, K.; Kasireddy, V.; Akinci, B.; Fieguth, P. A review on computer vision based defect detection and condition assessment of concrete and asphalt civil infrastructure. *Adv. Eng. Informatics* **2015**, *29*, 196–210. [[CrossRef](#)]
50. Kim, B.; Cho, S. Automated Multiple Concrete Damage Detection Using Instance Segmentation Deep Learning Model. *Appl. Sci.* **2020**, *10*, 8008. [[CrossRef](#)]
51. Bai, Y.; Sezen, H.; Yilmaz, A. End-to-end Deep Learning Methods for Automated Damage Detection in Extreme Events at Various Scales. In Proceedings of the 2020 25th International Conference on Pattern Recognition (ICPR), Milan, Italy, 10–15 January 2020.
52. Huang, H.; Cheng, W.; Zhou, M.; Chen, J.; Zhao, S. Towards Automated 3D Inspection of Water Leakages in Shield Tunnel Linings Using Mobile Laser Scanning Data. *Sensors* **2020**, *20*, 6669. [[CrossRef](#)]
53. Choi, W.; Cha, Y. SDDNet: Real-Time Crack Segmentation. *IEEE Trans. Ind. Electron.* **2020**, *67*, 8016–8025. [[CrossRef](#)]
54. Chen, H.; Lin, H.; Yao, M. Improving the Efficiency of Encoder-Decoder Architecture for Pixel-Level Crack Detection. *IEEE Access* **2019**, *7*, 186657–186670. [[CrossRef](#)]
55. Chen, L.C.; Zhu, Y.; Papandreou, G.; Schroff, F.; Adam, H. Encoder-decoder with atrous separable convolution for semantic image segmentation. In Proceedings of the European Conference on Computer Vision (ECCV), Munich, Germany, 8–14 September 2018; pp. 801–818.
56. Long, J.; Shelhamer, E.; Darrell, T. Fully convolutional networks for semantic segmentation. In Proceedings of the IEEE Conference on Computer Vision and Pattern Recognition (CVPR), Boston, MA, USA, 7–12 June 2015; pp. 3431–3440.
57. Badrinarayanan, V.; Kendall, A.; Cipolla, R. Segnet: A deep convolutional encoder-decoder architecture for image segmentation. *IEEE Trans. Pattern Anal. Mach. Intell.* **2017**, *39*, 2481–2495. [[CrossRef](#)]
58. Wang, A.; Togo, R.; Ogawa, T.; Haseyama, M. Detection of Distress Region from Subway Tunnel Images via U-net-based Deep Semantic Segmentation. In Proceedings of the IEEE 8th Global Conference on Consumer Electronics (GCCE), Osaka, Japan, 15–18 October 2019; pp. 766–767.

Article

Implementation of Construction Waste Recycling under Construction Sustainability Incentives: A Multi-Agent Stochastic Evolutionary Game Approach

Ying Sun and Zhaolin Gu *

School of Human Settlement and Civil Engineering, Xi'an Jiaotong University, Xi'an 710049, China; sunying.cerys@outlook.com

* Correspondence: guzhaoln@mail.xjtu.edu.cn

Abstract: Because of the rapid development of the economy and the process of urbanization, construction waste recycling is becoming increasingly important and should be considered. Motivated by effectively managing the construction waste recycling under sustainability incentives, the multi-agent stochastic game model is used to evaluate the evolutionary behavior of the government agencies, waste recyclers, and waste producers. To capture the uncertainty existing in the external environment, the replicator dynamic formula is integrated with Gaussian noise, and the Lyapunov exponent diagram is analyzed to illustrate the nonlinear dynamic behavior. The numerical approximations are then solved by utilizing the random Taylor expansion formula. Finally, a numerical simulation is performed to evaluate the evolutionary trajectories of the participants involved. The findings revealed that: (1) the government agency should adopt a positive supervision approach, which can encourage waste producers and recyclers to collaborate around each other; (2) lower sorting and disposal costs can enhance construction waste recycling; and (3) the existence of uncertainty in the environment around different participants will influence one's strategy selection.

Citation: Sun, Y.; Gu, Z.

Implementation of Construction Waste Recycling under Construction Sustainability Incentives: A Multi-Agent Stochastic Evolutionary Game Approach. *Sustainability* **2022**, *14*, 3702. <https://doi.org/10.3390/su14063702>

Academic Editors: Carlos Morón Fernández and Daniel Ferrández Vega

Received: 7 February 2022

Accepted: 16 March 2022

Published: 21 March 2022

Publisher's Note: MDPI stays neutral with regard to jurisdictional claims in published maps and institutional affiliations.



Copyright: © 2022 by the authors. Licensee MDPI, Basel, Switzerland. This article is an open access article distributed under the terms and conditions of the Creative Commons Attribution (CC BY) license (<https://creativecommons.org/licenses/by/4.0/>).

Keywords: construction waste recycling; sustainability incentives; multi-agent stochastic game model

1. Introduction

Construction waste is an issue that has attracted increasing worldwide attention recently. With the rapid development of socioeconomic and urbanization in China, the building industry has emerged as a pillar of the national economy. In particular, a large number of raw materials are used and massive construction waste is generated along a gradient of increasing urbanization, resulting in environmental pollution and scarcity of nature resource [1,2]. According to a study published by the Chinese Academy of Engineering, construction waste increased by 15.4% per year from 1990 to 2000, and by 16.2% per year from 2000 to 2013 [1,3]. Because of limited technology, e.g., a lack of professional construction waste recycling enterprises, and a lack of unified technical standards, China's construction waste resource rate is less than 10%, which is far below the developed countries [1,3]. Furthermore, to the best of our knowledge, the traditional disposal methods of construction waste in many countries in China are landfill and open-air stacking, which not only cause secondary pollution to soil, groundwater, rivers, and air, but also continuously occupy valuable land resources. To that end, representatives from the Chongqing Technology Evaluation and Transfer Service Center of the Chongqing Academy of Science and Technology suggested that the government should do everything possible to supervise construction waste recycling and ensure that it meets the requirements of construction sustainability development [2,4].

At present, construction waste recycling has been proven to be the most effective method of managing construction trash. In the meantime, many existing works [5–9] have already investigated its positive social, environmental, and sustainable influences and

pointed out that many factors, such as positive government agency supervision, or waste recyclers implement waste recycling, can influence construction waste recycling. Huang et al. [7] pointed out that government takes a decisive role in directing and promoting construction waste recycling in China. Furthermore, Bakshan et al. [10] used Bayesian network analysis to investigate the causal behavioral determinants of practice improvement in construction waste management, and they concluded that proper supervision is critical in construction waste recycling systems. Lately, Fu et al. [11] further investigated the influence of the government's supervision for waste recycling enterprises. Tam et al. [12] emphasized that the government's incentives can encourage construction waste producers and waste recyclers to actively recycle construction waste. However, these studies almost discussed construction waste recycling from the standpoint of an interview and questionnaire survey, and there are no existing studies that focus on how different factors influence the behavior between government and recycling enterprises.

To address the above mentioned issues, Ma et al. [1] introduced a dynamic evolutionary game theory into the construction management system and investigated the effects of government incentive policies on the evolution process. The experiments show that: (1) government subsidies for waste enterprises are critical for construction waste recycling; (2) government subsidies for waste recyclers are not always necessary since the behavior of waste recyclers is influenced by the waste producers. Furthermore, increasing the landfill cost will encourage cooperation when the government does not provide a subsidy. In contrast, Long et al. [13] investigated the evolutionary game theory between construction waste producers and construction waste recyclers in the context of the government's reward-penalty mechanism. However, it focuses primarily on the dynamic evolution process between different enterprises with and without government incentives, ignoring how the government influences the behavior of construction waste producers and waste recyclers during the evolution process. To this end, Su [2] stated that recycling construction waste is extremely beneficial for reducing environmental pollution and conserving resources, and the three-party evolutionary game theory is investigated, which included government agencies, construction waste producers, and construction waste recyclers. In particular, it was discovered that the government plays different roles during different construction waste recycling periods. Du et al. [14] presented a theoretical evolutionary game theory framework to analyze the behavior of governments, construction contractors, and the public. It first investigated the impact of various factors on stakeholders' decision-making and discovered that incentives and penalties can reduce the illegal dumping of construction waste. To that end, this paper mainly investigated what is the best choice for penalties and incentives selection.

Many significant efforts have been made to use evolutionary game theory to investigate the impact of various factors on construction waste recycling, e.g., construction sustainability incentives, positive/negative government supervision, etc. However, in these existing works [1,2,13,14], the evolutionary game process analysis for construction waste recycling is based on a deterministic model that ignores the effect of external uncertainty. It is well understood that various random factors play an important role in decision-making between each participant during the evolution process, which should be taken into account in terms of construction waste recycling [15,16]. The purpose of this paper is to build a three-party stochastic game framework that can answer the following corresponding questions. (1) How should the three-party payoff matrix and replicator dynamic formula for the construction recycling system be defined? (2) Is there an equilibrium solution in the random replicator dynamic differential formula when Gaussian white noise is introduced? If so, what kinds of boundary conditions must be met?

To address the aforementioned issues, a three-party stochastic game framework is proposed for construction waste recycling based on bounded rationality theory, in which the payoff matrix is first constructed and then the replicator dynamic equation is formalized. In particular, the Lyapunov exponent diagram is employed to investigate the nonlinear dynamic characteristics of replicator dynamic equations based on the Benettin

method, and then Gaussian white noise is introduced into the *Itô* equation. The numerical approximations are then solved using the Taylor expansion method. Finally, a numerical simulation is run to demonstrate the dynamic evolutionary trajectory. In conclusion, the following contributions have been made:

- The three-party stochastic game structure, which includes government agencies, construction waste producers, and construction waste recyclers, is first presented.
- The Lyapunov exponent diagram is next analyzed to capture the nonlinear dynamic behavior of the replicator dynamic equation based on Benettin method.
- Next, the Gaussian white noise is inserted into the replicator dynamic equation as an uncertain that exists in the external environment. Furthermore, the existence and stability of the equilibrium solutions of the *Itô* stochastic differential equation are investigated.
- Finally, the numerical simulations are conducted to show the evolutionary trajectory in terms of the stability based on Taylor expansion.

2. Literature Review

2.1. Construction Waste Recycling and Management

In recent years, with the rapid development of the economy and the acceleration of urbanization, construction and demolition waste (C&D) has increased dramatically recent years, accounting for 30–40% of city waste in China and more than 40% of all municipal waste in Europe [7–9]. However, the recycling of C&D waste is not optimistic. According to the National Bureau of Statistics of China, 1.3 billion tonnes of construction waste were produced in China in 2017, which is five times the total quantity of residential waste produced in the same year [3]. According to Ma et al. [1], 80% of the construction waste can be recycled. However, the construction waste recycling rate in China is less than 10%, which is much lower compared with 94% for the Netherland and 95% for Japan. A large gap is observed between China and developed countries in the construction waste recycling industry. In other words, construction waste recycling and management have received considerable attention from scholars both at home and abroad. Duan et al. [17] and Yang et al. [18] said that the traditional method of processing construction waste is landfill and 84% of the construction waste is landfilled in recent years in Shengzhen City, China. However, there is insufficient capacity in this area to landfill construction waste. As a result, construction waste recycling and resourcing have become a national primary objective for improving environmental effects, and the question about how to process construction waste effectively and rationally has become an urgent one. Lately, Kabirifar et al. [19] presented a framework to assess the effectiveness of construction and demolition waste management (CDWM) using construction and demolition waste stakeholders' attitudes (CDWSA), CDWM within project life cycles (CDWPLC), which pointed out that CDWAS was the most effective factor in CDWM and CDWPLC was the least effective factor in CDWN. Finally, it was stated that the most effective CDWM strategies were recycle, reuse, and reduce. Furthermore, motivated by sustainability concepts, Ghafourian et al. [20] investigated the sustainable construction and demolition waste management (SCDWM) by introducing sustainability dimensions in CDWM, which further analyzed the impacts of factors that contribute to sustainability aspects of CDWM on waste management hierarchy, such as reduce, reuse, recycle, and disposal strategies.

Recently, Bao et al. [21] treated Shengzhen as a case study and provided a decision-support framework for construction waste recycling planning. This framework intends to assist in the planning of on-site and off-site construction waste recycling in Shenzhen, China, using qualitative research methodologies such as case studies, site visits, and semi-structured interviews. Lu et al. [22] investigated a data-driven approach to obtain the bulk densities of inert and non-inert construction waste by analyzing a big dataset of 4.9 million loads of construction waste in Hong Kong in the years 2017 to 2019. Hoang et al. [23] studied the financial and economic evaluation of construction and demolition waste recycling in Hanoi, Vietnam from the supply and demand perspective. However, informal

processing the construction waste, e.g., land-filling, has increased the government costs. Ma et al. [1] constructed an evolutionary game model including construction enterprises and recycling enterprises and analyzed the behavior evolution trajectory of participants in the construction waste recycling management system. Moreover, Su [2] studied the multi-agent evolutionary game, including government agencies, waste recycles, and waste producers, in the recycling utilization of construction waste. Most of the above literature analyzes the importance of recycling construction waste. Moreover, it only considers the deterministic replicator dynamics equations, without further consideration that environmental uncertainty on the behavioral decision of participants, which plays an essential role in constructing the evolutionary game theory model. Compared with the deterministic model, which assumes that parameters are deterministic, Yazdani et al. [24] studied a waste collection routing problem by considering uncertain and proposed a novel simheuristic approach based on an integrated simulation optimization. In particular, an efficient hybrid genetic algorithm is used to optimize vehicle route planning for construction and demolition waste collection from construction projects to recycling facilities.

2.2. Evolutionary Game Theory for Construction Waste

Evolutionary game theories are flexible and powerful tools for understanding evolutionary dynamics of group interactions [25]. Many significant efforts have been made towards using evolutionary game theory to manage construction waste recycling. Ma et al. [1] developed a dynamic evolutionary game model on construction waste recycling to analyze the symbiotic evolution between the behavior of construction enterprises and recycling enterprises, in situations with or without government incentives. Moreover, the authors also studied how government incentive policy affects the dynamic evolution process of construction waste recycling. Lately, Su [2] further studied the multi-agent evolutionary decision-making process and stable strategies among three stakeholders, including government agencies (GA), waste recycles (WR) and waste producer (WP), in the recycling utilization of construction waste. In particular, Su analyzed the main factors that affected the strategies of the stakeholders and provide the tripartite evolutionary game model.

However, considering the existence of uncertainties, in reality, it is difficult to reflect the actual situation of construction waste recycling in reality only by using the general deterministic evolutionary game model. So it is necessary to introduce the random disturbance for analysis [15] and judge the stability of stochastic evolution [26]. Li et al. [16] constructed a multiplayer stochastic evolutionary game model to study the impact of innovation subsidy on enterprise innovation development. Liu et al. [27] introduced Gaussian white noise to analyze the corporate governance issues, and found that random interference factors can affect the trajectory of the equilibrium strategy.

3. Three-Party Evolutionary Game Framework

3.1. Problem Formulation

As for recycling construction waste, the strategy bank of government agencies, waste recycles, and waste producers are $S_{GA} = \{PS, NS\}$, $S_{WR} = \{IR, NIR\}$, and $S_{WP} = \{I, NI\}$, respectively. In particular, *PS* and *NS* represent positive and negative supervision, *IR* and *NIR* indicate implement construction waste recycling and not implement construction waste recycling. The tripartite evolutionary game model, including government agencies, waste recycles, and waste producers are as follows:

The government agencies, waste recycles, and waste producers are the members of the construction waste recycling system. In this system, government agency aims to increase the proportion of implementing construction waste recycling to realize and promote the construction sustainability development. As for waste recycles and producers, they try to maximize their interests. It is worth noting that if waste producers do not implement construction waste recycling, the construction waste will increase, which will further pollute the environment and lead to higher environmental management costs [28,29]. Therefore, strategies from waste recycles and producers play an essential role for the environment

and eco-system, the more these two enterprises adopt waste recycling, the less pollution led by construction waste. Following Ref. [2], this work first introduces a more precise multi-agent evolutionary model by introducing environmental benefits and penalties for waste recyclers and producers, respectively. In particular, it is assumed that government is more prone to support waste recyclers than waste producers. Then the evolution behavior of three participants is analyzed during the procedure of construction waste recycling through the evolutionary game framework. The description of corresponding parameters is given in Table 1.

Table 1. Model parameter descriptions.

| Para. | Descriptions |
|--------------|--|
| C_0 | If waste recyclers and producers do not implement construction waste recycling, then waste producers need to send the produced construction wastes to landfill for disposal, and the cost is C_0 , where $C_0 > 0$. |
| P_j | The waste recyclers generate construction materials by using natural materials, and the benefits is P_j , where $P_j > 0$. |
| E_g | The environment governance cost is paid by government agencies if the waste recyclers and producers do not implement construction waste recycling, where $E_g > 0$. |
| λ | Revenue distribution factor if waste recyclers and waste producers adopt construction waste recycling, where $0 < \lambda \leq 1$. |
| R | Total revenue if waste recyclers and producers adopt waste recycling, $R > 0$. |
| η | Effort level when waste producers implement construction waste recycling. ($0 < \eta \leq 1$). |
| C | C Total costs of the entire recycling procedure from sorting to re-production ($C > 0$). |
| C_1 | Sorting cost of construction waste ($0 < C_1 \leq C$). |
| C_g | Supervision cost of government agencies ($0 < C_g \leq C$). |
| ΔC_j | The losses if waste producers do not implement construction waste recycling while the waste recyclers adopt construction waste recycling strategies. |
| G | Social benefits were achieved when the government conducted positive supervision, e.g., good reputation. |
| S_1 | Environment benefits brought by the waste recyclers implement construction waste recycling, such as environmental improvement, etc. |
| S_2 | Environment benefits brought by the waste producers implement construction waste recycling, such as environmental improvement, etc. |
| G_1 | Good reputation achieved by government agency although their positive supervision cannot effectively evade construction waste generation. |
| S_s | Subsidies offered by the government agencies to waste producers when it implements waste recycling. |
| S_j | Subsidies provided by GA to waste recyclers when it implements waste recycling. |
| F_1 | Penalties are issued by GA to waste recyclers when it does not implement waste recycling. |
| F_2 | Penalties are issued by GA to waste producers when it does not implement waste recycling, where $0 < F_1 < F_2$ |
| x | The probability when government agency conducting positive supervision. |
| y | The probability that waste recyclers conduct construction waste recycling. |
| z | The probability that waste producers implement construction waste recycling. |

Among them, the assumptions are summarized as follows:

- The government agencies, waste recyclers, and waste producers have individually bounded rationality and try to find the maximization value of their interests.
- The waste recyclers have enough spaces to recycle waste if the waste producers are “conducting” waste recycling strategy.
- They are able to adjust their strategies when the environment changes in the construction waste recycling process.
- Assuming x indicates the probability when government agency conducts positive supervision, $1 - x$ denotes the probability when government agency conducts negative supervision. Similarly, y denotes the probability that waste recyclers conduct

construction waste recycling, $1 - y$ indicates the probability that waste recyclers do not conduct construction waste recycling. If z denotes the probability that waste producers implement construction waste recycling, $1 - z$ represents the probability that waste producers do not implement construction waste recycling.

- In the stochastic evolutionary system, the higher the strategy payoff than the average payoff is, the higher probability different enterprises conduct this strategy. Generally, this principle can be represented by replicator dynamics formulas.
- The uncertainty exists around different participants, which will bring random disturbance into the evolutionary system. To this end, it is necessary to consider this random noise in the replication dynamic differential formula.

3.2. Payoff Matrix and Replicator Dynamics Equations

Table 2 gives the payoff matrix of the government agencies, waste recyclers and waste producers, which is defined based on the principles shown in Figure 1 and each element of the Payoff Matrix are shown in Equation (1).

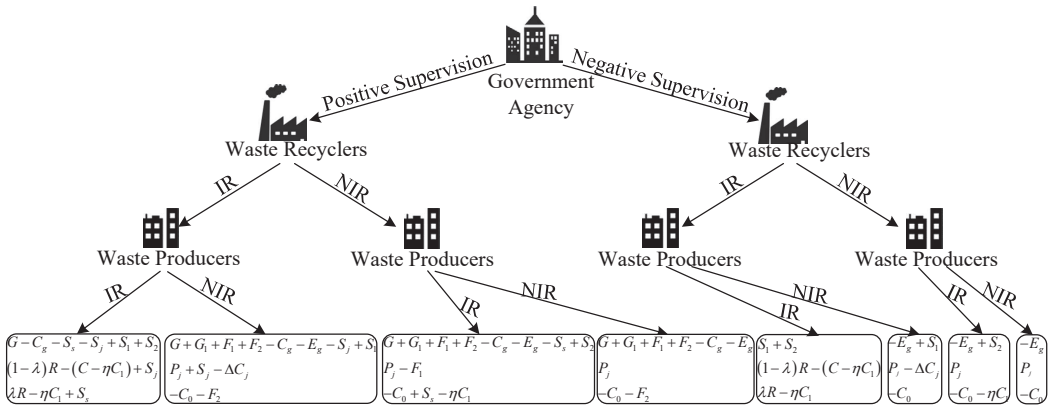


Figure 1. The three-party game tree of government agencies, waste recyclers and waste producers.

Table 2. The payoff matrix of the three-party evolutionary game for construction waste recycling.

| | | | Waste Producer | | |
|-------------------|------------------------------|------------------|---------------------------------|---------------------------------|-------------------|
| | | | Implement Recycling z | Not Implement Recycling $1 - z$ | |
| Government Agency | Positive Supervision x | Waster Recyclers | Implement Recycling y | (a_1, b_1, c_1) | (a_2, b_2, c_2) |
| | | | Not Implement Recycling $1 - y$ | (a_3, b_3, c_3) | (a_4, b_4, c_4) |
| | Negative Supervision $1 - x$ | Waster Recyclers | Implement Recycling y | (a_5, b_5, c_5) | (a_6, b_6, c_6) |
| | | | Not Implement Recycling $1 - y$ | (a_7, b_7, c_7) | (a_8, b_8, c_8) |

$$\begin{bmatrix} G - C_g - S_s - S_j + S_1 + S_2 & (1 - \lambda)R - (C - \eta C_1) + S_j & \lambda R - \eta C_1 + S_s \\ G + G_1 + F_1 + F_2 - C_g - E_g - S_j + S_1 & P_j + S_j - \Delta C_j & -C_0 - F_2 \\ G + G_1 + F_1 + F_2 - C_g - E_g - S_s + S_2 & P_j - F_1 & -C_0 + S_s - \eta C_1 \\ G + C_1 + F_1 + F_2 - C_g - E_g & P_j & -C_0 - F_2 \\ S_1 + S_2 & (1 - \lambda)R - (C - \eta C_1) & \lambda R - \eta C_1 \\ -E_g + S_1 & P_j - \Delta C_j & -C_0 \\ -E_g + S_2 & P_j & -C_0 - \eta C_1 \\ -E_g & P_j & -C_0 \end{bmatrix} \quad (1)$$

Let N_{11} and N_{12} denote the expected utility when government agency conducts positive supervision and negative supervision, respectively, and their average is represented by \bar{N}_1 .

$$\begin{aligned} N_{11} = & yz(G - C_g - S_s - S_j + S_1 + S_2) + y(1 - z)(G + G_1 + F_1 + F_2 - C_g - E_g - S_j + S_1) \\ & + (1 - y)z(G + G_1 + F_1 + F_2 - C_g - E_g - S_s + S_2) + (1 - y)(1 - z) \\ & (G + G_1 + F_1 + F_2 - C_g - E_g) \end{aligned} \quad (2)$$

$$\begin{aligned} N_{12} = & yz(S_1 + S_2) + y(1 - z)(-E_g + S_1) + (1 - y)z(-E_g + S_2) + (1 - y)(1 - z)(-E_g) \\ = & yz(E_g) - yS_1 + zS_2 - E_g \end{aligned} \quad (3)$$

$$\bar{N}_1 = x \times N_{11} + (1 - x) \times N_{12} \quad (4)$$

Then the replicator dynamic formula of government agency conducting positive supervision is given, as shown in Equation (5):

$$\begin{aligned} F(x) = & \frac{dx}{dt} = x(N_{11} - \bar{N}_1) = x(1 - x)(N_{11} - N_{12}) \\ = & x(1 - x)[yz(-G_1 - F_1 - F_2) - yS_j - zS_s + (G + G_1 + F_1 + F_2 - C_g)] \end{aligned} \quad (5)$$

Similarly, let N_{21} and N_{22} represent that waste recycler enterprise selects to implement and not implement construction waste recycling, respectively. And \bar{N}_2 denotes the average revenues.

$$\begin{aligned} N_{21} = & xz[(1 - \lambda)R - (C - \eta C_1)] + x(1 - z)(P_j + S_j - \Delta C_j) \\ & + (1 - x)z[(1 - \lambda)R - (C - \eta C_1)] + (1 - x)(1 - z)(P_j - \Delta C_j) \\ = & -xzS_j + xS_j + z[(1 - \lambda)R - (C - \eta C_1) - P_j + \Delta C_j] + (P_j - \Delta C_j) \end{aligned} \quad (6)$$

$$N_{22} = xz(P_j - F_1) + x(1 - z)P_j + (1 - x)zP_j + (1 - x)(1 - z)P_j = P_j - xzF_1 \quad (7)$$

$$\bar{N}_2 = y * N_{21} + (1 - y) * N_{22} \quad (8)$$

Then, according to Equations (6) and (7), the replicator dynamic equation of waste producers conducting construction waste recycling strategy is given as follows:

$$\begin{aligned} F(y) = & \frac{dy}{dt} = y(N_{21} - \bar{N}_2) = y(1 - y)(N_{21} - N_{22}) \\ = & y(1 - y)\{-xzS_j + xS_j + z[(1 - \lambda)R - (C - \eta C_1) - P_j + \Delta C_j] + xzF_1 - \Delta C_j\} \end{aligned} \quad (9)$$

Finally, let N_{31} and N_{32} denote the expected utility that the waste producer chooses to implement and not implement the waste recycling and their average is represented by \bar{N}_3 , which are formulated as follows:

$$\begin{aligned}
 N_{31} &= xy(\lambda R - \eta C_1 + S_s) + x(1 - y)(-C_0 + S_s - \eta C_1) \\
 &\quad + (1 - x)y(\lambda R - \eta C_1) + (1 - x)(1 - y)(-C_0 - \eta C_1) \\
 &= xS_s + y(\lambda R + C_0) - C_0 - \eta C_1
 \end{aligned}
 \tag{10}$$

$$\begin{aligned}
 N_{32} &= xy(-C_0 - F_2) + x(1 - y)(-C_0 - F_2) - (1 - x)yC_0 - (1 - x)(1 - y)C_0 \\
 &= -xF_2 - C_0
 \end{aligned}
 \tag{11}$$

$$\bar{N}_3 = z \times N_{31} + (1 - z) \times N_{32}
 \tag{12}$$

Then, the replicator dynamic formula of waste recycler conducting construction waste recycling strategy is defined as follows:

$$\begin{aligned}
 F(z) &= \frac{dz}{dt} = z(N_{31} - \bar{N}_3) = z(1 - z)(N_{31} - N_{32}) \\
 &= z(1 - z)[x(S_s + F_2) + y(\lambda R + C_0) - C_0 - \eta C_1]
 \end{aligned}
 \tag{13}$$

3.3. Replicator Dynamics Analysis

According to Equations (5), (9) and (13), the multi-agent dynamic replication formula of construction waste recycling system is achieved, i.e.,

$$\begin{cases}
 F(x) = x(1 - x)[yz(-G_1 - F_1 - F_2) - yS_j - zS_s + (G + G_1 + F_1 + F_2 - C_g)] \\
 F(y) = y(1 - y)\{-xzS_j + xS_j + z[(1 - \lambda)R - (C - \eta C_1) - P_j + \Delta C_j] + xzF_1 - \Delta C_j\} \\
 F(z) = z(1 - z)[x(S_s + F_2) + y(\lambda R + C_0) - C_0 - \eta C_1]
 \end{cases}
 \tag{14}$$

Let $\begin{cases} F(x) = 0 \\ F(y) = 0 \\ F(z) = 0 \end{cases}$, 8 corresponding strategy solutions for the construction waste recycling system can be achieved, i.e., $A1(0, 0, 0)$, $A2(0, 0, 1)$, $A3(0, 1, 0)$, $A4(0, 1, 1)$, $A5(1, 0, 0)$, $A6(1, 0, 1)$, $A7(1, 1, 0)$, and $A8(1, 1, 1)$. Additionally, there also exists a mixed strategy solution $O((x^*, y^*, z^*))$, which satisfies Equation (15)

$$\begin{cases}
 F(x^*) = y^*z^*(-G_1 - F_1 - F_2) - y^*S_j - z^*S_s + (G + G_1 + F_1 + F_2 - C_g) = 0 \\
 F(y^*) = -x^*z^*S_j + x^*S_j + z^*[(1 - \lambda)R - (C - \eta C_1) - P_j + \Delta C_j] + x^*z^*F_1 - \Delta C_j = 0 \\
 F(z^*) = x^*(S_s + F_2) + y^*(\lambda R + C_0) - C_0 - \eta C_1 = 0
 \end{cases}
 \tag{15}$$

Therefore, the following equations can be achieved

$$x^* = \frac{C_0 + \eta C_1}{S_s + F_2}
 \tag{16}$$

$$y^* = \frac{C_0 + \eta C_1}{\lambda R + C_0}
 \tag{17}$$

$$z^* = \frac{(S_s + F_2)\Delta C_j - (C_0 + \eta C_1)S_j}{(C_0 - \eta C_1)(F_1 - S_j) + (S_s + F_2)[(1 - \lambda)R - (C - \eta C_1) - P_j + \Delta C_j]}
 \tag{18}$$

where $0 < x^* < 1$, $0 < y^* < 1$ and $0 < z^* < 1$.

In addition, it is obvious that $1 - x$, $1 - y$, and $1 - z$ are non-negative, so they will not influence the results of the evolution analysis. Next, the replicator dynamic formulas of government agencies, waste recyclers, and waste producers can be rewritten as:

$$\begin{cases}
 F(x) = dx/dt = x[yz(-G_1 - F_1 - F_2) - yS_j - zS_s + (G + G_1 + F_1 + F_2 - C_g)] \\
 F(y) = dy/dt = y\{-xzS_j + xS_j + z[(1 - \lambda)R - (C - \eta C_1) - P_j + \Delta C_j] + xzF_1 - \Delta C_j\} \\
 F(z) = dz/dt = z[x(S_s + F_2) + y(\lambda R + C_0) - C_0 - \eta C_1]
 \end{cases}
 \tag{19}$$

3.4. Nonlinear Dynamic System Chaotic Analysis

To the best of our knowledge, Equation (19) is a nonlinear dynamic formula, meaning some parameters will bring chaos into this system. Chaotic represents an irregular and random movement that exists in a deterministic nonlinear system, e.g., butterfly effect. To study if the chaotic characteristic exists in the nonlinear dynamic formula in the setting of some threshold values, the Lyapunov exponent diagram is used to analyze the characteristic of the nonlinear dynamic system [30]. The Lyapunov exponent graph is used to analyze the convergence of adjacent trajectories. Especially, the nonlinear dynamic system shows stability characteristics when $LLE < 0$, where LLE means largest Lyapunov exponent. In contrast, if $LLE = 0$, the nonlinear dynamic system bifurcates at that point; if $LLE > 0$, the nonlinear dynamic system shows chaotic behavior [31].

Taking the three-party evolutionary game framework construction waste recycling system as examples, the LLE graphs are obtained based on Benettin algorithm. As shown in Figure 2, fixing other parameters, $LLE < 0$ when construction waste sorting cost C_1 belongs to $(0, 8.1)$, $(9.8, 10.2)$, $(10.8, 12.4)$, $(17.6, 18.5)$, $(19.8, 20)$, resulting in stable construction waste recycling system. In contrast, if $LLE > 0$, where $C_1 \in (8.1, 9.8)$, $(10.2, 10.8)$, $(12.4, 17.6)$ and $(18.5, 19.8)$, the construction waste recycling system is going to show chaotic characteristic (as shown in Figure 2a). From Figure 2b, it can be observed that $LLE < 0$ if $C_0 \in (4.2, 4.8)$, $(5.8, 6.5)$, $(6.8, 8.2)$, $(8.5, 9.7)$, $(10.7, 11.5)$, $(16.1, 16.3)$, $(16.9, 18.1)$, and $C_0 \in (18.3, 19.8)$, respectively and the system stay in stable state. If $C_0 \in (0, 4.2)$, $(4.8, 5.8)$, and $C_0 \in (6.5, 6.8)$, $(8.2, 8.5)$, $(9.7, 10.7)$, $(11.5, 16.1)$, $(16.3, 16.9)$, $(18.1, 18.3)$, $(19.8, 20)$, respectively, then $LLE > 0$ and the nonlinear dynamic system shows chaotic characteristic. It is also observed $LLE > 0$ when $\eta \in (0.32, 0.44)$, $(0.49, 0.71)$, $(0.74, 0.78)$, $(0.83, 0.84)$, and $\eta \in (0.91, 0.92)$, $(0.99, 1)$ in Figure 2c. This also make system show chaotic characteristic.

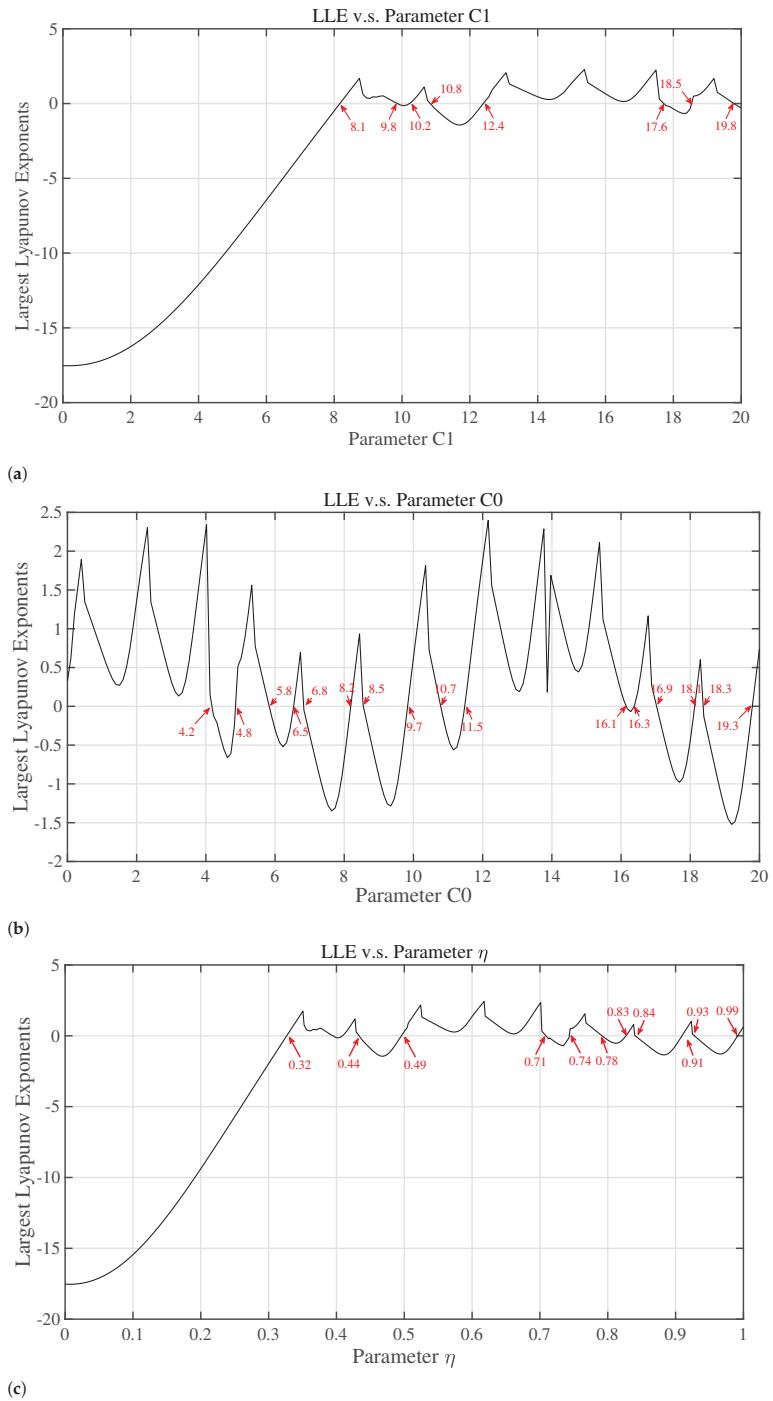


Figure 2. Largest Lyapunov exponent diagram of tripartite stochastic evolutionary game system with fixed parameters are $S_s = 10$, $S_j = 10$, $F_1 = 15$, $F_2 = 20$, $G = 30$, $G_1 = 15$, $E_g = 8$, $C_g = 5$, $P_j = 15$, $\Delta C_j = 8$, $C = 30$, $\lambda = 0.2$, $R = 45$. (a) $C_0 = 10, \eta = 0.7$. (b) $C_1 = 20, \eta = 0.7$. (c) $C_0 = 10, C_1 = 20$.

4. Stochastic Evolutionary Game Framework

4.1. Multi-Agent Stochastic Evolutionary Game Framework

To the best of our knowledge, there exist high uncertainty in the game among the government agencies, waste recyclers, and waste producers because the complexity of the external environment. To this end, the different participants will have different strategic selections because of their profits. In particular, there always exists random noise in the replicator dynamics formula, leading to bad performance for the deterministic evolutionary game framework, since the existing uncertainty around different participants. Therefore, it is necessary to take random noise into account in the tripartite game model. To further improve the previous deterministic game model, in this study, the replicator dynamic formula is combined with Gaussian white noise, which results in the multi-agent stochastic evolutionary game framework, as follows:

$$\begin{cases} dx(t) = [yz(-G_1 - F_1 - F_2) - yS_j - zS_s + (G + G_1 + F_1 + F_2 - C_g)]x(t)dt + \delta x(t)d\omega(t) \\ dy(t) = \{-xzS_j + xS_j + z[(1 - \lambda)R - (C - \eta C_1) - P_j + \Delta C_j] + xzF_1 - \Delta C_j\}y(t)dt + \delta y(t)d\omega(t) \\ dz(t) = [x(S_s + F_2) + y(\lambda R + C_0) - C_0 - \eta C_1]z(t)dt + \delta z(t)d\omega(t) \end{cases} \quad (20)$$

where $\omega(t)$ is Brownian movement. $d\omega(t)$ denotes Gaussian white noise, where $t > 0$ should stratify and h is time step, $h > 0$. $\Delta\omega(t) = \omega(t + h) - \omega(t)$ and it can be represented as normal distribution $N(0, \sqrt{h})$, and δ denotes noise intensity.

To this end, the Equation (20) denotes one-dimensional multi-agent stochastic differential formula, which also describes the tripartite evolutionary replicator dynamics equation of government agency, waste recyclers, and waste producers under random noise, respectively.

4.2. Equilibrium Solutions Analysis

It is known that Equation (20) is $It\delta$ -type stochastic differential formula, therefore, at initial time $x(0) = 0$, $y(0) = 0$, and $z(0) = 0$, respectively. Then according to Equation (20), the following equations are given:

$$\begin{cases} dx(t) = [yz(-G_1 - F_1 - F_2) - yS_j - zS_s + (G + G_1 + F_1 + F_2 - C_g)] \cdot 0 + \delta x(t)d\omega(t) \\ dy(t) = \{-xzS_j + xS_j + z[(1 - \lambda)R - (C - \eta C_1) - P_j + \Delta C_j] + xzF_1 - \Delta C_j\} \cdot 0 + \delta y(t)d\omega(t) \\ dz(t) = [x(S_s + F_2) + y(\lambda R + C_0) - C_0 - \eta C_1] \cdot 0 + \delta z(t)d\omega(t) \end{cases} \quad (21)$$

Based on Equation (21), it can be seen that $d\omega(t)|_{t=0} = \omega'(t)dt|_{t=0} = 0$, and there at least have zero solution, which indicates the construction waste recycling system will stay in this state without the interference of external white noise. To this end, zero solution is the best in this situation.

However, the construction recycling system will always be disturbed by the internal and external environment, which influences system stability. Therefore, the system stability under random noise circumstances must be considered and analyzed.

Given stochastic differential equation [16]

$$\begin{cases} dx(t) = f(t, x(t))dt + g(t, x(t))d\omega(t) \\ x(t_0) = x_0 \end{cases} \quad (22)$$

It is assumed that there has a function $V(t, x)$ for which there exist positive constant σ_1, σ_2 , such that

$$\sigma_1|x|^p \leq V(t, x) \leq \sigma_2|x|^p, t \geq 0 \quad (23)$$

Then, two kinds of specific scenarios are analyzed concerning system stability.

I. If a positive constant α is existing, making $LV(t, x) \leq -\alpha V(t, x), t \geq 0$, the null solution of Equation (22) is therefore globally exponentially stable in p-th mean. Then, $E|x(t, x_0)|^p < \frac{\sigma_2}{\sigma_1}|x_0|^p e^{-\alpha t}, t \geq 0$.

II. When a positive constant α is existing, making $LV(t, x) \geq \alpha V(t, x), t \geq 0$. In this case, the null solution of Equation (22) is not exponentially stable in p -th mean. Then, $E|x(t, x_0)|^p \geq \frac{\sigma_2}{\sigma_1}|x_0|^p e^{-\alpha t}, t \geq 0$.

To this end, for the Equation (19), let $V(t, x) = x(t)$, $V(t, y) = y(t)$, and $V(t, z) = z(t)$, where $x, y, z \in [0, 1]$. In particular, when $\sigma_1 = \sigma_2 = 1, p = 1$, and $\alpha = 1$, the following equations can be attained:

$$\begin{aligned} LV(t, x) &= f(t, x) = x[yz(-G_1 - F_1 - F_2) - yS_j - zS_s + (G + G_1 + F_1 + F_2 - C_g)] \\ LV(t, y) &= f(t, y) = y\{-xzS_j + xS_j + z[(1 - \lambda)R - (C - \eta C_1) - P_j + \Delta C_j] + xzF_1 - \Delta C_j\} \\ LV(t, z) &= f(t, z) = z[x(S_s + F_2) + y(\lambda R + C_0) - C_0 - \eta C_1] \end{aligned} \tag{24}$$

So, if the conditions

$$\begin{aligned} x[yz(-G_1 - F_1 - F_2) - yS_j - zS_s + (G + G_1 + F_1 + F_2 - C_g)] &\leq -x \\ y\{-xzS_j + xS_j + z[(1 - \lambda)R - (C - \eta C_1) - P_j + \Delta C_j] + xzF_1 - \Delta C_j\} &\leq -y \\ f(t, z) = z[x(S_s + F_2) + y(\lambda R + C_0) - C_0 - \eta C_1] &\leq -z \end{aligned} \tag{25}$$

are satisfied, the null solutions of Equation (19) are globally exponentially stable in p -th mean, respectively.

4.3. Taylor Expansion of Evolution Equation

It is known that there is no clear solution for a nonlinear $It\delta$ stochastic differential formula. To this end, the random Taylor expansion for $It\delta$ equation is conducted and the numerical approximations are used to solve it.

For a existing stochastic differential equation, i.e., Equation (26)

$$dx(t) = f(t, x(t))dt + g(t, x(t))d\omega(t) \tag{26}$$

where $t \in [t_0, T], x(t_0) = x_0, x_0 \in R$, and $\omega(t)$ is the standard winner process. Assume that, when $h = (T - t_0)/N, t_n = t_0 + nh$, the equation of random Taylor expansion is given in Equation (26)

$$x(t_{n+1}) = x(t_n) + I_0f(x(t_n)) + I_1g(x(t_n)) + I_{11}L^1g(x(t_n)) + I_{00}L^0f(x(t_n)) + R \tag{27}$$

where $L^0 = f(x)\frac{\partial}{\partial x} + \frac{1}{2}g^2(x)\frac{\partial^2}{\partial x^2}, L^1 = g(x)\frac{\partial}{\partial x}, I_0 = h, I_1 = \Delta\omega_n, I_{00} = \frac{1}{2}h^2, I_{11} = \frac{1}{2}[(\Delta\omega_n)^2 - h]$, and R is the remainder of the Taylor expansion.

Therefore, Equation (27) can be rewritten as follows

$$\begin{aligned} x(t_{n+1}) &= x(t_n) + hf(x(t_n)) + \Delta\omega_n g(x(t_n)) + \frac{1}{2}[(\Delta\omega_n)^2 - h]g(x(t_n))g'(x(t_n)) \\ &+ \frac{1}{2}h^2 \left[f(x(t_n))f'(x(t_n)) + \frac{1}{2}g^2(x(t_n))f''(x(t_n)) \right] + R \end{aligned} \tag{28}$$

To this end, the Milstein approach is used to solve the approximation problem. The Taylor expansions are further conducted for government agencies, waste recyclers, and waste producers, which leads to

$$\begin{aligned} x(t_{n+1}) &= x(t_n) + h(y(t_n)z(t_n)(-G_1 - F_1 - F_2) - y(t_n)S_j - z(t_n)S_s + \\ &+ (G + G_1 + F_1 + F_2 - C_g))x(t_n) + \frac{1}{2}((\Delta\omega_n)^2 - h)\sigma^2x(t_n) + \frac{1}{2}h^2(y(t_{n+1})z(t_{n+1}) \\ &(-G_1 - F_1 - F_2) - y(t_{n+1})S_j - z(t_{n+1})S_s + (G + G_1 + F_1 + F_2 - C_g))^2x(t_n) + \Delta\omega_n\sigma x(t_n) + R_1 \end{aligned} \tag{29}$$

$$y(t_{n+1}) = y(t_n) + h \left(-x(t_n)z(t_n)S_j + x(t_n)S_j + z(t_n) \left[(1-\lambda)R - (C - \eta C_1) - P_j + \Delta C_j \right] \right. \\ \left. + x(t_n)z(t_n)F_1 - \Delta C_j \right) y(t_n) + \frac{1}{2} [(\Delta\omega_n)^2 - h] \sigma^2 y(t_n) + \frac{1}{2} h^2 \left(-x(t_n)z(t_n)S_j + x(t_n)S_j \right. \quad (30)$$

$$\left. + z(t_n) \left[(1-\lambda)R - (C - \eta C_1) - P_j + \Delta C_j \right] + x(t_n)z(t_n)F_1 - \Delta C_j \right)^2 y(t_n) + \Delta\omega_n \sigma y(t_n) + R_2 \\ z(t_{n+1}) = z(t_n) + h \left(x(t_n)(S_s + F_2) + y(t_n)(\lambda R + C_0) - C_0 - \eta C_1 \right) z(t_n) + \frac{1}{2} h^2 \left(x(t_n)(S_s \right. \quad (31) \\ \left. + F_2) + y(t_n)(\lambda R + C_0) - C_0 - \eta C_1 \right)^2 z(t_n) + \Delta\omega_n \sigma z(t_n) + \frac{1}{2} \left((\Delta\omega_n)^2 - h \right) \sigma^2 z(t_n) + R_3$$

5. Numerical Simulations

To the best of our knowledge, it is hard to achieve the precise solution of nonlinear *Itô* differential formula. To this end, numerical simulation is applied to simulate the trajectory of three-party dynamic evolution. Especially, in this study, a three participants stochastic evolutionary game framework is proposed for construction waste recycling by analyzing the effect principle of sorting cost of construction waste, construction waste producer disposal cost when recyclers and producers do not implement construction waste recycling, effort level when waste producer implement construction waste recycling, and Gaussian white noise on the three-party evolutionary trajectory. In addition, the stability and convergence rate of the evolutionary trajectory is also analyzed. In the beginning, the following two different cases are considered: (1) for the numerical study of sorting costs and effort level, let both waste recyclers and producers implement waste recycling under positive government supervision. In this case, $x = 0.5$, which means the government agency conducts the positive supervision. In particular, the government agency does not favor any one of the positive and negative strategies at the game start, and the same with the waste producers and waste recyclers. To this end, the initial points are defined as $x_0 = y_0 = z_0 = 0.5$. (2) In contrast, for the disposal costs study, let both waste recyclers and producers do not want to implement waste recycling, while government agency tends to negative supervision strategies at the beginning. Here $x = 0.4$. While the waste producers and recyclers do not implement construction waste recycling. Therefore the initial points are defined as $x = 0.4, y_0 = 0.2, z_0 = 0.3$.

5.1. Sorting Cost of Construction Waste

Sorting cost is an essential factor when conducting construction waste recycling. Therefore, it is necessary for the waste producers and recyclers to take this factor into consideration. Figure 3 shows the results of the evolutionary trajectory of government agencies, waste recyclers, and waste producers, respectively. From Figure 3a, it is observed that with the increase of waste sorting cost, government agency always keeps the state under positive supervision. From the perspective of stability of evolution system and convergence rate, $C_1 = 5$ is the first one to reach the equilibrium point, while $C_1 = 2$ tends to reach the stable point. However, when the value of sorting cost (i.e., $C_1 = 19$) belongs to some ranges that lead to $LLE > 0$, the evolutionary trajectory of the three parties shows a very instability characteristic. Meanwhile, it can be seen from Figure 3b,c, the waste producers and recyclers also can implement waste recycling with the increasing sorting costs. However, when sorting cost $C_1 = 19$, the trajectories show strong instability.

Furthermore, the analysis of sorting cost between the waste recyclers and producers without external interference ($\delta = 0$) is conducted. In particular, from Figure 4, it can be seen that when $C_1 = 2$ and $C_1 = 5$, the trajectory of recyclers and producers presents a fast convergence to implement construction waste recycling, and there exist Nash equilibrium. This means that if waste producers and recyclers bear fewer sorting costs, it will promote its enthusiasm to implement construction waste recycling. This is because the more sorting is, the more complex the dynamic system will show. Furthermore, with the increase of

the sorting cost, the probabilities of waste producers and recyclers choosing to implement construction recycling will reduce.

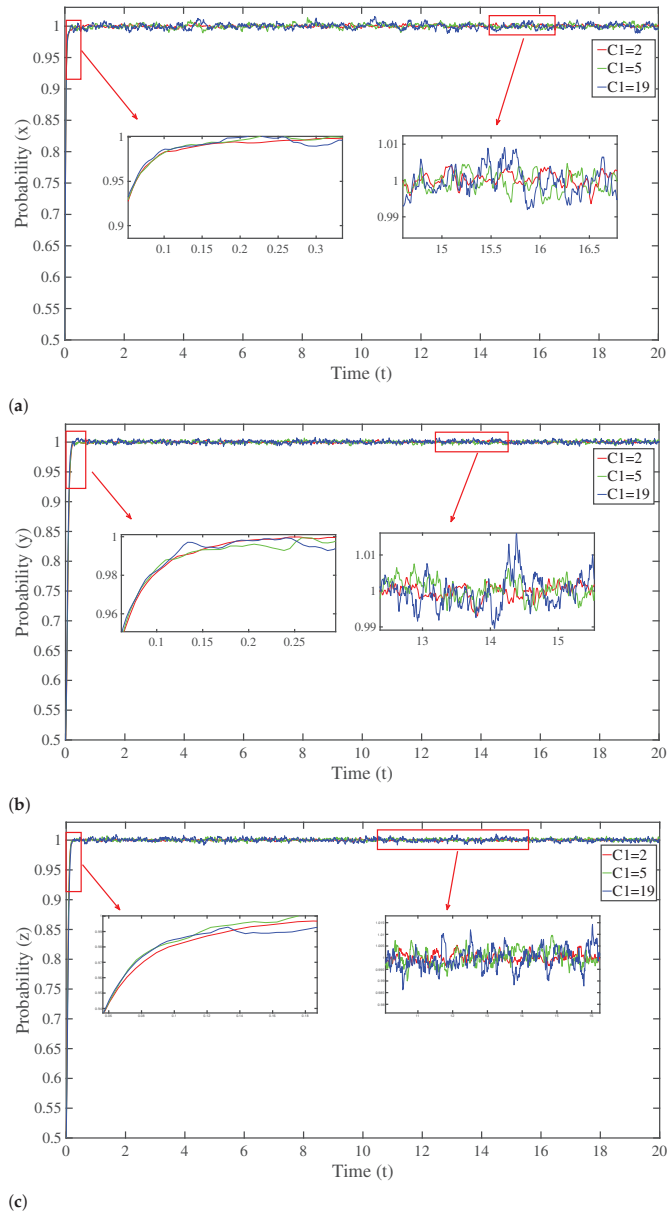


Figure 3. Multi-agent dynamic evolutionary trajectories under different construction waste sorting costs. (a) The probability when government agency conducting positive supervision. (b) The probability when waste recyclers implement construction waste recycling. (c) The probability when waste producers implement construction waste recycling. When $S_s = 10$, $S_j = 10$, $F_1 = 15$, $F_2 = 20$, $G = 30$, $G_1 = 15$, $E_g = 8$, $C_g = 5$, $P_j = 15$, $\Delta C_j = 8$, $C = 30$, $\lambda = 0.2$, $R = 45$, $\eta = 0.3$, $C_0 = 11$, $\delta_1 = \delta_2 = \delta_3 = 0.1$.

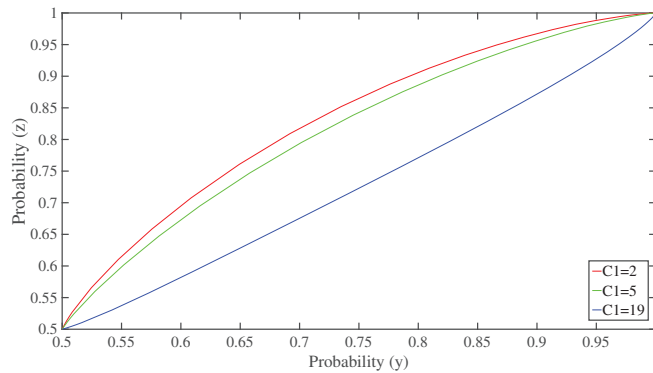


Figure 4. Evolution of waste recycles and waste producers.

Therefore, the waste producers and recyclers should find a suitable sorting cost that enhances their enthusiasm for construction waste recycling under the positive supervision of government agencies.

5.2. Disposal Costs from Waste Producers

An essential assumption in the construction waste recycling management system is that if both waste producers and recyclers do not implement waste recycling. The producers should pay the fee for waste landfills. To this end, how disposal cost affects the waste recycling system is further studied. Figure 5 shows the numerical simulation results. From the perspective of the government agency, the suitable C_0 leads the evolutionary trajectory to quickly converge to the stability points. However, unsuitable value brings disturbance to the dynamic system, which makes the construction recycling system is easily affected by external factors. In contrast, it can be seen that waste recyclers and producers are prone to not implement waste recycling when the value of C_0 results in $LLE > 0$. This means although an unreasonable value of C_0 can speed the trajectory evolution, the system is easily influenced by the external environment. In addition, the government agency can quickly reach the equilibrium point with a reasonable C_0 and choose positive supervision. Waste recyclers and producers aim to not conduct recycling construction waste in this situation.

5.3. Effects of Effort Level of Waste Producers

The effort level represents how waste producers implement waste recycling. Generally, the smaller η is, the rougher the waste producers dispose of the construction waste. In contrast, the larger η represents the waste producers dispose of the construction waste finer. Therefore, how effort level affects the dynamic system is also considered. To this end, the effect of effort level is discussed. Figure 6 gives the results. From Figure 6a, it is observed that reasonable and higher value of effort level make the government agency reach the equilibrium faster and more stable under positive supervision. In contrast, a lower reasonable value of η also reduces the convergence time of the system, which even brings disturbance to the system. And when selecting the unreasonable value of η , the system will be more easily affected by the external environments. In this case, the waste recyclers select to implement waste recycling under positive supervision from the government agency. A larger and reasonable value of effort level will make a faster and more stable system. This means waste recyclers can quickly reach the balance and a lower value of effort level will bring disturbance for the system. In contrast, waste producers reach the balance under the reasonable effort level value. In addition, the dynamic shows more vulnerable characteristics under the unreasonable effort level.

In the construction waste recycling system, the more effort from waste producers to recycle the construction waste is, the more enthusiasm for government agencies imple-

menting positive supervision is and the more enthusiasm for waste recyclers implementing waste recycling is. This undoubtedly brings great benefits for the construction waste recycling system. Therefore, the waste producers need to try their best to recycle the construction waste generated by themselves, which will promote the activities of government agencies and waste recyclers.

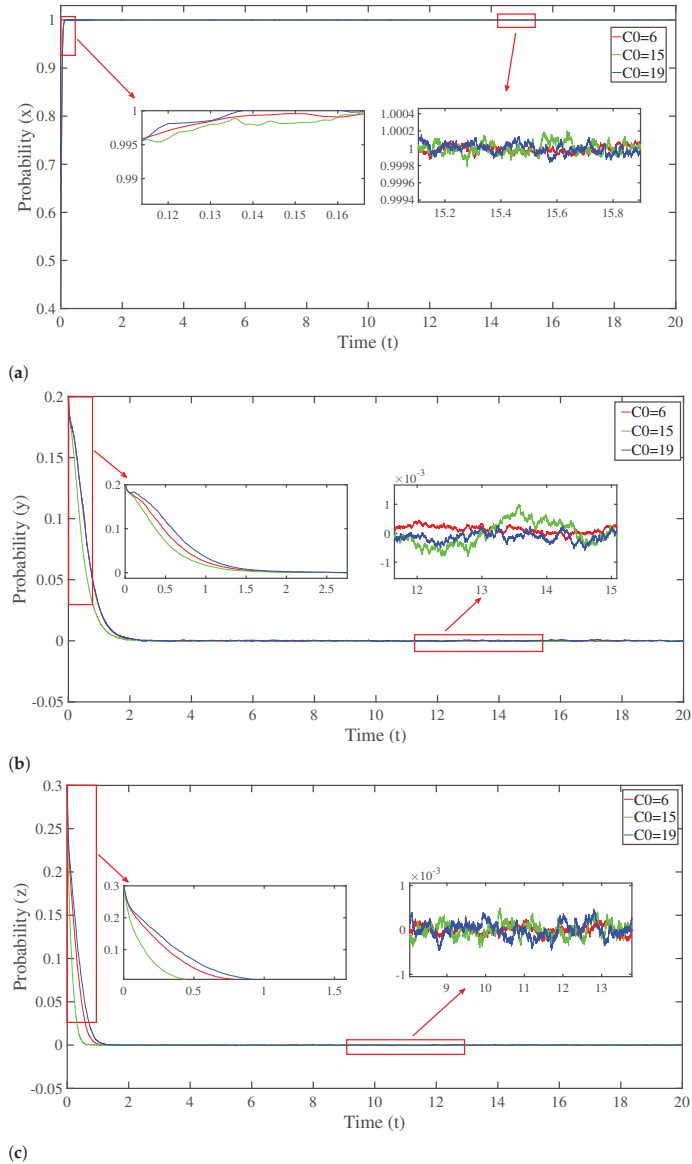


Figure 5. Multi-agent dynamic evolutionary trajectories under different disposal costs. (a) The probability when government agency conducting positive supervision. (b) The probability when waste recyclers implement construction waste recycling. (c) The probability when waste producers implement construction waste recycling. When $S_g = 10$, $S_j = 10$, $F_1 = 15$, $F_2 = 20$, $G = 30$, $G_1 = 15$, $E_g = 8$, $C_g = 5$, $P_j = 15$, $\Delta C_j = 8$, $C = 30$, $\lambda = 0.2$, $R = 45$, $\eta = 0.3$, $C_1 = 5$, $\delta_1 = \delta_2 = \delta_3 = 0.1$.

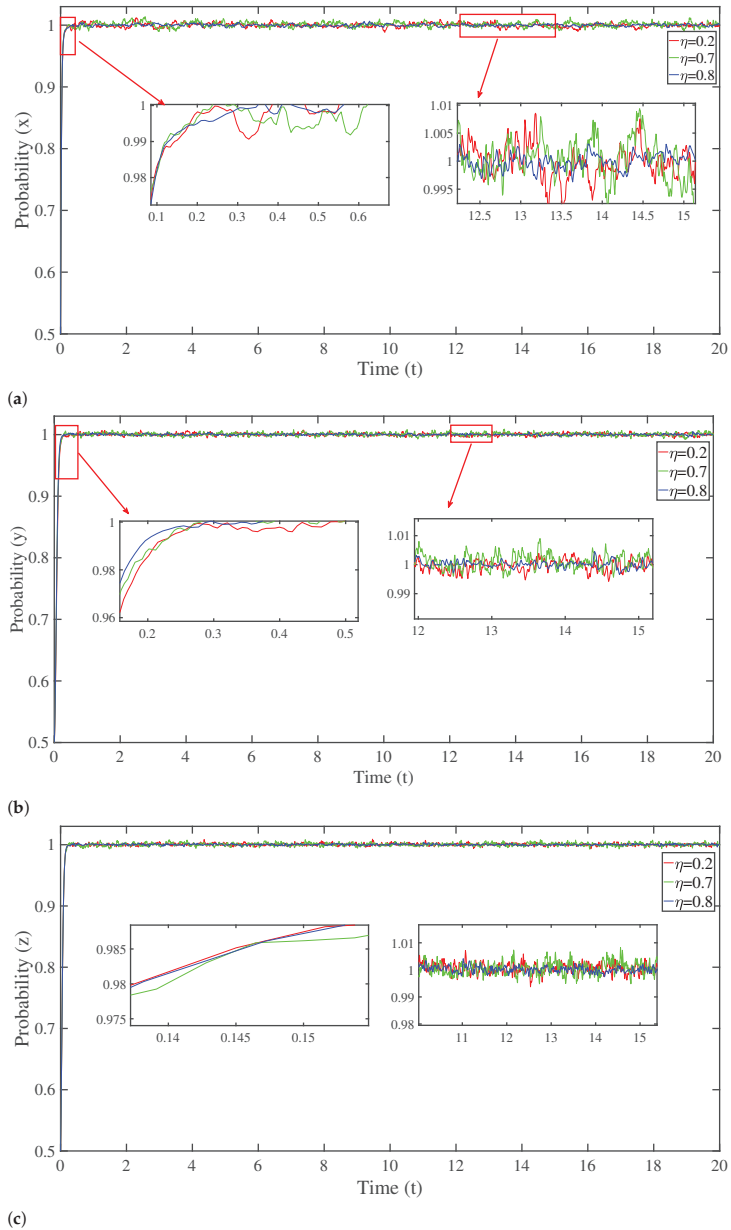
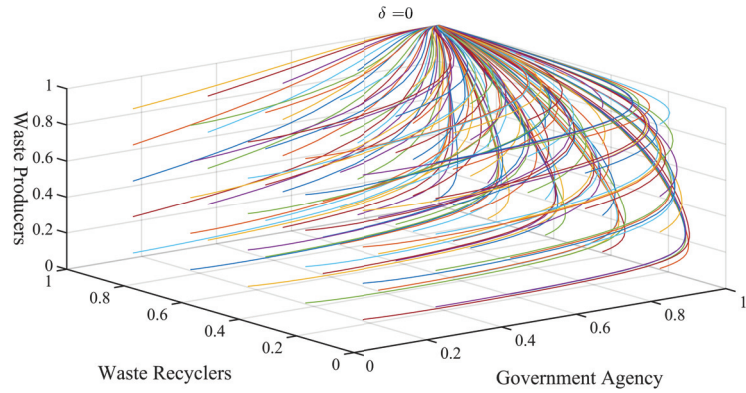


Figure 6. Multi-agent dynamic evolutionary trajectories under different effort level. (a) The probability when government agency conducting positive supervision. (b) The probability when waste recyclers implement construction waste recycling. (c) The probability when waste producers implement construction waste recycling. When $S_s = 10$, $S_j = 10$, $F_1 = 15$, $F_2 = 20$, $G = 30$, $G_1 = 15$, $E_g = 8$, $C_g = 5$, $P_j = 15$, $\Delta C_j = 8$, $C = 30$, $\lambda = 0.2$, $R = 45$, $C_0 = 6$, $C_1 = 5$, $\delta_1 = \delta_2 = \delta_3 = 0.1$.

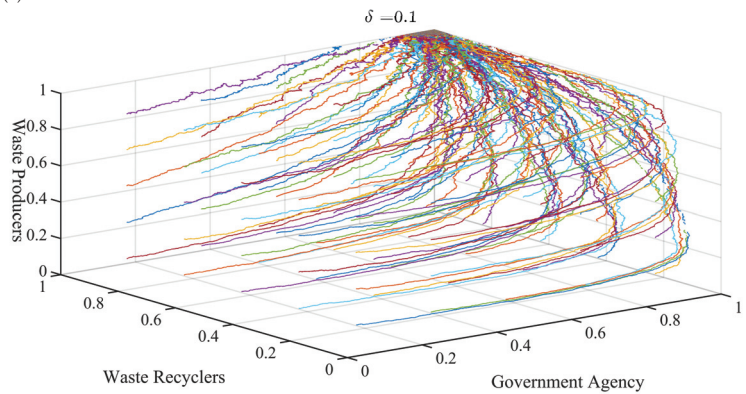
5.4. The Effect of Noise Intensity

Further simulations are conducted to discuss how noise intensity affects the trajectory of the evolutionary game model. Figure 7 shows the results. It can be observed that the uncertainty will bring random disturbance into the evolution process and then affect the

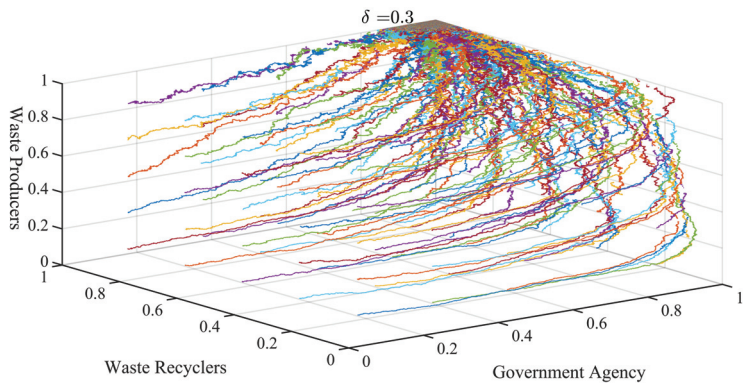
evolution process. In addition, it also can be seen that the higher the noise intensity is, the more fluctuation exists in the evolutionary trajectories. This means the uncertainty can affect the strategy choice of the government agencies, waste recyclers, and waste producers.



(a)



(b)



(c)

Figure 7. Multi-agent dynamic evolutionary trajectories under different noise intensity. (a) The probability when government agency conducting positive supervision. (b) The probability when waste recyclers implement construction waste recycling. (c) The probability when waste producers implement construction waste recycling. When $S_s = 10$, $S_j = 10$, $F_1 = 15$, $F_2 = 20$, $G = 30$, $G_1 = 15$, $E_g = 8$, $C_g = 5$, $P_j = 15$, $\Delta C_j = 8$, $C = 30$, $\lambda = 0.2$, $R = 45$, $C_0 = 6$, $C_1 = 5$, $\eta = 0.8$.

6. Discussion

An important exploration of the development of construction waste recycling systems is the study of the game interaction between the government agency and different recyclers, as well as the evolutionary trajectory of participants. Due to the lack of effective management strategies in the past, construction waste recycling has brought significant impacts on the environment and human health [7,32]. To improve environmental quality, many countries' governments have enacted a variety of environmental incentive policies [1]. However, there are multiple parties involved in the construction waste recycling system, and the existence of conflicts of interest makes it difficult to effectively implement environmental incentive policies. In particular, the existence of uncertainty in the external environment, makes the behavior of participants in the construction waste recycling system more complicated [15]. Under the premise of bounded rationality, the stochastic evolutionary game model is built to analyze the complex behavior of participants, in which the Gaussian white noise is introduced to describe the impacts of uncertainty factors on stakeholders' decision evolution trajectories. Balancing the interests of participants is the key to improving the quality of construction waste recycling. For example, China established a Processing Fund for Waste Electrical and Electronic Products in 2012 to assist the formal recycling sectors of the electronic waste dismantling industry. The dismantling fund has lost \$8 billion since its establishment, with the fund already stagnant in 2017. As a result, the management of e-waste recycling cannot rely solely on subsidies, but also on corresponding punitive measures, which is consistent with previous research [33] and also useful for construction waste recycling. According to Andrew et al. [34], different policies must be implemented based on the characteristics of different countries in order to improve governance quality. Furthermore, environmental uncertainty is a significant factor that must be considered during the decision-making process. The random interference factors can influence the equilibrium strategy's trajectory [16]. In addition, certain critical values are determined so that the system behaves chaotically.

There are also some limitations in this paper. There are differences in construction recycling management and environment incentive policies in different countries. This paper built a stochastic evolutionary game model for a case study of China, which would be greater applicability by considering different environmental incentive policies in different countries. In addition, this paper only considers the government agencies, waste producers, and waste recyclers, and introduce Gaussian white noise, China's dual government systems also play an important role in construction waste recycling. More practical conclusions would be obtained by considering the combination of political concentration and economic decentralization of dual government systems.

Base on above analysis, some implications are proposed as follows:

- With the construction waste recycling system, greater attention must be paid to the game interaction between waste producers and waste recyclers. Different enterprises have different willingness in different states, which makes the behavior of participants in the construction waste recycling system more complicated. It is therefore incredibly important to coordinate the different waste recycling enterprises' interests and obligations to ensure the effective implementation of waste recycling and to improve environmental quality.
- As regulators of the construction waste recycling system, the government agency must adopt a subsidy-penalty coordination mechanism in order to improve construction waste recycling's environmental quality and increase subsidies for qualified recyclers and default penalties for collusion.
- When making decisions, the government agency must fully consider the existence of uncertain factors in order to ensure the smooth implementation of environmental incentive policies and improve construction waste recycling quality.

7. Conclusions

Facilitating the implementation of construction waste recycling is the primary basis to realize construction sustainability and it has great practical significance for the quality improvement of construction waste recycling. In this study, the three-party *Itô* stochastic evolutionary game framework is proposed for construction waste recycling, making the payoff matrix and combining the Gaussian white noise with replicator dynamic formula. Then the random Taylor expansion is used to solve the numerical approximation, and finally, the numerical simulations are conducted to study the dynamic evolution between the government agencies, waste recyclers, and waste producers. The main conclusions are as follows: (1) Smaller sorting costs make the group strategy more stable and effective. (2) Larger disposal costs make waste producers do not implement construction waste recycling. (3) The more Waste producer put into disposing of the construction waste recycling, the more efforts government make to guide construction recycling, and the more enthusiasm the waste recyclers recycle construction waste. (4) Based on the comparative analysis of Gaussian white noise intensity, the effect of uncertainty external environments brings the random disturbance into the evolution trajectory of different participants, which leads to fluctuation of a smooth curve. To evade strategy fluctuation for different participants, it is necessary to let government agencies actively guide the waste producers and waste recyclers.

In a brief, this paper investigated the tripartite *Itô* stochastic evolutionary game model for construction waste recycling policies analysis, filling the multi-agent stochastic game study of construction waste recycling and offering a practical basis for different agencies to implement construction waste recycling.

Author Contributions: Conceptualization, Y.S. and Z.G.; methodology, Y.S.; software, Y.S.; validation, Y.S. and Z.G.; formal analysis, Y.S.; investigation, Y.S.; resources, Y.S.; data curation, Y.S.; writing—original draft preparation, Y.S.; writing—review and editing, Z.G.; visualization, Y.S.; supervision, Z.G.; project administration, Z.G.; funding acquisition, Z.G. All authors have read and agreed to the published version of the manuscript.

Funding: The author(s) disclosed receipt of the following financial support for the research, authorship, and/or publication of this article: This work was supported by the project of Basic Work of the Ministry of Science and Technology (No. SB2013FY112500).

Institutional Review Board Statement: Not applicable.

Informed Consent Statement: Not applicable.

Data Availability Statement: Not applicable.

Conflicts of Interest: The authors declare no conflict of interest.

References

1. Ma, L.; Zhang, L. Evolutionary game analysis of construction waste recycling management in China. *Resour. Conserv. Recycl.* **2020**, *161*, 104863. [\[CrossRef\]](#)
2. Multiagent evolutionary game in the recycling utilization of construction waste. *Sci. Total. Environ.* **2020**, *738*, 139826. [\[CrossRef\]](#) [\[PubMed\]](#)
3. Zheng, L.; Wu, H.; Zhang, H.; Duan, H.; Wang, J.; Jiang, W.; Dong, B.; Liu, G.; Zuo, J.; Song, Q. Characterizing the generation and flows of construction and demolition waste in China. *Constr. Build. Mater.* **2017**, *136*, 405–413. [\[CrossRef\]](#)
4. Li, X.; Huang, R.; Dai, J.; Li, J.; Shen, Q. Research on the evolutionary game of construction and demolition waste (CDW) recycling units' green behavior, considering remanufacturing capability. *Int. J. Environ. Res. Public Health* **2021**, *18*, 9268. [\[CrossRef\]](#) [\[PubMed\]](#)
5. Tseng, M.L.; Wong, W.P.; Soh, K.L. An overview of the substance of resource, conservation and recycling. *Resour. Conserv. Recycl.* **2018**, *136*, 367–375. [\[CrossRef\]](#)
6. Gálvez-Martos, J.L.; Styles, D.; Schoenberger, H.; Zeschmar-Lahl, B. Construction and demolition waste best management practice in Europe. *Resour. Conserv. Recycl.* **2018**, *136*, 166–178. [\[CrossRef\]](#)
7. Huang, B.; Wang, X.; Kua, H.; Geng, Y.; Bleischwitz, R.; Ren, J. Construction and demolition waste management in China through the 3R principle. *Resour. Conserv. Recycl.* **2018**, *129*, 36–44. [\[CrossRef\]](#)

8. Wang, H.; She, H.; Xu, J.; Liang, L. A Three-Point Hyperbolic Combination Model for the Settlement Prediction of Subgrade Filled with Construction and Demolition Waste. *Materials* **2020**, *13*, 1959. [[CrossRef](#)]
9. Kabirifar, K.; Mojtahedi, M.; Wang, C.; Tam, V.W. Construction and demolition waste management contributing factors coupled with reduce, reuse, and recycle strategies for effective waste management: A review. *J. Clean. Prod.* **2020**, *263*, 121265. [[CrossRef](#)]
10. Bakshan, A.; Srour, I.; Chehab, G.; El-Fadel, M.; Karaziwan, J. Behavioral determinants towards enhancing construction waste management: A Bayesian Network analysis. *Resour. Conserv. Recycl.* **2017**, *117*, 274–284. [[CrossRef](#)]
11. Fu, J.; Zhong, J.; Chen, D.; Liu, Q. Urban environmental governance, government intervention, and optimal strategies: A perspective on electronic waste management in China. *Resour. Conserv. Recycl.* **2020**, *154*, 104547. [[CrossRef](#)]
12. Tam, V.W.; Le, K.N.; Wang, J.; Illankoon, I. Practitioners recycling attitude and behaviour in the Australian construction industry. *Sustainability* **2018**, *10*, 1212. [[CrossRef](#)]
13. Long, H.; Liu, H.; Li, X.; Chen, L. An evolutionary game theory study for construction and demolition waste recycling considering green development performance under the chinese government's reward–penalty mechanism. *Int. J. Environ. Res. Public Health* **2020**, *17*, 6303. [[CrossRef](#)] [[PubMed](#)]
14. Du, L.; Feng, Y.; Lu, W.; Kong, L.; Yang, Z. Evolutionary game analysis of stakeholders' decision-making behaviours in construction and demolition waste management. *Environ. Impact Assess. Rev.* **2020**, *84*, 106408. [[CrossRef](#)]
15. Foster, D.; Young, P. Stochastic evolutionary game dynamics. *Theor. Popul. Biol.* **1990**, *38*, 219–232. [[CrossRef](#)]
16. Li, J.; Ren, H.; Zhang, C.; Li, Q.; Duan, K. Substantive innovation or strategic innovation? Research on multiplayer stochastic evolutionary game model and simulation. *Complexity* **2020**, *2020*, 9640412. [[CrossRef](#)]
17. Duan, H.; Li, J. Construction and demolition waste management: China's lessons. *Waste Manag. Res.* **2016**, *34*, 397–398. [[CrossRef](#)]
18. Yang, H.; Xia, J.; Thompson, J.R.; Flower, R.J. Urban construction and demolition waste and landfill failure in Shenzhen, China. *Waste Manag.* **2017**, *63*, 393–396. [[CrossRef](#)]
19. Kabirifar, K.; Mojtahedi, M.; Wang, C.C.; Tam, V.W. Effective construction and demolition waste management assessment through waste management hierarchy; a case of Australian large construction companies. *J. Clean. Prod.* **2021**, *312*, 127790. [[CrossRef](#)]
20. Ghafourian, K.; Kabirifar, K.; Mahdiyari, A.; Yazdani, M.; Ismail, S.; Tam, V.W. A synthesis of express analytic hierarchy process (EAHP) and partial least squares-structural equations modeling (PLS-SEM) for sustainable construction and demolition waste management assessment: The case of Malaysia. *Recycling* **2021**, *6*, 73. [[CrossRef](#)]
21. Bao, Z.; Lu, W. A decision-support framework for planning construction waste recycling: A case study of Shenzhen, China. *J. Clean. Prod.* **2021**, *309*, 127449. [[CrossRef](#)]
22. Lu, W.; Yuan, L.; Xue, F. Investigating the bulk density of construction waste: A big data-driven approach. *Resour. Conserv. Recycl.* **2021**, *169*, 105480. [[CrossRef](#)]
23. Hoang, N.H.; Ishigaki, T.; Kubota, R.; Tong, T.K.; Nguyen, T.T.; Nguyen, H.G.; Yamada, M.; Kawamoto, K. Financial and economic evaluation of construction and demolition waste recycling in Hanoi, Vietnam. *Waste Manag.* **2021**, *131*, 294–304. [[CrossRef](#)] [[PubMed](#)]
24. Yazdani, M.; Kabirifar, K.; Frimpong, B.E.; Shariati, M.; Mirmozaffari, M.; Boskabadi, A. Improving construction and demolition waste collection service in an urban area using a simheuristic approach: A case study in Sydney, Australia. *J. Clean. Prod.* **2021**, *280*, 124138. [[CrossRef](#)]
25. Zhang, C.; Lin, K.; Wang, L. Incentive and Supervisory Contract between Special Committees and CEO Based on the Evolutionary Game Model. *Math. Probl. Eng.* **2020**, *2020*, 4089634. [[CrossRef](#)]
26. Cobb, L. Stochastic catastrophe models and multimodal distributions. *Behav. Sci.* **1978**, *23*, 360–374. [[CrossRef](#)]
27. Liu, X.; Lin, K.; Wang, L.; Zhang, H. Stochastic evolutionary game analysis between special committees and ceo: Incentive and supervision. *Dyn. Games Appl.* **2021**, *11*, 538–555. [[CrossRef](#)]
28. Ortiz, O.; Pasqualino, J.; Castells, F. Environmental performance of construction waste: Comparing three scenarios from a case study in Catalonia, Spain. *Waste Manag.* **2010**, *30*, 646–654. [[CrossRef](#)]
29. Di Maria, A.; Eyckmans, J.; Van Acker, K. Downcycling versus recycling of construction and demolition waste: Combining LCA and LCC to support sustainable policy making. *Waste Manag.* **2018**, *75*, 3–21. [[CrossRef](#)]
30. Arshad, M.H.; Kassas, M.; Hussein, A.E.; Abido, M.A. A Simple Technique for Studying Chaos Using Jerk Equation with Discrete Time Sine Map. *Appl. Sci.* **2021**, *11*, 437. [[CrossRef](#)]
31. Manera, M. Perspectives on Complexity, Chaos and Thermodynamics in Environmental Pathology. *Int. J. Environ. Res. Public Health* **2021**, *18*, 5766. [[CrossRef](#)] [[PubMed](#)]
32. Ding, Z.; Yi, G.; Tam, V.W.; Huang, T. A system dynamics-based environmental performance simulation of construction waste reduction management in China. *Waste Manag.* **2016**, *51*, 130–141. [[CrossRef](#)] [[PubMed](#)]
33. Zhao, Y.; Wang, W.; Ni, Y. EPR system based on a reward and punishment mechanism: Producer-led product recycling channels. *Waste Manag.* **2020**, *103*, 198–207. [[CrossRef](#)]
34. Chapman, A.; Fujii, H.; Managi, S. Key drivers for cooperation toward sustainable development and the management of CO₂ emissions: Comparative analysis of six Northeast Asian countries. *Sustainability* **2018**, *10*, 244. [[CrossRef](#)]

Article

Evaluation of a Chongqing Industrial Zone Transformation Based on Sustainable Development

Xiaoyan Zhang ^{1,2,3,*}, Yuehao Cao ⁴, Mingfang Tang ^{1,*}, Enyi Yu ¹, Yiqun Zhang ^{1,2} and Gang Wu ^{1,2}

¹ State Key Laboratory of Urban and Regional Ecology, Research Center for Eco-Environmental Sciences, Chinese Academy of Sciences, Beijing 100085, China; eyyu@rcees.ac.cn (E.Y.); zhangyiqun999@126.com (Y.Z.); wug@rcees.ac.cn (G.W.)

² University of Chinese Academy Sciences, Beijing 100049, China

³ Institute of Architecture Design and Research, Chinese Academy of Sciences, Beijing 100086, China

⁴ School of Architecture and Urban Planning, Chongqing University, Chongqing 400030, China; urban_cao@foxmail.com

* Correspondence: xyzhang1_st@rcees.ac.cn (X.Z.); mftang@rcees.ac.cn (M.T.)

Abstract: With rapid urban expansion and the increasing demand of industrial development, the existing industrial zones require transformation and upgrading to achieve the sustainable development of society, economy, and environment. The green transformation of industrial zones lacks overall theoretical guidance and a systematic evaluation system. This research aims at developing effective methods to integrate the elements of existing industrial zones within the same framework for the purpose of optimizing the sustainability of the whole system. In this study, the connotation of a composite ecosystem in existing industrial zones was analyzed using the theory of sustainable development, and an evaluation model of existing industrial zone was constructed. Taking the green transformation of Chongqing Gepai Wire and Cable Co., Ltd. as an example, the sustainability of land, architecture, industry, ecology, landscape, culture, and other elements has been fully considered in the transformation process. Through the evaluation results, it can be seen that the sustainability of all aspects of the industrial zone have been effectively improved, which is 16% to 40% higher than that before the transformation. The research results illustrate that, in the process of the green transformation of industrial zones, using interdisciplinary methods to select indicators and dynamically evaluate the sustainable development of industrial zones can systematically and comprehensively consider the elements of industrial zones and promote the role of various majors in the transformation of industrial zones.

Keywords: existing industrial zone; green transformation; sustainable development; evaluation model

Citation: Zhang, X.; Cao, Y.; Tang, M.; Yu, E.; Zhang, Y.; Wu, G. Evaluation of a Chongqing Industrial Zone Transformation Based on Sustainable Development. *Sustainability* **2022**, *14*, 5122. <https://doi.org/10.3390/su14095122>

Academic Editors: Carlos Morón Fernández and Daniel Ferrández Vega

Received: 6 March 2022

Accepted: 20 April 2022

Published: 24 April 2022

Publisher's Note: MDPI stays neutral with regard to jurisdictional claims in published maps and institutional affiliations.



Copyright: © 2022 by the authors. Licensee MDPI, Basel, Switzerland. This article is an open access article distributed under the terms and conditions of the Creative Commons Attribution (CC BY) license (<https://creativecommons.org/licenses/by/4.0/>).

1. Introduction

China's existing industrial zones form a complex and massive system that is continuously undergoing development and, in many regions, degradation [1,2]. In the process of transformation, cultural excavation and economic and social development are typically not considered. Large-scale demolition and construction in existing industrial zones constitute a huge waste of resources [3–5]. Construction waste accounts for 30–40% of municipal solid waste [6–8].

In terms of the green transformation of industrial zones, some theories and methods are relatively well-developed. For example, in terms of industrial production, clean production and a circular economy can be adopted to reduce pollution emissions [9–12]. In industrial zones that have caused serious pollution, ecological environmental restoration measures can be adopted to transform brownfields [13,14]. Regarding building utilization in industrial areas, the protection and reuse of architectural heritage sites can be strengthened gradually [15–17]. The core ideas are to reduce damage to nature, utilize and conform

to nature, realize the symbiosis between human and nature, improve eco-efficiency, abandon waste, improve resource recycling, use renewable energy, promote multi-disciplinary resource management [18,19], and combine environment and economy [20–22]. However, implementing transformation often unilaterally emphasizes the green transformation of one aspect in the industrial zone and lacks an overall evaluation system and transformation method for the total factors of green transformation in the industrial zone.

Ma and Wang proposed the concept of an asocial-economic-natural complex ecosystem in 1979 and the idea of “sustainable development” from the perspective of a complex ecosystem [23]. Wang et al. (1989) further explained and enriched the concept of the social-economic-natural complex ecosystem from the perspective of cybernetics [24–26]. Later, Zhao explained the concept of sustainable development from a philosophical perspective and proposed the principles of establishing a sustainable development indicator system [27–29]. Niu, Lü et al., and Ye and Chen analyzed sustainable development from different perspectives; however, they all emphasize that sustainable development requires overall systematic coordination [30–33].

On the premise of sustainable development, starting from the concept of green economy, this paper quantitatively analyzes the eco-economic system of industrial zones from the perspectives of flow of capital, energy, and material. For example, PSR and DPSIR models are employed to evaluate the index system of environmental sustainable development [34–40]. Regarding the transformation of existing industrial buildings, the evaluation is mostly carried out from the perspectives of green buildings and the impact of the whole life cycle of buildings on the environment [41–48]. With regard to landscape evaluation, it is mostly conducted from the perspectives of culture, material, and emotion [49]. The innovation of this research lies in the integration of sustainable development ideas in the fields of ecology, urban planning and design, landscape design, green transformation of existing industrial zones, and the design of comprehensive indicators of the dynamic process of industrial zone transformation and development in view of society, economy, and environment.

This study constructs a sustainable development evaluation model of the existing industrial zone and applies this evaluation system to an existing industrial zone, Chongqing Pigeon Brand Wire and Cable Co., Ltd., to determine the sustainable development potential of this area. The evaluation system reflects the integrity, systematic nature, and dynamics of the green transformation of the industrial zone, rather than pursuing the sustainability of one aspect of the industrial zone.

2. Materials and Methods

2.1. Study Area

Pigeon Brand Wire and Cable Co., Ltd., situated near Chongqing University, is an enterprise specialized in wires and cables and is mainly engaged in the processing of products such as electrical porcelain products and wires. The company is the backbone of this industry in China. The company has been established for more than 60 years, which has not only developed the local economy but also provided many jobs. The factory has, over the course of its long history, become an integral part of the collective memory and identity of the community.

In June 2006, Pigeon Brand moved its wire and cable production to a new industrial zone, leaving the old factory idle. According to relevant planning, innovation-capable regions should be built around the Chongqing University. To improve the area, the old site of the original Pigeon Brand cable factory will be upgraded to become the Design and Creation Industry Zone of Chongqing University, covering an area of 1.87 ha (Figures 1 and 2). The project was launched in 2018. After completion, it is expected to accommodate a design team of 500 people. After more than three years of transformation, it has been put into use.



Figure 1. Transformation scope.



Figure 2. Before reconstruction.

2.2. Data Collection

In terms of data sources, several indicators were obtained from actual measurement, statistics, and literature, whereas others were determined from expert scoring and questionnaire surveys. This study contains six types of data, namely land, architecture, industry, ecology, landscape, and culture of the existing industrial zone. Land and building data are obtained through actual measurement. Industrial data are obtained by comparing the actual measured value with the relevant value of the national eco-industrial demonstration zone standard. Ecological data are mainly obtained by comparing the actual measurement with the relevant standards. For example, the soil scoring standard refers to the soil environmental quality standard, the water scoring standard refers to the national industrial wastewater discharge standard, and the noise evaluation standard refers to the acoustic environment quality standard. Landscape and cultural data are mainly obtained through questionnaires.

2.3. Method

The general goal of sustainable development in an existing industrial zone is realized through the synergy of the environmental, economic, and social subsystems that constitute the system, so as to eliminate the system's current degradation and stagnation and improve it considering the renewal and utilization of land resources as the goal [50–52]. This study emphasizes that, under the premise of a clear overall goal and vision, the favorable factors of social and economic subsystems can be used to create landscape on the material elements of the environmental subsystems (Figure 3) to achieve social, economic, and environmental improvements, and sustainable development [53–55].

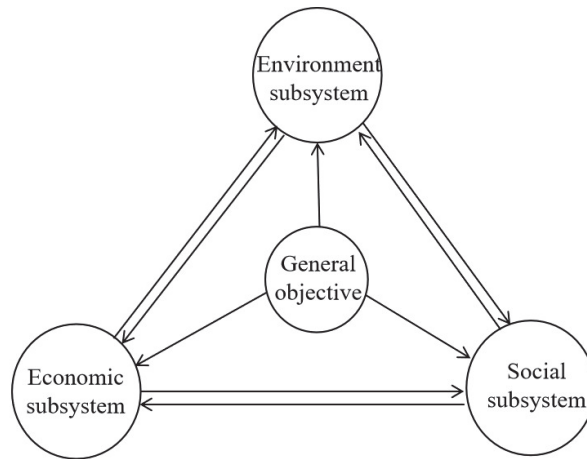


Figure 3. Relationship between subsystems in existing industrial zones.

An existing industrial zone is a composite ecosystem with economic development as its main body. The transformation and upgrading of existing industrial zones cover the most complex elements and combinations. In the meantime, the transformation and upgrading of existing industrial zones is a spiraling dynamic and sustainable development process, in which the industrial zone must be altered from its past state; this is the top priority in solving sustainable development issues in the human society. The main feature of the sustainable development evaluation model is to highlight the baseline status of ecosystem services, while considering how to improve the people's overall satisfaction as much as possible [36,56,57].

Existing industrial zones can be regarded as complete composite ecosystems [58,59]. On this basis, we constructed a green transformation and sustainable development evaluation model. Each subsystem was composed of the social, economic, and environmental elements of the existing industrial zones. We found that through the optimization of each element index, ecosystem services can be maintained and improved, with sustainable benefits provided to existing industrial zones. This model of a continuous optimization of the elements of existing industrial zones is called the sustainable development evaluation model of the green transformation of existing industrial zones.

The sustainable development evaluation model of existing industrial zones requires a complete data system embracing data on land, industry, ecology, architecture, culture, and landscape in the respective industrial zones [60–62]. In this process, the sustainable development of the existing industrial zone will be realized by means of industrial transformation and upgrading, compound land use, ground buildings, the green transformation of structures, ecological environment restoration, the construction of characteristic landscape, the continuation of culture, and so on (Figure 4).

The transformation of existing industrial zones is an evolving process (from unsustainable to sustainable). During the process of construction, dynamic monitoring and real-time data feedback can be implemented, while adjustments, improvements, and renovation can be made according to changes in the situation during the implementation process (Figure 5).

In the sustainable development evaluation model, an index system of six dimensions (land, building, industry, ecology, landscape, and culture) is constructed. Each dimension has its sustainability score and can be optimized in different dimensions under the premise of ensuring ecological constraints. In the process of green transformation, the data for each dimension are reflected in the indicators (Figure 6). Before and after the transformation, there will be changes in the indicator data. The comparison of sustainable development

evaluation reflects the green and ecological effects of the transformation means. According to the scoring results of each indicator, the improvement in each direction can be reflected.

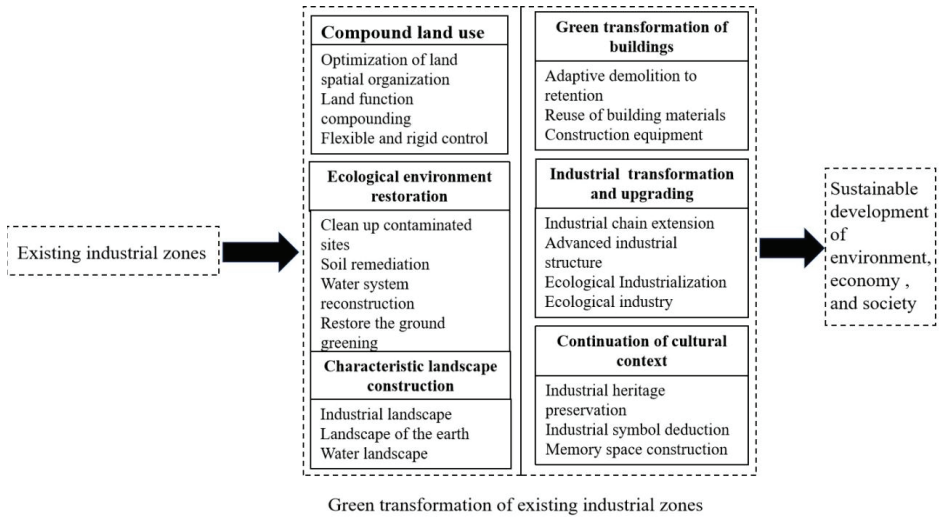


Figure 4. The transformation and upgrading of existing industrial zones.

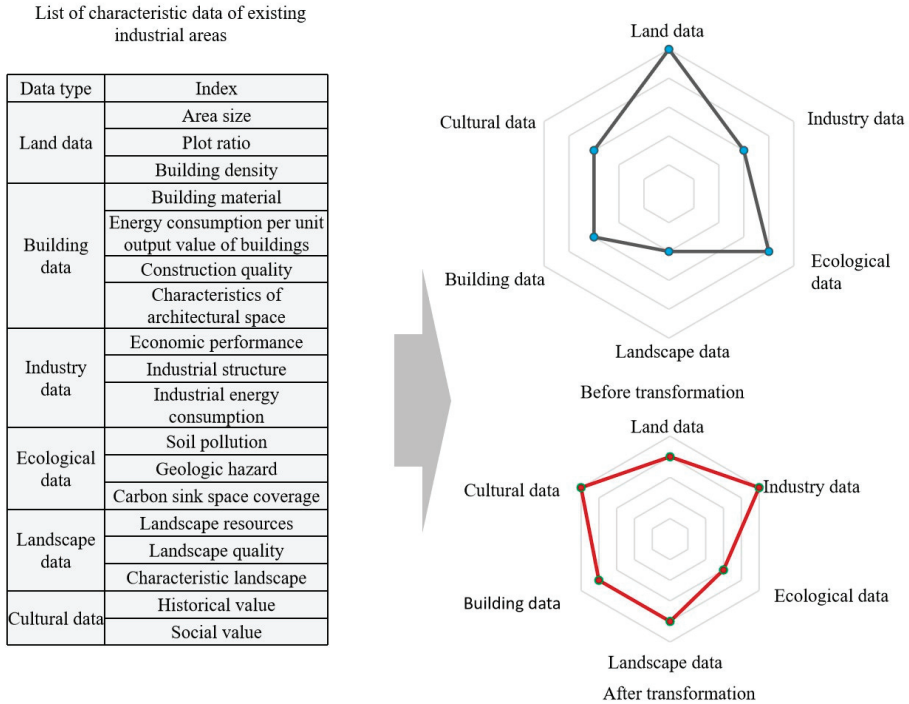


Figure 5. Data model of sustainable development in existing industrial zones.

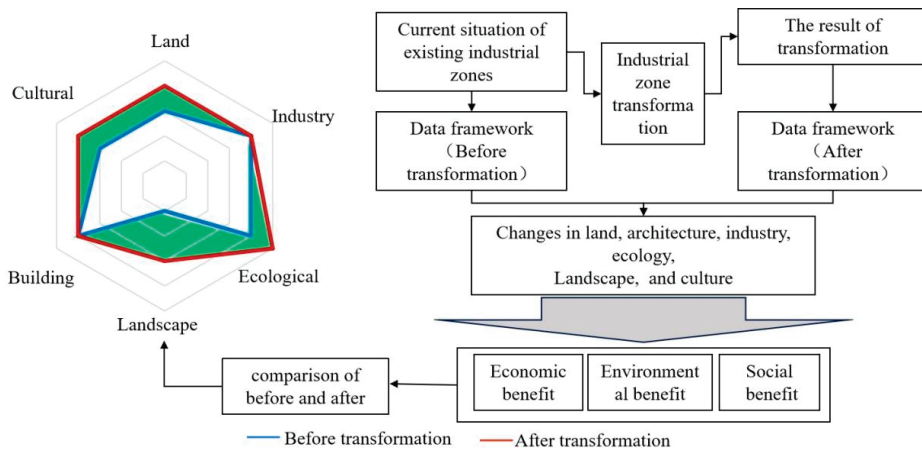


Figure 6. Comparison before and after transformation.

2.4. Evaluation Process

To make the evaluation results scientific, the construction of the index system follows the principles of comprehensiveness, systematicness, operability, and 3 Rs (reduction, reuse, and recycling). Through an on-site investigation, observation, and questionnaire survey of the project, the relevant government departments, project investors, relevant designers, users, and later, operation managers are consulted; the historical data, project planning scheme, transformation design drawings, and on-site actual information of buildings related to the transformation of the industrial zones are collected; and the factors affecting the whole process of the transformation of the industrial zones are analyzed and summarized. Through the analysis of the information, a list of indicators is made, following the general optimization principle of evaluation indicators. In addition, through repeated communication and argumentation with experts, combined with the actual development of the industrial zone, the preliminary framework of evaluation indicators for the transformation and sustainable development of the industrial zone is summarized from the three aspects of economy, society, and environment.

The analytic hierarchy process (AHP) can be used for qualitative and quantitative analyses and is suitable for multi-objective decision-making processes [63,64]. The hierarchical structure model designed in this study is based on the AHP. When selecting model indicators, the key elements that can be changed in the process of the transformation and upgrading of industrial zones are selected, and include aspects of land, architecture, industry, ecology, landscape, and culture. Overall, the indicators take green and low-carbon principle as the starting point, and can reflect the social, economic, and cultural characteristics of industrial zones. At the same time, the selection of indicators focuses on industrial transformation and the demand of landscape perception.

From the perspective of the current development status of existing urban industrial zones in China, the vast majority of industrial zones are in the dual dilemma of low-carbon transformation as well as development and economic benefit improvement. In the process of index selection, the economic value and utilization efficiency of industrial land are considered. Therefore, in terms of land, geographical conditions, area size, and land function are more important to the economic value of the renewal and transformation of the existing industrial zone. In addition, the indicators of plot ratio and building density are applied to judge the economic value and space utilization efficiency of zoning transformation according to the growth ratio before and after the transformation. In terms of industry, industrial structure, economic benefits, and industrial energy consumption should be considered. For building indicators, the reconstruction value of buildings is determined by the building materials and building quality, the type of buildings is determined by the

building space characteristics, and the energy consumption of buildings is measured by the building's energy consumption per unit output value. The ecological indicator mainly refers to the ecological stock in the industrial zone, including green ecological stock and gray ecological stock. Green ecological stock refers to the existing ecological space in the industrial zone. Gray ecological stock refers to the space that can be transformed into a certain ecological function after a certain transformation, such as roof space, corridor space, impervious ground, and square space. Landscape data include landscape perception and landscape feature data. Landscape perception data include landscape friendliness and attractiveness. Landscape feature data include characteristic buildings and structures and characteristic landscape nodes. In terms of culture, the historical, technological, artistic, and social values of the built space in the industrial zone are considered. Table 1 lists the main level 1 and 2 indicators determined in this study.

Table 1. Data types and contents of transformation.

| Data Type | Land Data | Building Data | Industry Data | Ecological Data | Landscape Data | Cultural Data |
|--------------|--|--|---|--|--|--|
| Data content | Geographic conditions; Area size; Land function; Plot ratio; Green space rate; Building density | Types of building functions; Building material; The age of Architecture; Building energy conservation; Construction quality; Type of building structure | Total output value of the park; Proportion of output value of high-tech industry; Carbon emissions per unit GDP decline | Green ecological capital; Grey ecological capital | Friendliness; landscape beauty; Landscape features | Historical value; Value of science and technology; Artistic value; Social value |

Regarding scoring standards, the ecological indicators are based on existing domestic standards, such as the national eco-industrial demonstration park standards, green building evaluation standards, soil environmental quality standards, etc. The indicators of landscape and culture are mainly evaluated subjectively in view of perceptual experience. Economic indicators are chiefly designed based on the national average level from characteristics and economic value of the park itself. For example, as far as the indicators of geographical conditions are concerned, considering that the distance between industrial areas and urban centers of cities of different sizes will be different, the distance judgment index is used to eliminate the impact of urban size, where L is the distance between the industrial zones and the urban centers, and S represents the urban administrative boundary area. When formulating the scoring standard, 50 cities with different grades and scales and their industrial areas were manually classified and compared with the K value. In this paper, three types of industrial zones are preliminarily demarcated, and when the demarcation range is: $0 < K \leq 0.06$, it is the urban type; when $0.06 < K \leq 0.2$, it is the suburban type; when $0.2 < K$, it is the outer suburban type. Subsequently, the geographical conditions of the industry are scored according to the interval value.

After obtaining the data, the indicators were scored according to the actual data. The weight can reflect the relative importance of each evaluation index in the evaluation system. In the model, a judgment matrix of each index was established. Eighteen experts in the six fields of land, architecture, industry, ecology, landscape, and culture were invited to rank the importance of each index in this field using the 1–9 scale method. The matrix value is the ratio of the importance of the two elements, and the index value in each level is the relative weight. The square root method was used to solve the normalized eigenvector and eigenvalue, and each feature vector was the weight of the evaluation factor. According to the weight of the judgment matrix, the score of each subsystem index was summed as the total score of the sustainable development degree in this field.

3. Results

Using the building indicators as an example (Tables 2 and 3), each indicator has corresponding secondary indicators and scoring standards. This is to obtain the building data scores before and after the transformation and then calculate the scores of the other five categories according to the same method.

Table 2. Indexing system for buildings.

| Target Layer | First Level Indicators | Secondary Indicators |
|-----------------|------------------------------|--|
| Building System | Building Type | Production plant, storage plant, auxiliary production plant, transportation building, and other buildings. |
| | Building Material | Brick wood (40 years), brick concrete (50 years), reinforced concrete (60 years), steel structure materials (80 years) |
| | Age of Architecture | 1840–1894; 1895–1936; 1937–1948; 1949–1976; 1976–present |
| | Building Energy Conservation | Energy consumption per unit output value of buildings |
| | Quality of Architecture | Good, medium, heavy, severe, cannot be used |
| | Type of Building Structure | “Large span type”, “conventional type”, “special type” |

Table 3. Score before and after reconstruction of the building system.

| Data Type | Data Content | Index Weight | Before Transformation | After Transformation |
|---------------|------------------------------|--------------|-----------------------|----------------------|
| Building data | Types of building functions | 0.097 | 0.27 | 0.38 |
| | Building material | 0.137 | 0.48 | 0.74 |
| | Age of Architecture | 0.115 | 0.43 | 0.45 |
| | Building energy conservation | 0.155 | 0.43 | 0.61 |
| | Construction quality | 0.306 | 0.57 | 1.01 |
| | Type of building structure | 0.19 | 0.65 | 0.76 |
| | Total | 1 | 2.83 | 3.95 |

The score of each group before and after the transformation is shown in the radar chart (Figure 7), and the development of each index can be intuitively understood. Following the transformation, we measured improvements of 33% for land, 40% for architecture, 35% for industry, 16% for ecology, 36% for landscape perception, and 39% for culture (Table 4).

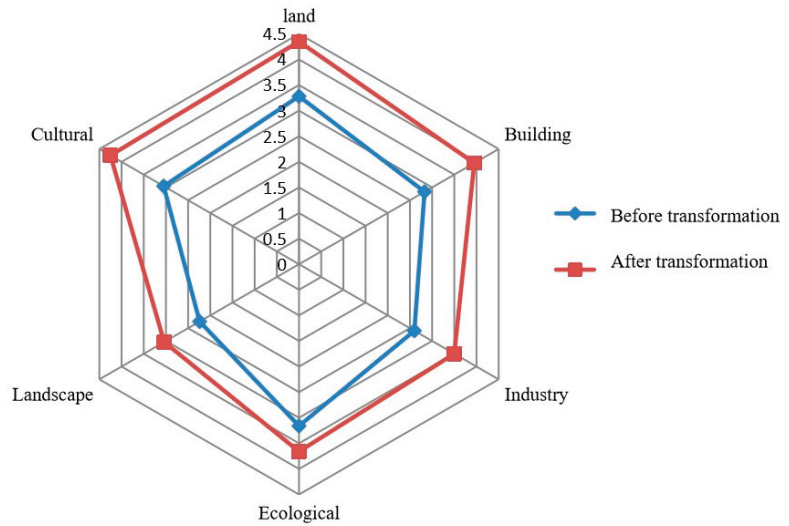


Figure 7. The evaluation model of Chongqing University Design and Creative Industrial zone.

Table 4. Comparison of indices before and after transformation.

| Index | Before Transformation | After Transformation | Changing Trend |
|------------|-----------------------|----------------------|----------------|
| Land | 3.28 | 4.35 | +33% |
| Building | 2.83 | 3.95 | +40% |
| Industry | 2.6 | 3.5 | +35% |
| Ecological | 3.16 | 3.66 | +16% |
| Landscape | 2.24 | 3.04 | +36% |
| Cultural | 3.05 | 4.25 | +39% |

In the process of reconstruction, the design team retain the original overall structure and fully respect the original appearance, and the historical significance of the old buildings is preserved and sublimated. Reusing building materials reduces waste generation, saves investment costs, and decreases the consumption of natural resources. Moreover, renovating existing buildings can make people deeply understand the impact of building on the environment and actively participate in the action of improving the environment.

At the same time, the company building kept the terrazzo floor, partial walls, large motors, warning signs, coils, and other devices left by the old cable factory. These articles are also the products of an era. Thus, the industrial culture and industrial spirit of the original cable factory are retained, and the industrial culture is continued. In the design process, the design team combined with Chongqing University's own historical and cultural heritage and the original architectural color; the industrial design style was adopted, with black, white, gray, bright red, and bright yellow as the main colors. This color matching is consistent with the style of Chongqing University, which will make the users of the zone continue to feel the essence of the Creative Industrial Zone and generate a sense of belonging and pride due to their emotional and spiritual cognition to Chongqing University [65,66].

4. Discussion

By changing land use and increasing building area and plot ratio, the indicator score of land increased from 3.28 to 4.35, an increase of 33%. By improving the existing building quality, optimizing the building space, making full use of the original buildings and facilities, and realizing the green transformation of the building, the indicator score of the building increased from 2.83 to 3.95, an increase of 40%.

In terms of industry, the cable manufacturing industry was transformed into a cultural and creative industry. After the transformation, the GDP of the industrial zone increased, the carbon emission per unit GDP decreased, and the proportion of high-tech industries increased. The final score increased from 2.6 to 3.5, an increase of 35%. In terms of ecology, positive changes included attempting to increase the number of trees, optimizing the green space structure, reducing patch fragmentation, strengthening connectivity, and reducing the proportion of impervious ground. After the transformation, the score increased from 3.16 to 3.66, and the ecological function will be gradually enhanced. Due to the short time interval before and after the transformation, the overall score increased by 16%.

In terms of landscape, mainly from the perspective of people's perception of the landscape, the principles of landscape creation were used to improve landscape friendliness by optimizing the comfort, accessibility, and participation of the landscape, focusing on building characteristic industrial buildings, public spaces, and landscape nodes. The score of landscape increased from 2.24 to 3.02, an increase of 36%. This kind of landscape contains a certain man-made and natural meaning and meets people's spiritual needs. This spirit is established above natural and artificial elements, which optimizes the benefit to mankind as well as achieving ecological sustainability.

In terms of culture, the industrial zone is combined with urban historical, cultural, and socio-economic factors. The cultural traces of the existing industrial zone in different periods were retained in different forms, and the historical, scientific, technological, and artistic value of the original buildings and facilities in the industrial zone were improved to improve people's perception of history and culture. The cultural score increased from 3.05 before the transformation to 4.25, an increase of 39%.

5. Conclusions

This study focuses on the construction of an evaluation system of an existing industrial zone using the principles of sustainable development, which takes the natural, economic, and social elements of the existing industrial zones into overall consideration and constructs an indicator system of six dimensions: land, building, industry, ecology, landscape, and culture.

Combined with the renovation of Chongqing Pigeon Brand Wire and Cable Co., Ltd., six categories of level 1 indicators and 43 categories of level 2 indicators were generated, and the data before and after the transformation were measured, calculated, and compared. After the transformation, the sustainability of land, architecture, industry, ecology, landscape perception, and culture increased by 33%, 40%, 35%, 16%, 36%, and 39%, respectively.

As far as the transformation of a complete industrial zone is concerned, both the time span and the space span are quite large. In different stages of the project, the content and importance of the indicators used for evaluation will be different, and there are some deficiencies in the comprehensiveness of the indicators. Due to the lack of early data in the old industrial zones, the operability of data calculation in development and construction is poor, and the objectivity of the scoring results is still insufficient. Furthermore, this study is primarily aimed at the transformation of old industrial zones into cultural, creative, and office zones, with a limited scope of application. The economic, social, and environmental indicators will change according to the types of industrial zones before transformation, and the functions and demands after transformation. Further study on the sustainable development evaluation of different transformation types would be needed to guide the implementation and promotion of the sustainable transformation of existing industrial zones.

From the perspective of multiple disciplines, this study runs the concept of sustainable development through the whole process of transformation, which is more conducive to the comprehensive sustainable development of industrial zones. The purpose of the evaluation is to promote the implementation of the transformation of industrial zones. Therefore, this study selects indicators from the fields of ecology, urban planning and design, and landscape design. It can be found that, in the transformation process of the

industrial zones, the cooperation of various disciplines is needed, and the concept of sustainable development in various professional fields runs through the whole process of transformation. Only in this way can it be more conducive to the comprehensive and sustainable development of the industrial zones. It is expected that this method can be used in the transformation of existing industrial zones.

Author Contributions: Conceptualization, X.Z. and M.T.; methodology, X.Z.; software, Y.C.; validation, X.Z. and Y.C.; formal analysis, X.Z.; investigation, Y.C. and Y.Z.; resources, E.Y.; data curation, Y.C.; writing—original draft preparation, X.Z.; writing—review and editing, E.Y.; visualization, Y.C.; supervision, X.Z.; project administration, X.Z.; funding acquisition, M.T. and G.W. All authors have read and agreed to the published version of the manuscript.

Funding: This work was supported by the National Key Research and Development Program of China [2016YFC0503603, 2018YFC0704900].

Institutional Review Board Statement: Not applicable.

Informed Consent Statement: Not applicable.

Data Availability Statement: The data presented in this study are available within the article.

Acknowledgments: The authors thank the reviewers for their valuable suggestions.

Conflicts of Interest: The authors declare no conflict of interest.

References

1. Song, X.L.; Xu, C.; Zhao, L.N.; Chen, B.; Yang, J.X. Review and Prospect of life cycle management. *Ecol. Econ.* **2010**, *3*, 47–51.
2. Huang, H.P. Critical review of life cycle management. *Acta Ecol. Sin.* **2017**, *37*, 4587–4598.
3. Zhang, G.Q.; Xu, F. *Sustainable Built Environment*; China Architecture & Building Press: Beijing, China, 2009.
4. Long, W.D. Building energy consumption proportion & target value of building energy saving. *Energy China* **2005**, *27*, 23–27.
5. Zhao, B. *Research on the Transformation and Upgrading of Industry Zones under the New Economic Background: Case Study on Jiangxi Province*; Economy and Management Publishing House: Beijing, China, 2017.
6. Zhou, T.H. *Studies on the Strategies for Urban Renewal in Industrial Areas*; Tsing Hua University: Beijing, China, 2010.
7. Zhu, D.F. *Studies on the Treatment of Constructionwastes in Urbanareas*; South East University: Nanjing, China, 2010.
8. Chen, S. *Studies on the Green Construction Management of Construction*; South East University: Nanjing, China, 2019.
9. Marjan, V. Clean production strategies: Developing preventive environmental management in the industrial economy. *Ecol. Econ.* **1993**, *12*, 84–85.
10. Yong, G.; Jia, F.; Sarkis, J.; Bing, X. Towards a national circular economy indicator system in china: An evaluation and critical analysis. *J. Clean. Prod.* **2012**, *23*, 216–224.
11. Lü, Y. *Research on the Theory and Practice of the Ecological Industrial Park Based on Low Carbon Utilization*; Tianjin University: Tianjin, China, 2011.
12. Xi, D.L. *Clean Production*; Chongqing University Press: Chongqing, China, 1995.
13. Liu, J. *Research on the Transformation of Brownfield Based on the Concept of Green Building*; Qingdao Technological University: Qingdao, China, 2016.
14. Hollander, J.B. Principles of brownfield regeneration: Cleanup, design, and reuse of derelict land. *J. Plan. Educ. Res.* **2010**, *31*, 229–231.
15. Chen, B. History beginning of Shenyang industrial architectural heritage and the double value. *Archit. Creat.* **2006**, *9*, 80–91.
16. Chen, X. *The Theoretical and Empirical Research on the Old Industrial Buildings (Group) Recycling*; Xi'an University of Architecture and Technology: Xi'an, China, 2010.
17. Lu, B.Y.; Zhao, J.Z. Ecological Industrial Garden: An Ideal Model of Sustainable Development. *Environ. Sci.* **2001**, *2*, 1–6.
18. Fu, L.N. *Research on Ecological Transformation of Industrial Park and Its Eco-Efficiency*; Central South University: Changsha, China, 2014.
19. Xiong, Y. Overview of Researches in Eco-Industrial Parks' Development. *J. China Univ. Geosci. Soc. Sci. Ed.* **2009**, *9*, 63–67.
20. Gan, Y.H. *Study on Industrial Symbiosis in Eco-Industrial Parks—Study on Circular Economy and Eco-Industrial Parks in Jiangxi Province*; Nanchang University: Nanchang, China, 2007.
21. Deng, J.H. *Industrial Ecology and Its Application in Industrial Park Planning*; Hunan University: Changsha, China, 2006.
22. Liu, D.M.; Gao, D.W. *Ecological Remediation: Theories and Technologies*; Harbin Institute of Technology: Harbin, China, 2020.
23. Ma, S.J.; Wang, R.S. The Social-Economic-Natural Complex Ecosystem. *Acta Ecol. Sin.* **1984**, *4*, 1–9.
24. Wang, R.S.; Ouyang, Z.Y. Ecological integration-scientific methods of human sustainable development. *Chin. Sci. Bull.* **1996**, *41*, 47–67.

25. Wang, R.S.; Ouyang, Z.Y. Social-Economic-Natural Complex Ecosystem and Sustainability. *Bull. Chin. Acad. Sci.* **2012**, *27*, 254, 337–345, 403–404. [[CrossRef](#)]
26. Wang, R.S.Z.T.; Liang, C.; Jingru, L.; Zhen, W. *Fundamentals of Industrial Ecology*; Xinhua Publishing House: Beijing, China, 2006.
27. Zhao, J.Z. Theoretical analysis of regional sustainable development. *Ecol. Econ.* **1991**, *2*, 12–15.
28. Zhao, J.Z. On sustainable development. *Sci. Technol. Rev.* **1992**, *4*, 13–16.
29. Zhao, J.Z.; Liu, X.Y.; Zhang, X.D. System analysis on the definition of sustainable development. *Acta Ecol. Sin.* **1999**, *3*, 3–5.
30. Chen, R.; Niu, W.Y. Recycling economy: An ideal economic model in the 21st century. *China Dev.* **2002**, *2*, 12–21.
31. Niu, W.Y. Three Basic Elements of Sustainable Development. *Bull. Chin. Acad. Sci.* **2014**, *29*, 410–415.
32. Lü, Y.L.; Wang, Y.C.; Yuan, J.J.; He, G.Z. Some thoughts on promoting the implementation of sustainable development goals in China. *China Popul. Resour. Environ.* **2018**, *28*, 1–9.
33. Ye, W.H.; Chen, G.Q. Theory of three models of production-The basic theory of sustainable development. *China Popul. Resour. Environ.* **1997**, *7*, 14–18.
34. Shang, J.; Zheng, Y. Research on comprehensive evaluation of eco-industrial parks based on green economy. *J. Huaqiao Univ. Nat. Sci.* **2015**, *36*, 698–703.
35. Zhou, J. *The Research of Evaluation Index System about Low-Carbon Industrial Park: Taking Hubei Province as an Example*; Huazhong University of Science & Technology: Wuhan, China, 2013.
36. Liu, K. *Research of Eco-System Health Assessment of Industrial Parks*; Dalian University of Technology: Dalian, China, 2016.
37. Yin, J. *Evaluation Index System and Upgrading Path of Industrial Zone-Empirical Analysis of Zhengjiang Economic and Technological Development Zone*; Jiangsu University: Zhengjiang, China, 2013.
38. Ma, G. *Study on Low-Carbon Evaluation Index System of Guangxi Industrial Park*; Guangxi Teachers Education University: Nanning, China, 2017.
39. Lin, H. *Construction of Urban Brownfield Redevelopment Technology System Based on Multidisciplinary Perspective: Changchun City as an Example*; Jilin University: Changchun, China, 2016.
40. Jin, G.; Song, H. Evaluation index system for ecological development of industrial parks based on DPSIR model. *Recycl. Resour. Circ. Econ.* **2014**, *17*, 7–10.
41. Zhu, R.; Wang, H. Research on indexes and weight of green retrofitting for existing buildings. *HV&AC* **2015**, *36*, 698–703.
42. Li, X.; Yang, H.; Zheng, Z. Evaluation on the Green Design of Reusing Industrial Buildings. *Constr. Technol.* **2016**, *45*, 81–87.
43. Su, Y. *Green Evaluation about Reconstruction Design Plan of Old Industrial Buildings*; Chongqing University: Chongqing, China, 2015.
44. Hill, R.; Bowen, P. Sustainable construction: Principles and a frame work for attainment. *Constr. Manag. Econ.* **1997**, *15*, 223–239.
45. Zhang, Y.; Fan, S.; Li, H. Research on assessment index system for the green regeneration of old industrial buildings. *Xi'an Univ. Archit. Technol. Ind. Constr.* **2014**, *44*, 56–59.
46. Wu, H. *Environmental Impact Analysis of Building Based on Life Cycle Assessment*; Dalian University of Technology: Dalian, China, 2006.
47. Tan, L. *Recycling: Research on Sustainable Utilization of Buildings*; Chongqing University: Chongqing, China, 2004.
48. Li, H.; Tian, W.; Yan, R. Constituting recycling evaluation index system for old industrial buildings (Group). *Xi'an Univ. Arch. Tech. Nat. Sci. Ed.* **2013**, *45*, 772–777.
49. Li, N. *Research on Visual Evaluation and Optimal Design of Industrial Heritage Landscape*; Yanshan University: Qinhuangdao, China, 2020.
50. Zhao, J.Z. Theoretical studies on the assessment criteria for the sustainable development of the social-economic-natural complex ecosystem. *Acta Ecol. Sin.* **1995**, *15*, 327–330.
51. Zhao, J.Z. Theoretical considerations on ecological civilization development and assessment. *Acta Ecol. Sin.* **2013**, *33*, 4552–4555. [[CrossRef](#)]
52. Zhou, T.H. *A Study of Urban Planning Policy for the Urban Regeneration in the Old Industrial District—Beijing as the Model*; Tsinghua University: Beijing, China, 2005.
53. Li, J. *Study on Evaluation Factor System of Reuse Value of Old Industrial Buildings*; Southwest Jiaotong University: Chengdu, China, 2011.
54. Antonella, P.; Marco, T. Re-naturing the city: Linking urban political ecology and cultural ecosystem services. *Sustainability* **2021**, *13*, 1786.
55. Frosch, R.A. The industrial Ecology of the 21st century. *Sci. Am.* **1995**, *273*, 178–181.
56. Millennium. *Ecosystem Assessment, Ecosystems and Human Well-Being: A Framework for Assessment*; Island press: Washington, DC, USA, 2003.
57. Shang, H.; Qu, Y. Assessment of sustainable development of eco-industrial parks based on material flow analysis. In Proceedings of the 2nd International Workshop on Sino-German Sustainable Development and Management of Industrial Parks, Beijing, China, 14–16 May 2007; pp. 437–443.
58. Wu, J. Landscape sustainability science: Ecosystem services and human well-being in changing landscapes. *Landsc. Ecol.* **2013**, *28*, 999–1023. [[CrossRef](#)]
59. Yang, P. Applying ecosystem concepts to the planning of industrial areas: A case study of Singapore's Jurong Island. *J. Clean. Prod.* **2004**, *12*, 1011–1023. [[CrossRef](#)]
60. Wang, X. Study on Spatial Structure Transformation of Suburban Industrial Development Zone. *Planners* **2011**, *27*, 93–98.

61. Zhao, R.N.; Ma, Z.; Qiao, Q.; Chang, D.H.; Zhang, Y.; Xie, M.H.; Guo, J. Comparative Analysis of Green Development Policies of China's Industrial Parks and Countermeasure Research. *Res. Environ. Sci.* **2020**, *33*, 511–518.
62. Grunsven, L.V. Industrial regionalization and urban-regional transformation in Southeast Asia: The SIJORI growth triangle considered. *Malays. J. Trop. Geogr.* **1995**, *26*, 1.
63. Deng, H.B.; Qiu, S.; Zheng, X.Y.; Shen, Y. Research on landsenses evaluation method. *Acta Ecol. Sin.* **2020**, *40*, 8022–8027.
64. Haiert, T.; Wang, H.D.; Wang, L.H.; Peng, Y.D. The comprehensive evaluation method of urban sustainable development. *China Popul. Resour. Environ.* **1997**, *7*, 46–50.
65. Crowell, S. *Husserl, Heidegger, and the Space of Meaning: Paths Toward Transcendental Phenomenology*; Northwestern University Press: Evanston, IL, USA, 2001.
66. Norberg-Schulz, C. Genius Loci: Toward a Phenomenology of Architecture. In *Historic Cities: Issues in Urban Conservation*; Cody, J., Siravo, F., Eds.; Academy Editions: Winterbourne, UK, 1980.

Article

Investigation of the Geopolymerization Potential of a Waste Silica-Rich Diabase Mud

Maria Spanou¹, Sokrates Ioannou², Konstantina Oikonomopoulou³, Pericles Savva^{4,*}, Konstantinos Sakkas⁵, Michael F. Petrou³ and Demetris Nicolaides¹

- ¹ Frederick Research Center, P.O. Box 24729, Nicosia 1303, Cyprus; res.mas@frederick.ac.cy (M.S.); d.nicolaides@frederick.ac.cy (D.N.)
- ² Department of Civil Engineering, Abu Dhabi Men's Campus Higher Colleges of Technology, Abu Dhabi 25026, United Arab Emirates; sioannou@hct.ac.ae
- ³ Department of Civil and Environmental Engineering, University of Cyprus, 75 Kallipoleos Av., P.O. Box 20537, Nicosia 1678, Cyprus; oikonomopoulou.konstantina@ucy.ac.cy (K.O.); petrou@ucy.ac.cy (M.F.P.)
- ⁴ Latomia Pharmakas, 23 Themistokli Dervi Av., S.TA.D.Y.L. Building, P.O. Box 23504, Nicosia 1066, Cyprus
- ⁵ RECS Civil Engineers & Partners LLC, 23 Themistokli Dervi Av., S.TA.D.Y.L. Building, P.O. Box 23504, Nicosia 1066, Cyprus; ksakkas@recsengineering.com
- * Correspondence: psavva@pharmakas.com

Abstract: Diabase mud (DM) is a silica-rich residue yielding from aggregate crushing and washing operations in quarries. This work focuses on identifying the geopolymerization potential of a diabase mud through characterization of its mineralogical composition, investigation of its reactivity, and assessment of the early compressive strengths of alkali activated mixtures formulated based on the mud's dissolution results. The findings suggest that considerably low amounts of Al and Si metals were dissolved following the dissolution tests conducted on DM, however, the incorporation of small quantities of CEM I, gypsum, and metakaolin (MK) moderately at a $\text{Na}_2\text{SiO}_3\text{:NaOH}$ ratio of 50:50 and with a molarity of NaOH of 4 M enhanced the geopolymerization compared to low L/S ratio mixtures cured at different conditions. When M was increasing, the high L/S ratio mixtures exhibited fluctuations in strengths, especially beyond a 10 M NaOH molarity. Maximum strengths of mixtures at equivalent molarity of 10 were achieved when the $\text{Na}_2\text{SiO}_3\text{:NaOH}$ ratio reached 30:70, regardless of the ambient conditions and the presence of CEM I. The curing conditions, the ratio of $\text{Na}_2\text{SO}_3\text{:NaOH}$, and the presence of CEM I in the DM-based mixtures did not appear to significantly affect the mixture when NaOH concentration was between 2 M and 4 M; at higher molarities, however, these enhanced the strengths of the geopolymerized DM.

Keywords: waste diabase mud; geopolymer binders; alkali activated materials; materials valorisation; sustainability; mix design; early age compressive strength

Citation: Spanou, M.; Ioannou, S.; Oikonomopoulou, K.; Savva, P.; Sakkas, K.; Petrou, M.F.; Nicolaides, D. Investigation of the Geopolymerization Potential of a Waste Silica-Rich Diabase Mud. *Materials* **2022**, *15*, 3189. <https://doi.org/10.3390/ma15093189>

Academic Editors: Carlos Morón Fernández and Daniel Ferrández Vega

Received: 4 April 2022

Accepted: 20 April 2022

Published: 28 April 2022

Publisher's Note: MDPI stays neutral with regard to jurisdictional claims in published maps and institutional affiliations.



Copyright: © 2022 by the authors. Licensee MDPI, Basel, Switzerland. This article is an open access article distributed under the terms and conditions of the Creative Commons Attribution (CC BY) license (<https://creativecommons.org/licenses/by/4.0/>).

1. Introduction

The exponential demand for cement production—which currently reaches over 4.3 billion tonnes per annum worldwide [1]—imposes considerable pressure on the industries towards developing initiatives for minimizing the environmental impact associated with the cement's embodied CO_2 emissions. Backed by the desire to deliver sustainable and cost-effective solutions in construction, the conversion of waste into secondary raw materials is an imperative initiative within the framework of the Circular Economy agenda for the European Union [2]. In this perspective, one of the most promising methods for utilizing byproducts and industrial waste is the geopolymerization. Within this technology, the reaction mechanism to form inorganic polymers is essentially based on an alkali-based activation i.e., dissolution of the solid precursor by alkaline hydrolysis, gelation, and finally rearrangement and reorganisation to a three-dimensional network that resembles a zeolitic-like structure. The alkaline activators are usually concentrated solutions of Na,K-hydroxides and Na,K-silicates, whereas most typically used solid precursors are Al-Si- and

Ca-Si-rich materials in nature. Prominent examples of such precursors are fly ash from coal combustion, metakaolin, and ground granulated blast furnace slag. Since these byproducts are associated with a considerably low embodied carbon footprint (for example, 4 kg of CO₂ emitted per tonne of fly ash produced; 52 kg of CO₂ emitted per tonne of slag produced [3]), the alkali activation of these materials certainly offers environmental advantages as well as promising durability, both aspects that have been indeed extensively researched [4–17]. The particular technology, in what is known as alkali-activated cement technology, has unveiled a promising potential, especially when considering slag, fly ash, and metakaolin for developing low carbon binders in non-structural applications, as featured in extensive research reviews [18–22].

In Cyprus, while slag and fly ash are in little to non-existent amounts due to the non-presence of steel industries or coal on the island. There is, however, an equally challenging issue to be addressed, and this is the large amounts of deposits of diabase mud (DM) accumulated as a sludge waste from the quarries. DM is a form of sludge waste that derives from solid fractions following aggregate crushing and/or aggregate washing operations. It is a residue yielded with a humidity content ranging between 25–30% and with a mineralogical composition consisting mainly of Al and Si oxides. This essentially makes it a promising candidate for potential alkali activation. At the same time, the accumulation rate of DM in quarries in Cyprus is indeed high, as certain plants were reported to exhibit an annual production of nearly 25,000 tonnes. Further, disposing of the mud in landfills within the production facilities is considerably limiting their storage capabilities. Considering the abovementioned issues, if a possible activation of the DM occurs to a sufficient degree so as to yield a durable, low carbon hydraulic binder, then there would be a leeway for the current issues of mud storage/accumulation/disposal in Cyprus to be controlled. At the same time, the possibility of sustainable solutions will be developed and offered to the market. Moreover, it would cater to the EU legislation related to recycling requirements of waste materials in Cyprus (which were introduced in 2012 [23]), thus ultimately enabling routes for the state to set regulations and targets related to industrial waste management.

The degree of the reactivity of the DM that is yielded from quarry operations for potential use in geopolymerization has not been researched to a considerable extent. Previous work [24–26] suggests that the quarry sludges or aggregate wash muds—depending on the oxide contents and reactivity—may scantily compete as a suitable precursor for potential alkali activation for yielding durable alkali-activated binders. There is, in addition, the important issue of the mineralogical variability of these residue muds due to the variations in the aggregate compositions existing in quarries in different geographic regions. Such variability, combined with additional key parameters that affect both the reactivity of the aluminosilicates (i.e., amorphism, fineness, specific surface area) as well as the precursor consumption (quantity and modulus of the alkali solutions for defining Si/Al or (Si + Al)/Na ratios of the mixtures), needs to be carefully taken into consideration when examining a by-product as a candidate for geopolymerization [5–18]. It is therefore critical to characterize and quantify the contents of key soluble elements, especially Al and Si, along with the crystallinity profile of the material and the corresponding phase amounts at the highest possible accuracy, so as to enable drawing conclusions on whether the material is capable of being geopolymerized—and thus defining its potential for use in developing sustainable and durable alkali-activated binders.

In light of the above, this work seeks to define the geopolymerization potential of a diabase mud received from a Cyprus quarry through a comprehensive experimental program, which consisted of characterizing, initially, the DM, followed by quantification of its reactivity potential through dissolution tests, and finally investigating of early mechanical properties of formulations developed based on the reactivity of the material.

2. Materials and Methods

2.1. Experimental Program

The experimental program consisted of three distinct stages, as described below:

- Characterization of the DM material as received from quarry;
- Examining the DM material's reactivity through dissolution tests (i.e., determining the soluble Al, Si contents) as a basis for then establishing properly proportioned inorganic polymer formulations; and
- Development of the above selected inorganic polymer formulations incorporating a combination of solids and alkaline solutions and investigating their stability through early age compressive strength tests at varying curing conditions and varying mixing parameters.

2.2. Characterization of the DM

The first stage of the experimental program, as received DM from Pharmakas Quarries in Cyprus, was initially characterized through X-Ray Diffraction Analysis (XRD), Thermogravimetric Analysis (TGA), Energy Dispersive X-Ray Fluorescence (ED-XRF), and density tests. For these tests, the DM was oven-dried at 110 °C until constant mass, followed by being crushed into fine particles using a Los Angeles abrasion machine at 2000 cycles and then sieved through a 0.063 mm sieve.

X-ray diffraction analysis was conducted using a BRUKER D8 X-Ray Diffractometer (BRUKER, Billerica, MA, USA) with Cu K α 1 (Ni filtered) radiation in the 2-theta range of 2° to 60° and on a 0.02°/s step. X-ray diffractogram of the material is shown in Figure 1. The composition, as observed by the peaks, appeared to be mainly crystalline, comprising of quartz (SiO₂), albite (NaAlSi₃O₈ or Na_{1.0-0.9}Ca_{0.0-0.1}Al_{1.0-1.1}Si_{3.0-2.9}O₈), labradorite (Ca, Na)(Al, Si)₄O₈, as well as minor traces of calcite (CaCO₃).

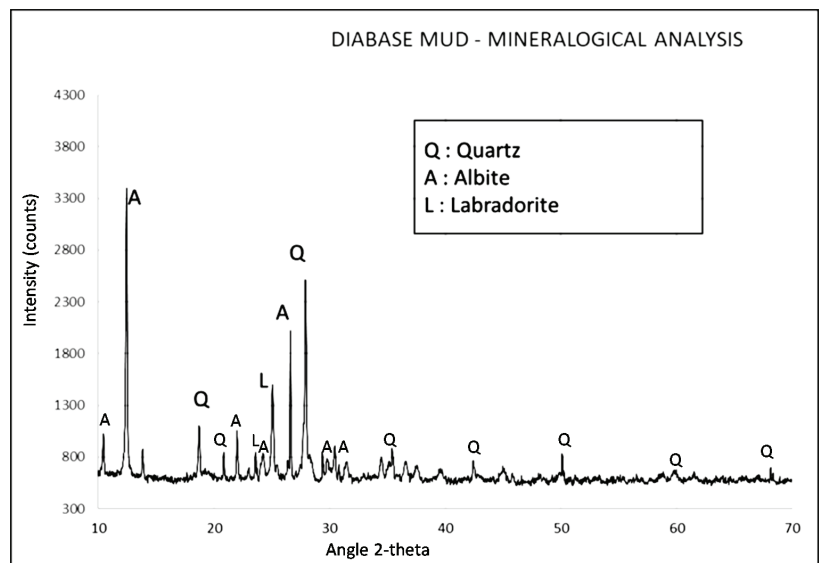


Figure 1. XRD diffractograms of the investigated DM material.

The differential thermal/thermogravimetric (DT/TGA) analysis (Figure 2), which was conducted from less than 100 °C to 1100 °C at nitrogen atmosphere and at a rate of 15 °C/min, confirmed the disintegration of the abovementioned phases with mass losses occurring mainly within the dehydroxylation range (i.e., 1.75% mass loss of labradorite/portlandite at 500–650 °C), as well as within the decarbonation range (i.e., approximately 1.2% mass loss of labradorite/calcite at 700–800 °C). It has to be noted that the recorded

initial mass loss was attributed to the loss of humidity, whereas the transformation of quartz was not observed during the analysis, as the phenomenon is taking place in higher temperatures.

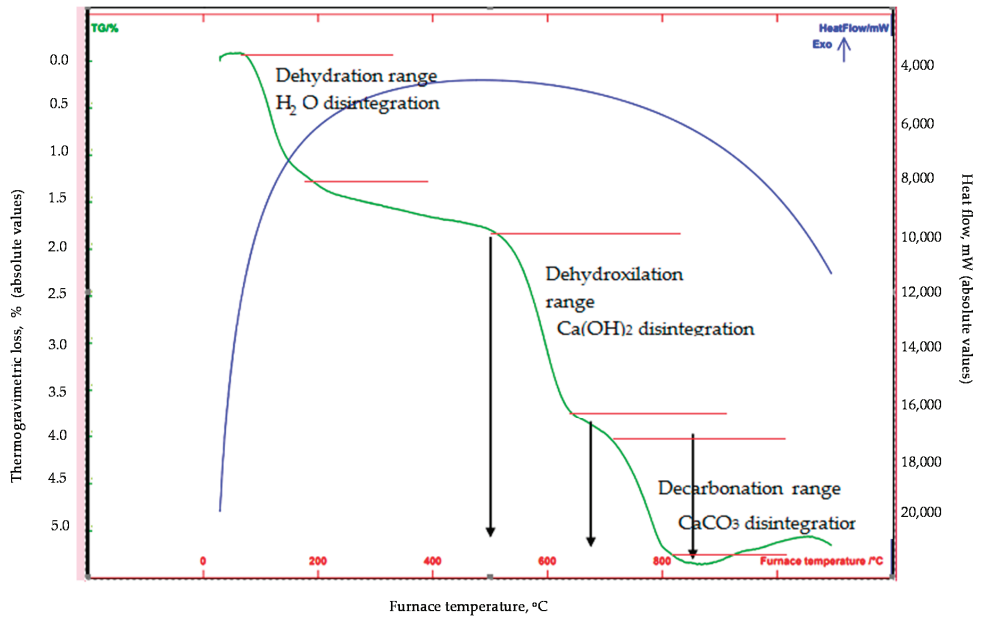


Figure 2. DT/TGA curves of the investigated DM material.

For obtaining the oxide contents of the DM, ED-XRF analysis was conducted using a SPECTRO XEPOS elemental spectrometer, the results of which are shown in Table 1. The results were validated through Atomic Absorption Analysis (Fusion method), as well. By observing the oxide contents, the DM appeared to be a silicate-rich material with almost 41% SiO₂ content, which, in combination with 11% of Al₂O₃, indirectly provided a good degree of reactivity potential and indicated a promising precursor for geopolymerization, even though its amorphousness profile may have seemed less favorable.

Table 1. Oxide composition of the DM material from ED X-Ray Fluorescence (XRF) analysis.

| | Na ₂ O | MgO | Al ₂ O ₃ | SiO ₂ | CaO | ZnO | FeO |
|---|-------------------|------|--------------------------------|------------------|------|------|-------|
| % | 2.53 | 8.87 | 11.14 | 40.91 | 5.36 | 1.71 | 13.65 |

2.3. Density of DM

Density measurements were obtained by oven-drying the as-received sample at 105 °C until constant mass, followed by grinding the material using pestle and mortar in sizes less than 63 microns and using a Quantachrome pycnometer to determine the density of the powdered sample. Four measurements were obtained, and the average density was reported as 2362 kg/m³ (standard deviation = 25.2 kg/m³). This value was slightly lower than the average reported density of the aggregates crushed and processed in the particular local quarry in Cyprus.

2.4. Reactivity (Dissolution Tests) and Basis of Establishing Formulations

Dissolution tests were conducted on the basis of assessing the reactivity of DM. Reactivity is defined as the concentration of leached-out soluble elements (Si, Al) following a

specific time frame. The test, therefore, provided the basis for establishing and developing inorganic polymer formulations incorporating solids with alkaline solutions for the subsequent experimental phase. The leaching reagents used were either NaOH or KOH at molarities of 2 M, 4 M, 6 M, 8 M, 10 M, 12 M, and 16 M, and at a liquid to solid ratio (L/S ratio) of 250. The test involved adding 0.2 g of the DM sample in 50 g leaching reagent in a tube which was shaken for 24 h, and then centrifuging the mixture for 15 min at 3000 rpm, followed by filtrating the supernatant at 0.45 micron membrane-filter and analyzing the residue through inductively coupled plasma atomic emission spectroscopy (ICP-AES). Results of the dissolution tests are shown in Figure 3. Based on the leached contents of both Al and Si metals, the highest dissolution percentage was noted at 12 M of NaOH or KOH molarity, beyond which, however, the efficiency of both reagents appeared to decline. The leaching amounts of both metals were higher when NaOH was used as the reagent compared to the case when KOH was used, although the contents were still very low to render the DM as a proper precursor for geopolymerization in both cases. The results from Figure 3 essentially suggest that DM may not be sufficiently dissolved in any of the two alkaline activators (i.e., a max. dissolution of 2.54%, which is considerably lower than typical Al-Si dissolutions of fly ash or metakaolin), and this is mainly attributed to the presence of high amounts of crystalline phases in DM that are unable to be dissolved, even in highly alkaline concentrations. A minimum, commonly suggested, dissolution percentage required to create a stable geopolymeric material based on previous research [18,19,27,28] is approximately 10%, which typically yields formulations of appreciable compressive strengths without the addition of other materials. A linear correlation, moreover, appears to exist [8,10,18,19] between the metal dissolution contents and the mechanical properties of the inorganic polymers; i.e., higher amounts of metal dissolutions were reported to lead to higher compressive strengths. Therefore, to establish appropriate inorganic polymer formulations that promote the dissolution of the metals, it was decided to incorporate small quantities of suitable hydraulic materials that promote greater amorphicity of phases within the matrix and thus enhance the geopolymerization of the DM. The materials selected are discussed in the following section.

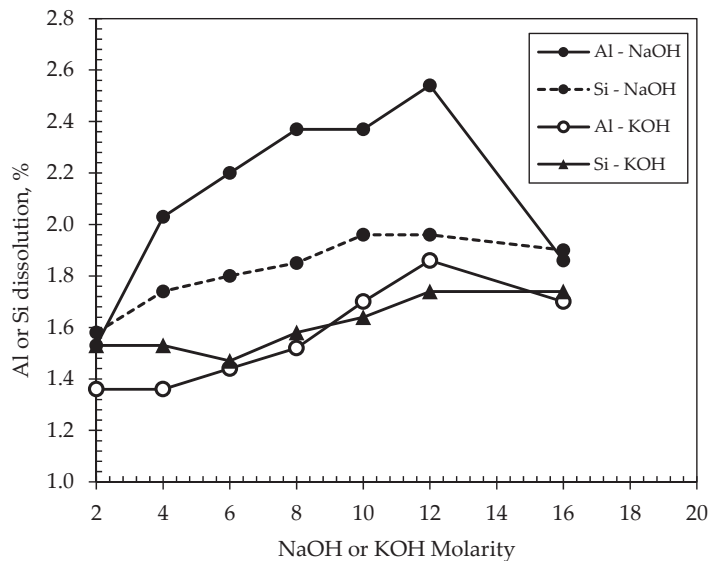


Figure 3. Results of dissolution of Al and Si elements of the investigated DM material.

2.5. Solids, Alkaline Solutions and Basis of Establishing Formulations

For achieving stability of the geopolymerized formulations, commercially available materials of portland cement (CEM I to EN 197-1:2020), gypsum (calcium sulfate dihydrate,

CaSO₄·2H₂O to EN 13279-1:2008), as well as commercially available metakaolin (MK), were all strategically incorporated in the mixtures at defined percentages (thereon all referred to as ‘solids’). The solids were added on the basis of promoting amorphicity in the matrix and thus enhancing the geopolymerization of the DM.

For preparing the alkaline activator solution, a combination of NaOH and Na₂SiO₃ solutions were used at progressively varying Na₂SiO₃:NaOH ratios ranging from 10:90 to 90:10, although predominantly considered ones were the 50:50 and 40:60 ratios. The NaOH solution was prepared in molarities of 2 M, 4 M, 6 M, 8 M, 10 M, and 12 M by mixing solid pellets with appropriate amounts of deionized water (to maintain constant properties of water),—the amount of which was determined based on NaOH molar mass for producing the required concentrations—and then stirring the mixture for 5 min using a magnetic stirrer. The solution was insulated for 24 h in ambient conditions and mixed with a commercially available Na₂SiO₃ solution in the abovementioned percentages to develop the alkaline activator (thereon referred to as ‘liquid’). Properties of all solids and alkaline solutions used are shown in Table 2.

Table 2. Properties of alkaline solutions and solid used in the experimental.

| Material | Conformity Standard | Nomenclature | Particle Size (Median, μm) | Specific Gravity | pH | Specific Surface (m ² /kg) |
|---------------------------|---------------------|--------------------------------------|----------------------------|------------------|-------|---------------------------------------|
| Portland cement CEM I | EN 197-1:2020 | CEM I | 19.6 | 3.1 | 12.5 | 330 |
| Metakaolin | NF P18-513 | MK | 1.2 | 2.5 | 5 | 14,200 |
| Gypsum | EN 13279-1:2008 | CaSO ₄ ·2H ₂ O | 24.5 | 2.82 | 7.2 | 260 |
| Sodium Silicate solution | - | Na ₂ SiO ₃ | - | 1.37 | 11.35 | - |
| Sodium Hydroxide solution | - | NaOH | - | 2.13 | 13 | - |

Three different cases of inorganic polymer mixtures were investigated:

- Case 1 included the development of 12 mixtures of varying molarities (2–12 M, at 2 M increment) and varying NaOH/Na₂SiO₃ ratios for a liquid to solid (L/S) ratio of 0.69, incorporating DM, CEM I and gypsum and oven-cured for 48 h at 70 °C;
- In Case 2, a total of nine mixtures were developed using DM, CEM I and MK at a low L/S ratio of 0.38, again with varying molarities (2–10 M, at 2 M increment) and varying NaOH/Na₂SiO₃ ratios, air-cured at 20 °C and 65% RH for 72 h prior to testing;
- And lastly, a Case 3 was considered where a total of eight mixtures were developed using DM and MK at a low L/S ratio (0.38), again with varying molarities (2–10 M, at 2 M increment) and varying NaOH/Na₂SiO₃ ratios and being conditioned in the oven at 50 °C for 72 h prior to testing.

The nature of the DM (i.e., being a waste material with mineralogical variability due to the differences in the compositions of aggregates existing in quarries in different geographic regions of the island), in combination with the very limited previous references on the characterization and valorization of the material, demanded the investigation of a wide spectrum of factors potentially influencing its activation. Therefore, the three Cases mentioned above were selected after a considerable number of small-scale preliminary trial mixtures and combinations, based on the evaluation of the results related to the characterization of the DM and either previous experiences of the research team, or some similar cases reported in the literature [28]. It is important to be noted that it was not the intention of the research team to perform a direct comparison of the results obtained from the three Cases under investigation. Instead, the selection of the three Cases and the variation of the parameters were all aimed to reveal the factors that would positively affect the activation of the DM. Compressive strength values at 24 and 48 h were obtained for the mixtures in Case 1, whereas 72-h strengths were determined for the mixtures developed in Cases 2 and 3. All the varied parameters of the experimental program are shown in Table 3 below.

Table 3. Mix proportions and properties of the developed formulations used in the experimental program.

| Curing Condition | Formulation Nomenclature | L/S Ratio | DM % by wt. Solids | CEMI % by wt. Solids | Gypsum % by wt. Solids | MK % by wt. Solids | Na ₂ SiO ₃ :NaOH Ratio %: % by wt. | M _{NaOH} | 24 h Average Compressive Strength (MPa) | 48 h Average Compressive Strength (MPa) | 72 h Average Compressive Strength (MPa) | |
|---|--|-------------|--------------------|----------------------|------------------------|--------------------|--|-------------------|---|---|---|------|
| CASE1: 24 h or 48 h in the oven at 70 °C | M1 | | | | | | 50:50 | 12 | 1.94 | 3.36 | - | |
| | M4 | | | | | | 40:60 | 12 | 2.1 | 4.23 | - | |
| | M5 | | | | | | 50:50 | 10 | 3.01 | 4.36 | - | |
| | M6 | | | | | | 40:60 | 10 | 3.73 | 5.4 | - | |
| | M7 | | | | | | 50:50 | 8 | 5.65 | 7.66 | - | |
| | M8 | 0.69 | | | | | 40:60 | 8 | 2.56 | 5.29 | - | |
| | M9 | | 68 | 16 | | | 50:50 | 6 | 4.19 | 6.49 | - | |
| | M10 | | | | | | 40:60 | 6 | 4.55 | 6.45 | - | |
| | M11 | | | | | | 50:50 | 4 | 6.3 | 8.31 | - | |
| | M12 | | | | | | 40:60 | 4 | 5.16 | 6.95 | - | |
| | M13 | | | | | | 50:50 | 2 | 5.49 | 6.82 | - | |
| | M14 | | | | | | 40:60 | 2 | 7.26 | 5.94 | - | |
| | CASE 2: Air cured at 20 °C, 65% RH (72 h) | CyDIA-0007g | | | | | | 50:50 | 10 | - | - | 9.43 |
| | | CyDIA-0008g | | | | | | 40:60 | 10 | - | - | 4.14 |
| CyDIA-0009g | | | | | | | 30:70 | 10 | - | - | 7.25 | |
| CyDIA-0010g | | | | | | | 10:90 | 10 | - | - | 4.46 | |
| CyDIA-0011g | | 0.38 | 82 | 4 | | 14 | 0:100 | 10 | - | - | 3.27 | |
| CyDIA-0012g | | | | | | | 50:50 | 8 | - | - | 9.34 | |
| CyDIA-0013g | | | | | | | 50:50 | 6 | - | - | 4.22 | |
| CASE 3: Oven cured 50 °C for 72 h | CyDIA-0014g | | | | | | 50:50 | 4 | - | - | 1.64 | |
| | CyDIA-0015g | | | | | | 50:50 | 2 | - | - | 1.12 | |
| | CyDIA-0004f | | | | | | 50:50 | 10 | - | - | 6.72 | |
| | CyDIA-0003f | | | | | | 30:70 | 10 | - | - | 7.53 | |
| | CyDIA-0002f | | | | | | 20:80 | 10 | - | - | 2.91 | |
| | CyDIA-0001f | | | | | | 0:100 | 10 | - | - | 1.73 | |
| | CyDIA-0004h | 0.38 | 82 | - | | 18 | 30:70 | 8 | - | - | 5.89 | |
| CyDIA-0003h | | | | | | 30:70 | 6 | - | - | 3.04 | | |
| CyDIA-0002h | | | | | | 30:70 | 4 | - | - | 1.93 | | |
| CyDIA-0001h | | | | | | 30:70 | 2 | - | - | 1.32 | | |

The paper aims to present, discuss and evaluate the results obtained from each of the three Cases under study, and reveal the factors that could enhance the alkali activation of the three hybrid mixtures. It should be noted that due to the nature and origin of the DM, as well as due to the lack of any previous knowledge related to the potential of the material to be valorized through geopolymerisation, a variety of experimental investigations were necessary to draw conclusions on this aspect. In a subsequent paper, the most promising mixtures developed based on the information summarised in this paper will be presented, along with the obtained physical and mechanical properties, durability characteristics, and optimized curing regimes.

2.6. Proportioning, Mixing, Casting, Curing, and Properties Tested

The inorganic polymers were prepared by carefully mixing the liquids and solids described in the previous section at the selected proportions shown in Table 3 for a total mixing duration of 5 min. The paste was then cast in copolymer-based cubic moulds ($50 \times 50 \times 50 \text{ mm}^3$) in accordance to ASTM C109–20, and was vibrated using a vibrating table for 1 min. The early age uniaxial compressive strengths of the samples were then determined using a 2000 kN CONTROLS hydraulic compression machine at either 24 and 48 h (for Case 1), or 72 h (for Cases 2 and 3), and at a loading rate of 0.2 MPa/s in accordance to ASTM C109–20 [20].

3. Results and Discussion

Average compressive strength developments and NaOH concentrations of all investigated formulations are shown in Table 3, along with the relevant mix proportions of solids and liquids incorporated in the mixtures. Relationships between compressive strengths, molarity and $\text{Na}_2\text{SiO}_3:\text{NaOH}$ ratios of 50:50 and 40:60 for mixtures in Case 1 are shown in Figure 4, whereas the same relationships related to Cases 2 and 3 are shown in Figures 5–7. The compressive strength values were determined as the averages of three samples for each value, and the standard deviations are included in the figures.

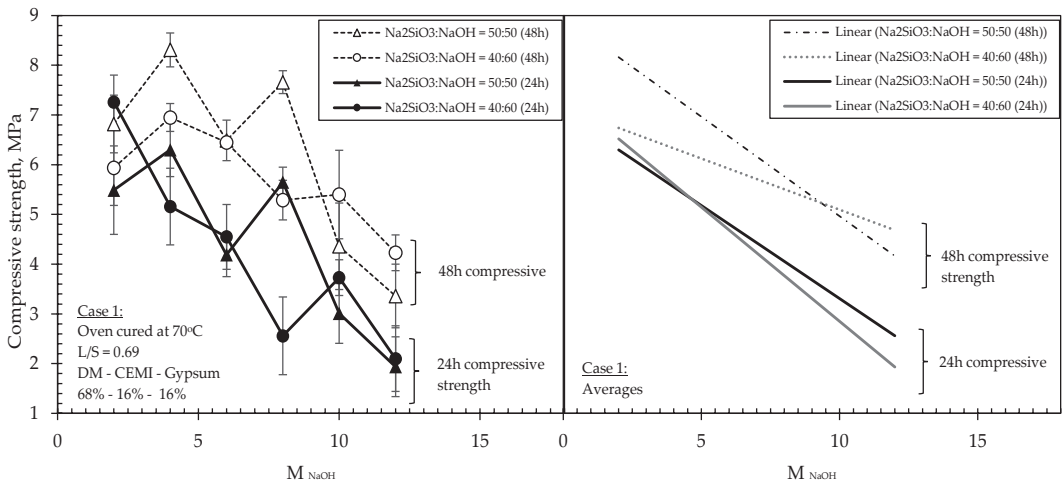


Figure 4. Effect of molarity of NaOH on the 24 h and 48 h compressive strength of formulations investigated in Case 1.

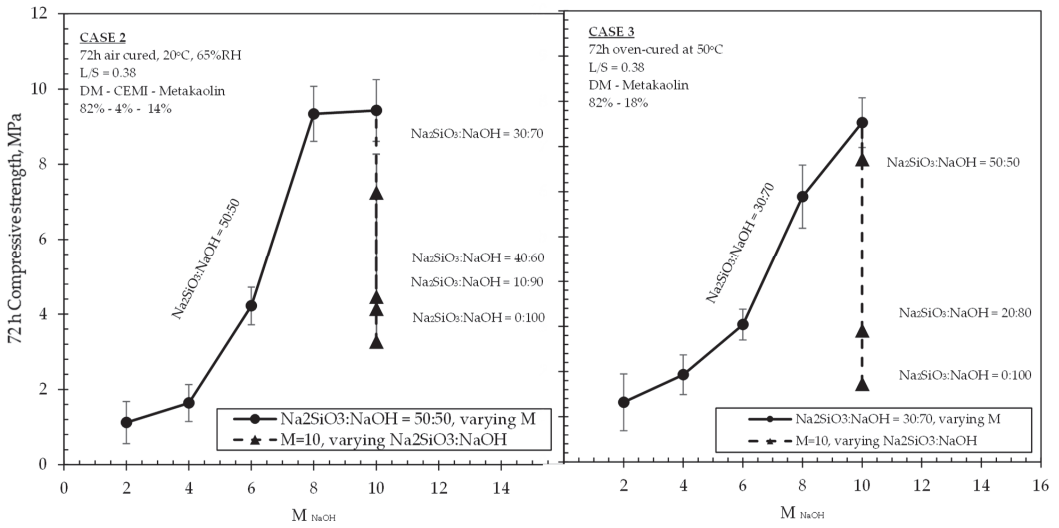


Figure 5. Effect of NaOH molarity and Na₂SiO₃: NaOH ratio on the 72 h strength of formulations at Cases 2 (left) and Case 3 (right).

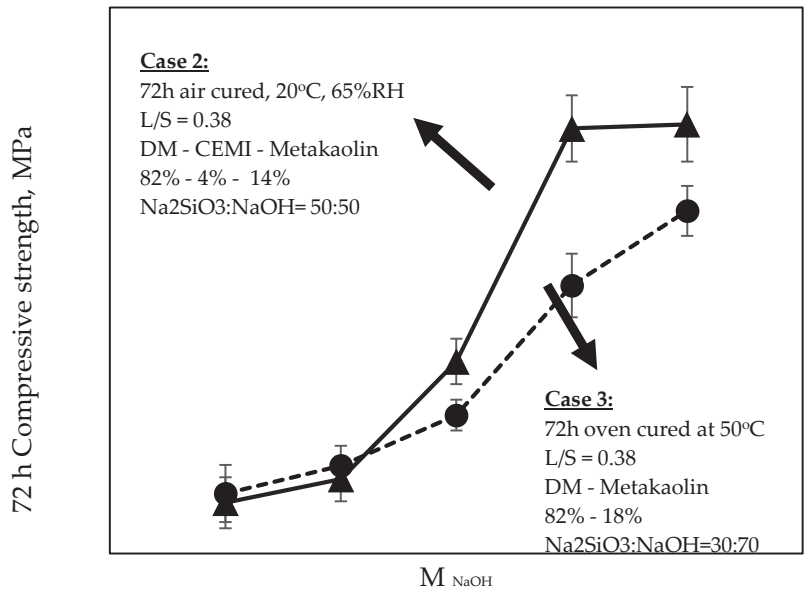


Figure 6. Relationship between 72 h compressive strength and NaOH molarity of formulations in Cases 2 and Case 3 at Na₂SiO₃:NaOH ratios of 50:50 and 30:70, respectively.

The results obtained from Case 1 showed that the relationship between compressive strengths and molarities at both Na₂SiO₃:NaOH tested ratios (i.e., 50:50 and 40:60) and at both ages (i.e., 24 h and 48 h), was overall inversely proportional, i.e., showcasing a declining rate, although however, changing the molarities caused fluctuations on the compressive strengths, especially in the mixtures having a Na₂SiO₃:NaOH ratio of 50:50. In these particular mixtures, when the highest molarity NaOH was incorporated in the liquids (i.e., 12 M), a significant strength loss (66% reduction) was recorded compared to its highest strength value, which was observed at a molarity of 4 M. Another interesting point obtained

was that the mixtures with $\text{Na}_2\text{SiO}_3:\text{NaOH}$ ratios of 50:50 exhibited approximately 10–20% higher 48 h compressive strengths than those of the 40:60 ratio, however, this occurred only up to molarity of 8 M; beyond which, the mixtures of 50:50 ratio suffered a drastic 48 h strength loss of 66% when molarity was increased from 8 M to 10 M, and these eventually became weaker than the mixtures of 40:60 ratio, with nearly 10% lower 48 h strengths.

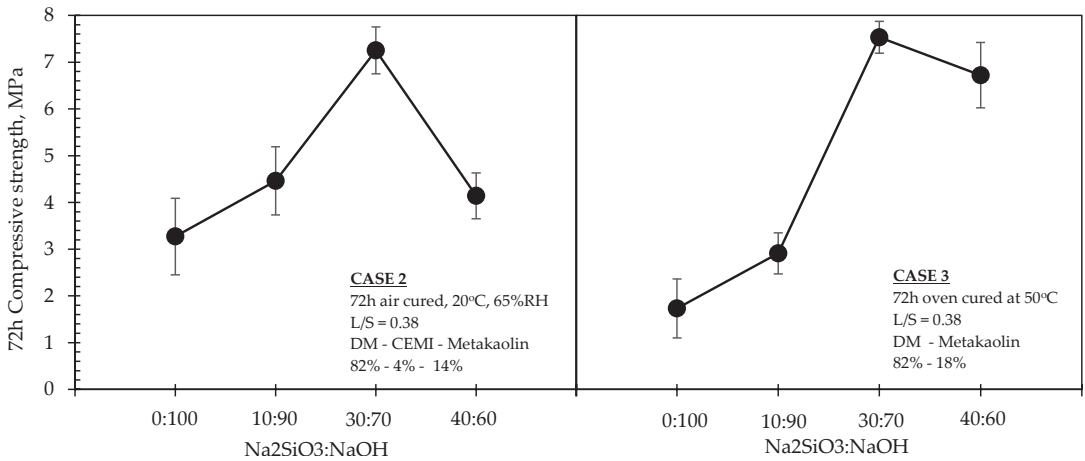


Figure 7. Effect of $\text{Na}_2\text{SiO}_3:\text{NaOH}$ ratio on the 72 h strength of formulations in Cases 2 (left) and 3 (right), for $M_{\text{NaOH}} = 10$.

The results in Figure 4 suggest that formulations of relatively high L/S ratio (i.e., 0.69) developed with a $\text{Na}_2\text{SiO}_3:\text{NaOH}$ ratio of 50:50 and with a molarity of NaOH solution of 4 M exhibited the highest strengths from all compared formulations. However, the particular mixtures appeared to be highly sensitive to variations in the molarity, leading to significant fluctuations in strengths when molarities were progressively increased, and eventually suffering drastic strength losses beyond 10 M NaOH concentrations. In mixtures of a ratio of 40:60, the fluctuations in strengths were less significant when molarities were progressively increasing, although strengths were still declining across the tested molarities.

In Case 1 and according to Figure 4, a general trend of compressive strength decrease with the increase of the alkalinity was observed with minor differentiations in the strengths (within a range of 10–15%). This trend is attributed to the fact that the DM cannot be dissolved in the alkaline solution, according to the results obtained from the dissolution tests. Therefore, the alkali presence and the increase of molarity did not affect the materials' geopolymeric formation and the development of strength. In contrast, the increase of alkalinity seems to decrease the compressive strengths, since no geopolymeric reaction is taking place. On the other hand, the mix designs for Case 1 contain two pozzolanic materials (i.e., cement and gypsum) that favour the presence of water for developing high strengths. In mixtures of lower alkalinity, the cement and gypsum hydration reactions become dominant (due to a higher amount of unbound water, i.e., water not participating in the alkaline solution), thus resulting in higher strengths, as recorded.

Results of investigations carried on mixtures of Cases 2 and 3 are shown in Figures 5–7. It should be noted that, while observations were made and provided within the text, no correlations could be made between the two Cases (i.e., 2 and 3) due to the variation of multiple parameters governing each case, such as the curing regime, the mixture design, the ambient conditions, and also possible different activation mechanisms. As has been aforementioned, it was not the intention of this research to perform a direct comparison of the results obtained from the three Cases under study. Instead, the selection of these Cases and the variation of the parameters were aimed to reveal the factors that would positively

affect the activation of the DM, and therefore to maximise the effective utilization of the DM content in mixtures.

Cases 2 and 3 are summarized in Figures 5–7 together due to the common presence of metakolin in the two different formulations, their identical age of testing (i.e., 72 h), and also some similar trends observed in the obtained experimental results. It was observed that the progressive increase in NaOH molarity caused an increase in the 72 h strengths of both sets of mixtures with an almost identical effect on strength values for 2 M and 4 M, and then, at higher molarities, reaching up to 9.43 MPa (Case 2) and 7.53 MPa (Case 3), respectively. When the molarity value increased from 6 M to 8 M, both sets of formulations experienced their highest increase rate in strengths (121% and 93% increase for Cases 2 and 3, respectively). Beyond 8 M and towards 10 M, Case 3 mixtures still exhibited an appreciable increase in strengths, which was even higher than that observed from 4 M to 6 M. In the same concentrations, however, the mixtures of Case 2 were not associated with any significant increase, indicating an optimum concentration between 8–10 M for their highest achievable strengths. The results in Figures 5 and 7 suggest that the addition of small quantities (4%) of CEM I in low L/S ratio DM-MK mixtures (i.e., Case 2), when conditioned in air ambient temperatures, led to a more significant increase in strengths at NaOH concentrations between 6 M and 8 M within the 50:50 Na₂SiO₃:NaOH ratio, although this effect was ceased at concentrations beyond 8 M and towards 10 M. This difference can be also observed in Figure 6 when comparing strength values between the 6 M–8 M range. At the same figure, when incorporating NaOH of molarity 2 M and 4 M, both air-cured and oven-cured mixtures yielded almost identical strengths regardless of their different Na₂SiO₃ ratios and regardless of the presence of CEM I in the formulation. Beyond a concentration of 4 M, and at least until the 8 M, there is a significant increase in strengths, which appears to be considerably sharper in the Case 2 mixtures. However, such an increase was less significant beyond 8 M in Case 2, in contrast to Case 3 mixtures. An additional observation for Case 3 made in Figure 5 (right hand part of the graph) was that a low L/S ratio DM-MK mixture with a 20:80 alkaline solution and its NaOH molarity at 10 M yields approximately the same strength as that of a mixture at 30:70 alkaline solution with a NaOH molarity of 6 M.

When both Cases were compared at equivalent molarity of 10 M (Figure 7), the maximum achievable strengths were found at 30:70 Na₂SiO₃:NaOH ratio, regardless of the presence of CEM I and regardless of the ambient conditions. It can be also seen, on the same figure, that the absence of CEM I in Case 3 appeared to have enhanced the strengths more significantly when the ratio was tending from 10:90 towards 30:70 when compared to Case 2 (i.e., when containing CEM I).

Fundamentally, the increase in compressive strengths in both Cases may be attributed to the increase of the alkalinity, which is mainly attributed to the presence of metakaolin in the mixtures, which predominantly reacts with the alkaline activator. Moreover, in Cases 2 and 3, the addition of the sodium silicate solution seems to have a positive effect on the evolution of the compressive strength. The continuous increase of Si content enhanced the content of dissolved elemental silicon, and the increase of Si(OH)₄ monomer promotes the formation of more -Si-O-Si- bonds, thus forming a more stable bond structure.

Generally, the higher the Si content, the more stable it is, since the chemical bond strength of -Si-O-Si- is higher than the corresponding of -Si-O-Al- and -Al-O-Al-, and therefore higher energy is required to break the particular bond.

With Si/Al ratio increasing up to a certain extent (i.e., Case 3), the content of elemental silicon dissolved in the system is much higher than that of aluminum. Meanwhile, a part of Si(OH)₄ will form a dimer after condensation reaction and then react with Al(OH)₃ to form a stable long chain (-Si-O-Al-O-Si-O-) PSS polymer (Si/Al = 2) or more stable long chain (-Si-O-Al-O-Si-O-Si-O-) PSDS polymer (Si/Al = 3). This phenomenon is not presented in Case 2, since the presence of cement creates C-S-H phases in parallel that are not enhanced with the presence of additional Si, while it in contrast intercepts the geopolymerisation process, and thus the compressive strength decreases (Figure 7).

4. Conclusions

The potential for geopolymerization of a diabase mud received from a Cyprus quarry was investigated in this paper and the following conclusions were drawn, based on the results:

- Considerably low amounts of Al and Si metals were dissolved following the dissolution tests conducted on DM, which essentially suggests that the material alone did not possess sufficient reactivity potential so as to give chemically stable alkali activated binders.
- Based on the above, mixtures of high L/S ratio incorporating CEM I, gypsum and MK at a $\text{Na}_2\text{SiO}_3\text{:NaOH}$ ratio of 50:50 and with a molarity of NaOH of 4 M enhanced the geopolymerization of the DM, but appeared to be highly sensitive when M was increasing, leading to significant fluctuations in strengths and eventually suffering drastic strength losses beyond a 10 M NaOH molarity.
- The curing conditions, the ratio of $\text{Na}_2\text{SO}_3\text{:NaOH}$, and the presence of CEM I in the DM-based mixtures did not appear to significantly affect the compressive strengths when the NaOH concentration was between 2 M and 4 M (i.e., Cases 2 and 3); at higher molarities, however, these enhanced the strengths of the geopolymerized DM.
- Maximum strengths of mixtures at equivalent molarity of 10 were achieved when the $\text{Na}_2\text{SiO}_3\text{:NaOH}$ ratio reached 30:70, regardless of the ambient conditions and regardless of the presence of CEM I.
- A low L/S ratio DM-Metakaolin mixture with a 20:80 alkaline solution with its NaOH molarity at 10M yields almost identical 72 h strength to that of a mixture at 30:70 alkaline solution with a NaOH molarity of 6 M.

Author Contributions: Conceptualization: D.N., M.S., K.S., P.S., S.I., K.O. and M.F.P.; Data curation: M.S., P.S., S.I., K.O., K.S., M.F.P. and D.N.; Formal analysis: M.S., P.S., S.I., K.O., K.S., M.F.P. and D.N.; Funding acquisition: D.N., K.S., P.S., M.F.P., M.S., K.O. and S.I.; Investigation: M.S., P.S., S.I., K.S., K.O., M.F.P. and D.N.; Methodology: M.S., P.S., K.S., S.I., K.O., D.N. and M.F.P.; Project administration: P.S., S.I., D.N. and M.F.P.; Resources: M.S., P.S., S.I., K.S., D.N. and M.F.P.; Supervision: D.N., P.S. and M.F.P.; Validation: D.N., P.S. and M.F.P.; Writing—original draft: S.I. and M.S.; Writing—review & editing: M.S., P.S., S.I., K.S., M.F.P. and D.N. All authors have read and agreed to the published version of the manuscript.

Funding: This research was funded by the Cyprus Research & Innovation Foundation (RIF) and the European Regional Development Fund, RESTART Research, Technological Development and Innovation Programs 2016–2020 (Project Budget: €248,748.00, Project Contract Number: ENTERPRISES/0618/0041).

Institutional Review Board Statement: Not applicable.

Informed Consent Statement: Not applicable.

Acknowledgments: The authors would like to express their sincere gratitude to the Cyprus Research & Innovation Foundation and the European Regional Development Fund for funding the research project entitled “Valorization of diabase mud for the development of innovative building materials” (Contract Number: ENTERPRISES/0618/0041). Special thanks also go to the undergraduate students at Frederick University who contributed to the experimental work, especially Christos Antoniou and Gregoria Miltiadous for their contribution to the experimental work.

Conflicts of Interest: The authors declare no conflict of interest.

References

1. OFCOM. Cement Production Worldwide from 1995 to 2021. Statista. 2021. Available online: <https://www.statista.com/statistics/1087115/global-cement-production-volume/> (accessed on 3 April 2022).
2. European Commission. Directive 2018/851 Amending Directive 2008/98/EC on Waste Framework. *Off. J. Eur. Union*. 2018. (L150/109-L 150/140). Available online: <https://eur-lex.europa.eu/legal-content/EN/TXT/PDF/?uri=CELEX:32018L0851&from=EN> (accessed on 4 April 2022).

3. BCA, CSMA, UKQAA. Fact Sheet 18 [P1]: Embodied CO₂ of UK Cement, Additions and Cementitious Material. 2009. Available online: http://cement.mineralproducts.org/downloads/fact_sheets.php (accessed on 4 April 2022).
4. Tänzler, R.; Buchwald, A.; Stephan, D. Effect of slag chemistry on the Hydration of alkali-activated slag: Comparison with ordinary Portland cement blast-furnace slag. *Mater. Struct.* **2015**, *48*, 629–641. [[CrossRef](#)]
5. Glukhovskiy, V.D.; Rostovskaya, G.S.; Rumyna, G.V. High strength slag-alkali cement. In Proceedings of the 7th International Congress on the Chemistry of Cements, Paris, France, 1 January 1980; Editions Septima: Paris, France, 1980.
6. Bernal, S.A.; Mejía de Gutiérrez, R.; Pedraza, A.L.; Provis, J.; Rodriguez, E.D.; Delvasto, S. Effect of binder content on the performance of alkali-activated slag concretes. *Cem. Concr. Res.* **2011**, *41*, 1–8. [[CrossRef](#)]
7. Shi, C.; Roy, D.; Krivenko, P. *Alkali-Activated Cements and Concretes*; CRC Press: Boca Raton, FL, USA, 2003.
8. Puertas, F.; Martínez-Ramírez, S.; Alonso, S.; Vazquez, T. Alkali-activated fly ash/slag cements: Strength behaviour and hydration products. *Cem. Concr. Res.* **2000**, *30*, 1625–1632. [[CrossRef](#)]
9. Koenig, A.; Wuestermann, A.; Gatti, F.; Rossi, L.; Fuchs, F.; Fessel, D.; Dathe, F.; Dehn, F.; Minelli, F. Flexural behaviour of steel and macro-PP fibre reinforced concretes based on alkali-activated binders. *Constr. Build. Mater.* **2019**, *211*, 583–593. [[CrossRef](#)]
10. Amer, I.; Kohail, M.; El-Feky, M.S.; Rashad, A.; Khalaf, M.A. Evaluation of using cement in alkali-activated slag concrete. *Int. J. Sci. Technol. Res.* **2020**, *9*, 245–248.
11. Angulo-Ramírez, D.E.; de Gutiérrez, R.M.; Puertas, F. Alkali-activated Portland blast-furnace slag cement: Mechanical properties and hydration. *Constr. Build. Mater.* **2017**, *140*, 119–128. [[CrossRef](#)]
12. Aliabdo, A.A.; Elmoaty, A.E.M.A.; Emam, M.A. Factors affecting the mechanical properties of alkali activated ground granulated blast furnace slag concrete. *Constr. Build. Mater.* **2019**, *197*, 339–355. [[CrossRef](#)]
13. Patel, Y.J.; Shah, N. Enhancement of the properties of ground granulated blast furnace slag based self compacting geopolymer concrete by incorporating rice husk ash. *Constr. Build. Mater.* **2018**, *171*, 654–662. [[CrossRef](#)]
14. Fang, G.; Ho, W.K.; Tu, W.; Zhang, M. Workability and mechanical properties of alkali-activated fly ash-slag concrete cured at ambient temperature. *Constr. Build. Mater.* **2018**, *172*, 476–487. [[CrossRef](#)]
15. Weil, M.; Dombrowski, K.; Buchwald, A. Life-cycle analysis of geopolymers. In *Geopolymers*; Elsevier: Amsterdam, The Netherlands, 2009; pp. 194–210.
16. Mendes, B.; Pedroti, L.G.; Vieira, C.M.F.; Marvila, M.; Azevedo, A.R.G.; Carbalho, J.M.F.; Ribeiro, J.C.L. Application of eco-friendly alternative activators in alkali activated materials: A review. *J. Build. Eng.* **2021**, *35*, 102010. [[CrossRef](#)]
17. Oliveira, L.B.; Azevedo, A.R.G.; Marvila, M.T.; Pereira, E.C.; Fediuk, R.; Vieira, C.M.F. Durability of geopolymers with industrial waste. *Case Stud. Constr. Mater.* **2022**, *16*, e00839. [[CrossRef](#)]
18. Palomo, A.; Grutzeck, M.W.; Blanco, M.T. Alkali-activated fly ashes: A cement for the future. *Cem. Concr. Res.* **1999**, *29*, 1323–1329. [[CrossRef](#)]
19. Roy, D.M. Alkali-activated cements opportunities and challenges. *Cem. Concr. Res.* **1999**, *29*, 249–254. [[CrossRef](#)]
20. *ASTM C109-20*; Standard Test Method for Compressive Strength of Hydraulic Cement Mortars. ASTM International: West Conshohocken, PA, USA, 2020.
21. Amer, I.; Kohail, M.; El-Feky, M.S.; Rashad, A.; Halaf, M. A review on alkali activated slag concrete. *Ain Shams Eng. J.* **2021**, *12*, 1475–1499. [[CrossRef](#)]
22. Wang, S.; Pu, X.; Scrivener, K.L.; Pratt, P.L. Alkali-activated slag cement and concrete: A review of properties and problems. *Adv. Cem. Res.* **1995**, *7*, 93–102. [[CrossRef](#)]
23. Bio, Bre, ICEDD, RPS, VTT and FCT. Construction and Demolition Waste Management in Cyprus. European Commission. 2015. Available online: https://ec.europa.eu/environment/pdf/waste/studies/deliverables/CDW_Cyprus_Factsheet_Final.pdf (accessed on 4 April 2022).
24. Thapa, V.B.; Waldmann, D.; Simon, C. Gravel wash mud, a quarry waste material as supplementary cementitious material (SCM). *Cem. Concr. Res.* **2019**, *124*, 105833. [[CrossRef](#)]
25. Largo, O.R.; Kacimi, L.; López-Delgado, A.; Frias, M. Characterization of Algerian reservoir sludges for use as active additions in cement: New pozzolans for eco-cement manufacture. *Constr. Build. Mater.* **2013**, *40*, 275–279.
26. Hameed, M.S.; Sekar, A.S.S. Properties Of Green Concrete Containing Quarry Rock Dust and Marble Sludge Powder as Fine Aggregate. *ARPN J. Eng. Appl. Sci.* **2009**, *4*, 83–89.
27. Sakkas, K.; Nomikos, P.; Sofianos, A.; Panias, D. Sodium based fire resistant geopolymer for passive fire protection. *J. Fire Mater.* **2015**, *3*, 259–270. [[CrossRef](#)]
28. Nikoloutsopoulos, N.; Sotiropoulou, A.; Kakali, G.; Tsvivilis, S. The effect of Solid/Liquid ratio on setting time, workability and compressive strength of fly ash based geopolymers. *Materialstoday* **2018**, *5*, 27441–27445. [[CrossRef](#)]

Article

Evolutionary Game Analysis of Energy-Saving Renovations of Existing Rural Residential Buildings from the Perspective of Stakeholders

Ming-Qiang Huang ^{1,*} and Rui-Juan Lin ²¹ School of Civil Engineering & Architecture, Xiamen University of Technology, Xiamen 361024, China² Third Institute of Oceanography, Ministry of Natural Resources, Xiamen 361005, China; linruijuan@tio.org.cn

* Correspondence: 2014110905@xmut.edu.cn

Abstract: To promote the orderly development of energy-saving renovations of existing rural residential buildings, it is necessary to coordinate the interests of various stakeholders. This study selects three key stakeholders—the government, energy-saving service enterprises and rural residents—as the research subjects and analyzes their interests and rights. In the meantime, a tripartite evolutionary game model is constructed to analyze the evolutionary rules and evolutionary stable strategies of tripartite behaviors, on the basis of which the influencing factors are analyzed. The research results show that: (1) as the supervisor and advocate of energy-saving renovations in existing rural residential buildings, the government, by adopting subsidies and fines, effectively fosters enthusiasm about energy-saving service enterprises among rural residents, encouraging them to participate in energy-saving renovations of existing rural residential buildings; (2) when the income of energy-saving renovations exceeds their cost, changes in the initial willingness ratio of the stakeholders, the government subsidies and fines only affect the evolution of the system so that it reaches a balanced and stable state, without changing the three parties' behavioral strategy choices in the game; (3) when the income from energy-saving renovations is lower than the cost, the behavioral strategies of the three parties in the game are all uncooperative; (4) key factors affecting tripartite cooperation in the game are as follows: government subsidies and fines, the overall interests of society, government supervision costs, loss of corporate image, standardization of the skills and services provided by enterprises, and willingness of rural residents to participate in the transformation.

Keywords: evolutionary game analysis; energy-saving renovation; the existing rural residential buildings; stakeholders' perspective

Citation: Huang, M.-Q.; Lin, R.-J. Evolutionary Game Analysis of Energy-Saving Renovations of Existing Rural Residential Buildings from the Perspective of Stakeholders. *Sustainability* **2022**, *14*, 5723. <https://doi.org/10.3390/su14095723>

Academic Editor: Alberto-Jesus Perea-Moreno

Received: 11 March 2022

Accepted: 6 May 2022

Published: 9 May 2022

Publisher's Note: MDPI stays neutral with regard to jurisdictional claims in published maps and institutional affiliations.



Copyright: © 2022 by the authors. Licensee MDPI, Basel, Switzerland. This article is an open access article distributed under the terms and conditions of the Creative Commons Attribution (CC BY) license (<https://creativecommons.org/licenses/by/4.0/>).

1. Introduction

1.1. The Energy Crisis Is Becoming Severe in China

With the rapid development of the social economy and the acceleration of urbanization, climate change, the energy crisis and biodiversity loss—caused by resource depletion and noticeable environmental pollution problems—are seriously threatening the sustainable development of the social economy and have become the biggest challenge for the progress of human society. China's economy has long maintained a good momentum of high-speed growth, which requires the support of sufficient energy resources. As a country with relatively scarce oil and gas resources, China requires a large amount of energy, such as coal and oil, to ensure its normal functioning and future development. Beyond that, it faces the requirement for an unyielding supply of energy due to the demand caused by extensive development, and the contradiction between economic development and resource shortages. According to the statistics released by the International Energy Agency (IEA), the total energy consumption of oil equivalent worldwide in 2018 was 9,937,702 kilotons, while the total energy consumption of oil equivalent in China was as high as 2,057,666 kilotons, accounting for 20.71% of the world's total, far higher than the 16.04% used by the United

States, thus making China the largest energy consumer in the world [1]. This low energy efficiency not only wastes energy, but also causes serious environmental pollution problems. According to the data from the BP World Energy Statistics Yearbook 2021, China's total carbon dioxide emissions in 2020 totaled 9.899 billion tons, accounting for 30.7% of the world's total emissions, compared with 20.9% in 2005 [2]. Therefore, considering the need for energy conservation and pollution control, it is urgent to "decouple" China's economic growth from energy consumption and carbon dioxide emissions.

1.2. The Construction Industry Is the Focus of Energy Conservation and Emission Reductions

Energy consumption and greenhouse gas emissions are often closely related to industrial production and development, to which the construction industry is a great contributor [3]. As one of the main driving forces to promote economic development, the construction industry plays a key role in economic and social development, but is one of major factors affecting the sharp increase in energy consumption and carbon emissions each year. In 2018, the total energy consumption of the global construction industry was as high as 2,109,205 kilotons of oil equivalent, and produced 2033 MtCO₂ [1]. In Britain, the total energy consumed by buildings accounted for about 40% of the total consumption and the carbon emissions caused by this account for 50% of the total emissions [4]. In the European Union, buildings consume about 50% of the total energy and produce about 50% of the carbon emissions during their life cycle [5,6]. In Malaysia, the construction industry consumed about 7750 GWh of energy and released about 5301 kilotons of carbon dioxide in 2008 [7,8]. In Canada, the total energy consumption of residential buildings and commercial buildings accounts for 30% of the national total, forming about 29% of carbon emissions [9]. For China, in terms of energy consumption, by 2018, the energy consumption of the national construction industry reached 2,109,205 kilotons of oil equivalent and produced 391MtCO₂ [10]. Moreover, the building construction sectors in countries all over the world, when combined, are responsible for over one-third of the global final energy consumption, and the carbon emissions share of the building sector will reach 50% by 2050, as estimated based on the current energy usage and emission intensity [11–13]. Buildings will, therefore, add substantial pressure to the primary energy supply if further policy actions are not taken at a global level to improve their efficiency [14,15].

1.3. Energy-Saving Renovation of Existing Rural Residential Buildings Is Key to the Sustainable Development of the Construction Industry in China

The urbanization rate in China grew from 42.99 percent in 2005 to 63.89 percent in 2020, and is expected to exceed 80 percent by 2050. With the increase in the urbanization rate, the rural population will gradually decrease, but the energy consumption of rural residential buildings still accounts for a very high proportion of the total energy consumption of buildings in China. In 2005, the energy use by rural residential buildings accounted for around 65% of total building energy use in China (including traditional biomass). Even with rapid urbanization, this is still expected to take up a quarter of China's building energy use in 2050 [16–19]. Due to serious lagging in the technical standards for rural residential building planning, design and construction, there are a great deal of problems in the construction of rural residential buildings, such as the over-simplified technical standards and the delay in the adoption of energy-saving evaluations. Compared with the 50% standard for building energy-efficiency in urban residential buildings, few strict energy-saving measures have been taken in the construction of most rural residential buildings in China. The low heating and cooling efficiency of residential buildings, and their poor thermal insulation performance, are also notable. At present, there are almost no accurate statistical data on the energy consumption of rural residential buildings in China. The evaluation of the energy consumption of rural residential buildings in China remains weak in all aspects. For instance, there is no effective evaluation system for the energy-saving performance and grading of rural residential buildings. In addition, the construction of rural residential buildings mainly utilizes the self-built and decentralized modes. Hence,

the commercialization rate of residential buildings is extremely low, and the engineering quality, functional quality and environmental quality of residential buildings are poor. In terms of residential construction technology, traditional techniques and methods are frequently adopted, such as manual masonry, a brick–concrete structure, few prefabricated components, low modular and assembly components, low labor productivity and low application levels for new technology. Since energy saving techniques have not been integrated into the design, planning and initial construction [20], these buildings consume a large amount of energy and emit large amounts of greenhouse gases. Therefore, it is imperative to carry out energy-saving renovations of existing rural residential buildings. This is an important part of the new rural construction and urbanization process, and is widely accepted as the best solution for aging residential buildings. Moreover, this could have various benefits, such as saving energy, decreasing environmental pollution, and promoting inhabitants' health [21,22].

2. Literature Review and Methods

2.1. Literature Review

Compared with new buildings, energy-saving renovations of existing buildings have greater potential for reductions in carbon emissions. The existing building area exceeds 60 billion square meters in China, and more than 60 percent of buildings are without energy conservation due to low construction standards and delayed maintenance. The large-scale demolition and reconstruction of existing buildings will not only cause a great waste of resources, but also lead to environmental degradation. A previous study has shown that buildings are responsible for 40% of the primary energy consumption and lead to over 30% of global greenhouse gas emissions [23]. While new energy efficiency regulations are applied to new buildings, the existing building stock remains energetically inefficient. Therefore, energy-saving renovations to the existing buildings are considered the most scientific and effective solution to reduce total energy consumption and global greenhouse gas emissions. However, the implementation of energy-saving renovations to existing buildings in China is still relatively slow. There are so many stakeholders involved in the process of energy-saving renovations to existing buildings. As the main body regulating energy-saving renovations of existing buildings, the participation intentions of the government, energy saving service enterprises and village residents directly affect the promotion of energy-saving renovations of existing buildings. Only when the government, energy saving service enterprises and village residents have the subjective willingness to participate can energy-saving renovations of the existing buildings be effectively promoted. However, previous studies on energy-saving renovations to existing buildings mainly focused on evaluation methods [20,24–27], retrofitting influence factors [28,29], cost–benefit analysis of retrofitting [30–34], evaluations of the effectiveness of retrofitting [35,36], barriers to retrofitting [37], and technical or scheme retrofittings [38–42]. In addition, some scholars are committed to reducing existing building energy consumption through energy modernization of buildings. Richarz et al. emphasized that modernizing existing non-residential buildings can significantly contribute to declared emission reduction targets. And they presented a mixed-integer linear program that schedules measures for a building energy system including envelope and supply system [43]. Dorota presented a case study for theoretical and real effect of the school's thermal modernization and found that the real energy use reduction after the thermal modernization effect was 33% [44]. Moreover, research on buildings from other regions of Poland has shown similar possibilities of reducing energy demands by up to 64% [45–47]. Staniūnas et al. made an ecological–economical assessment of multi-dwelling houses modernization and revealed that a complete replacement of windows would help decline total emissions approximately by 30% and thus greatly fulfilled initial expectations [48]. Pozo et al. analyzed the tax incentives to modernize the energy efficiency of the housing in Spain and the analysis showed that tax benefits are insufficient to promote energy efficiency, especially in those of old construction [49]. Belany et al. dealt with the possibilities the lighting retrofit and the life cycle cost analysis economic analysis

in the process of increasing the energy efficiency of buildings [50]. Furthermore, most prior studies focused on urban existing buildings, commercial buildings [27,31], historical buildings [32], educational buildings [39], and office buildings [41]. Only some of the literature discusses energy-saving renovations to existing rural residential buildings, such as the work of Hu et al. [51], Tahsidoost and Zomorodian [52], Liu et al. [53], Alev et al. [54], and Rocchi et al. [55]. However, they still focused on technical or scheme retrofitting, a cost–benefit analysis of retrofitting and evaluation methods, while ignoring the influence of stakeholders’ willingness to participate in energy-saving renovations to existing rural residential buildings. In particular, energy-saving renovations of existing rural residential buildings do not have the complete policies and regulations that are implemented for urban buildings in China. Moreover, the intention of each stakeholder to participate in energy conservation transformation may only be to maximize their own interests, but it is worth investigating the best way in which to make decisions that can increase the intention of participation.

2.2. Evolutionary Game Theory

Evolutionary game theory is different from the assumption of the completely rational man in traditional game theory, which holds that man is a bounded rationality. The research object of game theory is multiple market participants, and it discusses the dynamic evolution of system groups. In evolutionary game theory, the participating groups have an active learning ability, can constantly choose and try to make mistakes through mutual imitation and learning, and can constantly change the basic behavior strategies of the game players, so as to maximize their own benefits. Smith proposed that the basis of constructing the evolutionary game model was mutation and choice [56]. Mutation refers to the solution to diversity stability in evolutionary games. Choice refers to the process of making choices by learning or imitating in groups and constantly optimizing one’s own choices, that is, the process of generating higher payments [57]. According to the mutation and choice theory in evolutionary game theory, replication dynamic equation and evolutionary stability strategy constitute the core of the evolutionary game model. Copying the dynamic equation is actually a dynamic strategy adjustment mechanism. It is assumed that the game players (insiders) are all bounded, rational people, and the individuals in the group with a lower income than the average will change their strategies and learn from the surrounding group members whose income is higher than their own. Therefore, the probability of each strategy choice of the game players in the group will change accordingly. Evolutionary Stable Strategy (ESS), as another core concept in evolutionary game theory, reflects the stable state of the equilibrium solution of the system. Evolutionary stability strategy thinks that the optimal equilibrium of people’s game is a function to be revised, so evolutionary stability strategy cannot be achieved at the beginning. It can only be achieved through trial and error and learning, and through the repetition of games by players to modify and improve individual strategies. Among the current research, Fan et al. developed an evolutionary game model to analyze the operation mechanism of local governments’ different expenditure preferences regarding the production behavior of industrial polluting enterprises [58]; Liu et al. applied an evolutionary game model to analyze the necessity and effect of orderliness–synergy in the sustainable development of China’s power generation industry during the transition period [59]; Su investigated the evolutionary decision-making process and stable strategies of three stakeholders involved in the construction waste recycling industry based on the evolutionary game model [60]. However, no scholar has thus far employed the evolutionary game model to analyze the behavioral strategies of stakeholders involved in energy-saving renovations of existing rural residential buildings. In this work, we construct a tripartite evolutionary game model to analyze the evolutionary rules and stable strategies of tripartite behaviors regarding energy-saving renovations of existing rural residential buildings, and analyze the influencing factors accordingly.

3. Dilemma Analysis of Energy-Saving Renovations of Existing Rural Residential Buildings

3.1. Positive Externality of Energy-Saving Renovation Market

Positive externality means that the marginal private cost is greater than the marginal social cost, that is, the marginal private benefit is less than the marginal social benefits, such as energy conservation, emission reductions, and low-carbon construction. At present, China has made some achievements in improving energy efficiency, but there is still a long way to go in terms of energy-saving renovations to existing buildings due to strong positive externalities and proneness to “market failure”. In the energy-saving renovation of existing rural residential buildings, participants often only consider the benefits and costs related to their own interests, ignoring all other unrelated factors. For example, rural residents, as users of existing buildings, can not only improve their living standards, reduce building energy consumption, save use and maintenance costs, and benefit their physical and mental health, but also reduce the total energy consumption of the whole society, reduce environmental pollution, and improve the surrounding living environment. However, in the market mechanism, rural residents predominantly care about the maximization of their own interests, instead of the marginal benefits brought to society, since this “extra income” will not bring them extra rewards. In addition, the process of energy-saving renovations will inconvenience residents’ daily life and will increase their economic burden. Rural residents’ attention is drawn to the renovation costs, ignoring the “positive externalities” brought about by energy-saving renovations of existing rural residential buildings to the wider society. As a result, many of them choose to forego energy-saving renovations.

3.2. Market Information Asymmetry

Information asymmetry is a common phenomenon in many economic fields at present. Many participants are involved in energy-saving renovations of existing rural residential buildings, with different interests and unequal amounts of renovation information. For example, when choosing energy-saving renovation technology, rural residents often do not have the ability to distinguish between good and bad, and cannot obtain reliable quality information about whether an energy-saving technology is advanced, economical or feasible. On the other hand, energy-saving service enterprises hold a great deal of relevant information on energy-saving technology, meaning that there is serious information asymmetry regarding the knowledge of energy-saving transformation technology.

In addition, information asymmetry also exists between the government and rural residents, and between the government and energy-saving service enterprises. In this case, the information-superior party will make a self-interested market choice, taking advantage of its information superiority, while the information-inferior party will be unable to make a correct judgment on the energy-saving effect of the purchased products due to the lack of information. Therefore, the information-inferior party will assume that all construction products in the construction market are of low value, and tend to choose construction products with lower prices. To maximize their own profits, the information-superior party will cater to the purchasing behavior of the information-inferior party, and produce building materials of poor quality at a low price, forcing high-quality, energy-saving building materials to withdraw from the market because their manufacturers cannot find suitable trading partners. Ultimately, the result of this is that most of the products left on the market are low-value products, which exemplifies the phenomenon of “inferior products driving out good products” [61,62].

3.3. The Existing Rural Residential Buildings Have a Large Stock That Is Difficult to Transform

Although the majority of building regulations and standards in China are targeting new and future buildings, existing buildings still constitute the largest share of the buildings stock [38]. Energy-saving construction in existing rural residential buildings is the key to building energy-saving work, and has always been a neglected but urgent problem that remains to be solved. In recent years, Chinese people’s living standards have been

greatly improved, accompanied by the rapid increase in building energy consumption. As one of the most important aspects of the total energy consumption in China, more attention should be paid to rural residential building energy consumption [63]. According to the Statistical Bulletin of Urban and Rural Construction in 2016, by 2016, the rural residential building area in China was about 32.32 billion square meters, accounting for 84.4% of the total area of villages and towns in China [64]. With the increase in per capita income in rural areas, the living standards of farmers have gradually improved, and the construction of rural residential buildings has reached an unprecedentedly high level. In 2019, the per capita housing construction area of rural residential buildings in China reached 48.9 m²/person, 9.1 m² more than that of urban residents. The total number of houses has shown a continuously growing trend. As with the improvement in living quality, rural residents have also changed their energy consumption. In rural areas, people used to mainly rely on traditional biomass energy resources, such as firewood and straw [63,65,66], but these are gradually being replaced by commercial energy resources including coal, electricity, liquefied petroleum gas (LPG) and refined oil products, due to the low thermal efficiency and combustion-generated pollution of these biomass resources [63,66,67]. Thus, with the increase in the total number of rural residential buildings, the buildings' energy consumption levels are bound to rise. As a result, this building category is one of the first places in which action should be taken to reduce energy consumption and pollutant emissions [68,69].

4. Subject Game Relationship

The energy-saving renovation of the existing rural residential buildings is a complex systematic project, which involves both collective and individual interests, national interests, enterprise interests and individual interests. Firstly, as the policy maker and supervisor of energy-saving renovations of existing rural residential buildings, the government represents the national interest, and has the highest degree of participation. Secondly, the energy-saving service enterprises, as participants in contracting the energy-saving renovations of existing rural residential buildings, possess the energy-saving renovation technology for the existing rural residential buildings, and are the main representatives of the interests of all enterprises. Thirdly, the rural residents, as the owners and users of the existing rural residential buildings, can benefit from the energy-saving renovations to the existing rural residential buildings, but, at the same time, face an increased cost of living, which affects their personal interests. All three parties are the main participants in the energy-saving renovations of existing rural residential buildings, and this study also focuses on their evolutionary game relationships. As for other auxiliary participants, such as banks, financial institutions, the environmentalists, etc., they have not directly participated in energy-saving renovation of existing rural residential buildings. Their suggestions or financial support can promote energy-saving renovation of existing rural residential buildings, but compared with the government and rural residents as funders and energy-saving service enterprises as designers and constructors, their impact is less. For example, suppose the environmentalists propose that energy-saving renovation of existing rural residential buildings is beneficial to protecting the ecological environment. However, if the government and rural residents do not realize or support it, their proposal will not be effectively solved. On the contrary, if the government and the rural residents are also aware of the importance of energy-saving renovation of existing rural residential buildings, and actively respond to the environmentalists' proposals, but the environmentalists are not involved in the related issues such as who will supervise, who will renovate, and who will bear the cost during the promotion process. These auxiliary participants will be a new field for our research team to further study in the future, but this study will focus on the main participants.

4.1. The Government

In the process of energy-saving renovations of existing rural residential buildings, the government, as the policy maker, shoulders the task of supervision, management and publicity, and regulates the behaviors of other participants by implementing economic incentive policies and administrative supervision, which mainly focuses on the social and environmental benefits brought by energy-saving renovations of existing rural residential buildings. Therefore, as a special participant, the government will pursue the long-term social and environmental benefits of energy-saving renovation, as well as the improvement in people's living standards and social stability.

4.2. Energy-Saving Service Enterprises

At present, the energy-saving renovation market for the existing residential buildings in China takes contract energy management as its main operation mode. The energy-saving service enterprises provide a package of professional energy-saving technical services, including energy-saving condition diagnosis, energy-saving project design, financing, renovation (construction, equipment installation and commissioning) and operation management, etc., for the energy-saving renovation of existing residential buildings. These enterprises are the main suppliers of energy-saving service products and they act as an internal driving force for the development of the energy-saving renovation market of existing residential buildings in China. The energy-saving service enterprises, as practitioners of the energy-saving renovation of existing rural residential buildings, have advanced energy-saving renovation technologies and resources. By signing renovation contracts with the government or rural residents and adhering to the government's incentive policies, they can obtain corresponding benefits according to contract stipulations or by reducing energy-saving renovation costs. In addition, energy-saving service enterprises have relatively complete information on the energy-saving renovation market of existing rural residential buildings, which may lead to more speculation in the process of energy-saving renovation, thus undermining the benign cooperation among energy-saving service enterprises, the government and rural residents. Therefore, the main purpose of energy-saving service enterprises participating in energy-saving renovations of existing rural residential buildings is to standardize their own behaviors and maximize their own interests while weighing the advantages and disadvantages.

4.3. Rural Residents

As users and direct beneficiaries of energy-saving renovations of existing rural residential buildings, residents' willingness to renovate and awareness of energy conservation and environmental protection will affect the development of the energy-saving renovation market and the improvements in the social environment. However, on August 1, 2008, the State Council of the People's Republic of China issued Regulations on Energy Conservation of Civil Buildings, which clearly stipulated that the cost of energy conservation renovations to existing buildings shall be borne jointly by the government and the building owner, and suggested that residents pay from 15 to 20 percent of the renovation cost. Therefore, as individuals, rural residents need to bear part of the cost of energy-saving renovation and accept the impact of the energy-saving renovation process on their normal work and life. Accordingly, residents in existing rural residential buildings are more concerned with their own financial status and the utility brought about by energy-saving transformations than with the maximization of social utility.

5. Game Model Construction

5.1. Basic Assumptions of the Model

Assumption 1. *The government, energy-saving service enterprises and rural residents are all bounded and rational.*

Assumption 2. All participants have two different selection strategies: government behavior strategy set $S_1 = [\text{regulatory incentives, laissez-faire}]$; service enterprise behavior strategy set $S_2 = [\text{providing energy-saving services, not providing energy-saving services}]$; rural residents' behavior strategy set $S_3 = [\text{fulfill energy-saving transformation, refuse energy-saving transformation}]$.

Assumption 3. Based on the assumption of bounded rationality, the probability that the government will supervise and encourage the energy-saving renovation of existing rural residential buildings is x , and the probability of laissez-faire is $1 - x$; the probability of the energy-saving service enterprises choosing to provide energy-saving services is y , and the probability of them choosing not to provide energy-saving services is $1 - y$; the probability of residents performing energy-saving renovations is z , and the probability of them refusing energy-saving renovations is $1 - z$, in which x, y and $z \in [0,1]$.

On the basis of on-the-spot investigation and the literature review, comprehensive analyses of the parameter settings of the cost, benefit and loss variables that affect the government, energy-saving service enterprises and rural residents' decisions are shown in Table 1.

Table 1. Symbols and meanings of parameters.

| Participants | Parameters | Meanings |
|----------------------------------|------------|--|
| Government | S_1 | Subsidies offered by the government to encourage the energy-saving service enterprises that provide standardized energy-saving services. |
| | S_2 | Subsidies offered by the government to village and town residents who voluntarily perform energy-saving transformation |
| | F_1 | Fines imposed by the government on the energy-saving service enterprises that do not provide standardized energy-saving services, where $F_1 > S_1$ |
| | F_2 | Fines imposed by the government on the residents of the existing rural residential buildings who refuse to perform energy-saving renovations, in which $F_2 > S_2$ |
| | R_1 | Under the supervision and encouragement of the government, the social and environmental benefits of the cooperative strategies adopted by the energy-saving service enterprises and the rural residents. |
| | R_2 | Under the government's laissez-faire, the social and environmental benefits produced by the cooperative strategies from the energy-saving service enterprises and the rural residents. |
| | L_1 | Loss of social and environmental benefits caused by speculative behavior or failure to provide energy-saving services by the energy-saving service enterprises. |
| | L_2 | Loss of social and environmental benefits caused by residents' refusal to carry out energy-saving renovations in the existing rural residential buildings. |
| | C_1 | The supervision costs paid by the government when implementing supervision incentives. |
| Energy saving service enterprise | E_1 | The income of the energy-saving service enterprises when they choose to provide standardized energy-saving services and the rural residents perform energy-saving transformations. |
| | C_2 | The costs paid by the energy-saving service enterprises when they choose to provide energy-saving services in a standardized way. |
| | C_3 | Credit loss caused by the energy-saving service enterprises not providing energy-saving services or providing non-standard energy-saving services. |
| | C_4 | Loss caused by residents' refusal to carry out energy-saving renovations in villages. |
| Rural resident | E_2 | The rural residents choose to perform energy-saving transformation and the energy-saving service enterprises provide standardized energy-saving services. |
| | C_5 | The costs paid by residents in the existing rural residential buildings when performing energy-saving renovations. |
| | C_6 | Loss caused by the energy-saving service enterprises refusing to provide energy-saving services or providing non-standard energy-saving services. |

5.2. Construction of Evolutionary Game Revenue Matrix

According to the above-mentioned capital construction conditions and profit and loss parameters, a tripartite game model of the government, energy-saving service enterprises and rural residents is constructed, and an evolutionary game income matrix is obtained, as shown in Table 2.

Table 2. Evolutionary game income matrix.

| Participants | | Rural Resident | | |
|--------------|----------------------------------|--|---|---|
| | | Fulfill Energy-Saving Transformation (z) | Refuse Energy-Saving Transformation (1 - z) | |
| Government | Regulatory incentives (x) | Providing energy-saving services (y) | $R_1 - S_1 - S_2 - C_1,$ $E_1 + S_1 - C_2,$ $E_2 + S_2 - C_5$ | $F_2 - S_1 - L_2 - C_1,$ $S_1 - C_4,$ $-F_2$ |
| | | Not providing energy-saving services (1 - y) | $F_1 - S_2 - L_1 - C_1,$ $-F_1 - C_3,$ $S_2 - C_6$ | $F_1 + F_2 - L_1 - L_2 - C_1,$ $-F_1,$ $-F_2$ |
| | Laissez-faire (1 - x) | Providing energy-saving services (y) | $R_2,$ $E_1 - C_2,$ $E_2 - C_5$ | $-L_2,$ $-C_4,$ 0 |
| | | Not providing energy-saving services (1 - y) | $-L_1,$ $-C_3,$ $-C_6$ | $-L_1 - L_2,$ $0,$ 0 |
| | Energy saving service enterprise | | | |

6. Equilibrium Analysis of Tripartite Evolutionary Game

6.1. Expectation Function Construction

(1) The expected return of the government’s choice of regulatory incentives:

$$\begin{aligned}
 P_{11} &= yz(R_1 - S_1 - S_2 - C_1) + y(1 - z)(F_2 - S_1 - L_2 - C_1) + (1 - y)z(F_1 - S_2 - L_1 - C_1) + \\
 &(1 - y)(1 - z)(F_1 + F_2 - L_1 - L_2 - C_1) \\
 &= yzR_1 + y(L_1 - S_1 - F_1) + z(L_2 - S_2 - F_2) + (F_1 + F_2 - L_1 - L_2 - C_1)
 \end{aligned}
 \tag{1}$$

The expected return of the government’s laissez-faire:

$$P_{12} = yzR_2 = y(1 - z)(-L_2) + (1 - y)z(-L_1) + (1 - y)(1 - z)(-L_1 - L_2) = yzR_2 + yL_1 + zL_2 - L_1 - L_2 \tag{2}$$

Average expected revenue of government:

$$\begin{aligned}
 P_1 &= xP_{11} + (1 - x)P_{12} = xyzR_1 - xyzR_2 - xyS_1 - xyF_1 - xzS_2 - xzF_2 + xF_1 + xF_2 \\
 &- xC_1 + yzR_2 + zL_2 + yL_1 - L_1 - L_2
 \end{aligned}
 \tag{3}$$

Replication dynamic equation of government’s choice of regulatory incentives:

$$F(x) = \frac{dx}{dt} = x(P_{11} - P_1) = x(1 - x)[y(zR_1 - zR_2 - S_1 - F_1) - z(S_2 + F_2) + F_1 + F_2 - C_1] \tag{4}$$

(2) The expected benefits of the energy-saving service enterprises choosing to provide energy-saving services:

$$\begin{aligned}
 P_{21} &= xz(E_1 + S_1 - C_2) + x(1 - z)(S_1 - C_4) + (1 - x)z(E_1 - C_2) + (1 - x)(1 - z)(-C_4) \\
 &= xS_1 + zE_1 - zC_2 - C_4 + zC_4
 \end{aligned}
 \tag{5}$$

Expected benefits of the energy-saving service enterprises choosing not to provide energy-saving services:

$$P_{22} = xz(-F_1 - C_3) + x(1 - z)(-F_1) + (1 - x)z(-C_3) + (1 - x)(1 - z) \times 0 = -xF_1 - zC_3 \tag{6}$$

Average expected income of the energy-saving service enterprises:

$$P_2 = yP_{21} + (1 - y)P_{22} = xyS_1 + yzE_1 + yzC_4 - yzC_2 - yC_4 - xF_1 - zC_3 + xyF_1 + yzC_3 \quad (7)$$

Replication dynamic equation of the energy-saving service enterprises choosing to provide energy-saving services:

$$F(y) = \frac{dy}{dt} = y(P_{21} - P_2) = y(1 - y)[z(E_1 + C_3 + C_4 - C_2) + x(S_1 + F_1) - C_4] \quad (8)$$

(3) The expected income of rural residents who choose to perform energy-saving transformations:

$$P_{31} = xy(E_2 + S_2 - C_5) + x(1 - y)(S_2 - C_6) + (1 - x)y(E_2 - C_5) + (1 - x)(1 - y)(-C_6) \\ = xS_2 + yE_2 + yC_6 - yC_5 - C_6 \quad (9)$$

The expected benefits of rural residents choosing to refuse energy-saving renovations:

$$P_{32} = xy(-F_2) + x(1 - y)(-F_2) + (1 - x)y \times 0 + (1 - x)(1 - y) \times 0 = -xF_2 \quad (10)$$

Average expected income of rural residents:

$$P_3 = zP_{31} + (1 - z)P_{32} = xz(S_2 + F_2) + zy(E_2 + C_6 - C_5) - xF_2 - zC_6 \quad (11)$$

Replication dynamic equation of rural residents choosing to perform energy-saving transformations:

$$F(z) = \frac{dz}{dt} = z(P_{31} - P_3) = z(1 - z)[x(S_2 + F_2) + y(E_2 + C_6 - C_5) - C_6] \quad (12)$$

6.2. Asymptotic Stability Analysis of Evolutionary Game

In the process of energy-saving renovations of existing rural residential buildings, there is serious information asymmetry between the government, energy-saving service enterprises and rural residents in terms of energy-saving renovation information. The three parties in the game will choose the strategies that maximize their own interests in the process of trial and error. When all three parties reach a stable state, all the participants in the game achieve Nash equilibrium through the process of trial and error. According to the stability principle of differential equations, the duplicated dynamic equation of the tripartite subject strategy is simultaneously established. By setting $F(x) = F(y) = F(z) = 0$, we find that there are eight pure strategy equilibrium points in the equation, namely (0,0,0); (1,0,0); (0,1,0); (0,0,1); (1,1,0); (1,0,1); (0,1,1); (1,1,1).

In view of the asymptotic stability of the equilibrium points, this study uses the Lyapunov discriminant method (indirect method) to judge, list the Jacobian matrix (as in Formula (13)), and discuss the stability of the above equilibrium points. Firstly, the Jacobian matrix is calculated as in Formula (14):

$$\begin{bmatrix} \frac{dx/dt}{dx} & \frac{dx/dt}{dy} & \frac{dx/dt}{dz} \\ \frac{dy/dt}{dx} & \frac{dy/dt}{dy} & \frac{dy/dt}{dz} \\ \frac{dz/dt}{dx} & \frac{dz/dt}{dy} & \frac{dz/dt}{dz} \end{bmatrix} \quad (13)$$

$$\begin{bmatrix} (1 - 2x)[y(zR_1 - zR_2 - S_1 - P_1) - z(S_2 + P_2) + P_1 + P_2 - C_1] & x(1 - x)(zR_1 - zR_2 - S_1 - P_1) & x(1 - x)(yR_1 - yR_2 - S_2 - P_2) \\ y(1 - y)(S_1 + P_1) & (1 - 2y)[z(E_1 + C_3 + C_4 - C_2) + xS_1 + xP_1 - C_4] & y(1 - y)(E_1 + C_3 + C_4 - C_2) \\ z(1 - z)(S_2 + P_2) & z(1 - z)(E_3 + C_6 - C_5) & (1 - 2z)[x(S_2 + P_2) + y(E_3 + C_6 - C_5) - C_6] \end{bmatrix} \quad (14)$$

According to Lyapunov's stability theorem, when the characteristic roots of the Jacobian matrix are all negative, the equilibrium point is a stable node. By substituting the equilibrium points into the Jacobian matrix, the eigenvalue corresponding to each equilibrium point can be obtained, as shown in Table 3.

Table 3. Eigenvalues corresponding to pure strategy equilibrium points.

| Equilibrium Point | Eigenvalue | Positive and Negative | Stability | Asymptotically Stable Condition |
|------------------------|--|-----------------------|-----------------|---------------------------------|
| H ₁ (0,0,0) | $\lambda_1 = P_1 + P_2 - C_1$ | – | Stable point | / |
| | $\lambda_2 = -C_4$ | – | | |
| | $\lambda_3 = -C_6$ | – | | |
| H ₂ (0,0,1) | $\lambda_1 = P_1 - C_1 - S_2$ | – | Unstable point | / |
| | $\lambda_2 = E_1 + C_3 - C_2$ | + | | |
| | $\lambda_3 = C_6$ | + | | |
| H ₃ (0,1,0) | $\lambda_1 = -S_1 + P_2 - C_1$ | – | Unstable point | / |
| | $\lambda_2 = C_4$ | + | | |
| | $\lambda_3 = E_3 - C_5$ | + | | |
| H ₄ (0,1,1) | $\lambda_1 = R_1 - R_2 - S_1 - S_2 - C_1$ | Uncertain | Uncertain point | $R_1 < R_2 + S_1 + S_2 + C_1$ |
| | $\lambda_2 = -E_1 - C_3 + C_2$ | – | | |
| | $\lambda_3 = -E_3 + C_5$ | – | | |
| H ₅ (1,0,0) | $\lambda_1 = -P_1 - P_2 + C_1$ | + | Unstable point | / |
| | $\lambda_2 = S_1 + P_1 - C_4$ | + | | |
| | $\lambda_3 = S_2 + P_2 - C_6$ | + | | |
| H ₆ (1,0,1) | $\lambda_1 = S_2 - P_1 + C_1$ | + | Unstable point | / |
| | $\lambda_2 = E_1 + C_3 - C_2 + S_1 + P_1$ | + | | |
| | $\lambda_3 = -S_2 - P_2 + C_6$ | – | | |
| H ₇ (1,1,0) | $\lambda_1 = S_1 - P_2 + C_1$ | + | Unstable point | / |
| | $\lambda_2 = -S_1 - P_1 + C_4$ | – | | |
| | $\lambda_3 = S_2 + P_2 + E_3 - C_5$ | + | | |
| H ₈ (1,1,1) | $\lambda_1 = -R_1 + R_2 + S_1 + S_2 + C_1$ | Uncertain | Uncertain point | $R_1 > R_2 + S_1 + S_2 + C_1$ |
| | $\lambda_2 = -E_1 - C_3 + C_2 - S_1 - P_1$ | – | | |
| | $\lambda_3 = -S_2 - P_2 - E_3 + C_5$ | – | | |

It can be seen from Table 3 that there are three situations in which evolutionary stability can be achieved to meet the eigenvalue requirements of the Lyapunov discriminant method (indirect method).

Scenario 1: If the external conditions remain unchanged, only equilibrium point H₁ (0,0,0) can meet the requirements of Liapunov's discriminant method (indirect method) for the eigenvalue, and other equilibrium points cannot form evolutionary stability, that is, the equilibrium point H₁ (0,0,0) (laissez-faire, no energy-saving service, no energy-saving renovations) is an evolutionary stability strategy. The phase diagram is shown in Figure 1.

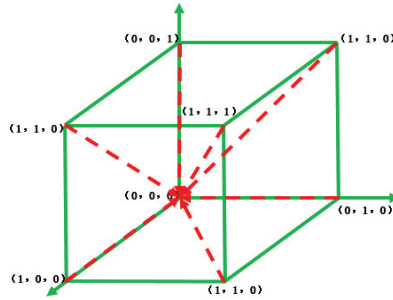


Figure 1. Phase diagram of equalization point H_1 (0,0,0).

Scenario 2: if the external conditions change, i.e., $R_1 < R_2 + S_1 + S_2 + C_1$, then equilibrium points H_1 (0,0,0) and H_4 (0,1,1) can achieve evolutionary stability, that is, H_1 (0,0,0) (laissez-faire, not providing energy-saving services, refusing energy-saving renovations) and H_4 (0,1,1) (laissez-faire, providing energy-saving services, fulfilling energy-saving renovations) are evolutionary stable strategies. The phase diagram is shown in Figure 2.

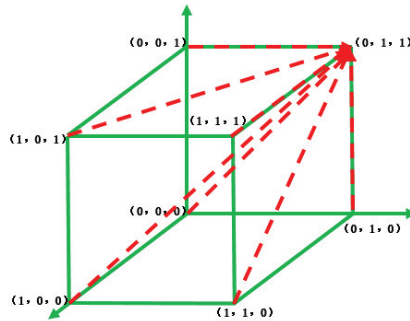


Figure 2. Phase diagram of equilibrium point H_4 (0,1,1) when $R_1 < R_2 + S_1 + S_2 + C_1$.

Scenario 3: if the external conditions change, i.e., $R_1 < R_2 + S_1 + S_2 + C_1$, then equilibrium points H_1 (0,0,0) and H_8 (1,1,1) can achieve evolutionary stability, that is, H_1 (0,0,0) (laissez-faire, not providing energy-saving services, refusing energy-saving renovations) and H_8 (1,1,1) (supervision and encouragement, providing energy-saving services, fulfilling energy-saving renovations) are evolutionary stable strategies. The phase diagram is shown in Figure 3.

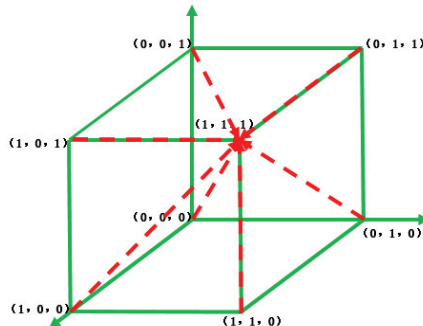


Figure 3. Phase diagram of equalization point H_8 (1,1,1) when $R_1 > R_2 + S_1 + S_2 + C_1$.

However, in the case of a laissez-faire approach by the government, the energy-saving service enterprises choose to provide energy-saving renovation services by themselves, and this provides an ideal state for rural residents to perform energy-saving renovations by themselves, without considering the renovation costs and the impact on their daily lives. According to the evolutionary game hypothesis, the government, energy-saving service enterprises and the rural residents are all bounded and rational. Therefore, under the premise of bounded rationality, all players in the three-party game hope to maximize their interests. Without the support of incentive policies and the guidance of relevant energy-saving renovation policies, low enthusiasm is displayed by energy-saving service enterprises and rural residents in the existing rural residential buildings to actively carry out energy-saving renovations, as is also confirmed in the actual investigation. Therefore, during the energy-saving renovations of existing rural residential buildings, the equilibrium points for realizing the tripartite evolutionary and stable strategy among the government, energy-saving service enterprises and rural residents are mainly H_1 (0,0,0) [laissez-faire, no energy-saving service, no energy-saving renovation] and H_8 (1,1,1) [supervision and encouragement, providing energy-saving service, fulfilling energy-saving renovations]. This study also focuses on these two situations.

7. Numerical Simulation Analysis

To further verify the accuracy of the model and more intuitively show the results that the government, energy-saving service enterprises and rural residents in the existing rural residential buildings achieved, as well as the evolutionary stability under different constraints and strategies, this study uses MATLAB2020A to analyze the evolution of equilibrium points H_1 (0,0,0) and H_8 (1,1,1) from the perspective of cost and benefit, subsidies and penalties, combined with the replication of dynamic equations and assumptions.

7.1. When the Benefits of Energy-Saving Renovations Are Greater than the Cost, the Change in the Initial Proportion of the Three Parties in the Game Will Affect the Evolution Results

Suppose x_0 , y_0 and z_0 represent the initial proportions of the government's choice to implement supervision and incentive strategies, energy-saving service enterprises' choice to provide energy-saving service strategies and rural residents' choice to implement energy-saving transformation strategies, respectively. The initial test time is 0, the evolution end time is 5, and the initial states are (0.1, 0.2, 0.3), (0.4, 0.5, 0.6), (0.7, 0.8, 0.9). $F_1 = 40$, $F_2 = 10$, $S_1 = 30$, $S_2 = 5$, $R_1 = 300$, $R_2 = 180$, $E_1 = 120$, $E_2 = 50$, $C_1 = 60$, $C_2 = 40$, $C_3 = 15$, $C_4 = 8$, $C_5 = 25$, $C_6 = 5$. The stability of the equilibrium point and system evolution results are shown in Figure 4.

It can be found that when the profits of energy-saving renovations are greater than the cost of energy-saving renovations, no matter which initial state the three parties chose, the three parties choose the cooperative strategy H_8 (1,1,1) (supervision and encouragement, providing energy-saving services and performing energy-saving renovations), but the time taken to reach a stable and balanced state differs. Figure 4 shows that when the government, the energy-saving service enterprises and the rural residents choose supervision and encouragement, providing energy-saving services and performing energy-saving transformations with a strategy ratio of 0.1, 0.2 and 0.3, the system reaches an evolutionary stable equilibrium state at around $t = 3.5$. When the initial ratio increases by 0.3 or 0.6, that is, 0.4, 0.5, 0.6 or 0.7, 0.8, 0.9, the system reaches an evolutionary stable equilibrium state at about $t = 2.5$ or $t = 1.8$. This shows that, when the government chooses to implement supervision and incentive strategies for energy-saving renovations of existing rural residential buildings, energy-saving service enterprises choose to provide energy-saving service strategies, and rural residents choose to improve the proportion of energy-saving renovation, this helps to shorten the system evolution and achieve a stable and balanced state, which also helps to stimulate participants' enthusiasm for energy-saving renovations of existing rural residential buildings, and promote the development of energy-saving renovations of existing rural residential buildings.

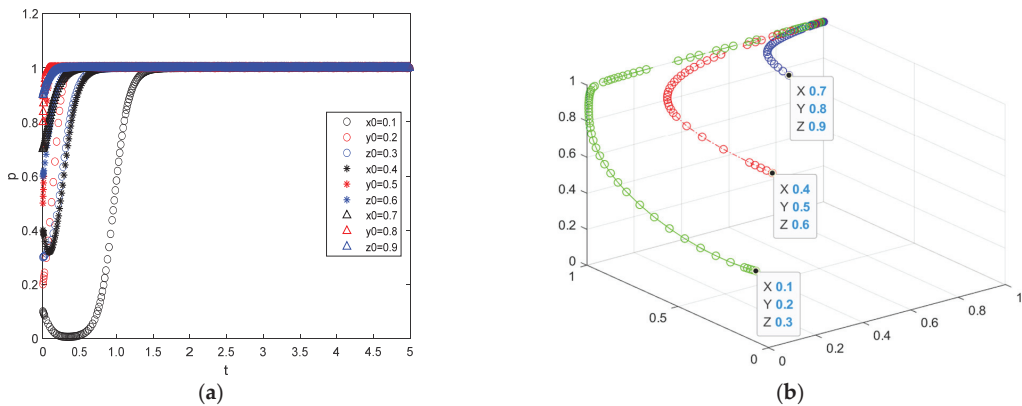


Figure 4. System evolution results under different initial intentions when the benefits of energy-saving renovations outweigh the costs. (a) The time at which the system evolves to a stable state. (b) Evolution rate.

7.2. When the Cost of Energy Savings Is Greater than the Income, the Change in the Initial Proportion of the Three Parties in the Game Will Affect the Evolution Result

It is assumed that the initial test time is 0, the evolution end time is 5, the initial states are (0.1, 0.2, 0.3), (0.2, 0.3, 0.4), (0.4, 0.6, 0.8), and the parameters are $F_1 = 20$, $F_2 = 10$, $S_1 = 15$, $S_2 = 5$, $R_1 = 100$, $R_2 = 60$, $E_1 = 80$, $E_2 = 30$, $C_1 = 160$, $C_2 = 100$, $C_3 = 40$, $C_4 = 10$, $C_5 = 30$, $C_6 = 8$. The stability of the equilibrium point and system evolution results is shown in Figure 5. Through the simulation results, it can be found that when the cost of energy-saving renovation is greater than the profits, the choice strategies of the tripartite government, energy-saving service enterprises and rural residents will not change due to the change in the initial state ratio; they all choose the behavior strategy H_1 (0,0,0), in which energy-saving service enterprises do not provide energy-saving renovation services, and rural residents do not perform energy-saving renovations. The reason for this is that, as the number of rational people is limited, the ultimate goal of the energy-saving service enterprises and the rural residents participating in the energy-saving renovations of existing rural residential buildings is to obtain relevant benefits. Therefore, when the cost of energy-saving renovation is greater than the profits, because the renovations are unprofitable, energy-saving service enterprises and rural residents naturally choose to revoke their participation, and the ultimate behavior strategy of the three parties in the game is uncooperative.

7.3. Influence of Changes in Government Subsidies and Fines on Evolution Results When Energy-Saving Benefits Outweigh Costs

(1) When the benefits of energy-saving renovations are greater than the cost, the government subsidies increase. As shown in Figure 6, assuming that the initial state remains unchanged, the subsidies obtained by energy-saving service enterprises and rural residents voluntarily participating in the energy-saving renovations of existing rural residential buildings under the government's regulatory incentive policy are increased from $S_1 = 30$, $S_2 = 5$ to $S_1 = 35$, $S_2 = 8$. The ultimate behavior strategy of the three parties in the game is still H_8 (1,1,1) (regulatory incentive, providing energy-saving services and performing energy-saving renovation). However, when comparing Figure 4 with Figure 6, due to the improvement in government subsidies, the energy-saving service enterprises and the rural residents can be fully mobilized to participate in energy-saving renovations of existing rural houses, and the benefits of both can be increased. Therefore, the rate at which an evolutionary stable equilibrium state is reached accelerates with the increase in the initial ratio. However, increasing government subsidies will increase the cost of supervision and the incentives for the government to participate in energy-saving renovations of existing

rural residential buildings. Therefore, by comparing Figures 4a and 6a, it can be found that no matter which initial state is chosen, the ultimate behavior strategy of the government is to implement supervision and incentive policies. However, in the same initial state, increasing subsidies will obviously slow down the process and bias the government's behavior strategy towards the implementation of supervision and incentive policies. The time needed for the system to evolve to an equilibrium and stable state is, therefore, also prolonged. By comparing Figure 4b with Figure 6b, it can be found that, in the same initial state, the curvatures of the three curves in Figure 4b are larger than the corresponding three curves in Figure 6b, and the trend rate of (1,1,1) is obviously larger. This conclusion can be verified again in conjunction with Figure 7. When the initial state is the same as (0.4, 0.5, 0.6), and when the government subsidy increases from $S_1 = 30, S_2 = 5$ to $S_1 = 35, S_2 = 8$, although the increase in the subsidy is moderate for energy-saving service enterprises and rural residents, their behavior strategies with regard to providing energy-saving services and performing energy-saving renovations are consistent, and the rate of the curve-biased cooperative strategy is also accelerated. However, raising subsidies has a significant impact on the government, which leads the three parties in the game taking more time to reach an evolutionary stable equilibrium state. The reason for this lies in the increase in subsidies, which increases the cost of government supervision.

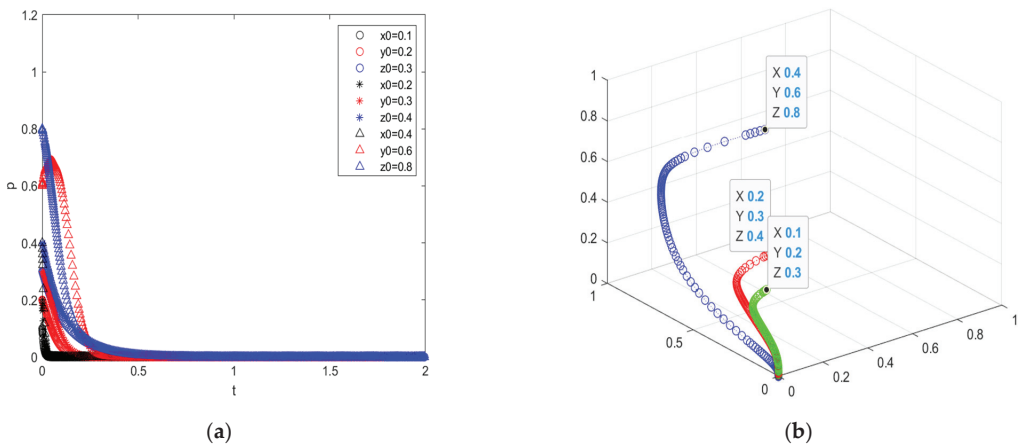


Figure 5. System evolution results under different initial intentions when the cost of energy-saving renovations is greater than the benefit. (a) The time at which the system evolves to a stable state. (b) Evolution rate.

(2) When the income of energy-saving renovations is greater than the renovation costs, the government increases its fines. As shown in Figure 8a, when other conditions are unchanged, and the initial state is (0.4, 0.5, 0.6), government fines will increase from $F_1 = 40$ and $F_2 = 10$ to $F_1 = 60$ and $F_2 = 15$. The ultimate behavioral strategy of the three parties in the game is still H_8 (1,1,1) (supervision and encouragement, providing energy-saving services and performing energy-saving transformations). However, it can also be seen from Figure 8 that when government fines increase, the time needed for the three parties in the game to reach an evolutionary stable equilibrium state is shortened on the premise that the income from energy-saving renovation is still greater than the renovation costs. At the same time, combined with Figure 8b, it can be seen that, when $F_1 = 60, F_2 = 15$, and the initial state increases from (0.2, 0.3, 0.4) to (0.5, 0.6, 0.7), the time needed for the three parties to reach an evolutionary stable equilibrium state is also shortened. When ensuring that the income created by energy-saving renovations is greater than the renovation costs, a moderate increase in government punishment will serve as a warning to energy-saving service enterprises providing standardized energy-saving services and rural residents

who refuse to perform energy-saving renovations. On the premise of the rational person, the energy-saving service enterprises and rural residents will choose to participate in the energy-saving renovations of existing rural residential buildings to ensure the maximization of their own interests after weighing the benefits and costs.

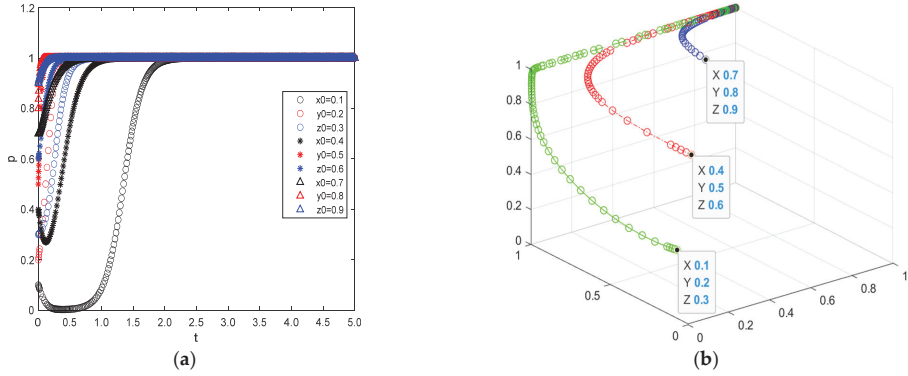


Figure 6. System evolution results under different initial intentions when subsidies are increased. (a) The time at which the system evolves to a stable state. (b) Evolution rate.

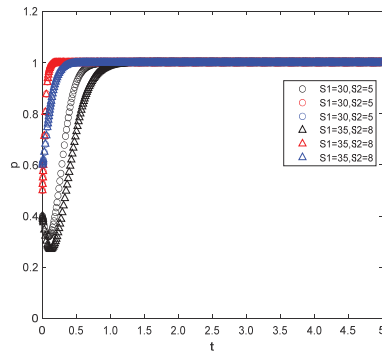


Figure 7. Evolution results of subsidy enhancement system under the same initial state.

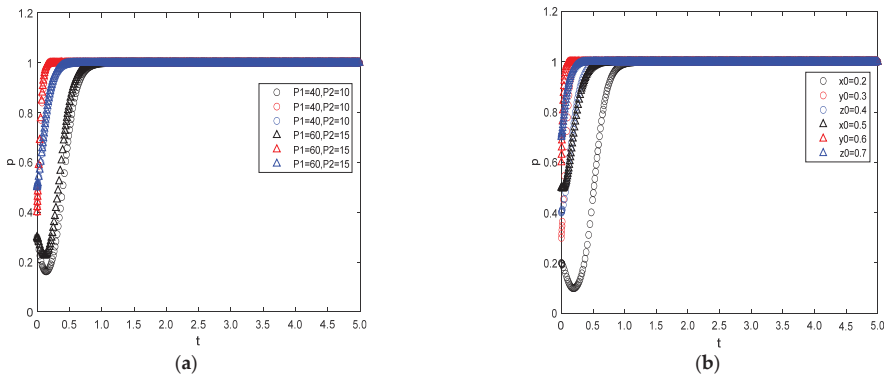


Figure 8. System evolution results under different initial intentions when punishment is increased. (a) The time at which the system evolves to a stable state. (b) Evolution rate.

8. Conclusions

Energy-saving renovations of existing rural residential buildings is an important part of national energy-saving and emission-reduction work, which is of great significance for saving energy, improving the indoor thermal environment, reducing greenhouse gas emissions, and promoting the transformation of development mode in the field of housing, urban–rural construction, and sustainable economic and social development. In this paper, the evolutionary game theory of bounded rationality is used to analyze the evolution law of the behavior strategies of the main bodies involved in energy-saving renovations of existing rural residential buildings, and an evolutionary game model and dynamic decision equations of the three-party behavior bodies of the government, energy-saving service enterprises and rural residents are constructed. By solving the stability points of these dynamic equations, the stability strategies and influencing factors of tripartite actors in different situations are analyzed.

(1) In energy-saving renovations of existing rural residential buildings, as the decision-maker and supervisor, the government's behavior strategies are mainly influenced by supervision cost and incentive policies. When the government does not supervise energy-saving service enterprises and rural residents, they have relatively low willingness to participate in existing rural buildings on the premise of limited rationality, and choose uncooperative behavioral strategies, that is, $H_1 (0,0,0)$ (laissez-faire, providing no energy-saving services, rejecting energy-saving renovations). However, in order to promote energy-saving renovations of existing rural residential buildings, and achieve energy conservation and emission reductions, the government tends to supervise the choice of behavior strategies. Therefore, in the process of supervision, the appropriate fines and subsidies provided by the government to energy-saving service enterprises and rural residents will help to mobilize their enthusiasm to participate in energy-saving transformations, and the behavior strategies of the three parties will tend towards $H_8 (1,1,1)$ (supervision incentives, providing energy-saving services and performing energy-saving transformations).

(2) The energy-saving service enterprises are the information-superior party, and they have complete information on energy-saving technologies. When participating in energy-saving renovations of existing rural residential buildings, their behavior strategies are mainly affected by the benefits and costs of providing standardized energy-saving services, and the loss caused by providing unstandardized energy-saving services. Therefore, when the benefits of participating in energy-saving transformation outweigh the costs, the behavior strategy of the energy-saving service enterprises is to provide standardized energy-saving services, regardless of whether the government subsidies or penalties are increased.

(3) As the inferior-information party, rural residents participate in energy-saving renovations of existing rural residential buildings in the hope of not only improving their living conditions, but also of obtaining certain government subsidies. The main influencing factors are the government subsidies, the loss caused by the unqualified energy-saving services provided by the energy-saving service enterprises and the extra economic expenses incurred during the energy-saving renovations. Hence, when the subsidies provided by the government are greater than the loss caused by unqualified energy-saving services provided by energy-saving service enterprises and the extra economic expenditure generated during the energy-saving transformation, the behavior strategy of rural residents is to carry out energy-saving transformations.

(4) The limitation of the research. The main limitation in this study is the research on the behavior strategy of market participants in energy-saving renovation of existing rural residential buildings only starts with three core participants, and the related auxiliary participants in energy-saving renovation of existing rural residential buildings have not been analyzed. That is because in the process of energy-saving renovation of existing rural residential buildings, the behaviors and strategies of the government, energy-saving service enterprises and rural residents have a relatively large mutual restriction and influence, while other related auxiliary participants may have an influence on a certain participant, but not all of them. For example, the bank's behavior strategy may have a greater impact

on the government and energy-saving service enterprises, but it has a less impact on rural residents. Therefore, the impact on the research results is not great, but it can be a direction for further research in the future.

Therefore, in the process of energy-saving renovations of existing rural residential buildings, the government, energy-saving service enterprises and rural residents, as the three main participants, will choose the most favorable behavior strategies, weighing the government subsidies and fines and the cost of their own participation to maximize their own interests under limited rationality. Therefore, in order to realize the energy-saving renovations of existing rural residential buildings, participants' cooperation is needed. In future research, we will further discuss the impact of increased stakeholder participation in energy-saving renovations of existing rural residential buildings, and analyze their development path, as influenced by various factors.

Author Contributions: Conceptualization, M.-Q.H. and R.-J.L.; methodology, M.-Q.H.; software, M.-Q.H.; validation, R.-J.L.; formal analysis, R.-J.L.; investigation, M.-Q.H. and R.-J.L.; data curation, M.-Q.H.; writing—original draft preparation, M.-Q.H. and R.-J.L.; writing—review and editing, M.-Q.H. All authors have read and agreed to the published version of the manuscript.

Funding: This research was supported by the National Natural Science Foundation of China (NSFC) (Grant No. 71503224) and Fujian Natural Science Foundation (Grant No. 2019J01865). The work described in this paper was also funded by Fujian Social Natural Science Foundation (Grant No. FJ2015C110), University Outstanding Young Scientific Research Talent Cultivation Program Project in Fujian Province, Project of “Scientific Research Climbing Plan” of Xiamen University of Technology (Grant No. XPDKT20034), and China-APEC Cooperation Fund-Study and Training on Marine Spatial Planning in APEC Region (Grant No. 12117000000200012).

Institutional Review Board Statement: Not applicable.

Informed Consent Statement: Not applicable.

Data Availability Statement: Not applicable.

Conflicts of Interest: The authors declare no conflict of interest.

References

1. International Energy Agency (IEA). Data and Statistics. Available online: <https://www.iea.org/data-and-statistics/?country=WORLD&fuel=Energy+consumption> (accessed on 10 August 2021).
2. BP. World Energy Statistics Yearbook. 2021. Available online: <https://www.bp.com/en/global/corporate/energy-economics/statistical-review-of-world-energy.html> (accessed on 10 August 2021).
3. Huang, M.Q.; Wang, B. Evaluating green performance of building products based on gray relational analysis and analytic hierarchy process. *Environ. Prog. Sustain. Energy*. **2014**, *33*, 1389–1395. [CrossRef]
4. Pan, W.; Garmston, H. Compliance with building energy regulations for new-build dwellings. *Energy* **2012**, *48*, 11–22. [CrossRef]
5. Pataki, D.; Emmi, P.; Forster, C.; Mills, J.; Pardyjak, E.; Peterson, T.; Thompson, J.; Dudley-Murphy, E. An integrated approach to improving fossil fuel emissions scenarios with urban ecosystem studies. *Ecologi. Complex*. **2009**, *6*, 1–14. [CrossRef]
6. Li, D.Z.; Chen, H.X.; Hui, E.C.M.; Zhang, J.B.; Li, Q.M. A methodology for estimating the life-cycle carbon efficiency of a residential building. *Build. Environ.* **2013**, *59*, 448–455. [CrossRef]
7. GEF. Malaysia: Buildings Sector Efficiency Project. 2008. Available online: <http://www.thegef.org/gef/sites/thegef.org/files/repository/11-30-09%20ID3598%20-%20Council%20letter.pdf> (accessed on 10 August 2021).
8. Yau, Y.H.; Hasbi, S. A review of climate change impacts on commercial buildings and their technical services in the tropics. *Renew. Sustain. Energy Rev.* **2013**, *18*, 430–441. [CrossRef]
9. Wang, W.M.; Zmeureanu, R.; Rivard, H. Applying multi-objective genetic algorithms in green building design optimization. *Build. Environ.* **2005**, *40*, 1512–1525. [CrossRef]
10. International Energy Agency (IEA). Data and Statistics. Available online: <https://www.iea.org/data-and-statistics/data-browser/?country=CHINA&fuel=CO2%20emissions&indicator=CO2BySource> (accessed on 10 August 2021).
11. International Energy Agency (IEA). Buildings-A source of enormous untapped efficiency potential. Available online: <https://www.iea.org/topics/buildings> (accessed on 10 August 2021).
12. Rhodes, C. The 2015 Paris climate change conference: COP21. *Sci. Prog.* **2016**, *99*, 97–104. [CrossRef] [PubMed]
13. Liu, Z.J.; Zhou, Q.X.; Tian, Z.Y.; He, B.-J.; Jin, G. A comprehensive analysis on definitions, development, and policies of nearly zero energy buildings in China. *Renew. Sustain. Energy Rev.* **2019**, *114*, 109314. [CrossRef]

14. International Energy Agency. Modernising Building Energy Codes to Secure Our Global Energy Future, Policy Pathway Publications, OECD/IEA and United Nations Development Programme (UNDP). 2013. Available online: <https://www.iea.org/publications/freepublications/publication/PolicyPathwaysModernisingBuildingEnergyCodes.pdf> (accessed on 10 August 2021).
15. Sesana, M.M.; Salvalai, G. A review on Building Renovation Passport: Potentialities and barriers on current initiatives. *Energy Build.* **2018**, *173*, 195–205. [\[CrossRef\]](#)
16. Evans, M.; Yu, S.; Song, B.; Deng, Q.; Liu, J.; Delgado, A. Building energy efficiency in rural China. *Energy Policy* **2014**, *64*, 243–251. [\[CrossRef\]](#)
17. National Bureau of Statistics of China. *China Energy Statistical Yearbook*; China National Bureau of Statistics: Beijing, China, 2006.
18. IEA. *Energy Balances of Non-OECD Countries*, 2007th ed.; IEA: Paris, France, 2007.
19. Yu, S.; Eom, J.; Evans, M.; Clarke, L. A long-term, integrated impact assessment of alternative building energy code scenarios in China. *Energy Policy* **2014**, *67*, 626–639. [\[CrossRef\]](#)
20. Ouyang, J.L.; Wang, C.Y.; Li, H.F.; Hokao, K. A methodology for energy-efficient renovation of existing residential buildings in China and case study. *Energy Build.* **2011**, *43*, 2203–2210. [\[CrossRef\]](#)
21. Papadopoulos, A.; Theodosiou, T.; Karatzas, K. Feasibility of energy saving renovation measures in urban buildings: The impact of energy prices and the acceptable pay back time criterion. *Energy Build.* **2002**, *34*, 455–466. [\[CrossRef\]](#)
22. Jakob, M. Marginal cost and co-benefits of energy efficiency investments: The case of the Swiss residential sector. *Energy Policy* **2006**, *34*, 172–187. [\[CrossRef\]](#)
23. Li, J.; Ng, S.T.; Skitmore, M. Review of low-carbon refurbishment solutions for residential buildings with particular reference to multi-story buildings in Hong Kong. *Renew. Sustain. Energy Rev.* **2017**, *73*, 393–407. [\[CrossRef\]](#)
24. Zheng, D.L.; Yu, L.J.; Wang, L.; Tao, J. Integrating willingness analysis into investment prediction model for large scale building energy saving retrofit: Using fuzzy multiple attribute decision making method with Monte Carlo simulation. *Sustain. Citie Soc.* **2019**, *44*, 291–309. [\[CrossRef\]](#)
25. Fan, Y.L.; Xia, X.H. Energy-efficiency building retrofit planning for green building compliance. *Energy Build.* **2018**, *136*, 312–321. [\[CrossRef\]](#)
26. Zhao, J.; Wu, Y.; Zhu, N. Check and evaluation system on heat metering and energy efficiency retrofit of existing residential buildings in northern heating areas of China based on multi-index comprehensive evaluation method. *Energy Policy* **2009**, *37*, 2124–2130. [\[CrossRef\]](#)
27. Ho, M.Y.; Lai, J.H.K.; Hou, H.Y.; Zhang, D. Key Performance Indicators for Evaluation of Commercial Building Retrofits: Shortlisting via an Industry Survey. *Energies* **2021**, *14*, 7327. [\[CrossRef\]](#)
28. Dolšak, J.; Hrovatin, N.; Zorić, J. Factors impacting energy-efficient retrofits in the residential sector: The effectiveness of the slovenian subsidy program. *Energy Build.* **2020**, *229*, 110501. [\[CrossRef\]](#)
29. Morelli, M.; Harrestrup, M.; Svendsen, S. Method for a component-based economic optimisation in design of whole building renovation versus demolishing and rebuilding. *Energy Policy* **2014**, *65*, 305–314. [\[CrossRef\]](#)
30. Oberegger, U.F.; Permetti, R.; Lollini, R. Bottom-up building stock retrofit based on leveled cost of saved energy. *Energy Build.* **2020**, *210*, 109757. [\[CrossRef\]](#)
31. Zheng, L.Z.; Lai, J. Environmental and economic evaluations of building energy retrofits: Case study of a commercial building. *Build. Environ.* **2018**, *145*, 14–23. [\[CrossRef\]](#)
32. Ciulla, G.; Galatioto, A.; Ricciu, R. Energy and economic analysis and feasibility of retrofit actions in Italian residential historical buildings. *Energy Build.* **2016**, *128*, 649–659. [\[CrossRef\]](#)
33. Ouyang, J.L.; Ge, J.; Hokao, K. Economic analysis of energy-saving renovation measures for urban existing residential buildings in China based on thermal simulation and site investigation. *Energy Policy* **2009**, *37*, 140–149. [\[CrossRef\]](#)
34. Wang, X.T.; Lu, M.J.; Mao, W.; Ouyang, J.; Zhou, B.; Yang, Y. Improving benefit-cost analysis to overcome financing difficulties in promoting energy-efficient renovation of existing residential buildings in China. *Appl. Energy* **2015**, *141*, 119–130. [\[CrossRef\]](#)
35. Piccardo, C.; Dodoo, A.; Gustavsson, L. Retrofitting a building to passive house level: A life cycle carbon balance. *Energy Build.* **2020**, *223*, 110135. [\[CrossRef\]](#)
36. Rakhshan, K.; Friess, W.A. Effectiveness and viability of residential building energy retrofits in Dubai. *Build. Engrg.* **2017**, *13*, 116–126. [\[CrossRef\]](#)
37. Yau, Y.; Hou, H.Y.; Yip, K.C.; Qian, Q.K. Transaction Cost and Agency Perspectives on Eco-Certification of Existing Buildings: A Study of Hong Kong. *Energies* **2021**, *14*, 6375. [\[CrossRef\]](#)
38. Liu, X.; Wang, C.C.; Liang, C.Z.; Feng, G.H.; Yin, Z.K.; Li, Z.H. Effect of the energy-saving retrofit on the existing residential buildings in the typical city in northern China. *Energy Build.* **2018**, *177*, 154–172.
39. Pohoryles, D.A.; Maduta, C.; Bournas, D.A.; Kouris, L.A. Energy performance of existing residential buildings in Europe: A novel approach combining energy with seismic retrofitting. *Energy Build.* **2020**, *233*, 110024. [\[CrossRef\]](#)
40. Javid, A.S.; Aramoun, F.; Bararzadeh, M.; Avami, A. Multi objective planning for sustainable retrofit of educational buildings. *Build. Engrg.* **2019**, *24*, 100759. [\[CrossRef\]](#)
41. Charles, A.; Mahid, W.; Ouellet-Plamondon, C.M. Case study of the upgrade of an existing office building for low energy consumption and low carbon emissions. *Energy Build.* **2019**, *183*, 151–160. [\[CrossRef\]](#)
42. Salvalai, G.; Sesana, M.M.; Lannaccone, G. Deep renovation of multi-storey multi-owner existing residential buildings—A pilot case study in Italy. *Energy Build.* **2017**, *148*, 23–36. [\[CrossRef\]](#)

43. Richarz, J.; Henn, S.; Osterhage, T.; Müller, D. Optimal scheduling of modernization measures for typical non-residential buildings. *Energy* **2022**, *238*, 121871. [[CrossRef](#)]
44. Dorota, A.K. Theoretical and real effect of the school's thermal modernization—A case study. *Energy Build.* **2014**, *81*, 30–37.
45. Sadowska, B.; Woroniak, J.P.; Woroniak, G.; Sarosiek, W. Energy and Economic Efficiency of the Thermomodernization of an Educational Building and Reduction of Pollutant Emissions—A Case Study. *Energies* **2022**, *15*, 2886. [[CrossRef](#)]
46. Michalak, P.; Szczotka, K.; Szymiczek, J. Energy Effectiveness or Economic Profitability? A Case Study of Thermal Modernization of a School Building. *Energies* **2021**, *14*, 1973. [[CrossRef](#)]
47. Siuta-Oлча, A.; Cholewa, T. Energy demand for space heating of residential buildings in Poland. In *Environmental Engineering III*; CRC Press: Boca Raton, FL, USA, 2010.
48. Staniūnas, M.; Medineckienė, M.; Zavadskas, E.K.; Kalibatas, D. To modernize or not: Ecological–economical assessment of multi-dwelling houses modernization. *Arch. Civ. Mech. Eng.* **2013**, *13*, 88–98. [[CrossRef](#)]
49. Pozo, M.V.; Bustos, J.P.G. Tax incentives to modernize the energy efficiency of the housing in Spain. *Energy Policy* **2019**, *128*, 530–538. [[CrossRef](#)]
50. Belany, P.; Hrabovsky, P.; Kolkova, Z. Combination of lighting retrofit and life cycle cost analysis for energy efficiency improvement in buildings. *Energy Rep.* **2021**, *7*, 2470–2483. [[CrossRef](#)]
51. Hu, X.Y.; Xiang, Y.M.; Zhang, H.; Lin, Q.; Wang, W.; Wang, H. Active–passive combined energy-efficient retrofit of rural residence with non-benchmarked construction: A case study in Shandong province, China. *Energy Rep.* **2021**, *7*, 1360–1373. [[CrossRef](#)]
52. Tahsildoost, M.; Zomorodian, Z. Energy, carbon, and cost analysis of rural housing retrofit in different climates. *Build. Engng.* **2020**, *30*, 101277. [[CrossRef](#)]
53. Liu, Z.J.; Wu, D.; He, B.J.; Wang, Q.; Yu, H.; Ma, W.; Jin, G. Evaluating potentials of passive solar heating renovation for the energy poverty alleviation of plateau areas in developing countries: A case study in rural Qinghai-Tibet Plateau, China. *Sol. Energy* **2019**, *187*, 95–107. [[CrossRef](#)]
54. Aleva, Ü.; Eskolab, L.; Arumägi, E.; Jokisalo, J.; Donarelli, A.; Siren, K.; Broström, T.; Kalamees, T. Renovation alternatives to improve energy performance of historic rural houses in the Baltic Sea region. *Energy Build.* **2014**, *77*, 58–66. [[CrossRef](#)]
55. Rocchi, L.; Kadziński, M.; Menconi, M.E.; Grohmann, D.; Miebs, G.; Paolotti, L.; Boggia, A. Sustainability evaluation of retrofitting solutions for rural buildings through life cycle approach and multi-criteria analysis. *Energy Build.* **2018**, *173*, 281–290. [[CrossRef](#)]
56. Smith, J.M. The theory of games and the evolution of animal conflicts. *Theor. Biol.* **1974**, *47*, 209–211. [[CrossRef](#)]
57. Yamamoto, H.; Ishida, K.; Ohta, T. Modeling Reputation Management System on Online C2C Market. *Comput. Mathe. Organi. Theory* **2004**, *10*, 165–178. [[CrossRef](#)]
58. Fan, W.; Wang, S.; Gu, X.; Zhou, Z.; Zhao, Y.; Huo, W. Evolutionary game analysis on industrial pollution control of local government in China. *Environ. Manag.* **2021**, *298*, 113499. [[CrossRef](#)]
59. Liu, P.K.; Peng, H.; Wang, Z.W. Orderly-synergistic development of power generation industry: A China's case study based on evolutionary game model. *Energy* **2020**, *211*, 118632.
60. Su, Y.B. Multi-agent evolutionary game in the recycling utilization of construction waste. *Sci. Total Environ.* **2020**, *738*, 139826. [[CrossRef](#)] [[PubMed](#)]
61. Huang, M.Q.; Cui, S.H.; Li, X.F. Analysis on the Influence Factors of Energy-saving Building Product Promotion and Application by Structural Equation Model. *J. Huaqiao Univ.* **2016**, *4*, 447–450. (In Chinese)
62. MHuang, Q.; Lin, R.J. Analysis on the difficulties and countermeasures of energy saving reconstruction of existing rural residential buildings. In Proceedings of the 2020 3rd International Workshop on Environment and Geoscience, Chengdu, China, 20–22 July 2020.
63. He, B.J.; Yang, L.; Ye, M.; Mou, B.; Zhou, Y. Overview of rural building energy efficiency in China. *Energy Policy* **2014**, *69*, 385–396. [[CrossRef](#)]
64. Statistical Bulletin of Urban and Rural Construction in 2016. Available online: https://www.mohurd.gov.cn/gongkai/fdzdgnkr/sjfb/tjxx/tjgb/201708/20170822_232983.html (accessed on 10 August 2021).
65. Wang, X.H.; Feng, Z.M. Rural household energy consumption with the economic development in China: Stages and characteristic indices. *Energy Policy* **2001**, *29*, 1391–1397.
66. Zeng, X.; Ma, Y.; Ma, L. Utilization of straw in biomass energy in China. *Renew. Sustain. Energy Rev.* **2007**, *11*, 976–987.
67. Chang, J.; Leung, D.Y.; Wu, C.Z.; Yuan, Z. A review on the energy production, consumption, and prospect of renewable energy in China. *Renew. Sustain. Energy Rev.* **2003**, *7*, 453–468.
68. Ferrante, A. Energy retrofit to nearly zero and socio-oriented urban environments in the Mediterranean climate. *Sustain. Cities Soc.* **2014**, *13*, 237–253. [[CrossRef](#)]
69. Fotopoulou, A.; Semprini, G.; Cattani, E.; Schihin, Y.; Weyer, J.; Gulli, R.; Ferrante, A. Deep renovation in existing residential buildings through façade additions- A case study in a typical residential building of the 70s. *Energy Build.* **2018**, *166*, 258–270. [[CrossRef](#)]

Review

A Review on the Effect of Mechanical Properties and Durability of Concrete with Construction and Demolition Waste (CDW) and Fly Ash in the Production of New Cement Concrete

Sérgio Roberto da Silva and Jairo José de Oliveira Andrade *

Graduation Program in Materials Engineering and Technology, Pontifical Catholic University of Rio Grande do Sul (PGETEMA/PUCRS), Porto Alegre 90610-900, Brazil; sergio.roberto@acad.pucrs.br

* Correspondence: jairo.andrade@pucrs.br

Abstract: The search for new alternative materials for employment in the construction industry is necessary for more sustainable development. The construction demolition waste (CDW), as well as by-products generated by initiatives, such as slag, fly ash (FA), palm oil fuel ash (POFA), metakaolin (MK), silica fume (SF), and rice husk ash (RHA), are objects of studies in several segments of the civil construction sector. The addition of these wastes to the materials currently used to produce concrete and mortar can be one of the significant efforts to achieve more sustainable construction. The use of these wastes in the construction sector can bring considerable benefits in terms of costs, energy efficiency, and environmental and ecological benefits. Over the years, many types of research have been developed aiming at the possibility of a practical use of CDW as an aggregate and industrial by-product (FA, POFA, MK, SF, RHA) as pozzolans. Based on recent studies, this paper reviews the current state of knowledge about the production of concrete with partial replacement of natural aggregates by recycled aggregates from CDW and the use of fly ash (FA) as pozzolan in partial replacement with Portland cement. This work discussed the following concrete properties: compressive strength, water absorption, chloride penetration, carbonation, and modulus of elasticity.

Keywords: concrete; construction and demolition waste; fly ash; mechanical properties; carbonation

Citation: da Silva, S.R.; Andrade, J.J.d.O. A Review on the Effect of Mechanical Properties and Durability of Concrete with Construction and Demolition Waste (CDW) and Fly Ash in the Production of New Cement Concrete. *Sustainability* **2022**, *14*, 6740. <https://doi.org/10.3390/su14116740>

Academic Editors: Carlos Morón Fernández and Daniel Ferrández Vega

Received: 8 April 2022
Accepted: 21 May 2022
Published: 31 May 2022

Publisher's Note: MDPI stays neutral with regard to jurisdictional claims in published maps and institutional affiliations.



Copyright: © 2022 by the authors. Licensee MDPI, Basel, Switzerland. This article is an open access article distributed under the terms and conditions of the Creative Commons Attribution (CC BY) license (<https://creativecommons.org/licenses/by/4.0/>).

1. Introduction

The increased rate of industrialization and urbanization due to economic and population growth has made the construction industry one of the segments that most consumes natural resources and generates solid waste that negatively impacts the environment. According to Mehta and Monteiro [1], during the most recent 100 years, the total populace has developed from 1.5 to 6 billion people, with almost 3 billion living around cities. It is estimated that the global world population will reach around 10 billion by 2060, which can be attributed to the technological, medical, and logistical advances that have improved living and health standards since the Industrial Revolution [2,3].

Concrete employed in the construction of cities plays a crucial role in socio-economic development. Still, it also has a rather significant adverse effect on the environment and the depletion of natural resources. Over the years, infrastructures have been basically built with concrete, steel, and wood, as well as glass, which are considered the primary materials used in contemporary construction [4]. However, in volume, the most significant manufactured product in the world today is concrete [1], and it is also considered to be the second most consumed material on Earth after water [4].

The construction industry is responsible for significant environmental impacts due to the extraction of raw materials and a considerable portion of the waste generation that negatively influences the environment [5,6]. It is also responsible for generating large amounts of carbon dioxide (CO₂) generated by the cement industries and by the

burning of fossil fuels used in the equipment employed in the extraction and processing of raw materials.

The extraction of raw materials, the processing of materials for civil construction, the construction of buildings, as well as renovations and demolitions, generate solid waste that, when disposed of improperly, can cause various problems, such as the proliferation of disease-carrying agents, the degradation of springs and permanent protection areas, the obstruction of drainage systems, silting up of rivers and streams, and the occupation of roads that degrade the urban landscape [6]. Aiming to use natural resources in a more sustainable way, several researchers have been seeking alternative uses for the solid waste from construction and demolition as a by-product for reuse in the construction industry as brick waste [7,8], ceramic [9,10], glass [11,12], from rubber [13,14], from concrete [15,16], and mixed waste [17,18].

Studies verifying the feasibility of using construction and demolition waste (CDW) as a partial replacement for natural aggregate for concrete production have presented relevant results. The different compositions of CDW directly influence the mechanical properties and durability of concrete [19]. Limbachiya, Meddah, and Ouchagour [20], Lotfy and Al-Fayez [21], and Poon, Kou, and Lam [22] observed that the replacement of coarse aggregate with recycled coarse aggregate at levels lower than 30% does not have a significant adverse effect on concrete performance when compared to natural concrete. According to the authors, CDW, as a more porous aggregate, has a high-water absorption capacity. This water adhered to the recycled aggregate can be used as an internal curing agent, especially for concretes with fly ash that requires longer wet curing for the pozzolanic reaction.

However, the significant variability of existing waste, with different compositions, and physical and mechanical properties, can present negative results due to increased porosity, roughness, and water absorption, which leads to higher a/c ratios, making the cement paste weaker and more porous [19,23–25]. Other studies evaluate the mechanical bonding in the Interfacial Transition Zone between the mortar and the substrate [19,26], which ultimately decreases the compressive strength of the material [10], which limits the use of recycled aggregate with a percentage higher than 30% in structural concrete [27].

The construction sector is also responsible for the generation and release into the atmosphere of large amounts of carbon dioxide (CO₂). Asia alone produces more than 80% of cement in the world and, as a consequence, releases approximately 80% of the CO₂ generated by Portland cement production [4]. According to Meyer [28] and Aprianti [29], the reduction of Portland cement production would be one of the alternatives to reduce the environmental impact. Another way would be the use of by-products generated by industrial processes, agricultural waste, and recycled materials. Among the various types of products that can be used, there is fly ash, which is a by-product generated by thermoelectric plants powered by mineral coal. According to Acar and Atalay [30], many thermoelectric plants were built in the world in a period of 80 years due to the growing demand for electricity generation. It is estimated that the annual global production of fly ash varies between 0.75 and 1 billion tons. Other works have already been performed, employing the fly ash and recycled aggregate in concretes simultaneously [5,17,31–37].

Limbachiya, Meddah, and Ouchagour [20] and Lima et al. [31], observed that the use of fly ash as a partial replacement for Portland cement in the production of concrete improves its durability as well as contributes to the reduction of CO₂ emissions. For a deeper understanding of the influence of fly ash in concrete, Payá et al. [38], Sakai et al. [39], Moon et al. [40], and Shaikh [33] investigated the role of this by-product in cement hydration, as well as the pozzolanic reaction process.

Dabhade, Chaudari, and Gajbhaye [5] verified a slight increase in axial compressive strength in concretes with recycled aggregate and with 10% of fly ash compared to concrete with recycled aggregate only. Lima et al. [31] concluded that the addition of fly ash in concretes with recycled aggregate, in general, improves workability as well as mechanical and durability properties, reducing the harmful effects of recycled aggregate.

The scope of this investigation was to gather and analyze the published information about the effects on the mechanical properties and durability of concretes with construction and demolition waste (CDW) and fly ash (fly ash). Based on this study, it was sought to identify the most suitable composition of concrete mixtures with construction and demolition waste and fly ash to reach a consensus on the most appropriate contents of these wastes to achieve results of mechanical properties and durability closer to the reference concretes. To seek a deeper understanding of the effect of fly ash in concretes with a recycled aggregate, a microstructural analysis was performed in the transition zone of the interface between the aggregate and the paste.

2. Importance of the Study

Considering the search for a solution for the appropriate disposal of waste generated by the construction industry segment, many studies have been developed with the objective of reusing this waste as by-products in order to reduce the consumption of natural resources and, consequently, reduce the negative impacts that this waste can cause to the environment.

In concrete, Portland cement is responsible for 74–81% of total CO₂ emissions, while coarse aggregate is responsible for 13–20% of CO₂ emissions. Fine aggregates generate less equivalent CO₂ as they are not crushed. The mixing of the conventional concrete process with Portland cement ranged only between 0.29 and 0.32 t CO₂-e/m³. It was found that the addition of fly ash is able to reduce between 13 and 15% of CO₂ emissions in concrete mixes [41]. Large amounts of waste from construction and demolition are generated every day by the construction industry, which, inappropriately deposited, can bring great harm to biodiversity. The use of these recycled aggregates in partial replacement of natural aggregates can be essential for the concrete eco-efficiency, as well as producing significant economic advantages [42].

There are already many studies focusing on the reuse of waste from construction and demolition (CDW), as well as waste generated by cement industries, such as fly ash (FA), for the production of mortar and concrete. However, there are few studies employing combined wastes, such as CDW and FA for new concrete production.

Analysis of publications focusing on the production of concrete with a combined use of CDW and FA was performed, initially in English, between January 2007 and December 2021. The databases investigated were ANTE (Abstract in New Technologies and Engineering), ASTM International, Aluminium Industry Abstract, and ACS Journals Search. The keywords used for the search were “concrete” + “fly ash” + “construction and demolition waste” or “concrete” + “fly ash” + “waste concrete aggregate” or “concrete” + “fly ash” + “recycled aggregate”. A total of 259 published articles were found, and their distribution by year is shown in Figure 1.

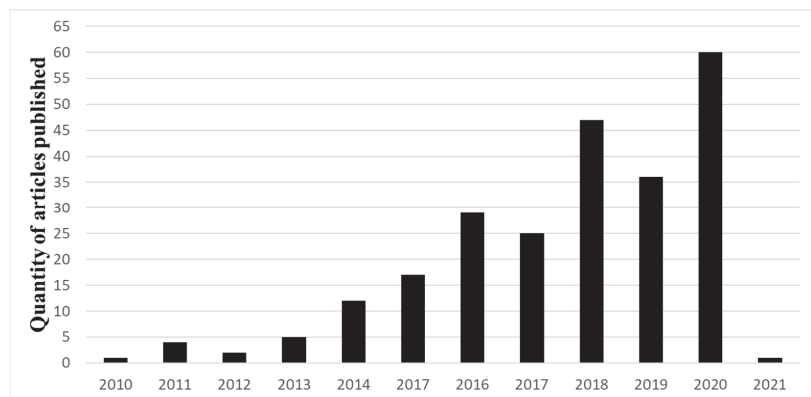


Figure 1. Number of articles published on the use of construction and demolition waste (CDW) with fly ash in concrete production.

Considering the different types of waste generated in the construction and demolition process, as well as the significant variability of these wastes, it is imperative that studies be conducted for a better understanding of the behavior of concretes with combined wastes. In this regard, this literature review is essential to have a more profound knowledge of the use of these wastes in the production of new cement concretes.

The main objective of this work is to establish an innovative concept in order to minimize the effects caused to the environment, which are: reduction of CO₂ emissions caused by cement industries and reduction of natural aggregates extraction from the environment.

3. Factors That Influence the Properties of Concrete with Recycled Aggregate and Fly Ash

3.1. Properties of Construction and Demolition Waste That Influence New Concretes

According to Meddah [4], recycled concrete aggregate is the most abundant waste due to the availability of its origin, which comes from the continuous demolition of old buildings and sidewalks. According to Morales-Martins et al. [43], recycled concrete coarse aggregates that are composed of original aggregate and adhered mortar contain impurities, such as clay bricks and crushed ceramic materials, and gypsum, which contribute to the existence of contaminants. These adhered products negatively influence the physical and mechanical properties of concrete produced with the recycled coarse aggregate [44,45]. Many studies have announced the contrasts between the characteristics of recycled concrete aggregates compared to natural aggregates [46–49], since the physicochemical and mechanical properties of recycled aggregates influence the properties of concrete [50,51], which are presented in the following.

3.1.1. Bulk Density and Water Absorption

Verian et al. [52] observed in their studies that there is a correlation between the water absorption of coarse aggregates and their density because the higher the absorption, the lower the density. The results observed by the authors Verian et al. [52] for recycled coarse aggregates were 14.50%, 12.50%, 12.44%, and 12.10% for water absorption, while for the bulk density, it was 2.05 kg/dm³, 2.18 kg/dm³, 2.21 kg/dm³ and 2.28 kg/dm³, respectively. For natural coarse aggregates, the water absorption was 2.30%, 1.98%, and 1.70%, while the bulk density was 2.69 kg/dm³, 2.74 kg/dm³, and 2.78 kg/dm³, respectively. The same behavior was verified in recycled and natural sands. In natural sand, the absorption was approximately 3.0% and 2.11%, while the specific mass was approximately 2.63 kg/dm³ and 2.68 kg/dm³. Agrela et al. [53] observed the correlation between the concrete content and the dry density of the saturated surface. The results obtained by the authors were: concrete with absorption of 2.48%, 5.1%, 7.49%, 10.2%, and 12.5% have a saturated surface dry density of 2.59 kg/dm³, 2.35 kg/dm³, 2.15 kg/dm³, and 2.08 kg/dm³, respectively.

Kisku et al. [51] also observed, based on their studies, that the presence of the old mortar contained in the recycled aggregate increases the absorption capacity and decreases the specific mass of recycled aggregates compared to natural aggregates. According to da Silva and Andrade [17], the evaluation of water absorption is an essential point that should be considered because the durability performance of concrete is a property of the pervasion qualities of materials, considering the trustworthiness of concrete against aggressive agents.

There are many studies that use different types of waste as aggregate for the production of concretes whose water absorption and bulk density are quite varied. Table 1 presents some comparisons of bulk density and water absorption.

Table 1. Bulk density and water absorption of different types of construction and demolition waste.

| Recycled Aggregate | Bulk Density (kg/m ³) | Water Absorption (%) | Authors |
|--------------------|-----------------------------------|----------------------|---|
| Brick | 974–2548 | 5.96–8.6 | Sharba et al. [54], Zachariah et al. [55], Dang et al. [56] |

Table 1. Cont.

| Recycled Aggregate | Bulk Density (kg/m ³) | Water Absorption (%) | Authors |
|--------------------|-----------------------------------|----------------------|--|
| RCA ¹ | 2265–2560 | 4.0–6.92 | Yang et al. [57], Jian and Wu [58], Sahoo and Singh [59] |
| MRA ² | 1250–2340 | 5.0–8.79 | Martínez et al. [60], Cantero et al. [61], Silva et al. [17], Robalo et al. [42] |
| Rubber | 539–1050 | 0.9–1.7 | Kasmi et al. [62], Yang et al. [57], Feng et al. [63] |
| Glass | 800–880 | 0.002–0.4 | Omoding et al. [64], Balan et al. [65], Yang et al. [66] |

¹ RCA—recycled aggregate concrete, ² MRA—mixed recycled aggregate.

The glass waste had the lowest percentages of water absorption, which ranged between 0.002 and 0.04% when compared to bricks, rubber, and glass. These percentages were also observed in the studies of Penacho, Brito, and Veigas [67]. However, the recycled concrete and mixed aggregates absorbed the most water, ranging from 4.0 to 8.79%. Cantero et al. [61] observed in their studies that the percentages of absorption of these materials varied between 4.49 and 10%. The bricks presented the most significant variation in bulk density (974 to 2548 kg/m³), and this is due to the characteristics of the clays as well as the preparation and burning temperature. The rubbers also present bulk density varying between 539 and 1050 kg/m³. Agrela et al. [53] recommend a classification into three groups for recycled aggregates from construction and demolition, based on the following proportions:

1. Recycled concrete aggregate for mixtures containing less than 10% ceramic and more than 90% concrete;
2. Mixed recycled aggregate for mixtures containing less than 30% ceramic and between 70 and 90% concrete;
3. Ceramic recycled aggregate for mixtures containing more than 30% ceramic and less than 70% concrete.

Based on their studies, the authors concluded that recycled aggregate with many ceramic particles causes an increase in water absorption and a decrease in the density of recycled aggregate. However, Robalo et al. [42] suggest the classification of recycled aggregates by their dry density, resulting in four classes:

- (a) Class A—dry density between 2400 and 2600 kg/m³;
- (b) Class B—dry density between 2100 and 2300 kg/m³;
- (c) Class C—dry density between 1800 and 2000 kg/m³;
- (d) Class D—dry density lower than 1800 kg/m³.

The classification was generated from a relative decrease in compressive strength of concrete with recycled aggregate obtained through the study of Robalo et al. [42], and some researchers. According to Robalo et al. [42], this classification allows for the estimation of the minimum compressive strength of the concretes based on the substitution content of recycled aggregate.

All wastes present variations in bulk density and water absorption. This variation is closely linked to the feasibility of the compositions of materials contained in the waste (RCA, RMA), the type and combination of materials for production (glass, rubber), as well as the selection, handling, and firing processes of ceramic materials.

3.1.2. Interfacial Transition Zones (ITZ)

Recycled aggregate is formed of two Interfacial Transition Zones (ITZ), one between the natural aggregate and the old cement matrix and the other between the old cement matrix and the new cement matrix [68–70]. A schematic diagram of the Interfacial Transition Zones (ITZ) in recycled concrete aggregate is presented in Figure 2.

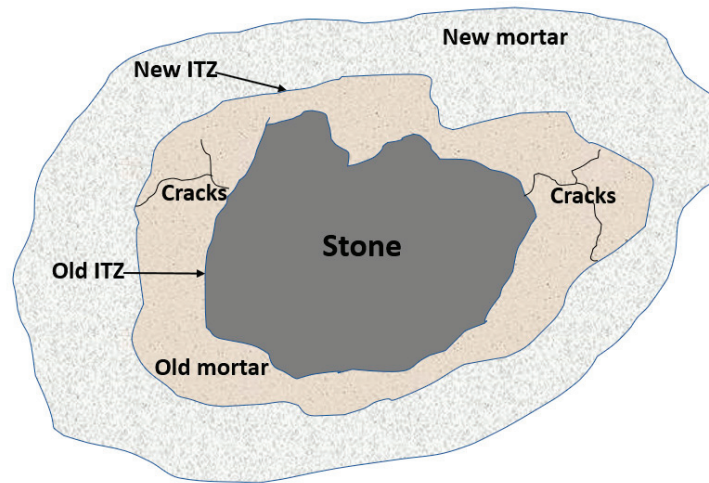


Figure 2. Schematic diagram of the old and new ITZ.

The old ITZ makes the microstructure of the concrete more brittle due to higher porosity and cracking; thus acting as the weakest link [49]. The method of crushing the source concrete has been observed in order to reduce the density of cracking in the old Interfacial Transition Zone (ITZ) [49]. According to Xiao et al. [69], the thickness of the old and new ITZ are in the same order of magnitude, with the new ITZ being thicker. It has been found that the increased ratio of mechanical properties, with respect to the modulus of elasticity and strength, of the old ITZ to the cement matrix, results in higher strength but lower ductility [71]. Zhao et al. [26] and Zhang et al. [72] suggest a third ITZ in the recycled aggregate.

The first ITZ is between the new aggregate and the new mortar, the second ITZ is located between the old mortar and the new mortar, and the third ITZ is between the old mortar and the new aggregate. According to the authors, the third ITZ presents stability in its mechanical properties; however, the addition of recycled aggregate in partial replacement of natural aggregate in concrete, Zhao observed in his studies, not only decreases the mechanical properties, such as mechanical strength and modulus of elasticity, but also decreases its durability, including chloride resistance. According to Zhang [72], the ITZ is characterized by its high porosity, high water permeability, and high diffusion coefficient. Consequently, the ITZ allows the ingress of harmful substances from the external environment, and the reaction between SO_4^{2-} and C-S-H tends to form first in the transition zone between the paste and the substrate, providing an earlier expansion in this zone than in other phases of the material. This expansion over time may be the key to understanding the macroscopic deterioration of concrete under external sulfate attack.

One of the methods employed to improve the microstructure of recycled concrete aggregate is the coating of aggregates with pozzolanic materials [73], and the Pozzolanic material that will be discussed next is fly ash.

3.1.3. Effect of the Recycled Aggregate Size on Strength and Elastic Modulus Properties

Kang and Weibin [74] developed a study to assess the impact of the recycled aggregate diameter on the mechanical properties of concrete (compressive strength and modulus of elasticity). The authors use three different diameters (5–15 mm, 15–20 mm, and 20–30 mm) of recycled aggregate. In this study, two types of recycled aggregate were used, one being crushed in the laboratory and the second crushed in a large crushing plant. It was observed that the larger the diameter of recycled aggregates, the greater the compressive strength. According to the authors, strength gain is related to the lower mortar content adhered to larger diameter aggregates when compared to smaller diameter aggregates. It was

observed that the control concrete elastic modulus was higher than the concrete elastic modulus with a recycled aggregate. However, the authors noted that concretes' modulus of elasticity with different diameters of recycled aggregate is closely linked to a variation in compressive strength performance. Musa and Saim [75] analyzed the compressive strength of concrete with natural coarse aggregate of different sizes (10 mm and 20 mm). The same behavior was observed by the authors, that the larger the particle size, the greater the compressive strength.

3.2. Fly Ash

The size and shape of the fly ash particles have a relevant effect on the binder properties (cement-waste ash). The pozzolanic reactivity is directly related to the fineness of the fly ash because the more significant the surface area, the higher the Pozzolanic Index [76,77]. Studies show that the smaller the fly ash particles, the higher the mechanical strength [77,78]. Furthermore, according to Blissett and Rowson [79], the chemical composition of fly ash has traditionally been the basis for evaluating its suitability for use as a cement replacement material. Another inherent factor in the properties of fly ash is, besides the physical and chemical characteristics, the crystalline structure in the hydration process [80].

There is a classification established by Ramachandran [81] for fly ash based on the amount of CaO. Fly ash with CaO contents below 10% is classified as pozzolanic material. Fly ash that has contents equal to or greater than 10% is classified as cementing materials. According to the author, fly ash consists predominantly of silicon oxide (SiO_2), calcium oxide (CaO), in addition to aluminum oxide (Al_2O_3), and iron oxide (Fe_2O_3). The amount of SiO_2 and CaO in the system influences the composition of the hydrate, as the greater the amount of SiO_2 , the smaller CaO/ SiO_2 ratio of the hydrates, that is, the lower the alkali-silica reaction due to the lower alkalinity of the pore solution [82]. According to Garzia et al. [83], an alkali-aggregate reaction, more precisely an alkali-silica reaction, can cause damage, such as the appearance of micro-cracks in concrete as well as loss of mechanical integrity properties and durability, which may even compromise the functionality of a structural part.

According to Mehta [84], the pozzolanic fly ash reaction compared to Portland cement is slower. Fly ash Oxides, when reacting with water and $\text{Ca}(\text{OH})_2$, result in a layer of C-S-H around the particle, making it difficult to access the innermost oxides. As a result, the hydration pozzolanic reaction forms more slowly; thus slowing down the resistance development. Concretes with fly ash addition, in partial replacement to Portland cement, may have lower mechanical strength compared to conventional ones at younger ages. However, the fly ash addition in partial replacement to Portland cement tends to reduce the effect of the alkali-aggregate reaction, which occurs between cement alkalis and reactive aggregates in the presence of moisture.

3.2.1. Effect of Fly Ash on the Compression, Tensile and Flexural in Concretes

When fly ash, cement, and water are mixed, silica (SiO_2) and alumina (Al_2O_3) progressively react with calcium hydroxide ($\text{Ca}(\text{OH})_2$), which is formed by the cement hydration process; thus producing the calcium silicate hydrate, known as secondary C-S-H. This reaction reduces the calcium hydroxide content and consequently reduces the concrete compressive strength. However, the cement hydration process allows the SiO_2 and Al_2O_3 reaction from the fly ash. The fly ash pozzolanic reaction depends on the $\text{Ca}(\text{OH})_2$ concentration, so it can be stated that the higher the $\text{Ca}(\text{OH})_2$ concentration, the higher the pozzolanic reaction rate [85]. The production of secondary C-S-H at older ages will depend on the $\text{Ca}(\text{OH})_2$ concentration, as the higher the concentration, the longer the pozzolanic reaction time [86]. The flexural strength exhibits similar behavior to the compressive strength. Tensile strength, on the other hand, depends on the shear zone of the interfaces between the paste and the substrate, which, in turn, improves with curing time. This improvement is closely linked to the fly ash pozzolanic reaction [85].

3.2.2. Bulk Density and Water Absorption

The Brazilian Standard NBR 12653/2014 classifies fly ash as class “C”, which is produced by burning mineral coal in thermoelectric power plants. However, the international standard ASTM C618:2012 classifies fly ash in “C” and “F”. Class “F” is produced by burning anthracite or bituminous coal and presents the exact limits of chemical compounds as the Brazilian standard (Table 2). Class “C” is produced by burning lignite or sub-bituminous coal that contains a combination of chemicals ($\text{SiO}_2 + \text{Al}_2\text{O}_3 + \text{Fe}_2\text{O}_3$) between 50% and 70%.

Table 2. Chemical characteristics required by ABNT NBR 12653: 2014 class “C” and by international standard ASTM C618:2012 class “F”.

| Properties (%) | ABNT NBR 12653:2014 | ASTM C 618:2012 | |
|--|------------------------|-----------------|-------------|
| | | Class C | Class F |
| $\text{SiO}_2 + \text{Al}_2\text{O}_3 + \text{Fe}_2\text{O}_3$ | ≥ 70.0 | ≥ 50.0 | ≥ 70.0 |
| SO_3 | ≤ 5.0 | ≤ 5.0 | ≤ 5.0 |
| Humidity (%) | ≤ 3.0 | ≤ 3.0 | ≤ 3.0 |
| Loss to fire | ≤ 10.0 | ≤ 10.0 | ≤ 10.0 |
| Alkalis available in Na_2O | ≤ 1.5 | ≤ 1.5 | ≤ 1.5 |
| Retained in the sieve 45 μm | $\leq 20\%$ | $\leq 34\%$ | $\leq 34\%$ |

Studies show that there is a significant variation in the number of oxides within the same class of fly ash. This variation is associated with its origin (characteristic of the coal) as well as the different forms of the process (calcination). Table 3 presents the variations of the oxides present in fly ash according to the literature.

Table 3. Range of oxides present in fly ash, as presented in the literature.

| Oxides | Class C (%) | Class F (%) | Authors |
|-----------------------------------|-------------|-------------|---------------------|
| CaO | 16.28–29.21 | 0.87–13.52 | [25,76,87–94] |
| SiO_2 | 27.05–37.67 | 49.2–70.70 | [25,76,87–94] |
| Al_2O_3 | 13.44–21.07 | 16.36–33.7 | [25,76,87–94] |
| Fe_2O_3 | 4.42–6.58 | 2.87–14.72 | [25,76,87–94] |
| MgO | 1.48–6.22 | 0.08–4.57 | [25,76,87–94] |
| K_2O | 0.35–1.25 | 0.58–2.16 | [25,76,88,89,91–94] |
| Na_2O | 0.33–1.91 | 0.0–2.82 | [25,76,88,91–94] |
| $\text{Na}_2\text{O}_{\text{eq}}$ | 0.50–1.43 | 1.16–4.24 | [76,87–89,93,94] |
| SO_3 | 1.43–7.65 | 0.25–1.47 | [25,76,87–89,91–94] |
| LOI | 0.12–15.73 | 0.49–4.01 | [25,76,87–90,92,94] |

Based on the Texas Department of Transportation database, the oxide content variations of approximately 5500 fly ash samples from 36 plants in and outside Texas were analyzed, and authors Du and Lukefahr [95] observed that the oxide contents of ASTM class F fly ash were more variable than those of class C fly ash. The authors observed that the main differences between class C and class F fly ash are CaO and SiO_2 , and class C fly ash has high CaO content, being mainly compounded with more than 25%. The CaO concentration in class C fly ash is higher than in class F fly ash, which was also observed by Oey et al. [96]. Already, according to the authors, Al_2O_3 and Fe_2O_3 showed very close results. According to Aboustait et al. [97], most of the particles of Class C fly ash have the highest contents of $\text{CaO} + \text{MgO} + \text{Na}_2\text{O} + \text{K}_2\text{O}$ than those of Class F fly ash. On the other hand, most of the particles of Class F fly ash have higher contents of $\text{SiO}_2 + \text{Al}_2\text{O}_3$, which is mainly due to the higher SiO_2 content in the particles of Class F fly ash.

Oey et al. [96] performed an alkali–silica reaction durability index analysis to verify the performance of fly ash in concretes, SiO_2 , Fe_2O_3 , Al_2O_3 , CaO, and equivalent alkali contents were used for calculation purposes. The alkali–silica reaction is an internal reaction between alkalis, such as Na^+ and K^+ , and hydroxyl ions (OH^-) of the cementitious material

and reactive silica in some aggregates, and the product of the reaction is an alkaline silica gel that has a high capacity to absorb water molecules from pore solution as well as from external sources [98]. The durability index of class C fly ash showed an average of 24.6, while that of class F fly ash was 51.3 [95]. According to Du, Lukefahr, and Naranjo [95], the use of fly ash in concrete can be more viable and productive if its durability index is considered.

According to Wright, Shafaatiann, and Rajabipour [93], for a reduction of the alkali-silica reaction expansion to occur, for class C fly ash with 27.3% CaO, it was necessary to replace 31% Portland cement, while for class F fly ash with 13.5% CaO, 18% replacement content was required. The reduction of the alkali-silica reaction occurs due to the decrease in alkalinity ([OH⁻]) of the pore solution, significantly decreasing the ionic diffusion coefficient of mortars, which is due, in part, to the reduction of porosity when Portland cement is replaced by fly ash of a lower density, and, in part, due to the pozzolanic reaction promoted by the high temperature and alkalinity of the system [94].

3.2.3. Physical and Mineralogical Properties of Fly Ash

According to the Brazilian Standard NBR 12653/2014 and the international standard ASTM C618:2012, the physical properties should be in accordance with the requirements established according to Table 4.

Table 4. Physical requirements for fly ash established in Brazilian (NBR 12653/2014) and international standards (ASTM C618:2012).

| Properties (%) | ABNT NBR 12653:2014 | ASTM C 618:2012 | |
|---|------------------------|-----------------|---------|
| | | Class C | Class F |
| Retained in the sieve 45 µm (% max.) | 34 | 34 | 34 |
| Pozzolanic activity Index at 28 days (% min.) | 75 | 75 | 75 |
| Required water (% max.) | 110 | 105 | 105 |

A high amount of coarse particles ($\varnothing > 1 \mu\text{m}$) causes an irregular distribution of the material and leads to high macroporosity [99]. However, finer particles tend to reduce water absorption due to the refinement of the capillary pores of the concretes [17].

Due to the employment of more advanced characterization techniques, such as scanning electron microscopy (SEM) imaging as well as energy-dispersive X-ray spectroscopy (EDS), it is possible to identify the morphology and the chemical hydration products formed. These techniques are widely employed for performing visual analysis to observe numbers and ranges of chemical compositions [17,92,99,100]. Through these applied techniques, it was observed that the fly ash used in the study of da Silva and Andrade [17] presented spherical and flat shapes while the Portland cement presented irregular and rough shapes.

For higher levels of fly ash incorporation, the workability of concrete increases due to the spherical and smooth shape of the particles that influence the rheological properties of the cement paste, causing a reduction in the water requirement [101]. By scanning electron microscopy (SEM), Tosun-Celikoglu et al. [92] noted that the particle size of class F fly ash is finer than that of class C fly ash particles.

The automated scanning electron microscopy (ASEM) technique employed by Aboustit et al. [97], allowed us to verify that the fly ash particles larger than 5.0 µm were more spherical than the smaller particles, and the particles with sizes between 0.1 and 1.0 µm were the least spherical. The authors also noted that class C fly ash seems to show a wider range of size distribution than those of class F. Furthermore, the pozzolanic reactivity is directly proportional to the fineness of the fly ash, as the finer the fly ash, the higher the Pozzolanic Index [76,102]. Tkaczewska [102] observe in his study that the finer fly ash (0–16 µm) increases the degree of depolymerization of SiO₄, which is responsible for the increase of pozzolanic reactivity.

The X-ray diffraction (XRD) technique is fundamental for knowing the crystalline structure and microstructure of a material to understand its properties. Silva and Andrade [30] used XRD on a fly ash particle for sample analysis. The authors observed a high concentration of quartz, calcite, and muscovite/illite as crystalline phases and amorphous phase content throughout the fly ash particles. Ma, Hu, and Ye [103] also used XRD in their studies, where they observed that the main crystalline phases of fly ash were quartz (SiO_2) and mullite ($3\text{Al}_2\text{O}_3, 2\text{SiO}_2$).

Durdzinski et al. [104] observed that the fly ash in studies was made of glassy material of amorphous nature, and because of that, the constituent materials largely include chemical reactions. According to the authors, fly ash with elevated amorphous substance is more viable in increasing the pozzolanic reaction.

4. Influence of Fly Ash Replacement in Concretes with Construction and Demolition Waste (CDW) in Concrete Properties

Feasibility studies of the use of construction and demolition waste (CDW) as a substitute for natural aggregate for the production of concrete in small quantities show promising results. However, the significant variability of existing waste, with different compositions, and physical and mechanical properties, can present adverse effects due to increased porosity, roughness, and water absorption that leads to higher w/c ratios, making the cement paste weaker and more porous [19,23–25]. To minimize the adverse effects regarding the significant variability of CDW, many studies have been adding fly ash as a partial replacement for Portland cement and will be presented as follows.

4.1. A General Overview

Many studies have investigated the influence of the use of fly ash and CDW on the physical–mechanical properties of concretes, showing that the results improve the mechanical properties and durability in ages longer than 28 days, as presented in Table 5.

Table 5. Some recent studies on the mechanical and durability properties of concrete with fly ash.

| Properties | RCD Types | Replacements | Authors |
|----------------------|------------------|---|---------------------------|
| Compressive strength | RCA ¹ | (RA ⁴ , 0% 50% 100%) (FA ⁵ , 0% 30% 60%) | Kurad et al. [37] |
| | MRA ² | (RA ⁴ , 0% 25% 50% 75% 100%) (FA ⁵ , 0% 15% 20% 25% 30%) | da Silva and Andrade [17] |
| | RCA ¹ | (RA ⁴ , 0% 100%) (FA ⁵ , 0% 20% 30%) | Sunayana and Barai [34] |
| | RCA ¹ | (RA ⁴ , 0% 25% 50%) (FA ⁵ , 0% 10%) | Shaikh [33] |
| | RCA ¹ | (RA ⁴ , 0% 50% 100%) (FA ⁵ , 0% 25% 35% 55%) | Kou and Poon [32] |
| | RMA ³ | (RA ⁴ , 0% 30% 40% 50%) (FA ⁵ , 0% 15%) | Zong, Fei, and Zhang [7] |
| Tensile strength | MRA ² | (RA ⁴ , 0% 25% 50% 75% 100%) (FA ⁵ , 0% 15% 20% 25% 30%) | da Silva and Andrade [17] |
| | RCA ¹ | (RA ⁴ , 0% 25% 50%) (FA ⁵ , 0% 10%) | Shaikh [33] |
| | RCA ¹ | (RA ⁴ , 0% 50% 100%) (FA ⁵ , 0% 25% 35% 55%) | Kou and Poon [32] |
| | RCA ¹ | (RA ⁴ , 0% 100%) (FA ⁵ , 0% 20% 30%) | Sunayana and Barai [34] |

Table 5. Cont.

| Properties | RCD Types | Replacements | Authors |
|-------------------------------|------------------|---|---------------------------|
| Modulus of elasticity | RCA ¹ | (FA ⁴ , 0% 100%) (FA ⁵ , 0% 20% 30%) | Sunayana and Barai [34] |
| | RCA ¹ | (RA ⁴ , 0% 50% 100%) (FA ⁵ , 0% 25% 35% 55%) | Kou and Poon [32] |
| Carbonation coefficient (k) | RCA ¹ | (RA ⁴ , 0% 50% 100%) (FA ⁵ , 0% 25% 35% 55%) | Kou and Poon [32] |
| | RCA ¹ | (RA ⁴ , 0% 20% 40% 60% 80%) (FA ⁵ , 0% 10% 20% 30%) | Geng and Sun [35] |
| | MRA ² | (RA ⁴ , 0% 25% 50% 75% 100%) (FA ⁵ , 0% 15% 20% 25% 30%) | da Silva and Andrade [17] |
| Sulfate resistance | RMA ³ | (RA ⁴ , 0% 30% 40% 50%) (FA ⁵ , 0% 15%) | Zong, Fei, and Zhang [7] |
| Permeability to chloride ions | RCA ² | (RA ⁴ , 0% 25% 50%) (FA ⁵ , 0% 10%) | Shaikh [33] |
| | RCA ² | (RA ⁴ , 0% 30% 60% 100%) (FA ⁵ , 0% 15% 30%) | Sim and Park [36] |
| Water absorption | MRA ³ | (RA ⁴ , 0% 25% 50% 75% 100%) (FA ⁵ , 0% 15% 20% 25% 30%) | da Silva and Andrade [17] |
| | RCA ¹ | (RA ⁴ , 0% 25% 50%) (FA ⁵ , 0% 10%) | Shaikh [33] |
| | RMA ³ | (RA ⁴ , 0% 30% 40% 50%) (FA ⁵ , 0% 15%) | Zong, Fei, and Zhang [7] |

¹ RCA = recycled concrete aggregate; ² MRA = mixed recycled aggregate; ³ RMA = recycled masonry aggregate
⁴ RA = recycled aggregate; ⁵ FA = fly ash.

In general, the addition of fly ash in partial replacement of Portland cement presents a positive influence with respect to mechanical strength and durability in concretes with recycled aggregate from construction and demolition when compared to concretes with recycled aggregate and without fly ash at higher ages of healing. Kamal et al. [105] analyzed sample data where more than a thousand pieces of information was extracted from the literature, and through the nonlinear model, the effect of fly ash on the resistance properties of concrete was investigated. The study involved high cement replacement content by fly ash (up to 70%), different water/binder ratios, and a 90-day curing period. The authors observed, through mathematical models, that there is a good correlation between compressive strength and the water/cement ratio in cured concrete up to 90 days without fly ash, but no correlation was verified between compressive strength and water/binder ratio in concrete with cured fly ash up to 90 days. A good correlation was also verified between compressive strength and tensile and bending strength. According to the authors, compressive strength can be calculated through mathematical models constructed through the suggested methodology.

According to Limbachiya, Meddah, and Ouchgour [20], whenever recycled aggregate (RA) is added to concrete with 30% fly ash in partial replacement to natural aggregate, regardless of the content to be replaced, the tendency of durability and mechanical strength is to decrease, and shrink drying is increased.

According to Limbachiya, Meddah, and Ouchagour [20], as the content of substitution of natural coarse aggregate by recycled concrete aggregate increases (ARC), the strengths (compression and traction), and the modulus of elasticity decrease. On the other hand, shrinkage by drying increases. It is a consensus among all authors that the use of recycled aggregate in concrete decreases the mechanical properties and durability, but with replacement levels below 30% of natural aggregate by the recycled aggregate, the adverse effects are not so significant. The addition of fly ash in small proportions in concretes with recycled

aggregate tends to minimize the adverse effects, but the impact of fly ash is observed in concretes with higher ages, where, according Lorca et al. (2014), the fly ash reacts with calcium hydroxide released by the cement hydration product in older ages.

Some studies have developed mathematical models to estimate the mechanical strength of concrete with pozzolanic materials as well as with recycled aggregate [105–107]. Shahr Piro et al. [105] used five different models to estimate the compressive strength of concrete with carbon nanotubes. Therefore, the artificial neural network model, M5P tree model, nonlinear regression model, and multilinear model have been used. The variables used in the model were curing time in days, coarse aggregate content, water/binder ratio, cement intake in kg/m^3 , and carbon nanotube. As a methodology, the authors used information such as the reference concrete compressive strength and concrete with different contents of carbon nanotube. Based on sample data with 282 records analyzed statistically, the authors developed a multiscale model to estimate the compressive strength of the concretes. Another very relevant study developed by the authors [107] was the analysis of the correlation between compressive strength and electrical resistivity of concrete slag residue. The models used for this study were the multi logistic regression model, complete quadratic model, M5P tree model, and neural network. Barkhordari et al.'s [106] mathematical models have been used to estimate the compressive strength of concrete with fly ash. The models used were super apprentice algorithm, simple average, weighted average, and stacking employed. The database contained information from 270 samples that were collected and preprocessed. Next, some recent research on the use of fly ash in concretes with recycled aggregate will be presented.

4.2. Mechanical Properties

4.2.1. Compressive Strength

Thus, concretes with the addition of fly ash in partial replacement to Portland cement may present lower compressive strength compared to conventional ones in the smallest ages. Below will be a few studies of the combined effect of different levels of fly ash and with 50% recycled aggregate in the compressive strength in concrete at 28 days of curing (Figure 3).

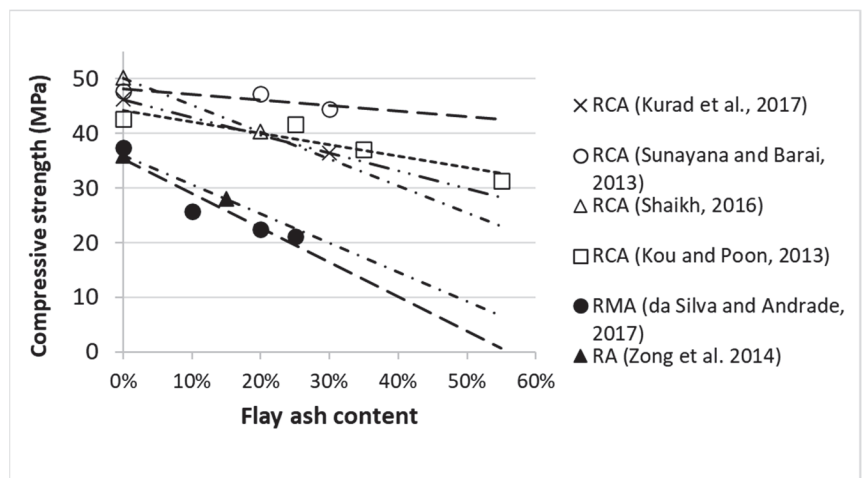


Figure 3. Compressive strength of concrete with: recycled aggregate of concrete (RCA), mixed recycled aggregate (RMA), and ceramic bricks (RA). Data from Zong et al. [7], da Silva and Andrade [17], Kou and Poon [32], Shaikh [33], Sunayana and Barai [34] and Kurad et al. [37].

The addition of fly ash in partial replacement to Portland cement tends to reduce the compressive strength of concrete in the smallest ages. According to Mehta [84], this is

because the oxides when reacting with water and $\text{Ca}(\text{OH})_2$ form a layer of C-S-H around the particle making it difficult to access the oxides of the inner part. With this, the hydration heat of the pozzolanic reaction forms more slowly making the development of resistance slower.

According to Kurad et al. [37], the actual decrease in the combined fly ash effect and recycled aggregate concrete (RCA) on compressive strength is less than the sum of the individual fly ash effect and RCA, especially after 28 days of cure. According to the authors, one of the factors that led to this behavior is the pozzolanic reaction between silicon dioxide (SiO_2) of fly ash and calcium hydroxide ($\text{Ca}(\text{OH})_2$) of RCA. With the increase of $\text{Ca}(\text{OH})_2$ due to the increasing reason for the incorporation of recycled aggregate, fly ash SiO_2 will have more Calcium Oxide (CaO) in the not hydrated particles of the old cement to produce more C-S-H, which is the main contributor to the development of concrete resistance.

In 2017, Kurad et al. [37] verified the effect of incorporating high volumes of recycled concrete aggregates and fly ash on the mechanical strength of new concretes. The authors produced concrete with axial compressive strength of 20 MPa at 28 days. At the same age (28 days) the concretes were crushed, and only after 10 months, the recycled concrete aggregate (RCA) was used in the mixture as coarse and fine aggregates for the production of new concretes. The sum of the main oxides of the fly ash used in this study ($\text{SiO}_2 + \text{Al}_2\text{O}_3 + \text{Fe}_2\text{O}_3$) was 86.1% of the total mass. The axial compressive strength designed for the original concrete was 37 MPa, and the slump of the cone was 80 ± 10 mm in all mixtures.

In this study, the authors replaced Portland cement with fly ash in the following proportions: 0%, 30%, and 50% of fly ash, and the binder consumption were 350, 235, and 140 kg/m^3 , respectively. The authors produced concrete with 0% and 100% replacement content of natural aggregate by recycled sand. Some of the concrete mixtures were repeated with the addition of a 1% superplasticizer.

The authors observed that, in general, the replacement of natural aggregate with recycled aggregate (RCA) is prejudicial to the compressive strength. The incorporation of RCA as fine aggregate is more detrimental than its incorporation as coarse aggregate. The authors also observed that when incorporating fly ash in mixtures with recycled aggregate (RCA), the compressive strength of concretes has the tendency to decrease at early ages. However, the rate of increase of concrete strength is directly proportional to the rise in incorporation levels of RCA and FA.

According to Kurad et al. [37], the decrease of the combined effect of the joint employment of fly ash and RCA is smaller than the individual effect of the components, especially after 28 days of curing. According to the authors' study, one of the factors that led to this behavior is the pozzolanic reaction between the Silicon Dioxide (SiO_2) of the fly ash and Calcium Hydroxide ($\text{Ca}(\text{OH})_2$) present in the RCA. With the increase of $\text{Ca}(\text{OH})_2$ due to the increasing ratio of incorporation of recycled aggregate, the SiO_2 of the fly ash will have more Calcium Oxide (CaO) from the extra particles of the old cement to produce more C-S-H, which is the main reason for the development of concrete strength [37].

According to Corinaldesi and Moriconi [108], concretes with a recycled concrete aggregate present an improvement in the interfacial transition zone (ITZ) as a result of the internal curing effect due to water being returned by the recycled aggregate particles, which have high porosity, and in the C-S-H particles, probably contained in recycled aggregates coming from the old mortar [108]. According to the authors, recycled aggregates also have $\text{Ca}(\text{OH})_2$ particles that should help improve the pozzolanic activity of fly ash. To analyze the TZs between natural aggregate and cement paste in conventional concrete and between recycled concrete aggregate and cement paste in RCA concrete and fly ash, the authors used the scanning electron microscopy (SEM) technique. The results showed that the ITZs of the concrete mixes made with fly ash and recycled concrete aggregates were better than those of the original concrete.

Corinaldesi and Moriconi [108] verified that the high amount of old cement particles increases the $\text{Ca}(\text{OH})_2$ content, and the fly ash also contains large amounts of SiO_2 . Soon the

amount of CSH increments and fills the ITZ and works on the interfacial connection among aggregates and paste. This behavior was also observed by other authors [20,106,109].

In 2017, da Silva and Andrade [17] produced concretes with mixed recycled aggregate consisting of 8% ceramic, 13% natural aggregate, and 79% concrete. The sum of the main oxides of the fly ash used in this study ($\text{SiO}_2 + \text{Al}_2\text{O}_3 + \text{Fe}_2\text{O}_3$) was 80.6%. The Portland cement used in this research was similar to ASTM C 150 III, whose levels of substitution of natural coarse aggregate by recycled aggregate proportions employed in the experiment were 25%, 50%, 75%, and 100%, with 15%, 20%, 25%, and 30% of cement substitution by fly ash. The axial compressive strength of the reference concrete at 28 days was 54.1 MPa, and the slump of the cone was approximately 80 ± 10 mm in all mixtures. The w/binder ratios employed were 0.40, 0.45, 0.50, 0.55, and 0.65. Based on a nonlinear regression model, the authors observed that by replacing natural coarse aggregate with mixed recycled coarse aggregate, the growth rate of axial compressive strength of the concretes without fly ash between the ages of 28 and 91 days was low for the w/b ratio of 0.4. However, as the replacement content of Portland cement by fly ash is increased, the growth rate of compressive strength increases significantly, and as the w/b ratio is increased, this growth rate is even higher (Table 6).

Table 6. Influence of the ratio w/b in the growth rate of the concrete compressive strength 25% RCA.

| Mix | Relationship f_{c91}/f_{c28} | | |
|--------|--------------------------------|---------|---------|
| | w/b 0.4 | w/b 0.5 | w/b 0.6 |
| R0F0 | 1.09 | 1.11 | 1.13 |
| R25F0 | 1.09 | 1.11 | 1.13 |
| R25F15 | 1.14 | 1.16 | 1.18 |
| R25F20 | 1.17 | 1.21 | 1.27 |
| R25F25 | 1.21 | 1.26 | 1.36 |
| R25F30 | 1.27 | 1.34 | 1.46 |

According to da Silva and Andrade [17], the pozzolanic reaction between fly ash and $\text{Ca}(\text{OH})_2$ in concretes with mixed recycled aggregate showed significant improvements in mechanical properties, tending to approach the reference concretes at older ages. The results verified in this study are in agreement with those observed by Kurad et al. [37].

The addition of fly ash in concretes with clay brick waste with a strength of approximately 10 MPa as coarse aggregate replacing natural coarse aggregate was the subject of a study by Zong, Fei, and Zhang [7]. The sum of the principal oxides in the fly ash ($\text{SiO}_2 + \text{Al}_2\text{O}_3 + \text{Fe}_2\text{O}_3$) was 86.91% of the total mass. The cement employed in this study was ordinary Portland cement. The proportions used in this study were 30%, 40%, and 50% recycled aggregate, and 15% fly ash. A high-performance polycarboxylate admixture was used for water reduction. The water content in the concrete was the standard amount of water required for reference concrete plus additional water based on the increased water absorption of the recycled aggregate. The authors observed a significant reduction in the density of the concretes with recycled aggregate compared to the reference concrete. According to the authors, this behavior is related to the low density of the recycled aggregate of ceramic material. According to the authors, the reference concrete had a density of 2476 kg/m³, while concretes with 30, 40, and 50% of recycled aggregate content presented 2352 kg/m³, 2316 kg/m³, and 2175 kg/m³, respectively. According to the authors, the reference concrete had a density of 2476 kg/m³, while concretes with 30, 40, and 50% of recycled aggregate content presented 2352 kg/m³, 2316 kg/m³, and 2175 kg/m³, respectively. According to the authors, the reduction in density of the concretes with recycled aggregate is related to the low density of the recycled aggregate of ceramic material.

Fei and Zhang [7] observed that the reduction in mechanical strength was more significant in concretes with 50% recycled aggregate and 15% fly ash compared to the reference concrete, which was 44% at 28 days of curing. Based on the authors' results, the concrete with only 15% fly ash presents compressive strength of 48 MPa and flexural

strength of 11 MPa. For concretes with 15% fly ash and 30, 40, and 50% recycled aggregate, the compressive strength was 42 MPa, 35 MPa, and 28 MPa, respectively, while the tensile strength was 4.8 MPa, 4.6 MPa, and 3.9 MPa, respectively. According to the authors, this behavior occurred because the recycled aggregate used in this study presents much lower strength than the natural aggregates.

In a general way, it can be noticed that the reduction in the mechanical strength of concrete when recycled aggregate is used is closely related to the type of waste. Recycled concrete aggregates tend to present higher mechanical resistance in comparison to recycled aggregates from clay bricks, and consequently present a higher strength decrease. The addition of fly ash in concretes with recycled aggregate has a very significant contribution because it produces an excellent pozzolanic reaction in the long term and has a pore filling effect due to the fine particles of the ash. The higher the content of adding fly ash in partial replacement to Portland cement, the lower the degree of reaction in the initial ages of cure [110].

4.2.2. Tensile Strength

Tensile strength showed behavior similar to compressive strength, although, according to a study carried out by Gonzalez-Corominas [111], if the curing process is steam, the tensile strength tends to improve. This behavior is closely linked to the addition of fly ash in partial replacement to Portland cement that results in a concrete with lower cement content, and consequently lower availability of calcium hydroxide in the concrete matrix (FILHO [112]), as shown in Figure 4.

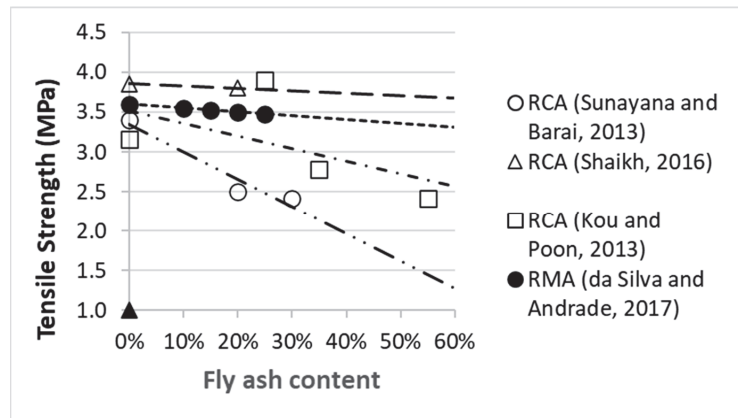


Figure 4. Results of tensile strength of concrete with recycled aggregate of concrete (RCA), mixed recycled aggregate (RMA), and ceramic bricks (RA) from some researchers. Data from da Silva and Andrade [17], Kou and Poon [32], Shaikh [33] and Sunayana and Barai [34].

Regarding the tensile strength, the results of several research studies are convergent. Kou and Poon [32] evaluated such property by employing replacement levels of 50% and 100% of natural aggregate by the coarse recycled concrete aggregate, with the addition of fly ash at three replacement levels (25%, 35%, and 50%) to the Portland cement ASTM Type I. The sum of the principal oxides of the fly ash employed in this study ($\text{SiO}_2 + \text{Al}_2\text{O}_3 + \text{Fe}_2\text{O}_3$) was 90.31%. The w/b ratio was 0.55, the slump was kept constant for all mixtures (120 mm), and the tensile strengths were estimated at ages of 28 days, 1, 3, 5, and 10 years. It was observed that the concretes produced with natural aggregate and fly ash in the proportions 0%, 25%, 35%, and 55% (R0F0, R0F25, R0F35, and R0F55) showed an increase in splitting tensile strength by 38.9%, 43.0%, 44.1%, and 39.8%, respectively, in the period between 28 days and 10 years. The concretes with 100% coarse recycled aggregate and fly ash in the same proportions showed an increase in strength of 57.8%, 62.5%, 67.2%, and 70.9%,

respectively, in the period between 28 days and 10 years. After 10 years, the concrete with 100% coarse recycled aggregate and 25% fly ash (R100F20) presented the highest tensile strength. However, the concrete with 100% coarse recycled aggregate and 55% fly ash (R100F55) was the one that showed the highest resistance gain. According to the authors, this behavior is closely related to the incorporation of fly ash into the recycled aggregate, which improves the microstructure of the ITZ, which, in turn, increases the adhesion between the aggregates and the paste. Mehta and Monteiro [1] suggest that the concentration of calcium hydroxide crystals in the ITZ may be reduced by chemical reactions when a pozzolanic mixture or a reactive aggregate is present. The authors suggest that possible chemical interaction between calcium hydroxide and the calcareous aggregate is probably the reason for the increased tensile strength of concrete.

In another study, Kou et al. [113] produced concretes with different w/c ratios (0.45, 0.50, and 0.55), Portland cement ASTM Type I and fly ash whose sum of the principal oxides ($\text{SiO}_2 + \text{Al}_2\text{O}_3 + \text{Fe}_2\text{O}_3$) is 90.31%. The absorption of the recycled aggregate varied between 4.26% and 8.69%. In this study, the authors produced reference concretes with 20, 50, and 100% recycled aggregate content and concretes with 25% addition of fly ash in partial replacement of Portland cement and 0%, 20%, 50%, and 100% of recycled aggregate in partial replacement of natural aggregate.

According to the authors, the tensile strength at 91 days of concrete with 100% recycled aggregate for w/b ratios 0.50, 0.45, and 0.40 were 12%, 10%, 9%, and 10% lower than that of the reference concrete, respectively. By using the addition of fly ash as a partial replacement for Portland cement, the strength of concretes with 100% recycled aggregate increment by 3%, 6%, and 8%, respectively, contrasted with cement without fly ash. Kou et al. [113] suggest that such an increase in strength in the concretes with fly ash can be credited to the densification of the concrete because of the possible reduction in porosity and to the pozzolanic reaction of the fine fly ash particles.

The result of the influence of fly ash in concretes with mixed recycled aggregate in the tensile strength in concretes was produced by da Silva and Andrade [17], between the period of 28 days and 91 days. The authors observed that the addition of fly ash in concretes with recycled aggregate would, in general, constrict the adverse effects that the recycled aggregate may cause in the tensile strength of concretes.

The authors observed that the negative effect in concretes with 25% of RCA and with an increasing amount of fly ash was smaller than in concrete with 20% of fly ash when the content of replacement of RCA increased. This behavior is due to the reduction of concrete porosity due to the filling of voids by fly ash particles. The addition of fly ash in concretes with recycled aggregate, by containing very fine materials, has a pore plugging effect in the recycled aggregates and makes a denser paste, and consequently reduces the harmful effects of the incorporation of recycled aggregate.

4.2.3. Elastic Modulus

According to Neville [96], the elastic modulus of concrete depends on the elastic modulus of the aggregate and the volume proportion of the aggregate in concrete. Studies show that the elastic modulus decrease in concretes with fly ash and recycled aggregate in the early ages. Sunayana and Barai [34] and Kou and Poon [32] observed similar behavior of the elastic modulus of concrete produced with different fly ash contents and with 50% recycled aggregate, as shown in Figure 5.

However, the improvement in elastic modulus was observed in concretes with RCA in the older ages by some authors. Sunayana and Barai [34] used two groups of recycled concrete aggregate as coarse aggregate for the production of fly ash concretes. The first group of recycled concrete aggregate consists of a particle packing method (PPM), which consists of adopting a continuous particle size range between 4.75 mm and 20 mm because, according to the authors, the voids between larger particles are filled by the smaller particles to achieve the lower amount of voids in a concrete mix. The mixing method used for the production of concrete with recycled aggregate and fly ash was in the following steps:

- (a) Mix for 15 s the natural aggregates and recycled aggregate;
- (b) Add fly ash and mix for another 15 s;
- (c) Portland cement is added and mixed for another 30 s;
- (d) Add water and superplasticizer to the dry material and mix for another 60 s.

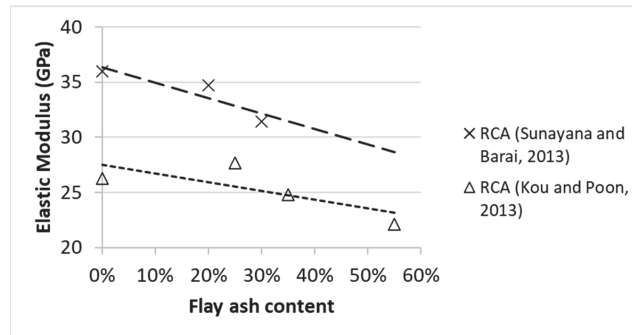


Figure 5. Elastic Modulus of concrete with recycled aggregate of concrete (RCA). Data from Kou and Poon [32] and Sunayana and Barai [34].

Cylindrical samples were fitted with a compressometer to measure the displacement at each load increment, which was subsequently converted to strain. The load was applied for three load cycles up to 1/3 compressive strength of similar cylinders and converted to strain. The stress–strain relationship in the linear elastic region was used to find the modulus of elasticity (E) and to minimize the effect of compressive strength. The parameter ($E/f_c^{0.5}$) was found to be in the range of 4461–5507. Based on the authors’ results, the reference concrete presented a compressive strength of approximately 43 MPa, while the concretes with 20 and 30% fly ash and RCA presented an average of 41 MPa and 42 MPa, respectively. The modulus of elasticity of the reference concrete was 36,000 MPa, while concretes with 20 and 30% fly ash and RCA had an average of 34,808 MPa and 31,340 MPa, respectively. The relationship between the modulus of elasticity and the compressive strength ($E/f_c^{0.5}$) for the reference concrete was approximately 5505 and for the concretes with 20 and 30% fly ash and RCA, it was around 5443 and 4764, respectively.

Based on the results, the authors observed a 5 to 10% reduction in elastic modulus in concretes with NAC compared to natural aggregate for 20% and 30% of fly ash replacement presented a decrease for RAC + FA20 compared to NAC for the same w/b ratio of 0.45. This behavior is due to the lower elastic properties of recycled aggregate due to the presence of adhered mortar compared to natural aggregates.

Kou and Poon [32] produced concretes with coarse recycled concrete aggregate in the replacement of 50% and 100% of coarse natural aggregate. The PC used in this research was equivalent to ASTM Type I. The sum of the principal oxides of the fly ash employed ($\text{SiO}_2 + \text{Al}_2\text{O}_3 + \text{Fe}_2\text{O}_3$) was 90.31%, and the proportions of the addition of fly ash in replacement of PC were 25%, 35%, and 50%. The w/b ratio was 0.55, and the concrete was kept constant at 120 mm. The static elastic modulus was determined according to ASTM C 469 (2002) in specimens at 28 days, 1 year, 3 years, 5 years, and 10 years.

Based on the results, the authors observed that in the first year of curing, there was a gain in the elastic modulus for R100 R100F25, R100F35, and R100F5 mixtures of 7.2%, 7.9%, 11.2%, and 14.8%, respectively. However, at higher ages, the increase in percentages in the elastic modulus was much higher, corresponding to 31.3%, 33.9%, 40.7%, and 46.1%, respectively, between 28 days and 10 years. The authors also observed that, compared to the control mixture, the utilization of a considerable quantity of recycled aggregate in the concrete diminished the modulus increment following 10 years of curing.

According to Neville [114], the modulus of elasticity increases with concrete strength, but the growth in the concrete modulus of elasticity is smaller than the growth in compressive

sive strength. The elastic modulus of concrete is closely linked to the elastic modulus of the binder matrix and aggregates. As recycled aggregate presents lower stiffness when compared to natural aggregate due to its composition and highly porous internal structure, it is expected that the higher the content of recycled aggregate substitution for natural aggregate, the lower the concrete elasticity modulus will be [42]. In the study by Kou and Poon [32], a good correlation was observed between compressive strength and modulus of elasticity for all concrete mixes with recycled concrete aggregate and fly ash. That is, as the compressive strength increases, the modulus of elasticity increases. For this analysis, the authors employed an equation based on ACI 318-08 to estimate the modulus of elasticity in terms of the compressive strength of natural concrete.

Thus, since the elastic modulus of concretes depends on the aggregate characteristics (considering the same properties for cement paste), it can be challenging to determine an adequate correlation between the elasticity modulus and concretes produced with recycled aggregate since the elasticity modulus of aggregates presents a significant variability, depending mainly on their type and origin.

4.3. Durability Properties

4.3.1. Water Absorption

According to Zhang et al. [115], there are several aggressive agents present in nature that contribute to the deterioration of the concrete structure, reducing its service life, whose action is associated with climatic and environmental conditions, such as CO_2 , Cl^- , O_2 , and H_2O . In addition, $\text{Ca}(\text{OH})_2$ gives concrete high alkalinity, maintaining the pH of the mixture between 12 and 13, but it is a leachable product and in contact with CO_2 present in the environment, and relative humidity of approximately 60–80% initiates the carbonation process, which reduces the pH to values close to 8–9, leaving the concrete exposed to chemical attacks. Limbachiya, Meddah, and Ouchagour [20] produced concretes with 0%, 30%, 50%, and 100% ratio of natural coarse aggregate to recycled concrete aggregate and with 30% fly ash in place of Portland cement CEM I 42.5 N. The mixtures were classified into three grades according to the 28-day design compressive strength (C20, C30, and C35 considering a 28-day design compressive strength of 20, 30, and 35 MPa, respectively).

The method employed for testing water absorption in concretes by the authors consisted of measuring the rate at which water, through a known surface area, flows into the capillary network of concrete pores with a fixed scale of 10 min. The estimation of volumetric flow is obtained by measuring the length of flow along a capillary of known size. The initial surface absorption (ISA) of the various mixtures was determined in 150 mm cubes.

The authors observed that the initial surface absorption (10 min) versus RCA content for all investigated mixtures showed an increase in the initial surface absorption (ISA) as the replacement content of the recycled concrete aggregate was increased. However, the authors observed that concretes with 30% fly ash in partial replacement of Portland cement showed a reduction in water absorption when compared to concretes without fly ash. According to Limbachiya, Meddah, and Ouchagour [20], this behavior is linked to the pozzolanic reaction and the pore structure refinement that reduces the water flux. The same behavior was verified by da Silva and Andrade [17].

To analyze the water absorption in concretes with recycled aggregate and 10% ultrafine fly ash (UFFA), Shaikh [48] used 10% ultrafine fly ash (UFFA) and two levels of substitution (25% and 50%) of coarse recycled aggregate from construction and demolition waste (CDW) in partial replacement of natural aggregate. The CDW used was constituted of approximately 78% concrete, 13% bricks, 2.3% asphalt, and 5.7% other materials. The water absorption of the recycled aggregate was 4.88%. The sum of the fly ash oxides ($\text{SiO}_2 + \text{Al}_2\text{O}_3 + \text{Fe}_2\text{O}_3$) was 95.5%, with a surface area of $2.51 \text{ m}^2/\text{g}$. Concrete water absorption over a period of 6 h was adjusted by linear regression, and, to describe the absorption, the slope of the equation was used. The absorption rate (mm) for the investigated concretes at 7, 28, and 90 days.

Based on the analysis through linear regression based on R^2 values greater than 0.98 for all mixtures, the authors observed that the water absorbed in the concrete increased as recommended in Fick's first law equation [33]. The concretes with recycled aggregate presented higher water absorption than the reference concretes. According to Shaikh [33], the rate of water absorption through concrete is a function of the permeability of the pore structure where, due to capillary increase, the rate of water percolation is controlled mainly in unsaturated concretes. Based on the results obtained the authors noticed that as the age of cure increases, the rate of water absorption of recycled aggregates decreases. This behavior is related to the continuous hydration reaction and the formation of calcium silicate hydrate (C-S-H), which generally fills the micropores in the matrix [33]. It was also found that the addition of 10% UFFA significantly reduced the water absorption rate of concretes containing recycled coarse aggregate and natural coarse aggregate at all ages [33]. The high pozzolanic activity, the secondary C-S-H due to the pozzolanic reaction of ultrafine fly ash (UFFA) with calcium hydroxide (CH), as well as the fineness of fly ash, may have significantly contributed to the reduction of water absorption [17,116].

In general, studies have shown that recycled aggregates are, for the most part, more permeable than natural aggregates. The higher the replacement level of natural aggregate by the recycled aggregate, the greater the water absorption. The addition of fly ash in concretes with recycled aggregate reduces the negative effect that the recycled aggregate causes in the concretes due to the refinement of the porous capillary network that makes these concretes denser, improving their mechanical resistance and reducing the flow of water through the concretes.

4.3.2. Chloride Ingress

The chloride ions do not cause significant damage to concrete itself, but they contribute to corrosion of reinforcement in structural elements and can negatively affect the serviceability and safety limit states [31,117]. Sim and Park [36] performed chloride ion penetration tests on concrete with recycled concrete sand, whose water absorption was 6.45%. The sum of the principal oxides of the fly ash employed in this study ($\text{SiO}_2 + \text{Al}_2\text{O}_3 + \text{Fe}_2\text{O}_3$) was 30.3%, with high CaO content (61.2%). The water/binder ratio was equal to 0.485, and the replacement contents of natural sand with recycled concrete sand were 30%, 60%, and 100%. The addition of fly ash in replacement of Portland cement CEM I was 15% and 30% by weight. The authors analyzed the depth of chloride ion penetration measured at different cure times compared to the addition of fly ash at the ages of 21 days and 56 days.

Based on the results, it is observed that the penetration of chloride ions at 21 days reduces significantly according to by how much the partial replacement of cement by fly ash is increased. For the concrete, at 56 days, the reduction was not so significant when compared to the reference concrete. According to the authors [36], the concretes with recycled aggregate for applications in structural elements obtained sufficient resistance to chloride ion penetration, and the resistance can be maximized by the addition of fly ash. Similar behaviors were observed by other authors [31,112].

Shaikh [33] used the method proposed by ASTM C1202 31 for the mitigation of chlorides in concretes with ultrafine fly ash and coarse aggregate from construction and demolition waste. The authors analyzed the effects of ultrafine fly ash (UFFA) on the permeability of chloride ions in concrete containing coarse recycled aggregates. The authors observed that for reference concretes (OPC), as the age of the concrete increases, the penetration of chloride ions decreases. By replacing the natural coarse aggregate with recycled coarse aggregate (RCA), there is a significant increase in chloride ion penetration compared to reference concretes (OPC). However, when adding 10% ultrafine fly ash (UFFA) in partial replacement of Portland cement, it is observed that there is a significant improvement in permeability at all ages. It is also observed that the addition of 10% UFFA will, in general, expand the chloride ion resistance of recycled aggregate concretes since, according to Shaikh [33], it serves to promote hydration and block the capillary spaces in the concrete matrix.

Thus, the chloride ions will penetrate the concretes with recycled aggregate more quickly due to a higher permeability rate in function of the capillary pores in the matrix of the cement and recycled aggregate. The addition of fly ash in concretes with recycled aggregate fills the capillary pores of the recycled aggregates making a denser concrete, and consequently improves the resistance of concretes to chloride ion penetration.

4.3.3. Carbonation Depth

Carbonation has a significant influence on concrete durability because this reaction reduces the pH of the water in the pores of the cement paste from approximately 12.6 to 8.3 [114]. When the low pH reaches the surface of the reinforcement, the thin passivation layer of oxides that is strongly adhered to the steel in the presence of moisture is destroyed, causing the beginning of the corrosive process [114]. According to Khunthongkeaw et al. [118], mortars with fly ash contents lower than 30% have carbonation proposals similar to the reference mortars. Thus, it is crucial to know the resistance to carbonation of concretes with recycled aggregate and fly ash so that these concretes can be used in structural elements.

Geng and Sun [35] used recycled concrete aggregate as sand with a fineness modulus equal to 2.7. The fly ash employed in this study presented a sum of 88% in its principal oxides ($\text{SiO}_2 + \text{Al}_2\text{O}_3 + \text{Fe}_2\text{O}_3$). The w/b ratio was 0.40, and the levels of substitution of natural sand for recycled sand were 20%, 40%, 60%, and 80% by weight, and the levels of substitution of ordinary Portland cement for fly ash were 10%, 20%, and 30% by weight. To perform the carbonation depth tests, the accelerated carbonation test was employed at a temperature of 20 ± 5 °C, with a relative humidity of 70 ± 5 and a carbon dioxide (CO_2) concentration of 3%. The carbonation depth was measured after 7, 14, and 28 days of exposure to CO_2 . The authors compared the carbonation depth between the reference concrete (FC0), concrete with 40% replacement content of natural sand by recycled sand (FC14), and concrete with 40% replacement of natural sand by recycled sand combined with 10% (FCF1), 20% (FCF2), and 30% (FCF3) of replacement of Portland cement by fly ash, respectively.

In the first 7 days of curing, all concretes, with the exception of LC14 (4 cm), have practically zero carbonation depth. After 14 days of curing, the LC0 concrete remained with a carbonation depth close to zero. Concretes LCF2, LCF3, LCF1, and LC14 presented carbonation depths of 0.24 cm, 0.26 cm, 0.49 cm, and 0.78 cm, respectively. At 28 days of cure, the authors observed that the LC0 and LCF2 concrete had very similar carbonation depths (0.48 cm). The LCF3 concrete has a carbonation depth greater than the LCF2 concrete, which was 0.98 cm and 0.75 cm, respectively. The LC14 concrete has a carbonation depth of 1.49 cm.

Carbonation depth of the concretes with recycled sand and fly ash is lower than the concretes with only recycled sand. According to Geng and Sun [35], the effect of cement replacement by fly ash on carbonation depth reveals that carbonation initially decreases and then increases with a replacement rate from 10% to 30%, and then reaches the minimum at 20%. However, according to the authors, the amount of cement decreases with increasing fly ash replacement content, which leads to a decrease in the alkalinity of the pore solution, which is unfavorable for the carbonation resistance capacity of the concrete. This behavior was also observed by Limbachiya, Meddah, and Ouchagour [20] and Silva and Andrade [17]. Khunthongkeaw, Tangtermsirikul, and Leelawat [100] and Silva and Andrade [17] suggest that this behavior may be related, in addition to the reduction of calcium hydroxide (CH) due to the reduction of cement content, to the pozzolanic reaction of the fly ash, which predominates in the refinement of the pores, since there is a slowing of the initial hydration process [35]. Limbachiya, Meddah, and Ouchagour [20] also state that the reduction of the initial CaO content in the cement matrix leads to a decrease in the pH of the concrete, which will contribute to accelerating the carbonation rate.

Silva and Andrade [17] evaluated the resistance to CO_2 of concretes with fly ash and mixed recycled coarse aggregate subjected to accelerated carbonation with a CO_2 concentration of 3%, moisture content between 65 and 75%, and a total exposure period

of 23 weeks. The first measurement of carbonation depth was at 15 days of exposure, and the other measures were taken every 30 days. They observed that the carbonation coefficient (adjusted according to Fick's second law) tends to be higher in concretes with recycled coarse aggregate and fly ash compared to reference concretes. This analysis was performed with reference concrete (R0F0), concrete with a 25% replacement of natural coarse aggregate by recycled coarse aggregate (R25F0), concrete with a 25% replacement of natural coarse aggregate by the recycled coarse aggregate, and 30% addition of fly ash in partial replacement of Portland cement, for a w/b ratio of 0.50.

The relationship between K ($\text{mm}/\text{month}^{0.5}$) and t (months) was analyzed in all concretes and based on the authors' results. All concretes presented in the carbonation coefficient with increasing time of exposure to CO_2 . This behavior was observed in all concretes. In the first 15 days of exposure to CO_2 , the reference concrete was a carbonation coefficient of 4.9, while the R25F0 and R25F30 concretes were a carbonation coefficient of 5.9 and R25F30. At 145 days of exposure to CO_2 , the reference concrete was a carbonation coefficient of 3.97, while the concretes R25F0 and R25F30 were a carbonation coefficient of 3.98 and R25F30. According to the authors, the carbonation process is straightforwardly associated with the exposure time of the specimens to CO_2 , and the carbonation coefficient will, in general, balance out after some time. Similar behaviors were observed by Meddah and Ouchagour [20], Khunthongkeaw, Tangtermsirikul, Leelawat [113], and Atiş [119].

In general, it is found that with a partial replacement of Portland cement with fly ash, the CH decreases and makes the concrete more vulnerable to CO_2 penetration. However, the pozzolanic reaction of the fly ash in the pore refinement, which occurs in concretes with higher ages, contributes to the carbonation resistance. Thus, it is possible to observe in the studies that initially, the carbonation resistance is lower at early ages, and as the age increases, the carbonation resistance is improved.

4.3.4. Microstructural Analyses

Microstructural analyses are essential to verify the products formed due to the chemical reactions between the components of the cement matrix and the aggregates, especially on the ITZ. Li, Xiao, and Zhou [120] observed the ITZ employing scanning electron microscopy (SEM). The authors investigated the properties of two groups of concretes: in the first (A) part of the mixing, water was mixed with a pozzolanic powder consisting of fly ash, silica fume, and blast furnace slag for 60 s in order to produce a paste with a relatively low water/binder ratio; then recycled concrete aggregate (RAC) was added to the paste and mixed for another 60 s to coat the surfaces of the recycled aggregate; finally, the remaining water, sand, and Portland cement were added to the mixture and mixed for another 120 s. The second group (B) mixtures were performed in a conventional way and without the pre-mixing of the recycled aggregate.

Microstructural analyses were performed on the concretes RC04A and RC04B to verify the influence of different types of the mixture on the ITZ of the two concretes that present the same proportions of materials. For concrete production, recycled aggregate from an old cement sidewalk was used, whose apparent density was $2.497 \text{ g}/\text{cm}^3$ and water absorption of 4.6%. The amount of binder and water was established at $500 \text{ kg}/\text{m}^3$ and $220 \text{ kg}/\text{m}^3$, respectively. A superplasticizer was added in a fixed amount of 0.8% to the binder in all mixtures. The density (in g/cm^3) of the fly ash, silica fume, and blast furnace slag were 2.38, 2.20, and 2.75, and specific surface area values (in m^2/kg) were 410, 20,000, and 240, respectively.

According to the authors, the RC04A concrete has a denser ITZ, and the hydrates are mainly composed of uniform CSH gel. With the new mixing technique, the pozzolanic coating layer forms a barrier that prevents water penetration. Workability is improved, and the ITZ is strengthened. On the other hand, concrete RC04B showed a crack with a length of 30–40 μm (perpendicular to the ITZ), and a large amount of CH crystals was observed in the ITZ. According to the authors, the occurrence of the cracks may be due to the water absorption from the paste by the recycled aggregate. After the water evaporation, it was

verified the occurrence of voids that correspond to the cracks in the ITZ. Thus, it can be observed that different mixing techniques can contribute to making the material denser and with fewer cracks. The use of recycled aggregate without pre-mixing, resulting in a weaker ITZ, was also verified by Poon, Shui, and Lam [68] and Sidorova et al. [121].

To evaluate the ITZ bond, Juan-Valdéz et al. [122] produced concretes with 50% replacement of natural aggregate with mixed recycled aggregate whose composition was 44.11% stone, 33.56% bricks, tiles, sanitary ware, 17.51% stone with mortar, 0.44% asphalt, 0.75% glass, 3.48% gypsum, and 0.16% other materials. The authors used a Hitachi S-4800 scanning electron microscope with tungsten as the X-ray source, a Si/Li detector, and a Bruker XFlash 5030 EDS analyzer to verify the EDX elemental mappings. It was found that aggregates (natural and recycled) developed ITZ with satisfactory properties [122]. According to the authors, this result was due to the wetting of the recycled aggregate before its addition to the concrete mixture. Thus, it can be seen that saturation of recycled aggregates results in beneficial effects regarding the improvement of concrete microstructure, making a denser paste that improves ITZ properties.

5. General Analysis

In general, construction and demolition waste can be used in the production of concrete components, mortar, paving blocks, subfloor, and masonry in urban infrastructures such as sidewalks and curbs. These materials can also be used in the regularization and gravel of unpaved streets, as well as in the base, sub-base, and reinforcement of the pavement subgrade. The use of waste (recycled aggregates) and fly ash (binder), although there are many studies, has still been little used in the construction industry, as it requires the systematization of quality control technology, public policies, standards, and technical specifications for use on a large scale. Based on what was exposed in this review, it is possible to estimate the practical application of this waste in some segments of civil construction, as shown in Table 7.

Table 7. Possible to estimate the practical application.

| Usage with 20% of Fly Ash | Replacement Rate | | |
|--|------------------|--------|------|
| | 0–25% | 25–50% | >50% |
| Structural cement concrete (20–25 MPa) | X | | |
| Non-structural cement concrete (<20 MPa) | X | X | |
| Permeable cement concrete | X | X | |
| Mortars | X | X | |
| Paving (base, sub-base, and sub-bed reinforcement) | X | X | X |

For use in paving, some basic requirements, such as particle size composition, maximum characteristic dimension, and shape index, are necessary. For cement concretes, the minimum required control requirements are particle size composition, water absorption, and control of contaminants, such as chlorides, sulfates, and non-mineral materials.

6. Conclusions

Considering the several works published in the literature, the following considerations can be drawn:

- There are already several studies exploring the most suitable composition of concrete mixtures with construction and demolition waste and fly ash to reach a consensus on the most appropriate contents of these wastes to achieve results of mechanical properties and durability closer to the reference concretes;
- Although there is an intense debate regarding the use of construction and demolition waste for the production of new concretes due to the significant variability of this waste, many researchers agree that small amounts of substitution of natural aggregates by recycled aggregates are quite feasible;

- The addition of fly ash as a partial replacement for Portland cement in concretes with recycled aggregate from construction and demolition waste, besides improving the adverse effects caused by recycled aggregates in terms of mechanical properties and durability, can contribute significantly to reducing CO₂ generation in the environment;
- The use of this solid waste in the production of concrete and mortar will make a significant contribution to reducing the consumption of natural resources as well as reducing production costs.

7. Suggestions for Further In-Depth Studies

In view of the current holes in the past studies, the accompanying suggestions are proposed for future exploration:

- There is a need for an establishment of methodologies for cost evaluation per m³ of concretes with recycled aggregate and fly ash;
- A study of the mechanical properties and durability in concretes with recycled aggregate and fly ash under different environmental conditions;
- Further investigations are necessary to determine ranges for an adequate w/b ratio for concretes with recycled aggregate and fly ash, given the variability of the physical–chemical characteristics of such materials;
- As the curing temperature directly affects the chemical reactions of fly ash activation, an evaluation of the mechanical properties and durability of concretes with recycled aggregate and fly ash is necessary;
- Life cycle analysis (LCA) that includes the recycling or reuse process to incorporate the product in the construction process is needed in order to give information for the decision-making process.
- Prediction of compressive strength of concrete modified with fly ash: applications of neuro-swarm and neuro-imperialism models;
- Systematic multiscale models to predict the compressive strength of fly ash-based geopolymer concrete at various mixture proportions and curing regimes;
- Soft computing techniques: systematic multiscale models to predict the compressive strength of HVFA concrete based on mix proportions and curing times;
- ANN, M5P-tree, and nonlinear regression approach with statistical evaluations to predict the compressive strength of cement-based mortar modified with fly ash;
- Characterizing and modeling the mechanical properties of the cement mortar modified with fly ash for various water-to-cement ratios and curing times;
- Model technics to predict the impact of the particle size distribution (PSD) of the sand on the mechanical properties of the cement mortar modified with fly ash;
- Compare the cost and environmental effect of the use of demolition construction waste for the production of new concrete.

Funding: This study was financed in part by the Coordenação de Aperfeiçoamento de Pessoal de Nível Superior—Brasil (CAPES)—Finance Code 001.

Institutional Review Board Statement: Not applicable.

Conflicts of Interest: The authors declare no conflict of interest.

References

1. Mehta, P.K.; Monteiro, P.J.M. *Concrete: Microstructure, Properties, and Materials*; McGraw-Hill: New York, NY, USA, 2006. [CrossRef]
2. Lanz, B.; Dietz, S.; Swanson, T. Global Population Growth, Technology, and Malthusian Constraints: A Quantitative Growth Theoretic Perspective. *Int. Econ. Rev.* **2017**, *58*, 973–1006. [CrossRef]
3. Dawson, I.G.J.; Johnson, J.E.V. Does Size Matter? A Study of Risk Perceptions of Global Population Growth. *Risk Anal.* **2017**, *37*, 65–81. [CrossRef] [PubMed]
4. Meddah, M.S. Recycled aggregates in concrete production: Engineering properties and environmental impact. *MATEC Web Conf.* **2017**, *101*, 05021. [CrossRef]
5. Dabhade, A.N.; Chaudari, S.R.; Gajbhaye, A.R. Effect of Flyash on Recycle Coarse Aggregate Concrete. *Int. J. Civ. Eng. Res.* **2014**, *5*, 2278–3652. Available online: <http://www.ripublication.com/ijcer.htm> (accessed on 8 November 2019).

6. Silva, R.V.; de Brito, J.; Dhir, R.K. Performance of cementitious renderings and masonry mortars containing recycled aggregates from construction and demolition wastes. *Constr. Build. Mater.* **2016**, *105*, 400–415. [[CrossRef](#)]
7. Zong, L.; Fei, Z.; Zhang, S. Permeability of recycled aggregate concrete containing fly ash and clay brick waste. *J. Clean. Prod.* **2014**, *70*, 175–182. [[CrossRef](#)]
8. Ge, Z.; Wang, Y.; Sun, R.; Wu, X.; Guan, Y. Influence of ground waste clay brick on properties of fresh and hardened concrete. *Constr. Build. Mater.* **2015**, *98*, 128–136. [[CrossRef](#)]
9. Ledesma, E.F.; Jiménez, J.R.; Ayuso, J.; Fernández, J.M.; de Brito, J. Maximum feasible use of recycled sand from construction and demolition waste for eco-mortar production—Part-I: Ceramic masonry waste. *J. Clean. Prod.* **2015**, *87*, 692–706. [[CrossRef](#)]
10. Evangelista, L.; de Brito, J. Mechanical behaviour of concrete made with fine recycled concrete aggregates. *Cem. Concr. Compos.* **2007**, *29*, 397–401. [[CrossRef](#)]
11. Mirzahosseini, M.; Riding, K.A. Effect of curing temperature and glass type on the pozzolanic reactivity of glass powder. *Cem. Concr. Res.* **2014**, *58*, 103–111. [[CrossRef](#)]
12. Wang, H.Y.; Zeng, H.H.; Wu, J.Y. A study on the macro and micro properties of concrete with LCD glass. *Constr. Build. Mater.* **2014**, *50*, 664–670. [[CrossRef](#)]
13. Guelmine, L.; Hadjab, H.; Benazzouk, A. Effect of elevated temperatures on physical and mechanical properties of recycled rubber mortar. *Constr. Build. Mater.* **2016**, *126*, 77–85. [[CrossRef](#)]
14. Ghizdävet, Z.; Ștefan, B.M.; Nastac, D.; Vasile, O.; Bratu, M. Sound absorbing materials made by embedding crumb rubber waste in a concrete matrix. *Constr. Build. Mater.* **2016**, *124*, 755–763. [[CrossRef](#)]
15. Dimitriou, G.; Savva, P.; Petrou, M.F. Enhancing mechanical and durability properties of recycled aggregate concrete. *Constr. Build. Mater.* **2018**, *158*, 228–235. [[CrossRef](#)]
16. Arulrajah, A.; Disfani, M.M.; Haghghi, H.; Mohammadinia, A.; Horpibulsuk, S. Modulus of rupture evaluation of cement stabilized recycled glass/recycled concrete aggregate blends. *Constr. Build. Mater.* **2015**, *84*, 146–155. [[CrossRef](#)]
17. da Silva, S.R.; de Andrade, J.J. Investigation of mechanical properties and carbonation of concretes with construction and demolition waste and fly ash. *Constr. Build. Mater.* **2017**, *153*, 704–715. [[CrossRef](#)]
18. Zieliński, K. Impact of Recycled Aggregates on Selected Physical and Mechanical Characteristics of Cement Concrete. *Procedia Eng.* **2017**, *172*, 1291–1296. [[CrossRef](#)]
19. Bravo, M.; de Brito, J.; Pontes, J.; Evangelista, L. Durability performance of concrete with recycled aggregates from construction and demolition waste plants. *Constr. Build. Mater.* **2015**, *77*, 357–369. [[CrossRef](#)]
20. Limbachiya, M.; Meddah, M.S.; Ouchagour, Y. Use of recycled concrete aggregate in fly-ash concrete. *Constr. Build. Mater.* **2012**, *27*, 439–449. [[CrossRef](#)]
21. Lotfy, A.; Al-Fayez, M. Performance evaluation of structural concrete using controlled quality coarse and fine recycled concrete aggregate. *Cem. Concr. Compos.* **2015**, *61*, 36–43. [[CrossRef](#)]
22. Poon, C.S.; Kou, S.C.; Lam, L. Influence of recycled aggregate on slump and bleeding of fresh concrete. *Mater. Struct.* **2007**, *40*, 981–988. [[CrossRef](#)]
23. Bravo, M.; de Brito, J.; Evangelista, L.; Pacheco, J. Superplasticizer’s efficiency on the mechanical properties of recycled aggregates concrete: Influence of recycled aggregates composition and incorporation ratio. *Constr. Build. Mater.* **2017**, *153*, 129–138. [[CrossRef](#)]
24. Wang, X.-Y.; Park, K.-B. Analysis of compressive strength development of concrete containing high volume fly ash. *Constr. Build. Mater.* **2015**, *98*, 810–819. [[CrossRef](#)]
25. Chousidis, N.; Ioannou, I.; Rakanta, E.; Koutsodontis, C.; Batis, G. Effect of fly ash chemical composition on the reinforcement corrosion, thermal diffusion and strength of blended cement concretes. *Constr. Build. Mater.* **2016**, *126*, 86–97. [[CrossRef](#)]
26. Zhao, Y.; Zeng, W.; Zhang, H. Properties of recycled aggregate concrete with different water control methods. *Constr. Build. Mater.* **2017**, *152*, 539–546. [[CrossRef](#)]
27. Kou, S.C.; Poon, C.S. Enhancing the durability properties of concrete prepared with coarse recycled aggregate. *Constr. Build. Mater.* **2012**, *35*, 69–76. [[CrossRef](#)]
28. Meyer, C. The greening of the concrete industry. *Cem. Concr. Compos.* **2009**, *31*, 601–605. [[CrossRef](#)]
29. Aprianti, E.; Shafiq, P.; Bahri, S.; Farahani, J.N. Supplementary cementitious materials origin from agricultural wastes—A review. *Constr. Build. Mater.* **2015**, *74*, 176–187. [[CrossRef](#)]
30. Acar, I.; Atalay, M.U. Characterization of sintered class F fly ashes. *Fuel* **2013**, *106*, 195–203. [[CrossRef](#)]
31. Lima, C.; Caggiano, A.; Faella, C.; Martinelli, E.; Pepe, M.; Realfonzo, R. Physical properties and mechanical behaviour of concrete made with recycled aggregates and fly ash. *Constr. Build. Mater.* **2013**, *47*, 547–559. [[CrossRef](#)]
32. Kou, S.C.; Poon, C.S. Long-term mechanical and durability properties of recycled aggregate concrete prepared with the incorporation of fly ash. *Cem. Concr. Compos.* **2013**, *37*, 12–19. [[CrossRef](#)]
33. Shaikh, F.U.A. Effect of ultrafine fly ash on the properties of concretes containing construction and demolition wastes as coarse aggregates. *Struct. Concr.* **2016**, *17*, 116–122. [[CrossRef](#)]
34. Sunayana, S.; Barai, S.V. Recycled aggregate concrete incorporating fly ash: Comparative study on particle packing and conventional method. *Constr. Build. Mater.* **2017**, *156*, 376–386. [[CrossRef](#)]
35. Geng, J.; Sun, J. Characteristics of the carbonation resistance of recycled fine aggregate concrete. *Constr. Build. Mater.* **2013**, *49*, 814–820. [[CrossRef](#)]

36. Sim, J.; Park, C. Compressive strength and resistance to chloride ion penetration and carbonation of recycled aggregate concrete with varying amount of fly ash and fine recycled aggregate. *Waste Manag.* **2011**, *31*, 2352–2360. [[CrossRef](#)]
37. Kurad, R.; Silvestre, J.D.; de Brito, J.; Ahmed, H. Effect of incorporation of high volume of recycled concrete aggregates and fly ash on the strength and global warming potential of concrete. *J. Clean. Prod.* **2017**, *166*, 485–502. [[CrossRef](#)]
38. Payá, J.; Borrachero, M.V.; Monzó, J.; Peris-Mora, E.; Bonilla, M. Long term mechanical strength behaviour in fly ash/Portland cement mortars prepared using processed ashes. *J. Chem. Technol. Biotechnol.* **2002**, *77*, 336–344. [[CrossRef](#)]
39. Sakai, E.; Miyahara, S.; Ohsawa, S.; Lee, S.H.; Daimon, M. Hydration of fly ash cement. *Cem. Concr. Res.* **2005**, *35*, 1135–1140. [[CrossRef](#)]
40. Moon, G.D.; Oh, S.; Choi, Y.C. Effects of the physicochemical properties of fly ash on the compressive strength of high-volume fly ash mortar. *Constr. Build. Mater.* **2016**, *124*, 1072–1080. [[CrossRef](#)]
41. Flower, D.J.M.; Sanjayan, J.G. Chapter 1—Greenhouse Gas Emissions Due to Concrete Manufacture. In *Handbook of Low Carbon Concrete*; Nazari, A., Sanjayan, J.G., Eds.; Butterworth-Heinemann: Oxford, UK, 2017; pp. 1–16. [[CrossRef](#)]
42. Robalo, K.; Costa, H.; Carmo, R.d.; Júlio, E. Experimental development of low cement content and recycled construction and demolition waste aggregates concrete. *Constr. Build. Mater.* **2021**, *273*, 121680. [[CrossRef](#)]
43. Martín-Morales, M.; Zamorano, M.; Ruiz-Moyano, A.; Valverde-Espinosa, I. Characterization of recycled aggregates construction and demolition waste for concrete production following the Spanish Structural Concrete Code EHE-08. *Constr. Build. Mater.* **2011**, *25*, 742–748. [[CrossRef](#)]
44. Tu, T.Y.; Chen, Y.Y.; Hwang, C.L. Properties of HPC with recycled aggregates. *Cem. Concr. Res.* **2006**, *36*, 943–950. [[CrossRef](#)]
45. Etxeberria, M.; Vázquez, E.; Mari, A.; Barra, M. Influence of amount of recycled coarse aggregates and production process on properties of recycled aggregate concrete. *Cem. Concr. Res.* **2007**, *37*, 735–742. [[CrossRef](#)]
46. Barbudo, A.; Agrela, F.; Beltrán, M.G.; Jiménez, J.R.; Galvín, A.P. Effect of cement addition on the properties of recycled concretes to reach control concretes strengths. *J. Clean. Prod.* **2014**, *79*, 124–133. [[CrossRef](#)]
47. Kapoor, K.; Singh, S.P.; Singh, B. Durability of self-compacting concrete made with Recycled Concrete Aggregates and mineral admixtures. *Constr. Build. Mater.* **2016**, *128*, 67–76. [[CrossRef](#)]
48. Medina, C.; Zhu, W.; Howind, T.; de Rojas, M.I.S.; Frías, M. Influence of mixed recycled aggregate on the physical-mechanical properties of recycled concrete. *J. Clean. Prod.* **2014**, *68*, 216–225. [[CrossRef](#)]
49. Shi, C.; Li, Y.; Zhang, J.; Li, W.; Chong, L.; Xie, Z. Performance enhancement of recycled concrete aggregate—A review. *J. Clean. Prod.* **2016**, *112*, 466–472. [[CrossRef](#)]
50. Lovato, P.S.; Possan, E.; Dal Molin, D.C.C.; Masuero, Á.B.; Ribeiro, J.L.D. Propriedades Mecânicas e de Durabilidade de Concretos com Agregados Reciclados. In Proceedings of the XII Congreso Latinoamericano de Patología y XIV Congreso de Calidad de la Construcción CONPAT, Cartagena, Colombia, 30 September–4 October 2013; pp. 1–10.
51. Kisku, N.; Joshi, H.; Ansari, M.; Panda, S.K.; Nayak, S.; Dutta, S.C. A critical review and assessment for usage of recycled aggregate as sustainable construction material. *Constr. Build. Mater.* **2017**, *131*, 721–740. [[CrossRef](#)]
52. Verian, K.P.; Ashraf, W.; Cao, Y. Properties of recycled concrete aggregate and their influence in new concrete production. *Resour. Conserv. Recycl.* **2018**, *133*, 30–49. [[CrossRef](#)]
53. Agrela, F.; de Juan, M.S.; Ayuso, J.; Gerdal, V.L.; Jiménez, J.R. Limiting properties in the characterisation of mixed recycled aggregates for use in the manufacture of concrete. *Constr. Build. Mater.* **2011**, *25*, 3950–3955. [[CrossRef](#)]
54. Sharba, A.A.K.; Altemen, A.A.G.A.; Hason, M.M. Shear behavior of exploiting recycled brick waste and steel slag as an alternative aggregate for concrete production. *Mater. Today Proc.* **2021**, *42*, 2621–2628. [[CrossRef](#)]
55. Zachariah, J.P.; Sarkar, P.P.; Pal, M. A study on the moisture damage and rutting resistance of polypropylene modified bituminous mixes with crushed brick aggregate wastes. *Constr. Build. Mater.* **2021**, *269*, 121357. [[CrossRef](#)]
56. Dang, J.; Zhao, J.; Pang, S.D.; Zhao, S. Durability and microstructural properties of concrete with recycled brick as fine aggregates. *Constr. Build. Mater.* **2020**, *262*, 120032. [[CrossRef](#)]
57. Li, Y.; Yang, X.; Lou, P.; Wang, R.; Li, Y.; Si, Z. Sulfate attack resistance of recycled aggregate concrete with NaOH-solution-treated crumb rubber. *Constr. Build. Mater.* **2021**, *287*, 123044. [[CrossRef](#)]
58. Jian, S.M.; Wu, B. Compressive behavior of compound concrete containing demolished concrete lumps and recycled aggregate concrete. *Constr. Build. Mater.* **2021**, *272*, 121624. [[CrossRef](#)]
59. Sahoo, S.; Singh, B. Punching shear capacity of recycled-aggregate concrete slab-column connections. *J. Build. Eng.* **2021**, *41*, 102430. [[CrossRef](#)]
60. Martínez-Lage, I.; Vázquez-Burgo, P.; Velay-Lizancos, M. Sustainability evaluation of concretes with mixed recycled aggregate based on holistic approach: Technical, economic and environmental analysis. *Waste Manag.* **2020**, *104*, 9–19. [[CrossRef](#)]
61. Cantero, B.; del Bosque, I.F.S.; Matías, A.; Medina, C. Statistically significant effects of mixed recycled aggregate on the physical-mechanical properties of structural concretes. *Constr. Build. Mater.* **2018**, *185*, 93–101. [[CrossRef](#)]
62. Kazmi, S.M.S.; Munir, M.J.; Wu, Y.F. Application of waste tire rubber and recycled aggregates in concrete products: A new compression casting approach. *Resour. Conserv. Recycl.* **2021**, *167*, 105353. [[CrossRef](#)]
63. Feng, W.; Liu, F.; Yang, F.; Jing, L.; Li, L.; Li, H.; Chen, L. Compressive behaviour and fragment size distribution model for failure mode prediction of rubber concrete under impact loads. *Constr. Build. Mater.* **2021**, *273*, 121767. [[CrossRef](#)]
64. Omoding, N.; Cunningham, L.S.; Lane-Serff, G.F. Effect of using recycled waste glass coarse aggregates on the hydrodynamic abrasion resistance of concrete. *Constr. Build. Mater.* **2021**, *268*, 121177. [[CrossRef](#)]

65. Anupam, B.R.; Balan, L.A.; Sharma, S. Thermal and mechanical performance of cement concrete pavements containing PVC-glass mix. *Road Mater. Pavement Des.* **2021**, *290*, 123238. [CrossRef]
66. Yang, S.; Lu, J.X.; Poon, C.S. Recycling of waste glass in dry-mixed concrete blocks: Evaluation of alkali-silica reaction (ASR) by accelerated laboratory tests and long-term field monitoring. *Constr. Build. Mater.* **2020**, *262*, 120865. [CrossRef]
67. Penacho, P.; de Brito, J.; Veiga, M.R. Physico-mechanical and performance characterization of mortars incorporating fine glass waste aggregate. *Cem. Concr. Compos.* **2014**, *50*, 47–59. [CrossRef]
68. Poon, C.S.; Shui, Z.H.; Lam, L. Effect of microstructure of ITZ on compressive strength of concrete prepared with recycled aggregates. *Constr. Build. Mater.* **2004**, *18*, 461–468. [CrossRef]
69. Xiao, J.; Li, W.; Sun, Z.; Lange, D.A.; Shah, S.P. Properties of interfacial transition zones in recycled aggregate concrete tested by nanoindentation. *Cem. Concr. Compos.* **2013**, *37*, 276–292. [CrossRef]
70. Duan, P.; Shui, Z.; Chen, W.; Shen, C. Effects of metakaolin, silica fume and slag on pore structure, interfacial transition zone and compressive strength of concrete. *Constr. Build. Mater.* **2013**, *44*, 1–6. [CrossRef]
71. Xiao, J.; Li, W.; Corr, D.J.; Shah, S.P. Effects of interfacial transition zones on the stress-strain behavior of modeled recycled aggregate concrete. *Cem. Concr. Res.* **2013**, *52*, 82–99. [CrossRef]
72. Zhang, H.; Ji, T.; Liu, H. Performance evolution of the interfacial transition zone (ITZ) in recycled aggregate concrete under external sulfate attacks and dry-wet cycling. *Constr. Build. Mater.* **2019**, *229*, 116938. [CrossRef]
73. Kong, D.; Lei, T.; Zheng, J.; Ma, C.; Jiang, J.; Jiang, J. Effect and mechanism of surface-coating pozzalanic materials around aggregate on properties and ITZ microstructure of recycled aggregate concrete. *Constr. Build. Mater.* **2010**, *24*, 701–708. [CrossRef]
74. Kang, M.; Weibin, L. Effect of the aggregate size on strength properties of recycled aggregate concrete. *Adv. Mater. Sci. Eng.* **2018**, *2018*. [CrossRef]
75. Musa, M.F.; bin Saim, A.A. *The Effect of Aggregate Size on the Strength of Concrete*; Universiti Teknologi Malaysia: Skudai, Malaysia, 2017; Volume 10, pp. 9–11. Available online: <http://sps.utm.my/thecolloquium/files/2017/09/TC-10-9-12.pdf> (accessed on 9 May 2021).
76. Myadraboina, H.; Setunge, S.; Patnaikuni, I. Pozzolanic Index and lime requirement of low calcium fly ashes in high volume fly ash mortar. *Constr. Build. Mater.* **2017**, *131*, 690–695. [CrossRef]
77. Gunasekara, C.; Law, D.W.; Setunge, S.; Sanjayan, J.G. Zeta potential, gel formation and compressive strength of low calcium fly ash geopolymers. *Constr. Build. Mater.* **2015**, *95*, 592–599. [CrossRef]
78. Kiattikomol, K.; Jaturapitakkul, C.; Songpiriyakij, S.; Chutubtim, S. A study of ground coarse fly ashes with different finenesses from various sources as pozzolanic materials. *Composites* **2001**, *23*, 335–343. [CrossRef]
79. Blissett, R.S.; Rowson, N.A. A review of the multi-component utilisation of coal fly ash. *Fuel* **2012**, *97*, 1–23. [CrossRef]
80. Durdziński, P.T.; Dunant, C.F.; Haha, M.B.; Scrivener, K.L. A new quantification method based on SEM-EDS to assess fly ash composition and study the reaction of its individual components in hydrating cement paste. *Cem. Concr. Res.* **2015**, *73*, 111–122. [CrossRef]
81. Ramachandran, V.S.P. *Concrete Admixtures Handbook—Properties, Science and Technology*, 12th ed.; William Andrew: Park Ridge, NJ, USA, 1984; 180p.
82. Shehata, M.H.; Thomas, M.D.A.; Bleszynski, R.F. The effects of fly ash composition on the chemistry of pore solution in hydrated cement pastes. *Cem. Concr. Res.* **1999**, *29*, 1915–1920. [CrossRef]
83. de Grazia, M.T.; Goshayeshi, N.; Gorga, R.; Sanchez, L.F.M.; Santos, A.C.; Souza, D.J. Comprehensive semi-empirical approach to describe alkali aggregate reaction (AAR) induced expansion in the laboratory. *J. Build. Eng.* **2021**, *40*, 102298. [CrossRef]
84. Mehta, P.K. Natural Pozzolan. In *Supplementary Cementing Materials*; Malhotra, V.M., Ed.; 1987; 427p, Available online: https://books.google.com/books/about/Supplementary_cementing_materials_for_co.html?id=PL9TAAAMAAMAJ (accessed on 9 May 2021).
85. Wang, Z.S. Influence of fly ash on the mechanical properties of frame concrete. *Sustain. Cities Soc.* **2011**, *1*, 164–169. [CrossRef]
86. Oner, A.; Akyuz, S.; Yildiz, R. An experimental study on strength development of concrete containing fly ash and optimum usage of fly ash in concrete. *Cem. Concr. Res.* **2005**, *35*, 1165–1171. [CrossRef]
87. Arezoumandi, M.; Looney, T.J.; Volz, J.S. Effect of fly ash replacement level on the bond strength of reinforcing steel in concrete beams. *J. Clean. Prod.* **2015**, *87*, 745–751. [CrossRef]
88. Rao, B.H.; Dinakar, P.; Mohanty, A.N.; Reddy, M.S.; Pavithra, P.; Satpathy, B.K. A mix design procedure for geopolymer concrete with fly ash. *J. Clean. Prod.* **2016**, *133*, 117–125. [CrossRef]
89. Alghazali, H.H.; Myers, J.J. Shear behavior of full-scale high volume fly ash-self consolidating concrete (HVFA-SCC) beams. *Constr. Build. Mater.* **2017**, *157*, 161–171. [CrossRef]
90. Komonwearaket, K.; Cetin, B.; Aydilek, A.H.; Benson, C.H.; Edil, T.B. Effects of pH on the leaching mechanisms of elements from fly ash mixed soils. *Fuel* **2015**, *140*, 788–802. [CrossRef]
91. Gholampour, A.; Ozbakkaloglu, T. Performance of sustainable concretes containing very high volume Class-F fly ash and ground granulated blast furnace slag. *J. Clean. Prod.* **2017**, *162*, 1407–1417. [CrossRef]
92. Tosun-Felekoğlu, K.; Gödek, E.; Keskinates, M.; Felekoğlu, B. Utilization and selection of proper fly ash in cost effective green HTPP-ECC design. *J. Clean. Prod.* **2017**, *149*, 557–568. [CrossRef]
93. Wright, J.R.; Shafaatian, S.; Rajabipour, F. Reliability of chemical index model in determining fly ash effectiveness against alkali-silica reaction induced by highly reactive glass aggregates. *Constr. Build. Mater.* **2014**, *64*, 166–171. [CrossRef]

94. Shafaatian, S.M.H.; Akhavan, A.; Maraghechi, H.; Rajabipour, F. How does fly ash mitigate alkali-silica reaction (ASR) in accelerated mortar bar test (ASTM C1567)? *Cem. Concr. Compos.* **2013**, *37*, 143–153. [[CrossRef](#)]
95. Du, L.; Lukefahr, E.; Naranjo, A. Texas Department of Transportation Fly Ash Database and the Development of Chemical Composition-Based Fly Ash Alkali-Silica Reaction Durability Index. *J. Mater. Civ. Eng.* **2012**, *25*, 70–77. [[CrossRef](#)]
96. Oey, T.; Timmons, J.; Stutzman, P.; Bullard, J.W.; Balonis, M.; Bauchy, M.; Sant, G. An improved basis for characterizing the suitability of fly ash as a cement replacement agent. *J. Am. Ceram. Soc.* **2017**, *100*, 4785–4800. [[CrossRef](#)]
97. Aboustait, M.; Kim, T.; Ley, M.T.; Davis, J.M. Physical and chemical characteristics of fly ash using automated scanning electron microscopy. *Constr. Build. Mater.* **2016**, *106*, 1–10. [[CrossRef](#)]
98. Schumacher, K.A.; Ideker, J.H. New Considerations in Predicting Mitigation of Alkali-Silica Reaction Based on Fly Ash Chemistry. *J. Mater. Civ. Eng.* **2014**, *27*, 04014144. [[CrossRef](#)]
99. Gunasekara, C.; Law, D.W.; Setunge, S. Long term permeation properties of different fly ash geopolymer concretes. *Constr. Build. Mater.* **2016**, *124*, 352–362. [[CrossRef](#)]
100. Du, W.; Zhang, C.-Y.; Kong, X.-M.; Zhuo, Y.-Q.; Zhu, Z.-W. Mercury release from fly ashes and hydrated fly ash cement pastes. *Atmos. Environ.* **2018**, *178*, 11–18. [[CrossRef](#)]
101. Chindaprasirt, P.; Homwuttivong, S.; Sirivivatnanon, V. Influence of fly ash fineness on strength, drying shrinkage and sulfate resistance of blended cement mortar. *Cem. Concr. Res.* **2004**, *34*, 1087–1092. [[CrossRef](#)]
102. Tkaczewska, E. Effect of size fraction and glass structure of siliceous fly ashes on fly ash cement hydration. *J. Ind. Eng. Chem.* **2014**, *20*, 315–321. [[CrossRef](#)]
103. Ma, Y.; Hu, J.; Ye, G. The effect of activating solution on the mechanical strength, reaction rate, mineralogy, and microstructure of alkali-activated fly ash. *J. Mater. Sci.* **2012**, *47*, 4568–4578. [[CrossRef](#)]
104. Durdziński, P.T.; Snellings, R.; Dunant, C.F.; Haha, M.B.; Scrivener, K.L. Fly ash as an assemblage of model Ca-Mg-Na-aluminosilicate glasses. *Cem. Concr. Res.* **2015**, *78*, 263–272. [[CrossRef](#)]
105. Shahr, N.; Salih, A.; Hamad, S.M.; Kurda, R. Comprehensive multiscale techniques to estimate the compressive strength of concrete incorporated with carbon nanotubes at various curing times and mix proportions. *J. Mater. Res. Technol.* **2021**, *15*, 6506–6527. [[CrossRef](#)]
106. Barkhordari, M.S.; Armaghani, D.J.; Mohammed, A.S. Data-Driven Compressive Strength Prediction of Fly Ash Concrete Using Ensemble Learner Algorithms. *Buildings* **2022**, *12*, 132. [[CrossRef](#)]
107. Shahr, N.; Mohammed, A.; Hamad, S.M.; Kurda, R. Electrical resistivity-Compressive strength predictions for normal strength concrete with waste steel slag as a coarse aggregate replacement using various analytical models. *Constr. Build. Mater.* **2022**, *327*, 127008. [[CrossRef](#)]
108. Corinaldesi, V.; Moriconi, G. Influence of mineral additions on the performance of 100% recycled aggregate concrete. *Constr. Build. Mater.* **2009**, *23*, 2869–2876. [[CrossRef](#)]
109. Lorca, P.; Calabuig, R.; Benlloch, J.; Soriano, L.; Payá, J. Microconcrete with partial replacement of Portland cement by fly ash and hydrated lime addition. *Mater. Des.* **2014**, *64*, 535–541. [[CrossRef](#)]
110. Poon, C.S.; Lam, L.; Wong, Y.L. Study on high strength concrete prepared with large volumes of low calcium fly ash. *Cem. Concr. Res.* **2000**, *30*, 447–455. [[CrossRef](#)]
111. Gonzalez-Corominas, A.; Etxeberria, M.; Poon, C.S. Influence of steam curing on the pore structures and mechanical properties of fly-ash high performance concrete prepared with recycled aggregates. *Cem. Concr. Compos.* **2016**, *71*, 77–84. [[CrossRef](#)]
112. Filho, J.H. *Sistemas Cimento, Cinza Volante e Cal Hidratada: Mecanismo de Hidratação, Microestrutura e Carbonatação do Concreto*; Escola Politécnica da Universidade de São Paulo: Sao Paulo, Brazil, 2008.
113. Kou, S.C.; Poon, C.S.; Chan, D. Influence of fly ash as a cement addition on the hardened properties of recycled aggregate concrete. *Mater. Struct.* **2008**, *41*, 1191–1201. [[CrossRef](#)]
114. Neville, A.M. *Propriedades do Concreto*, 2nd ed.; Editora Pini Ltd.: São Paulo, Brazil, 1997.
115. Zhang, W.; Huang, Q.; Jiang, Z.; Dou, X.; Gu, X. Numerical analysis of the effect of coarse aggregate distribution on concrete carbonation. *Constr. Build. Mater.* **2012**, *37*, 27–35. [[CrossRef](#)]
116. Supit, S.W.M.; Shaikh, F.U.A.; Sarker, P.K. Effect of ultrafine fly ash on mechanical properties of high volume fly ash mortar. *Constr. Build. Mater.* **2014**, *51*, 278–286. [[CrossRef](#)]
117. Ann, K.Y.; Moon, H.Y.; Kim, Y.B.; Ryou, J. Durability of recycled aggregate concrete using pozzolanic materials. *Waste Manag.* **2008**, *28*, 993–999. [[CrossRef](#)]
118. Khunthongkeaw, J.; Tangtermsirikul, S.; Leelawat, T. A study on carbonation depth prediction for fly ash concrete. *Constr. Build. Mater.* **2006**, *20*, 744–753. [[CrossRef](#)]
119. Atiş, C.D. Accelerated carbonation and testing of concrete made with fly ash. *Constr. Build. Mater.* **2003**, *17*, 147–152. [[CrossRef](#)]
120. Li, J.; Xiao, H.; Zhou, Y. Influence of coating recycled aggregate surface with pozzolanic powder on properties of recycled aggregate concrete. *Constr. Build. Mater.* **2009**, *23*, 1287–1291. [[CrossRef](#)]
121. Sidorova, A.; Vazquez-Ramonich, E.; Barra-Bizinotto, M.; Roa-Rovira, J.J.; Jimenez-Pique, E. Study of the recycled aggregates nature's influence on the aggregate-cement paste interface and ITZ. *Constr. Build. Mater.* **2014**, *68*, 677–684. [[CrossRef](#)]
122. Juan-Valdés, A.; Rodríguez-Robles, D.; García-González, J.; Guerra-Romero, M.I.; Morán-del Pozo, J.M. Mechanical and microstructural characterization of non-structural precast concrete made with recycled mixed ceramic aggregates from construction and demolition wastes. *J. Clean. Prod.* **2018**, *180*, 482–493. [[CrossRef](#)]

Article

Identifying the Barriers to Sustainable Management of Construction and Demolition Waste in Developed and Developing Countries

Ali Al-Otaibi ^{1,*}, Patrick Aaniamenga Bowan ², Mahmoud M. Abdel daiem ^{1,3}, Noha Said ³, John Obas Ebohon ⁴, Aasem Alabdullatief ⁵, Essa Al-Enazi ⁶ and Greg Watts ⁷

- ¹ Civil Engineering Department, College of Engineering, Shaqra University, Al-Dawadmi 11911, Saudi Arabia; mmabdeldaim@zu.edu.eg
 - ² Department of Civil Engineering, School of Engineering, Dr. Hilla Limann Technical University (Formerly Wa Polytechnic), Wa P.O. Box 553, Ghana; p.a.bowan@dhltu.edu.gh
 - ³ Environmental Engineering Department, Faculty of Engineering, Zagazig University, Zagazig 44519, Egypt; nsmohammed@zu.edu.eg
 - ⁴ School of Built Environment and Architecture, London South Bank University (LSBU), London SE1 0AA, UK; ebohono@lsbu.ac.uk
 - ⁵ Department of Architecture and Built Environment, College of Architecture and Planning, King Saud University, Ar Riyadh 11451, Saudi Arabia; aasem@ksu.edu.sa
 - ⁶ General Administration for Investment and Privatization, Ministry of Education, Ar Riyadh 11451, Saudi Arabia; arch_esa@hotmail.com
 - ⁷ School of Science, Engineering and Environment, University of Salford, Salford M5 4NT, UK; g.n.watts@salford.ac.uk
- * Correspondence: alialotaibi@su.edu.sa; Tel.: +966-505117740

Citation: Al-Otaibi, A.; Bowan, P.A.; Abdel daiem, M.M.; Said, N.; Ebohon, J.O.; Alabdullatief, A.; Al-Enazi, E.; Watts, G. Identifying the Barriers to Sustainable Management of Construction and Demolition Waste in Developed and Developing Countries. *Sustainability* **2022**, *14*, 7532. <https://doi.org/10.3390/su14137532>

Academic Editors: Carlos Morón Fernández and Daniel Ferrández Vega

Received: 23 April 2022

Accepted: 13 June 2022

Published: 21 June 2022

Publisher's Note: MDPI stays neutral with regard to jurisdictional claims in published maps and institutional affiliations.



Copyright: © 2022 by the authors. Licensee MDPI, Basel, Switzerland. This article is an open access article distributed under the terms and conditions of the Creative Commons Attribution (CC BY) license (<https://creativecommons.org/licenses/by/4.0/>).

Abstract: The construction industry is a vital part of every nation's economy. Construction activities influence the social, environmental, and economic aspects of sustainability. There are so many barriers to sustainable construction and demolition waste management (C&DWM). This study aims to identify barriers for effective sustainable C&DWM in developed and developing countries. To achieve the objective, 11 barriers have been selected and identified based on an excessive and comprehensive literature review, and then reviewed by experts. These reviewed barriers were further examined by various experts within different organizations using a questionnaire survey. Ranking of the barriers was carried out using the Relative Importance Index (RI), and the results were statistically analyzed using Statistical Package for Social Sciences (SPSS). Practical solutions were proposed to overcome the identified barriers. The overall ranking of barriers by RI indicates that insufficient attention paid to C&DWM, lack of law enforcement, lack of regulation, and financial constraints represent the four major barriers to sustainable C&DWM in these countries. The findings of this study and the proposed solutions are enablers for decision-makers to develop effective strategies to tackle construction and demolition wastes in sustainable manners.

Keywords: barriers; sustainability; construction and demolition waste; waste management; relative importance index

1. Introduction

The population and economic growth due to urbanization have increased the amount of municipal waste, notably construction and demolition waste (C&DW) generated from increased demand for housing and municipal expansion [1]. This massive amount of C&DW creates environmental burdens, for example by depleting resources, reducing green space, and increasing air and land pollution and toxic waste discharge [2,3].

Consequently, the rapid increase in global urbanization has increased the demands placed upon the construction industry [4,5]. The construction industry now not only needs

to meet this increasing demand for urban spaces but also effectively address all the negative externalities associated with increased urbanization. This includes the large-scale clearance of agricultural land, high energy consumption, and rising environmental degradation [6]. The amount of C&DW generated by the industry is also increasing at a rapid rate. Globally, more than 10 billion tons of C&DW are produced every year [7,8]. The construction industry is seen as a major generator of waste and pollution, as waste from construction activities significantly pollutes the environment [8,9]. The proper management of this waste is a challenge in many countries, particularly developing countries. Moreover, construction projects in most developing countries have been characterized by poor performance in terms of sustainability [10]. C&DW mainly consists of inert and non-biodegradable materials such as concrete, plaster, wood, metal, broken tiles, bricks, and masonry [11]. In some parts of the world, the disposal of C&DW often creates additional hazards as it is disposed of indiscriminately and illegally on any available space, including on the shoulders of major roads [12].

Although the construction industry has a vital role in developing cities, its contribution to environmental degradation is widely acknowledged [13]. Infrastructural development can lead to significant C&DW generation if it is not designed and constructed sustainably. The C&DW is considered the largest waste flow worldwide, and has reached 30–40% of the total solid waste (SW) [14–16], for instance, the European construction sector produces 820 million tons of C&DW every year, which is around 46% of the total amount of SW generated in Europe [17]. Sustainable construction has become a focal point for countries worldwide, as the Earth's resources are under severe pressure due to increasing population and economic expansion. As a result of this, many countries are striving to implement sustainable construction practices in their construction industries [10].

Sustainable management of C&DW is therefore of paramount importance to mitigate and reduce the environmental impacts of C&DW. Thus, it takes into consideration reducing raw material consumption, reusing materials, appropriate recycling mechanisms, and minimizing waste generation from construction and demolition tasks [18]. Despite great previous efforts, the current practice in the construction industry is far from reaching the goals of sustainability to fully achieve sustainable construction. Recent research has shown that the construction industry requires significant transformation to fully implement sustainable practices to contribute to the achievement of sustainable development goals [1].

Understanding the barriers to sustainable development can promote the development of eco-friendly, socially harmless, and economically viable strategies [1]. Prior studies have assessed the barriers to sustainable construction and demolition waste management (C&DWM). Some studies showed that the economic concerns are the most influential in C&DWM from both governmental and institutional perspectives [18,19]. Negash et al. [1] found that the eliminating regulatory and social barriers can significantly enhance the performance of C&DWM. Also, Dong et al. [20] showed that the technical barriers areas are important due to the complexity of waste management; technical resources such as appropriate processes, procedures, and people are needed for waste management activities. Furthermore, Ghaffar et al. [21] emphasized that improvement in the regulatory system, social awareness, technical practices, and the development of waste infrastructure using innovation to treat waste are necessary to achieve sustainable C&DWM.

Therefore, this research contributes to provide qualitative information about the challenges and barriers to sustainable C&DWM and aims to investigate, identify, and rank the barriers to C&DWM. Effectively, the identifications of these barriers may help decision makers to develop the strategies required to mitigate them.

This study is organized as follows: Section 1 introduces the research; Section 2 is focused on literature reviews on the barriers to achieve sustainable C&DWM; Section 3 outlines the methodology used in this study including identification barriers and data analysis procedures; Section 4 presents and discusses the results including categorization of the construction industry, evaluation of the barriers to effective and sustainable C&DWM, suggestion solutions to tackle the barriers to effective sustainable C&DWM, and statistical

analysis for the obtained results; Section 5 states the main conclusions from the present study, summarizes limitations, and presents recommendations for future studies.

2. Literature Review

The construction industry encompasses the design, construction, maintenance, and demolition of assets, buildings, engineering, and infrastructure works. It involves the entire life cycle of buildings and infrastructure from concept and design, to development, use, and ultimate demolition [22] and the importance of the construction industry to the economy of a country cannot be underestimated. It has been argued that a country's construction industry is vital to its economic development and national growth [23], yet stakeholders are increasingly demanding construction companies take responsibility beyond their economic contribution to include their impact upon the wider environment and society [24]. Unlike many industries, the construction industry also operates almost wholly in the public eye and so is subject to a greater level of scrutiny over its practices, specifically around waste minimization, reuse, and recycling practices. The construction industry involves several participants and stakeholders, their consciousness and commitment can have a major impact on the effectiveness of C&DWM.

C&DWM is considered to be one of the most important environmental challenges faced by policymakers worldwide because of the rate of increase and associated pollution. Accordingly, many researchers have identified many barriers to effective C&DWM around the world. Bufoni et al. [25] identified socio-political, technological, regulatory, financial, and human resources constraints as the barriers to effective C&DWM. This is supported by Menegaki and Damigos [26], who also identified the lack of regulatory and financial resources as hindrances to sustainable C&DWM. Similarly, Udawatta et al. [27] found that the main barriers to effective C&DWM include the rigidity of construction practices, construction project characteristics, awareness, experience and commitment, and the rudimentary nature of waste management systems, and human and technical factors. Aghimien et al. [28] revealed that the major barriers to sustainable construction practices are fear of higher investment costs, no local green certification available, lack of government policies or support, and lack of financial incentives. Opoku and Ahmed [29] recognized the importance of public awareness and proper knowledge and understanding of sustainability as being essential to the successful promotion of sustainable construction practices in the various construction organizations. Aghimien et al. [28] noted that sustainability awareness and the knowledge-related factor are crucial barriers to sustainable construction. Karji et al. [5] found that pre-construction constraints, managerial constraints, legislative constraints, and financial and planning constraints are the most influential challenges that the industry faces to foster sustainable construction. Furthermore, the barriers to effective C&DWM are classified under three dimensions: behavioral, technical, and legal [30]. Huang et al. [31] also acknowledged that ineffective management systems, immature recycling technology, under-developed market for recycled C&DW products, and immature recycling market operations constitute barriers to C&DWM. Also of note is the findings that barriers to effective C&DWM vary from country to country and regions of the world. This is hardly surprising given the differences in levels of socio-economic cultural norms, institutions, energy sources, and climate [32].

Prior studies highlighted that the consideration of economic barriers is essential because contractors usually seek and give high priority to financial gains [19,33]. Lockrey et al. [34] underlined that economic viability is a significant barrier and has a substantial effect on contractors' performance, practices, and behaviors regarding C&DWM. Chen et al. [19] identified economic barriers as having the most influence on both government institutions' and contractors' management strategies. Negash et al. [1] revealed that the economic barriers are significant and should be investigated to improve the understanding of the obstacles to managing waste generated from construction works and provide solutions that address these obstacles. Moreover, technical barriers that involve the absence of the right expertise, knowledge, and technologies needed to promote sustainability are obstacles

to implement C&DWM [35,36]. Mahpour [30] argues that technical, legal, and social barriers are fundamental barriers that make it difficult to achieve sustainability. Negash et al. [1] noted that the technical weaknesses are significant sources of problems related to C&DWM and need to be considered. Social barriers, such as the lack of contractor awareness and lack of community involvement, significantly hinder the implementation of sustainability practices [34]. Abarca-Guerrero et al. [37] argue that social awareness affects the sustainability performance of C&DWM. Insufficient or the lack of management regulations, such as weak policies and inadequate supervision, create significant challenges for attaining sustainability in construction works [15,30,38]. Similarly, Negash et al. [1] indicate that it is necessary to consider the significance of regulatory barriers when assessing C&DWM.

On the other hand, policymakers and industry practitioners must improve their awareness and efforts to promote and implement effective C&DWM [39]. Albeit, the emergence of building information modeling technology provides new opportunities to reduce construction waste generation and project costs by enhancing the quality of design and construction management with inherent capabilities like material quantity take-off, spatial conflict analysis, and multidisciplinary data communications. However, few studies have focused on how to more effectively manage demolition waste generated from existing buildings with the aid of building information modeling applications [39,40]. Han et al. [39] identified the main barriers hindering the extensive adoption of building information modeling in C&DWM as the inefficient building data acquisition and integration process, moreover, existing waste management software and inherent waste analytic functionalities are not compatible with building information modeling.

3. Methodology

This study used data from the Science Direct and Web of Science database during the years 2019–2021 to explore research published in journals, books, chapters, and studies on the sustainable construction industry. The main keywords to search the database included construction industry, sustainable waste management, sustainable C&DWM, challenges, barriers and obstacles to sustainable C&DWM, management of C&DW in developed and developing countries, Egypt, Ghana, UK, and KSA, statistical analysis, relative importance (RI), proposed solutions to eliminate and overcome barriers to sustainable construction, etc. The papers included in this study were published between the years 1998 and 2021. This was done to identify barriers to sustainable C&DWM in some developed and developing countries as well as to investigate the possible solutions to tackle the barriers. The initial search yielded more than 300 publications in the English language. They were analyzed individually to assess if they focused on sustainable C&DWM in developed and developing countries. Thus, general and non-relevant articles were excluded from these articles. At the end, a total of 78 research items has been retained including 77 research articles and 1 technical report.

The methodology of the study consists of three main steps: In the first step, identify the barriers based on the literature review. In the second step, the questionnaire was assessed by experts in construction projects. In the third step, the reviewed questionnaire was sent to respondents to identify and rank the barriers. Ranking of the barriers was carried out using the RI, and the results were statistically analyzed using Statistical Package for Social Sciences (SPSS). Practical solutions were proposed to overcome the identified barriers. Figure 1 shows the methodology for the current research.

3.1. Identification of Barriers

There are so many barriers that hinder the effective and sustainable implementation of waste management policies and strategies in construction projects. In the first phase, 82 papers were reviewed and eleven barriers were identified; later, 24 papers were reviewed and the selected barriers were the same. This is due to the overlap of suggested barriers investigated through the reviewed papers, as well as experts' recommendations, as indicated in Table 1. All these barriers are widely acknowledged in the literature and are

highly applicable in the current context of this study. The literature review focused mainly on two criteria for journal selection: indexed in Science Citation Index and a publication focusing on waste management.

Table 1. Barriers to effective C&DWM.

| Serial Number | Barriers to Effective C&DWM | References |
|---------------|--------------------------------------|---|
| B1 | Institutional Fragmentation | [4,27,31,33,41–47] |
| B2 | Lack of Fundamental Data on C&DW | [27,30,43,48–52] |
| B3 | Lack of Law Enforcement | [2,15,30,31,41,50,53–56] |
| B4 | Insufficient Attention Paid to C&DWM | [2,15,27,33] |
| B5 | Socio-political | [1,10,21,25,46,52,53,57] |
| B6 | Technological | [1,20,25–27,30,33,42–46,48,51,52,57] |
| B7 | Lack of Regulation | [1,2,10,15,21,25,26,31,33,43,45,49–51,53–56,58] |
| B8 | Financial | [1,10,15,25,26,31,43,44,52,53,57–59] |
| B9 | Human Resources Constraints | [2,4,25,27,30,42,52,54,55] |
| B10 | Construction Project Characteristics | [27,46,53,60] |
| B11 | Rigidity of Construction Practices | [27,52,60–62] |

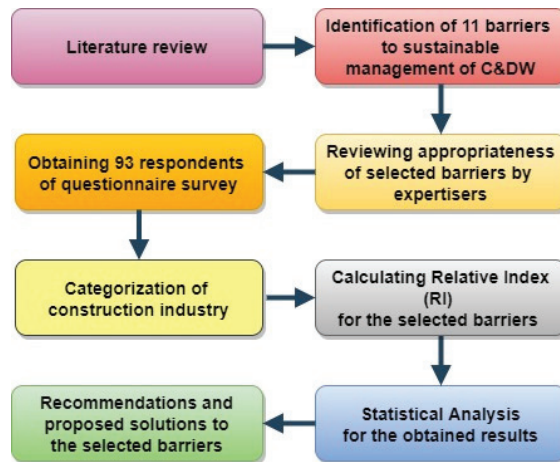


Figure 1. Research methodology scheme.

B1: Institutional Fragmentation.

Several institutions are involved in waste management, and as often as it is the case, many of these institutions reneged on their responsibilities, hoping other institutions would tackle the problem. This scenario occurs mostly under extensive bureaucracy where there are no clearly defined lines of responsibilities [2,46,47]. Institutional fragmentation is particularly a major challenge to effective and sustainable C&DWM, and rather than a weak and bureaucratic waste management system, requires effective and strong institutional arrangements for waste management [4,41,63,64].

B2: Lack of Fundamental Data on C&DW.

Sustainable waste management requires reliable data on rates of generation and composition of the wastes. However, the fundamental data on C&DW that will inform effective planning for sustainable C&DWM is absent in many developing countries and woefully inadequate in some developed countries [27,51,52]. Notwithstanding this, C&DW comprises the largest waste stream in most developed countries and is also increasing at alarming rates in the developing world, due to an increasing rate of urbanization [65].

B3: Lack of Law Enforcement.

Many countries have a long history of safeguarding the environment, including attempts in ensuring proper C&DWM, and have enacted appropriate legislations; nonetheless, the enforcement of legislations is a major challenge in many countries, particularly in developing countries [41]. The non-compliance and non-enforcement of laws and regulations governing C&DW have significantly contributed to poor C&DWM in many countries [2,30,41,54].

B4: Insufficient Attention Paid to C&DWM.

Stakeholders in the construction industry usually focus more on completing the project within budget, at the expected time, and to the desired quality, and much less attention is paid to the waste emanating from construction activities [15,27,33,66]. This has given a bad image to the construction industry, as improper disposal of C&DW results in far-reaching environmental consequences [2].

B5: Socio-political factor.

The construction industry, like other industries, is characterized by cultural and socio-political differences across firms' types, age, and size. Consequently, several studies have linked the construction industry's culture with its waste intensiveness [1,10,21,52,67]. This means that an effective and sustainable waste management system cannot be established unless the cultural and socio-political patterns of construction firms are fully understood [25,46,53,57].

B6: Technological.

The C&DW technology and management choices in many countries have become very complicated, especially when reductions in greenhouse gasses, elimination of landfill sites, and land reclamation are targeted goals [42,44]. The C&DW sector has become a specialized industry involving huge and indivisible capital requirements, and sophisticated technology, requiring in-depth experience and expertise in research and engineering [26,30,43–46,51,57]. Technical information and guidance, advanced technologies and methodologies for sustainable construction represent important requirements for effective C&DWM [1,20,52].

B7: Lack of Regulation.

Environment regulation, including C&DWM, is essential for ensuring effective and sustainable environmental management and governance [1,2,10,21]. However, weak enforcement of environmental regulations in many countries allows construction firms to flout regulations on C&DWM without sanctions [50,51,55].

B8: Financial.

Financial resources are critical for effective waste management; however, these are generally scarce in many countries [25,44]. Poor economic policies, coupled with extreme poverty and infrastructure deficit, make the financial consideration one of the obvious constraints to developing appropriate C&DWM systems in most developing countries [1,10,26,43,52,68].

B9: Human Resources Constraints.

Human resources are essential for effective waste management, especially the daily operations of C&DWM [2,52]. Nonetheless, many countries do not have the human resources with the requisite expertise required for the effective and sustainable management of a C&DW system [25,27,30,42,54,55].

B10: Construction Project Characteristics.

Several construction project characteristics have the potential to influence C&DWM, which include: the complexity of the project, type of project, size of project, location of the project, the importance for the project to be completed on time, the form of contract, and project funding [27,46,53,60].

B11: Rigidity of Construction Practices

Many stakeholders are involved in the construction industry who play varied and crosscutting roles. The effectiveness of a C&DWM system in a particular location or country depends on the performance of these stakeholders in terms of their awareness of the impact of construction SW on the environment, and flexibility or rigidity in their practices [27,61,62]. With high public awareness about the problems posed by inadequate C&DWM, broad consultation and the involvement of all stakeholders are needed for the sustainable development of C&DWM strategies and policies [52,60].

3.2. Data Collection and Analysis

The questionnaire is a systematic technique of data collection and it is used to obtain professional opinions. A questionnaire survey was distributed amongst various stakeholders within different organizations to investigate barriers to effective waste management implementation in the construction industry in the selected countries. In this study, the construction industry in the studied countries was categorized in terms of ownership (public or private), type of the organization, size of the organization, role of the respondent in the organization, and experience of the respondent in the construction industry. A two-step procedure was adopted to assess its appropriateness and rationality. In the first step, the questionnaire was assessed by 15 persons having expertise in construction projects, to ensure clarity and technical applicability. In the second step, the reviewed questionnaire was sent to respondents to identify and rank the frequency (i.e., 1 = Never, 2 = Rarely, 3 = Occasionally, 4 = Sometimes, 5 = Frequently, 6 = Usually, and 7 = Always) of the eleven barriers.

The distribution was conducted across various countries, mainly the UK, the KSA, Ghana, and Egypt. Due to the ongoing COVID-19 pandemic, the Google questionnaire survey form was used. Around 150 experts in the construction field were invited to participate in the study and 93 responses were collected over the course of two months in 2020. A convenience sampling approach was adopted to select participants from each country; 93 valid responses were received and considered for analysis (UK: 18, KSA: 31, Ghana: 32, and Egypt: 12). All results were reported descriptively with the aid of Statistical Package for Social Sciences (SPSS), Microsoft Excel, and RI.

The study adopts the RI research method to identify and rank the critical barriers to the sustainable implementation of construction demolition waste management in the countries investigated. The RI is widely used in the analysis of construction strategies and policies. Equation (1) [69,70] depicts the RI measurement.

$$RI = \sum (ax) \times \frac{100}{7} \quad (1)$$

where: a = constant (weight) 1 to 7, x = n/N, n = Frequency of responses, N = Total responses.

Finally, the questionnaire included the reasons for organizations' engagement in effective C&DWM. It was investigated by asking the respondents "Why do you think your organization should engage in effective C&DWM activities?" This was performed to know the current trends and needs to achieve sustainable C&DWM in their organizations.

4. Results and Discussion

The results discussed under this section are based on the extensive literature review that produced the barriers to effective C&DWM and the responses to the questionnaire by experts from the UK, the KSA, Egypt, and Ghana. Thus, the responses of 93 experts in the construction industry are discussed.

4.1. Categorization of the Construction Industry

The classifications of respondents in relation to ownership of the organizations are shown in Figure 2a. It can be seen that 49.5% of the respondents were from the public sector, whereas 50.5% work in the private sector. Thus, both the public and private sectors of the economy were equally represented.

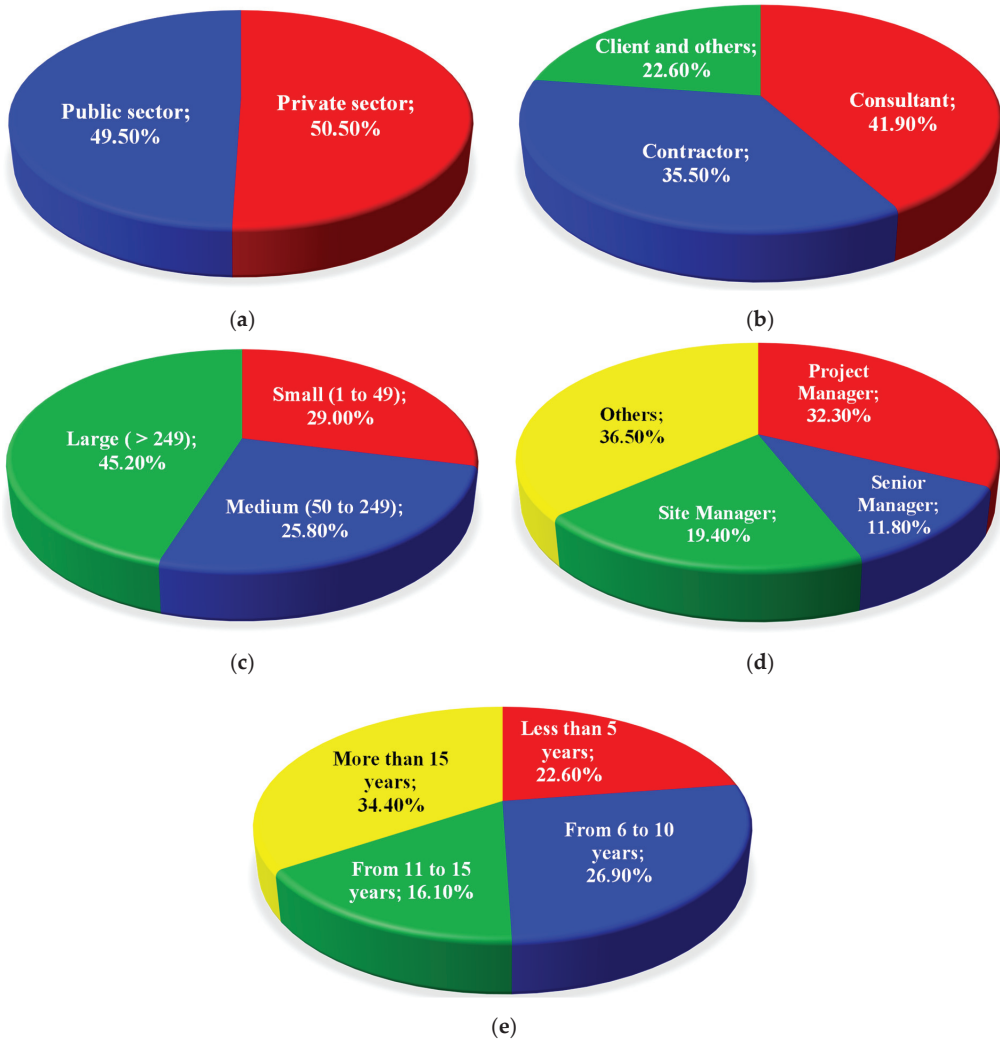


Figure 2. Categorization of the Construction Industry: (a) Ownership of the organization, (b) type of organization, (c) size of organization, (d) position in organization, and (e) years of experience.

Also, on the type of construction industry, a majority of the respondents (41.9%) were from consultancy firms and remaining respondents were contractors, clients, and other built environment professionals, as indicated in Figure 2b. These represent the main stakeholders in the construction industry of the four countries under study. Furthermore, Figure 2c indicates percentages of organizational size based on the number of employees. The organizations were categorized in sizes as: large organization (<249 employees), medium organization (50 to 249 employees), and small organization (>49 employees). The large size organization accounted for the highest percentage of respondents at 45.2% of all respondents.

In addition, the position of respondents in the organizations are classified in Figure 2d. Project managers recorded 32.8% of respondents, and the significance of this is that they were well placed to assess the barriers to an effective and sustainable C&DWM system. The classification of respondents according to the years of experience is shown in Figure 2e.

The category of respondents with more than 15 years of experience stood at 34.4%, whereas those with 6 to 10 years' experience constituted 26.9% of respondents.

It can be observed from the characteristics of respondents that the majority are from consultancy firms, large organizations, project managers, and have considerable experience of the workings of the construction industry in their respective countries.

4.2. Organizations' Engagement in Effective and Sustainable C&DWM

The result on organizations' engagement in effective and sustainable C&DWM were obtained and illustrated in Figure 3. The most prominent reasons identified by 70% of respondents was the desire "to make a positive difference to society". This clearly shows that respondents are aware of the adverse environmental effects of construction activities on the natural environment, and the need for the industry to make a difference to society in the manners that it conducts its activities. Though not as significant, 15% of respondents hold the view that the primary objective of their organization's engagement with sustainable C&DWM is to meet the primary objectives of delivering quality projects timely and within costs.

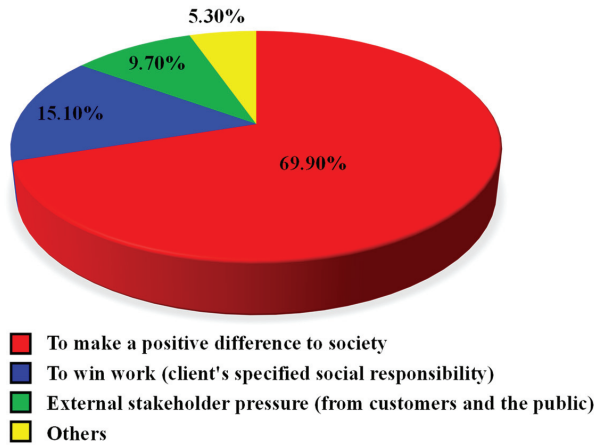


Figure 3. Reasons for organizations' engagement in effective C&DWM.

4.3. Evaluation of Barriers to Effective and Sustainable C&DWM

Based on the results obtained from the experts, the estimated RI values range from 0.45 to 0.70, as shown in Figure 4. These values were divided into three levels: strong barriers (0.60–0.70), moderate barriers (0.50–0.60), and weak barriers (<0.50).

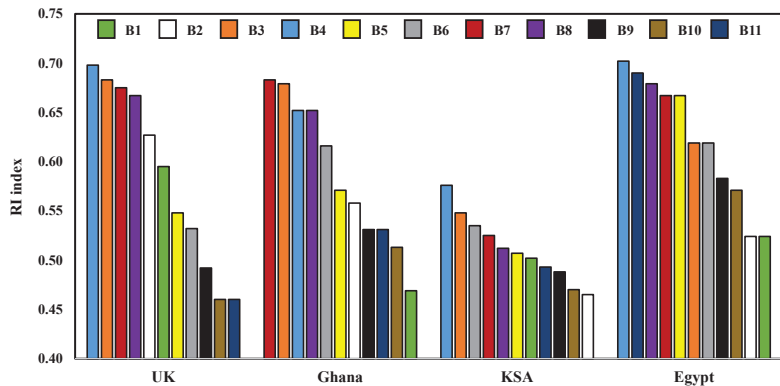


Figure 4. Variation of RI index for UK, Ghana, KSA, and Egypt.

4.3.1. Critical Barriers in the UK

According to the questionnaire in the UK, B4, B3, B7, B8, and B2 constitute the five strongest barriers to effective and sustainable C&DWM. Additionally, B1, B5, and B6 were regarded as moderate barriers to effective and sustainable C&DW. Notwithstanding these, the UK Government has been using a combination of regulations, economic instruments, and voluntary agreements to meet targets of ethical, social, and environmental performance in driving the waste management agenda [71,72]. Also, the UK implements legislative and fiscal measures which lead not only to construction waste reduction, but are directly related to the rising landfill tax, increasing cost for waste disposal, and compliance requirements with site waste management regulations from 2008 [73,74].

4.3.2. Critical Barriers in the KSA

The experts in the KSA indicated that the top seven barriers to sustainable C&DWM are B4, B3, B6, B7, B8, B5, and B1. Despite these barriers, the country has moderate RI values (0.50–0.60), the plurality of them is a major challenge to adopt feasible approaches to tackle the barriers. Identification of these barriers can support the efforts of decision makers in the Kingdom to meet their 2030 Vision. There are no data available on C&DW characterization [75]. Despite the fact that contractors play an important role in collecting C&DW from their sites by licensed waste haulers who are subcontracted to perform this task, the subcontractors usually dispose of these wastes indiscriminately in unapproved sites or by the roadsides, resulting in environmental and visual pollutions, and blockage to roads and drainage [2].

4.3.3. Critical Barriers in Egypt

The C&DWM challenges are not different in Egypt compared to the KSA and Ghana, as C&DWM is a major problem in the construction industry. Consequently, experts who responded to the study questionnaire identified seven strong barriers to sustainable C&DWM in Egypt. These barriers are B4, B11, B8, B7, B5, B3, and B6. The remaining barriers were regarded as moderate level barriers. Recently, Waste Management Law No.202 of 2020 has been adopted for waste management including construction and demolition waste in Egypt [76]. The main goals of the law are the development of an integrated municipal, industrial, agricultural wastes, and C&DWM system; to promote reuse; the recycling, treatment, and final disposal of waste; and to manage waste in a way that reduces damage to public health and the environment. The implementation of these policies will ensure effective and sustainable C&DWM in Egypt.

Notwithstanding this, Daoud et al. [77] posit that 5.8 million tons of C&DW is generated annually, which accounts for 6.4% of the total SW generation in Egypt. This figure may not reveal the extent of the problem owing to lack of accurate data on SW generation and characteristics in Egypt [78]. Similar to C&DW disposal in the KSA, C&DW is also usually dumped on roadsides and in open spaces. In the particular case of C&DW, contractors usually find it cheaper to transfer C&DW to illegal sites. This problem is continuing despite the new legislation, and this is due to several reasons including the existence of unregistered construction firms operating without permits, lack of regulatory enforcement, poor C&DW collection and disposal, limited local government participation, and poor financial commitments to C&DWM [77].

4.3.4. Critical Barriers in Ghana

The construction industry in Ghana, as with most others in sub-Saharan Africa, is underdeveloped, relying on imported materials and expertise to function. The relative underdevelopment of the sector is characterized by weak institutions and institution building capacity, hence the limited absorptive capacity for managerial, technology, technological innovations, as well as institutional development [10]. The current study indicates B7, B3, B4, B8, and B6 have the highest range of RI (0.60–0.70) and represent the major barriers to effective and sustainable C&DWM in Ghana. The other barriers are considered

moderate barriers and only B1 is disregarded based on its factor. In this context, previous studies showed that the additional financial cost of providing measures to improve the sustainability of construction works, the government policies, legislation and government commitment, the management of the construction industry, the technical information on sustainable construction, the desire of stakeholders in the construction industry to be committed to change, and congruent goals and objectives represented the main components for successful implementation of sustainable construction in the Ghanaian construction industry [10].

4.4. Common Barriers and Proposed Solutions

Opinion data from respondents were integrated and analyzed for all the countries studied. Table 2 indicates the descriptive information for the results and the overall ranking of barriers using the Relevance Index method. As can be observed, B4, B3, B7, and B8 are strong major barriers to sustainable C&DWM. However, the other barriers are considered as moderate barriers, with only B10 being considered as a weak barrier and can be disregarded due its low RI value (<0.50). The correlation coefficients of the results have also been determined to get the relationship between the different barriers. Table 3 shows the correlation coefficients, where the values between 0.5 and 1 indicate closely related barriers. The strongest relation has been found between B10 and B11 followed by the relation between B9 and B10. The lowest one has been detected between B1 and B10. These barriers can be mitigated and managed by organizations through proper management and leadership.

Table 2. Descriptive statistics of the received data and RI index for the overall countries.

| Barriers to Effective C&DWM | N | Minimum | Maximum | Mean | Std. Deviation | Variance | Confidence Level (95.0%) | RI | Rank |
|-----------------------------|----|---------|---------|------|----------------|----------|--------------------------|-------|------|
| B1 | 93 | 1 | 7 | 3.56 | 2.01 | 4.05 | 0.41 | 0.512 | 10 |
| B2 | 93 | 1 | 7 | 3.69 | 1.79 | 3.20 | 0.37 | 0.536 | 7 |
| B3 | 93 | 1 | 7 | 4.36 | 2.05 | 4.18 | 0.42 | 0.628 | 2 |
| B4 | 93 | 1 | 7 | 4.45 | 1.85 | 3.41 | 0.38 | 0.642 | 1 |
| B5 | 93 | 1 | 7 | 3.87 | 1.89 | 3.59 | 0.39 | 0.558 | 6 |
| B6 | 93 | 1 | 7 | 3.99 | 1.81 | 3.27 | 0.37 | 0.573 | 5 |
| B7 | 93 | 1 | 7 | 4.38 | 1.94 | 3.75 | 0.40 | 0.627 | 3 |
| B8 | 93 | 1 | 7 | 4.30 | 1.95 | 3.79 | 0.40 | 0.611 | 4 |
| B9 | 93 | 1 | 7 | 3.55 | 1.86 | 3.46 | 0.38 | 0.516 | 9 |
| B10 | 93 | 1 | 7 | 3.42 | 1.62 | 2.61 | 0.33 | 0.496 | 11 |
| B11 | 93 | 1 | 7 | 3.67 | 1.76 | 3.11 | 0.36 | 0.525 | 8 |

N: Number of valid Respondents, RI: Relative importance index.

Based on the evaluation of the barriers to effective and sustainable C&DWM in the four studied countries, practical solutions to overcoming barriers to effective and sustainable C&DWM have been proposed in Table 4. The proposed solutions to tackle the barriers to effective sustainable C&DWM include cooperation and collaboration among construction companies, providing complete data about the amount of C&DW and their composition, the reuse, recycling and reducing of waste and minimizing its negative impact on the environment, choosing the suitable material that can minimize waste or be reused or recycled, increasing the awareness of the benefits and the procedures used for deconstructing buildings and selective demolition that uses fewer tools and equipment, reduces pollution and toxicity in the removal process and increases the longevity of buildings, enforcing regulations on waste management, stakeholder's involvement in C&DWM, application of sustainability policies in C&DWM, and adoption of integrated waste management.

Table 3. Correlation coefficients and *p*-values of the barriers for the overall countries.

| | | B1 | B2 | B3 | B4 | B5 | B6 | B7 | B8 | B9 | B10 | B11 |
|-----|--------------|----------|----------|----------|----------|----------|----------|----------|----------|----------|----------|----------|
| B1 | C. | | 0.513 ** | 0.460 | 0.219 | 0.453 | 0.346 | 0.374 | 0.330 | 0.168 | 0.143 | 0.224 |
| | <i>p</i> -V. | | <0.001 | <0.001 | 0.019 * | <0.001 | 0.002 | 0.012 | 0.012 | 0.834 * | 0.529 * | 0.783 * |
| B2 | C. | 0.513 ** | | 0.739 ** | 0.590 ** | 0.551 ** | 0.508 ** | 0.624 ** | 0.393 | 0.169 | 0.271 | 0.269 |
| | <i>p</i> -V. | <0.001 | | <0.001 | <0.001 | <0.001 | <0.001 | <0.001 | 0.011 | 0.774 * | 0.115 * | 0.130 * |
| B3 | C. | 0.460 | 0.739 ** | | 0.692 ** | 0.517 ** | 0.509 ** | 0.679 ** | 0.450 | 0.220 | 0.281 | 0.270 |
| | <i>p</i> -V. | <0.001 | <0.001 | | <0.001 | <0.001 | 0.020 | <0.001 | 0.011 | 0.315 * | 0.195 * | 0.268 * |
| B4 | C. | 0.219 | 0.590 ** | 0.692 ** | | 0.562 ** | 0.540 ** | 0.643 ** | 0.596 ** | 0.422 | 0.458 | 0.553 ** |
| | <i>p</i> -V. | 0.019 * | <0.001 | <0.001 | | <0.001 | 0.001 | <0.001 | <0.001 | 0.001 | <0.001 | <0.001 |
| B5 | C. | 0.453 | 0.551 ** | 0.517 ** | 0.562 ** | | 0.652 ** | 0.580 ** | 0.485 | 0.216 | 0.176 | 0.282 |
| | <i>p</i> -V. | <0.001 | <0.001 | <0.001 | <0.001 | | <0.001 | <0.001 | <0.001 | 0.479 * | 0.045 | 0.189 * |
| B6 | C. | 0.346 | 0.508 ** | 0.509 ** | 0.540 ** | 0.652 ** | | 0.668 ** | 0.654 ** | 0.290 | 0.265 | 0.260 |
| | <i>p</i> -V. | 0.002 | <0.001 | 0.020 | 0.001 | <0.001 | | <0.001 | <0.001 | 0.075 * | 0.250 * | 0.507 * |
| B7 | C. | 0.374 | 0.624 ** | 0.679 ** | 0.643 ** | 0.580 ** | 0.668 ** | | 0.684 ** | 0.255 | 0.353 | 0.400 |
| | <i>p</i> -V. | 0.012 | <0.001 | <0.001 | <0.001 | <0.001 | <0.001 | | <0.001 | 0.285 * | 0.169 * | 0.024 |
| B8 | C. | 0.330 | 0.393 | 0.450 | 0.596 ** | 0.485 | 0.654 ** | 0.684 ** | | 0.536 ** | 0.483 | 0.494 |
| | <i>p</i> -V. | 0.012 | 0.011 | 0.011 | <0.001 | <0.001 | <0.001 | <0.001 | | <0.001 | 0.001 | <0.001 |
| B9 | C. | 0.168 | 0.169 | 0.220 | 0.422 | 0.216 | 0.290 | 0.255 | 0.536 ** | | 0.771 ** | 0.663 ** |
| | <i>p</i> -V. | 0.834 * | 0.774 * | 0.315 * | 0.001 | 0.479 * | 0.075 * | 0.285 * | <0.001 | | <0.001 | <0.001 |
| B10 | C. | 0.143 | 0.271 | 0.281 | 0.458 | 0.176 | 0.265 | 0.353 | 0.483 | 0.771 ** | | 0.775 ** |
| | <i>p</i> -V. | 0.529 * | 0.115 * | 0.195 * | <0.001 | 0.045 | 0.250 * | 0.169 * | 0.001 | <0.001 | | <0.001 |
| B11 | C. | 0.224 | 0.269 | 0.270 | 0.553 ** | 0.282 | 0.260 | 0.400 | 0.494 | 0.663 ** | 0.775 ** | |
| | <i>p</i> -V. | 0.783 * | 0.130 * | 0.268 * | <0.001 | 0.189 * | 0.507 * | 0.024 | <0.001 | <0.001 | <0.001 | |

C: Correlation, *p*-V.: *p*-Value, ** Correlation is significant and strong positive, * *p*-value is not significant.

Table 4. Proposed solutions to barriers to effective and sustainable C&DWM.

| Barriers to Effective C&DWM | Proposed Solution(s) | References |
|-----------------------------|--|--------------|
| B1 | The government, organizations, and individuals should establish effective communication tools to achieve cooperation and collaboration among construction companies. The government should have an appropriate framework to encourage and regulate companies' practices. Construction companies and their projects should realize the strategic importance of C&DWM and implement it at organizational and project levels. | [4,41] |
| B2 | Municipalities should provide fundamental data about the approximate amount of C&DW and their compositions based on the project type. Moreover, they should provide data about the protocols, procedures and alternatives for the available management of C&DW (reuse, recycle, reduction, and disposal). | [51,52] |
| B3 | Implementation of waste management rules and regulations by enforcing the environmental regulations and penalties regarding C&DWM. | [2,30,41] |
| B4 | Promote environmental awareness by organizing discussions, seminars, training, and workshops on sustainable construction and its importance for contractors, consultants, and stakeholders. Moreover, provide clear understanding about the benefits and the used procedure of deconstructing buildings and selective demolition. | [2,15,27,52] |

Table 4. Cont.

| Barriers to Effective C&DWM | Proposed Solution(s) | References |
|-----------------------------|--|------------|
| B5 | Social awareness, change in culture and attitude by branding and use of social media, as well as incentives such as tax reduction and applicable sustainability policies by government agencies can support sustainable C&DWM. | [10,52] |
| B6 | Technical information in sustainable construction, advanced technologies and methodologies, production and distribution of technical guidance documents for best practices should be available. | [46,52] |
| B7 | Governments should review and evaluate existing legislations and suggest amendments in coordination with responsible regulatory authorities. Moreover, governments with the support of stakeholders should develop legislation, regulations, codes, and standards relating to sustainable construction practices. | [2,10] |
| B8 | Additional financial cost should be provided for sustainability management. Reduction in costs by improving quality and reusing materials or recycled products, determining the best routes and use of waste transportation and material recycling to achieve economic and environmental gains by reducing fuel consumption. | [10,52] |
| B9 | Developing appropriate training for all levels of workers in order to develop their skills and knowledge. | [2,4,52] |
| B10 | The construction project characteristics should be provided to organize and achieve effective and sustainable C&DWM such as type, size, location, and complexity of the project, as well as the importance for the project to be completed on time, contract form, and project funding. | [46,60] |
| B11 | Creating and improving awareness and knowledge of sustainable construction amongst various actors in the construction industry, especially for stakeholders. Funded projects should include provisions that encourage and obligate the stakeholders and contractors towards proper C&DWM. | [52,61,62] |

5. Conclusions

The large amount of C&DW with poor management has severely affected sustainability. Sustainable construction efforts in some countries have been unsuccessful due to so many barriers to its successful implementation. This study identified sustainability barriers to effective and sustainable C&DWM in four countries (UK, KSA, Egypt, and Ghana). Eleven barriers (institutional fragmentation, lack of fundamental data on C&DW, lack of law enforcement, insufficient attention paid to C&DWM, socio-political, technological, lack of regulation, financial, human resources constraints, construction project characteristics, and rigidity of construction practices) have been identified and ranked by RI. The overall ranking of barriers indicated that the insufficient attention paid to C&DWM, lack of law enforcement, lack of regulation, and financial constraints represent the four major barriers to effective and sustainable C&DWM. Consequently, practical solutions to tackle the barriers have been proposed. The proposed solutions include cooperation and collaboration among construction companies, providing complete data about the amount of C&DW and its composition, enforcing regulations on waste management, stakeholder's involvement in C&DWM, application of sustainability policies in C&DWM, and adoption of integrated waste management. These findings can support decision makers to achieve effective and sustainable C&DWM.

Although this study identified and ranked the barriers to sustainable C&DWM and suggested solutions to tackle these barriers, there are still some limitations to the study. The barriers and suggested solutions were identified based on the literature review. The number of respondents was limited. Future studies should consider more barriers hindering the adoption of building information modeling and increase the number of respondents from different countries to be more reliable and closer to the real conditions.

Author Contributions: Conceptualization, A.A.-O., P.A.B., M.M.A.d., N.S., J.O.E., A.A., E.A.-E. and G.W.; Data curation, A.A.-O. and P.A.B.; Formal analysis, M.M.A.d. and N.S.; Investigation, A.A.-O., P.A.B., M.M.A.d. and N.S.; Methodology, A.A.-O., P.A.B., M.M.A.d. and N.S.; Software, A.A.-O., P.A.B., M.M.A.d. and N.S.; Supervision, A.A.-O., P.A.B., M.M.A.d. and N.S.; Writing—original draft, M.M.A.d.; Writing—review and editing, M.M.A.d. All authors have read and agreed to the published version of the manuscript.

Funding: This research received no external funding.

Institutional Review Board Statement: Not applicable.

Informed Consent Statement: Not applicable.

Acknowledgments: The authors would like to thank the Deanship of Scientific Research at Shaqra University for supporting this work.

Conflicts of Interest: The authors declare no conflict of interest.

References

1. Negash, Y.T.; Hassan, A.M.; Tseng, M.-L.; Wu, K.-J.; Ali, M.H. Sustainable construction and demolition waste management in Somaliland: Regulatory barriers lead to technical and environmental barriers. *J. Clean. Prod.* **2021**, *297*, 126717. [[CrossRef](#)]
2. Blaisi, N.I. Construction and demolition waste management in Saudi Arabia: Current practice and roadmap for sustainable management. *J. Clean. Prod.* **2019**, *221*, 167–175. [[CrossRef](#)]
3. Bamgbade, J.A.; Kamaruddeen, A.M.; Naw, M.N.M.; Adeleke, A.Q.; Salimon, M.G.; Ajibike, W.A. Analysis of some factors driving ecological sustainability in construction firms. *J. Clean. Prod.* **2019**, *208*, 1537–1545. [[CrossRef](#)]
4. Alotaibi, A.; Edum-Fotwe, F.; Price, A.D.F. Critical barriers to social responsibility implementation within mega-construction projects: The case of the Kingdom of Saudi Arabia. *Sustainability* **2019**, *11*, 1755. [[CrossRef](#)]
5. Karji, A.; Namian, M.; Tafazzoli, M. Identifying the key barriers to promote sustainable construction in the United States: A principal component analysis. *Sustainability* **2020**, *12*, 5088. [[CrossRef](#)]
6. Tang, S.; Yang, J.; Lin, L.; Peng, K.; Chen, Y.; Jin, S.; Yao, W. Construction of physically crosslinked chitosan/sodium alginate/calcium ion double-network hydrogel and its application to heavy metal ions removal. *Chem. Eng. J.* **2020**, *393*, 124728. [[CrossRef](#)]
7. Liu, J.; Wu, P.; Jiang, Y.; Wang, X. Explore potential barriers of applying circular economy in construction and demolition waste recycling. *J. Clean. Prod.* **2021**, *326*, 129400. [[CrossRef](#)]
8. Wu, H.; Zuo, J.; Yuan, H.; Zillante, G.; Wang, J. A review of performance assessment methods for construction and demolition waste management. *Resour. Conserv. Recycl.* **2019**, *150*, 104407. [[CrossRef](#)]
9. Manowong, E. Investigating factors influencing construction waste management efforts in developing countries: An experience from Thailand. *Waste Manag. Res.* **2012**, *30*, 56–71. [[CrossRef](#)]
10. Ametepye, O.; Aigbavboa, C.; Ansah, K. Barriers to successful implementation of sustainable construction in the Ghanaian construction industry. *Procedia Manuf.* **2015**, *3*, 1682–1689. [[CrossRef](#)]
11. Meckwan, A.; Patel, D. Construction & Demolition Waste Management Practices in Construction Industry in Vadodara. *Int. Res. J. Eng. Technol. IRJET* **2019**, *6*, 824–828.
12. Ali, A.; Ezeah, C.; Khatib, J. Estimating Construction and Demolition (C&D) Waste Arising in Libya. In Proceedings of the 31st International Conference on Solid Waste Technology and Management, Philadelphia, PA, USA, 3–6 April 2016.
13. Dubinski, D.; Won, S.Y.; Konczalla, J.; Mersmann, J.; Geisen, C.; Herrmann, E.; Seifert, V.; Senft, C. The Role of ABO Blood Group in Cerebral Vasospasm, Associated Intracranial Hemorrhage, and Delayed Cerebral Ischemia in 470 Patients with Subarachnoid Hemorrhage. *World Neurosurg.* **2017**, *97*, 532–537. [[CrossRef](#)] [[PubMed](#)]
14. Zhao, W.; Leeftink, R.B.; Rotter, V.S. Evaluation of the economic feasibility for the recycling of construction and demolition waste in China—The case of Chongqing. *Resour. Conserv. Recycl.* **2010**, *54*, 377–389. [[CrossRef](#)]
15. Jin, R.; Li, B.; Zhou, T.; Wanatowski, D.; Piroozfar, P. An empirical study of perceptions towards construction and demolition waste recycling and reuse in China. *Resour. Conserv. Recycl.* **2017**, *126*, 86–98. [[CrossRef](#)]
16. Akhtar, A.; Sarmah, A.K. Construction and demolition waste generation and properties of recycled aggregate concrete: A global perspective. *J. Clean. Prod.* **2018**, *186*, 262–281. [[CrossRef](#)]
17. Gálvez-Martos, J.-L.; Styles, D.; Schoenberger, H.; Zeschmar-Lahl, B. Construction and demolition waste best management practice in Europe. *Resour. Conserv. Recycl.* **2018**, *136*, 166–178. [[CrossRef](#)]
18. Ghafourian, K.; Kabirifar, K.; Mahdiyari, A.; Yazdani, M.; Ismail, S.; Tam, V.W.Y. A synthesis of express analytic hierarchy process (EAHP) and partial least squares-structural equations modeling (PLS-SEM) for sustainable construction and demolition waste management assessment: The case of Malaysia. *Recycling* **2021**, *6*, 73. [[CrossRef](#)]
19. Chen, J.; Hua, C.; Liu, C. Considerations for better construction and demolition waste management: Identifying the decision behaviors of contractors and government departments through a game theory decision-making model. *J. Clean. Prod.* **2019**, *212*, 190–199. [[CrossRef](#)]

20. Dong, J.; Liu, D.; Wang, D.; Zhang, Q. Identification of key influencing factors of sustainable development for traditional power generation groups in a market by applying an extended MCDM model. *Sustainability* **2019**, *11*, 1754. [[CrossRef](#)]
21. Ghaffar, S.H.; Burman, M.; Braimah, N. Pathways to circular construction: An integrated management of construction and demolition waste for resource recovery. *J. Clean. Prod.* **2020**, *244*, 118710. [[CrossRef](#)]
22. Tsiga, Z.D.; Emes, M.; Smith, A. Critical success factors for the construction industry. *PM World J.* **2016**, *5*, 1–12.
23. Ahady, S.; Gupta, S.; Malik, R.K. A critical review of the causes of cost overrun in construction industries in developing countries. *Int. Res. J. Eng. Technol.* **2017**, *4*, 2550–2558.
24. Watts, N.; Amann, M.; Arnell, N.; Ayeb-Karlsson, S.; Belesova, K.; Boykoff, M.; Byass, P.; Cai, W.; Campbell-Lendrum, D.; Capstick, S. The 2019 report of The Lancet Countdown on health and climate change: Ensuring that the health of a child born today is not defined by a changing climate. *Lancet* **2019**, *394*, 1836–1878. [[CrossRef](#)]
25. Bufoni, A.A.L.; Oliveira, L.B.L.; Rosa, L.L.P. The declared barriers of the large developing countries waste management projects: The STAR model. *Waste Manag.* **2016**, *52*, 326–338. [[CrossRef](#)]
26. Menegaki, M.; Damigos, D. A review on current situation and challenges of construction and demolition waste management. *Curr. Opin. Green Sustain. Chem.* **2018**, *13*, 8–15. [[CrossRef](#)]
27. Udawatta, N.; Zuo, J.; Chiveralls, K.; Yuan, H.; Zillante, G.; Elmualim, A. Major factors impeding the implementation of waste management in Australian construction projects. *J. Green Build.* **2018**, *13*, 101–121. [[CrossRef](#)]
28. Aghimien, D.O.; Oke, A.E.; Aigbavboa, C.O. Barriers to the adoption of value management in developing countries. *Eng. Constr. Archit. Manag.* **2018**, *25*, 818–834. [[CrossRef](#)]
29. Opoku, A.; Ahmed, V.; Cruickshank, H. Leadership style of sustainability professionals in the UK construction industry. *Built Environ. Proj. Asset Manag.* **2015**, *5*, 184–201. [[CrossRef](#)]
30. Mahpour, A. Prioritizing barriers to adopt circular economy in construction and demolition waste management. *Resour. Conserv. Recycl.* **2018**, *134*, 216–227. [[CrossRef](#)]
31. Huang, B.; Wang, X.; Kua, H.; Geng, Y.; Bleischwitz, R.; Ren, J. Construction and demolition waste management in China through the 3R principle. *Resour. Conserv. Recycl.* **2018**, *129*, 36–44. [[CrossRef](#)]
32. Zorpas, A.; Voukkali, I.; Loizia, P. Socio Economy Impact in Relation to Waste Prevention. Sustainable Economic Development. Springer International Publishing. 2017, pp. 31–48. Available online: <https://www.springerprofessional.de/en/socio-economy-impact-in-relation-to-waste-prevention/10750872>. (accessed on 4 March 2022).
33. Yuan, H. Barriers and countermeasures for managing construction and demolition waste: A case of Shenzhen in China. *J. Clean. Prod.* **2017**, *157*, 84–93. [[CrossRef](#)]
34. Lockrey, S.; Nguyen, H.; Crossin, E.; Verghese, K. Recycling the construction and demolition waste in Vietnam: Opportunities and challenges in practice. *J. Clean. Prod.* **2016**, *133*, 757–766. [[CrossRef](#)]
35. Tura, N.; Hanski, J.; Ahola, T.; Stähle, M.; Piiparinen, S.; Valkokari, P. Unlocking circular business: A framework of barriers and drivers. *J. Clean. Prod.* **2019**, *212*, 90–98. [[CrossRef](#)]
36. Tsai, F.M.; Bui, T.-D.; Tseng, M.-L.; Wu, K.-J. A causal municipal solid waste management model for sustainable cities in Vietnam under uncertainty: A comparison. *Resour. Conserv. Recycl.* **2020**, *154*, 104599. [[CrossRef](#)]
37. Abarca-Guerrero, L.; Maas, G.; Van Twillert, H. Barriers and motivations for construction waste reduction practices in Costa Rica. *Resources* **2017**, *6*, 69. [[CrossRef](#)]
38. Munyasya, B.M.; Chileshe, N. Towards sustainable infrastructure development: Drivers, barriers, strategies, and coping mechanisms. *Sustainability* **2018**, *10*, 4341. [[CrossRef](#)]
39. Han, D.; Kalantari, M.; Rajabifard, A. Building Information Modeling (BIM) for Construction and Demolition Waste Management in Australia: A Research Agenda. *Sustainability* **2021**, *13*, 12983. [[CrossRef](#)]
40. Koutamanis, A. Building information modeling for construction and demolition waste minimization. In *Advances in Construction and Demolition Waste Recycling*; Elsevier: Amsterdam, The Netherlands, 2020; pp. 101–120. [[CrossRef](#)]
41. Bowan, P.A.; Kayaga, S.; Cotton, A.; Fisher, J. Municipal Solid Waste Management Performance. *J. Stud. Soc. Sci.* **2020**, *19*, 1–28.
42. Park, J.; Tucker, R. Overcoming barriers to the reuse of construction waste material in Australia: A review of the literature. *Int. J. Constr. Manag.* **2017**, *17*, 228–237. [[CrossRef](#)]
43. Ulubeyli, S.; Kazaz, A.; Arslan, V. Construction and Demolition Waste Recycling Plants Revisited: Management Issues. *Procedia Eng.* **2017**, *172*, 1190–1197. [[CrossRef](#)]
44. Aslam, M.S.; Huang, B.; Cui, L. Review of construction and demolition waste management in China and USA. *J. Environ. Manag.* **2020**, *264*, 110445. [[CrossRef](#)] [[PubMed](#)]
45. Bao, Z.; Lu, W. Developing efficient circularity for construction and demolition waste management in fast emerging economies: Lessons learned from Shenzhen, China. *Sci. Total Environ.* **2020**, *724*, 138264. [[CrossRef](#)] [[PubMed](#)]
46. Kabirifar, K.; Mojtahedi, M.; Wang, C.; Tam, V.W.Y. Construction and demolition waste management contributing factors coupled with reduce, reuse, and recycle strategies for effective waste management: A review. *J. Clean. Prod.* **2020**, *263*, 121265. [[CrossRef](#)]
47. de Oliveira, J.A.P. Intergovernmental relations for environmental governance: Cases of solid waste management and climate change in two Malaysian States. *J. Environ. Manag.* **2019**, *233*, 481–488. [[CrossRef](#)] [[PubMed](#)]
48. Won, J.; Cheng, J.C.P. Identifying potential opportunities of building information modeling for construction and demolition waste management and minimization. *Autom. Constr.* **2017**, *79*, 3–18. [[CrossRef](#)]

49. Wu, Z.; Fan, H.; Liu, G. Forecasting Construction and Demolition Waste Using Gene Expression Programming. *J. Comput. Civ. Eng.* **2015**, *29*, 04014059. [CrossRef]
50. Giorgi, S.; Lavagna, M.; Campioli, A. Guidelines for Effective and Sustainable Recycling of Construction and Demolition Waste. In *Designing Sustainable Technologies, Products and Policies*; Springer International Publishing: Cham, Switzerland, 2018; pp. 211–221.
51. Faruqi, M.H.Z.; Siddiqui, F.Z. A mini review of construction and demolition waste management in India. *Waste Manag. Res.* **2020**, *38*, 708–716. [CrossRef]
52. Correia, J.M.F.; de Oliveira Neto, G.C.; Leite, R.R.; da Silva, D. Plan to Overcome Barriers to Reverse Logistics in Construction and Demolition Waste: Survey of the Construction Industry. *J. Constr. Eng. Manag.* **2021**, *147*, 4020172. [CrossRef]
53. Wu, Z.; Yu, A.T.W.; Shen, L. Investigating the determinants of contractor's construction and demolition waste management behavior in Mainland China. *Waste Manag.* **2017**, *60*, 290–300. [CrossRef]
54. Karunasena, G.; Amaratunga, D. Capacity building for post disaster construction and demolition waste management: A case of Sri Lanka. *Disaster Prev. Manag.* **2016**, *25*, 137–153. [CrossRef]
55. Schamne, A.N.; Nagalli, A. Reverse logistics in the construction sector: A literature review. *Electron. J. Geotech. Eng.* **2016**, *21*, 691–702.
56. Saadi, N.; Ismail, Z.; Alias, Z. A review of construction waste management and initiatives in malaysia. *J. Sustain. Sci. Manag.* **2016**, *11*, 101–114.
57. Ajayi, S.O.; Oyedele, L.O.; Bilal, M.; Akinade, O.O.; Alaka, H.A.; Owolabi, H.A.; Kadiri, K.O. Waste effectiveness of the construction industry: Understanding the impediments and requisites for improvements. *Resour. Conserv. Recycl.* **2015**, *102*, 101–112. [CrossRef]
58. Mak, T.M.W.; Yu, I.K.M.; Wang, L.; Hsu, S.C.; Tsang, D.C.W.; Li, C.N.; Yeung, T.L.Y.; Zhang, R.; Poon, C.S. Extended theory of planned behaviour for promoting construction waste recycling in Hong Kong. *Waste Manag.* **2019**, *83*, 161–170. [CrossRef] [PubMed]
59. Chisholm, J.M.; Zamani, R.; Negm, A.M.; Said, N.; Abdel daiem, M.M.; Dibaj, M.; Akrami, M. Sustainable waste management of medical waste in African developing countries: A narrative review. *Waste Manag. Res.* **2021**, *39*, 1149–1163. [CrossRef] [PubMed]
60. Luangcharoenrat, C.; Intrachooto, S.; Peansupap, V.; Sutthinarakorn, W. Factors influencing construction waste generation in building construction: Thailand's perspective. *Sustainability* **2019**, *11*, 3638. [CrossRef]
61. Sarhan, J.; Xia, B.; Fawzia, S.; Karim, A.; Olanipekun, A. Barriers to implementing lean construction practices in the Kingdom of Saudi Arabia (KSA) construction industry. *Constr. Innov.* **2018**, *18*, 246–272. [CrossRef]
62. Xu, Z.; Zayed, T.; Niu, Y. Comparative analysis of modular construction practices in mainland China, Hong Kong and Singapore. *J. Clean. Prod.* **2020**, *245*, 118861. [CrossRef]
63. Spoann, V.; Fujiwara, T.; Seng, B.; Lay, C.; Yim, M. Assessment of public–private partnership in municipal solid waste management in Phnom Penh, Cambodia. *Sustainability* **2019**, *11*, 1228. [CrossRef]
64. Kabera, T.; Wilson, D.C.; Nishimwe, H. Benchmarking performance of solid waste management and recycling systems in East Africa: Comparing Kigali Rwanda with other major cities. *Waste Manag. Res.* **2019**, *37*, 58–72. [CrossRef]
65. Islam, R.; Nazifa, T.H.; Yuniarto, A.; Uddin, A.S.; Salmiati, S.; Shahid, S. An empirical study of construction and demolition waste generation and implication of recycling. *Waste Manag.* **2019**, *95*, 10–21. [CrossRef] [PubMed]
66. Ajayi, S.O.; Oyedele, L.O.; Akinade, O.O.; Bilal, M.; Owolabi, H.A.; Alaka, H.A.; Kadiri, K.O. Reducing waste to landfill: A need for cultural change in the UK construction industry. *J. Build. Eng.* **2016**, *5*, 185–193. [CrossRef]
67. D'Angelo, A.; Buck, T. The earliness of exporting and creeping sclerosis? The moderating effects of firm age, size and centralization. *Int. Bus. Rev.* **2019**, *28*, 428–437. [CrossRef]
68. Luttenberger, L.R. Waste management challenges in transition to circular economy—Case of Croatia. *J. Clean. Prod.* **2020**, *256*, 120495. [CrossRef]
69. Wong, C.H.; Holt, G.D.; Cooper, P.A. Lowest price or value? Investigation of UK construction clients' tender selection process. *Constr. Manag. Econ.* **2000**, *18*, 767–774. [CrossRef]
70. Zhao, Z.-Y.; Zhao, X.-J.; Zuo, J.; Zillante, G. Corporate social responsibility for construction contractors: A China study. *J. Eng. Des. Technol.* **2016**, *14*, 614–640. [CrossRef]
71. Velenturf, A.P.M.; Purnell, P.; Tregent, M.; Ferguson, J.; Holmes, A. Co-producing a vision and approach for the transition towards a circular economy: Perspectives from government partners. *Sustainability* **2018**, *10*, 1401. [CrossRef]
72. Tunji-Olayeni, P.; Kajimo-Shakantu, K.; Osunrayi, E. Practitioners' experiences with the drivers and practices for implementing sustainable construction in Nigeria: A qualitative assessment. *Smart Sustain. Built Environ.* **2020**, *9*, 443–465. [CrossRef]
73. Osmani, M. Construction waste minimization in the UK: Current pressures for change and approaches. *Procedia Soc. Behav. Sci.* **2012**, *40*, 37–40. [CrossRef]
74. Ajayi, S.O.; Oyedele, L.O. Policy imperatives for diverting construction waste from landfill: Experts' recommendations for UK policy expansion. *J. Clean. Prod.* **2017**, *147*, 57–65. [CrossRef]
75. Ouda, O.K.M.; Peterson, H.P.; Rehan, M.; Sadef, Y.; Alghazo, J.M.; Nizami, A.S. A case study of sustainable construction waste management in Saudi Arabia. *Waste Biomass Valorization* **2018**, *9*, 2541–2555. [CrossRef]
76. Egyptian Environmental Affairs Agency. Natural Protectorates Description. 2020. Available online: <https://www.eea.gov.eg/en-us/topics/nature/protectorates.aspx> (accessed on 4 March 2022).

77. Daoud, A.O.; Othman, A.A.E.; Robinson, H.; Bayyati, A. An investigation into solid waste problem in the Egyptian construction industry: A mini-review. *Waste Manag. Res.* **2020**, *38*, 371–382. [[CrossRef](#)] [[PubMed](#)]
78. Ibrahim, M.I.M.; Mohamed, N.A.E.M. Towards sustainable management of solid waste in Egypt. *Procedia Environ. Sci.* **2016**, *34*, 336–347. [[CrossRef](#)]

Article

Use of Carbonated Water as Kneading in Mortars Made with Recycled Aggregates

David Suescum-Morales ¹, José Ramón Jiménez ^{1,*} and José María Fernández-Rodríguez ^{2,*}

¹ Departamento de Ingeniería Rural, Escuela Politécnica Superior de Belmez, Universidad de Córdoba, 14240 Córdoba, Spain; p02sumod@uco.es

² Departamento de Química Inorgánica e Ingeniería Química, Escuela Politécnica Superior de Belmez, Universidad de Córdoba, 14240 Córdoba, Spain

* Correspondence: jrjimenez@uco.es (J.R.J.); um1feroj@uco.es (J.M.F.-R.)

Abstract: The increased concern about climate change is revolutionising the building materials sector, making sustainability and environmental friendliness increasingly important. This study evaluates the feasibility of incorporating recycled masonry aggregate (construction and demolition waste) in porous cement-based materials using carbonated water in mixing followed (or not) by curing in a CO₂ atmosphere. The use of carbonated water can be very revolutionary in cement-based materials, as it allows hydration and carbonation to occur simultaneously. Calcite and portlandite in the recycled masonry aggregate act as a buffer for the low-pH carbonated water. Carbonated water produced better mechanical properties and increased accessible water porosity and dry bulk density. The same behaviour was observed with natural aggregates. Carbonated water results in an interlaced shape of carbonate ettringite (needles) and fills the microcracks in the recycled masonry aggregate. Curing in CO₂ together with the use of carbonated water (concomitantly) is not beneficial. This study provides innovative solutions for a circular economy in the construction sector using carbonated water in mixing (adsorbing CO₂), which is very revolutionary as it allows carbonation to be applied to in-situ products.

Keywords: carbonated water; CO₂ sequestration; accelerated carbonation; circular economy; construction demolition waste

Citation: Suescum-Morales, D.; Jiménez, J.R.; Fernández-Rodríguez, J.M. Use of Carbonated Water as Kneading in Mortars Made with Recycled Aggregates. *Materials* **2022**, *15*, 4876. <https://doi.org/10.3390/ma15144876>

Academic Editors: Carlos Morón Fernández and Daniel Ferrández Vega

Received: 23 May 2022

Accepted: 8 July 2022

Published: 13 July 2022

Publisher's Note: MDPI stays neutral with regard to jurisdictional claims in published maps and institutional affiliations.

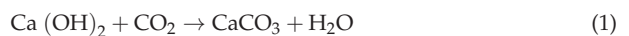


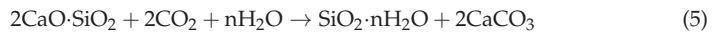
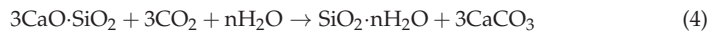
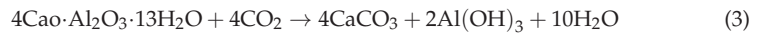
Copyright: © 2022 by the authors. Licensee MDPI, Basel, Switzerland. This article is an open access article distributed under the terms and conditions of the Creative Commons Attribution (CC BY) license (<https://creativecommons.org/licenses/by/4.0/>).

1. Introduction

Cement and concrete are used in building and construction work worldwide. The construction industry producing cement and concrete can be regarded as the world's largest industry [1–3]. Construction is responsible for a great amount of CO₂ release [4,5]. One tonne of cement emits approximately 0.6 to 0.8 tonnes of CO₂ [1,6–8]. The CO₂ concentration in the atmosphere has increased from 280 to 420 ppm in 2020 [9]. The incorporation of waste and the proper use of resources are leading global challenges to control the negative environmental impact of cement and concrete and preserve the planet.

High-emission countries are actively exploring carbon capture and utilisation (CCU) or storage technologies. CCU is a novel method to reduce CO₂ and turn CO₂ into a commercially interest product [10–12]. The carbonation and chemical reactions in cement-based materials (CBMs) (Equations (1) to (5)) [13–18] occurs with CO₂, affects cement hydration products, and increases CaCO₃ production [5,19,20]. As early as 1970, the idea of CO₂ capture through carbonation with CBM appeared [21]. Carbonation of CBM, as an alternate to CCU, reduces water absorption and curing time (useful in the precast industry), increases density, and improves fragmentation resistance and mechanical properties [22–24].





The concentration of CO₂ in the environment must be increased for accelerated carbonation in different ways [14,15,18,23–30]. To increase this level of CO₂, a carbonation chamber is usually necessary [13] with or without pressure [31,32], with different levels of CO₂ or even submerging the samples in mixtures of different gases [33–35]. A review on the effect of CO₂ in cement-based materials on the physico-mechanical properties was previously described in another study by Suescum-Morales et al. [36]. The carbonation rate is determined by the diffusion of CO₂ gas in the samples [35]. Carbonation products make samples more dense, preventing the easy entry of CO₂. The need for a high amount of CO₂ in the curing environment implies the need for an accelerated carbonation chamber. An attractive alternative is to apply carbonation technology during cement kneading. To avoid the difficulty of CO₂ diffusion and make CBM carbonation apply to in-situ products, the kneading water is replaced by carbonated water (water with high CO₂ content). Thus, it is possible to start the carbonation simultaneously with the hydration process of the cement and increase carbonation [20,37]. Furthermore, the hydration reaction of the cement occurs much faster than that under normal curing conditions [5].

Construction and demolition waste (CDW) is produced during the demolition phases of several types of construction building or infrastructures (over 30 billion tonnes per year worldwide) [13,38,39]. CDW is composed of several types of waste, in addition to concrete and ceramics, such as glass, stone, bituminous material, and others. Recycled aggregates (RAs) are obtained from CDW with appropriate treatment (recycling plant treatment). A possible simple classification of RA may be made, in a simple way [25]: (i) if the waste is ceramic, the aggregate might be called recycled ceramic aggregates; (ii) if is concrete waste, may be called recycled concrete aggregates (RCA); and (iii) if it is a mixture of the two above, mixed recycled aggregates (MRA) [36,40].

Mixed recycled aggregate (MRA) is the most widely produced RA in the world. The non-existence of regulations and different sources is still limited the use of MRA [41]. Recycled masonry aggregate (RMA) differs from natural aggregates (NAs) mainly in terms water absorption, higher porosity, and lower density [42,43]. MRA has had different uses: as aggregates for masonry mortar, and as an aggregate for alkaline activated material or CBM [41–48]. RMA is a type of MRA obtained from screening and crushing walls waste [36,49–52].

There are two ways to produce accelerated carbonation in RCA [14]: in the aggregate itself [7,42,53–55] or in the mixture of RCA with Portland cement [24,27,28,56]. However, these studies do not investigate the effect of CO₂ on CBMs made with RMA or RCA using carbonated water as kneading water. This research would fill this information gap. Nor has any literature been found that studies the simultaneous use of carbonated water and CO₂ curing.

This study mainly investigates the physico-mechanical properties of a porous CBM with RMA, and carbonated water as kneading water and for subsequent curing in CO₂. To observe the effect of carbonated water on the microstructure of the hardened samples, with NA and RMA, and cured under both regimes, scanning electron microscopy (SEM), energy dispersive X-ray spectroscopy (EDS), and backscattered electron (BSE) were performed. Thermogravimetric analysis and differential thermal analysis (TGA/DTA) was also performed to determine the amount of CaCO₃ in all cases. No studies have been found that simultaneously use carbonated water as kneading water, under accelerated curing, and using RMA as aggregate. The production of precast or in-situ non-reinforced CBM products could be possible with the following approach: incorporation of waste (RMA), with the added value to CO₂, and inclusion of carbonated water as kneading water, which can be very revolutionary.

2. Materials and Methods

2.1. Materials

NA was used as a reference. NA and RMA were used in previous research [25,36,49,50]. The components of RMA according to UNE EN 933-11:2009 were: red ceramic bricks (53.9%), masonry mortar (39.8%), unbound aggregates (5.7%), concrete (0.4%), and gypsum particles (0.2%). Water absorption and dry bulk density (DBD) were measured according to UNE-EN 1097-6:2013 [57]. DBD for NA and RMA was $2.63 \text{ g}\cdot\text{cm}^{-3}$ and $2.14 \text{ g}\cdot\text{cm}^{-3}$, respectively. The amount of CaCO_3 for NA and RMA (197 and $239 \text{ kg}/\text{m}^3$ respectively) was calculated using TGA/DTA. Water absorption was 0.79% for NA and 9% for RMA. CEM II/A-V 42.5 R was used as cement [58] with a DBD of $2.89 \text{ g}\cdot\text{cm}^{-3}$ according to the characteristics provided by the manufacturer.

As kneading water, two types of commercial water were used: normal water (H_2O) and carbonated water ($\text{CO}_2\cdot\text{H}_2\text{O}$), both from the manufacturer Fuente Primavera, Spain. For H_2O , the pH value was 7.7 and the initial concentration of CO_2 was between $0.2\text{--}0.5 \text{ mg}\cdot\text{L}^{-1}$. For $\text{CO}_2\cdot\text{H}_2\text{O}$, these values were 4.8 (for pH) and $14.1\text{--}14.4 \text{ mg CO}_2\cdot\text{L}^{-1}$.

2.2. Experimental Design and Curing Conditions

NA and RMA were sieved: 2/4, 1/2, 0.5 /1, 0.25/0.5, 0.125/0.25, and 0/0.125 fractions to reconstitute the lower limit indicated by ASTM C 144-04 [59]. Two gaps were achieved by deleting the following fractions: 0.25/0.5 and <0.125 mm. Its mineral skeleton (with two gaps) can facilitate the input of CO_2 and total carbonation of the mix (more porous). Table 1 shows the reconstituted particle size distribution of NA.

Table 1. Spindle-shaped particle size limits.

| Size (mm) | ASTM C 144-04 (Limit) | Fraction Size | Original Percentage Retained | Application of 2 Gaps | Particle Size Distribution Obtained (Passing) |
|-----------|-----------------------|---------------|------------------------------|-----------------------|---|
| 4 | 100 | >4 | 0 | 0 | 100 |
| 2 | 88 | 2/4 | 12 | 16 | 84 |
| 1 | 62 | 1/2 | 26 | 35 | 49 |
| 0.5 | 32 | 0.5/1 | 30 | 40 | 9 |
| 0.25 | 8 | 0.25/0.5 | 24 | 0 | 9 |
| 0.125 | 1 | 0.125/0.25 | 7 | 9 | 0 |
| 0.075 | 0 | <0.125 | 1 | 0 | 0 |
| 0.063 | | TOTAL | 100 | 100 | - |

Equations (6) and (7) calculate the dry mass of each component:

$$\text{Dry mass of cement} = \frac{V \cdot 1 \cdot \rho_{rd \text{ cement}}}{6} \quad (6)$$

$$\text{Dry mass of NA} = \frac{V \cdot 5 \cdot \rho_{rd \text{ natural aggregate}}}{6} \quad (7)$$

where $\rho_{rd \text{ cement}} = 2.89 \text{ g}/\text{cm}^3$ and $\rho_{rd \text{ natural aggregate}} = 2.63 \text{ g}/\text{cm}^3$, which are the DBD of cement and NA, respectively. A volume (V) of 1600 cm^3 was manufactured in each mix. According to Equation (7), the mass of NA was 3507 g. The mass of each fraction for NA (Table 2) were obtained according to the 2 gap realized in Table 1. A total substitution of NA by RMA in volume fraction by fraction was realized. To replace NA by RMA, the bulk density was used [60].

Table 2. Aggregate weights used by different fractions.

| Mixes | NA | | | RMA 100% | |
|--------------------|-------------------------------|---------------------------|---------------------------|---------------------------|-----------------|
| Fraction Size (mm) | Weight Used (g) | BD * (g/cm ³) | Volume (cm ³) | BD * (g/cm ³) | Weight Used (g) |
| >4 | 0 | - | - | - | - |
| 2/4 | 561 | 1.44 | 388.38 | 0.99 | 386 |
| 1/2 | 1216 | 1.49 | 813.53 | 1.05 | 855 |
| 0.5/1 | 1403 | 1.55 | 900.01 | 1.17 | 1053 |
| 0.25/0.5 | 0 | - | - | - | - |
| 0.125/0.25 | 327 | 1.38 | 235.80 | 1.19 | 279 |
| <0.125 | 0 | - | - | - | - |
| TOTAL | 3507 (Equation (7)) | | | | 2574 |

* BD = Bulk density.

The samples were subjected to two curing environments (both with $21 \pm 2^\circ\text{C}$ and $65 \pm 10\%$ of relative humidity): (i) normal climatic chamber (CC) and (ii) accelerated carbonation chamber ($\text{CO}_2\cdot\text{C}$). For the CC, the CO_2 concentration was 0.04%, and for the $\text{CO}_2\cdot\text{C}$ it was 5%. The CO_2 used for this condition was provided by Linde (99.99995% purity). Figure 1 shows the experimental design carried out.

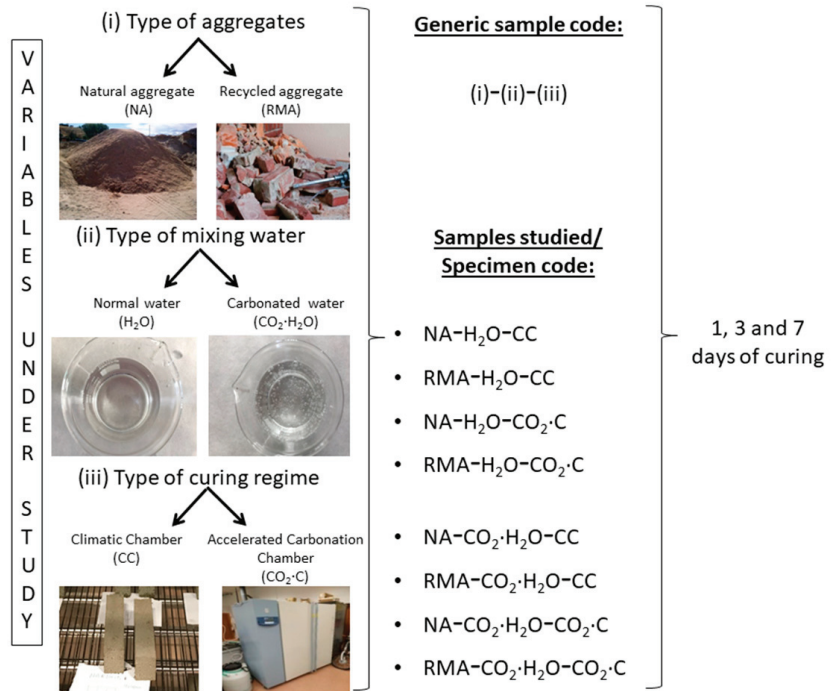


Figure 1. Experimental design carried out.

2.3. Kneading Process

Table 3 shows the composition of the mixes studied. The aggregates were pre-saturated, according to the water absorption of each one of them (NA or RMA). Therefore the w/c ratio used can be considered as effective. The kneading process was in accordance with previous research [25,36].

Table 3. Weights used for the different mixes (g).

| Mortar Type | NA RMA | | Cement | | Saturation Water | | Effective Water | | Total Water | w/c | Consistency Index (mm) |
|---|--------|------|--------|-----|------------------|-----------------------------------|------------------|-----------------------------------|-------------|--------|------------------------|
| | | | | | H ₂ O | CO ₂ ·H ₂ O | H ₂ O | CO ₂ ·H ₂ O | | | |
| NA-H ₂ O- ^(*) | 3507 | - | 771 | 28 | - | 308 | - | 336 | 0.4 | 80 ±10 | |
| RMA-H ₂ O- ^(*) | - | 2574 | 771 | 232 | - | 308 | - | 540 | 0.4 | 80 ±10 | |
| NA-CO ₂ ·H ₂ O- ^(*) | 3507 | - | 771 | - | 28 | - | 308 | 336 | 0.4 | 80 ±10 | |
| RMA-CO ₂ ·H ₂ O- ^(*) | - | 2574 | 771 | - | 232 | - | 308 | 540 | 0.4 | 80 ±10 | |

(^{*}) CC or CO₂-C.

Prismatic 40 × 40 × 160 mm casts were used [61]. The samples were kept in the mould for 3 h. The samples were covered to prevent CO₂ input/output during this time. After this time (3 h), the samples were demoulded because the aim was to demould the samples very quickly, similar to what happens in a precast plant. According to Pan et al. [35], this pre-curing time is crucial to avoid water-saturated capillary pores resulting in a low penetration rate of CO₂ for the samples cured in CO₂-C. The samples were then cured in two chambers: CC and CO₂-C for 1, 3, and 7 days of curing.

2.4. Test Methods

X-ray fluorescence spectrometry analysis (XRF) was realized with ZSX PRIMUS IV, Rigaku equipment. A Bruker D8 Discover A 25 diffractometer were used for to obtain X-ray diffraction (XRD) patterns. A CuK α radiation ($\lambda = 1.54050 \text{ \AA}$; 40 Kv; 30 mA) was used and scan angles between 10° to 70° (2 θ) were programmed. The speed used was of 0.02 2 θ min⁻¹. For identifying the diffractograms, the International Database ICDD 2003 was used [62].

TGA/DTA were performed using a Setaram Setys Evolution 16/18 instrument with a resolution of 0.002–0.02 μg . The heating increase was 5° min⁻¹.

The flexural (FS) and compressive strength (CS) were obtained according to the European Standard EN 1015-11 [61] for 1, 3, and 7 d of curing. The dry bulk density (DBD) of hardened samples was determined according to European Standard EN 1015-10 [63]. Accessible porosity for water (APW) were measured according to European Standard UNE 83980 [64].

The morphology and composition of the mixes with NA and RMA under the CC regime were studied using H₂O and CO₂·H₂O. SEM, EDS, and BSE were obtained using JEOL JSM 7800F at the age of 7 d. The objective was to observe the effect of carbonated water on the microstructure of the hardened samples, with NA and RMA cured under CC regime. They were then sputtered with gold to obtain the maximum image quality.

All the above tests were carried out in triplicate.

3. Results and Discussion

3.1. Characterization of Raw Materials

Figure 2 shows the XRD patterns of NA, RMA, and cement. Quartz (SiO₂) (05-0490) [62] was the main phase for NA and RMA. Other minority phases were also found and were described in greater detail in other research [25,36]. The diffractogram of the cement was in agreement with the finding of other authors [65–69]. Table 4 shows the XRF results found for NA, RMA, and cement, which are in agreement with the phases found in XRD.

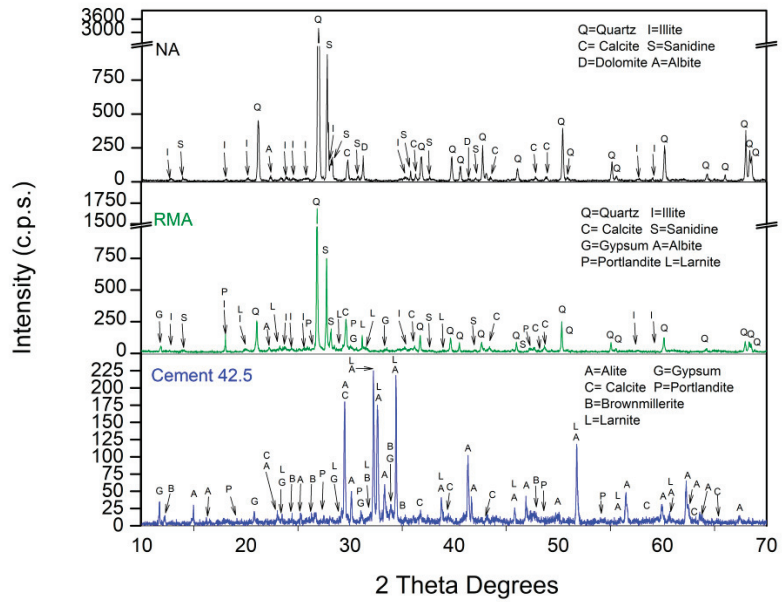


Figure 2. XRD patterns of NA, RMA, and cement.

Table 4. XRF results for NA, RMA, and Cement.

| Oxides | NA | RMA | Cement |
|--------------------------------|-------|-------|--------|
| F ₂ O | - | 0.74 | - |
| Na ₂ O | 0.82 | 0.71 | 0.29 |
| MgO | 1.06 | 1.65 | 1.00 |
| Al ₂ O ₃ | 5.82 | 10.79 | 6.59 |
| SiO ₂ | 49.63 | 34.44 | 18.29 |
| P ₂ O ₅ | 0.07 | 0.12 | 0.13 |
| SO ₃ | 0.03 | 2.52 | 4.02 |
| Cl ₂ O ₃ | - | 0.05 | 0.07 |
| K ₂ O | 1.52 | 2.18 | 1.09 |
| CaO | 5.60 | 12.18 | 45.61 |
| TiO ₂ | 0.27 | 0.54 | 0.41 |
| Cr ₂ O ₃ | 0.04 | 0.02 | - |
| MnO ₂ | 0.04 | 0.06 | 0.05 |
| Fe ₂ O ₃ | 1.74 | 3.55 | 2.85 |
| CuO | - | - | 0.04 |
| ZnO | - | 0.02 | 0.02 |
| SrO | - | 0.03 | 0.05 |
| Rb ₂ O | - | - | 0.01 |
| BaO | 0.03 | 0.03 | 0.06 |
| BALANCE CO ₂ | 32.32 | 30.61 | 19.43 |
| TOTAL | 67.68 | 69.39 | 80.57 |

3.2. Compressive and Flexural Strength

Figure 3 shows the CS results for the four mixes and two curing regimes at ages of 1, 3, and 7 days of curing. When comparing NA-H₂O-CC with NA-CO₂-H₂O-CC at 1 day of age, CS decreased by 8.6%. According to Valdemir dos Santos et al. [20], this result is related to the reduced AFm formation in the microstructure during the early hydration period [20]. Similar results were reported by Lippiatt et al. [5] in a cement paste aged 1 d using carbonated water. In addition, the low pH value of carbonated water (4.8) can negatively affect the strength [70], delay the setting [71], and produce changes

in the cement paste structure [72]. It is possible that a low pH leads to the reduction of hydrated calcium silicate and hydrated calcium aluminate because the reactions of equations 8–10 occur. Additionally, the amount of Portlandite present decreases. Therefore, the structure of the cement paste will be weaker. Nevertheless, at 3 and 7 d, an increment of 18% and 12.5% was obtained, respectively, when using carbonated water for the NA mixture and CC regime. When kneading cement and water, the pH increases rapidly, and this solution becomes saturated with $\text{Ca}(\text{OH})_2$ after 24 h [73,74]. Furthermore, the calcite phase found in NA (Figure 2) can act as a buffer when added to carbonated water, as observed by Lippiatt et al. [5] to achieve simultaneous hydration and carbonation in cement. This saturated solution of $\text{Ca}(\text{OH})_2$, together with CO_2 in the carbonated water, favoured the carbonation reaction and increased CS at 3 and 7 d [22–24]. Equations (8)–(10) show the chemical reaction with carbonated water [20].

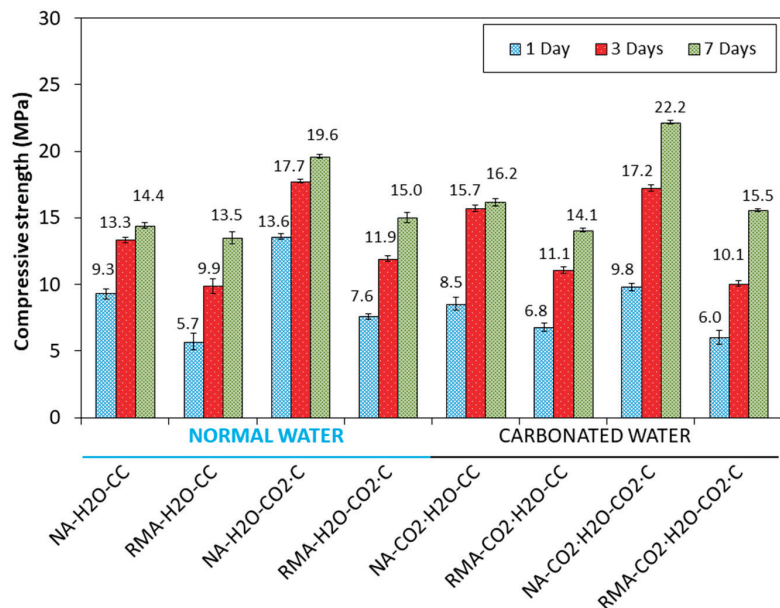
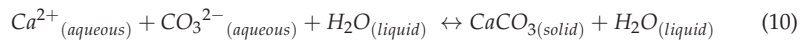
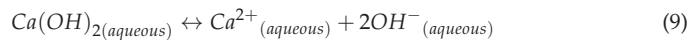
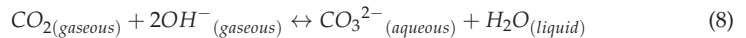


Figure 3. Compressive strength at different curing ages and hardening environments.

Compared to NA, RMA mixture under CC regime, using carbonated and normal water (RMA-H₂O-CC and RMA-CO₂-H₂O-CC), had slightly lower CS. This loss of mechanical properties agreed with other studies when the percentage of substitution of NA for RA was 100% [14,75–79]. However, compared to normal water, the carbonated water was beneficial in this case for all ages of curing (19.3%, 12.1%, and 4.4% for 1, 3, and 7 d, respectively) due to the presence of CaCO_3 and $\text{Ca}(\text{OH})_2$ in RMA (Figure 2). These phases act as a buffer of carbonated water [5], increase pH, avoid the loss of mechanical resistance, and delay hydration [70,71] that occur in the mixture with NA with 1 d of curing. Thus, carbonated water with RMA can improve the mechanical strength under the CC regime.

For NA and RMA mixtures, the increase in CS in samples cured with CO₂-C (NA-H₂O-CC vs. NA-H₂O-CO₂-C and RMA-H₂O-CC vs. RMA-H₂O-CO₂-C) agree with the

results in [13,14,18,24,27,28,56,80–82]. For NA mixtures, with 1 d and under CO₂-C, when using carbonated water in the kneading, compared with normal water, decreased the CS by 38.77% (NA-H₂O-CO₂-C vs. NA-CO₂-H₂O-CO₂-C). The low pH value of carbonated water along with accelerated carbonation (CO₂-C) results in a negative effect on strength [70] and delayed setting [71], which lowers the pH values of the mix [83–85]. For 3 d of curing, the effect of carbonated water on CS was still negative. For 7 d of curing, an increment of 13.3% was observed. This could indicate the regulation of pH [22–24] and the carbonation of the sample.

The same behaviour was observed in the samples with RMA (RMA-H₂O-CO₂-C vs. RMA-CO₂-H₂O-CO₂-C), although with minor decreases for 1 and 3 d. This is again due to CaCO₃ and Ca(OH)₂ in RMA (Figure 2) acting as a buffer of carbonated water [5], maintaining a pH higher than that with NA. Thus, carbonated water under accelerated carbonation (with NA and RMA) is beneficial only after 7 d of curing.

The FS results for all the mixes under CC and CO₂-C at the ages of 1, 3, and 7 d, in Figure 4, reveal the same trend as CS.

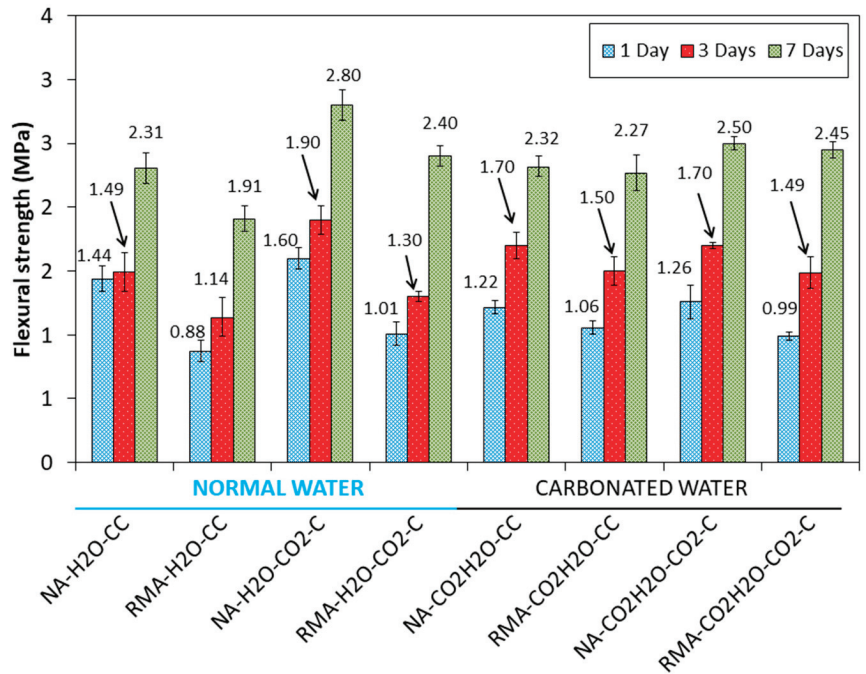


Figure 4. Flexural strength at different curing ages and hardening environments.

3.3. DBD and APW

DBD and APW are shown in Figure 5 for 7 d of curing under CC and CO₂-C. On the NA mixture, under the CC regime, the use of carbonated water as kneading water, compared with normal water, incremented the DBD by 3.3%. This result agrees with the increase in the mechanical properties in Figures 3 and 4. Carbonated water favours the carbonation reaction at 7 d of curing, increasing the DBD [22–24]. The APW also increased by 5.28% when using carbonated water during kneading. This result is in accordance with Valdemir et al. [20], who found that CO₂ released by the carbonated water could generate additional porosity. The same behaviour was observed with RMA (RMA-H₂O-CC and RMA-CO₂-H₂O-CC), in which DBD increased by 0.8% and APW by 19.06%.

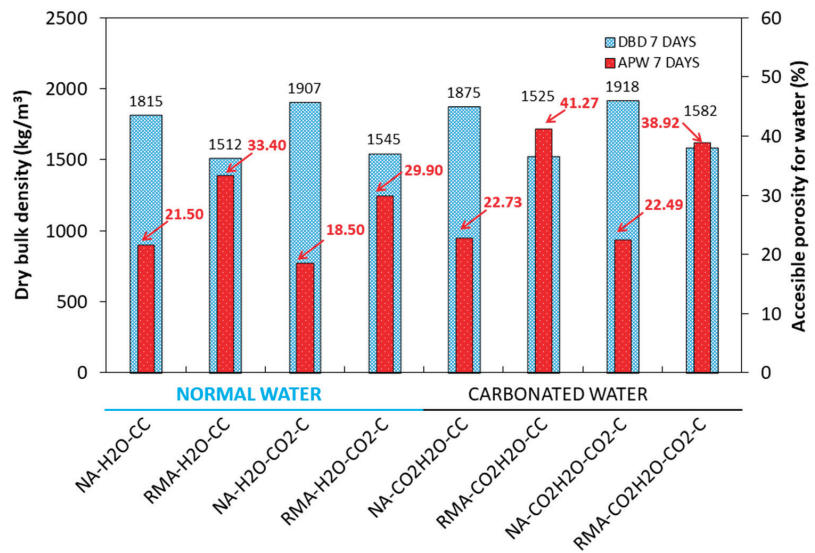


Figure 5. DBD and APW for 7 d under CC and CO₂-C.

For the RMA mixture under the CC regime, when using carbonated and normal water (RMA-H₂O-CC and RMA-CO₂-H₂O-CC), DBD and APW were higher than those in the same mixtures with NA. This agrees with the lower particle dry density, and higher water absorption of RMA reported in [51,79,86].

For the NA and RMA mixtures, using normal water, an increase in DBD and a decrease in APW were observed for samples cured in CO₂-C (NA-H₂O-CC vs. NA-H₂O-CO₂-C and RMA-H₂O-CC vs. RMA-H₂O-CO₂-C). These mechanical properties could be due to sample carbonation, as observed in [13,14,18,24,27,28,56,80]. Carbonated water for kneading water under accelerated carbonation, compared to normal water, increased the DBD and APW (NA-H₂O-CO₂-C vs. NA-CO₂-H₂O-CO₂-C and RMA-H₂O-CO₂-C vs. RMA-CO₂-H₂O-CO₂-C). These results agree with the mechanical properties observed in Figures 3 and 4.

3.4. XRD

XRD obtained for NA using normal and carbonated water as kneading water under CC are shown in Figure 6. For normal water at 1 d, the main phases found were quartz (05-0490) [62], calcite (05-0586) [62], dolomite (11-0078), albite (10-0393) [85], and microline (19-0926) [84], which agrees with the fundamental composition of NA in Figure 2. Hatrurite (86-0402) [62], larnite (33-0302) [62] from the cement used (Figure 2), portlandite (44-1481) [62], and ettringite (37-1479) [62] from the reaction products of Ordinary Portland cement (OPC) [87,88] were also observed. Comparing the phases found using normal or carbonated water as kneading water, a sharp decrease of the phases hatrurite and larnite were observed (Inset Figure 6 labelled “C₃S and C₂S”, red colour “1 day normal water”, purple colour “1 day carbonated water”). Furthermore, the formation of portlandite Ca(OH)₂ was affected by the carbonated water as kneading water (Inset Figure 7 labelled “Portlandite”, red colour “1 day normal water”, purple colour “1 day carbonated water”) and is in accordance with Equation (7). The loss of intensity of hatrurite and larnite peaks and delay in the formation of portlandite were also reported by Hou et al. [71] with acid water. The observed results can be because of the pH of the carbonated water (4.8) and decreased mechanical strength at 1 d of curing, as shown in Figures 4 and 5.

Comparing the diffractogram of 1 d with those obtained at the ages of 3 and 7 d for carbonated water, the same phases were identified but an increase in the intensity was observed in the calcite phase (Inset Figure 6 labelled “CaCO₃ (3 days)” and “CaCO₃ (7 days)”),

suggesting that carbonated water as kneading water produced carbonation [22–24]. This also explains the increased mechanical strength in Figures 3 and 4 and DBD in Figure 5.

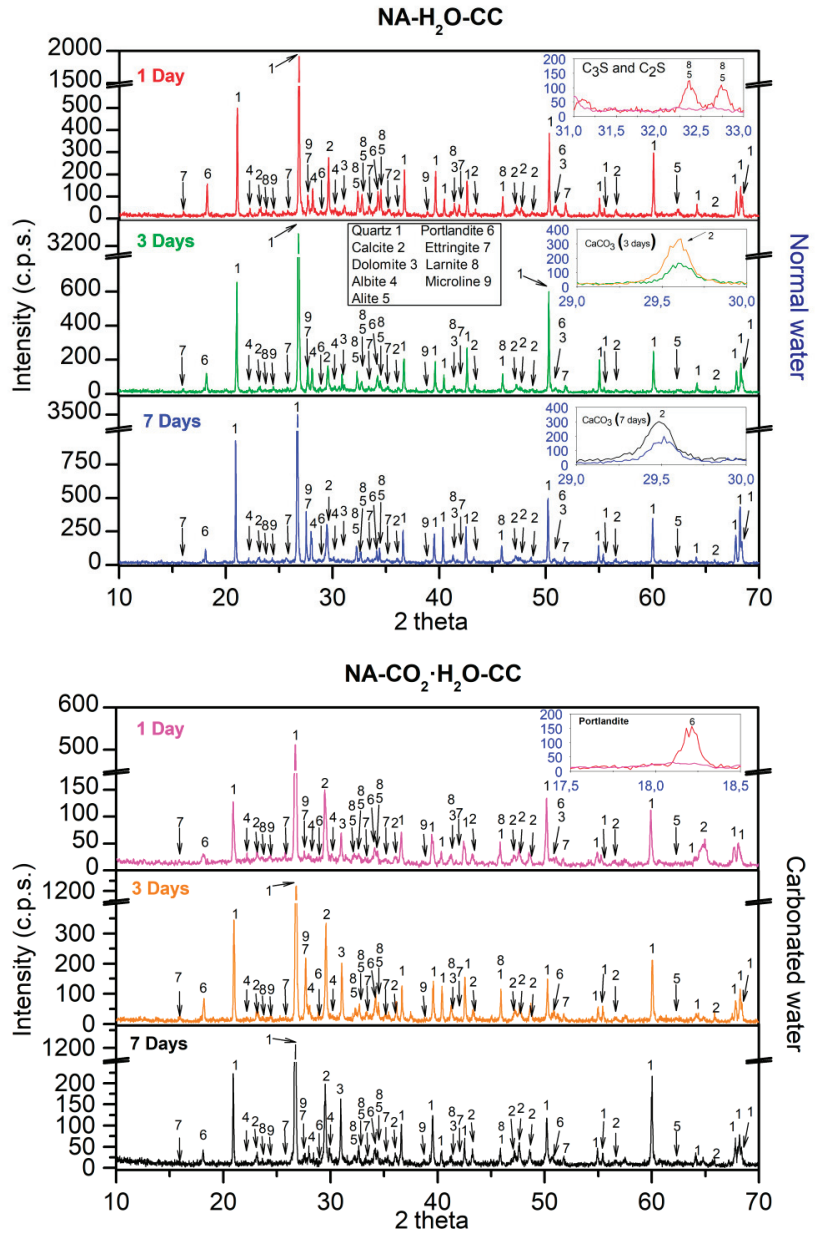


Figure 6. XRD for NA with normal and carbonated water under CC.

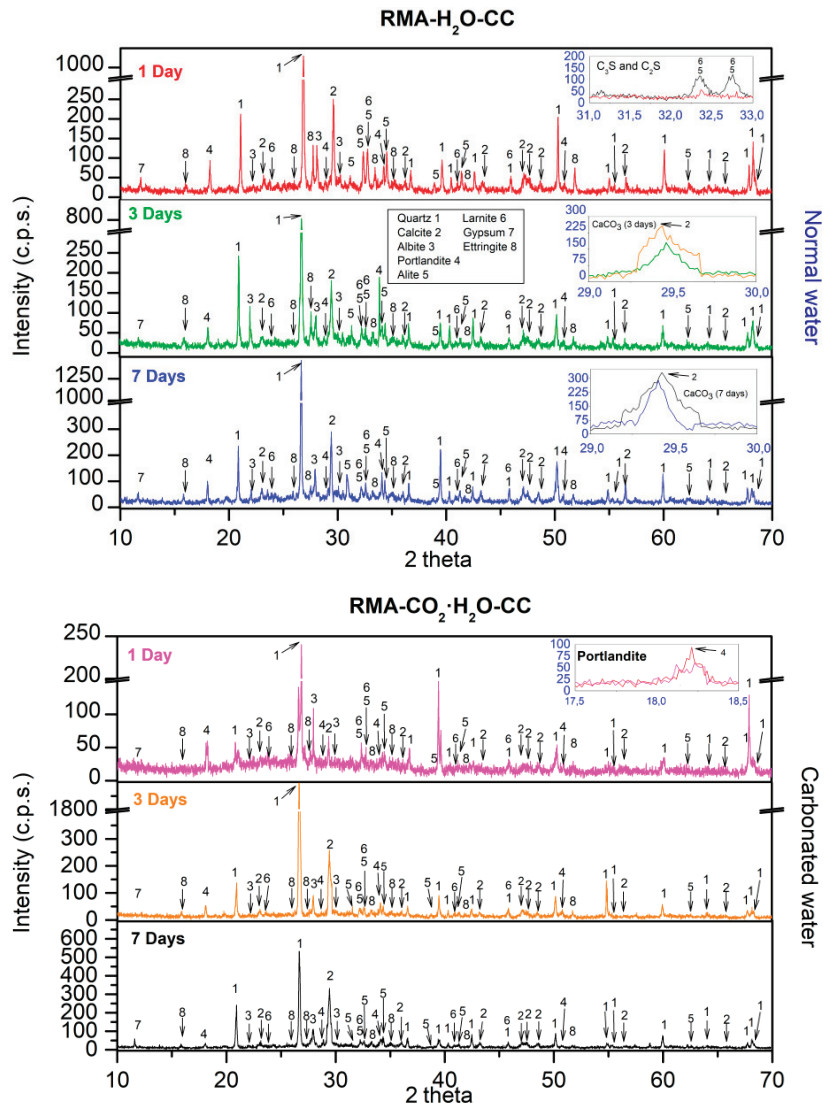


Figure 7. XRD for RMA with normal and carbonated water under CC.

XRD obtained for NA using normal and carbonated water as kneading water under CC are shown in Figure 7. With carbonated water (Figure 7 inset labelled “ C_3S and C_2S ”), we observed a decrease in the peaks of the phases hatrurite and larnite. In addition, the formation of portlandite $Ca(OH)_2$ was not significantly delayed when using carbonated water (Figure 8 inset labelled “Portlandite”). Both processes were due to the presence of $CaCO_3$ and $Ca(OH)_2$ in RMA (Figure 2). These phases acted as a buffer [5]. Hence, carbonated water can increase the mechanical properties at 1 d of age with RMA than with NA (Figures 3 and 4). These results highlight that RMA, acting as a buffer for carbonated water during kneading, avoids a decrease in pH without adding $CaCO_3$ or $Ca(OH)_2$, as previously proposed in [5,89]. Owing to its mineralogical composition, RMA has a similar effect as $CaCO_3$ and $Ca(OH)_2$.

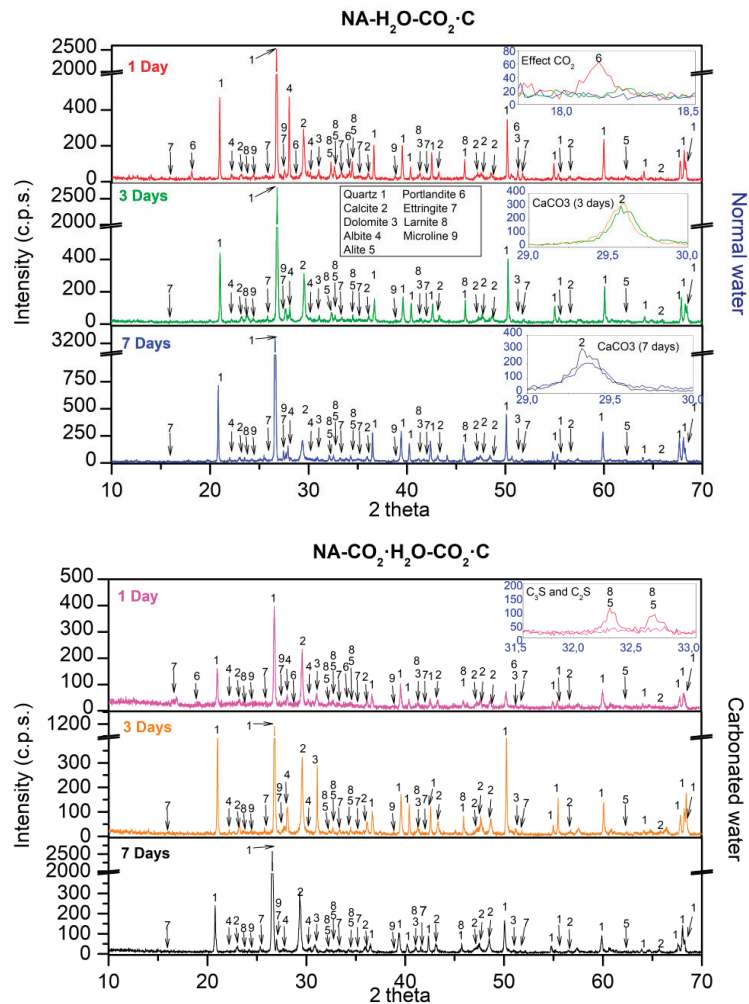


Figure 8. XRD for NA with normal and carbonated water under $\text{CO}_2\text{-C}$.

At 3 and 7 d with normal water, the same phases were identified as that of 1 d. Comparing these diffractograms with that obtained for 3 and 7 d using carbonated water, a higher intensity was observed in the calcite peaks (Figure 7 inset labelled “ CaCO_3 (3 days)” and “ CaCO_3 (7 days)”). This behaviour was already observed in the samples with NA (Figure 7) and indicates that the carbonated water produced carbonation [22–24]. This supports the increase in mechanical strength with carbonated water (in Figures 3 and 4) and DBD (in Figure 5).

XRD obtained for NA using normal and carbonated water as kneading water under $\text{CO}_2\text{-C}$ are shown in Figure 8. For 1 d, with normal water, the same phases as in CC were found. For 3 and 7 d, the disappearance of the portlandite phase was observed (Figure 8 inset labelled “Effect CO_2 ”), which shows the consumption portlandite when it comes into contact with CO_2 (Equation (1)). This concurs with an increase in the mechanical strength in samples cured in $\text{CO}_2\text{-C}$ (Figures 3 and 4). This was due to samples carbonation, as reported in [13,14,18,24,27,28,56,80]. The same phases were found for 1, 3, and 7 d with carbonated water. The portlandite also disappeared at the age of 3 and 7 d.

The effect of carbonated water at 1 d, under the CO₂-C regime, is almost the same as that under CC (Figure 6). However, a decrease in the peaks of the hatrurite and larnite phases were observed (Figure 8 inset labelled “C₃S and C₂S”). For 3 d, the effect of carbonated water (Figure 6) is negligible on the calcite formed with respect to the effect produced by the carbonation chamber (Figure 8), because the amount of CO₂ contributed by the CO₂-C regime is greater than that of the carbonated water (Figure 8 inset labelled “CaCO₃ (3 days)”), similar intensity found for CaCO₃ peaks). These results agree with the delay in setting [71] and strength development [70] due to the initial decrease in pH produced by combining carbonated water and CO₂-C regimes. At 7 d, a greater intensity was observed in the calcite phase, more with carbonated water than with normal water (Figure 8 inset labelled “CaCO₃ (7 days)”). This indicates that pH had been regulated [22–24] and that carbonation of the sample is better than in with normal water and agrees with the results of the mechanical properties in Figures 4 and 5 and DBD in Figure 6.

XRD obtained for RMA using normal and carbonated water as kneading water under CO₂-C are shown in Figure 9. At 1 d, with normal water, the phases found were the same as those found in the CC regime (Figure 7). For 3 and 7 d, the disappearance of the portlandite phase was observed (Figure 9 inset labelled “Effect CO₂”), indicating carbonation (Equation (1)) [13–17].

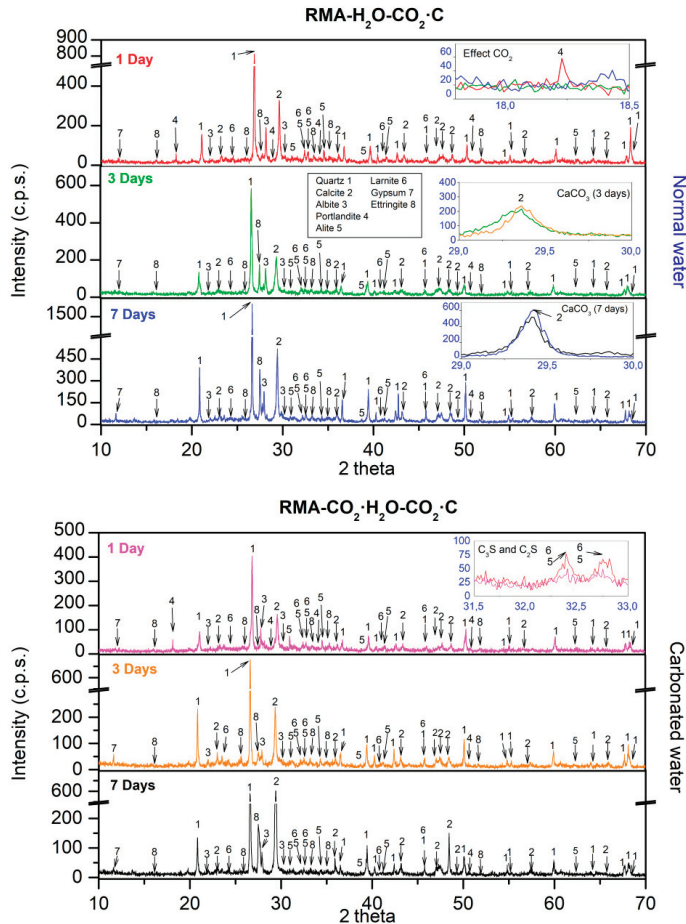


Figure 9. XRD for RMA with normal and carbonated water under CO₂-C.

With carbonated water, the same phases were observed as that with normal water. For 1 d, a light decrease of hatrurite and larnite were observed (Figure 9 inset labelled “ C_3S and C_2S ”, red colour “1 day normal water”, purple colour “1 day carbonated water”), indicating that carbonated water has a retarding effect on the development of mechanical properties at a young age. As with NA (Figure 8), the same behaviour, including calcite peak intensities, was observed at the age of 3 d (Figure 9 inset labelled “ $CaCO_3$ (3)”). The low pH value of carbonated water along with accelerated carbonation (CO_2 -C) which also lowers the pH, negatively affects the strength, although less in the case of NA (Figures 3 and 4). At 7 d of curing, the calcite peaks were similar with carbonated and normal water (Figure 9 inset labelled “ $CaCO_3$ (7)”) and agree with the mechanical properties in Figures 3 and 4 and DBD in Figure 5.

3.5. SEM

Figure 10 shows a general SEM and elemental composition mapping of the NA mixture with normal and carbonated water as kneading water under CC at low magnification (NA- H_2O -CC vs. NA- CO_2 - H_2O -CC). Two main zones were detected: siliceous aggregate and cement paste. The main element in the aggregates is Si and agrees with the chemical composition (Table 4), XRD (Figure 2) results. The main elements contained in the cement paste were Ca, Al, K, and Mg. At low magnification, no differences were observed using carbonated water.

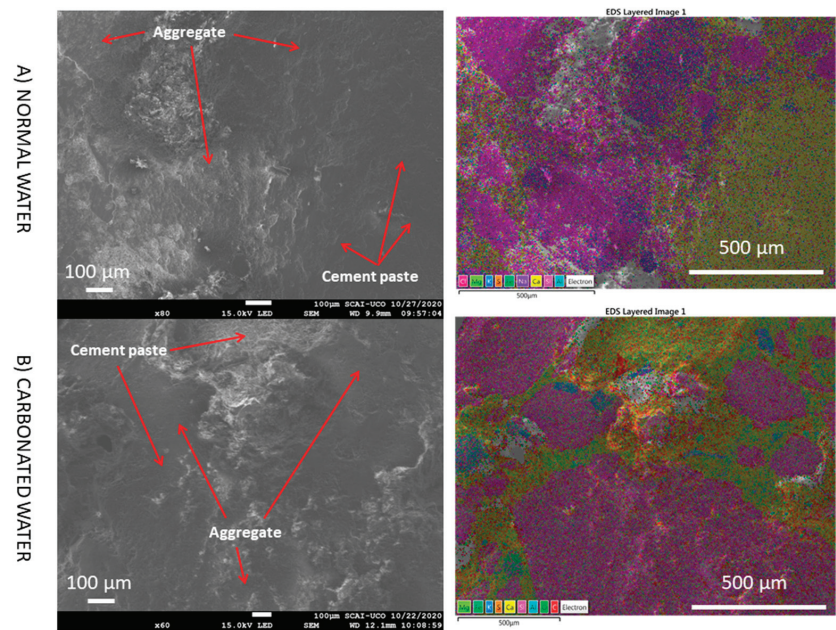


Figure 10. SEM images and elemental composition mapping of NA with normal and carbonated water under normal curing regime CC (NA- H_2O -CC vs. NA- CO_2 - H_2O -CC) at low magnification.

However, by increasing the magnification over the cement paste zone, significant differences were found when using carbonated water (Figure 11). First, it seems that the structure of the cement paste with carbonated water was more porous than that obtained with normal water. The qualitative analysis by SEM agrees with the highest APW found with carbonated water (Figure 5). With normal water, it can be seen that the grains with rounded faces and edges were formed around the cement particles. Nevertheless, with carbonated water, large amounts of well-developed and intertwined needles particles, with very high surface areas are observed. Considering the morphological similarities with

ettringite $\text{Ca}_6[\text{Al}(\text{OH})_6]_2(\text{SO}_4)_3 \cdot 26\text{H}_2\text{O}$, it can be speculated that the needle-like structure is a carbonated ettringite with the chemical formula $\text{Ca}_6[\text{Al}(\text{OH})_6]_2(\text{CO})_3 \cdot 26\text{H}_2\text{O}$ [37]. Because of the high CO_2 content of carbonated water, ion exchange occurs; that is, SO_4^{2-} is fully or partially replaced by CO_3^{2-} . A similar result was found by Pingping et al. [27] with water curing with CO_2 .

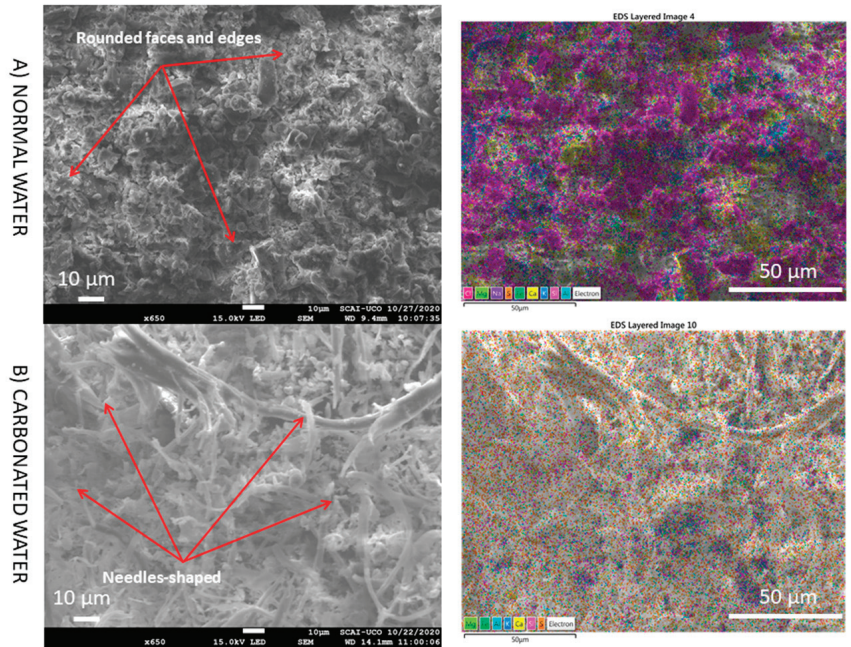


Figure 11. SEM images and elemental composition mapping of NA (zone cement paste) with normal and carbonated water under normal curing regime CC (NA- H_2O -CC vs. NA- CO_2 - H_2O -CC) at medium magnification.

SEM images with higher magnification were taken to confirm the above results (Figure 12). With normal water, grains with rounded faces and edges were observed. However, with carbonated water, hexagonal- or orthorhombic-shaped (1) and needle-shaped particles (2) were observed. EDS analysis of the hexagonal particle revealed the presence of Ca, C, and O, indicating the possibility of CaCO_3 [2,27]. This agrees with the greater intensity of calcite observed in XRD with carbonated water for NA (Figure 6 vs. Figure 7). For needle-shaped particles, EDS revealed a high concentration of C and O, indicating that SO_4^{2-} was fully or partially replaced by CO_3^{2-} to form carbonate ettringite [37]. Boumaza et al. [19] formed carbonated crystals having hexagonal or orthorhombic shapes between the needles of ettringite under a CO_2 environment. The interlaced shape of the carbonate ettringite and greater presence of calcite (due to the carbonation produced by CO_2 in the carbonated water) improved the mechanical properties (Figures 3 and 4) compared to normal water.

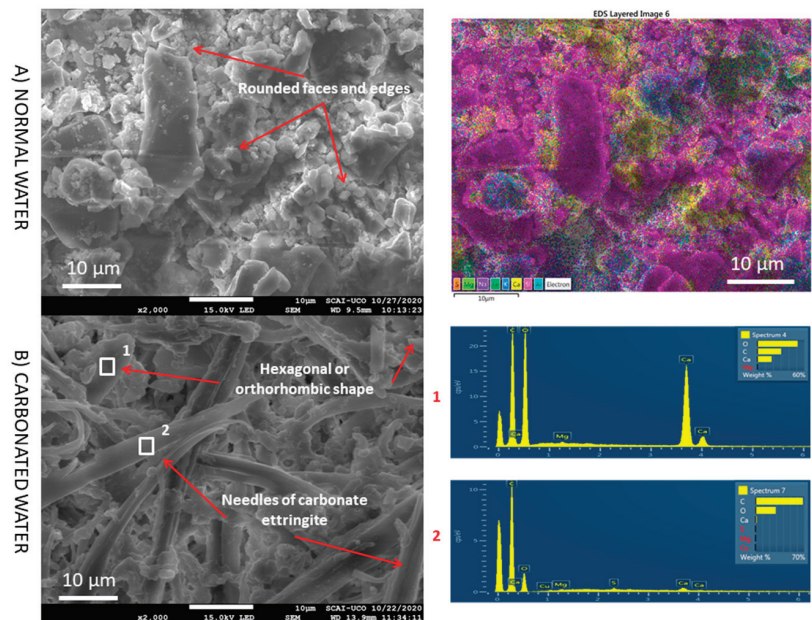


Figure 12. SEM images and EDS of NA (zone cement paste) with normal and carbonated water under normal curing regime CC (NA-H₂O-CC vs. NA-CO₂-H₂O-CC) at high magnification. Elemental composition mapping.

Figure 13 shows a general SEM and elemental composition mapping of the RMA mixture with normal and carbonated water under CC at low magnification (RMA-H₂O-CC vs. RMA-CO₂-H₂O-CC). In this case, two zones were observed: a siliceous aggregate or piece of brick, which is in accordance with the nature of the RMA (Figure 2), and cement paste containing Ca, Al, K, and Mg as the main elements. Furthermore, microcracks and a possible interfacial transition zone (ITZ), which is the area between the old and the new cement paste and is the weakest region in MRA mortar [3,90,91], were observed. These could explain the decrease in mechanical properties (Figures 3 and 4) with the replacement of NA by RMA (with normal and carbonated water under CC) and the higher porosity found with RMA (Figure 5). At this magnification, no differences were found between carbonated and normal water with RMA. The same areas as with normal water are also found. This is contrary to what is observed with NA (Figure 10).

With slightly higher magnification, microcracks were more visible (Figure 14). There were fewer microcracks when using carbonated water as the carbonation products (CaCO₃ particles) can gradually fill pores and micropores [22–24,35]. This agrees with the improvement in the mechanical properties observed with carbonated water in RMA under the CC regime (RMA-H₂O-CC vs. RMA-CO₂-H₂O-CC). Furthermore, this increase in carbonation products was also observed in the XRD analysis (Figure 7). Notably, when using RMA and carbonated water, the presence of carbonated ettringite was not observed, unlike when using NA (Figures 11 and 12) due to the existence of calcite and portlandite in RMA (Figure 2). Calcite and portlandite act as buffers for carbonated water [5], consuming CO₂ from carbonated water, especially portlandite (Equation (1)), thereby avoiding the full or partial replacement of SO₄²⁻ by CO₃²⁻.

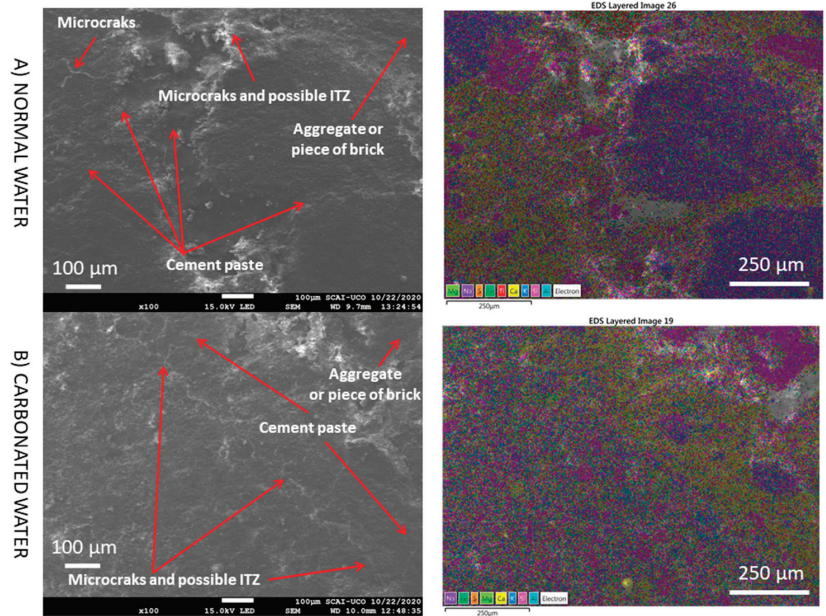


Figure 13. SEM images and elemental composition mapping of RMA with normal and carbonated water under normal curing regime CC (RMA-H₂O-CC vs. RMA-CO₂-H₂O-CC) at low magnification.

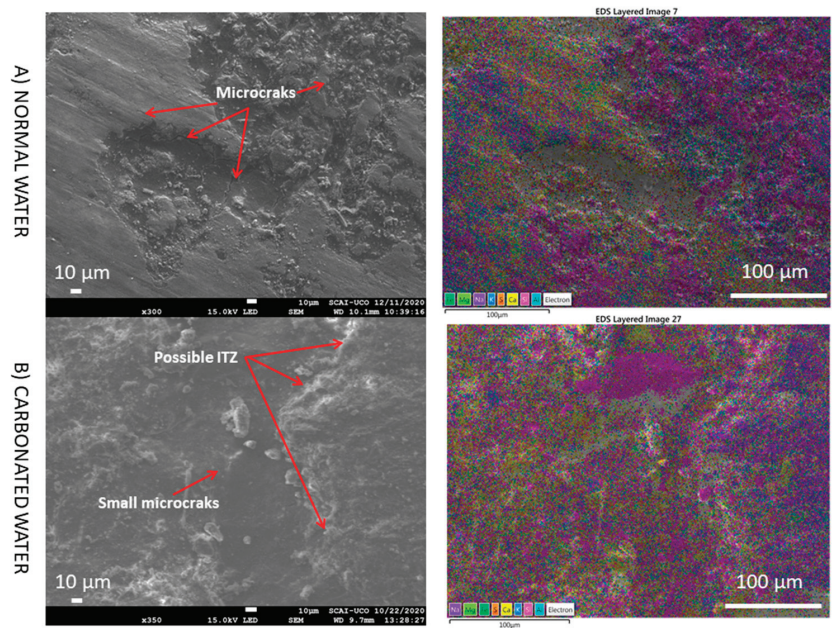


Figure 14. SEM images and elemental composition mapping of RMA with normal and carbonated water under normal curing regime CC (RMA-H₂O-CC vs. RMA-CO₂-H₂O-CC) at medium magnification.

At higher magnification (Figure 15), no microcracks were observed due to the filling of microcracks by the effect of carbonated water in the RMA. In addition, carbonate ettringite

(needle-shaped particles) is not observed. The same behaviour was observed at very high magnification (Figure 16). Therefore, carbonated water on the microstructure of RMA serves the purpose of filling the microcracks. Studies on the influence of carbonated water with RMA have not been found in the literature.

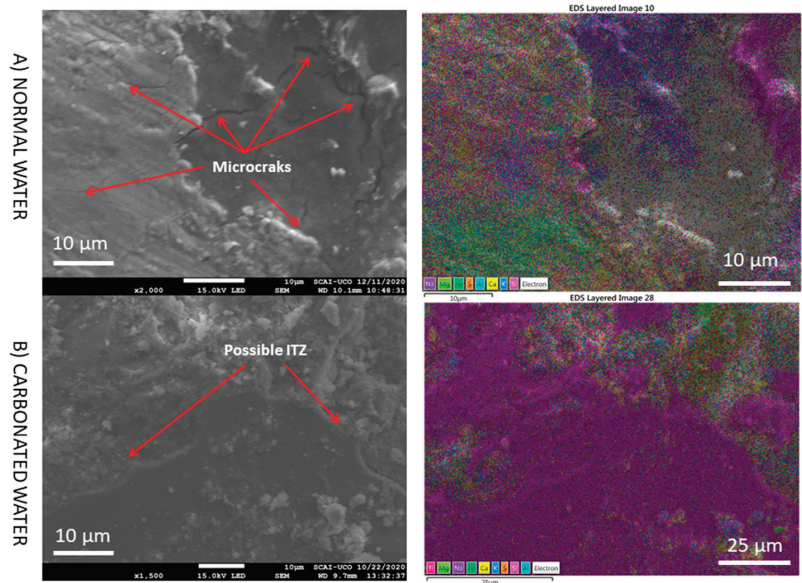


Figure 15. SEM images and elemental composition mapping of RMA with normal and carbonated water under normal curing regime CC (RMA-H₂O-CC vs. RMA-CO₂-H₂O-CC) at high magnification.

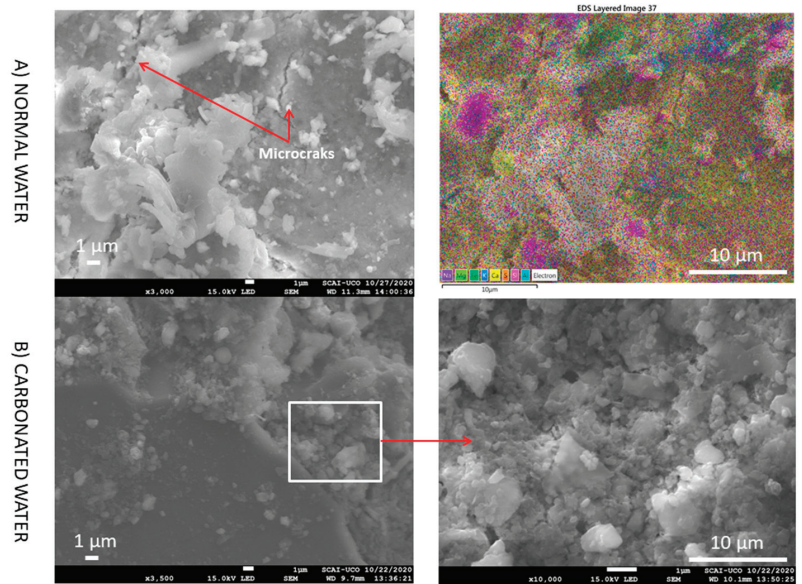


Figure 16. SEM images and elemental composition mapping of RMA with normal and carbonated water under normal curing regime CC (RMA-H₂O-CC vs. RMA-CO₂-H₂O-CC) at very high magnification.

3.6. TGA-DTA

To determine whether carbonated water produces a greater amount of CaCO_3 in the mixes with NA and RMA in CC regime, TGA/DTA was performed (Figure 17). Five stages were observed for all the mixes with normal and carbonated water. In the stage from 480 to 1000 °C, CaCO_3 decomposition occurred [2,56], attributed to the loss of mass resulting from calcium carbonate decomposition. A high loss of mass in this range indicates high calcium carbonate in the mix.

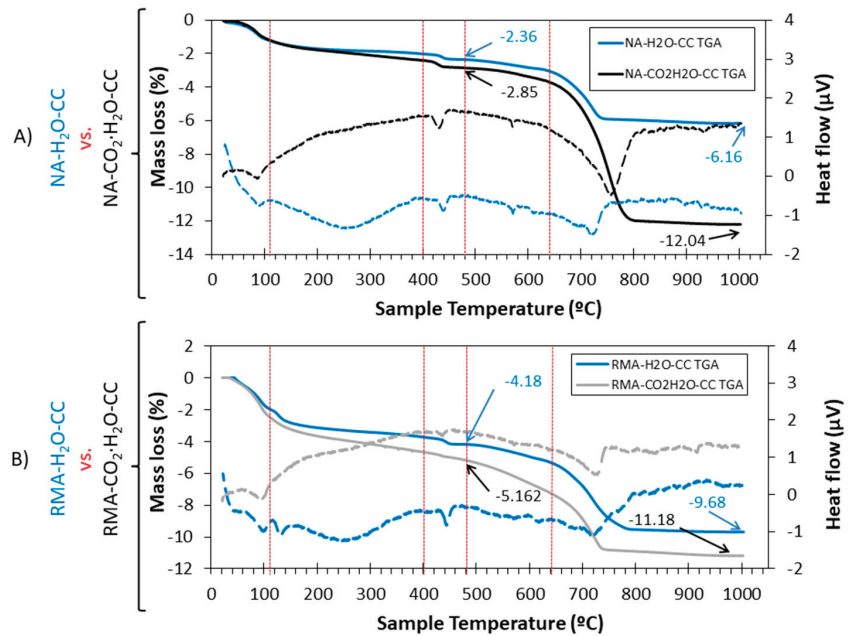


Figure 17. TGA (solid lines) and DTA (dotted lines) curves for (A) mix with NA and (B) mix with RMA. Use of normal and carbonated water.

For the mix with NA (Figure 17A), a mass loss of 3.8% and 9.19% were observed for normal and carbonated water, respectively, (NA-H₂O-CC vs. NA-CO₂-H₂O-CC) in the range of 480–1000 °C, indicating a greater amount of CaCO_3 (product of carbonation) formation with carbonated water. This is in agreement with the mechanical properties (Figures 3 and 4), DBD (Figure 6), XRD results (Figure 6), and SEM (Figures 10–12). The temperature of the decomposition peak of CaCO_3 is different between NA-H₂O-CC and NA-CO₂-H₂O-CC. This was due to the different “nature” of CaCO_3 . In the case of NA-H₂O-CC, this CaCO_3 is the result of the hardening process of the cement [36,92]. In the case of NA-CO₂-H₂O-CC, the calcium carbonate is the result of the carbonation produced in the sample and by them exist a delayed in the decomposition temperature. In contrast, for the mix with RMA (Figure 17B), the mass loss is 5.5 and 6.01 for normal and carbonated water, respectively (RMA-H₂O-CC vs. RMA-CO₂-H₂O-CC), between 480 and 1000 °C. In this case, the difference in calcium carbonate formation was not as important as in NA (although it is still greater with carbonated water than with normal water). This was already described in the analysis of the intensity for calcite peaks in XRD. The difference between the intensity of the peaks was greater in the NA mixture than in the RMA mixture, at the age of 7 d (see Figure 6 inset labelled “ CaCO_3 (7 days)” vs. Figure 7 inset labelled “ CaCO_3 (7 days)”).

4. Conclusions

This study presents an experimental study using carbonated water as kneading water and its impact on the physical-mechanical properties of a porous CBM made with NA and RMA. The main objective was to evaluate the influence of carbonated water together with whether or not subsequent curing in carbonation chamber on the mechanical properties and explain this behaviour using XRD, SEM, and TGA/DTA. The characterisation of the mix composition with different aggregates (NA or RMA), normal water or carbonated water as kneading water, and different hardening environments (different level of CO₂) were performed at 1, 3, and 7 d. The following conclusions were obtained:

- Carbonated water worsened mechanical properties at 1 d of curing with NA under the CC regime, compared to normal water. The phases of CaCO₃ and Ca(OH)₂ in the RMA, acted as a buffer for carbonated water.
- The low pH value of carbonated water and accelerated carbonation (CO₂·C) further lowers the pH, and negatively affects the strength at 1 d of normal curing for all the mixes. The simultaneous utilization of carbonated water as kneading water and subsequent curing in CO₂ is not recommended.
- In all the mixtures studied, the effect of carbonated water increased the DBD (due to carbonation) and APW, indicating that carbonated water generated additional porosity. The carbonation reaction that occurs with carbonated water under CC explains the increase in mechanical strength at 7 d of curing for NA and RMA. A greater intensity in the CaCO₃ peaks (XRD) and increased weight loss of calcite decomposition (TGA/DTA) was also observed.
- The presence of interlaced needles of ettringite carbonate observed by SEM and the increased presence of calcite (due to the carbonation produced by CO₂ in the carbonated water) resulted in better mechanical properties than normal water. Carbonated water on the microstructure of the RMA results in the filling of microcracks (shown in the SEM images). Ettringite carbonate was not observed in this case because of portlandite in RMA, which consumed CO₂ from carbonated water. Carbonated water as kneading water using RMA could allow for the production of precast CBM products with good mechanical properties without the need for CO₂ curing chamber.

The utilization of carbonated water as kneading water in CBM with recycled aggregates (circular economy) can be a novel and interesting procedure to obtain a more environmentally friendly building material without the use of a carbonation chamber. At the same time, it improves mechanical properties and contributes to climate change mitigation.

Author Contributions: Conceptualization, D.S.-M. and J.M.F.-R.; Methodology, J.R.J.; writing—original draft preparation, D.S.-M.; writing—review and editing, J.M.F.-R. and J.R.J.; supervision, J.M.F.-R.; project administration, J.M.F.-R. and J.R.J. All authors have read and agreed to the published version of the manuscript.

Funding: This research was funded by Andalusian regional government UCO-FEDER 20 research project (Ref. 1381172-R) and the Ministry of Science and Innovation of the Government of Spain through the PRECAST-CO₂ research project (Ref. PID2019-111029RB-I00).

Institutional Review Board Statement: Not applicable.

Informed Consent Statement: Not applicable.

Data Availability Statement: Not applicable.

Acknowledgments: D. Suescum-Morales acknowledges funding from MECD-Spain (<http://www.mecd.gob.es/educacion-mecd/>) FPU 17/04329. D. Suescum-Morales also want to thank Cesar Javier Ramos and Maria Esther Jiménez for their help in measuring the initial CO₂ concentration of normal and carbonated water.

Conflicts of Interest: The authors declare no conflict of interest.

References

- Lippiatt, N.; Ling, T.-C.; Pan, S.-Y. Towards carbon-neutral construction materials: Carbonation of cement-based materials and the future perspective. *J. Build. Eng.* **2020**, *28*, 101062. [[CrossRef](#)]
- Zhan, B.J.; Xuan, D.; Poon, C.S.; Shi, C.J. Mechanism for rapid hardening of cement pastes under coupled CO₂-water curing regime. *Cem. Concr. Compos.* **2019**, *97*, 78–88. [[CrossRef](#)]
- Wang, R.; Yu, N.; Li, Y. Methods for improving the microstructure of recycled concrete aggregate: A review. *Constr. Build. Mater.* **2020**, *242*, 118164. [[CrossRef](#)]
- Burek, J.; Nutter, D. Life cycle assessment of grocery, perishable, and general merchandise multi-facility distribution center networks. *Energy Build.* **2018**, *174*, 388–401. [[CrossRef](#)]
- Lippiatt, N.; Ling, T.-C.; Eggermont, S. Combining hydration and carbonation of cement using super-saturated aqueous CO₂ solution. *Constr. Build. Mater.* **2019**, *229*, 116825. [[CrossRef](#)]
- Higuchi, T.; Morioka, M.; Yoshioka, I.; Yokozeki, K. Development of a new ecological concrete with CO₂ emissions below zero. *Constr. Build. Mater.* **2014**, *67*, 338–343. [[CrossRef](#)]
- Sanjuán, M.; Andrade, C.; Mora, P.; Zaragoza, A. Carbon Dioxide Uptake by Mortars and Concretes Made with Portuguese Cements. *Appl. Sci.* **2020**, *10*, 646. [[CrossRef](#)]
- Kaliyavaradhan, S.K.; Ling, T.-C.; Mo, K.H. CO₂ sequestration of fresh concrete slurry waste: Optimization of CO₂ uptake and feasible use as a potential cement binder. *J. CO₂ Util.* **2020**, *42*, 101330. [[CrossRef](#)]
- Yuan, J. Vertical Profiles of Carbon Dioxide in the Lower Troposphere at Manua Loa Observatory, Hawaii, Determined with a Multi-Copter Drone. In Proceedings of the Ocean Sciences Meeting, San Diego, CA, USA, 16–21 February 2020.
- Qiu, R.; Zhang, H.; Zhou, X.; Guo, Z.; Wang, G.; Yin, L.; Liang, Y. A multi-objective and multi-scenario optimization model for operation control of CO₂-flooding pipeline network system. *J. Clean. Prod.* **2020**, *247*, 119157. [[CrossRef](#)]
- Yu, S.; Horing, J.; Liu, Q.; Dahowski, R.; Davidson, C.; Edmonds, J.; Liu, B.; McJeon, H.; McLeod, J.; Patel, P.; et al. CCUS in China's mitigation strategy: Insights from integrated assessment modeling. *Int. J. Greenh. Gas Control* **2019**, *84*, 204–218. [[CrossRef](#)]
- Suescum-Morales, D.; Cantador-Fernández, D.; Jiménez, J.; Fernández, J. Mitigation of CO₂ emissions by hydrotalcites of Mg₃Al-CO3 at 0 °C and high pressure. *Appl. Clay Sci.* **2020**, *202*, 105950. [[CrossRef](#)]
- Liang, C.; Pan, B.; Ma, Z.; He, Z.; Duan, Z. Utilization of CO₂ curing to enhance the properties of recycled aggregate and prepared concrete: A review. *Cem. Concr. Compos.* **2019**, *105*, 103446. [[CrossRef](#)]
- Kaliyavaradhan, S.K.; Ling, T.-C. Potential of CO₂ sequestration through construction and demolition (C&D) waste—An overview. *J. CO₂ Util.* **2017**, *20*, 234–242. [[CrossRef](#)]
- Lu, B.; Shi, C.; Zheng, J.; Ling, T.-C. Carbon dioxide sequestration on recycled aggregates. In *Carbon Dioxide Sequestration in Cementitious Construction Materials*; Woodhead Publishing: Sawston, UK, 2018. [[CrossRef](#)]
- Quesada Carballo, L.; del Rosario Perez Perez, M.; Cantador Fernandez, D.; Caballero Amores, A.; Fernandez Rodriguez, J.M. Optimum Particle Size of Treated Calcites for CO₂ Capture in a Power Plant. *Materials* **2019**, *12*, 1284. [[CrossRef](#)]
- Hang, J.; Shi, C.; Li, Y.; Pan, X.; Poon, C.-S.; Xie, Z. Performance Enhancement of Recycled Concrete Aggregates through Carbonation. *J. Mater. Civ. Eng.* **2015**, *27*. [[CrossRef](#)]
- Rostami, V.; Shao, Y.; Boyd, A.J. Carbonation Curing versus Steam Curing for Precast Concrete Production. *J. Mater. Civ. Eng.* **2012**, *24*, 1221–1229. [[CrossRef](#)]
- Boumaaza, M.; Huet, B.; Turcry, P.; Ait-Mokhtar, A. The CO₂-binding capacity of synthetic anhydrous and hydrates: Validation of a test method based on the instantaneous reaction rate. *Cem. Concr. Res.* **2020**, *135*, 106113. [[CrossRef](#)]
- Dos Santos, V.; Tonoli, G.H.D.; Mármol, G.; Savastano, H. Fiber-cement composites hydrated with carbonated water: Effect on physical-mechanical properties. *Cem. Concr. Res.* **2019**, *124*, 105812. [[CrossRef](#)]
- Zhang, D.; Ghouleh, Z.; Shao, Y. Review on carbonation curing of cement-based materials. *J. CO₂ Util.* **2017**, *21*, 119–131. [[CrossRef](#)]
- Zhan, B.; Poon, C.S.; Liu, Q.; Kou, S.; Shi, C. Experimental study on CO₂ curing for enhancement of recycled aggregate properties. *Constr. Build. Mater.* **2014**, *67*, 3–7. [[CrossRef](#)]
- Kou, S.-C.; Zhan, B.-J.; Poon, C.-S. Use of a CO₂ curing step to improve the properties of concrete prepared with recycled aggregates. *Cem. Concr. Compos.* **2014**, *45*, 22–28. [[CrossRef](#)]
- Shi, C.; He, F.; Wu, Y. Effect of pre-conditioning on CO₂ curing of lightweight concrete blocks mixtures. *Constr. Build. Mater.* **2012**, *26*, 257–267. [[CrossRef](#)]
- Suescum-Morales, D.; Fernández-Rodríguez, J.M.; Jiménez, J.R. Use of carbonated water to improve the mechanical properties and reduce the carbon footprint of cement-based materials with recycled aggregates. *J. CO₂ Util.* **2022**, *57*, 101886. [[CrossRef](#)]
- Kashef-Haghighi, S.; Shao, Y.; Ghoshal, S. Mathematical modeling of CO₂ uptake by concrete during accelerated carbonation curing. *Cem. Concr. Res.* **2015**, *67*, 1–10. [[CrossRef](#)]
- He, P.; Shi, C.; Tu, Z.; Poon, C.S.; Zhang, J. Effect of further water curing on compressive strength and microstructure of CO₂-cured concrete. *Cem. Concr. Compos.* **2016**, *72*, 80–88. [[CrossRef](#)]
- Zhan, B.J.; Poon, C.S.; Shi, C.J. Materials characteristics affecting CO₂ curing of concrete blocks containing recycled aggregates. *Cem. Concr. Compos.* **2016**, *67*, 50–59. [[CrossRef](#)]
- Zhan, B.; Poon, C.; Shi, C. CO₂ curing for improving the properties of concrete blocks containing recycled aggregates. *Cem. Concr. Compos.* **2013**, *42*, 1–8. [[CrossRef](#)]

30. Liu, S.; Guan, X.; Zhang, S.; Xu, C.; Li, H.; Zhang, J. Sintering red mud based imitative ceramic bricks with CO₂ emissions below zero. *Mater. Lett.* **2017**, *191*, 222–224. [[CrossRef](#)]
31. Monkman, S.; Shao, Y. Carbonation Curing of Slag-Cement Concrete for Binding CO₂ and Improving Performance. *J. Mater. Civ. Eng.* **2010**, *22*, 296–304. [[CrossRef](#)]
32. Shi, C.; Wu, Y. Studies on some factors affecting CO₂ curing of lightweight concrete products. *Resour. Conserv. Recycl.* **2008**, *52*, 1087–1092. [[CrossRef](#)]
33. Ben Ghacham, A.; Pasquier, L.-C.; Cecchi, E.; Blais, J.-F.; Mercier, G. Valorization of waste concrete through CO₂ mineral carbonation: Optimizing parameters and improving reactivity using concrete separation. *J. Clean. Prod.* **2017**, *166*, 869–878. [[CrossRef](#)]
34. Pan, X.; Shi, C.; Farzadnia, N.; Hu, X.; Zheng, J. Properties and microstructure of CO₂ surface treated cement mortars with subsequent lime-saturated water curing. *Cem. Concr. Compos.* **2019**, *99*, 89–99. [[CrossRef](#)]
35. Pan, X.; Shi, C.; Hu, X.; Ou, Z. Effects of CO₂ surface treatment on strength and permeability of one-day-aged cement mortar. *Constr. Build. Mater.* **2017**, *154*, 1087–1095. [[CrossRef](#)]
36. Suescum-Morales, D.; Kalinowska-Wichrowska, K.; Fernández, J.M.; Jiménez, J.R. Accelerated carbonation of fresh cement-based products containing recycled masonry aggregates for CO₂ sequestration. *J. CO₂ Util.* **2021**, *46*, 101461. [[CrossRef](#)]
37. Kwasny, J.; Basheer, P.A.M.; Russell, M.; Doherty, W.; Owens, K.; Ward, N. CO₂ sequestration in cement-based materials during mixing process using carbonated water and gaseous CO₂. In Proceedings of the 4th International Conference on the Durability of Concrete Structures, West Lafayette, IN, USA, 24–26 July 2014; pp. 72–79. [[CrossRef](#)]
38. Li, Y.; Fu, T.; Wang, R. An assessment of microcracks in the interfacial transition zone of recycled concrete aggregates cured by CO₂. *Constr. Build. Mater.* **2020**, *236*, 117543. [[CrossRef](#)]
39. Amin, M.; Tayeh, B.A.; Agwa, I.S. Effect of using mineral admixtures and ceramic wastes as coarse aggregates on properties of ultrahigh-performance concrete. *J. Clean. Prod.* **2020**, *273*, 123073. [[CrossRef](#)]
40. Tam, V.W.Y.; Soomro, M.; Evangelista, A.C.J. A review of recycled aggregate in concrete applications (2000–2017). *Constr. Build. Mater.* **2018**, *172*, 272–292. [[CrossRef](#)]
41. Ferreira, R.L.S.; Anjos, M.A.S.; Maia, C.; Pinto, L.; de Azevedo, A.R.G.; de Brito, J. Long-term analysis of the physical properties of the mixed recycled aggregate and their effect on the properties of mortars. *Constr. Build. Mater.* **2020**, *274*, 121796. [[CrossRef](#)]
42. Pavlu, T.; Fortova, K.; Divis, J.; Hajek, P. The Utilization of Recycled Masonry Aggregate and Recycled EPS for Concrete Blocks for Mortarless Masonry. *Materials* **2019**, *12*, 1923. [[CrossRef](#)]
43. Mora-Ortiz, R.S.; Munguía-Balvanera, E.; Díaz, S.A.; Magaña-Hernández, F.; Del Angel-Meraz, E.; Bolaina-Juárez, Á. Mechanical Behavior of Masonry Mortars Made with Recycled Mortar Aggregate. *Materials* **2020**, *13*, 2373. [[CrossRef](#)]
44. Cuenca-Moyano, G.M.; Martín-Pascual, J.; Martín-Morales, M.; Valverde-Palacios, I.; Zamorano, M. Effects of water to cement ratio, recycled fine aggregate and air entraining/plasticizer admixture on masonry mortar properties. *Constr. Build. Mater.* **2020**, *230*, 116929. [[CrossRef](#)]
45. Tan, J.; Cai, J.; Li, X.; Pan, J.; Li, J. Development of eco-friendly geopolymers with ground mixed recycled aggregates and slag. *J. Clean. Prod.* **2020**, *256*, 120369. [[CrossRef](#)]
46. Cantero, B.; del Bosque, I.S.; Matias, A.; Medina, C. Statistically significant effects of mixed recycled aggregate on the physical-mechanical properties of structural concretes. *Constr. Build. Mater.* **2018**, *185*, 93–101. [[CrossRef](#)]
47. Zhang, L.; Sojobi, A.; Kodur, V.; Liew, K.M. Effective utilization and recycling of mixed recycled aggregates for a greener environment. *J. Clean. Prod.* **2019**, *236*, 117600. [[CrossRef](#)]
48. Cantero, B.; Bravo, M.; de Brito, J.; del Bosque, I.S.; Medina, C. Mechanical behaviour of structural concrete with ground recycled concrete cement and mixed recycled aggregate. *J. Clean. Prod.* **2020**, *275*, 122913. [[CrossRef](#)]
49. Jiménez, J.R.; Ayuso, J.; López, M.; Fernández, J.M.; De Brito, J.M.C.L. Use of fine recycled aggregates from ceramic waste in masonry mortar manufacturing. *Constr. Build. Mater.* **2013**, *40*, 679–690. [[CrossRef](#)]
50. Ledesma, E.F.; Jiménez, J.R.; Ayuso, J.; Fernández, J.M.; de Brito, J. Maximum feasible use of recycled sand from construction and demolition waste for eco-mortar production—Part-I: Ceramic masonry waste. *J. Clean. Prod.* **2015**, *87*, 692–706. [[CrossRef](#)]
51. Silva, R.; de Brito, J.; Dhir, R. Performance of cementitious renderings and masonry mortars containing recycled aggregates from construction and demolition wastes. *Constr. Build. Mater.* **2016**, *105*, 400–415. [[CrossRef](#)]
52. Silva, Y.F.; Robayo, R.A.; Matthey, P.E.; Delvasto, S. Properties of self-compacting concrete on fresh and hardened with residue of masonry and recycled concrete. *Constr. Build. Mater.* **2016**, *124*, 639–644. [[CrossRef](#)]
53. Pacheco, J.; de Brito, J.; Chastre, C.; Evangelista, L. Experimental investigation on the variability of the main mechanical properties of concrete produced with coarse recycled concrete aggregates. *Constr. Build. Mater.* **2019**, *201*, 110–120. [[CrossRef](#)]
54. Silva, R.V.; Jiménez, J.; Agrela, F.; de Brito, J. Real-scale applications of recycled aggregate concrete. In *New Trends in Eco-efficient and Recycled Concrete*; Woodhead Publishing: Sawston, UK, 2018; pp. 573–589. [[CrossRef](#)]
55. Lopez-Uceda, A.; Ayuso, J.; Jiménez, J.R.; Galvín, A.P.; Del Rey, I. Feasibility study of roller compacted concrete with recycled aggregates as base layer for light-traffic roads. *Road Mater. Pavement Des.* **2018**, *21*, 276–288. [[CrossRef](#)]
56. Sáez del Bosque, I.F.; Van den Heede, P.; De Belie, N.; de Rojas, M.S.; Medina, C. Carbonation of concrete with construction and demolition waste based recycled aggregates and cement with recycled content. *Constr. Build. Mater.* **2020**, *234*, 117336. [[CrossRef](#)]
57. UNE-EN-1097-6:2013; Tests for Mechanical and Physical Properties of Aggregates. Part 6: Determination of Particle Density and Water Absorption. CEN: Brussels, Belgium, 2013.

58. UNE-EN-197-1:2011; Part 1: Composition, Specifications and Conformity Criteria for Common Cements. BSI: London, UK, 2011.
59. ASTM-C-144; Standard Specification for Aggregate for Masonry Mortar. American Society for Testing and Materials: West Conshohocken, PA, USA, 2004.
60. EN-1015-6:1999; Methods of Test Mortar for Mansory. Part 6: Determination of Bulk Density of Fresh Mortar. SIST: Ljubljana, Slovenia, 1999.
61. EN-1015-11:2000; Methods of Test for Mortar for Mansory. Part 11: Determination of Flexural and Compressive Strenght of Hardened Mortar. SIS: Stockholm, Sweden, 2000.
62. JCPDS. Joint Committee on Power Diffraction Standard-International Centre for Diffraction. 2003.
63. EN-1015-10:2000; Methods of Test Mortar for Mansory. Part 6: Determination of Bulk Density of Hardened Mortar. AENOR: Madrid, Spain, 2000.
64. UNE-83980:2014; Concrete Durability. Test Methods. Determination of the Water Absorption, Density and Accesible Porosity for Water in Concrete. Spanish Association for Standardization: Madrid, Spain, 2014.
65. Roncero, J.; Valls, S.; Gettu, R. Study of the influence of superplasticizers on the hydration of cement paste using nuclear magnetic resonance and X-ray diffraction techniques. *Cem. Concr. Res.* **2002**, *32*, 103–108. [[CrossRef](#)]
66. Tang, S.; Cai, X.; He, Z.; Shao, H.; Li, Z.; Chen, E. Hydration process of fly ash blended cement pastes by impedance measurement. *Constr. Build. Mater.* **2016**, *113*, 939–950. [[CrossRef](#)]
67. Abed, M.; Nemes, R.; Lubl6y, E. Performance of Self-Compacting High-Performance Concrete Produced with Waste Materials after Exposure to Elevated Temperature. *J. Mater. Civ. Eng.* **2020**, *32*, 05019004. [[CrossRef](#)]
68. Suescum-Morales, D.; R6os, J.D.; De La Concha, A.M.; Cifuentes, H.; Jim6nez, J.R.; Fern6ndez, J.M. Effect of moderate temperatures on compressive strength of ultra-high-performance concrete: A microstructural analysis. *Cem. Concr. Res.* **2021**, *140*, 106303. [[CrossRef](#)]
69. Esquinas, R.; Motos-P6rez, D.; Jim6nez, M.; Ramos, C.; Jim6nez, J.R.; Fern6ndez, J. Mechanical and durability behaviour of self-compacting concretes for application in the manufacture of hazardous waste containers. *Constr. Build. Mater.* **2018**, *168*, 442–458. [[CrossRef](#)]
70. Sumra, Y.; Payam, S.; Zainah, I. The pH of Cement-based Materials: A Review. *J. Wuhan Univ. Technol. Sci. Ed.* **2020**, *35*, 908–924. [[CrossRef](#)]
71. Hou, W.; Bao, J. Evaluation of cement retarding performance of cellulosic sugar acids. *Constr. Build. Mater.* **2019**, *202*, 522–527. [[CrossRef](#)]
72. Bao, H.; Xu, G.; Wang, Q.; Peng, Y.; Liu, J. Study on the deterioration mechanism of cement-based materials in acid water containing aggressive carbon dioxide. *Constr. Build. Mater.* **2020**, *243*, 118233. [[CrossRef](#)]
73. Li, X.; Shui, Z.; Sun, T.; Liu, K.; Wang, X. The hydration mechanism of cement-based materials served in marine environment during early-age magnesium precipitation. *Constr. Build. Mater.* **2020**, *230*, 117010. [[CrossRef](#)]
74. Lothenbach, B.; Winnefeld, F. Thermodynamic modelling of the hydration of Portland cement. *Cem. Concr. Res.* **2006**, *36*, 209–226. [[CrossRef](#)]
75. Jim6nez, J.R.; Fern6ndez-Ledesma, E.; Ayuso, J.; Corinaldesi, V.; Iglesias, F.J. A proposal for the maximum use of recycled concrete sand in masonry mortar design. *Mater. Construcci6n* **2016**, *66*, e075. [[CrossRef](#)]
76. Duan, Z.; Hou, S.; Xiao, J.; Li, B. Study on the essential properties of recycled powders from construction and demolition waste. *J. Clean. Prod.* **2020**, *253*, 119865. [[CrossRef](#)]
77. Mart6nez, P.S.; Cortina, M.G.; Mart6nez, F.F.; S6nchez, A.R. Comparative study of three types of fine recycled aggregates from construction and demolition waste (CDW), and their use in masonry mortar fabrication. *J. Clean. Prod.* **2016**, *118*, 162–169. [[CrossRef](#)]
78. Gonzalez-Corominas, A.; Etxeberria, M. Properties of high performance concrete made with recycled fine ceramic and coarse mixed aggregates. *Constr. Build. Mater.* **2014**, *68*, 618–626. [[CrossRef](#)]
79. Silva, J.; de Brito, J.; Veiga, R. Recycled Red-Clay Ceramic Construction and Demolition Waste for Mortars Production. *J. Mater. Civ. Eng.* **2010**, *22*, 236–244. [[CrossRef](#)]
80. Li, X.; Ling, T.-C. Instant CO₂ curing for dry-mix pressed cement pastes: Consideration of CO₂ concentrations coupled with further water curing. *J. CO₂ Util.* **2020**, *38*, 348–354. [[CrossRef](#)]
81. Suescum-Morales, D.; Cantador-Fern6ndez, D.; Jim6nez, J.R.; Fern6ndez, J.M. Potential CO₂ capture in one-coat limestone mortar modified with Mg₃Al- CO_3 calcined hydrotalcites using ultrafast testing technique. *Chem. Eng. J.* **2021**, *415*, 129077. [[CrossRef](#)]
82. Suescum-Morales, D.; Fern6ndez, D.C.; Fern6ndez, J.M.; Jim6nez, J.R. The combined effect of CO₂ and calcined hydrotalcite on one-coat limestone mortar properties. *Constr. Build. Mater.* **2020**, *280*, 122532. [[CrossRef](#)]
83. Zhao, K.; Liang, Y.; Ji, T.; Lu, Y.; Lin, X. Effect of activator types and concentration of CO₂ on the steel corrosion in the carbonated alkali-activated slag concrete. *Constr. Build. Mater.* **2020**, *262*, 120044. [[CrossRef](#)]
84. Vogler, N.; Lindemann, M.; Drabetzki, P.; K6hne, H.-C. Alternative pH-indicators for determination of carbonation depth on cement-based concretes. *Cem. Concr. Compos.* **2020**, *109*, 103565. [[CrossRef](#)]
85. Seigneur, N.; Kangni-Foli, E.; Lagneau, V.; Dauz6res, A.; Poyet, S.; Le Bescop, P.; L'H6pital, E.; de Lacaillerie, J.-B.D. Predicting the atmospheric carbonation of cementitious materials using fully coupled two-phase reactive transport modelling. *Cem. Concr. Res.* **2020**, *130*, 105966. [[CrossRef](#)]

86. De Hita, P.R.; Pérez-Gálvez, F.; Morales-Conde, M.J.; Pedreño-Rojas, M.A. Characterisation of recycled ceramic mortars for use in prefabricated beam-filling pieces in structural floors. *Mater. Construcción* **2019**, *69*, e189. [[CrossRef](#)]
87. Gonçalves, T.; Silva, R.V.; De Brito, J.; Fernández, J.M.; Esquinas, A.R. Mechanical and durability performance of mortars with fine recycled concrete aggregates and reactive magnesium oxide as partial cement replacement. *Cem. Concr. Compos.* **2020**, *105*, 103420. [[CrossRef](#)]
88. Lozano-Lunar, A.; Dubchenko, I.; Bashynskiy, S.; Rodero, A.; Fernández, J.; Jiménez, J. Performance of self-compacting mortars with granite sludge as aggregate. *Constr. Build. Mater.* **2020**, *251*, 118998. [[CrossRef](#)]
89. Qian, X.; Wang, J.; Fang, Y.; Wang, L. Carbon dioxide as an admixture for better performance of OPC-based concrete. *J. CO2 Util.* **2018**, *25*, 31–38. [[CrossRef](#)]
90. Wu, C.-R.; Hong, Z.-Q.; Zhang, J.-L.; Kou, S.-C. Pore size distribution and ITZ performance of mortars prepared with different bio-deposition approaches for the treatment of recycled concrete aggregate. *Cem. Concr. Compos.* **2020**, *111*, 103631. [[CrossRef](#)]
91. Dang, J.; Zhao, J.; Pang, S.D.; Zhao, S. Durability and microstructural properties of concrete with recycled brick as fine aggregates. *Constr. Build. Mater.* **2020**, *262*, 120032. [[CrossRef](#)]
92. Ye, G.; Liu, X.; De Schutter, G.; Poppe, A.-M.; Taerwe, L. Influence of limestone powder used as filler in SCC on hydration and microstructure of cement pastes. *Cem. Concr. Compos.* **2007**, *29*, 94–102. [[CrossRef](#)]

Article

Uniaxial Compressive Stress–Strain Relation of Recycled Coarse Aggregate Concrete with Different Carbonation Depths

Kun Tu ^{1,2}, Jin Wu ^{1,2,*}, Yiyuan Wang ^{1,2}, Huachao Deng ^{1,2} and Rui Zhang ³

¹ Department of Civil and Airport Engineering, Nanjing University of Aeronautics and Astronautics, 29 Yudao Street, Nanjing 210016, China

² Jiangsu Airport Infrastructure Safety Engineering Research Center, 29 Yudao Street, Nanjing 210016, China

³ School of Kangda, Nanjing Medical University, 88 Chunhui Road, Lianyungang 222000, China

* Correspondence: wujin@nuaa.edu.cn

Highlights:

- Uniaxial compressive stress–strain curves of recycled aggregate concrete (RAC) with different carbonation depth were investigated.
- The effect of carbonation depth on peak stress, strain, elastic modulus, and the relative toughness of RAC was studied.
- Stress–strain models of recycled aggregate concrete with different carbonation depths were established.

Abstract: The stress–strain relation of recycled aggregate concrete (RAC) after carbonation is very important to the assessment of the durability of RAC. The objective of this study is to investigate the uniaxial compressive stress–strain curves of RAC after carbonation. In this study, the specimens were prepared with 70-mm diameter and 140-mm height cylinders, and the carbonation of the specimens was accelerated after curing 28 days. Then a uniaxial compressive loading test on the specimens was performed by using a mechanical testing machine. The results show that the peak stress (σ_0) and elastic modulus (E_c) of all specimens increase with the increase of carbonation depth. The ratio of ultimate strain to peak strain (ϵ_u/ϵ_0) and relative toughness of the specimens decrease with the increase of carbonation depth. Furthermore, carbonation has a stronger effect on natural coarse aggregate concrete (NAC) than the 50% replacement rate of RAC with similar compressive strength. Stress–strain models of recycled aggregate concrete with different carbonation depths were established according to experimental results.

Keywords: recycled coarse aggregate concrete; carbonation; uniaxial compressive loading; stress–strain curves; fitting analysis

Citation: Tu, K.; Wu, J.; Wang, Y.; Deng, H.; Zhang, R. Uniaxial Compressive Stress–Strain Relation of Recycled Coarse Aggregate Concrete with Different Carbonation Depths. *Materials* **2022**, *15*, 5429. <https://doi.org/10.3390/ma15155429>

Academic Editors: Daniel Ferrández Vega, Jean-Marc Tulliani and Carlos Morón Fernández

Received: 6 April 2022

Accepted: 3 August 2022

Published: 7 August 2022

Publisher's Note: MDPI stays neutral with regard to jurisdictional claims in published maps and institutional affiliations.



Copyright: © 2022 by the authors. Licensee MDPI, Basel, Switzerland. This article is an open access article distributed under the terms and conditions of the Creative Commons Attribution (CC BY) license (<https://creativecommons.org/licenses/by/4.0/>).

1. Introduction

With the development of the construction industry has come a myriad of construction waste and great damage to the environment [1]. In China, 2.36 billion tons of construction waste was generated annually in the most recent decade [2]. Consequently, it is urgent to use recycled construction and demolition materials. The use of recycled aggregate (RA) in concrete opens a whole new range of possibilities for reusing materials in construction. Reuse of waste concrete as RA in new concrete is beneficial from the viewpoint of environmental protection and preservation of resources, as it reduces the use of natural materials used in concrete production [3]. It presents a more environmentally friendly alternative destination for this waste [4]. Using recycled aggregate could save about 60% of limestone resources and reduce CO₂ emissions by about 15–20% [5]. However, the strength of RAC decreases with the increase of the replacement percentage of recycled aggregate due to the presence of micro-cracks and old cement paste that has adhered to

the original aggregates [6–8]. Azevedo pointed out that the substitution of more than 25% of construction and demolition waste (CDW) for sand requires relatively larger amounts of water in the mortar, and the water absorption of the mortar increased with the levels of incorporated CDW [9]. Because of the high variability in the characteristics of recycled aggregates, in order to obtain better properties, a deeper classification of the constituents should be carried out [10]. The premix process can fill up some pores and cracks, resulting in a denser concrete, an improved interfacial zone around recycled aggregate, and thus a higher strength when compared with the traditional mixing approach [11].

In addition, many researchers have argued that the carbonation resistance of RAC was worse than that of natural aggregate concrete (NAC) [12–14], which may lead to the corrosion of reinforcement, causing safety hazards and great economic losses [15]. There are many factors affecting the carbonation of RAC, such as the cement matrix, aggregate, mixing method, external load, and external environment, etc. [14]. Consequently, it is necessary to strengthen recycled coarse aggregate (RCA) or recycled aggregate concrete (RAC) itself in order to obtain RAC with better properties.

Some researchers found that the properties of RAC could be improved by adding pozzolan, silica fume, and rubber particles and fibers into RAC [16–20]. Other researchers found that the properties of RAC can be improved by carbonation which includes carbon conditioning and carbon curing. Carbon conditioning is the injection of CO₂ into recycled aggregate, accomplished with the assistance of a sealable carbonation chamber [21]. Zhang et al. [22] and Zhan et al. [23] found carbonation can improve RCA in physical and mechanical properties. The apparent density of RCA was significantly increased, whereas the water absorption and crushing value of RCA were significantly decreased after carbonation. Carbon curing relies upon carbonation reaction between CO₂ and cement paste, and it carbonates entire concrete blocks after concrete mixing [18]. Zhan et al. [24] found that carbon curing improved rapidly the compressive strength of RAC with strength gains ranging from 108% to 151% higher than conventional moisture curing. Zhan et al. [25] and Xuan et al. [26] found that carbon-curing conditions will lead to improvements of RAC strength.

The widespread adoption of RAC requires not only a better understanding of its mechanical properties and durability but also the availability of guidelines on designing reliable RAC structures [27]. In order to guide the design of RAC structures, the stress–strain relationship of RAC has been preliminarily investigated [28–31]. In addition, Luo et al. [32] investigated stress–strain curves of fully carbonated RAC and found that carbonated RAC improved the compressive strength and elastic modulus of RAC. However, less information is available on the effect of carbonation depth on the stress–strain relation of RAC.

The objective of this study is to evaluate the peak stress, elastic modulus, strain, relative toughness and establish the stress–strain model of RAC with different carbonation depths according to experimental results.

2. Experimental Method

2.1. Materials and Mixture Proportions

Ordinary Portland cement of grade 42.5 was used in this study. The cement properties are shown in Table 1, and river sand with particle size less than 4.75 mm was used as fine aggregates. NCA was from gravel, and RCA was produced from Nanjing Shoujia Renewable Resources Utilization Company (Nanjing, China). After the concrete residues were transported to the company, a jaw crusher was employed in order to reduce the size of the large pieces of concrete residues. After being crushed, the residues were cleaned and graded ready for the planned tests. The crushing values of NCA and RCA were measured according to Pebbie and crushed stone for building (GB/T14685-2011) in China. The size grading of RCA and NCA were similar to ranging from 5 mm to 20 mm, and satisfied the standard for technical requirements and test method of sand and crushed stone (or gravel) for ordinary concrete (JGJ52-2006) in China. Figure 1 shows the sieving results of aggregates, and the properties of NCA and RCA are shown in Table 2.

Table 1. Properties of cement.

| Property | Value |
|--|----------|
| Type and class | P.O 42.5 |
| Specific surface area (m ² kg ⁻¹) | 335 |
| Initial and final setting times (min) | 215/265 |
| 28-day compressive and flexural strength (MPa) | 49.8/8.7 |
| SO ₃ (%) | 2.4 |
| MgO (%) | 1.8 |
| CaO (%) | 62.6 |
| SiO ₂ (%) | 21.2 |
| Al ₂ O ₃ (%) | 5.6 |
| Fe ₂ O ₃ (%) | 4.6 |

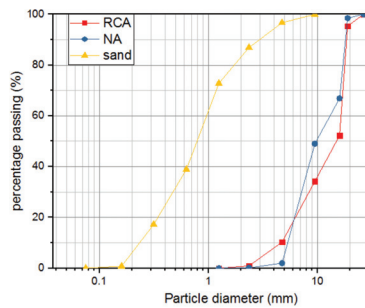


Figure 1. Grading curve of aggregates.

Table 2. Properties of the NCA and RCA.

| Aggregate Type | Coarse Aggregate Grading (mm) | Apparent Density (kg/m ³) | Water Absorption (%) | Crushing Value (%) |
|----------------|-------------------------------|---------------------------------------|----------------------|--------------------|
| NCA | 5–20 | 2773 | 1.08 | 3.2 |
| RCA | 5–20 | 2541 | 5.12 | 14.2 |

Due to the high water absorption of RCA, pre-soaking was used to make RCA reach the saturated surface dry (SSD) condition. The mix design proportions of RAC and NAC are listed in Table 3. Note that the replacement ratio of specimens is calculated by volume. The water–cement ratio and sand ratio were adjusted to obtain similar 28-day compressive strengths of NAC and RAC based on the technical code on the application of recycled concrete (DG/TJ08-2018) in China.

Table 3. Mix design proportions of NAC and RAC.

| Concrete Type | Water (kg/m ³) | Cement (kg/m ³) | Water to Cement Ratio | NCA (kg/m ³) | RCA (kg/m ³) | Fine Aggregates (kg/m ³) |
|---------------|----------------------------|-----------------------------|-----------------------|--------------------------|--------------------------|--------------------------------------|
| NAC | 195 | 274.6 | 0.71 | 1131.1 | 0.0 | 754.1 |
| RAC50 | 200 | 333.3 | 0.60 | 566.8 | 519.0 | 694.2 |
| RAC100 | 205 | 410.0 | 0.50 | 0.0 | 1006.6 | 643.5 |

The specimens with 70-mm diameter and 140-mm height cylinders were cast in a PVC mould. After curing for 28 days, the compressive strengths of RAC cubes (100 mm × 100 mm × 100 mm) with replacement ratios of 0%, 50% and 100% were 37.5 MPa, 36.4 MPa and 31.1 MPa, respectively.

2.2. Accelerated Carbonation Procedure

The acceleration of concrete carbonation was performed in a carbonation experiment chamber. The temperature was 20 °C, the humidity was 60% and the CO₂ concentration was 20%. All specimens were wax-sealed at both ends to conduct side-only carbonation. To achieve different carbonation depths, carbonation periods were set to 0, 14, 28, 42, 56, 70, and 84 days.

The carbonation depth is a quantity index that characterizes the degree of carbonation. A 1/3-length cylinder was split when measuring carbonation depth, and the cross-section of the remaining piece was sealed with wax for further carbonation and measurement. For the piece after splitting, drop 1% phenolphthalein alcohol solution (alcohol solution contains 20% distilled water) on the cross-section. Then a measurement point was marked every 45° on the circular section and the depth of carbonation was measured at each measurement point. The average value of carbonation depth was taken as the carbonation depth of the specimens,

$$\bar{d}_t = \frac{1}{n} \sum_{i=1}^n d_i \quad (1)$$

where d_t is the average carbonation depth (mm) after carbonation t (d) of the test, d_i is the carbonation depth of measuring point (mm), and n is the total number of measuring points.

2.3. Uniaxial Compressive Loading Test

A uniaxial compressive loading test was performed by using a mechanical testing machine. Two displacement meters were fixed on the middle part of both sides of the specimen, and the displacement in the middle part of the specimen (170–180 mm) was measured in this test as shown in Figure 2. A load sensor was placed under the steel pads. The dynamic data acquisition system was used to collect the test data.



Figure 2. Test setup of loading and measurement.

The peak strain (ϵ_0) is the strain corresponding to peak stress and the ultimate strain (ϵ_u) is the strain corresponding to the stress which is 50% of peak stress at the descending part of the stress–strain curve.

The elastic modulus (E_c) was calculated with the following expression [33,34]:

$$E_c = \frac{\sigma_{0.4} - \sigma_0}{\epsilon_{0.4} - \epsilon_0}, \quad (2)$$

where σ_0 is peak stress and $\sigma_{0.4}$ is the stress corresponding to 40% of the peak stress, ϵ_0 is the peak strain, and $\epsilon_{0.4}$ is the corresponding to $\sigma_{0.4}$.

3. Experimental Results and Discussion

3.1. Carbonation Depth

Figure 3 shows carbonated specimens with 0%, 50%, and 100% RCA replacement ratios. The correlation between carbonation depths and carbonation periods is shown in Figure 4. It can be seen that the carbonation depth of specimens increased as the replacement ratio of RCA increased due to the increase of the porosity of RAC. This agreed with the findings observed by C. Thomas and Miguel Bravo [35,36].

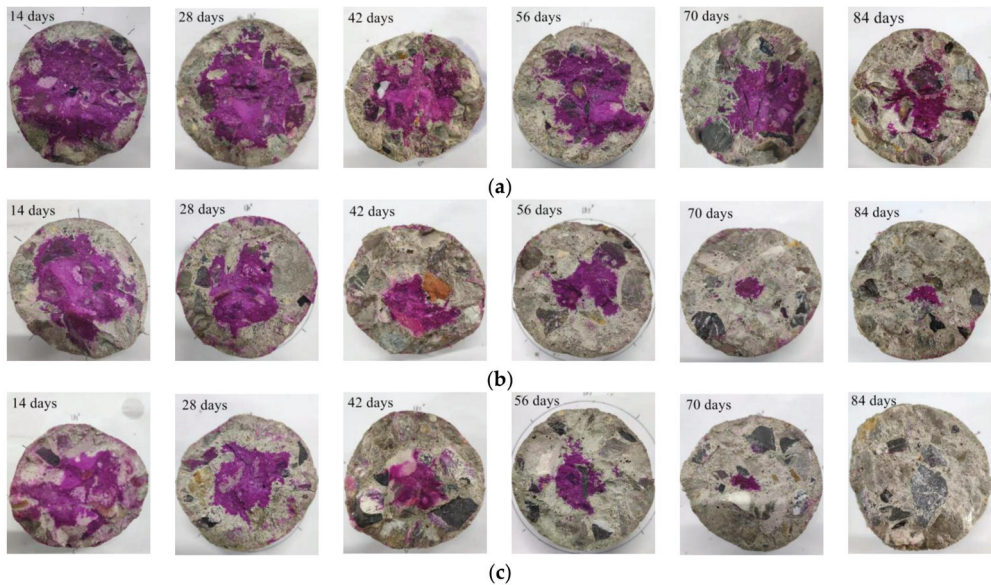


Figure 3. Typical specimens after different carbonation periods. (a) NAC; (b) RAC50; (c) RAC100.

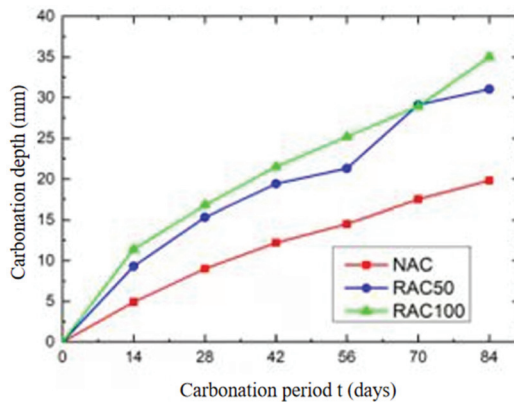


Figure 4. Carbonation depth versus carbonation periods.

Moreover, the RAC100 was fully carbonated at 35.0 mm of carbonation depth, whereas RAC50 and NAC were carbonated at 31.0 and 19.2 mm, respectively. Notably, the carbonation depth of RAC50 was 12% higher than that of NAC under a similar 28-day compressive strength. However, the carbonation resistance of RAC can be improved upon by adding other materials, such as fly ash [14], etc. Consequently, it is possible to apply RAC in field applications.

3.2. Failure Pattern

Failure patterns of RAC and NAC specimens with different carbonation depths are compressive failure modes, as shown in Figure 5. For non-carbonated RAC and NAC specimens, there were a few cracks that were parallel to the loading direction, and the surfaces were slightly spalling. There is no significant difference in failure patterns of uncarbonated RAC and NAC specimens, as shown in Figure 5a–c. In contrast, for highly carbonated RAC50 and RAC100 specimens, as shown in Figure 5e,f, lots of short cracks were parallel to the loading direction, but these short cracks formed one or several long cracks. Finally, there were diagonal cracks that passed through the whole specimens, as shown in Figure 6. However, carbonated NAC specimens had the same failure pattern with uncarbonated NAC, and the spalling happened in carbonated NAC, as shown in Figure 5d. Therefore, the effect of carbonation on the failure pattern of RAC is more obvious than that of NAC. This is explained as follows: for carbonated RAC, carbonation did not change the pore and microcrack in RCA, but there were obvious micro-cracks on the interface between RCA and the new cement matrix, and the structure was looser in the interface transition zone (ITZ). Yang et al. [37] found the above phenomenon by comparing scanning electron micro-graphs of carbonated RAC with that of carbonated NAC. Consequently, carbonation mainly changes the microstructure of the paste and interface transition zone. Short cracks occurred in RAC with the increase of loading, but the more pore and microcracks in RCA prevented the development of short cracks. Therefore, lots of short cracks occurred and formed one or several long diagonal cracks, resulting in the diagonal band failure of specimens.

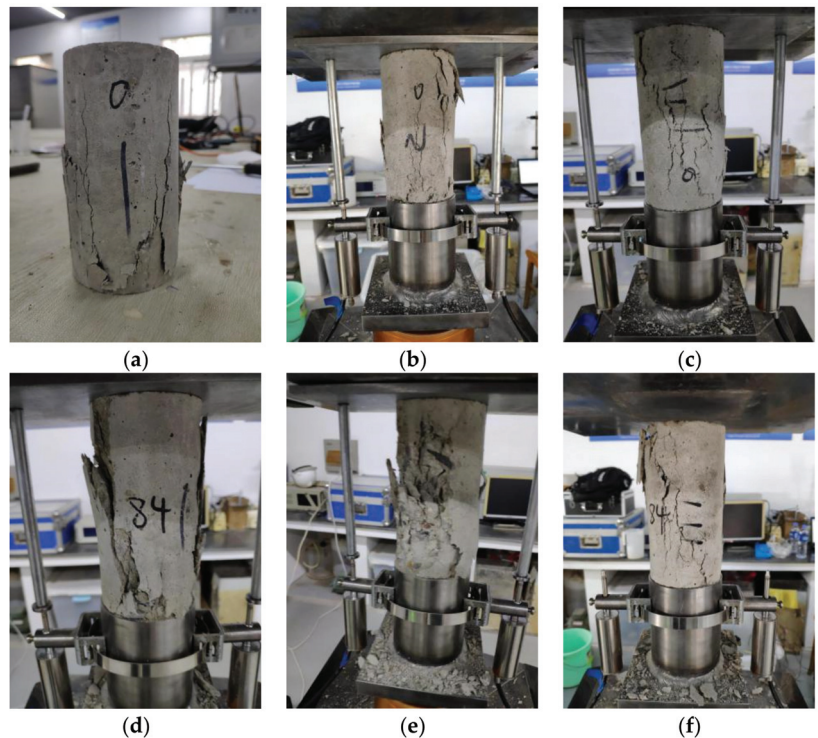


Figure 5. The failure pattern of RAC and NAC specimens. (a) NAC-0.0 mm; (b) RAC50-0.0 mm; (c) RAC100-0.0 mm; (d) NAC-19.8 mm; (e) RAC50-31.0 mm; and (f) RAC100-35.0 mm.

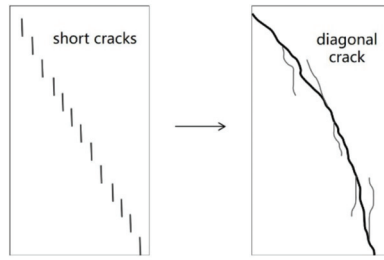


Figure 6. The development of the failure of carbonated RAC specimens.

In Figure 5f, the failure mode of RAC100-35.0 mm, which was fully carbonated, is similar to the findings in the literature [38]. Although the interior of the fully carbonated concrete has a high degree of compactness, a large number of original cracks inside RCA was responsible for the failure of carbonated RAC.

3.3. Uniaxial Compressive Stress–Strain Curves

The uniaxial compressive stress–strain curves of the specimens with different carbonation depths are shown in Figure 7. It is shown that the stress–strain curves of the specimens exhibit similar features, whereas the replacement rate of RCA and carbonation depth showed an obvious impact on the stress–strain relation of RAC.

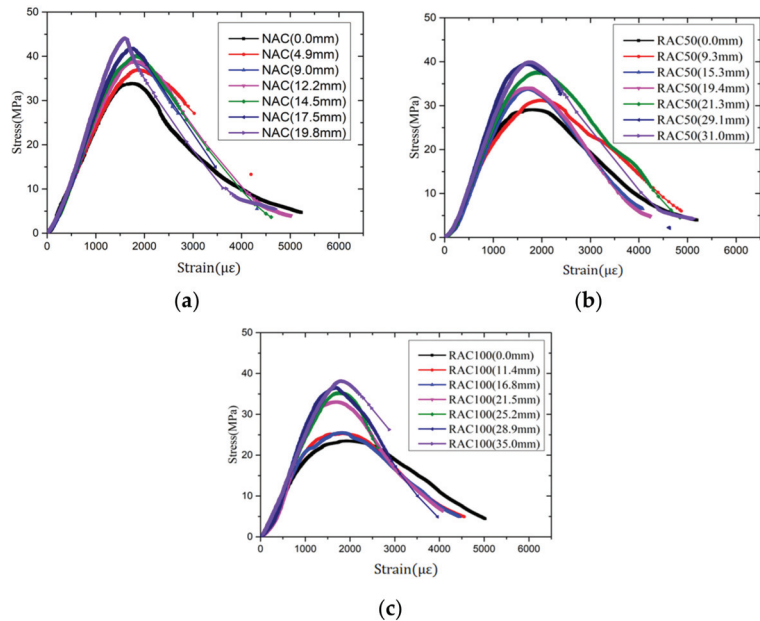


Figure 7. Uniaxial stress–strain curves of the specimens with different carbonation depth. (a) NAC; (b) RAC50; and (c) RAC100.

The peak stress and slope of the ascending part of the curve declined with the increase of the replacement rate of RCA, which conformed to findings from other researchers [29,38]. Furthermore, as carbonation depths increased, peak stress increased and both the ascending and descending part of the stress–strain curves became steeper. During a uniaxial compressive loading experiment, the highly carbonated specimens were more brittle.

3.3.1. Peak Stress

Figure 8 shows the relationship between peak stress and carbonation depth. The results show that the peak stress of NAC, RAC50, and RAC100 specimens increased with the increase of carbonation depth. This is caused by the reactions between CO₂ and hydration products of cement, such as Ca(OH)₂ and C-S-H, which can reduce the porosity of concrete [33,34,37–39]. The peak stress of the concrete was increased by reducing the porosity [40–42].

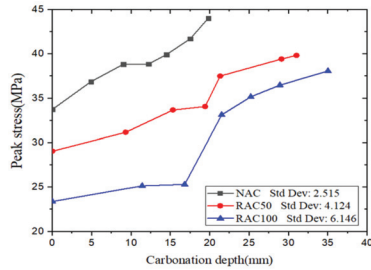


Figure 8. Peak stress versus carbonation depth.

When the carbonation depth reached about 20 mm, the peak stress of NAC, RAC50, and RAC100 specimens increased by about 30.5%, 17.6%, and 41.6%, respectively, compared with uncarbonated specimens. The result shows that the peak stress of NAC increased much more than that of RAC50 with the same carbonation depths. Moreover, the peak stress of fully carbonated RAC100 increased by about 62.8%; hence carbonation can increase the strength of RAC, which is consistent with findings by other researchers [24–26]. In Figure 8, it is found that the standard deviation values of the peak stress of RAC100 is higher than that of RAC50 and NAC, the peak stress has a clear jump from 16.8 to 21.5 mm of carbonation of RAC100. The reason may be due to the discreteness of RAC. Further experiments need to be performed in order to investigate the phenomenon.

3.3.2. Strain

The peak strain and ultimate strain of the specimens with different carbonation depths are shown in Figure 9. It shows that carbonation depth has no significant effect on the peak strain of all specimens. However, the ultimate strain of NAC and RAC100 decreased with the increase of carbonation depth.

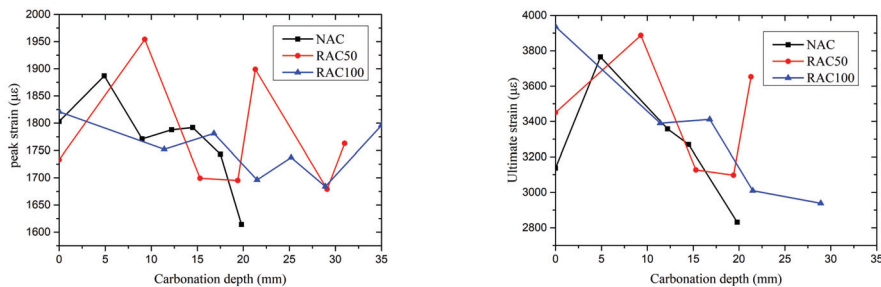


Figure 9. Peak strain and ultimate strain versus carbonation depth.

The ratio of the ultimate strain to peak strain (ϵ_u/ϵ_0) describes the trend of the descending part of stress–strain curves [43]. Figure 10 shows the relationship between the ratio of ultimate strain to peak strain and carbonation depth. The results show that the ratio of ultimate strain to peak strain of RAC50 is roughly larger than that of NAC. This means

the descending part of the stress–strain curve of RAC50 is flatter than that of NAC, and the results match with the descending part of stress–strain curves. Additionally, the ratios of ultimate strain to peak strain of NAC, RAC50, and RAC100 specimens decreased with the increase of carbonation depth. This means the descending part of the stress–strain curves of these specimens becomes steeper and steeper due to the carbonation. This is consistent with the rapid destruction of specimens after carbonation.

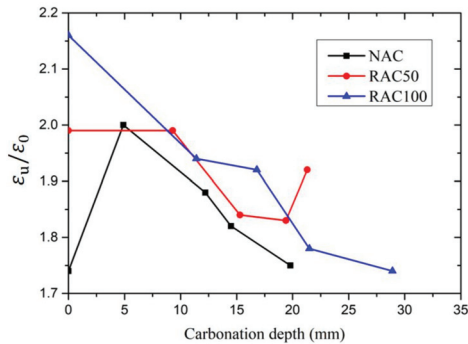


Figure 10. Ratio of ultimate strain to peak strain versus carbonation depth.

3.3.3. Elastic Modulus

Figure 11 shows the relationship between the elastic modulus and carbonation depth. It can be observed that the elastic modulus of RAC50 is significantly lower than that of NAC. The reasons are as follows. On the one hand, the decrease in the elastic modulus of RAC50 was attributed to the weak and porous recycled coarse aggregates [5,44]. On the other hand, the elastic modulus may decrease due to the cracks between old mortar and aggregates and the micro-cracks which occur in the process of the production of RCA [45].

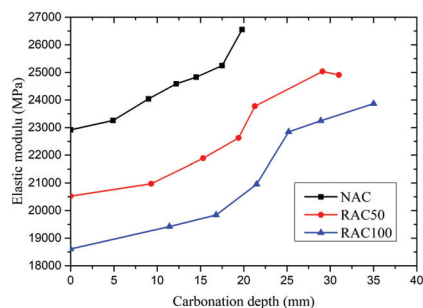


Figure 11. Elastic modulus versus carbonation depth.

Moreover, the elastic modulus of NAC, RAC50, and RAC100 specimens increased with the increase of carbonation depth. Oğuzhan Çopuroğlu [46] and Han Jian De [47] obtained similar results by using nanoindentation technology. Concrete specimens become denser with the increase of carbonation depth, which is due to the carbonation of concrete. In the carbonation, the chemical reaction between CO₂ entered in the concrete and Ca(OH)₂ in the cement produces insoluble CaCO₃, which deposits in the pores of concrete.

When the carbonation depth reached about 20 mm, the elastic modulus of NAC, RAC50, and RAC100 specimens increased by about 15.8%, 10.2%, and 12.6%, respectively, compared to uncarbonated specimens. The result shows that the elastic modulus of NAC is higher than that of RAC50 with the same carbonation depth. When the RAC100 is fully carbonated, its elastic modulus has increased by about 28.3%.

3.3.4. Relative Toughness

The area under the stress–strain curve can generally be considered as a measure of the toughness of materials [48]. However, researchers' definition of toughness is not universal. Wengui Li [41] and Sufen Dong [49] regarded the area under the stress–strain curve as toughness directly. Zemei Wu [50] and Jinyang Jiang [51] defined the relative toughness as the ratio of the area under the curve to that of the ascending portion before the peak stress.

To avoid misjudgment due to much higher peak stress after carbonation, the ratio of the area under the curve before 50% of peak stress at the descending part to that of before peak stress was defined as relative toughness in this study. Figure 12 shows the relationship between relative toughness and carbonation depth. The relative toughness of uncarbonated NAC is higher than that of RAC50. This may be due to the weak and porous RCA. The relative toughness of NAC, RAC50, and RAC100 specimens decreased overall with the increase of carbonation depth. When the carbonation depth reached about 20 mm, the relative toughness of NAC, RAC50, and RAC100 specimens decreased by about 14.6%, 7.1%, and 16.2%, respectively, compared with non-carbonated specimens. The results show that the relative toughness of NAC reduced faster than that of RAC50 with the increase of carbonation depth.

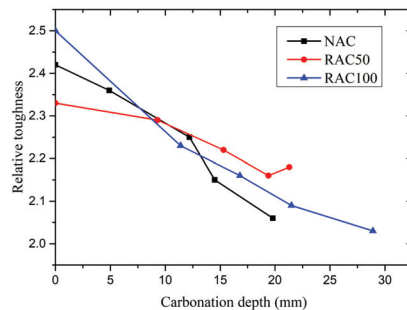


Figure 12. Relative toughness versus carbonation depth.

4. Stress–Strain Relation of Carbonated RAC and NAC

Xiao [29] and Wu [31] found that the analytical equations proposed by Guo [52] and adopted by the code for design of concrete structures (GB 50010-2002) in China to describe the complete stress–strain curve of NAC were also applicable to RAC. Hence, in this study, the equations are adopted to analyze the stress–strain relation of carbonated RAC and NAC are shown as follows:

$$y = \begin{cases} ax + (3 - 2a)x^2 + (a - 2)x^3, & x \leq 1 \\ \frac{x}{b(x-1)^2 + x}, & x \geq 1 \end{cases} \quad (3)$$

$$x = \frac{\varepsilon}{\varepsilon_c}, y = \frac{\sigma}{\sigma_c}$$

where a and b are parameters affecting the ascending and descending part of the curve, respectively; ε_0 is the peak strain; σ_0 is the peak stress.

The First Optimization software developed by 7D-Soft High Technology Inc. was used to find the optimum parameters of the ascending part and the descending part according to the test data based on Equation (3). Parameter a , b and corresponding correlation coefficients are shown in Table 4. The fitting results of the stress–strain relation are shown in Figure 13. The results show that the test values are in good agreement with the theoretical values and correlation coefficients are over 0.9. It is proven that Equation (3) is also applicable to carbonated RAC and NAC.

Table 4. Fitting results.

| Specimens | Coefficient a | Correlation Coefficient | Coefficient b | Correlation Coefficient |
|----------------|-----------------|-------------------------|-----------------|-------------------------|
| NAC-0.0 mm | 1.057 | 0.998 | 3.568 | 0.993 |
| NAC-4.9 mm | 0.871 | 0.999 | 1.835 | 0.960 |
| NAC-9.0 mm | 0.624 | 0.999 | 3.010 | 0.950 |
| NAC-12.2 mm | 0.653 | 0.999 | 3.432 | 0.947 |
| NAC-14.5 mm | 0.674 | 0.999 | 3.466 | 0.944 |
| NAC-17.5 mm | 0.473 | 0.999 | 3.648 | 0.999 |
| NAC-19.8 mm | 0.214 | 0.997 | 4.706 | 0.988 |
| RAC50-0 mm | 1.099 | 0.990 | 2.170 | 0.943 |
| RAC50-9.3mm | 1.213 | 0.997 | 2.284 | 0.943 |
| RAC50-15.3 mm | 0.540 | 0.998 | 2.813 | 0.950 |
| RAC50-19.4 mm | 0.766 | 0.996 | 3.065 | 0.931 |
| RAC50-21.3 mm | 0.926 | 0.996 | 2.554 | 0.911 |
| RAC50-29.1mm | 0.571 | 0.997 | 3.434 | 0.930 |
| RAC50-31.0 mm | 0.613 | 0.999 | 3.505 | 0.959 |
| RAC100-0 mm | 1.841 | 0.986 | 1.962 | 0.921 |
| RAC100-11.4 mm | 1.482 | 0.985 | 2.220 | 0.926 |
| RAC100-16.8 mm | 1.551 | 0.988 | 2.445 | 0.945 |
| RAC100-21.5 mm | 0.636 | 0.986 | 3.104 | 0.972 |
| RAC100-25.2 mm | 0.636 | 0.999 | 3.032 | 0.957 |
| RAC100-28.9 mm | 0.558 | 0.995 | 3.193 | 0.944 |
| RAC100-35.0 mm | 0.705 | 0.999 | 2.005 | 0.999 |

Parameter a represents the relative slope of the ascending part of the curve, and a smaller value means a flatter ascending part [50]. Parameter a of uncarbonated NAC and RAC50 are similar, whereas that of RAC100 is nearly 70% higher than them. This potentially indicates that parameter a depends on the compressive strength more than the replacement rate of RCA. Besides, parameter a generally shows a downward trend with the increases in the carbonation depth. This means carbonation increased the relative flatness of the ascending part of stress–strain curves.

Parameter b presents the relative slope of the descending part of the curve. A bigger b value means a steeper descending part of the curve and therefore poorer toughness performance [51]. It can be clearly observed that parameter b increases with the increase of carbonation depth, meaning that carbonation increased the relative steepness of the descending part of stress–strain curves.

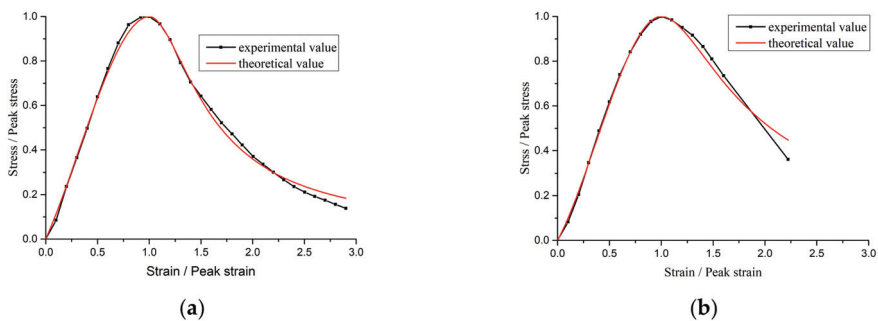
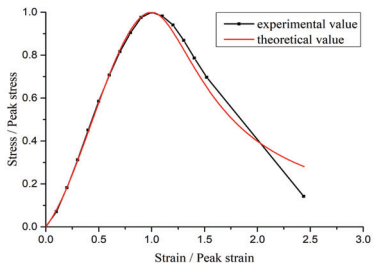
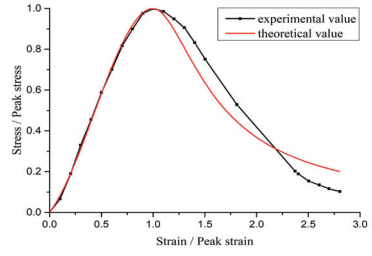


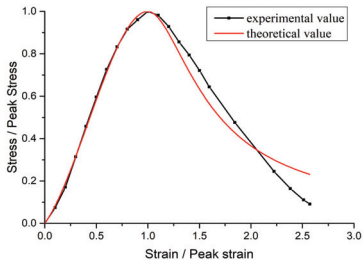
Figure 13. Cont.



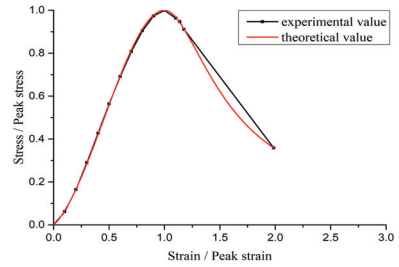
(c)



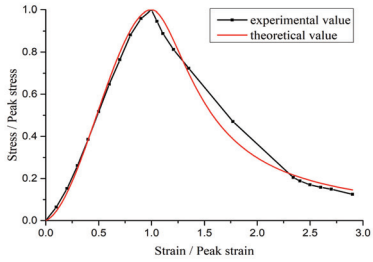
(d)



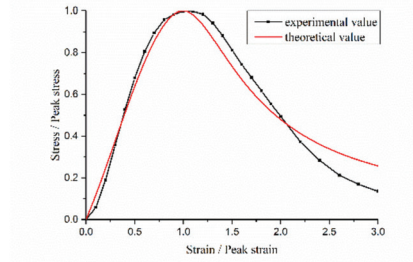
(e)



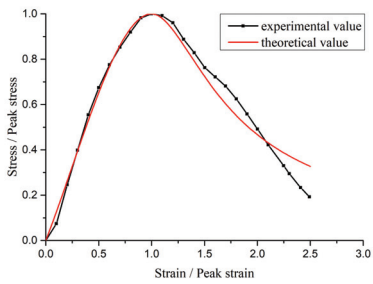
(f)



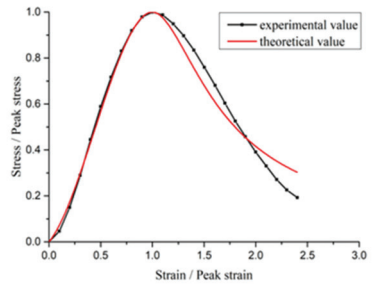
(g)



(h)

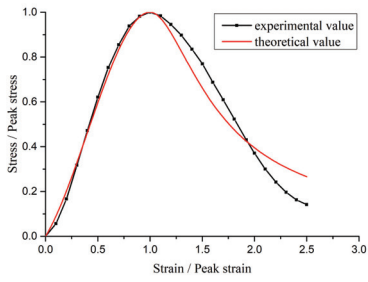


(i)

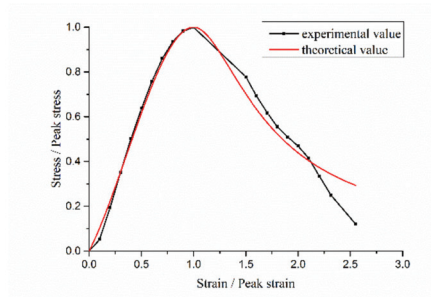


(j)

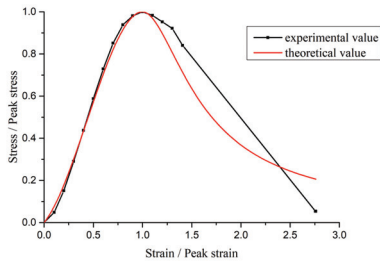
Figure 13. Cont.



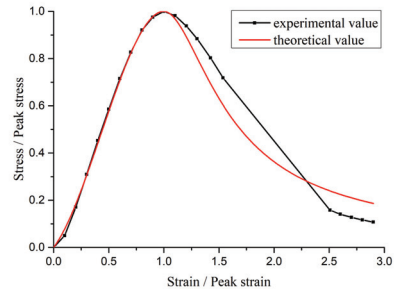
(k)



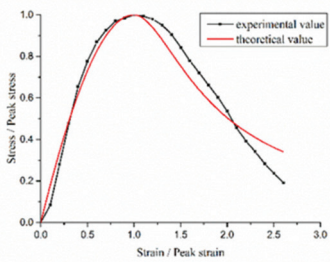
(l)



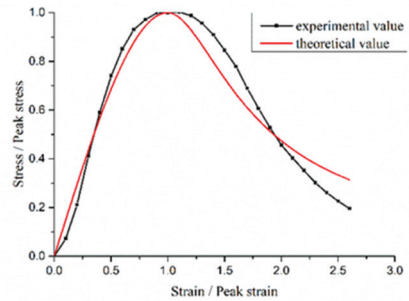
(m)



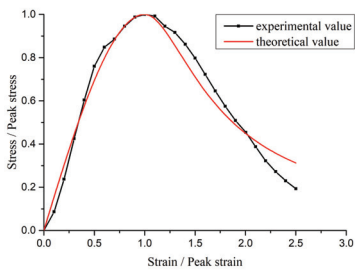
(n)



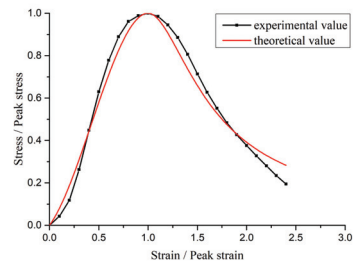
(o)



(p)



(q)



(r)

Figure 13. Cont.

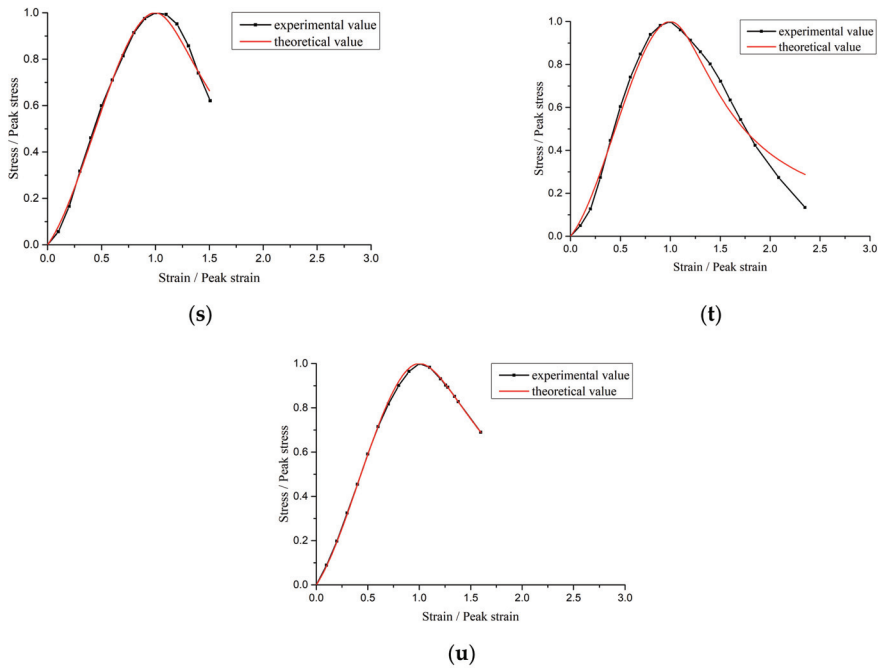


Figure 13. The fitting results of stress–strain relation. (a) NAC-0.0 mm; (b) NAC-4.9 mm; (c) NAC-9.0 mm; (d) NAC-12.2 mm; (e) NAC-14.5 mm; (f) NAC-17.5 mm; (g) NAC-19.8 mm; (h) RAC50-0.0 mm; (i) RAC50-9.3 mm; (j) RAC50-15.3 mm; (k) RAC50-19.4 mm; (l) RAC50-21.3 mm; (m) RAC50-29.1 mm; (n) RAC50-31.0 mm; (o) RAC100-0.0 mm; (p) RAC100-11.4 mm; (q) RAC100-16.8 mm; (r) RAC100-21.5 mm; (s) RAC100-25.2 mm; (t) RAC100-28.9 mm; and (u) RAC100-35.0 mm.

In addition, the correlation coefficients of NAC are higher than those of RAC50 and RAC100, which may be due to the discreteness of RAC [28].

The research results show that low strength of interfacial transition zone is the main factor of the size effect of concrete. Consequently, the size effect on the strength of recycled aggregate concrete becomes obvious because the strength of interfacial transition zone of recycled aggregate concrete is lower than that of ordinary concrete [53]. The compressive stress–strain model of recycled coarse aggregate concrete in this study is mainly used in the finite element method (FEM) analysis of concrete structure. The element size in the concrete structure analysis is small, so the size effect on strength and brittleness will be small. Therefore, the experimental results in Figure 13 will be directly applied to FEM analysis of concrete structure in the engineering practice.

5. Summary

In this study, the uniaxial compressive behavior of RAC with different carbonation depths was experimentally investigated, and the effects of carbonation depths on NAC and RAC were compared by experimental results. The main results are summarized as follows.

- (1) During the accelerated carbonation, the values of the carbonation depth of RAC increases as the replacement ratio of recycled coarse aggregate increases. At 84 days, RAC100 was fully carbonated and the carbonation depth was 35.0 mm, whereas that of RAC50 and NAC were 31.0 and 19.2 mm, respectively.
- (2) The peak stress and elastic modulus of RAC and NAC specimens increased with the increase of carbonation depth, and the peak stress of fully carbonated RAC100 increased by about 62.8% and elastic modulus has increased by about 28.3%. The ratio

of ultimate strain to peak strain and relative toughness of RAC and NAC specimens decreased overall with the increase of carbonation depth. When the carbonation depth reached about 20 mm, the relative toughness of RAC50 and RAC100 specimens decreased by about 7.1% and 16.2%, respectively, compared with non-carbonated specimens.

- (3) Stress–strain models of recycled aggregate concrete with different carbonation depths were established, and the experimental values are in good agreement with the theoretical values and correlation coefficients are over 0.9. Carbonation decreased the relative slope of the ascending part and increased the relative steepness of the descending part of stress–strain curves of recycled aggregate concrete.

Author Contributions: Conceptualization, J.W.; Data curation, H.D.; Formal analysis, K.T.; Investigation, K.T. and H.D.; Methodology, Y.W.; Resources, K.T., J.W., Y.W. and R.Z.; Supervision, J.W.; Validation, H.D.; Visualization, H.D.; Writing—original draft, H.D.; Writing—review & editing, H.D. All authors have read and agreed to the published version of the manuscript.

Funding: This research was funded by the subproject of the 13th Five-Year Plan National Key R&D Plan: Study on recycled aggregate concrete for construction waste and preparation of composite wall panel (2018YFD1101001-2), 2018–2022.

Acknowledgments: This work was supported by the subproject of the 13th Five-Year Plan National Key R&D Plan: Study on recycled aggregate concrete for construction waste and preparation of composite wall panel (2018YFD1101001-2), 2018–2022.

Conflicts of Interest: The authors declare no conflict of interest.

References

1. Vieira, C.S.; Pereira, P.M. Use of recycled construction and demolition materials in geotechnical applications: A review. *Resour. Conserv. Recycl.* **2015**, *103*, 192–204. [[CrossRef](#)]
2. Zhang, J.H.; Ding, L.; Li, F.; Peng, J.H. Recycled aggregates from construction and demolition wastes as alternative filling materials for highway subgrades in China. *J. Clean. Prod.* **2020**, *225*, 120–223. [[CrossRef](#)]
3. Fonseca, N.; de Brito, J.; Evangelista, L. The influence of curing conditions on the mechanical performance of concrete made with recycled concrete waste. *Cem. Concr. Compos.* **2011**, *33*, 637–643. [[CrossRef](#)]
4. Rao, M.C.; Bhattacharyya, S.K.; Barai, S.V. Influence of field recycled coarse aggregate on properties of concrete. *Mater. Struct.* **2011**, *44*, 205–220. [[CrossRef](#)]
5. Xiao, J.Z.; Li, W.G.; Fan, Y.H.; Huang, X. An overview of study on recycled aggregate concrete in China (1996–2011). *Constr. Build. Mater.* **2012**, *31*, 364–383. [[CrossRef](#)]
6. Lima, C.; Caggiano, A.; Faella, C.; Martinelli, E.; Pepe, M.; Realfonzo, R. Physical properties and mechanical behaviour of concrete made with recycled aggregates and fly ash. *Constr. Build. Mater.* **2013**, *47*, 547–559. [[CrossRef](#)]
7. Kou, S.C.; Poon, C.S. Enhancing the durability properties of concrete prepared with coarse recycled aggregate. *Constr. Build. Mater.* **2012**, *35*, 69–76. [[CrossRef](#)]
8. Topc, L.B.; Sengel, S. Properties of concretes produced with waste concrete aggregate. *Cem. Concr. Res.* **2004**, *34*, 1307–1312. [[CrossRef](#)]
9. Azevedo, A.R.G.; Cecchin, D.; Carmo, D.F.; Silva, F.; Campos, C.; Shtrucka, T.; Marvila, M.; Monteiro, S. Analysis of the compactness and properties of the hardened state of mortars with recycling of construction and demolition waste (CDW). *J. Mater. Res. Technol.* **2020**, *9*, 5942–5952. [[CrossRef](#)]
10. Barbudo, A.; Agrela, F.; Ayuso, J.; Jiménez, J.R.; Poon, C.S. Statistical analysis of recycled aggregates derived from different sources for sub-base applications. *Constr. Build. Mater.* **2012**, *28*, 28–129. [[CrossRef](#)]
11. Tam, V.W.Y.; Gao, X.F.; Tam, C.M. Microstructural analysis of recycled aggregate concrete produced from two-stage mixing approach. *Cem. Concr. Res.* **2005**, *35*, 1195–1203. [[CrossRef](#)]
12. Sagoe-Crentsil, K.K.; Brown, T.; Taylor, A.H. Performance of concrete made with commercially produced coarse recycled concrete aggregate. *Cem. Concr. Res.* **2001**, *31*, 707–712. [[CrossRef](#)]
13. Cui, Z.L.; Yang, L.H.; Ohaga, Y. Durability test investigation on the recycled aggregate concrete. *Bull. Chin. Ceram. Soc.* **2007**, *26*, 1107–1111. [[CrossRef](#)]
14. Zeng, X.C. Progress in the research of carbonation resistance of RAC. *Constr. Build. Mater.* **2020**, *230*, 116976. [[CrossRef](#)]
15. Lu, W.S.; Tam, V.W.Y. Construction waste management policies and their effectiveness in Hong Kong: A longitudinal review. *Renew. Sustain. Energy Rev.* **2013**, *23*, 214–223. [[CrossRef](#)]
16. Omrane, M.; Kenai, S.; Kadri, E.H.; Abdelkarim, A.M. Performance and durability of self compacting concrete using recycled concrete aggregates and natural pozzolan. *J. Clean. Prod.* **2017**, *165*, 415–430. [[CrossRef](#)]

17. Xie, J.H.; Fang, C.; Lu, Z.H.; Li, Z.J.; Li, L.J. Effects of the addition of silica fume and rubber particles on the compressive behaviour of recycled aggregate concrete with steel fibres. *J. Clean. Prod.* **2018**, *197*, 656–667. [[CrossRef](#)]
18. Ahmed, T.W.; Mohammed Ali, A.A.; Zidan, R.S. Properties of high strength polypropylene fiber concrete containing recycled aggregate. *Constr. Build. Mater.* **2020**, *241*, 118010. [[CrossRef](#)]
19. Hanumesh, B.M.; Harish, B.A.; Ramana, N.V. Influence of Polypropylene Fibres on Recycled Aggregate Concrete. *Mater. Today Proc.* **2018**, *5*, 1147–1155. [[CrossRef](#)]
20. Zhu, Y.G.; Kou, S.C.; Poon, C.S.; Dai, J.G.; Li, Q.Y. Influence of silane-based water repellent on the durability properties of recycled aggregate concrete. *Cem. Concr. Compos.* **2013**, *35*, 32–38. [[CrossRef](#)]
21. Vivian, W.Y.; Tam, A.B.; Khoa, N.L.; Li, W.G. Utilising CO₂ technologies for recycled aggregate concrete: A critical review. *Constr. Build. Mater.* **2020**, *250*, 118903. [[CrossRef](#)]
22. Zhang, J.K.; Shi, C.J.; Li, Y.K.; Pan, X.Y.; Poon, C.S.; Xie, Z.B. Influence of carbonated recycled concrete aggregate on properties of cement mortar. *Constr. Build. Mater.* **2015**, *98*, 1–7. [[CrossRef](#)]
23. Zhan, B.J.; Poon, C.S.; Liu, Q.; Kou, S.; Shi, C.J. Experimental study on CO₂ curing for enhancement of recycled aggregate properties. *Constr. Build. Mater.* **2014**, *67*, 3–7. [[CrossRef](#)]
24. Zhan, B.J.; Poon, C.; Shi, C.J. CO₂ curing for improving the properties of concrete blocks containing recycled aggregates. *Cem. Concr. Compos.* **2013**, *42*, 1–8. [[CrossRef](#)]
25. Zhan, B.J.; Xuan, D.X.; Poon, C.S.; Shi, C.J. Effect of curing parameters on CO₂ curing of concrete blocks containing recycled aggregates. *Cem. Concr. Compos.* **2016**, *71*, 122–130. [[CrossRef](#)]
26. Xuan, D.X.; Zhan, B.J.; Poon, C.S. A maturity approach to estimate compressive strength development of CO₂-cured concrete blocks. *Cem. Concr. Compos.* **2018**, *85*, 153–160. [[CrossRef](#)]
27. Xiao, J.Z.; Zhang, K.J.; Akbarnezhad, A. Variability of stress-strain relationship for recycled aggregate concrete under uniaxial compression loading. *J. Clean. Prod.* **2018**, *181*, 753–771. [[CrossRef](#)]
28. Bairagi, N.K.; Ravande, K.; Pareek, V.K. Behaviour of concrete with different proportions of natural and recycled aggregates. *Resour. Conserv. Recycl.* **1993**, *9*, 109–126. [[CrossRef](#)]
29. Xiao, J.Z.; Li, J.B.; Zhang, C. Mechanical properties of recycled aggregate concrete under uniaxial loading. *Cem. Concr. Res.* **2005**, *35*, 1187–1194. [[CrossRef](#)]
30. Xiao, J.Z.; Du, J.T. Complete stress-strain curve of concrete with different recycled coarse aggregates under uniaxial compression. *J. Build. Mater.* **2008**, *11*, 111–115. (In Chinese)
31. Wu, J.; Jing, X.H.; Wang, Z. Uni-axial compressive stress-strain relation of recycled coarse aggregate concrete after freezing and thawing cycles. *Constr. Build. Mater.* **2017**, *134*, 210–219. [[CrossRef](#)]
32. Luo, S.; Ye, S.C.; Xiao, J.Z.; Zheng, J.L.; Zhu, Y.T. Carbonated recycled coarse aggregate and uniaxial compressive stress-strain relation of recycled aggregate concrete. *Constr. Build. Mater.* **2018**, *188*, 956–965. [[CrossRef](#)]
33. Sormeh, K.H.; Shao, Y.X.; Ghoshal, S. Mathematical modeling of CO₂ uptake by concrete during accelerated carbonation curing. *Cem. Concr. Res.* **2015**, *67*, 1–10. [[CrossRef](#)]
34. Lee, H.S.; Wang, X.Y. Evaluation of compressive strength development and carbonation depth of high volume slag-blended concrete. *Constr. Build. Mater.* **2016**, *124*, 45–54. [[CrossRef](#)]
35. Thomas, C.; Setién, J.; Polanco, J.A.; Alaejos, P.; Sánchez de Juan, M. Durability of recycled aggregate concrete. *Constr. Build. Mater.* **2013**, *40*, 1054–1065. [[CrossRef](#)]
36. Bravo, M.; Brito, J.D.; Pontes, J.; Evangelista, L. Durability performance of concrete with recycled aggregates from construction and demolition waste plants. *Constr. Build. Mater.* **2015**, *77*, 357–369. [[CrossRef](#)]
37. Yang, H.F.; Deng, Z.H.; Li, X.L. Microscopic mechanism study on carbonation resistance of recycled aggregate concrete. *Adv. Mater. Res.* **2011**, *194–196*, 1001–1006. [[CrossRef](#)]
38. Chen, T.W.; Wu, J.; Dong, G.Q. Mechanical properties and uniaxial compression stress-strain relation of recycled coarse aggregate concrete after carbonation. *Materials* **2021**, *14*, 2215. [[CrossRef](#)]
39. Morandea, A.; Thiéry, M.; Dangla, P. Investigation of the carbonation mechanism of CH and C-S-H in terms of kinetics, microstructure changes and moisture properties. *Cem. Concr. Res.* **2014**, *56*, 153–170. [[CrossRef](#)]
40. Della, M.R.; George, R.G. Porosity-Strength Relation in Cementitious Materials with Very High Strengths. *J. Am. Ceram. Soc.* **1973**, *56*, 549–550. [[CrossRef](#)]
41. Powers, T.C. Structure and Physical Properties of Hardened Portland Cement Paste. *J. Am. Ceram. Soc.* **1958**, *41*, 1–6. [[CrossRef](#)]
42. Khan, M.I.; Lynsdale, C.J.; Waldron, P. Porosity and strength of PFA/SF/OPC ternary blended paste. *Cem. Concr. Res.* **2000**, *30*, 1225–1229. [[CrossRef](#)]
43. Li, L.; Poon, C.S.; Xiao, J.Z.; Xuan, D.X. Effect of carbonated recycled coarse aggregate on the dynamic compressive behavior of recycled aggregate concrete. *Constr. Build. Mater.* **2017**, *151*, 52–62. [[CrossRef](#)]
44. Xiao, J.Z.; Li, W.G.; Sun, Z.H.; David, A.; Lange, S.P.S. Properties of interfacial transition zones in recycled aggregate concrete tested by nanoindentation. *Cem. Concr. Compos.* **2013**, *37*, 276–292. [[CrossRef](#)]
45. Shaikh, F.U.A. Mechanical and durability properties of fly ash geopolymer concrete containing recycled coarse aggregates. *Int. J. Sustain. Built Environ.* **2016**, *5*, 277–287. [[CrossRef](#)]
46. Çopuroğlu, O.; Schlangen, E. Modeling of frost salt scaling. *Cem. Concr. Res.* **2008**, *38*, 27–39. [[CrossRef](#)]

47. De Han, J.; Pan, G.H.; Sun, W.; Wang, C.H.; Cui, D. Application of nanoindentation to investigate chemomechanical properties change of cement paste in the carbonation reaction. *Sci. China Technol. Sci.* **2012**, *55*, 616–622. [[CrossRef](#)]
48. Zhao, S.J.; Fan, J.J.; Sun, W. Utilization of iron ore tailings as fine aggregate in ultra-high performance concrete. *Constr. Build. Mater.* **2014**, *50*, 540–548. [[CrossRef](#)]
49. Dong, S.F.; Han, B.G.; Yu, X.; Ou, J.P. Dynamic impact behaviors and constitutive model of super-fine stainless wire reinforced reactive powder concrete. *Constr. Build. Mater.* **2018**, *184*, 602–616. [[CrossRef](#)]
50. Wu, Z.M.; Shi, C.J.; He, W.; Wang, D.H. Uniaxial compression behavior of ultra-high performance concrete with hybrid steel fiber. *J. Mater. Civ. Eng.* **2016**, *28*, 06016017. [[CrossRef](#)]
51. Jiang, J.Y.; Feng, T.T.; Chu, H.Y.; Wu, Y.R.; Wang, F.J.; Zhou, W.J.; Wang, Z.F. Quasi-static and dynamic mechanical properties of eco-friendly ultra-high-performance concrete containing aeolian sand. *Cem. Concr. Compos.* **2019**, *97*, 369–378. [[CrossRef](#)]
52. Guo, Z. *Strength and Constitutive Relations of Concrete—Principle and Application*; China Construction Industry Press: Beijing, China, 2004; pp. 42–44. (In Chinese)
53. Bai, L.L. *Experimental Study on Compressive Strength and Microscopic Properties of Recycled Concrete with Reinforced Coarse Aggregate*; Xi'an University of Architecture and Technology: Xi'an, China, 2019; pp. 58–59. (In Chinese)

Article

Evaluation of Performance of Polyacrylamide-Modified Compacted Clay as a Gas Barrier: Water Retention and Gas Permeability and Diffusion Characteristics

Yu-Zhang Bi ^{1,†}, Jia-Ming Wen ^{1,2,†}, Hao-Liang Wu ³ and Yan-Jun Du ^{1,*}

¹ Jiangsu Key Laboratory of Urban Underground Engineering & Environmental Safety, Institute of Geotechnical Engineering, Southeast University, Nanjing 210096, China

² Zijin (Changsha) Engineering Technology Co., Ltd., Changsha 410006, China

³ School of Civil Engineering, Sun Yat-sen University, Guangzhou 510275, China

* Correspondence: duyanjun@seu.edu.cn

† These authors contributed equally to this work.

Abstract: In this paper, the performance of a gas barrier that consisted of polyacrylamide (PAM)-modified compacted clayey soil was experimentally explored. The moisture content and water loss characteristics of the tested soils were adopted as indicative indices of water retention capacity (WRC). The gas permeability (K_p) and gas diffusion coefficient (D_p) of the modified compacted clays were evaluated via gas permeability and gas diffusion tests. The test results showed that the moisture content of the modified compacted clay samples subjected to drying tests increased with increasing polyacrylamide content. K_p and D_p decreased with increasing PAM content. Compared with 0.2% PAM content, the K_p of the sample with 1.0% PAM was reduced by ten times, and the D_p was reduced to ~35%. Compared to the unmodified clay, the liquid limit of the PAM-modified clay increased by 45~55%. Comparison of the liquid limit tests between this study and previous studies revealed that the liquid limit ratio of the zwitterionic polyacrylamide (ZP)-modified soil was much higher than the other material-modified soils. The results of this study are useful to facilitate the application of modified compacted clays as gas barrier materials at industrial contaminated sites.

Keywords: compacted clay; polyacrylamide; gas barrier performance; gas permeability; gas diffusion coefficient

Citation: Bi, Y.-Z.; Wen, J.-M.; Wu, H.-L.; Du, Y.-J. Evaluation of Performance of Polyacrylamide-Modified Compacted Clay as a Gas Barrier: Water Retention and Gas Permeability and Diffusion Characteristics. *Appl. Sci.* **2022**, *12*, 8379. <https://doi.org/10.3390/app12168379>

Academic Editors: Carlos Morón Fernández and Daniel Ferrández Vega

Received: 2 May 2022

Accepted: 9 June 2022

Published: 22 August 2022

Publisher's Note: MDPI stays neutral with regard to jurisdictional claims in published maps and institutional affiliations.



Copyright: © 2022 by the authors. Licensee MDPI, Basel, Switzerland. This article is an open access article distributed under the terms and conditions of the Creative Commons Attribution (CC BY) license (<https://creativecommons.org/licenses/by/4.0/>).

1. Introduction

The compacted clay cover (CCC), as one of the main horizontal barriers, is widely applied in industrial organics contaminated sites to effectively control upward migration of volatile organic compound (VOC) and semi-volatile organic compound (SVOC) vapors or gases [1]. Studies reveal that gas migration through the CCC in landfills is predominated by diffusion [2]. Diffusion of VOC and SVOC gases through CCC may lead to the emission of toluene gas in landfills, migrating from pollution sources in deep soil to the air [3]. Upward migration of gas in clay occurs via advection [4] and diffusion [5]. Diffusion is the primary mechanism of VOC and SVOC gas migration in clayey soils on most occasions [6,7]. Advection can affect the migration of VOC or SVOC gas only when the temperature and vapor pressure in clays are relatively high, e.g., during the summer season [8,9]. In real projects, the CCC stays unsaturated on most occasions, except for relatively heavy rainfall infiltration. There are three indicators that quantify gas advection in clays when air pressure is high, gas permeability, air-water relative permeability, and moisture content [10]. A critical step in evaluating a CCC's performance against VOCs or SVOCs is to measure the permeation and diffusion of gas while they change with the moisture contents of CCC.

The influence of moisture content in clay is significant for gas migration. In recent years, a geosynthetic clay liner (GCL) has been extensively used as the VOC/SVOC gas

barrier in contaminated sites. However, the bentonite in GCL is usually sodium-activated calcium bentonite in China, and the barrier performance is not as good as sodium bentonite GCL. This is because the high-quality sodium bentonite resources in China are scarce. Previous studies [11,12] found that the gas permeability of the sodium bentonite GCL decreased with increasing moisture content under different pressures. Studies have shown that the gas permeability changes after hydration from 1.0×10^{-18} to 1.0×10^{-11} m² [13–15]. After drying, the gas permeability of the GCL can range between 0.03 and 0.21 m² [16]. The VOC/SVOC gas migration from contaminated soil through GCL into the air is mainly controlled by pressure and concentration gradients. The advection governs gas flow caused by differential pressures, and the gas advection indicator is reflected by the gas permeability [17]. Gas migration due to a concentration gradient is controlled by the gas diffusion coefficient [18]. Rouf et al. [19] demonstrated that when the apparent degree of saturation (ADOS) of the sodium bentonite GCL increased greater than approximately 65%, both the gas diffusion coefficient and gas permeability of the GCL were considerably reduced. The ADOS is defined as the gravimetric water content (w) of a GCL at a given time, divided by the maximum gravimetric water content (w_{ref}) that the same GCL reaches during hydration under the same applied stress conditions [19]. It can be anticipated that the gas diffusion and gas permeability of CCC increase significantly with the decrease in both gravimetric water content and ADOS [20]. Extremely low moisture content will lead to VOC gas migration into clay by diffusion and advection more easily, thus impairing the CCC gas barrier efficacy. Low moisture contents in compacted clay can cause fissures due to water loss [21]. Ultimately, a crack network may develop from the fissures, becoming the preferential and dominant pathway for the upward advection of VOC or SVOC gas released from the unsaturated contaminated soils. Through laboratory tests, Drumm et al. [22] found that the hydraulic conductivity near soil cracks increased sharply as compared to intact soil that is not intact, confirming the existence of dominant flow paths after the soil cracked.

Adopting modified materials in CCC is one potential approach to suppress cracking caused by water loss and improve the gas barrier performance. Super absorbent polymers (SAP) are a type of polymers with strong water-absorbing capability, composed of many hydrophilic functional groups, such as carbonyls, hydroxyls, and quaternary ammonium salts. One of the most commonly used SAPs is polyacrylamide (PAM), which is usually adopted as a water retention agent in agriculture, due to its long-term water retention capabilities [23,24]. Studies [25–27] have shown that polymers are adsorbed on the surface of soil particles through physicochemical reactions. A polymer is one of the promising materials recently applied to soil stabilization. It has a long chain of monomers connected to each other by sufficiently strong and flexible Van der Waals forces. The polymer can encapsulate the soil particles and connect them through polymer chain expansion, thereby improving the soil's water retention capacity (WRC). As a result, the hydraulic properties, erosion resistance, and gas impermeability of the modified soils can be improved. Qi et al. [28] researched the dried cracking of clay modified by PAM through a constant temperature evaporation test and image processing technology. They found that PAM is effective in mitigating soil cracking and even inhibiting crack formation. In addition, Yu et al. [29] conducted column tests to compare the cracking of the GCL before and after PAM modification at different temperatures. They demonstrated that the number of GCL cracks decreased after PAM modification at 40 °C. Therefore, using PAM to modify the CCC is promising, as it may improve the WRC and enhance the gas barrier performance. Nevertheless, previous studies mainly focused on polymer-modified clay's WRC and hydraulic properties. The barrier performance of GCLs/CCCs containing VOC/SVOC gases should be evaluated not only by gas permeability and WRC, but also by the gas diffusion coefficient.

The primary purpose of this study was to investigate the gas barrier performance of PAM-modified CCCs. A series of laboratory tests were conducted, which included liquid limit, water retention, gas permeability, and gas diffusion tests. The results are

useful in facilitating CCC design and its application as gas barriers in VOC and SVOC contaminated sites.

2. Materials and Methods

2.1. In-Site Clay

Sampling the in situ CCCs was based on ASTM D3441 [30], The *Geotechnical Engineering Investigation Handbook* [31] and other references [32,33]. The specific sampling procedure was displayed in the authors' previous study [18]. A total of 40 sampling points were set up. Sampling depth was one-half of the CCC thickness. The GXY-1 engineering driller was adopted for rotary drilling sampling. The methods of the drilling operation were employed as per the *Geotechnical Engineering Investigation Handbook* [34], Standard practice for Classification of Soils for Engineering Purposes [35], and Geotechnical design, Part 2: Ground investigation and testing [36]. Samples should be wrapped in an impermeable material (plastic sealing bag) and stored in a shockproof box (filled with foam buffer) to prevent transport disturbance. The soil's fundamental physical properties were tested based on the standards of GB/T 50145–2007 [37] and ASTM D2487 [38]. Test results were shown in Table 1. Figure 1 is the plasticity chart to identify the soil classification. As the organic content of the CCC sample is only 4.2%, the soil of the contaminated site can be classified as clay with low LL, based on Figure 1 and ASTM D2487.

Table 1. Basic physical indicators of the clay used in the test.

| Parameters | Number of Samples | Mean | Test Method |
|----------------------------------|-------------------|-------|--------------------|
| Natural moisture content (%) | 40 | 22.5 | ASTM D2216 [31,39] |
| Specific gravity, G_s | 40 | 2.72 | ASTM D854 [40] |
| Liquid limit, LL (%) | 40 | 38.14 | ASTM D4318 [41] |
| Plastic limit, PI (%) | 40 | 14.90 | ASTM D4318 [41] |
| Optimal moisture content (%) | 6 | 25.6 | ASTM D7382 [42] |
| Maximum dry density (g/cm^3) | 6 | 1.78 | ASTM D4253 [43] |
| Organic content, C_{oc} (%) | 6 | 4.2 | ASTM D2974 [44] |

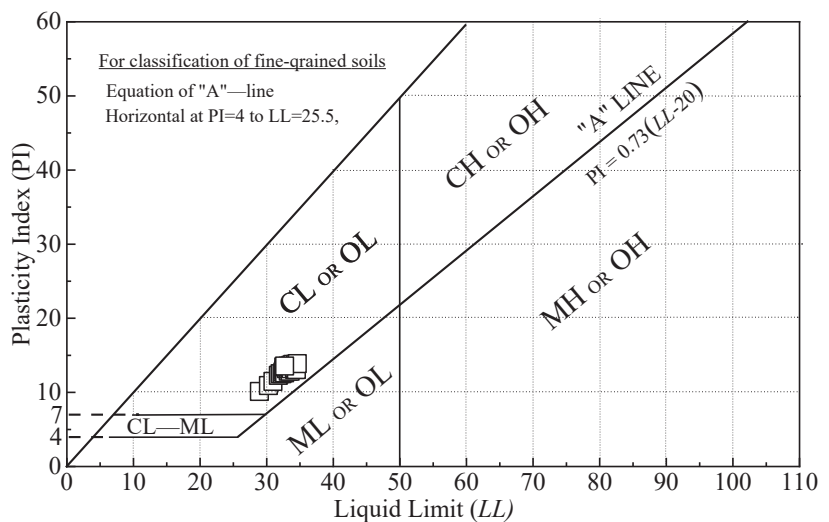


Figure 1. Plasticity chart for classification of fine-grained soils.

2.2. Polyacrylamide

There are four kinds of PAM in the market, cationic PAM (CP), anionic PAM (AP), nonionic PAM (NP), and zwitterion PAM (ZP). According to the authors' preliminary test

results (see Supplementary Materials), the zwitterionic PAM worked best in inhibiting the cracking of CCCs. The modified clay had a much lower gas permeability (K_p) and gas diffusion coefficient (D_p) with good gas barrier performance than that modified by cationic, anionic, and nonionic polyacrylamide. Hence, zwitterionic polyacrylamide was selected as the tested modifier in this research, which was provided by Henan Zhengzhou Lvjie Environmental Protection Material Co., Ltd. (Zhengzhou, China), with a molecular weight of 12 million and solid content no less than 90%. The parameters of PAM were shown in Table 2.

Table 2. Testing program and parameters of this study.

| Testing Parameters | Values |
|----------------------|---|
| Polymer type | Zwitterionic polyacrylamide (ZP) |
| Molecular weight | 12 million |
| Admixture amount (%) | 0, 0.2, 0.4, 0.6, 0.8, 1.0 |
| Drying time (h) | 0, 3.5, 7, 10.5, 14, 17.5 |
| Testing program | Moisture content, water loss, gas permeability, gas diffusion, liquid limit |

2.3. CCC Sample Preparation

The compacted clay samples were prepared according to the w_{opt} and ρ_{dmax} of the clay materials. The soil can reach the maximum degree of compaction only when it satisfies the w_{opt} and ρ_{dmax} . This is because Ralph R. Proctor proposed a compaction test, where a soil sample is compacted by means of a set of blows of a hammer per lift, which prove that the maximum dry density (ρ_{dmax}) of soil is related to certain moisture, called the optimum moisture content (w_{opt}) [45]. The soil samples with the size of 61.8×20 mm were prepared by the static compression method. The dry density and moisture content of all the compacted clay samples were 1.78 and 25.6%, respectively. The moisture content was in accordance with the optimum water content (w_{opt}).

The degree of compaction was designed based on the authors' previous study [46], which proved that compacted clays with 90% degree of compaction had superior gas barrier performance than those with lower degrees of compaction. The specific ZP-modified compacted samples were prepared as follows: (1) thoroughly mix the air-dried in-situ soils with a certain amount of ZP powder. The ZP dosage is shown in Table 2 (2) distilled water was added until the moisture content reached 25.6%, and the soil–water mixture was thoroughly stirred using a glass rod until uniform; (3) the above soil–water mixture was added into a rigid mold with a size of 61.8×20 mm, and it was statically compacted using a hydraulic jack to the designed degree of compaction of 90%; (4) CCC samples were sealed with plastic bags and cured in the curing room for 14 days until the samples reached the moisture balance.

The CCC samples used in the gas permeability and gas diffusion tests were prepared with the same method with that used in the WRC tests samples. It is noted that the samples were subjected to drying at various times of 0 h, 3.5 h, 7 h, 10.5 h, 14 h, and 17.5 h, respectively, and the drying temperature was 100 °C (see Table 2).

2.4. Test Methods

2.4.1. WRC Tests

After soil sample preparation, the compacted clay samples were placed in aluminum boxes. The opening percentage of the aluminum box was greater than 85%. The opening percentage is the ratio of hole area to the total lid area. Studies [47] show that PAM solutions can maintain at least half their original viscosity for more than 8 years at 100 °C and for approximately 2 years at 120 °C. Its backbone can remain stable at high temperatures. So, the soil samples were dried in an oven with a temperature of 100 °C in order to save time. The quality changes in the samples were recorded every 3.5 h, and Equations (1) and (2) were used to calculate the moisture content and water loss rates after drying.

The water loss rates of the clay samples after drying were calculated as follows:

$$W_s = \frac{m_0 - m_t}{m_s \times 25.6\%} \times 100\% \quad (1)$$

where w is the moisture content; m_s is the sum of the mass of the clay and polyacrylamide (g); m_0 is the mass of a compacted clay sample before being baked (g); m_t is the mass of a compacted clay sample after drying for time t (g), and W_s is the water loss rate (%).

2.4.2. Clay Gas Permeability Tests

The CCC samples used in the gas permeability tests were prepared with the same method as those used in the WRC samples. It is noted that the samples were subjected to drying at various times of 0 h, 3.5 h, 7 h, 10.5 h, 14 h, and 17.5 h, respectively, and the drying temperature was 100 °C. Gas permeability is defined according to Darcy's equation as the factor of proportionality between the ratio of gas flow and the pressure gradient along the flow distance. The gas permeability of the CCC samples was measured immediately after drying for 10.5 h at 100 °C. The air permeability of soil was measured using the Eijkelkamp-type air permeability apparatus (model 08.07, Eijkelkamp Agrisearch Equipment, The Netherlands) with the following procedures: firstly, the instrument should be tested for tightness before the test. The preliminary test results revealed that it had good airtightness and no air leakage. Secondly, a thick rubber sealing ring (inside diameter: 50 mm, outside diameter: 70 mm, thickness: 10 mm), a perforated plate (diameter: 53 mm, thickness: 1 mm, the diameter of the hole: 1 mm), and a compacted soil sample were placed into a sample holder (inside diameter: 105 mm, outside diameter: 150 mm, height: 50 mm, material: stainless steel) in turn and fixed with a clamp for subsequent sealing. Finally, the flow meter (range: 0.1~10 L/min, accuracy: 1.25%) was switched on by turning the button counterclockwise to a vertical position to control the air pressure within an acceptable range for measurement. Each measurement was repeated for 5 replications within a max. of 10 min and enabled the quantification of pneumatic soil properties.

The testing time should be kept as short as possible during the experiments. This is because gas will dry out the soil sample. Three identical samples were prepared for testing. The air pressure was set as 10 kPa. It is noted that the gravimetric moisture content change in the samples before and after the tests was found to be insignificant, i.e., within 3%. This is attributed to the relatively low gas flow rate (0.5 L/min) and short testing time (10 min). Rouf et al. have proven that a maximum variation in gravimetric moisture content of $\pm 5\%$ was deemed acceptable during the gas permeability tests [48].

The gas permeability (K_p) of the compacted clay samples in the tests was derived in accordance with the published studies [49,50].

$$K_p = \frac{k \cdot \rho_1 \cdot g}{\mu} \quad (2)$$

$$Q = \frac{k \cdot A \cdot P}{\mu \cdot L} \quad (3)$$

$$Q = v \cdot A = \frac{v}{t \cdot A} \cdot A = \frac{v}{t} \quad (4)$$

$$K_p = \rho_1 \cdot g \cdot \frac{V \cdot L}{t \cdot P \cdot A} \quad (5)$$

where K_p is the gas permeability of a clay sample (m^2); k is the permeability coefficient (m/s); ρ_1 is the air density (kg/m^3); t is the test time (s); V is the amount of air passing through the sample within time t (m^3); L is the thickness of the compacted clay sample to be tested (m); p is the actual pressure value (MPa), and A is the bottom area of the sample (m^2).

2.4.3. Gas Diffusion Tests

The CCC samples used in the gas permeability tests were prepared with the same method as that used in the WRC tests samples. It is noted that the samples were subjected to drying at various times of 0 h, 3.5 h, 7 h, 10.5 h, 14 h, and 17.5 h, respectively, and the drying temperature was 100 °C. The testing apparatus used for this study is schematically shown in Figure 2. The apparatus consisted of a 3D printing gas diffusion chamber, an oxygen sensor (KE-25, Figaro Inc., Tokyo, Japan) with the accuracy of $\pm 1\%$, and a data logger (CR1000, Campbell Scientific, Inc., Logan, UT, USA), and a computer. The oxygen sensor was used to measure the concentration of oxygen with a unit of % (the concentration defined based on the content of oxygen in the atmosphere, 21%). The location of this oxygen sensor is in the bottom of the diffusion chamber. The size of the diffusion chamber is shown in Figure 2. The soil sample is placed at the top of the diffusion chamber; thus, the oxygen gas can only migrate into the chamber through the soil sample. A soil sample can be rapidly inserted into the apparatus and sealed to prevent the loss of gases and water and can be removed without further soil disturbance. The steps of gas tightness self-tests were conducted as follows: (1) an air-tight PVC lib was covered on the top of the chamber, and (2) the nitrogen gaseous were released to fill the chamber. The oxygen concentration should be decreased to the threshold of 0.3–0.6%. (3) It can be considered that the chamber has good air tightness when the variation range of oxygen concentration is less than 0.3%. The specific practical steps were listed as follows: (1) the samples were placed at the top of the diffusion chamber; (2) the silicon grease was evenly applied to the contact part between the samples and the inner wall of the diffusion chamber. Applying the silicon grease was found to be effective in preventing gas migration through the gap in the contact part; (3) the air inlet and outlet valves were opened, and the nitrogen gas container was opened to introduce nitrogen into the diffusion chamber through the inlet. Furthermore, we adjusted the flow control valve to make nitrogen enter the diffusion chamber evenly and steadily through the inlet. The oxygen sensor was installed to monitor the oxygen concentration change in the diffusion chamber until all the oxygen was discharged, and (4) the oxygen was released when the oxygen concentration decreased to the threshold of 0.3–0.6%. The inlet was closed after injecting nitrogen for 5–15 s.

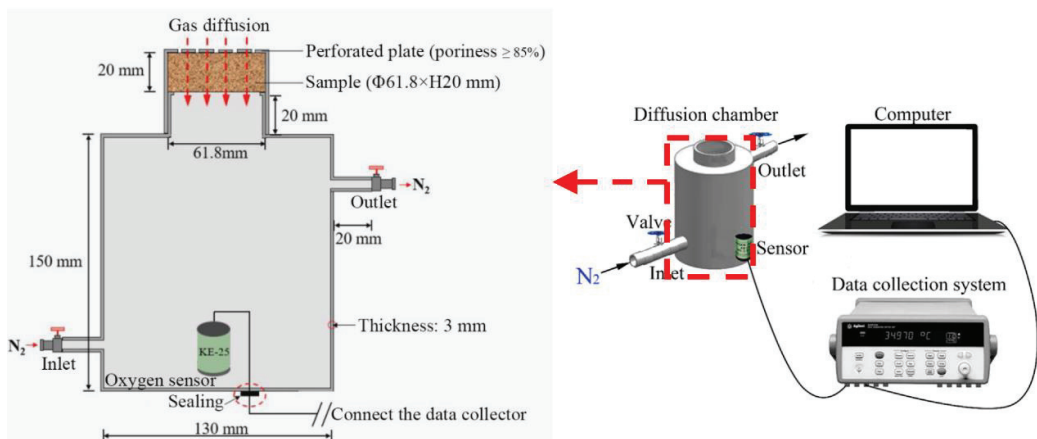


Figure 2. The 3D printing gas diffusion chamber.

In this research, a data acquisition instrument was applied to record the oxygen concentration in the diffusion chamber (C_t) every 5 min until the concentration was equal to the oxygen in the atmosphere (C_0), i.e., a steady state was reached.

The gas diffusion coefficients D_p of the compacted clay samples were calculated based on the previous studies [51,52] and combined with Fick's first law.

$$D'_p = h_s \cdot h_c \cdot k \tag{6}$$

$$\ln\left(\frac{\Delta C_t}{\Delta C_0}\right) = k \cdot t \tag{7}$$

$$K_j = \frac{D_p}{D'_p} = \frac{\varepsilon}{\alpha_1^2} \cdot \frac{1}{h_s \cdot h_c} \tag{8}$$

$$\varepsilon = 1 - \frac{\rho_b}{\rho_s} - \theta_v \tag{9}$$

where D_p is the correction gas diffusion coefficient (m^2/s); D'_p is the gas diffusion coefficient before calibration (m^2/s); h_s is the height of the compacted clay sample (m); h_c is the height of the diffusion chamber (m); k is the slope of the straight line in the scatter diagram of $\ln(\Delta C_t/\Delta C_0)$ (dimensionless); ΔC_t is the difference between OC at both ends of the clay sample at time t (g/cm^3); ΔC_0 is the difference between OC at both ends of the clay sample at time t_0 (t_0 means initial stage); K_j is the corrected coefficient introduced with changes in the storage capacity of OC; α_1 is the first solution of the equation $(\alpha \times h_s)\tan(\alpha \times h_s) = (h_s \times \varepsilon)/h_c$ greater than 0; ε is the gas-filled porosity [53]; ρ_b is the bulk density of the soil sample (g/cm^3); ρ_s is the particle density of the clay (g/cm^3); and θ_v is the volumetric moisture content of the clay sample.

2.4.4. Liquid Limit Test

The liquid limit test was conducted according to ASTM D4318 [39]. The liquid limit and plastic limit data were obtained from a liquid-plastic combined tester according to the standard test method SL237-007-1999 [54].

3. Results and Discussion

3.1. Liquid Limit

Figure 3 shows the relationship between the liquid limit of the modified compacted clay and the content of ZP. The liquid limit increases with the increasing ZP, which is higher than the unmodified clay (in Table 1). The liquid limits of the compacted clay were 45%, 49%, 52%, 54%, and 55%, when the corresponding ZP content ranged from 0.2 to 1%. Previous studies have demonstrated [55–57] that the WRC of clay increases with LL values. This is because clay with high LL can retain more content of water in the soil pore, which in turn can reduce gas permeability.

To compare the effects of different modification materials on LL, a dimensionless parameter, LL_d , is proposed, which was defined as the ratio of LL to LL_{ck} , where LL_{ck} is the liquid limit of un-treated clay. The comparison results of LL_d are shown in Figure 3b. The results show that the ZP-modified soil has higher LL_d values when compared with other modifiers.

3.2. WRC

The evolution of the moisture content with various ZP contents is shown in Figure 4. For the untreated samples, the initial moisture content was 25.6%. It decreased significantly with the increase in drying time from 0 h to 7 h; the moisture significantly decreased from 9% to 13%. After 17.5 h of drying, the moisture content of the compacted clay mixed with ZP of 0.2%, 0.4%, 0.6%, 0.8%, and 1.0% were 4%, 7%, 8%, 9%, and 12%, respectively. The moisture of the soil treated with 1.0% ZP content was 193% higher as compared to the soil with 0.2% ZP. Studies have proven [37] that ZP has a large specific surface area with many hydrophilic groups. Due to the electrostatic attraction between the anions and the penetration disparity induced by the differing concentrations of cations inside and outside, PAM expands linearly to form a three-dimensional network structure [25,26]. Thus, the polymer network of ZP

has a strong physical adsorption effect on water molecules. Accordingly, ZP can effectively improve the WRC of compacted clay and inhibit the evaporation of clay moisture during the drying process. After drying, the moisture content of the clay increased with increasing ZP content, and the modification was the most prominent when the ZP content was 1%.

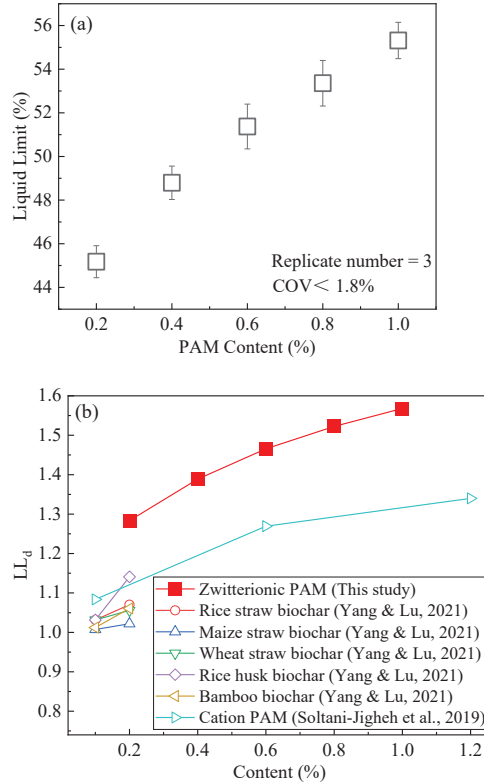


Figure 3. Liquid limit of CCC mixed with ZP. (a) Influence of PAM content on the LL of the compacted clay; (b) effect of different materials mixed with clay on LL/LL_{ck} of the compacted clay [58,59].

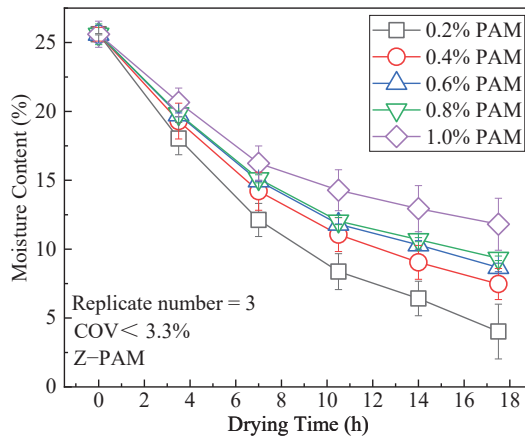


Figure 4. The moisture content of the compacted clay mixed with different PAM contents.

Figure 5 reflects the influence of ZP content on the water loss of the compacted clay after drying. After 17.5 h of drying at 100 °C, the water loss rates of the compacted clay mixed with different contents of ZP were 84%, 71%, 66%, 64%, and 54%, as the ZP content ranged from 0.2% to 1.0%. Therefore, increasing the content of modifier ZP can effectively reduce the water loss rate of clay and improve its WRC. Studies have indicated that the water loss of the clay mixed with various ordinary agricultural and forestry water-retaining agents varies from 55% to 63%, after they are dried for 360 min with a temperature of 60 °C [53]. However, when our research used 0.8% and 1.0% ZP for modification, the water loss rates of the clay after drying at 100 °C for 17.5 h were 64% and 54%. Furthermore, field monitoring results in the Changzhou contaminated site showed that [18] the highest atmospheric temperature was 45 °C, which was much lower than the test temperature of 100 °C in this paper. As a result, ZP plays a more prominent role in enhancing the WRC of CCC under low temperatures of 45 °C rather than 100 °C.

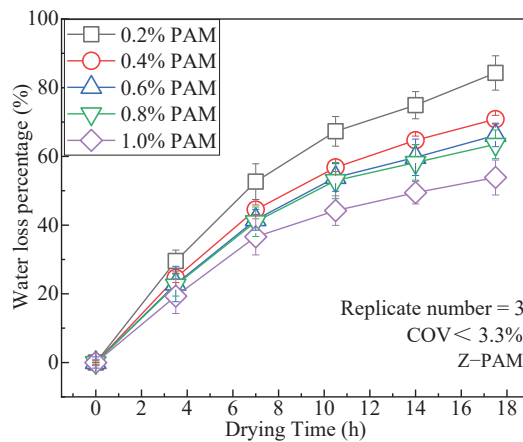


Figure 5. Water loss percentage of the compacted clay mixed with different contents of ZP.

Based on the preliminary test results, when the ZP content was than 1%, the clay with the same initial moisture content was too viscous to be blended homogeneously. Therefore, we did not test the soils with ZP content higher than 1.0%.

3.3. Gas Permeability

Figure 6 shows the relationship between the gas permeability and moisture content. It is noted that the gas permeability of the soils was measured immediately after drying for various times. It is observed the gas permeability of compacted clay increased with the rise in moisture. The relationship of GCL K_p and moisture content can be reflected in three stages in Figure 6. The first trend in stage I represents K_p decreasing sharply with increasing moisture content ranging from 4% to 30%. The second trend in stage II shows K_p very slightly decreasing with the increasing moisture content of 30~50%. The third trend in stage III represents K_p decreasing sharply with the increasing moisture content of 50~100%. According to the comparison between this study and geosynthetic clay liners in previous studies, as shown in Figure 6, the gas permeability of both CCC and GCL decreases with the rise in moisture content. In addition, the test results of Rouf et al. [11] showed that when the moisture content of the GCL was 5~100%, the gas permeability at 20 kPa overburden pressure varied from 10^{-13} m^2 to 10^{-16} m^2 , much lower than that of compacted clay. Only when the ZP content reached 1.0% was the gas permeability of ZP-modified compacted clay lower than that of the GCL, with moisture content in the range of 20% to 28%.

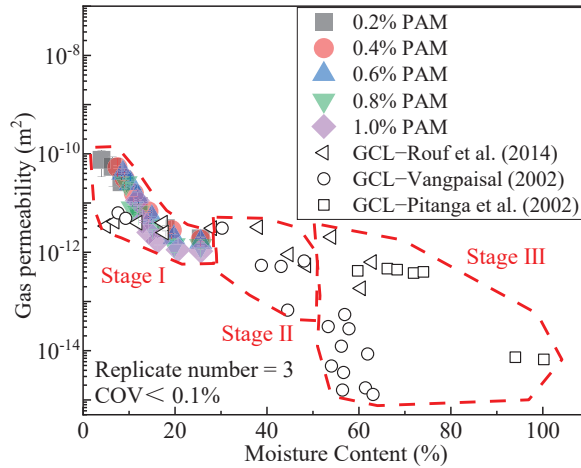


Figure 6. Relationship between the gas permeability and moisture content of compacted clay after ZP modification [11,13,60].

The CCC sample total drying time is 17.5 h. The CCC’s final state after drying can be compared to unveil the barrier performance under different ZP contents. Figure 7 shows the influence of ZP content on the gas permeability of the compacted clay after 17.5 h of drying. It can be observed that the moisture content of the clay enhanced as the content of ZP increased, while the gas permeability K_p gradually decreased. The moisture content and gas permeability showed an apparent negative correlation, meaning that gas permeability decreased with the rise in moisture content [11–13]. When the ZP content was 1.0%, the gas permeability of the clay after drying was $1.12 \times 10^{-11} m^2$, which was 97% lower than that of the ZP admixture content of 0.2%. As proved, ZP can increase the moisture content of clay after drying, thereby reducing its gas permeability. When the PAM content is 1%, the gas barrier performance of clay can be effectively improved by about one order of magnitude.

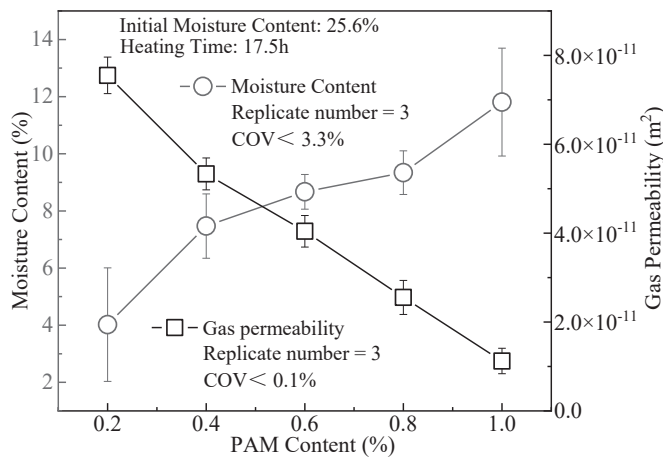


Figure 7. Influence of ZP content on gas permeability of the compacted clay.

3.4. Gas Diffusion Coefficient

Figure 8 displays the relationship between the gas diffusion coefficient and moisture content (after different times of drying with the initial moisture content of 25.6%) of the compacted clay after ZP modification. The relationship of GCL D_p and moisture content can be divided into two stages in Figure 8. The first trend in stage I represents D_p , which has no changes with the increasing moisture content, ranging from 8% to 42%. The second trend in stage II shows D_p , which decreases sharply with the increasing moisture content of 58~100%. The relationship between CCC D_p and moisture content follows the linear decreasing law; D_p decreases sharply with the increasing moisture content of 0~25.6%.

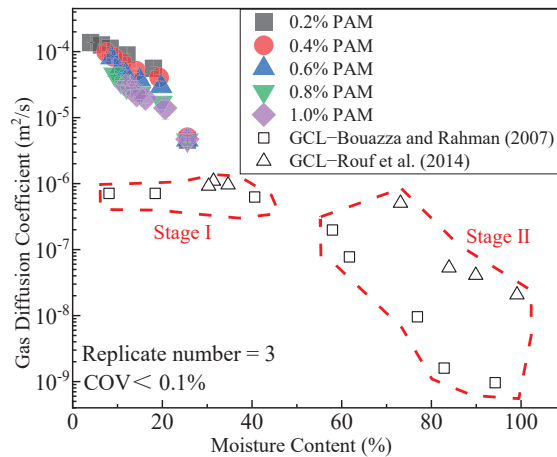


Figure 8. Relationship between the gas diffusion coefficient and moisture content of the compacted clay after PAM modification [11,57].

As the content of ZP ranged from 0.2% to 1.0%, the gas diffusion coefficient decreased with the rise in moisture. According to the analyses of the gas diffusion test results of Rouf and Bouazza [19,56] on the GCL, when the moisture content of the GCL was 8~100%, the gas diffusion coefficient was between 10^{-6} and 10^{-9} m^2/s , much smaller than that of compacted clay with the same moisture content.

As shown in Figure 8, when the moisture content was 25.6%, the gas diffusion coefficients of clay mixed with ZP at the contents of 0.2%, 0.4%, 0.6%, 0.8%, and 1.0% remained in the same order of magnitude, which was 4.56×10^{-6} m^2/s , 5.05×10^{-6} m^2/s , 4.72×10^{-6} m^2/s , 4.56×10^{-6} m^2/s , and 4.51×10^{-6} m^2/s , respectively. When the drying starts, the CCC samples present different gas barrier properties. The D_p of the CCC sample with 0.2% ZP content after 17.5 h drying is 1.37×10^{-4} m^2/s , while the D_p of the 1.0% ZP content sample is 3.06×10^{-5} m^2/s . This is because the CCC samples mixed with high content ZP have high WRC, which can reduce the microstructure of clay particles and enhance the barrier property of CCC.

The CCC sample's total drying time is 17.5 h. After drying, the CCC's final state can be compared to unveil the barrier performance under different ZP contents. Figure 9 presents the relationship between the gas diffusion coefficient and moisture content of the compacted clay after drying for 17.5 h with the change in ZP content. It can be observed that the D_p decreased with increasing moisture content. When the ZP content was 1%, the gas diffusion coefficient of the clay was 3.06×10^{-5} m^2/s , which was only 35% of that at the ZP content of 0.2%. Hence, ZP can effectively improve compacted clay's gas-barrier and anti-diffusion performance, and its modification effect increases with the rise in ZP admixture content.

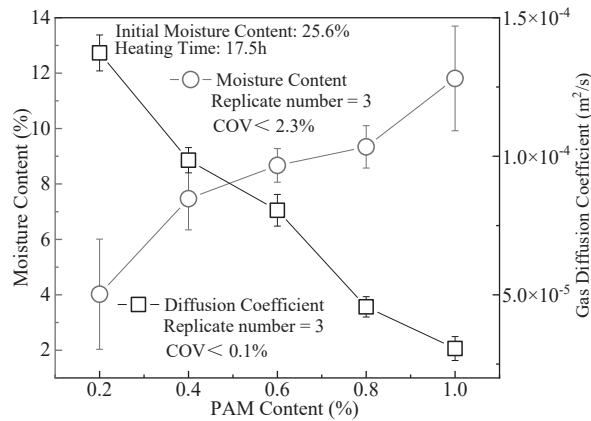


Figure 9. Influence of ZP content on the gas diffusion coefficient of the compacted clay.

4. Conclusions

This study investigated the gas barrier performance of CCC of an industrial contaminated site that was modified by zwitterion polyacrylamide (ZP). The water retention capacity (WRC) test, liquid limit (LL) test, gas permeability test, and gas diffusion test were conducted to unveil the barrier mechanism. Based on the results, the following conclusions can be drawn:

- (1) ZP could increase the moisture content of the compacted clay. The WRC is related to the linear expansion of polymer molecules after water adsorption. The moisture content of the clay after drying increases with the rise in the ZP admixture content. The modification had a prominent effect at a ZP content of 1%, and the moisture content after drying increased by 193% more than at the ZP content of 0.2%.
- (2) The WRC of compacted clay significantly improves after adding ZP. When the admixture content is 0.8% and 1.0%, the water loss rate after the clay is dried for 17.5 h at 100 °C is 64% and 54%. Its WRC is better than ordinary water-retention agents for agriculture and forestry.
- (3) The effects of ZP, i.e., reducing the clay gas permeability K_p and gas diffusion coefficient D_p , are not obvious. When the content is 1.0%, the K_p of CCC is about one order of magnitude lower than that at the ZP content of 0.2%. Its D_p is only 35% at the admixture content of 0.2%. For CCC with the same moisture content, the K_p and D_p decrease with the rise in ZP content.
- (4) The reasons for the slight improvement in the gas barrier performance of modified clay are as follows. ZP modification enhances the WRC of CCC after drying, thereby reducing the K_p and D_p .
- (5) ZP can increase the LL of compacted clay. When the admixture content varies from 0.2 to 1.0%, LL increases by 45~55% more than unmodified clay.

Further studies are warranted to explore the economic efficiency and long-term stability of ZP-modified CCCs. The data in this study offer modified materials as gas barriers in applying geotechnical engineering.

Supplementary Materials: The supporting information can be downloaded at: <https://www.mdpi.com/article/10.3390/app12168379/s1>. Figure S1: Clay cracking with different PAMs. Figure S2: Gas permeability and gas diffusion coefficient of clay under different PAMs. Table S1: The results of each sample.

Author Contributions: Data curation, Y.-Z.B., J.-M.W. and H.-L.W.; Funding acquisition, Y.-J.D. and Y.-Z.B.; Investigation, Y.-Z.B., J.-M.W. and H.-L.W.; Supervision, Y.-J.D. All authors have read and agreed to the published version of the manuscript.

Funding: This study was financially supported by the National Key Research and Development Program (Grant Nos. 2018YFC1803100), Jiangsu Province Key Research and Development Program of China (SBE2022740941), National Natural Science Foundation of China (Grant Nos. 41877248 and 42177133), Scientific Research Foundation of Graduate School of Southeast University (Grant No. YBJJ 1844), and Postgraduate Research and Practice Innovation Program of Jiangsu Province (Grant No. KYCX17_0130).

Institutional Review Board Statement: Not applicable.

Informed Consent Statement: Not applicable.

Data Availability Statement: The data that support the findings of this study are available from the first author, Yuzhang Bi, upon reasonable request.

Acknowledgments: We thank the anonymous referee for their careful reading and for providing insightful comments to improve the initial version of this paper. The corresponding author (Yan-Jun Du) would like to acknowledge the Jiangsu Province Key Research and Development Program of China (project name: Key Technology Research on Multi-Coordinated Low Carbon Cover Barrier for VOC Sites in Yangtze River Delta).

Conflicts of Interest: The authors declare no competing interests.

Nomenclature

| | |
|------------------|---|
| WRC | Water retention capacity |
| LL | Liquid limit |
| LL _d | The dimensionless results of LL |
| LL _{ck} | The LL of soil without any additive |
| CCC | Compacted clay cover |
| ADOS | Apparent degree of saturation |
| I _p | Plasticity index |
| CL | Clay with low LL |
| CH | Clay with high LL |
| ML | Silt with low LL |
| MH | Silt with high LL |
| OL | Low liquid limit organic clay or silt |
| OH | High liquid limit organic clay or silt |
| VOC | Volatile organic compound |
| PAM | Polyacrylamide |
| ZP | Zwitterion polyacrylamide |
| GCL | Geosynthetic clay liner |
| CK | Control blank |
| COV | Covariance (it is a measure of the joint variability of two random variables) |
| OC | Oxygen concentration |
| m _s | Sum of the mass of the clay and polyacrylamide (g) |
| m ₀ | The mass of a compacted clay sample before drying (g) |
| m _t | The mass of a compacted clay sample after drying for time t (g) |
| W _S | The water loss rate (%) |
| K _p | The gas permeability of a clay sample |
| k | The permeability coefficient (m ²) |
| ρ ₁ | The air density (kg/m ³) |
| t | The test time (s) |
| V | The amount of air passing through the sample within time t (m ³) |
| L | The thickness of the compacted clay sample to be tested (m) |
| p | The actual pressure value (hPa) |
| A | The bottom area of the sample (m ²) |
| D _p | The correction gas diffusion coefficient (m ² /s) |
| D _p ' | The gas diffusion coefficient before calibration (m ² /s) |
| h _s | The height of the compacted clay sample |
| h _C | The height of the diffusion chamber (cm) |

| | |
|--------------|---|
| k | The slope of the straight line in the scatter diagram of $\ln(\Delta C_t / \Delta C_0)$ (t) |
| ΔC_t | The difference between OC at both ends of the clay sample at time t |
| ΔC_0 | The difference between OC at both ends of the clay sample at time t_0 |
| FP | Filter paper |
| SSSM | Saturated salt solution method |
| RH | Relative humidity |

References

- Mahmoodlu, M.G.; Hassanizadeh, S.M.; Hartog, N.; Raoof, A.; van Genuchten, M.T. Evaluation of a horizontal permeable reactive barrier for preventing upward diffusion of volatile organic compounds through the unsaturated zone. *J. Environ. Manag.* **2015**, *163*, 204–213. [[CrossRef](#)] [[PubMed](#)]
- Xie, H.-J.; Wang, Q.; Yan, H.; Chen, Y.-M. Steady-state analytical model for vapour-phase volatile organic compound (VOC) diffusion in layered landfill composite cover systems. *Can. Geotech. J.* **2017**, *54*, 1567–1579. [[CrossRef](#)]
- Su, Y.; Pei, J.; Tian, B.; Fan, F.; Tang, M.; Li, W.; He, R. Potential application of biocover soils to landfills for mitigating toluene emission. *J. Hazard. Mater.* **2015**, *299*, 18–26. [[CrossRef](#)] [[PubMed](#)]
- Brusseau, M.L. Transport of organic chemicals by gas advection in structured or heterogeneous porous media: Development of a model and application to column experiments. *Water Resour. Res.* **1991**, *27*, 3189–3199. [[CrossRef](#)]
- Moldrup, P.; Olesen, T.; Gamst, J.; Schjønning, P.; Yamaguchi, T.; Rolston, D. Predicting the Gas Diffusion Coefficient in Repacked Soil Water-Induced Linear Reduction Model. *Soil Sci. Soc. Am. J.* **2000**, *64*, 1588–1594. [[CrossRef](#)]
- Foose, G.J.; Benson, C.H.; Edil, T.B. Comparison of solute transport in three composite liners. *J. Geotech. Geoenviron. Eng.* **2002**, *128*, 391–403. [[CrossRef](#)]
- You, K.; Zhan, H. Comparisons of diffusive and advective fluxes of gas phase volatile organic compounds (VOCs) in unsaturated zones under natural conditions. *Adv. Water Resour.* **2013**, *52*, 221–231. [[CrossRef](#)]
- Falta, R.W.; Javandel, I.; Pruess, K.; Witherspoon, P.A. Density-driven flow of gas in the unsaturated zone due to the evaporation of volatile organic compounds. *Water Resour. Res.* **1989**, *25*, 2159–2169. [[CrossRef](#)]
- Mendoza, C.A.; Frind, E.O. Advective-dispersive transport of dense organic vapors in the unsaturated zone: 2. Sensitivity analysis. *Water Resour. Res.* **1990**, *26*, 388–398. [[CrossRef](#)]
- Conant, B.H.; Gillham, R.W.; Mendoza, C.A. Vapor transport of trichloroethylene in the unsaturated zone: Field and numerical modeling investigations. *Water Resour. Res.* **1996**, *32*, 9–22. [[CrossRef](#)]
- Rouf, M.A.; Singh, R.M.; Bouazza, A.; Rowe, R.K.; Gates, W.P. Gas permeability of partially hydrated geosynthetic clay liner under two stress conditions. *Environ. Geotech.* **2016**, *3*, 325–333. [[CrossRef](#)]
- Mendes, M.; Pierson, P.; Touze-Foltz, N.; Mora, H.; Palmeira, E. Characterisation of permeability to gas of geosynthetic clay liners in unsaturated conditions. *Geosynth. Int.* **2010**, *17*, 344–354. [[CrossRef](#)]
- Suits, L.D.; Sheahan, T.C.; Pitanga, H.N.; Pierson, P.; Vilar, O. Measurement of Gas Permeability in Geosynthetic Clay Liners in Transient Flow Mode. *Geotech. Test. J.* **2011**, *34*, GTJ103000. [[CrossRef](#)]
- Bouazza, A.; Vangpaisal, T. Gas Advective Flux of Partially Saturated Geosynthetic Clay Liners. *Advances in Transportation and Geoenvironmental Systems Using Geosynthetics. Geotech. Spec. Publ.* **2000**, *103*, 54–67.
- Shan, H.-Y.; Yao, J.-T. Measurement of air permeability of geosynthetic clay liners. *Geotext. Geomembr.* **2000**, *18*, 251–261. [[CrossRef](#)]
- Smith, J.A.; Tisdale, A.K.; Cho, H.J. Quantification of natural vapor fluxes of trichloroethene in the unsaturated zone at Pi-catinny Arsenal, New Jersey. *Environ. Sci. Technol.* **1996**, *30*, 2243–2250. [[CrossRef](#)]
- Bouazza, A.; Vangpaisal, T. An apparatus to measure gas permeability of geosynthetic clay liners. *Geotext. Geomembr.* **2003**, *21*, 85–101. [[CrossRef](#)]
- Bi, Y.Z.; Fu, X.L.; Zhou, S.J.; Ni, J.; Du, Y. Field Investigation of Effect of Plants on Cracks of Compacted Clay Covers at a Contaminated Site. *Int. J. Environ. Res. Public Health* **2022**, *19*, 7248. [[CrossRef](#)]
- Rouf, A.; Bouazza, A.; Singh, R.M.; Gates, W.P.; Rowe, R.K. Gas flow unified measurement system for sequential measurement of gas diffusion and gas permeability of partially hydrated geosynthetic clay liners. *Can. Geotech. J.* **2016**, *53*, 1000–1012. [[CrossRef](#)]
- Kerry Rowe, R.; Rayhani, M.T.; Take, W.A. GCL hydration under simulated daily thermal cycles. *Geosynth. Int.* **2011**, *18*, 196–205. [[CrossRef](#)]
- Sjökvist, T.; Niklewski, J.; Blom, Å. Effect of wood density and cracks on the moisture content of coated Norway spruce (*Picea abies* (L.) Karst). *Wood Fiber Sci.* **2019**, *51*, 160–172. [[CrossRef](#)]
- Drumm, E.C.; Boles, D.R.; Wilson, G.V. Desiccation cracks result in preferential flow. *Geotech. News-Vanc.* **1997**, *15*, 22–26.
- Friedrich, S. Superabsorbent polymers (SAP). In *Application of Super Absorbent Polymers (sap) in Concrete Construction*; Springer: Dordrecht, The Netherlands, 2012; pp. 13–19.
- Mo, C.; Zhu, S.; Li, H.; Huang, Z. Synthesis of poly (acrylic acid)/sodium humate superabsorbent composite for agricultural use. *J. Appl. Polym. Sci.* **2006**, *102*, 5137–5143. [[CrossRef](#)]
- Theng, B.K.G. Interactions of clay minerals with organic polymers. Some practical applications. *Clays Clay Miner.* **1970**, *18*, 357–362. [[CrossRef](#)]
- Li, Y.; Shao, M.; Horton, R. Effect of Polyacrylamide Applications on Soil Hydraulic Characteristics and Sediment Yield of Sloping Land. *Procedia Environ. Sci.* **2011**, *11*, 763–773. [[CrossRef](#)]

27. Liu, J.; Chen, Z.; Kanungo, D.P.; Song, Z.; Bai, Y.; Wang, Y.; Li, D.; Qian, W. Topsoil reinforcement of sandy slope for preventing erosion using water-based polyurethane soil stabilizer. *Eng. Geol.* **2019**, *252*, 125–135. [[CrossRef](#)]
28. Qi, C.; Bai, Y.; Liu, J.; Bu, F.; Kanungo, D.P.; Song, Z.; He, X. Desiccation Cracking Behavior of Polyurethane and Polyacrylamide Admixed Clayey Soils. *Polymers* **2020**, *12*, 2398. [[CrossRef](#)]
29. Yu, B.; El-Zein, A.; Rowe, R.K. Effect of added polymer on the desiccation and healing of a geosynthetic clay liner subject to thermal gradients. *Geotext. Geomembr.* **2020**, *48*, 928–939. [[CrossRef](#)]
30. ASTM D3441-05; Standard Test Method for Mechanical Cone Penetration Tests of Soil. American Society for Testing and Materials: West Conshohocken, PA, USA, 2005.
31. Hunt, R.E. *Geotechnical Engineering Investigation Handbook*; CRC Press: Boca Raton, FL, USA, 2005.
32. Moore, J.E. *Field Hydrogeology: A Guide for Site Investigations and Report Preparation*; CRC Press: Boca Raton, FL, USA, 2016.
33. Hess-Kosa, K. *Environmental Site Assessment Phase I: A Basic Guide*; CRC Press: Boca Raton, FL, USA, 2007.
34. *CJJ-2008*; Code for Construction and Quality Acceptance of Road Works in City and Town. China Communications Press: Beijing, China, 2008.
35. Kaneko, K.; Nohara, S. Review of effective vegetation mapping using the UAV (Unmanned Aerial Vehicle) method. *J. Geogr. Inf. Syst.* **2014**, *6*, 733. [[CrossRef](#)]
36. Wong, W.S.D.; Lee, L. *Statistical Analysis of Geographic Information with ArcView GIS and ArcGIS*; Wiley: Hoboken, NJ, USA, 2005.
37. Mechtcherine, V.; Gorges, M.; Schroefl, C.; Assmann, A.; Brameshuber, W.; Ribeiro, A.B.; Cusson, D.; Custódio, J.; Da Silva, E.F.; Ichimiya, K.; et al. Effect of internal curing by using superabsorbent polymers (SAP) on autogenous shrinkage and other properties of a high-performance fine-grained concrete: Results of a RILEM round-robin test. *Mater. Struct.* **2013**, *47*, 541–562. [[CrossRef](#)]
38. Koerner, G.R.; Koerner, R.M. Long-term temperature monitoring of geomembranes at dry and wet landfills. *Geotext. Geomembr.* **2006**, *24*, 72–77. [[CrossRef](#)]
39. ASTM D2216-19; Standard Test Methods for Laboratory Determination of Water (Moisture) Content of Soil and Rock by Mass. American Society for Testing and Materials: West Conshohocken, PA, USA, 2019.
40. ASTM D854-14; Standard Test Methods for Specific Gravity of Soil Solids by Water Pycnometer. American Society for Testing and Materials: West Conshohocken, PA, USA, 2016.
41. ASTM D4318-17e1; Standard Test Methods for Liquid Limit, Plastic Limit, and Plasticity Index of Soils. American Society for Testing and Materials: West Conshohocken, PA, USA, 2018.
42. ASTM D7382-20; Standard Test Methods for Determination of Maximum Dry Unit Weight of Granular Soils Using a Vibrating Hammer. American Society for Testing and Materials: West Conshohocken, PA, USA, 2020.
43. ASTM D4253-16e1; Standard Test Methods for Maximum Index Density and Unit Weight of Soils Using a Vibratory Table. American Society for Testing and Materials: West Conshohocken, PA, USA, 2019.
44. Koerner, G.R.; Koerner, R.M. In-Situ Temperature Monitoring of Geomembranes. In Proceedings of the GRI-18 Conference on Geosynthetics Research and Development In-Progress, GeoFrontiers, ASCE, Austin, TX, USA, 24–26 January 2005; pp. 318–323.
45. Dantas, G.H.S.; Furlan, A.P.; Fabbri, G.T.P. On gyratory compaction of a clayey soil. *EJGE* **2016**, *21*, 5725–5733.
46. ASTM D2974-20e1; Standard Test Methods for Determining the Water (Moisture) Content, Ash Content, and Organic Material of Peat and Other Organic Soils. American Society for Testing and Materials: West Conshohocken, PA, USA, 2020.
47. Seright, R.S.; Campbell, A.R.; Mozley, P.S.; Han, P. Stability of partially hydrolyzed polyacrylamides at elevated temperatures in the absence of divalent cations. *SPE J.* **2010**, *15*, 341–348. [[CrossRef](#)]
48. Shackelford, C.D.; Benson, C.H.; Katsumi, T.; Edil, T.B.; Lin, L. Evaluating the hydraulic conductivity of GCLs permeated with non-standard liquids. *Geotext. Geomembr.* **2000**, *18*, 133–161. [[CrossRef](#)]
49. Moldrup, P.; Poulsen, T.G.; Schjønning, P.; Olesen, T.; Yamaguchi, T. Gas Permeability in Undisturbed Soils: Measurements and Predictive Models. *Soil Sci.* **1998**, *163*, 180–189. [[CrossRef](#)]
50. McCarthy, K.P.; Brown, K.W. Soil gas permeability as influenced by soil gas-filled porosity. *Soil Sci. Soc. Am. J.* **1992**, *56*, 997–1003. [[CrossRef](#)]
51. Taylor, S.A. Oxygen diffusion in porous media as a measure of soil aeration. *Proc. Soil Sci. Soc. Am.* **1949**, *14*, 55–61. [[CrossRef](#)]
52. Su, Z. *Using Gradient Method to Estimate Soil Surface CO₂ Flux in Crop and Grass Field*; China Agricultural University: Beijing, China, 2016. (In Chinese)
53. Zhang, J. *Comparative Analysis of Basic Properties to 11 Kind of Super-Absorbent-Polymers*; Northwest Sci-Tech University of Agricultural and Forestry: Xiayang, China, 2009. (In Chinese)
54. Republic of China. *Specification of Soil Test*; SL237-1999; China Architecture and Building Press: Beijing, China, 1999.
55. Scalia, I.V.J.; Benson, C.H.; Bohnhoff, G.L. Long-term hydraulic conductivity of a bentonite-polymer composite permeated with aggressive inorganic solutions. *J. Geotech. Geoenviron. Eng.* **2014**, *140*, 04013025. [[CrossRef](#)]
56. Lee, J.M.; Shackelford, C.D.; Benson, C.H.; Jo, H. Correlating index properties and hydraulic conductivity of geosynthetic clay liners. *J. Geotech. Geoenviron. Eng.* **2005**, *131*, 1319–1329. [[CrossRef](#)]
57. Bouazza, A.; Rahman, F. Oxygen diffusion through partially hydrated geosynthetic clay liners. *Civ. Eng.* **2007**, *57*, 767–772. [[CrossRef](#)]
58. Yang, C.D.; Lu, S.G. Effects of five different biochars on aggregation, water retention and mechanical properties of paddy soil: A field experiment of three-season crops. *Soil Tillage Res.* **2021**, *205*, 104798. [[CrossRef](#)]

59. Soltani-Jigheh, H.; Bagheri, M.; Amani-Ghadim, A.R. Use of hydrophilic polymeric stabilizer to improve strength and durability of fine-grained soils. *Cold Regions Sci. Technol.* **2019**, *157*, 187–195. [[CrossRef](#)]
60. Vangpaisal, T. Gas Permeability of Geosynthetic Clay Liners under Various Conditions. Ph.D. Thesis, Monash University, Melbourne, Australia, 2002.

Article

Study and Characterization of Special Gypsum-Based Pastes for Their Use as a Replacement Material in Architectural Restoration and Construction

María Paz Sáez-Pérez ¹, Jorge A. Durán-Suárez ², Amparo Verdú-Vázquez ^{3,*} and Tomás Gil-López ³

¹ Department of Architectural Constructions, Advanced Technical School of Building Engineering, University of Granada, c/ Severo Ochoa s/n, 18071 Granada, Spain

² Department of Sculpture, Faculty of Fine Arts, University of Granada, Andalucía s/n. Edif. Aynadamar, 18071 Granada, Spain

³ Departamento de Tecnología de la Edificación, Escuela Técnica Superior de Edificación, Universidad Politécnica de Madrid, 28040 Madrid, Spain

* Correspondence: amparo.verdu@upm.es

Abstract: Within the construction sector, the use of gypsum-based pastes features in the majority of monuments, giving this material significant relevance in conservation and restoration projects affecting the world's cultural heritage. In this research, we evaluated special gypsum-based colored pastes mixed with air lime, hydraulic lime and sodium silicate, and eight different pigments for their use as replacement materials in architectural restoration and construction. We analyzed the suitability of their physical and chemical properties and their hydric characteristics, mechanics and colorimetric implications in two different studies after 28 days and 120 days. The characterization of the products has mainly confirmed the suitability of the pastes containing pigments for use in the most common applications for these kinds of mixes, highlighting that their specific capacities are worth leveraging. The crystallization of gypsum minerals, observed in all of the mixes, helps to consolidate the shrinkage cracks which appear inside the pastes, improving their mechanical strength values. Another observation of the pastes is related to the amorphous silica precipitates in the mixes which contained sodium silicate: the latter provided to them good mechanical behavior. The improvement observed in the pastes containing the green earth pigment is substantial, due to the inclusion of aluminum silicates and Mg, which is partly responsible for the increased compressive strength of the pastes. Finally, the colorimetric analysis is of vital importance in determining the loss of intensity of the colors of the pastes used, since subjective observation leads to serious errors of interpretation.

Keywords: replacement pastes; water glass; pigments; chromatic evaluation; construction; cultural heritage

Citation: Sáez-Pérez, M.P.; Durán-Suárez, J.A.; Verdú-Vázquez, A.; Gil-López, T. Study and Characterization of Special Gypsum-Based Pastes for Their Use as a Replacement Material in Architectural Restoration and Construction. *Materials* **2022**, *15*, 5877. <https://doi.org/10.3390/ma15175877>

Academic Editor: Alessandro P. Fantilli

Received: 15 July 2022

Accepted: 22 August 2022

Published: 25 August 2022

Publisher's Note: MDPI stays neutral with regard to jurisdictional claims in published maps and institutional affiliations.



Copyright: © 2022 by the authors. Licensee MDPI, Basel, Switzerland. This article is an open access article distributed under the terms and conditions of the Creative Commons Attribution (CC BY) license (<https://creativecommons.org/licenses/by/4.0/>).

1. Introduction

Plaster is a commonly-used material due both to its abundance and the fact that it is easy to extract, transform and distribute [1]. In addition, there are other features, such as its easy preparation, durability and versatility [2], along with its quick setting and hardening when exposed to air. It is a material that is often used in the construction sector due to its low cost, its excellent thermal insulation and soundproofing properties, its high flame resistance and its low energy consumption during the production process [3,4]. It is also easy to recycle using suitable preparation processes based on the theory of hydration and dehydration [5].

In building construction, plaster is used for decorative trimmings and coatings of walls and ceilings; for stucco work and rendering; in interiors and exteriors; as a binder in ceramic and stone materials; and even for building products such as bricks and blocks, laminated plasterboards, plasterboard sandwich panels, etc. [6,7].

Despite its aforementioned advantages, its extreme fragility and limited mechanical strength and resistance to water mean that this material is unsuitable when its use requires it to withstand certain specific stresses, to bear shock loads or to be located in external environments [8].

For some time, research has been being carried out into how to improve the mechanical properties of pastes so as to broaden the scope of their use. This fact has led to new mixes being studied in which natural and artificial fibers are added [9–16]. Usually, in the case of plasters or gypsum-based pastes, the way that this is achieved is by reinforcing them using fiberglass [17–19].

The search for materials which have lower environmental impacts and greater efficiency has led to artificial fiber-based additives being replaced by others containing natural fibers [3]. However, the high cost of natural fiber in comparison with that of plaster, along with the limited interaction of these additives with the plaster matrix, mean that these compounds are not as competitive as artificial ones.

Within the construction sector, the use of gypsum-based pastes is necessary for the majority of monuments, giving this material significant relevance in conservation and restoration projects affecting the world's cultural heritage. Its origin dates back to the sixth millennium BC in Greece, and it was widely used and developed by the Romans [20]. Consequently, knowledge of this type of compound, and its application, is fundamental for mitigating the state of degradation and loss of built heritage [21–24]. Despite its importance, there has been little interest in studying it or defining new strategies for its use in conservation for a number of years.

Fortunately, in recent decades, the features of mortars and pastes have become a priority in material characterization studies, particularly those which have compositional or microstructural issues [25–34], excluding aesthetic matters [21,35–38]. In this regard, incorporating polymers in traditional building materials, such as mortars, adds great value when compared to conventional building materials. The addition of polymers makes it possible to obtain good levels of mechanical strength, good adhesion properties, abrasion and weathering resistance, waterproofing and excellent insulating properties [39].

New research projects seek to increase the durability of plaster pastes exposed to atmospheric influences. Recent studies have analyzed the improvements brought about by introducing modifying additives to the plaster binder, such as: polymeric compositions, fine minerals and nano-disperse components. Zhukov et al. have analyzed the addition of hardening resins to plaster through polycondensation and the application of nano-aggregates [40]. The addition of a polymer to the plaster mix produces a framework of dehydrated crystalline aggregates during the hydration of the plaster, whilst the resin, when it hardens, forms a continuous polymeric matrix. This causes the polymeric plaster to increase its strength over time due to the continuous polymerization of the resin.

Other research projects seek to analyze the influence of micro-aggregates (micro-spheres, hydroxyethyl methyl cellulose polymer and/or aerogel) on the thermal conductivity coefficient and thermal diffusivity. Using these additives makes it possible to reduce thermal conductivity by up to 23%, compared to the unmodified plaster samples [41]. The authors conclude that the polymer provoked a change in the structure of the plaster compound, giving it a lower density and greater porosity.

On the other hand, the porosity increasing can also have some disadvantages, since a key element to take into account in the conservation of gypsum-based pastes is the permeability of the compound [42]. As such, it is necessary to study the porosity, sphericity and pore size distribution, assessing the changes depending on the mortar composition [43]. Recent studies have made progress by using mercury intrusion porosimetry (MIP) and micro-computerized tomography (μ CT). Thanks to these techniques, it is possible to visualize pores, air voids, aggregates and binder distributions within a sample [25].

However, when it comes to heritage, the maintenance and preservation of buildings require broader interventions also addressing issues of aesthetic nature. In this respect, the colorimetry rules and studies can be key in the field of conservation and restoration [44–46]. Knowledge of the chromatic possibilities of pigments and their techniques is fundamental when the objective is to carry out an intervention for recovery of built heritage [47,48].

In this kind of intervention, where it is not possible to modify the aesthetic characteristics of the element, colorimetry has become a highly useful tool. In an intervention of this type, a

correct choice of materials must be made after evaluating the effectiveness of the procedures to be used and the chromatic modifications that can happen. In this way, it is necessary to develop a colorimetric study at least, before and during the preparation of the restorative pastes.

There are recent studies which have already applied the study of colorimetry in the field of monumental heritage, analyzing the performances of treated pigments [49–56]. For this reason, the use of pigments in different applications within the field of materials engineering and interventions in architectural heritage is necessary in order to achieve matching visual and aesthetic characteristics [57,58].

Generally, the colorimetry studies have focused on the characteristics of the pigments, mainly on production processes and their formulation, the saving of resources, the product finish and the most suitable application methods for protecting the environment. However, it is important to underline the conditions that the materials will be exposed for establishing their performance and effectiveness.

The present article focuses upon the application of different pigments in plaster-based pastes for use in construction, be it to new builds or to the restoration of cultural heritage sites. It analyzes the intended use of the pigments studied, the suitability of their physical and chemical properties and the characteristics of the materials. Their colorimetric implications were analyzed in two different studies after 28 days and 120 days.

2. Materials and Methods

The research carried out involved designing four gypsum-based pastes containing added pigments. Different binders and pigments were used to produce them, making it possible to add significant color to the pastes, and increase their final mechanical strengths without unduly reducing their insulation or water vapor permeability values.

Both the limes and plaster used were provided by CTS Spain. The plaster used contained a minimum of 90% of hemihydrate, giving it the highest quality, as can be seen in the XRD (Figure 1). According to the distributor, a microfiltration process is applied to the air lime after it has been slaked in tanks used specifically for that purpose, and it is then aged for a period of no less than six months. According to [59], air lime is a type CL90 calcium lime (CL), the CaO + MgO content of which is $\geq 90\%$. The MgO content is $\leq 5\%$, the CO₂ content is $\leq 4\%$, the SO₃ content is $\leq 2\%$ and the usable lime (Ca(OH)₂) content is $\geq 80\%$. Where hydraulic lime (NHL5) is concerned, this was genuinely natural pure lime obtained from the calcination of loamy limestone, without additives, at production temperatures of 1200 °C, which according to [59], has a usable lime (Ca(OH)₂) content of $\geq 15\%$, a SO₃ content of $\leq 2\%$ and compressive strengths ranging from 5 to 15 MPa. The sodium metasilicate (water glass) was acquired from Alquera Ciencia SL (Spain), with a SiO₂ content of $26.40 \pm 1.50\%$, Na₂O content of $8.00 \pm 0.60\%$ and water content of $65.60 \pm 2.00\%$. The true density is 38 ± 1.00 Be, and the pH is 12.50 ± 1.00 . The mixture has a viscosity of 80 MPa·s.

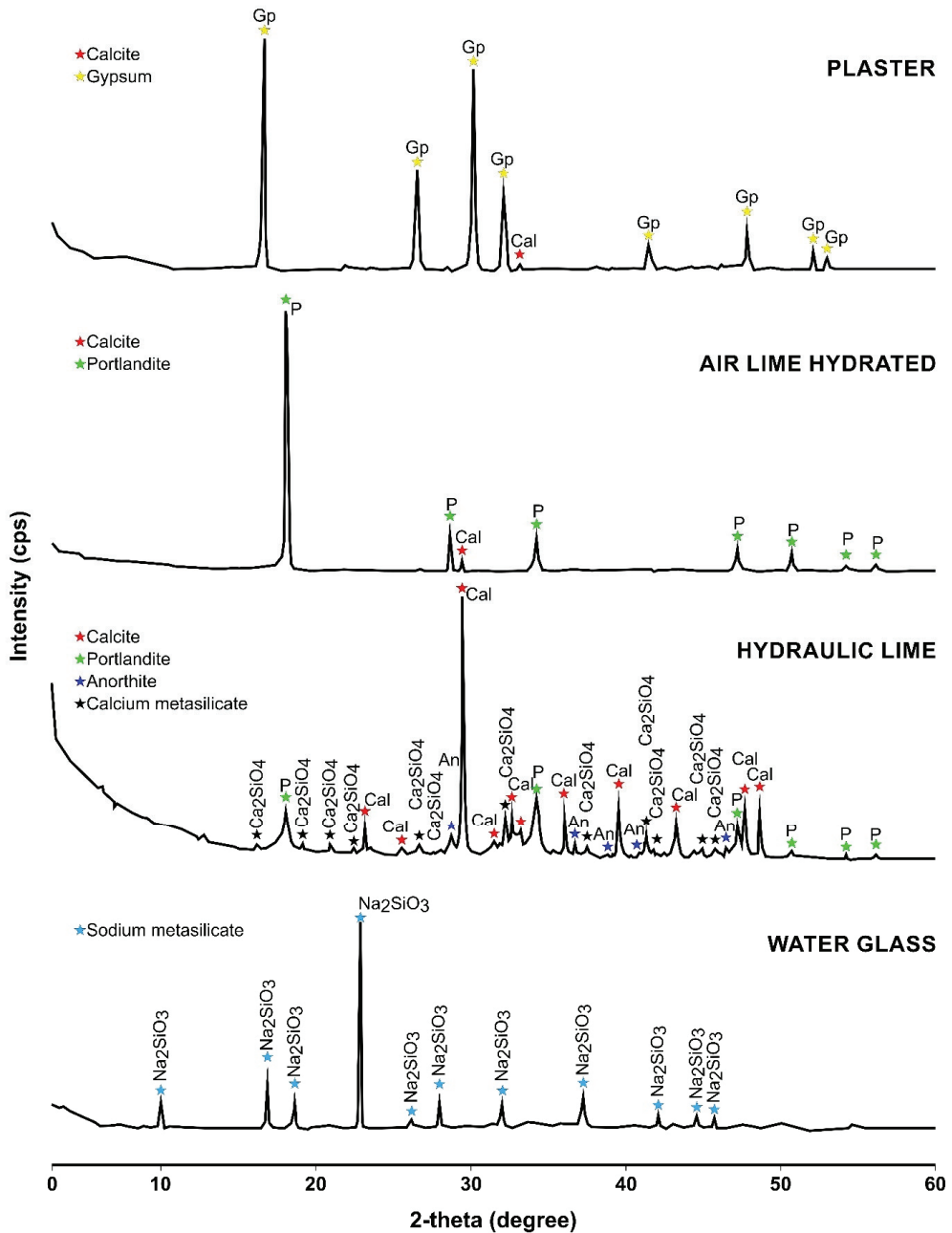


Figure 1. X-ray diffractograms for the plaster, hydrated air lime, hydraulic lime and water glass [60]. Abbreviations for names of rock-forming minerals.

In relation to the different pigments used (eight), these were supplied by Kremer Pigmente. The color range selected enables the use of a broad spectrum of red, blue, green, ochre and yellow colors, specifically for use in the preparation of pastes, putties and mortars for applications in architectural heritage work. The compositional parameters, by manufacturer, color code [61] and name, are set out in Tables 1 and 2.

Table 1. List of pigments along with an indication of the identification used in the study carried out, trade name, color index, composition and acronym.

| Name | Commercial Pigment/Binders [62,63] | Colour Index Name | Manufacturer's Composition | Acronym |
|------|------------------------------------|-------------------|--------------------------------------|---------|
| CY | Chromium yellow pigment | 77600 | Lead chromate | PY34 |
| MO | Molybdenum orange pigment | 77629 | Lead chromate, sulfate and molybdate | PR104 |
| O | Ochre pigment | 77492 | Iron hydroxide | PY43 |
| GE | Green earth pigment | 77009 | Iron (II) silicoaluminate, Mg and K | PG23 |
| CG | Chromium green pigment | 77288 | Chromium oxide | PG15 |
| NS | Natural sienna pigment | 77491-2 | Calcined natural iron oxide | PBr7 |
| ZY | Zinc yellow pigment | 77956 | Zinc chromate | PY36 |
| UB | Ultramarine blue pigment | 77007 | Sodium polysulfide-aluminosilicate | PB29 |

Table 2. List of raw materials used for binders along with an indication of the identification used in the study carried out, trade name, color index, composition and acronym.

| Name | Commercial Pigment/Binders [62,63] | Colour Index Name | Manufacturer's Composition | Acronym |
|------|------------------------------------|-------------------|---|---------|
| P | Plaster of paris | 77231 | Hemihydrate | PW25 |
| LW | Lime White | 77220 | Calcium hydroxide-Portlandite | PW18 |
| NHL | Natural hydraulic lime | 77230 | Silica calcium aluminates and calcium hydroxide | PW28 |
| WG | Water glass | 77007 | Sodium metasilicate | PB29 |

2.1. Binder Characterization

In order to study the mineralogical, chemical and colorimetric properties of the binders used in the present research, X-ray fluorescence (XRF), X-ray diffraction (XRD) and standard colorimetric observation methods were used, in line with the CIELab 1976 system.

A compact, high-performance wavelength dispersive X-ray fluorescence spectrometer, the Zetium model (Malvern Panalytical Company, Worcestershire, UK) by the brand PANalytical, was used to perform the X-ray fluorescence test (XRF) at the Scientific Instrumentation Centre of the University of Granada (CIC).

A Bruker D8 DISCOVER diffractometer (Dectris, Baden-Daettwil, Switzerland) with a DECTRIS PILATUS3R 100K-A detector (Dectris, Baden-Daettwil, Switzerland), from the Scientific Instrumentation Centre of the University of Granada (CIC), was used for the XRD test. The Xpowder [64] program (v. 8, Daniel, Granada, Spain) was used to determine the composition.

Figure 1 and Table 3 show the results obtained from the XRD and XRF tests.

Table 3. Chemical composition by XRF analysis (wt %) of each raw material. Data normalized to 100% (LOI-free), loss on ignition.

| SAMPLE (wt %) | SiO ₂ | Al ₂ O ₃ | Fe ₂ O ₃ | MnO | MgO | CaO | Na ₂ O | K ₂ O | TiO ₂ | P ₂ O ₅ | SO ₃ | Cl | LOI |
|-----------------|------------------|--------------------------------|--------------------------------|-------|-------|--------|-------------------|------------------|------------------|-------------------------------|-----------------|-------|--------|
| Plaster | 0.508 | 0.402 | 0.212 | 0.108 | 0.602 | 32.205 | | 0.047 | 0.196 | 0.021 | 45.450 | | 20.106 |
| Aerial lime | 0.202 | | 0.076 | | 0.516 | 76.292 | 0.128 | 0.068 | | 0.630 | 0.196 | 0.412 | 21.430 |
| Hidraulic lime | 12.908 | 4.052 | 1.902 | 0.028 | 0.944 | 58.653 | 0.098 | 0.925 | 0.247 | 0.052 | 0.093 | | 19.918 |
| Sodium silicate | 48.09 | 0.18 | 0.03 | | | 0.03 | 19.57 | 0.08 | 0.01 | 0.01 | 0.05 | | 31.78 |

The preparation of the samples involved grinding the raw materials in an agate pestle and paste and subsequently sieving them (mesh sieve ASTM N° 45, diameter <0.354mm).

A Konica Minolta CM-2500c Spectrophotometer (I.T.A. Aquateknica, S.A. Valencia, Spain) from the University of Granada was used in order to be able to carry out the colorimetric characterization and calculate the CIELab-1976 chromaticity coordinates [65] of the binders, pure pigments and their mixes after 28 and 120 days. The measurements obtained for diffuse spectral reflectance were in the visible range of 360–740 nm, at 5 nm

intervals, with a D65 illuminant at 10°. The specular reflection component was excluded from all of the measurements, following CIE recommendations [66].

2.2. Sample Design and Preparation

The research was carried out using four different pastes: the first composed entirely of pure plaster; the second made of plaster and air lime; the third made of plaster and hydraulic lime; and the fourth made of plaster and sodium silicate. In all four cases, the pastes were mixed with the pigments described above.

For the compression and flexural tests, several samples with dimensions of 160 × 40 × 40 mm were prepared in a plastic mold. For the permeability test, the samples dimensions were 40 × 40 × 20 mm, being prepared in a plastic mold.

A dosage was specified in terms of the volumes of the mixture components, the final compositions being those shown in Table 4. In order to prepare the samples, the different components (plaster, lime/plaster + pigment) were dry-mixed, before finally adding potable water in order to facilitate the mixing. For the samples containing plaster and water glass, the plaster binder and pigment were dry-mixed before adding the sodium silicate (liquid). This binder (sodium metasilicate) was purchased commercially in proportions of 25% active material, sodium silicate (Na₂SiO₃), and 75% water. The compaction times in the demountable molds and subsequent demolding were 24 h for all samples.

Table 4. Specification and dosage of each gypsum-based paste mix (by volume %).

| Name | Plaster | Aerial Lime | Hydraulic Lime | Sodium Silicate Solution (25–75%) | Pigment | Water Added |
|------|---------|-------------|----------------|-----------------------------------|---------|-------------|
| | % | % | % | % | % | parts |
| PPS | 80 | 0 | 0 | | 20 | 0.5 |
| PALS | 65 | 15 | 0 | | 20 | 0.5 |
| PHLS | 65 | 0 | 15 | | 20 | 0.5 |
| PWGS | 65 | | | 15 | 20 | |

All of the samples were placed in a Weiss Technik climatic chamber, ClimeEvent model (Xian LIB Environmental Simulation Industry, Shaanxi Province, China), with the following characteristics: temperature range −42 °C to 180 °C and relative humidity of 10–98%.

The environmental setting and hardening conditions for the PPS, PALS and PHLS mixtures were 22 °C and RH 70% inside of a climatic chamber for 120 days. The samples of the PWGS paste had particular conditions of 60 °C for 24 h in an oven, causing the concretion of the binder, and were subsequently kept in the same environmental conditions (in a climatic chamber) as the rest of the samples.

The average time used for sample setting was 28 days, except in the case of the PWGS mixes, which set after 24 h. All samples were considered to have fully hardened after 120 days.

Figure 2 shows both the pigments and the binders used in the research.

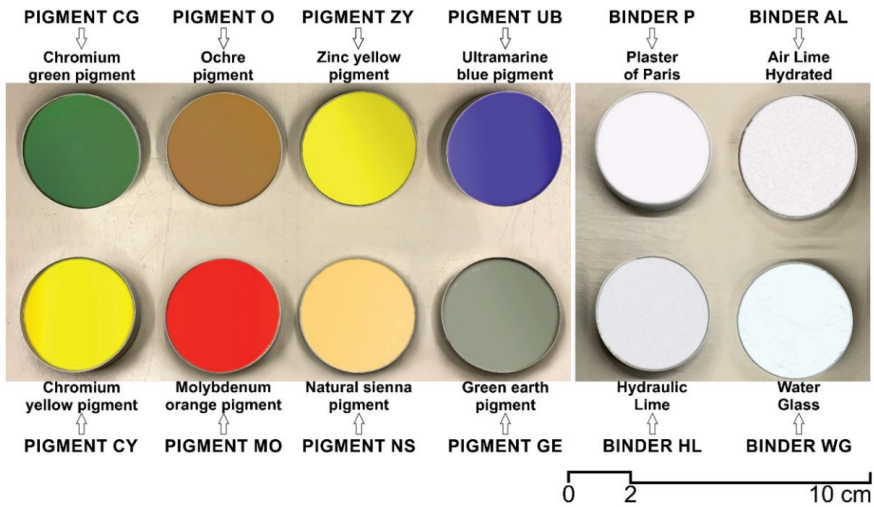


Figure 2. Samples of pigments and binders used in the research.

2.3. Methods

2.3.1. Scanning Electron Microscopy (SEM)

Using a GEMINI (FESEM) CARL ZEISS scanning electron microscope (SEM) (LEICA, Madrid, Spain), with a Röntec M Series EDX Detector (LEICA, Madrid, Spain), belonging to the Scientific Instrumentation Centre of the University of Granada (CIC) the mineralogical, microstructural and textural characterization of the mixes was performed. The results of the EDX analysis were collected by matrix spotting of the indicated samples.

2.3.2. Water Vapor Permeability

According to [67], sixty-four test pieces were analyzed for each paste type (two for each pigment) and two for each mix without added pigments (eight test pieces), after 120 days, in laboratory conditions (temperature: 20 ± 2 °C; RH: $65 \pm 5\%$). Their dimensions were $40 \times 40 \times 20$ mm. The edges of the samples were sealed using liquid paraffin; then they were placed in plastic recipients with covers, such that one part of the test piece was inside the recipient and the other was outside of it. The join between the test piece and the plastic recipient was sealed using liquid paraffin.

Granular calcium chloride was placed inside the plastic recipients as a drying agent, in sufficient volume in order to obtain a relative humidity of 0%. An air gap measuring approximately 10 mm was left between the drying agent and the base of each test piece.

After preparing the samples, the recipients were weighed in order to determine their initial mass.

The specimens were brought out from the climatic chamber to measure the weights. The same specimens were used to perform the water vapor permeability tests at both 28 and 120 days.

The test conditions were $50 \pm 1\%$ RH and 25 ± 0.5 °C, the samples being weighed every twenty-four hours until the weight difference every twenty-four hours did not exceed 5%.

2.3.3. Mechanical Tests

The flexural strength and compressive strength tests were carried out on each type of test piece, following a hardening time of 120 days. The total of samples used were 216. In order to calculate the strength, regulation [68] was used, for prismatic test pieces with dimensions of $160 \times 40 \times 40$ mm.

The press machine used to perform the break test was IBERTESTEUR TEST MD2 universal testing apparatus (Ibertest, Madrid, Spain). For a sampling interval of 64 mm, the test speed was 1 mm/min. The sample was broken by using a concentrated load on the central part, with the load cell set to 5 kN. In the compression testing, the speed used was 5 mm/min.

Using the average of the results for the three test pieces for each dosage and pigment used, the average mechanical strength value was obtained.

2.3.4. Color Tests

After preparing the samples, their diffuse spectral reflectance curves were measured. Five colorimetric determinations were performed for each one. Using Bessel's correction, the standard deviation was obtained for the values acquired, without this ever exceeding 3% of the associated average value [69].

Finally, SpectraMagic NX Color Data Software (I.T.A. Aquatecnica, S.A., Valencia, Spain) was used to present the simulations of the color variations for the samples studied.

3. Results

3.1. Scanning Electron Microscopy (SEM)

Figure 3 shows both the morphological analysis and EDX analysis of the samples.

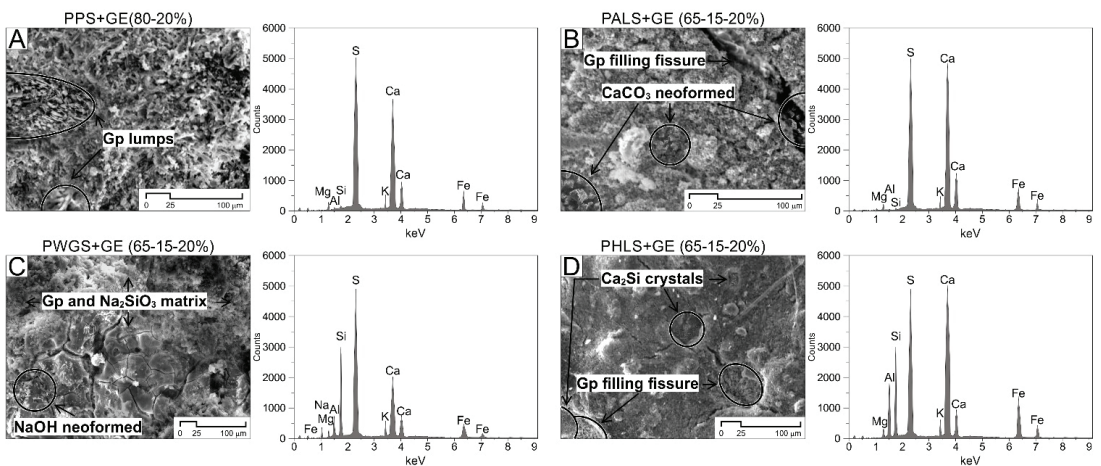


Figure 3. Scanning electron microscopy images corresponding to different pastes with the pigment, GE (Green Earth). The presence of gypsum lumps (A), several recrystallizations that are filling cracks (B,D) and other characteristic mineralization of the paste's matrix (B–D) are highlighted. The plot of the EDX analysis corresponds to the elemental composition of the matrix.

In the SEM study carried out 120 days after they were prepared, plaster crystallization was detected in specific areas of all of the samples, specifically in cavities with sizes of $\approx 20\text{--}35\ \mu\text{m}$, along with needle morphology in the case of the PPS + GE sample, where lumps of such crystallization were detected, and in PALS + GE and PHLS + GE samples. It may be speculated that this type of neoformed crystal generates a certain mechanical improvement in the pastes due to the filling and consolidation produced in cracks and micro-fractures.

Meanwhile, calcium carbonate crystallization was found in cavities in some samples, such as those of PALS + GE; belite crystallization (Ca_2Si , calcium silicate hydrate) was found in the PHLS + GE samples; and neoformed sodium hydroxide (NaOH) in the plaster and sodium metasilicate matrix of the PWGS + GE samples.

The EDX analyses of the matrixes of all of the samples provided results which are consistent with the quality of the samples. Elements associated with the Green Earth (GE) pigment stood out in all of them. This artificial pigment is obtained by combining two

types of hydrous phyllosilicate: celadonite ($\text{KMgFe}_3 + \text{Si}_4\text{O}_{10}(\text{OH})_2$) and glauconite ($\text{Fe}_3 +, \text{Al}, \text{Mg}_2\text{Si}, \text{Al}_4\text{O}_{10}(\text{OH})_2$). Apart from this, the elements associated with the matrix are those which are characteristic of each mix. S-Ca associations stand out, as they are typical in plaster and air lime (PPS and PALS), along with increases in Si, which is characteristic in samples containing hydraulic lime and water glass.

3.2. Water Vapor Permeability Test

The results of the water vapor permeability tests for both test periods, after 28 and 120 days, are shown in Table 5 and Figure 4.

Table 5. Results of the water vapor permeability test and standard deviation for the different white pastes tested.

| WVP ($\text{kg}/(\text{m}\cdot\text{Pa}\cdot\text{s})\cdot 10^{-12}$) | | | | | | | | |
|---|-----------------|-----------------|------------------|-----------------|------------------|------------------|------------------|------------------|
| 28 Days | | | | 120 Days | | | | |
| PIGMENT | PPS | PALS | PWGS | PHLS | PPS | PALS | PWGS | PHLS |
| Binder | 33.4 ± 1.50 | 27.2 ± 1.70 | 25.30 ± 0.40 | 22.8 ± 0.45 | 28.95 ± 1.35 | 25.89 ± 0.95 | 22.91 ± 0.83 | 20.96 ± 1.33 |
| CY | 33.1 ± 0.80 | 26.9 ± 1.10 | 24.90 ± 1.25 | 20.9 ± 1.17 | 31.4 ± 0.90 | 25.5 ± 0.95 | 23.6 ± 0.83 | 19.8 ± 1.33 |
| MO | 32.9 ± 1.10 | 26.5 ± 1.30 | 24.50 ± 1.10 | 20.5 ± 1.07 | 31.2 ± 1.30 | 25.1 ± 1.18 | 23.2 ± 1.13 | 19.4 ± 1.25 |
| O | 33.8 ± 1.70 | 26.9 ± 1.50 | 24.90 ± 1.33 | 21.1 ± 1.25 | 30.9 ± 0.80 | 25.5 ± 0.95 | 23.6 ± 1.06 | 20.5 ± 1.10 |
| GE | 32.3 ± 1.3 | 26.1 ± 1.20 | 24.10 ± 1.11 | 20.0 ± 1.50 | 30.5 ± 1.80 | 24.8 ± 0.91 | 22.9 ± 1.12 | 19.0 ± 1.30 |
| CG | 33.2 ± 0.70 | 27.4 ± 1.33 | 25.43 ± 1.20 | 21.5 ± 0.94 | 31.5 ± 1.20 | 26.3 ± 1.46 | 24.1 ± 1.38 | 20.4 ± 0.98 |
| NS | 32.3 ± 1.50 | 27.2 ± 0.95 | 25.72 ± 1.80 | 20.5 ± 1.37 | 32.1 ± 1.50 | 25.8 ± 1.13 | 23.9 ± 0.95 | 19.48 ± 1.80 |
| ZY | 33.3 ± 1.12 | 27.1 ± 1.17 | 25.47 ± 1.40 | 21.4 ± 1.22 | 31.6 ± 1.10 | 25.7 ± 1.20 | 23.8 ± 1.05 | 20.3 ± 1.10 |
| UB | 32.9 ± 1.13 | 26.5 ± 1.08 | 24.39 ± 1.18 | 20.5 ± 1.30 | 31.2 ± 1.10 | 25.1 ± 1.32 | 23.2 ± 0.88 | 19.8 ± 1.18 |

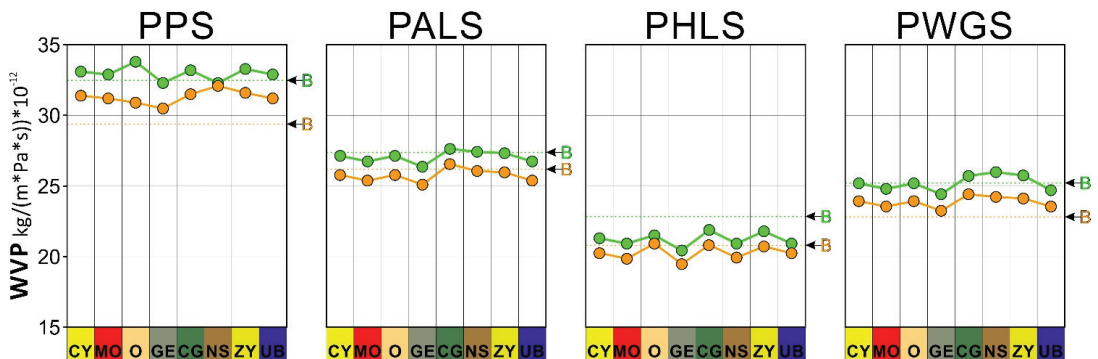


Figure 4. Water vapor permeability of the binders and their corresponding pigmented pastes (PPS, PALS, PHLS and PWGS). The green circles and the orange circles correspond to the permeability at 28 and 120 days respectively. The dotted line and the green letter B correspond to the specific binder at 28 days. The dotted line and the orange letter B correspond to the specific binder at 120 days.

After 28 days, the average permeability for the PPS + PIGMENT samples was $33\text{kg}/(\text{m}\cdot\text{Pa}\cdot\text{s})\cdot 10^{-2}$. The maximum value was $33.3 \pm 1.12\text{kg}/(\text{m}\cdot\text{Pa}\cdot\text{s})\cdot 10^{-12}$ for the sample containing the ZY pigment, and the minimum value was $32.3 \pm 1.3\text{kg}/(\text{m}\cdot\text{Pa}\cdot\text{s})\cdot 10^{-12}$ for the sample containing the GE pigment.

In the case of the PALS + pigment samples, the average representative value for the group is $26.83\text{kg}/(\text{m}\cdot\text{Pa}\cdot\text{s})\cdot 10^{-12}$. The maximum value was $27.4 \pm 1.33\text{kg}/(\text{m}\cdot\text{Pa}\cdot\text{s})\cdot 10^{-12}$ for the sample containing the CG pigment, and the minimum value was $26.1 \pm 1.20\text{kg}/(\text{m}\cdot\text{Pa}\cdot\text{s})\cdot 10^{-12}$ for the sample containing the GE pigment.

The average value of the PWGS + PIGMENT sample group was $24.8\text{kg}/(\text{m}\cdot\text{Pa}\cdot\text{s}) \cdot 10^{-12}$. There was a maximum value of $25.72 \pm 1.8\text{kg}/(\text{m}\cdot\text{Pa}\cdot\text{s}) \cdot 10^{-12}$ for the NS samples and a minimum value of $24.1 \pm 1.11\text{kg}/(\text{m}\cdot\text{Pa}\cdot\text{s}) \cdot 10^{-12}$ for the GE samples.

Finally, the lowest values were noticed in the plaster and hydraulic lime pastes (PHLS + PIGMENT), the average value being $20.8\text{kg}/(\text{m}\cdot\text{Pa}\cdot\text{s}) \cdot 10^{-12}$. The maximum value was $21.5 \pm 0.94\text{kg}/(\text{m}\cdot\text{Pa}\cdot\text{s}) \cdot 10^{-12}$ for the CG samples, and the minimum value was $20.0 \pm 1.50\text{kg}/(\text{m}\cdot\text{Pa}\cdot\text{s}) \cdot 10^{-12}$ for the GE samples.

It is deduced from the overall analysis that the substitution of the plaster (−15%) in the different pastes by air lime, sodium silicate and hydraulic lime resulted in lower permeability of the compound. In the different mixes, over time (120 days), it was observed that the values decreased in all cases, confirming compaction of the samples. We recorded reductions in the values of between 8.50% for the PPS + O samples and 0.60% for the PPS + NS samples, for the 28 and 120 days. For the remaining pastes, the values varied between 4% and 5% for each period of study.

3.3. Mechanical Tests

The results obtained in the mechanical tests display differences for the different mixes, in terms of both compressive and flexural strength, during the test period (120 days). The results obtained from the mechanical tests are set out in Table 6 (samples without added pigments) and Table 7 and Figure 5 (binders and samples after 120 days).

Table 6. Results of the mechanical tests (120 days) and standard deviation for the different pastes tested.

| Samples | Compressive Strength (MPa) | | Flexural Strength (MPa) | |
|---------|----------------------------|----------|-------------------------|----------|
| | | σ | | σ |
| PP | 5.40 | 0.02 | 2.25 | 0.03 |
| PAL | 5.62 | 0.04 | 2.93 | 0.06 |
| PHL | 9.79 | 0.03 | 3.90 | 0.05 |
| PWG | 8.65 | 0.01 | 3.51 | 0.04 |

Table 7. Results for mechanical tests and standard deviation for the different pastes containing added pigments tested after 120 days.

| Samples | Compressive Strength (MPa) | | Flexural Strength (MPa) | |
|-------------|----------------------------|----------|-------------------------|----------|
| | | σ | | σ |
| PPS | | | | |
| PPS + CY | 5.40 | 0.03 | 2.24 | 0.02 |
| PPS + MO | 5.42 | 0.05 | 2.25 | 0.04 |
| PPS + O | 5.43 | 0.04 | 2.24 | 0.03 |
| PPS + GE | 5.52 | 0.02 | 2.32 | 0.03 |
| PPS + CG | 5.42 | 0.03 | 2.26 | 0.02 |
| PPS + NS | 5.45 | 0.04 | 2.21 | 0.05 |
| PPS + ZY | 5.30 | 0.05 | 2.22 | 0.04 |
| PPS + UB | 5.36 | 0.03 | 2.23 | 0.03 |
| PALS | | | | |
| PALS + CY | 5.61 | 0.02 | 2.91 | 0.04 |
| PALS + MO | 5.64 | 0.05 | 2.92 | 0.05 |
| PALS + O | 5.63 | 0.04 | 2.93 | 0.06 |
| PALS + GE | 5.74 | 0.05 | 2.94 | 0.03 |
| PALS + CG | 5.56 | 0.03 | 2.91 | 0.06 |
| PALS + NS | 5.60 | 0.02 | 2.93 | 0.05 |
| PALS + ZY | 5.58 | 0.05 | 2.94 | 0.04 |
| PALS + UB | 5.62 | 0.03 | 2.92 | 0.02 |

Table 7. Cont.

| Samples | Compressive Strength (MPa) | | Flexural Strength (MPa) | |
|-------------|----------------------------|----------|-------------------------|----------|
| PPS | | | | |
| | | σ | | σ |
| PWGS | | | | |
| | | σ | | σ |
| PWGS + CY | 8.66 | 0.03 | 3.50 | 0.02 |
| PWGS + MO | 8.68 | 0.01 | 3.51 | 0.01 |
| PWGS + O | 8.67 | 0.02 | 3.50 | 0.06 |
| PWGS + GE | 8.72 | 0.01 | 3.52 | 0.04 |
| PWGS + CG | 8.68 | 0.04 | 3.52 | 0.05 |
| PWGS + NS | 8.71 | 0.05 | 3.48 | 0.03 |
| PWGS + ZY | 8.65 | 0.06 | 3.48 | 0.06 |
| PWGS + UB | 8.62 | 0.01 | 3.49 | 0.02 |
| PHLS | | | | |
| | | σ | | σ |
| PHLS + CY | 9.80 | 0.02 | 3.92 | 0.05 |
| PHLS + MO | 9.76 | 0.04 | 3.91 | 0.06 |
| PHLS + O | 9.73 | 0.01 | 3.93 | 0.04 |
| PHLS + GE | 9.91 | 0.02 | 3.92 | 0.03 |
| PHLS + CG | 9.80 | 0.05 | 3.94 | 0.03 |
| PHLS + NS | 9.82 | 0.03 | 3.91 | 0.05 |
| PHLS + ZY | 9.84 | 0.03 | 3.92 | 0.02 |
| PHLS + UB | 9.85 | 0.03 | 3.90 | 0.07 |

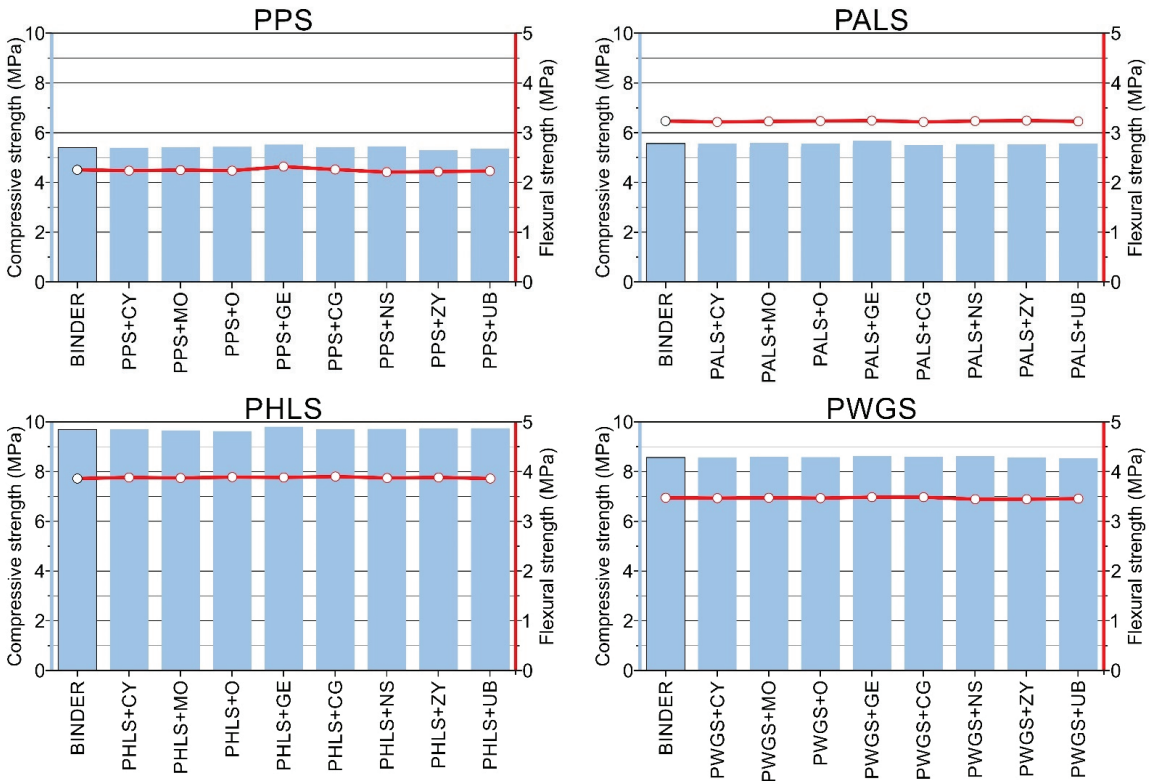


Figure 5. Mechanical strength values (MPa) of binders at 120 days and their corresponding pigment-colored pastes (PPS, PALS, PHLS and PWGS). Blue bar plot corresponds to compressive strength. Line plot with red circles corresponds to flexural strength.

3.3.1. Compressive Strength

PPS + Pigment Samples

In the plaster paste samples containing added pigment (PPS + PIGMENT), the maximum compressive strength after 120 days was $5.52 \text{ MPa} \pm 0.02$ for the PPS + PGE (Green Earth pigment) sample. The minimum value was $5.3 \text{ MPa} \pm 0.05$ for the PPS + PZY (Zinc yellow pigment) pigment sample.

In percentage terms, the variation among the pastes containing added pigment was 3.98%, and the difference among the pastes without added pigment was 2.17%. This shows full compatibility between the pastes and the pigments used.

PALS + Pigment Samples

The compressive strength of the plaster + lime pastes exhibits a slight increase in the results, compared to the previous group. In this case, the values range between $5.74 \text{ MPa} \pm 0.05$ for the PALS + PGE (Green Earth pigment) samples and $5.56 \text{ MPa} \pm 0.03$ for the PALS + PCG (chromium green pigment) samples. This represents an average increase of 3.74% compared to the pure plaster samples.

PWGS + Pigment Samples

The compressive strength levels of the plaster + sodium silicate pastes were higher compared to the previous groups. In this case, the values range between $8.72 \text{ MPa} \pm 0.01$ for the PWGS + PGE (Green Earth pigment) samples and $8.62 \text{ MPa} \pm 0.01$ for the PWGS + PUB (Ultramarine Blue pigment) samples. This represents average increases of 37.6% compared to the pure plaster samples and 35.2% compared to the plaster and air lime samples.

PHLS + Pigment Samples

The results for this group of samples are the highest of all those tested, reaching maximum values of $9.91 \text{ MPa} \pm 0.02$ for the samples containing added pigment (PHLS + PGE (Green Earth pigment) and $9.79 \text{ MPa} \pm 0.03$ for the samples without added pigment; percentage differences are less than 1% between them. In relation to the other groups, a significant increase was also confirmed, these being 45% compared to the pure plaster samples (PPS), 42.7% compared to the plaster and air lime (PALS) samples and 11.6% compared to the pastes containing geopolymers (PWGS).

Overall, it was observed that the compressive strength results for the samples containing pigments experienced improvements in resistance capacity, the least resistant being the PPS pastes, followed by the PALS and the PWGS, and the most resistant being the PHLS pastes.

The literature consulted [70,71] confirms that, in general, an increase in compressive strength for this type of paste is the consequence of a variation in the microstructure of the hardened matrix.

Furthermore, [72,73] established that an increase may also be the result of chemical reactions between the components (plaster + hydraulic lime) in the presence of water. The presence of plaster as a replacement for the lime results in faster hydration, and consequently, accelerated setting.

Meanwhile, it was observed that the addition of water glass to the mixes studied resulted in the formation of amorphous silica, which acted as a siliceous aggregate in the resulting paste, thereby increasing the mechanical strength.

Finally, in the samples containing hydraulic lime, an increase in the hydration rate was confirmed due to the presence of calcium silicates, whose role is that of an active additive (catalyst) in these pastes.

The analysis of the samples containing pigments for the four pastes concluded that in all cases, the maximum value was associated with the samples containing the PGE (Green Earth pigment). Previous studies [73–75] confirmed that MgO in both the pigment itself and in the binding material acts as a fraction of aggregate material, increasing the compressive strength of the mixes containing added pigments.

3.3.2. Flexural Strength

Where flexural strength is concerned, the results show a very similar tendency to those observed in the compressive strength testing (Tables 6 and 7). In this case, it is observed that strength increased when part of the plaster was replaced by other binders, such as air lime, sodium silicate or hydraulic lime.

During the period of study, the maximum values were obtained for the plaster + hydraulic lime samples (PHLS samples). Those maximum values were up to 3.94 MPa \pm 0.03 (average value of 3.92 MPa). Next were the plaster + water glass samples (PWGS samples), which reached an average value of 3.50 MPa, representing a percentage decrease of 10.7%. In third place were the plaster + air lime samples (PALS samples), which obtained average flexural strength of 2.93 MPa. Finally, the minimum values were achieved by the pure plaster samples (PPS samples), their average value being 2.25 MPa.

In percentage terms, the differences between the groups are significant. The plaster + hydraulic lime samples were 10.7% stronger than the plaster + water glass samples, 25.2% stronger than the plaster + air lime samples and 42.6% stronger than the pure plaster samples.

After comparing the results of the samples containing added pigments, no real difference was observed among them. On comparing the samples without added pigments with the colored samples in each group, it was observed that in the plaster + hydraulic lime samples (PHLS samples) the flexural strength results were very similar to those for the sample without added pigment, there being a difference of <1% in all cases. The samples containing plaster + water glass (GWS sample) obtained similar differences, slightly greater than for the previous group, although still less than <1%. The samples containing plaster + air lime (PALS samples) displayed differences of 2%. Lastly, for the pure plaster samples (PPS samples) the differences were also minor, slightly above 2% (2.17%).

3.4. Color Tests

Figure 6 shows the color coordinates L^* , a^* and b^* for the mixes studied in the different media tested, in the test phases after 28 and 120 days. Each pigment displays the luminosity values L^* on the left and the chromaticity diagram a^*-b^* on the right. In all cases, the black circles represent the coordinates of the pure pigment, the blue circles the binders, the white circles the pastes after 28 days and the grey circles the pastes after 120 days.

With regard to the binders, they all feature very small tonal amounts (a^*-b^*) of red and blue, except the water glass, whose tones are blue and green. The luminosities (L^*) are extremely high in all cases, with values which are very close to 100%, generating a visual impression that is very similar to white. Meanwhile, the pigments used in all of the mixes in proportions of 20% feature shades which are characteristic of the color palette designed, and they are obviously affected by their interactions with the different binders on forming the pastes.

In terms of shade, the CY pigment is composed of a significant proportion of yellow and also features a considerable amount of green (a^*-b^*). The luminosity of this chromium pigment is very close to 100%. The luminosity of the pastes hardened for 28 or 120 days tended to differ, darkening in some way by approximately 5%; the color saturation decreased more markedly—by up to 40%.

The MO pigment is largely composed of yellow and red tones (a^*-b^*), and the luminosity is low: slightly higher than 50%. The changes induced by the different binders increased the luminosity in all cases, this being greater after 120 days, with values of close to 13%. In the chromaticity diagram the saturation of the pastes drastically reduces to levels which are very close to those of the binders (\approx 80%). Equally noteworthy is the reduction induced by the binders in relation to the yellow shades, at the expense of the associated red shade.

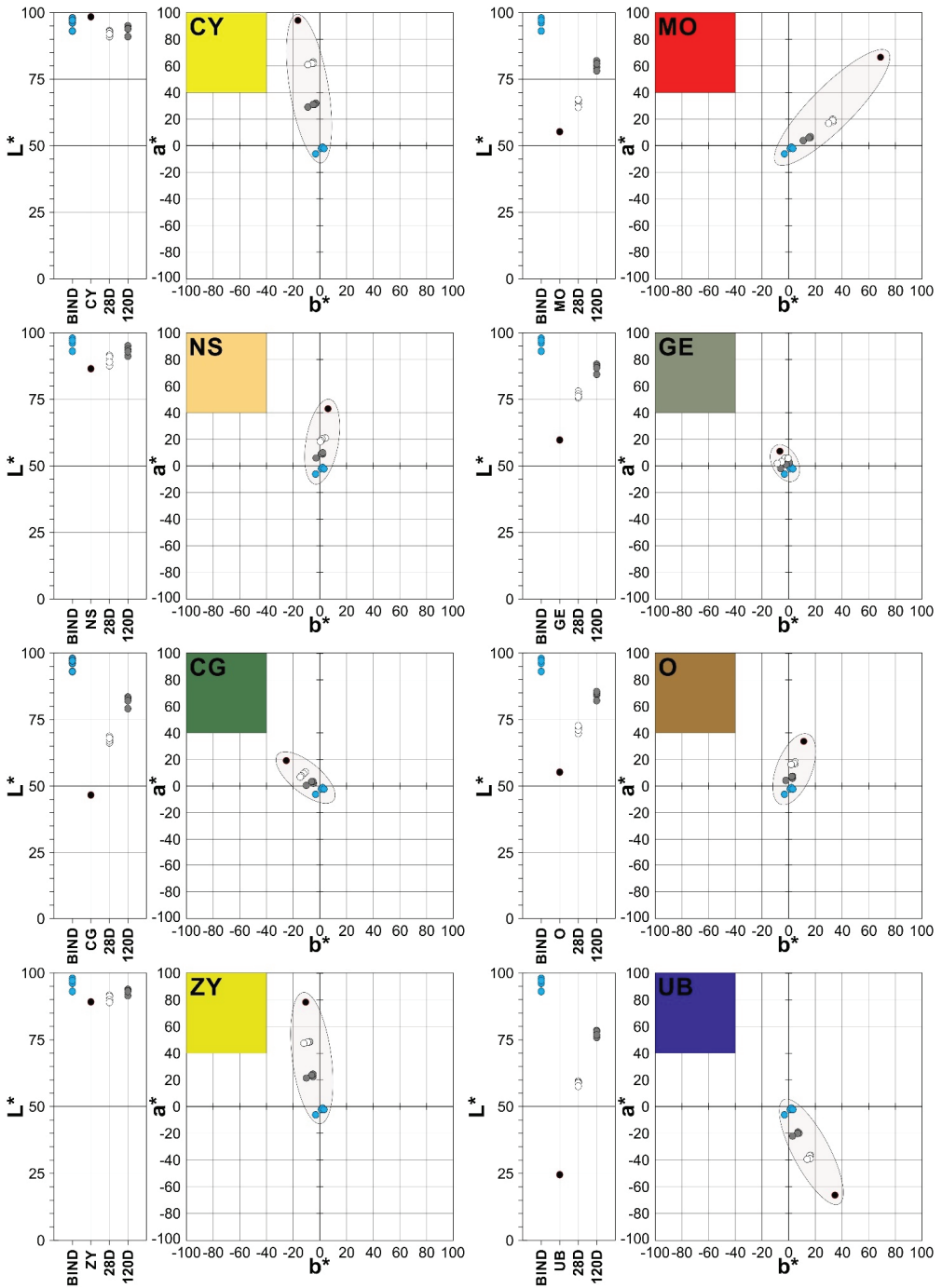


Figure 6. CIELab1976 colour space representation of binders and their corresponding pigment-coloured pastes (PPS, PALS, PHLS and PWGS). Plot L^* , indicates brightness values of the different samples. Plot a^*-b^* , indicates chromaticity values of the different samples. Blue circles are the binder samples without pigment; black circles are the pigment samples; white circles are the paste samples at 28 days; grey circles are the paste samples at 120 days.

The NS pigment has high luminosity (L^*) values, of close to 90%, and where chromaticity (a^*b^*) is concerned, yellow stands out as the principal shade alongside small amounts of red. The pastes obtained provoke subsaturation, with values which are close to those of the binders, although the relative reduction was $\approx 10\%$. The luminosity increased $\approx 14\%$. It is notable how there were significant reductions in the yellow and red shades, and the red was replaced by green in the PWGS paste, after 120 days.

The GE pigment has average luminosity ($\approx 60\%$) and chromaticity values (a^*b^*), along with comparatively small amounts of yellow and green. The pastes featured increased luminosity ($\approx 12\%$), particularly those measured after 120 days, contrary to what happens in the chromaticity diagram, where the pastes display relative subsaturation of $\approx 8\%$ after 28 and 120 days.

The CG pigment has low luminosity ($< 50\%$) and chromaticity components (a^*b^*) based on green and yellow shades. The variations in luminosity were significant, particularly the increase in white, which occurred in the pastes after 28 and 120 days ($\approx 15\%$). The most significant variations in terms of chromaticity stemmed from subsaturation, which arose in the mixes after 28 and 120 days; these have a clear tendency towards the binder values ($\approx 3\%$).

The O pigment reached luminosity values slightly higher than 50% and tonal proportions (a^*b^*) of yellow and red. The changes were similar to those experienced by the rest of the pigments and their pastes: a clear increase in luminosity ($\approx 6\%$) and a substantial loss of saturation ($\approx 14\%$). The PWGS sample after 120 days provided a slight green tone compared to the reddish tones of the other samples (PPS, PALS and PHLS).

The ZY pigment has very high luminosity values ($\approx 90\%$), whilst the chromaticity includes tonal components based on yellow and green. The variations experienced by the pastes on hardening with the binders were very similar to those described in all cases: increased luminosity ($\approx 3\%$) and loss of saturation ($\approx 30\%$).

The UB pigment has low L^* values, making it dark ($\approx 25\%$). The changes induced by the inclusion of the binders studied increased luminosity by up to ($\approx 11\%$) after 120 days. The chromaticity values include a blue tonal component, which dominates in relation to the red tone, which represents half the amount of the blue. The pastes provoked a loss of saturation which left it close to the binders' values ($\approx 33\%$).

Table 8 shows that all of the paste samples studied experienced total color variations (ΔE) clearly detectable by the human eye $\Delta E \geq 3$ [76] after 28 or 120 days. These changes are determined by the chroma variation (ΔC), which entails variations in saturation (subsaturations). This doubled after 120 days in the majority of cases, compared to the amount after 28 days. Likewise, the increased luminosity (ΔL) induced by the binders used to prepare the pastes is a decisive factor in the total color variation (ΔE). The only exception of note occurred in the mixes containing pigment O, whose variations just exceeded the limit of detection by the human eye.

Table 8. CIE Lab* 1976 values for the pigments and pastes used in this study and total color variations (ΔE), chromaticity variations (ΔC) and luminosity variations (ΔL) of the pigments used in the preparation of the pastes after 28 and 120 days.

| | 28D | | | 120D | | | 28D | 120D | 28D | 120D | 28D | 120D |
|-----------------------|--------|-------|-------|--------|-------|-------|------------|------------|------------|------------|------------|------------|
| | a^* | b^* | L^* | a^* | b^* | L^* | ΔE | ΔE | ΔC | ΔC | ΔL | ΔL |
| PIGMENT CY | -17.03 | 92.10 | 98.40 | -17.03 | 92.10 | 98.40 | 0.00 | 0.00 | 0.00 | 0.00 | 0.00 | 0.00 |
| PPS + CY (80–20%) | -5.00 | 62.00 | 93.20 | -3.99 | 31.09 | 95.02 | -23.80 | -23.84 | -31.46 | -62.32 | -5.20 | -3.38 |
| PALS + CY (65–15–20%) | -5.00 | 63.12 | 92.80 | -3.00 | 32.00 | 94.00 | -23.51 | -23.58 | -30.34 | -61.52 | -5.60 | -4.40 |
| PHLS + CY (65–15–20%) | -6.00 | 62.00 | 91.03 | -5.00 | 31.00 | 91.00 | -25.55 | -25.60 | -31.37 | -62.26 | -7.37 | -7.40 |
| PWGS + CY (65–15–20%) | -9.00 | 61.00 | 92.00 | -9.00 | 29.07 | 93.91 | -25.10 | -25.10 | -32.00 | -63.23 | -6.40 | -4.49 |
| \bar{X} | -6.25 | 62.03 | 92.26 | -5.25 | 30.79 | 93.48 | -24.49 | -24.53 | -31.29 | -62.33 | -6.14 | -4.92 |
| σ | 1.89 | 0.87 | 0.96 | 2.63 | 1.23 | 1.73 | 0.99 | 0.97 | 0.69 | 0.70 | 0.96 | 1.73 |

Table 8. Cont.

| | 28D | | | 120D | | | 28D | 120D | 28D | 120D | 28D | 120D |
|-----------------------|--------|--------|-------|--------|--------|-------|--------|--------|--------|--------|-------|-------|
| | a* | b* | L* | a* | b* | L* | ΔE | ΔE | ΔC | ΔC | ΔL | ΔL |
| PIGMENT MO | 74.20 | 65.13 | 55.40 | 74.20 | 65.13 | 55.40 | 0.00 | 0.00 | 0.00 | 0.00 | 0.00 | 0.00 |
| PPS + MO (80–20%) | 33.40 | 18.41 | 67.09 | 16.14 | 6.09 | 81.88 | −36.04 | −41.79 | −60.59 | −81.48 | 11.69 | 26.48 |
| PALS + MO (65–15–20%) | 33.00 | 20.01 | 67.00 | 16.15 | 7.00 | 81.00 | −35.89 | −41.45 | −60.14 | −81.13 | 11.60 | 25.60 |
| PHLS + MO (65–15–20%) | 32.99 | 19.05 | 65.00 | 15.08 | 6.03 | 78.14 | −37.87 | −43.82 | −60.63 | −82.49 | 9.60 | 22.74 |
| PWGS + MO (65–15–20%) | 30.00 | 17.02 | 66.00 | 11.00 | 4.00 | 81.00 | −38.74 | −44.17 | −64.24 | −87.03 | 10.60 | 25.60 |
| \bar{X} | 32.35 | 18.62 | 66.27 | 14.59 | 5.78 | 80.51 | −37.14 | −42.81 | −61.40 | −83.03 | 10.87 | 25.11 |
| σ | 1.58 | 1.25 | 0.98 | 2.45 | 1.27 | 1.63 | 1.40 | 1.39 | 1.91 | 2.72 | 0.98 | 1.63 |
| PIGMENT NS | 11.40 | 37.20 | 55.47 | 11.40 | 37.20 | 55.47 | 0.00 | 0.00 | 0.00 | 0.00 | 0.00 | 0.00 |
| PPS + NS (80–20%) | 5.00 | 16.99 | 71.80 | 2.79 | 5.88 | 85.00 | 6.20 | 6.08 | −21.20 | −32.40 | 16.33 | 29.53 |
| PALS + NS (65–15–20%) | 4.99 | 18.00 | 71.00 | 3.00 | 6.99 | 84.50 | 5.66 | 5.55 | −20.23 | −31.30 | 15.53 | 29.03 |
| PHLS + NS (65–15–20%) | 4.00 | 17.07 | 69.99 | 2.40 | 7.01 | 82.10 | 4.40 | 4.33 | −21.38 | −31.50 | 14.52 | 26.63 |
| PWGS + NS (65–15–20%) | 1.99 | 16.04 | 71.09 | −2.00 | 4.03 | 84.10 | 5.15 | 5.15 | −22.74 | −34.41 | 15.62 | 28.63 |
| \bar{X} | 4.00 | 17.03 | 70.97 | 1.55 | 5.98 | 83.93 | 5.35 | 5.28 | −21.39 | −32.40 | 15.50 | 28.46 |
| σ | 1.42 | 0.80 | 0.74 | 2.38 | 1.40 | 1.27 | 0.77 | 0.74 | 1.04 | 1.42 | 0.74 | 1.27 |
| PIGMENT GE | −6.00 | 10.00 | 59.15 | −6.00 | 10.00 | 59.15 | 0.00 | 0.00 | 0.00 | 0.00 | 0.00 | 0.00 |
| PPS + GE (80–20%) | −3.00 | 3.00 | 78.00 | −1.01 | 0.30 | 87.88 | 17.83 | 17.78 | −7.42 | −10.61 | 18.85 | 28.73 |
| PALS + GE (65–15–20%) | −3.00 | 4.00 | 77.00 | −1.00 | 1.00 | 87.62 | 16.87 | 16.82 | −6.66 | −10.25 | 17.85 | 28.47 |
| PHLS + GE (65–15–20%) | −2.99 | 3.02 | 76.13 | −2.00 | 0.99 | 84.40 | 15.96 | 15.93 | −7.41 | −9.43 | 16.98 | 25.25 |
| PWGS + GE (65–15–20%) | −6.09 | 1.99 | 76.99 | −6.07 | −2.00 | 86.85 | 16.97 | 16.97 | −5.26 | −5.27 | 17.84 | 27.70 |
| \bar{X} | −3.77 | 3.00 | 77.03 | −2.52 | 0.07 | 86.69 | 16.91 | 16.87 | −6.69 | −8.89 | 17.88 | 27.54 |
| σ | 1.55 | 0.82 | 0.76 | 2.41 | 1.42 | 1.59 | 0.76 | 0.76 | 1.02 | 2.46 | 0.76 | 1.59 |
| PIGMENT CG | −25.30 | 19.02 | 47.04 | −25.30 | 19.02 | 47.04 | 0.00 | 0.00 | 0.00 | 0.00 | 0.00 | 0.00 |
| PPS + CG (80–20%) | −12.00 | 9.00 | 68.00 | −5.00 | 2.00 | 83.00 | 12.94 | 12.08 | −16.65 | −26.27 | 20.96 | 35.96 |
| PALS + CG (65–15–20%) | −11.99 | 8.99 | 67.04 | −4.99 | 3.01 | 82.89 | 12.00 | 11.13 | −16.67 | −25.82 | 20.00 | 35.85 |
| PHLS + CG (65–15–20%) | −12.00 | 9.00 | 66.30 | −6.02 | 2.95 | 79.09 | 11.28 | 10.48 | −16.65 | −24.95 | 19.26 | 32.05 |
| PWGS + CG (65–15–20%) | −14.00 | 6.89 | 67.00 | −10.01 | 0.09 | 82.07 | 12.10 | 11.40 | −16.05 | −21.64 | 19.96 | 35.03 |
| \bar{X} | −12.50 | 8.47 | 67.09 | −6.51 | 2.01 | 81.76 | 12.08 | 11.27 | −16.50 | −24.67 | 20.05 | 34.72 |
| σ | 1.00 | 1.05 | 0.70 | 2.39 | 1.36 | 1.83 | 0.68 | 0.66 | 0.30 | 2.09 | 0.70 | 1.83 |
| PIGMENT O | 7.40 | 45.30 | 87.20 | 7.40 | 45.30 | 87.20 | 0.00 | 0.00 | 0.00 | 0.00 | 0.00 | 0.00 |
| PPS + O (80–20%) | 4.01 | 20.99 | 91.20 | 1.97 | 8.98 | 95.10 | −4.87 | −4.94 | −24.53 | −36.71 | 4.00 | 7.90 |
| PALS + O (65–15–20%) | 4.02 | 21.00 | 91.49 | 2.00 | 10.00 | 93.80 | −4.59 | −4.65 | −24.52 | −35.70 | 4.29 | 6.60 |
| PHLS + O (65–15–20%) | 4.00 | 20.98 | 89.04 | 2.00 | 9.00 | 91.25 | −6.98 | −7.04 | −24.54 | −36.68 | 1.84 | 4.05 |
| PWGS + O (65–15–20%) | 0.99 | 19.00 | 91.00 | −2.94 | 5.99 | 93.01 | −5.58 | −5.53 | −26.87 | −39.23 | 3.80 | 5.81 |
| \bar{X} | 3.26 | 20.49 | 90.68 | 0.76 | 8.49 | 93.29 | −5.50 | −5.54 | −25.12 | −37.08 | 3.48 | 6.09 |
| σ | 1.51 | 1.00 | 1.11 | 2.47 | 1.73 | 1.61 | 1.07 | 1.07 | 1.17 | 1.51 | 1.11 | 1.61 |
| PIGMENT ZY | −10.99 | 78.08 | 88.10 | −10.99 | 78.08 | 88.10 | 0.00 | 0.00 | 0.00 | 0.00 | 0.00 | 0.00 |
| PPS + ZY (80–20%) | −8.00 | 48.00 | 91.00 | −5.00 | 22.00 | 94.00 | −15.04 | −15.23 | −30.19 | −56.29 | 2.90 | 5.90 |
| PALS + ZY (65–15–20%) | −8.00 | 47.99 | 90.10 | −5.00 | 24.02 | 93.20 | −15.84 | −16.03 | −30.20 | −54.31 | 2.00 | 5.10 |
| PHLS + ZY (65–15–20%) | −9.00 | 48.03 | 89.00 | −6.00 | 23.20 | 91.40 | −16.70 | −16.92 | −29.98 | −54.89 | 0.90 | 3.30 |
| PWGS + ZY (65–15–20%) | −11.79 | 47.10 | 91.16 | −9.99 | 21.04 | 93.00 | −14.95 | −15.14 | −30.30 | −55.56 | 3.06 | 4.90 |
| \bar{X} | −9.20 | 47.78 | 90.32 | −6.50 | 22.57 | 92.90 | −15.63 | −15.83 | −30.17 | −55.26 | 2.22 | 4.80 |
| σ | 1.79 | 0.45 | 0.99 | 2.38 | 1.31 | 1.09 | 0.82 | 0.83 | 0.13 | 0.85 | 0.99 | 1.09 |
| PIGMENT UB | 36.60 | −65.67 | 24.98 | 36.60 | −65.67 | 24.98 | 0.00 | 0.00 | 0.00 | 0.00 | 0.00 | 0.00 |
| PPS + UB (80–20%) | 16.00 | −37.99 | 59.00 | 8.00 | −20.00 | 78.00 | −7.25 | −8.59 | −33.96 | −53.64 | 34.02 | 53.02 |
| PALS + UB (65–15–20%) | 15.99 | −37.00 | 58.04 | 7.00 | −19.04 | 77.08 | −8.56 | −10.04 | −34.87 | −54.89 | 33.06 | 52.10 |
| PHLS + UB (65–15–20%) | 16.01 | −38.98 | 57.51 | 6.82 | −20.04 | 75.90 | −7.93 | −9.41 | −33.04 | −54.01 | 32.53 | 50.92 |
| PWGS + UB (65–15–20%) | 14.02 | −39.40 | 58.70 | 3.00 | −22.10 | 78.03 | −7.15 | −8.46 | −33.36 | −52.88 | 33.72 | 53.05 |
| \bar{X} | 15.51 | −38.34 | 58.31 | 6.21 | −20.30 | 77.25 | −7.72 | −9.13 | −33.81 | −53.86 | 33.33 | 52.27 |
| σ | 0.99 | 1.07 | 0.67 | 2.20 | 1.29 | 1.00 | 0.66 | 0.74 | 0.81 | 0.84 | 0.67 | 1.00 |

All of these changes are represented in the form of a color chart in Figure 7, taking into account the average values for a*, b* and L* for each group of samples. For each pigment and paste type, the results are shown for 28 days and 120 days according to their color coordinates (CIELab 1976).

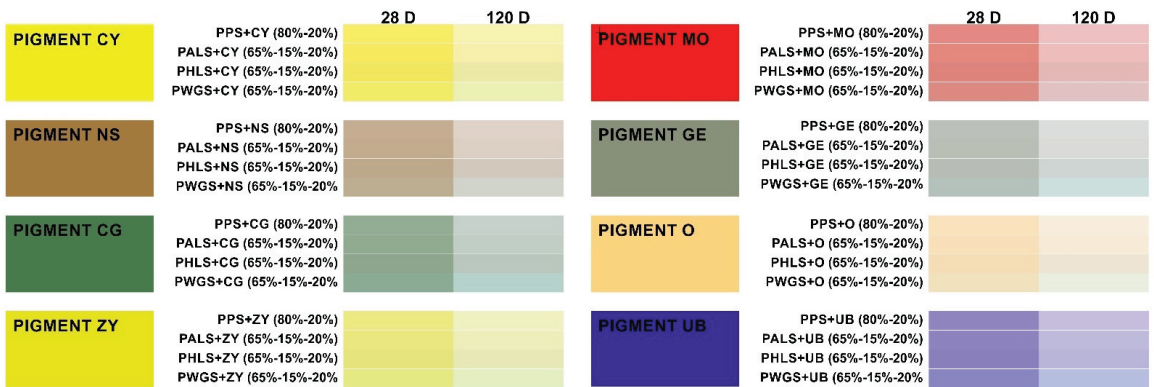


Figure 7. Color chart for the different mixes and inorganic pigments used, with an indication of their color code for both of the test phases (28 days and 120 days).

4. Conclusions

1. The characterization of the products primarily confirmed the suitability of the pastes containing pigments for use in the most common applications for mixes of this kind.
2. The results obtained in relation to mechanical strength confirmed the increases when air lime and hydraulic lime are used. Likewise, the inclusion of water glass induced improvements in all cases with regard to the samples containing plaster, whilst not outperforming the pastes containing hydraulic lime.
3. From previous studies and the mechanical results obtained, it can be concluded that the presence of magnesium silica aluminates could have been partly responsible for the increases in compressive strength of the mixes containing Green Earth pigment.
4. The crystallization of gypsum minerals, observed in all of the mixes, helped to consolidate the shrinkage cracks which appeared in them, improving their mechanical strength values, just as in the cases of neofomed calcium carbonate and belite originating in PALS and PHLS or sodium metasilicate in the PWGS samples.
5. The water vapor permeability values were high in all cases due to the dominant presence of plaster; nevertheless, the mixes of binders and pigments had reduced values: by around 15% for the pastes after 28 days, and by 25% for the mixes after 120 days.
6. Where the values obtained in the mechanical tests are concerned, the results either coincide with those observed in similar studies [77,78] or are even higher, as in the case of [79]. A similar observation can be made for amorphous silica precipitates in the mixes containing water glass.
7. The colorimetric analysis offered total color differences in the pastes containing added pigments, compared to the pure pigments, which were clearly detectable by the human eye in all cases, after 28 and 120 days. Pigment O and its mixes were at the limits of visual perception, the ΔE values being close to three. The main modifications were determined by the variations in chromaticity (ΔC), resulting in subsaturation and duplicating that perception in the majority of cases after 120 days. Meanwhile, the variation in luminosity induced by the whitish appearance of the binders was a decisive factor in the perception of the total color of the pastes.

Author Contributions: Conceptualization, M.P.S.-P. and J.A.D.-S.; methodology, M.P.S.-P. and J.A.D.-S.; validation, M.P.S.-P. and J.A.D.-S.; formal analysis, M.P.S.-P. and J.A.D.-S.; investigation, M.P.S.-P. and J.A.D.-S.; resources, M.P.S.-P., J.A.D.-S., A.V.-V. and T.G.-L.; data curation, M.P.S.-P. and J.A.D.-S.; writing—original draft preparation, M.P.S.-P. and J.A.D.-S.; writing—review and editing, M.P.S.-P., J.A.D.-S., A.V.-V. and T.G.-L.; supervision, M.P.S.-P. and J.A.D.-S., A.V.-V. and T.G.-L. All authors have read and agreed to the published version of the manuscript.

Funding: This research received no external funding.

Institutional Review Board Statement: Not applicable.

Informed Consent Statement: Not applicable.

Data Availability Statement: Not applicable.

Acknowledgments: This work was supported by the REMINE Programme for Research and Innovation Horizon 2020 Marie Skłodowska–Curie Actions and WARMEST H2020-MSCA-RISE-2020 (Marie Skłodowska–Curie Research and Innovation Staff Exchange and was carried out under the auspices of Research Groups RNM 0179 and HUM 629 of the Junta de Andalucía.

Conflicts of Interest: The authors declare no conflict of interest.

References

- Mileto, C.; Vegas, F.; La Spinali, V. Is Gypsum External Rendering Possible? The Use of Gypsum Mortar for Rendering Historic Façades of Valencia's City Centre. *Adv. Mater. Res.* **2011**, *250–253*, 1301–1304. [\[CrossRef\]](#)
- Rampazzi, L.; Corti, C.; Bugini, R.; Sansonetti, A.; Biraghi, M.; Castelletti, L.; Nobile, I.; Orsenigo, C. Thermal analysis and archaeological chronology: The ancient mortars of the site of Baradello (Como, Italy). *Thermochim. Acta* **2013**, *572*, 71–84. [\[CrossRef\]](#)
- Lucolano, F.; Boccarusso, L.; Langella, A. Hemp as eco-friendly substitute of glass fibres for gypsum reinforcement: Impact and flexural behavior. *Compos. Part B Eng.* **2019**, *175*, 107073. [\[CrossRef\]](#)
- Martias, C.; Joliff, Y.; Favotto, C. Effects of the addition of glass fibers, mica and vermiculite on the mechanical properties of a gypsum-based composite at room temperature and during a fire test. *Compos. Part B Eng.* **2014**, *62*, 37–53. [\[CrossRef\]](#)
- Henrik, L.N. Now: 100% wallboard recycling with gypsum recycling international. *Glob. Gypsum Mag.* **2017**, *98*, 122–129.
- Rashad, A.M. Phosphogypsum as a construction material. *J. Clean. Prod.* **2017**, *166*, 732–743. [\[CrossRef\]](#)
- Gencel, O.; Diaz, J.J.D.C.; Sutcu, M.; Koksall, F.; Rabanal, F.P.A.; Martínez-Barrera, G. A novel lightweight gypsum composite with diatomite and polypropylene fibers. *Constr. Build. Mater.* **2016**, *113*, 732–740. [\[CrossRef\]](#)
- Arikan, M.; Sobolev, K. The optimization of a gypsum-based composite material. *Cem. Concr. Res.* **2002**, *32*, 1725–1728. [\[CrossRef\]](#)
- Pang, M.; Sun, Z.; Huang, H. Compressive Strength and Durability of FGD Gypsum-Based Mortars Blended with Ground Granulated Blast Furnace Slag. *Materials* **2020**, *13*, 3383. [\[CrossRef\]](#)
- Flores Medina, N.; Barbero-Barrera, M.M. Mechanical and physical enhancement of gypsum composites through a synergic work of polypropylene fiber and recycled isostatic graphite filler. *Constr. Build. Mater.* **2017**, *131*, 165–177. [\[CrossRef\]](#)
- Wang, W.; Chou, N. The behaviour of coconut fibre reinforced concrete (CFRC) under impact loading. *Constr. Build. Mater.* **2017**, *134*, 452–461. [\[CrossRef\]](#)
- Firmo, J.P.; Correia, J.R.; Bisby, L.A. Fire behaviour of FRP-strengthened reinforced concrete structural elements: A state-of-the-art review. *Compos. Part B Eng.* **2015**, *80*, 198–216. [\[CrossRef\]](#)
- Asprone, D.; Cadoni, E.; Lucolano, F.; Prota, A. Analysis of the strain-rate behavior of a basalt fiber reinforced natural hydraulic mortar. *Cem. Concr. Compos.* **2014**, *53*, 52–58. [\[CrossRef\]](#)
- Hamzaoui, R.; Guessasma, S.; Mecheri, B.; Eshtiaghi, A.M.; Bennabi, A. Microstructure and mechanical performance of modified mortar using hemp fibres and carbon nanotubes. *Mater. Des.* **2014**, *56*, 60–68. [\[CrossRef\]](#)
- Lucolano, F.; Liguori, B.; Colella, C. Fibre-reinforced lime-based mortars: A possible resource for ancient masonry restoration. *Constr. Build. Mater.* **2013**, *38*, 785–789. [\[CrossRef\]](#)
- Thanon Dawood, E.; Meshal Mezal, A. The Properties of Fiber Reinforced Gypsum Plaster. *J. Sci. Res. Rep.* **2014**, *3*, 1339–1347.
- Álvarez, M.; Ferrández, D.; Morón, C.; Atanes-Sánchez, E. Characterization of a New Lightened Gypsum-Based Material Reinforced with Fibers. *Materials* **2021**, *14*, 1203. [\[CrossRef\]](#)
- Majumdar, A.J. Glass fibre reinforced cement and gypsum products. *Proc. Math. Phys. Eng. Sci.* **2006**, *319*, 69–78. [\[CrossRef\]](#)
- Eve, S.; Gomina, M.; Gmouh, A.; Samdi, A.; Moussa, R.; Orange, G. Microstructural and mechanical behaviour of polyamide fibre-reinforced plaster composites. *J. Eur. Ceram. Soc.* **2002**, *22*, 2269–2275. [\[CrossRef\]](#)
- Elsen, J. Microscopy of historic mortars—A review. *Cem. Concr. Res.* **2006**, *36*, 1416–1424. [\[CrossRef\]](#)
- Freire, M.T. Restoration of Ancient Portuguese Interior Plaster Coatings: Characterization and Development of Compatible Gypsum-Based Products. Ph.D. Thesis, University of Lisbon, Lisbon, Portugal, 2016.
- Vasconcelos, F. Considerations about decorative plasterwork. *Bol. Do Mus. Nac. Arte Antiga. V* **1966**, *1*, 34–43. (In Portuguese)
- Conde, M. *Interview to Vítor Serrão*; Pedra & Cal: Faro, Portugal, 2001; pp. 14–16.
- Vieira, E. Stuccos in the context of decorative arts in Portugal. In *I Encontro Sobre Estuques Port.*; Museu do estuque: Oporto, Portugal, 2008; pp. 19–26.
- Brunello, V.; Canevali, C.; Corti, C.; De Kock, T.; Rampazzi, L.; Recchia, S.; Sansonetti, A.; Tedeschi, C.; Cnudde, V. Understanding the Microstructure of Mortars for Cultural Heritage Using X-ray CT and MIP. *Materials* **2021**, *14*, 5939. [\[CrossRef\]](#) [\[PubMed\]](#)
- Brunello, V. Mortars: A Complex Material in Cultural Heritage a Multi-Analytical Procedure to Characterize Historical Mortars. Ph.D. Thesis, Università dell'Insubria, Varese, Italy, 2020.
- Brunello, V.; Corti, C.; Sansonetti, A.; Tedeschi, C.; Rampazzi, L. Non-invasive FTIR study of mortar model samples: Comparison among innovative and traditional techniques. *Eur. Phys. J. Plus* **2019**, *134*, 270. [\[CrossRef\]](#)
- Fischer, H.B.; Vtorov, B. Characterization of historical gypsum mortars. *ZKG Int.* **2002**, *55*, 92–99.

29. Sanz, D. Analysis of Gypsum Used in External Renders Using Geological Techniques. Ph.D. Thesis, Polytechnic University of Madrid, Madrid, Spain, 2009.
30. Franzoni, E.; Sandrolini, F.; Baldazzi, L. Characterization of gypsum-selenite plasters from historic buildings in the Emilia-Romagna region (Italy). In *RILEM TC 203-RHM Final Work, Proceedings of the 2nd Historic Mortars Conference (HMC2010), Prague, Czech Republic, 22–24 September 2011*; Válek, J., Groot, C., Hughes, J.J., Eds.; RILEM Publications s.a.r.l.: Bagneux, France, 2010; pp. 157–164.
31. Igea, J.; Lapuente, P.; Blanco-Varela, M.T.; Martínez-Ramírez, S. Ancient gypsum mortars from Sta. María Magdalena church (Zaragoza, Spain): Advances in technological manufacture. In *RILEM TC 203-RHM Final Work, Proceedings of the 2nd Historic Mortars Conference (HMC2010), Prague, Czech Republic, 22–24 September 2011*; Válek, J., Groot, C., Hughes, J.J., Eds.; RILEM Publications s.a.r.l.: Bagneux, France, 2010; pp. 197–205.
32. Igea, J.; Lapuente, P.; Martínez-Ramírez, S.; Blanco-Varela, M.T. Characterization of mudejar mortars from San Gil Abbot church (Zaragoza, Spain): Investigation of the manufacturing technology of ancient gypsum mortars. *Mater. Constr.* **2012**, *62*, 515–529. [[CrossRef](#)]
33. Igea, J.; Romera, J.; Martínez-Ramírez, S.; Lapuente, P.; Blanco-Varela, M.T. Assessment of the physico-mechanical behaviour of gypsum-lime repair mortars as a function of curing time. *Environ. Earth Sci.* **2013**, *70*, 1605–1618. [[CrossRef](#)]
34. Bel-Anzué, P.; Almagro, A.; Sáez Pérez, M.P.; Rodríguez-Navarro, C. Influence of the calcination process in traditional gypsum with structural behavior. *Ge-Conservación* **2017**, *11*, 79–85. [[CrossRef](#)]
35. Ranesi, A.; Faria, P.; Veiga, M.D.R. Traditional and Modern Plasters for Built Heritage: Suitability and Contribution for Passive Relative Humidity Regulation. *Heritage* **2021**, *4*, 2337–2355. [[CrossRef](#)]
36. Theodoridou, M.; Lofa, M.; Ioannou, I. Historic Gypsum Mortars from Cyprus: Characterization and Reinvention for Conservation Purposes. In Proceedings of the 3rd Historic Mortars Conference HMC2013, Glasgow, Scotland, 11–13 September 2013; pp. 1–8.
37. Middendorf, B.; Knöfel, D. Characterization of historic mortars from buildings in Germany and The Netherlands. In *Conservation of Historic Brick Structures*; Baer, N., Fitz, S., Livingstone, R.A., Eds.; Routledge: Oxfordshire, UK, 1998; pp. 178–196.
38. Tesch, V.; Middendorf, B. Optimised microstructure of calcium sulphate based mortars for the restoration of historic masonry. In *Repair Mortars for Historic Masonry*; Groot, C., Ed.; RILEM: Delft, The Netherlands, 2005; pp. 345–353.
39. Shen, J.; Liang, J.; Lin, X.; Lin, H.; Yu, J.; Yang, Z. Recent Progress in Polymer-Based Building Materials. *Int. J. Polym. Sci.* **2020**, *2020*, 8838160. [[CrossRef](#)]
40. Zhukov, A.D.; Bessonov, I.V.; Bobrova, E.Y.; Gorbunova, E.A.; Demissie, B.A. Materials based on modified gypsum for facade systems. *Nanotechnol. Constr.* **2021**, *13*, 144–149. [[CrossRef](#)]
41. Prałat, K.; Ciemnicka, J.; Koper, A.; Buczkowska, K.E.; Łoś, P. Comparison of the Thermal Properties of Geopolymer and Modified Gypsum. *Polymers* **2021**, *13*, 1220. [[CrossRef](#)] [[PubMed](#)]
42. Zhu, J.; Zhang, R.; Zhang, Y.; He, F. The fractal characteristics of pore size distribution in cement-based materials and its effect on gas permeability. *Sci. Rep.* **2019**, *9*, 17191. [[CrossRef](#)] [[PubMed](#)]
43. Zueno, M.; Tomasin, P.; Alberghina, M.F.; Longo, A.; Marrale, M.; Gallo, S.; Zendri, E. Comparison between mercury intrusion porosimetry and nuclear magnetic resonance relaxometry to study the pore size distribution of limestones treated with a new consolidation product. *Measurement* **2019**, *143*, 234–245. [[CrossRef](#)]
44. Justicia Muñoz, H.; Sáez-Pérez, M.P.; Durán-Suárez, J.A.; Villegas Broncano, M.Á. Estudio de materiales de construcción vernáculos empleados en el patrimonio cultural: Guía para la restauración arquitectónica del Colegio Máximo de Cartuja. Granada-España (siglo XIX). *Inf. Constr.* **2021**, *73*, e381. [[CrossRef](#)]
45. Durán-Suárez, J.A.; Sáez-Pérez, M.P.; Peralbo-Cano, R.; Fernández-Martínez, V.M. Classical construction techniques in 17th century Jesuit architecture. Tools for the restoration of historic heritage. *J. Cult. Herit.* **2018**, *35*, 139479511. [[CrossRef](#)]
46. Ramos Molina, J.; Durán Suárez, J.A.; Sebastián Pardo, E.; Sáez Pérez, M.P. Estudio del estado de conservación de las yeserías del Oratorio de la Madraza de Granada. Identificación, evaluación y análisis. *Inf. Constr.* **2017**, *69*, e175. [[CrossRef](#)]
47. Sáez-Pérez, M.P.; Durán-Suárez, J.A.; Verdú-Vázquez, A.; Gil-López, T. Characterization and chromatic evaluation of gypsum-based pastes for construction and heritage restoration. *Constr. Build. Mater.* **2021**, *307*, 124981. [[CrossRef](#)]
48. Rodríguez-Gordillo, J.; Sáez-Pérez, M.P.; Durán-Suárez, J.A.; García-Beltrán, A. Chromatic behavior of inorganic pigments in restoration mortars (nonhydraulic lime, hydraulic lime, gypsum, and portland cement). A comparative study. *Color Res. Appl.* **2007**, *32*, 65–70. [[CrossRef](#)]
49. Sansonetti, A.; Andreotti, A.; Bertasaa, M.; Bonaduce, I.; Corti, C.; Facchin, L.; La Nasa, J.; Spiriti, A.; Rampazzia, L. Territory and related artworks: Stuccoworks from the Lombard lakes. *J. Cult. Heritage* **2020**, *46*, 382–398. [[CrossRef](#)]
50. Vignola, M.; Bosia, D.; Pennacchio, R.; Zerbini, M. Mortars and plasters produced with earth-based sustainable mixes: A methodology proposal for recovery of vernacular architecture in Roero, Piedmont (Italy). The International Archives of the Photogrammetry, Remote Sensing and Spatial Information Sciences. In Proceedings of the HERITAGE2020 (3DPast+RISK-Terra) International Conference, Valencia, Spain, 9–12 September 2020; Volume XLIV-M-1-2020.
51. Melgosa, M.; Collado-Montero, F.J.; Fernández, E.; Medina, V.J. Estudio colorimétrico de los azulejos del Patio de las Doncellas del Real Alcázar de Sevilla (España). *Boletín Soc. Española Cerámica Y Vidr.* **2015**, *54*, 109–118. [[CrossRef](#)]
52. Rodríguez-Gordillo, J.; Durán-Suárez, J.A.; Sáez-Pérez, M.P. Efecto de Agentes Ambientales en el Cromatismo de Pigmentos con Aglutinantes Pictóricos para su Aplicación en Conservación y Restauración Patrimonial. *PH Investig.* **2014**, *3*, 35–53. Available online: <http://www.iaph.es/phinvestigacion/index.php/phinvestigacion/articulo/view/52> (accessed on 1 February 2022).

53. Rodríguez-Gordillo, J.; Sáez-Pérez, M.P.; Durán-Suárez, J.A. Evaluación Experimental del Comportamiento Cromático de Pigmentos Inorgánicos en Diversos Aglutinantes Pictóricos. *PH Investig.* **2013**, *1*, 41–53. Available online: <http://www.iaph.es/phinvestigacion/index.php/phinvestigacion> (accessed on 1 February 2022).
54. Pridmore, R.W. 14th century example of the four unique hues. *Color Res. Appl.* **2006**, *31*, 364–365. [[CrossRef](#)]
55. Reillon, V.; Berthier, S. Modelization of the optical and colorimetric properties of lusted ceramics. *Appl. Phys. A* **2006**, *83*, 257–265. [[CrossRef](#)]
56. Durán-Suárez, J.A.; García-Beltrán, A.; Sáez-Pérez, M.P.; Rodríguez-Gordillo, J. Evaluation of the chromatic effectiveness of color pigments in restoration materials (lime and Portland cement). *Color Res. Appl.* **2000**, *25*, 286–291. [[CrossRef](#)]
57. Kirchner, E.; van den Kieboom, G.-J.; Njo, L.; Supèr, R.; Gottenbos, R. Observation of visual texture of metallic and pearlescent materials. *Color Res. Appl.* **2007**, *32*, 256–266. [[CrossRef](#)]
58. Sáez-Pérez, M.P.; Rodríguez-Gordillo, J.; Durán-Suárez, J.A. Synthetic white pigments (white titanium and white zinc) in different binding media. Influence of environmental agents. *Constr. Build. Mater.* **2016**, *114*, 151–161. [[CrossRef](#)]
59. UNE-EN 459-1:2016; Cales Para la Construcción. Parte 1: Definiciones, Especificaciones y Criterios de Conformidad. UNE: Portland, ME, USA, 2016.
60. Whitney, D.L.; Evans, B.W. Abbreviations for names of rock-forming minerals. *Am. Mineral.* **2010**, *95*, 185–187. [[CrossRef](#)]
61. AATcc. Colour Index International. Bradford: American Association of Textile Chemist and Colorist and Society of Dyers and Colourists. 2002. Available online: <http://www.colour-index.com/> (accessed on 10 February 2022).
62. Available online: <https://sdc.org.uk/> (accessed on 7 January 2022).
63. Available online: <https://www.aatcc.org/> (accessed on 7 January 2022).
64. Martín Ramos, J.D. Using X Powder—A software package for powder X-ray diffraction analysis. Legal Deposit GR-1001/04; X Powder: Granada, Spain, 2004; ISBN 84-609-1497-6.
65. McLaren, K. The Development of the CIE 1976 (L*a*b*) Uniform Colour-Space and Colour-Difference Formula. *Coloration Technol.* **2008**, *92*, 338–341. [[CrossRef](#)]
66. Judd, D.B.; Wyszecki, G. *Color in Business, Science, and Industry*, 3rd ed.; Wiley-Interscience: New York, NY, USA, 1975; ISBN-13: 978-0471452126.
67. UNE-EN 15803:2010; Conservation of Cultural Property—Test Methods—Determination of Water Vapour Permeability (dp). UNE: Portland, ME, USA, 2010.
68. UNE-EN 1015-11:2000/A1:2007; Methods of Test for Mortar for Masonry—Part 11: Determination of Flexural and Compressive Strength of Hardened Mortar. UNE: Portland, ME, USA, 2007.
69. Fernández-Abascal, H.; Guijarro, M.; Rojo, J.L.; Sanz, J.A. *Cálculo de Probabilidades y Estadística*; Editorial Ariel: Barcelona, Spain, 1994; 282p, ISBN 84-344-2094-5.
70. Pacheco-Torgal, F.; Faria, J.; Jalali, S. Some considerations about the use of lime-cement mortars for building conservation purposes in Portugal: A reprehensible option or a lesser evil? *Constr. Build. Mater.* **2012**, *30*, 488–494. [[CrossRef](#)]
71. Salih, M.A.; Hussein, A.A. Enhancing the compressive strength property of gypsum used in walls plastering by adding lime. *J. Univ. Babylon Eng. Sci.* **2018**, *26*, 3.
72. Prasanna, K.A.; Sanjaya, K.P. Effect of lime and ferrochrome ash (FA) as partial replacement of cement on strength, ultrasonic pulse velocity and permeability of concrete. *Constr. Build. Mater.* **2015**, *94*, 448–457. [[CrossRef](#)]
73. Brunello, V.; Bersani, D.; Rampazzi, L.; Sansonetti, A.; Tedeschi, C. Gypsum based mixes for conservation purposes: Evaluation of microstructural and mechanical features. *Mater. Constr.* **2020**, *70*, 337. [[CrossRef](#)]
74. Atzeni, C.; Massidda, L.; Sanne, U. Magnesian lime. Experimental contribution to interpreting historical data. *Sci. Technol. Conserv. Cult. Herit.* **1996**, *5*, 29–36.
75. Dheilly, R.M.; Bouguerra, A.; Beaudoin, B.; Tudo, J.; Queneudec, M. Hydromagnesite development in magnesian lime mortars. *Mater. Sci. Eng. A* **1999**, *268*, 127–131. [[CrossRef](#)]
76. AATCC (2005) Test Method 173 CMC (TM-173-2005); Calculation of Small Differences for Acceptability. American Association of Textile Chemist and Colorist: Research Triangle, NC, USA, 2006; pp. 311–315.
77. Jara, L.M.S.; Yepes, J.A.F.; Pérez, J.J.P. Analysis of the Resistance to Bending of Gypsum with Added Graphene. *Coatings* **2021**, *11*, 650. [[CrossRef](#)]
78. Čáňková, M.; Konáková, D.; Vejmelková, E.; Bartončková, E.; Keppert, M.; Černý, R. Properties of lime-cement plasters incorporating ceramic powder. *Int. J. Comp. Meth. Exp. Meas* **2017**, *5*, 144–153. [[CrossRef](#)]
79. Krejsová, J.; Doleželová, M. Resistance of mortars with gypsum, lime and composite binders against molds. *Acta Polytech. CTU Proc.* **2019**, *21*, 16–20. [[CrossRef](#)]

Article

Mechanical Properties of Concrete Produced by Light Cement-Based Aggregates

Mais Abdulrazzaq Ibrahim ^{1,*}, Nihat Atmaca ², Ahmed Assim Abdullah ² and Adem Atmaca ³¹ Department of Civil Engineering, Cihan University-Erbil, Kurdistan Region, Erbil 44001, Iraq² Department of Civil Engineering, Engineering Faculty, Gaziantep University, Gaziantep 27310, Turkey³ Department of Mechanical Engineering, Engineering Faculty, Gaziantep University, Gaziantep 27310, Turkey

* Correspondence: mais.ibrahim@cihanuniversity.edu.iq; Tel.: +964-7518263926

Abstract: There is great growing concern regarding the environmental impact of the building and construction industry. Aggregate, one of the most crucial ingredients of concrete, is among the concerns in this regard. There will be a steady increase in demand for aggregates in the near future, but limited natural reserves will not be able to respond to this demand due to the risk of depletion. This current situation is forcing researchers to conduct new and artificial material production techniques that keep the resources within the allowed boundaries. Artificial aggregate production is one of the new methods for sustainable, environmentally friendly material production. The mechanical and environmental properties of lightweight concrete produced via artificial aggregates in different ratios were investigated in this study. Fly ash (FA), ground granulated blast-furnace slag (GGBFS), and quartz powder (QP) were utilized in the production of artificial lightweight aggregate (LWA) by using a special technique known as cold-bonding pelletization. The prepared concrete samples with the artificial aggregates were subjected to compressive, tensile, flexural, and bonding tests. The test results demonstrated that the bonding, tensile, and compressive strength values of lightweight concrete with a 20% GGBFS coarse aggregate replacement ratio of lightweight aggregates increased by 11%, 12%, and 30%, respectively. Moreover, it has been observed that a 41% increase in compressive strength is possible with a 40% QP coarse aggregate replacement ratio of lightweight aggregates. Finally, in addition to significantly impacting the mechanical properties of the lightweight concrete produced via artificial lightweight aggregates, we demonstrated that it is possible to control and reduce the harmful environmental effects of waste materials, such as FA, GGBFS, and QP in the present study.

Keywords: artificial aggregate; lightweight concrete; fly ash; ground granulated blast furnace slag; quartz powder

Citation: Ibrahim, M.A.; Atmaca, N.; Abdullah, A.A.; Atmaca, A. Mechanical Properties of Concrete Produced by Light Cement-Based Aggregates. *Sustainability* **2022**, *14*, 15991. <https://doi.org/10.3390/su142315991>

Academic Editors: Carlos Morón Fernández and Daniel Ferrández Vega

Received: 19 October 2022

Accepted: 29 November 2022

Published: 30 November 2022

Publisher's Note: MDPI stays neutral with regard to jurisdictional claims in published maps and institutional affiliations.



Copyright: © 2022 by the authors. Licensee MDPI, Basel, Switzerland. This article is an open access article distributed under the terms and conditions of the Creative Commons Attribution (CC BY) license (<https://creativecommons.org/licenses/by/4.0/>).

1. Introduction

It is crucial to keep industrial waste under control and to reduce its impact on the environment as much as possible. Due to rapid urbanization and a large increase in the world's population [1], a large amount of solid waste has been generated and this is increasing rapidly in Turkey. According to the Turkish Statistical Institute, up to 16 million tons of FA are being created yearly, but only two or three percent can be used efficiently in the cement and concrete industry. FA, GGBFS as a waste material of steel factories, and QP with high reserve areas in Turkey are capable of having alkali-activated binder properties in terms of concrete production technology. Therefore, the goal of this research is to determine the optimal amount of waste materials to use in the production of lightweight aggregate for concrete mixes. Some other discussions have been had in the literature regarding the recycling of waste materials into new building materials, such as municipal solid waste incineration bottom ash (MSWIBA), silica fume (SF), and rice husk ash (RHA) for use as cement replacement materials. It was found that the use of FA as

partial replacement for cement in concrete resulted in enhanced durability of the produced concrete in addition to reducing CO₂ emissions [2]. The influence of FA in the cement hydration process and its pozzolanic reaction inside concrete has been investigated by the authors in [3–5]. However, several researchers have investigated using FA and GGBFS in producing artificial LWA [6–13] such as: recycling bottom ash in artificial LWA to be used directly in concrete [14] and minimizing cumulative quantities and preserving the environment. The aggregate in concrete provides a large percentage of (often between 65 and 75 percent) and contributes significantly to the material's heavy weight; therefore, it makes sense to investigate the possibility of turning waste materials into lightweight artificial concrete. The different chemical and physical properties of waste materials directly affect the mechanical and durability of the produced concrete [15]. It was observed in some studies that the replacement of 30 percent of recycled aggregate with the natural aggregate had no significant impact on the performance of concrete when compared to natural concrete [16–18]. Therefore, the goal of this research was to determine the optimal amount of waste materials for use in the production of lightweight aggregate for concrete mixes.

Different materials and procedures may be used to produce artificial aggregate, such as cold-bonding and sintering techniques [7,19]. According to BS EN 13055, aggregates are considered lightweight aggregates if their particle densities do not exceed 2000 kg/m³. Lightweight artificial aggregate was produced via the sintering method using alkaline palm oil fuel ash (POFA) combined with silt [20]. Although sintering consumes more energy than cold bonding, the benefits of achieving the sintered aggregate properties in less time outweigh waiting 28 days for cold-bonded aggregate to cure [21].

Lightweight aggregate manufacture via cold bonding was developed in the early 2000s, and FA was used as the dry powder. In this process, a million tons of waste materials was employed to generate aggregate, and this was found to be an appropriate material for producing lightweight aggregates [22–25]. The cold-bonding process has been widely used to utilize various types of waste materials and protect the environment by controlling the leaching of pollutants [26]. The technique can thus be considered a proper treatment channel for recycling waste materials [27]. Moreover, the technique is more economical than the sintering method, but the crushing strength of aggregates usually gives lower results [10,28,29]. In addition, the technique has more advantages in terms of cost, energy consumption, and gas emissions [30].

Concrete with different compressive characteristics can be made from a wide variety of structural components around the world, simplifying construction while increasing durability and versatility. Depending on the intended function, concrete may be poured in almost any form, shape, or color. Concrete may now be found in many locations, thanks to the tremendous expansion in the building industry. However, concrete has some drawbacks including its low tensile strength and heavy weight. Many research studies have looked at ways to amplify these unfavorable traits. High-strength concrete may be enhanced with recycled cement kiln dust and fibers made from recycled polyethylene [31]. Artificial aggregates are also employed to reduce the concrete's weight. For industrial purposes, a variety of light aggregates have been employed successfully. For example, bottom FA, concrete waste powder, and pulverized granulated blast-furnace slag [32] may all be used when using a cold-bonding technique. Various studies examined the mechanical behaviors of concrete produced with cold-bonded lightweight FA aggregates [10,13]. Sintered and cold-bonded artificial aggregate produced by utilizing washed sludge ash (WAS) and GGBFS was used to produce concrete with mechanical properties comparable to ordinary concrete with a lower oven-dry density [33]. This form of artificial aggregate may be utilized in various concretes with varying mechanical properties. Depending on the aggregate content, the compressive strength may be readily achieved at concrete manufacture between 20 and 80 MPa. The use of 10% FA with recycled aggregate resulted in a slight increase in the axial compressive strength of the concrete [34]. Furthermore, the addition of FA to the concrete with recycled aggregate improved the workability—due to the spherical and flat shape of pellets—in addition to the mechanical and durability properties of concrete [2].

Although lightweight concrete has a lower strength than normal-weight concrete, it has some advantages such as having a reduced dead load, being eco-friendly, being low cost, and having higher seismic and fire resistant properties [35–37]. From an environmental protection point of view, using FA artificial aggregate as a fine aggregate in concrete could reduce CO₂ emissions by up to 60% compared to conventional concrete [38]. Furthermore, replacing 50% of the cement with FA as a binder could reduce greenhouse emissions by 54% [39]. In addition to the environmental impact of using an FA artificial aggregate, the cost of producing concrete can be reduced by 13–15% compared to conventional concrete [40]. Sintered artificial aggregate is widely preferred in concrete production in order to provide a higher strength. Using sintered FA aggregate in lightweight concrete production has resulted in good mechanical and durability properties [41]. Similarly, the fly ash cenosphere (FAC) features include being hollow spherical, lightweight, and air-filled [42]. It is favored in different industries due to its high workability, low conductivity and bulk density, and its thermal resistance [40]. FAC is also a fine aggregate in sustainable lightweight concrete production [43]. A combination of 50% FAC and 75% SFA is suitable for producing sustainable lightweight concrete [43]. However, a high volume of FAC and SFA (up to 75%) leads to a significant reduction in lightweight concrete strength; the strength could be enhanced by adding silica fume [44,45]. Based on these previous studies, it is observed that a high volume of FAC and SFA could be utilized in lightweight concrete production with the aid of silica fume.

There is a lack of research on the use of QP in manufacturing aggregate and its influence on the mechanical performance of the bond strength effects of lightweight aggregates between concrete and reinforcing bars in particular. Hence, this study was focused on the influence of an artificial aggregate made from FA, GGBFS, and QP powder on the properties of concrete. Additionally, the effect of lightweight aggregate on the adhesion of concrete to steel was examined. The experimental findings were compared with the outcomes of conventional concrete made using typical aggregate. Due to prior research, the optimal value of the aggregates was determined based on the water absorption, bulk density, and crushing strength. These aggregates were substituted for conventional coarse aggregate with varying ratios to assess the concrete's compressive strength, modulus of elasticity, and tensile strength, and the strength of the bond between the aggregates and the cement paste.

2. Materials and Methods

During this experimental study, concrete was cast using three different types of artificial LWAs to examine their influence on concrete's mechanical and fracture properties. Different replacement ratios (20%, 40%, and 60%) were applied with natural coarse aggregate by weight.

2.1. Materials

This experiment used the same cement for producing artificial aggregate and testing concrete containing artificial aggregate. The specific gravity of CEM I 42.5 R Portland cement is 3.14, and the Blaine fineness is 326 m²/kg. Table 1 shows the chemical qualities that were employed in this experiment.

Two types of coarse aggregate utilized in manufacturing lightweight aggregate concrete are cold-bonded artificial aggregates and normal aggregates. Materials utilized in artificial aggregate synthesis include FA, GGBFS, and Q powder (see Table 1). The decision was made to use a blend of river sand and crushed limestone sand as the final fine aggregate obtained from a local supplier.

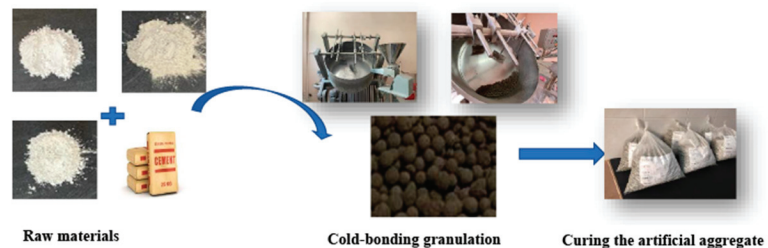
Slag from iron and steelmaking is known as GGBFS. FA from a thermal power plant in Turkey was utilized in this investigation with a specific gravity of 2.25 m²/kg and a fineness of 287 m²/kg. The GGBFS and QP qualities utilized in this experiment are shown in Table 1. Concrete mixes were made more manageable using a water-reducing additive with a specific gravity of 1.19. A superplasticizer (SP) was added to the mix.

Table 1. Physical and chemical properties of cement, FA, GGBFS, and QP.

| Chemical Composition (%) | Portland Cement | FA | QQBFS | QP |
|--------------------------------------|-----------------|--------|--------|-------|
| CaO | 62.58 | 4.24 | 34.12 | 0.28 |
| SiO ₂ | 20.25 | 56.20 | 36.41 | 89.05 |
| Al ₂ O ₃ | 5.31 | 20.17 | 10.39 | 5.03 |
| Fe ₂ O ₃ | 4.04 | 6.69 | 0.69 | 3.62 |
| MgO | 2.82 | 1.92 | 10.26 | – |
| SO ₃ | 2.73 | 0.49 | – | – |
| K ₂ O | 0.92 | 1.89 | 0.97 | 0.28 |
| Na ₂ O | 0.22 | 0.58 | 0.35 | – |
| Loss on ignition | 3.02 | 1.78 | 1.64 | – |
| Specific gravity | 3.15 | 2.25 | 2.79 | 2.65 |
| Blaine fineness (m ² /kg) | 326.00 | 287.00 | 418.00 | – |

2.2. Production of Artificial LWAs

The FA, GGBFS, and QP LWAs were made using the cold-bonding technique in a titled pan at ambient temperature with varied ratios of Portland cement (20%, 30%, and 50% by weight of cement). For the first 10 min, Figure 1 depicts the process whereby the dry materials were fed onto the disc and rotated at a constant speed to ensure uniformity. During the rotation, the dry mixture was sprayed with water to act as a coagulant and form pellets [9,12]. The process was repeated for 10–12 min in order to produce pellets with a diameter ranging between 6 mm and 12 mm. The aggregates were kept in plastic bags at 70% relative humidity for 28 days. The specific gravity, bulk density, water absorption, and crushing strength of the aggregates were determined following the curing period. This method was carried out for all the aggregate types manufactured.

**Figure 1.** The process of cold-bonding manufacturing the LWA [22].

2.3. Concrete Mix Proportions

The artificial aggregate types were produced to develop the concrete mixes in the experimental investigation. FA and GGBFS were combined with crushed QP powder in the LWA production process. The materials used to make the artificial aggregate and the replacement ratio with coarse aggregate are listed in Table 2. A complete list of the concrete mix proportions used in the investigation is provided in Table 3. FAAC, GGBFSAC, and QPAC refer to the FA, GGBFS, and QP aggregate concrete mixtures in Table 3. This also shows how much superplasticizer (SP) was needed to achieve appropriate workability.

Table 2. The design for concrete mixtures.

| Mix ID | Replacement Rate (%) | Cement (kg/m ³) | Water (kg/m ³) | River Sand (kg/m ³) | Natural Aggregate (kg/m ³) | Manufactured Aggregate (kg/m ³) | SP (kg/m ³) |
|---------|----------------------|-----------------------------|----------------------------|---------------------------------|--|---|-------------------------|
| FAAC | 20 | 360 | 158 | 733.3 | 589.4 | 80 | 4.45 |
| | 40 | 360 | 158 | 733.3 | 442 | 157.7 | 4.45 |
| | 60 | 360 | 158 | 733.3 | 294.7 | 236.7 | 4.45 |
| GGBFSAC | 20 | 360 | 158 | 733.3 | 589.3 | 93.7 | 4.45 |
| | 40 | 360 | 158 | 733.3 | 442 | 187.7 | 4.45 |
| | 60 | 360 | 158 | 733.3 | 294.7 | 281.3 | 4.45 |
| QPAC | 20 | 360 | 158 | 733.3 | 589.4 | 82.5 | 4.45 |
| | 40 | 360 | 158 | 733.3 | 442.1 | 165 | 4.45 |
| | 60 | 360 | 158 | 733.3 | 294.7 | 247.5 | 4.45 |

Table 3. Physical and mechanical properties of artificial LWA.

| Mix ID | Maximum Aggregate Size (mm) | Fineness Modulus | Specific Gravity | Apparent Specific Gravity | Density (kg/m ³) | Water Absorption (%) | Crushing Strength (N) |
|--------|-----------------------------|------------------|------------------|---------------------------|------------------------------|----------------------|-----------------------|
| FAA | 16 | 1.78 | 1.43 | 2.43 | 937.59 | 28.52 | 722.96 |
| GGBFSA | 12.5 | 2.67 | 1.74 | 2.43 | 1114.42 | 16.27 | 1038.98 |
| QA | 12.5 | 1.53 | 1.61 | 2.70 | 928.00 | 18.00 | 675.51 |

2.4. Concrete Casting and Specimen Preparation

Three series of concrete mixes were cast in this investigation according to the three types of artificial aggregates. The coarse aggregate was used in each case to make up 20%, 40%, and 60% of the original volume. In total, ten different concrete combinations and a control concrete mixture were prepared. According to ASTM C192-18, the control mixture was poured, whereas the artificial aggregate-containing mixture required further operations to be completed. To achieve a saturated surface dry state, it was essential to soak the lightweight aggregate pellets used in the concrete mixes overnight in water, and then dry them with a towel to remove the excess water. The concrete mixtures were prepared and created using a rotating pan mixer with a 40-litre capacity.

In accordance with TS EN 12350-2, a slump cone was used to test the workability of each combination once the mixing step was completed. The hardened characteristics of the concrete mixes were investigated once the workability was established. A total of six specimens were used in the investigation of hardened properties. These included three specimens of 100 mm cubes for compression strength testing, three specimens of 100 * 200 mm cylinders for splitting tensile and three-point load testing, three specimens of 75 * 75 * 280 mm for modulus of elasticity testing, and three specimens of 150mm cubes for the water permeability test. Water curing was performed for 28 days on all the concrete sample seeds that had been removed from the molds after 24 h of drying.

2.5. Test Methods

2.5.1. Aggregate Tests

The particle size distribution of artificial LWA was determined. The tests for the physical properties of the artificial LWA were conducted in terms of specific gravity, bulk density, and water absorption in accordance with ASTM 127. The crushing strength test was performed in accordance with BS 812 part 110 by placing the pellet between two parallel plates and applying a direct load until failure, an average of 10 pellets was taken as the crushing strength. Furthermore, mineralogy and microstructural analyses were performed on the manufactured pellets by using scanning electron microscopy (SEM).

2.5.2. Concrete Tests

Compressive strength was determined using cubic samples according to the ASTM C39-18. The splitting tensile strength was calculated using ASTM C496-17 and Equation (1):

$$f_s = \frac{2P}{\pi DL} \quad (1)$$

where f_s = splitting tensile strength (MPa), P = maximum load (N), D = specimen diameter (mm), and L = specimen length (mm).

The fracture energy was established in accordance with RILEM 50-FMC Technical Committee [46]. Figure 2 shows a beam with notches during the test. The notch-to-depth ratio was 0.4. An LVT transducer measured midspan deflection (LVDT). The area under the load–displacement curve was used to compute the fracture energy by using Equation (2):

$$G_F = \frac{W_0 + mg \frac{S}{U} \delta_s}{B(W - a)} \quad (2)$$

where G_F is the fracture energy (N/mm), W_0 is the area under load–displacement curve (N.mm), m is the specimen mass (kg), g is acceleration of gravity (m/s^2), S is the distance between support (mm), U is the specimen length (mm), δ_s is the specimen deflection (mm), B is the specimen width (mm), W is the specimen depth (mm), and a is the notch depth (mm).



Figure 2. A notch beam under fracture energy test.

Also, the notched beams were used to determine the net flexural strength in accordance with ASTM C1609, 2005 by using Equation (3) [47]:

$$f_{flex} = \frac{3P_{max}S}{2B(W-a)^2} \quad (3)$$

where f_{flex} is the failure load (MPa) and P_{max} is the maximum load (N).

Furthermore, to measure the characteristic length to indicate the brittleness of each specimen, Equation (4) was used: [48]

$$l_{ch} = \frac{EG_F}{f_s^2} \quad (4)$$

where l_{ch} is the characteristic length (mm) and E is the static modulus of elasticity (GPa).

RILEM RC6 requires $150 \times 150 \times 150$ mm cube specimens with embedded reinforcement bars with a 16 mm diameter at the center of the sample to determine the bond strength between the steel and the lightweight aggregate [49]; Equation (5) is used to measure the bond strength:

$$\tau = \frac{P}{\pi d_b L_b} \quad (5)$$

where τ is bond strength (MPa), d_b is the diameter of the embedded steel bar (16 mm), and L_b is the embedded length of the steel bar (150 mm).

3. Results and Discussion

3.1. Results of Aggregate Tests

The particle size distribution of artificial LWA is shown in Figure 3. The physical and mechanical properties are displayed in Table 3. It is noted that the GGBFSA recorded the highest crush strength value and minimum water absorption rate. The microstructure for each type of artificial LWA aggregate is shown in Figure 4. The minor differences between the artificial LWAs are that the QPA has sharp corners and the presence of voids in FAA is less than in GGBFSA and QPA. The FAA particles exhibited a denser surface structure when compared to the other types of aggregate. The core of the aggregate particles showed a porous structure that gives the lighter weight and the high water absorption, leading to a reduction in the strength and stiffness of artificial aggregate particles.

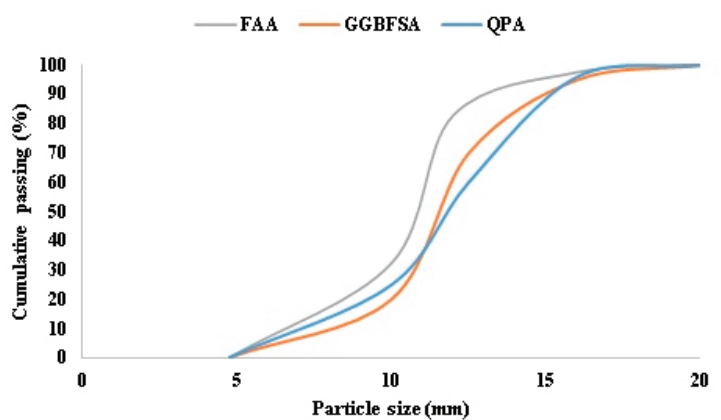


Figure 3. Particle size distribution of artificial LWAs.

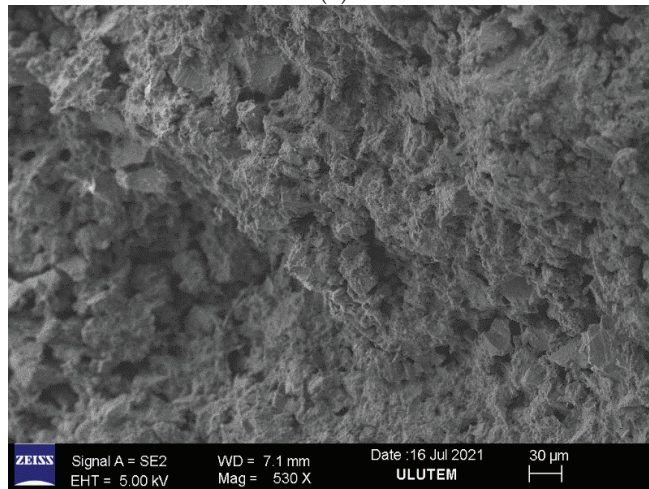
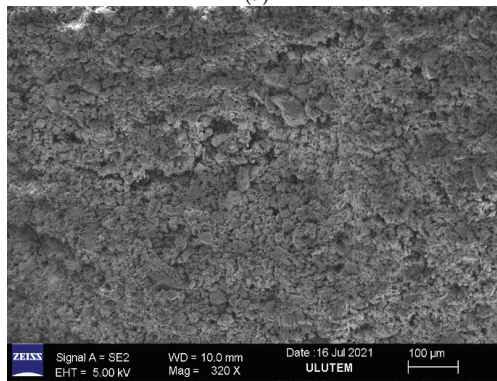
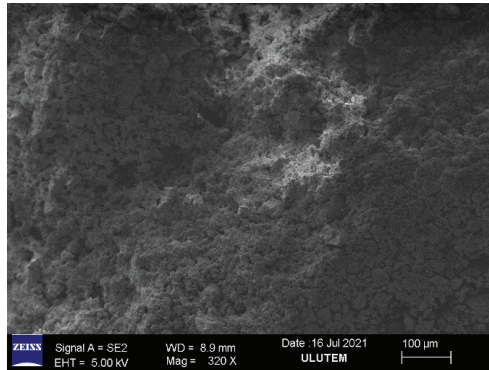


Figure 4. The microstructure of artificial LWAs (a) FAA, (b) GGBFSA, and (c) QPA.

3.2. Results of Concrete Tests

The results of compression, splitting tensile, flexure, bonding, and modulus of elasticity tests are discussed in detail below. Furthermore, the photographic views and graphical illustrations were added for a clear and detailed discussion and evaluation.

3.2.1. Compressive Strength

The average compressive strength results of the cube samples which were treated for 28 days are illustrated in Figure 5.

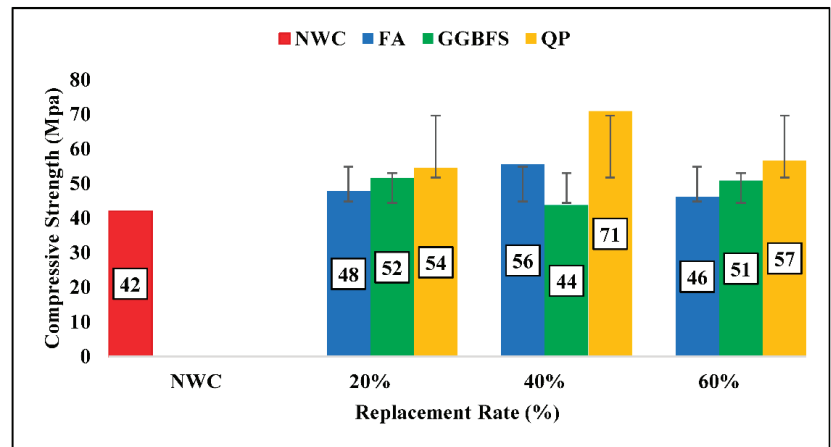


Figure 5. The compressive strength of LWA concretes.

All of the mixtures generated similar results when the pressures ranged between 40 MPa and 55 MPa, compared with the natural normal-weight concrete (NWC). According to these results, the artificial aggregate used up to 60% of the traditional coarse aggregate and may still offer appropriate compressive strength. The experimental results indicate that artificial LWA concrete requires a lower water-to-cement ratio than regular aggregate concrete. A higher cement percentage is needed to compensate for the artificial aggregate's increased porosity and softness and decreased hardness [50].

The maximum compressive strength was attained at a 40% volume replacement ratio for the mixture comprising quartz artificial aggregate in this experiment. Although the lowest value was obtained by replacing 60% of the natural aggregate with GGBFS artificial aggregate, it was still 1% higher than for the regular aggregate. However, when the artificial aggregate ratios were increased, compressive strength was slightly reduced. There is a reasonable amount of strength in the concrete formed using artificial aggregates, although it is not as strong as traditional concrete. According to the previous research, adding sintered FA LWA decreases the compressive strength by 10% to 13%. The results of this experiment confirm those of Nadesan [45].

3.2.2. Splitting Tensile Strength

A splitting tensile test assesses the concrete's tensile strength. It is a method through which a fracture occurs due to applied stress attempting to locate weaker paths. The average tensile strength was calculated using three 100 * 200 mm cylindrical samples. In this study, the tensile strength of the concrete with artificial LWA is equivalent to that of sound concrete, as shown in Table 2 and Figure 6. It is estimated that the performance of lightweight concrete created using artificial aggregate is comparable to that of control concrete prepared with ordinary coarse aggregates. Artificial aggregate has a reduced strength, round shape, and poor anchoring potential with cured cement paste, which are

the causes of limited improvement for the splitting tensile strength. For these reasons and because of artificial aggregates' moderate tensile strength, artificial LWA could not enhance the tensile strengths to levels higher than for ordinary concrete. Tensile strength is dependent on the shear of the interfaces zone between the cement paste and aggregate particles and this can be improved by the curing time and condition, for example, steam curing can improve the tensile strength more than water curing. Concrete is used for several purposes; however, the splitting tenacity results of concrete, including artificial aggregate, were satisfactory.

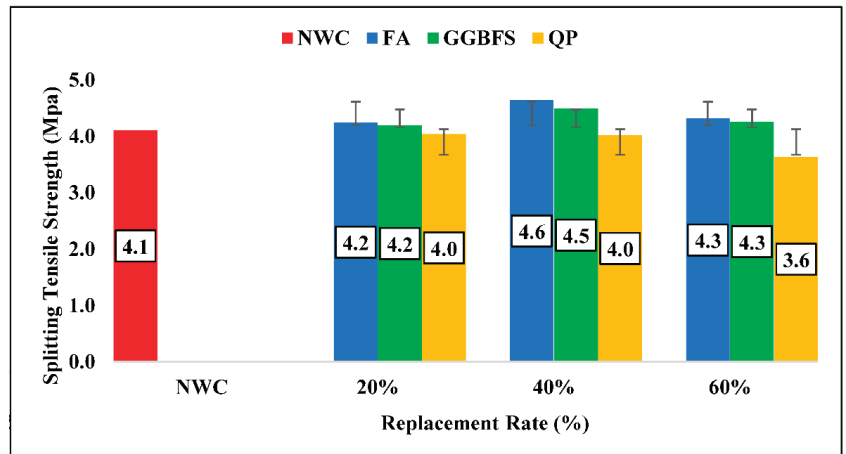


Figure 6. The splitting tensile strength of lightweight aggregate concretes.

3.2.3. Net Flexural Strength

A different type of tensile strength test, known as the net flexural strength, is shown in Figure 7. According to the results, concrete's net flexural strength was more significant than its splitting tensile strength. Concrete mixtures constructed with FA artificial LWA had values ranging from 5.41 MPa to 6.62 MPa, while GGBFS and QP artificial aggregates had values ranging from 4.48 MPa to 5.45 MPa and 5.56 MPa to 6.09 MPa, respectively. Particles with a higher crushing strength showed better flexural strength values. While the net flexural strength of artificial LWA concretes was lower than that of normal-weight concrete, the compressive, splitting, and net flexural strengths were all comparable to normal-weight aggregate concrete and it could be improved by improving the cement paste quality and reducing the water-cement ratio. Although the flexural strength of artificial LWA concretes was lower than that of natural normal-weight aggregate concrete, there was a consistency between the compressive strength, tensile strength, and net flexural strength for the artificial LWA concrete.

3.2.4. Load–Displacement Curves

Figure 6 shows typical load–displacement curves for concrete mixtures. Concretes with a lower compressive strength as demonstrated in Figure 8 have more significant displacements based on the load–displacement curve. Concretes constructed with lightweight artificial particles display ductile behavior because their maximum displacement values are more crucial. Adding artificial LWA to a concrete mix improves the concrete's ductility.

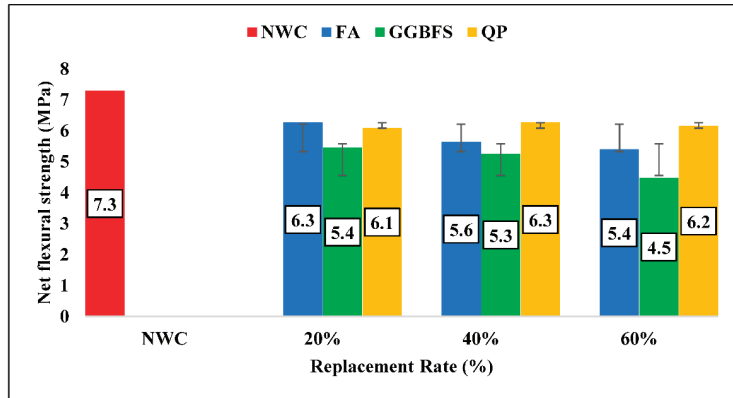
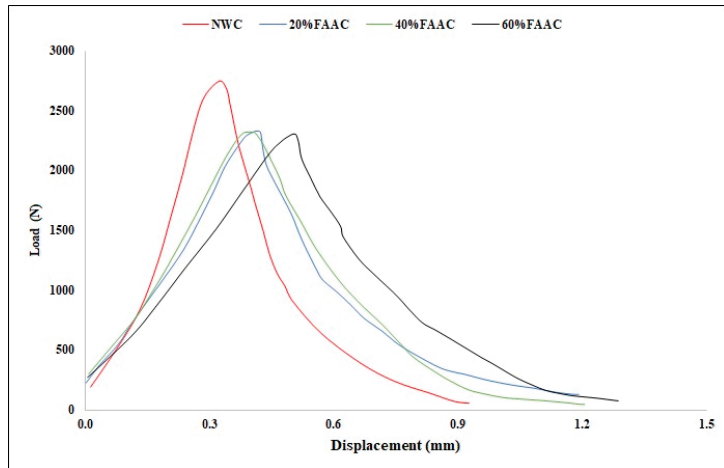
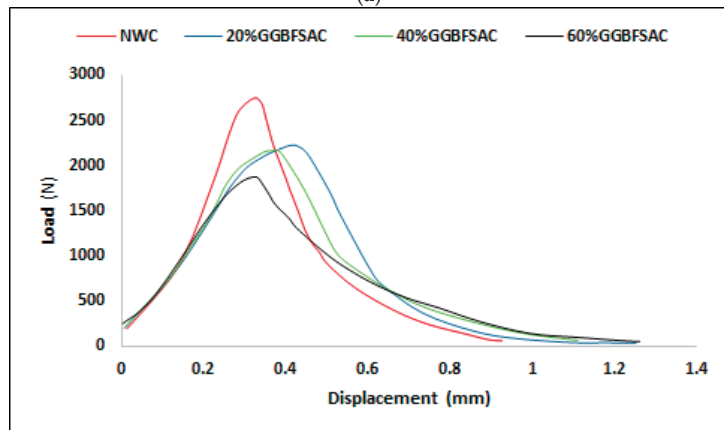


Figure 7. The net flexural strength of artificial aggregate concrete.



(a)



(b)

Figure 8. Cont.

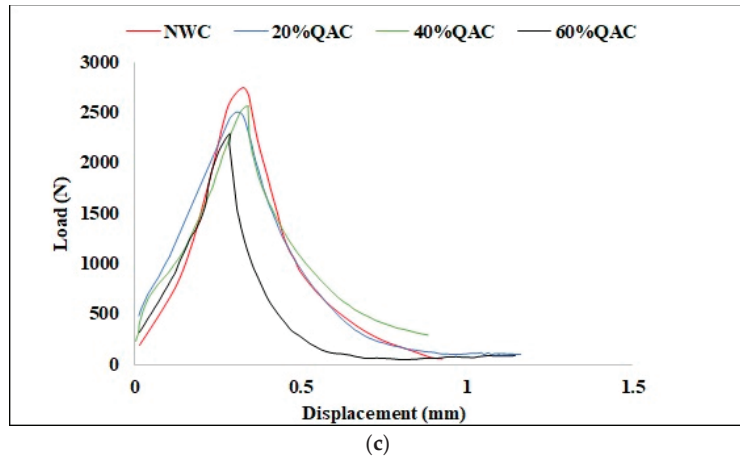


Figure 8. Load–displacement curves for (a) FAAC, (b) GGBFSAC, and (c) QAC.

3.2.5. Fracture Energy

A three-point bending machine was used to test a notched beam, and the results are shown in Figure 9. Artificial aggregate concretes constructed from FA, QP, and GGBFS fiber-reinforced materials had fracture energies of 391 MPa, 328 MPa, and 310 MPa, respectively. The strength of artificial LWA concrete was reduced when compared to natural normal-weight aggregate concrete. The fracture energy is the sum of the actuator’s energy and weight. The decreased fracture energy of artificial LWA concretes may be attributed to the results of this calculation. Because of the lower weight of the concrete, the amount of energy given by weight is reduced. The area under the load–displacement curves for concrete created using artificial LWA was less than for concrete manufactured with natural normal-weight aggregate. Since natural normal-weight aggregate has a lower density than artificial aggregate, the fracture energy provided by the actuator in the concrete will be more substantial.

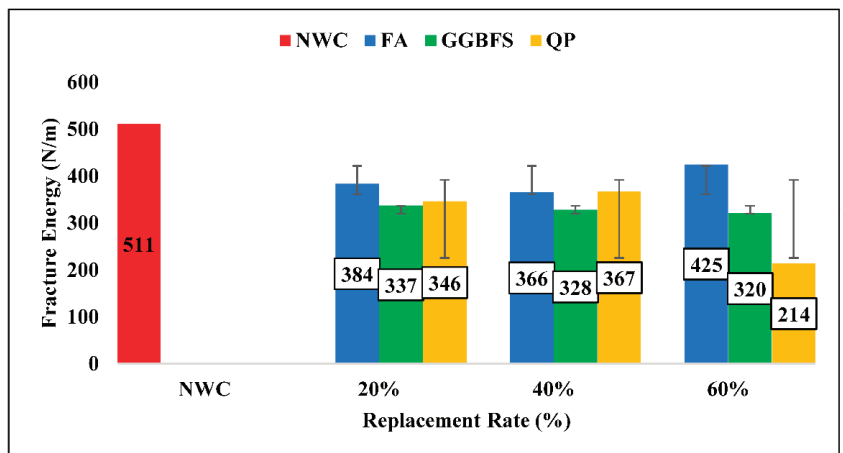


Figure 9. Fracture energy of artificial aggregate concretes.

3.2.6. Characteristic Length

Figure 10 depicts the characteristic length values, which are a brittleness measurement. The concrete mixes made using artificial lightweight particles had the most significant characteristic length values. With its distinctive length as a consequence, it is clear that artificial LWA makes concrete more ductile. Because of its higher compressive strength, the stronger concrete also had shorter characteristic length values. This provides further evidence that the ductility of concrete increases with its compressive strength.

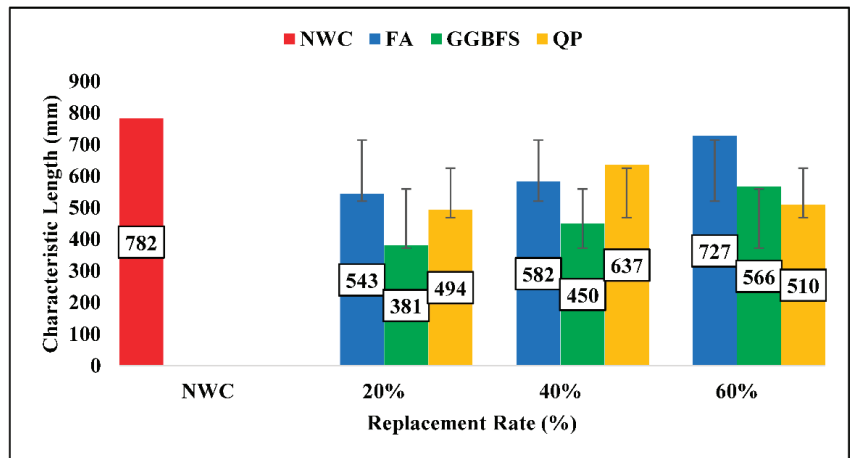


Figure 10. Characteristic length of artificial aggregate concretes.

3.2.7. Bond Strength

We could determine the concrete's binding strengths using the findings of this experiment. Increasing the FA artificial lightweight replacement boosts the concrete mix's binding strength. The results are shown in Figure 11. GGBFS artificial LWAs increased bond strength at a 20 percent replacement ratio by approximately 42 percent, while increasing the GGBFS content to 60 percent reduced bond strength by 18 percent. Almost all bond strength tests for quartz artificial aggregate concrete were passed. When compared to natural normal-weight aggregate, manufactured LWA was weaker. This, however, directly affects the steel bar–concrete relationship; pulling out the steel bar easily breaks or crushes the weaker aggregate of the implanted steel bar.

The findings of the other studies demonstrated that artificial LWA works well, if not exceptionally. As a result, concretes constructed using artificial LWA have lower bond strength than concretes made with normal-weight natural aggregate. Thus, bond strength was determined to be the least effective measure when assessing the entire performance of artificial LWA.

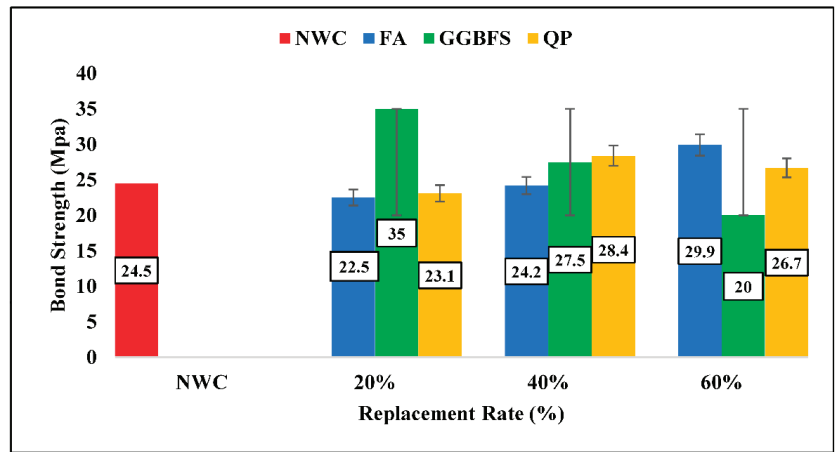


Figure 11. Bond strength of artificial aggregate concretes.

4. Conclusions

Based on the results gained from this experimental study, the following conclusions can be attained:

1. Artificial LWA was used to build concrete with compressive strengths of 40 MPa and 60 MPa. The maximum compressive strength was achieved for QPLWAC, which recorded 71 MPa at a 40 percent replacement ratio. The artificial LWA may be employed for any desired concrete strength class.
2. When used in concrete mixtures, artificial lightweight and ordinary weight particles produced splitting tensile strengths almost identically. Only slightly different changes were discovered. The lower splitting tensile strength values in concrete, including artificial LWA, are related to the lower crushing strength of artificial aggregates and the curing condition of the constructed concrete.
3. Artificial LWA concretes resulted in lower net flexural strength results when compared to normal concrete. However, the outcomes were satisfactory for all the concrete mixtures when the correlation between compressive strength and splitting tensile strength was taken into consideration. Regarding the concrete mixes, it was found that the higher ultimate loads occurred in the concrete, including natural, normal-weight aggregate. In contrast, more significant maximum displacement occurred in concrete containing artificial LWA. As a result, it can be concluded that concrete's tensile strength is reduced by using artificial LWA.
4. Because artificial LWA has a lower self-weight, the fracture energy of concrete is lower than that of concrete made with natural, heavier particles. Furthermore, this study's findings were consistent with previous research on the fracture energy of concrete mixes using artificial LWA. As a result, this shows that lightweight artificial aggregate may be used to make high-fracture-energy concretes.
5. Concrete ductility was enhanced as a consequence of using artificial LWA in concrete manufacturing, according to the findings regarding the characteristic length, which is a practical approach to quantify brittleness.
6. Artificial LWA used in concrete manufacturing considerably impacts the strength of the connection between the concrete and the reinforcing bar. There is a strong correlation between the reinforcing bar and the artificial LWA. Natural aggregate particles are more rigid than artificial LWA particles. As a result, the lower and comparable concrete resistance to normal concrete is generated after removing the reinforcing bar.

7. In conclusion, utilizing artificial LWA in concrete production has a significant impact, not only in terms of preserving the environment, but in the production of concrete with mechanical properties that are comparable with normal concrete and which can be applied in several construction fields.

Author Contributions: Conceptualization, M.A.I.; Methodology, M.A.I. and A.A.A.; Formal analysis, M.A.I.; Investigation, M.A.I. and A.A.A.; Resources, M.A.I.; Data curation, M.A.I.; Writing – original draft, M.A.I.; Writing – review & editing, M.A.I. and N.A.; Visualization, A.A.A.; Supervision, N.A. and A.A.A.; Funding acquisition, M.A.I. and A.A.A. All authors have read and agreed to the published version of the manuscript.

Funding: This research received no external funding.

Informed Consent Statement: Not applicable.

Acknowledgments: The authors would like to thank the Laboratory Unit at Gaziantep University for providing the support to finish this study.

Conflicts of Interest: The authors declare no conflict of interest.

References

1. Kodur, V.K.R.; Naser, M.Z.; Bhatt, P.P. *Energy Engineering*; Springer: Berlin/Heidelberg, Germany, 2017; pp. 113–122.
2. Lima, C.; Caggiano, A.; Faella, C.; Martinelli, E.; Pepe, M.; Realfonzo, R. Physical Properties and Mechanical Behaviour of Concrete Made with Recycled Aggregates and Fly Ash. *Constr. Build. Mater.* **2013**, *47*, 547–559. [[CrossRef](#)]
3. Paya, J.; Borrachero, M.V.; Monzo, J.; Peris-Mora, E.; Bonilla, M. Long Term Mechanical Strength Behaviour in Fly Ash/Portland Cement Mortars Prepared Using Processed Ashes. *J. Chem. Technol. Biotechnol. Int. Res. Process Environ. Clean Technol.* **2002**, *77*, 336–344.
4. Sakai, E.; Miyahara, S.; Ohsawa, S.; Lee, S.-H.; Daimon, M. Hydration of Fly Ash Cement. *Cem. Concr. Res.* **2005**, *35*, 1135–1140. [[CrossRef](#)]
5. Moon, G.D.; Oh, S.; Choi, Y.C. Effects of the Physicochemical Properties of Fly Ash on the Compressive Strength of High-Volume Fly Ash Mortar. *Constr. Build. Mater.* **2016**, *124*, 1072–1080. [[CrossRef](#)]
6. Cheeseman, C.R.; Virdi, G.S. Properties and Microstructure of Lightweight Aggregate Produced from Sintered Sewage Sludge Ash. *Resour. Conserv. Recycl.* **2005**, *45*, 18–30. [[CrossRef](#)]
7. Joseph, G.; Ramamurthy, K. Influence of Fly Ash on Strength and Sorption Characteristics of Cold-Bonded Fly Ash Aggregate Concrete. *Constr. Build. Mater.* **2009**, *23*, 1862–1870. [[CrossRef](#)]
8. Kayali, O. Fly Ash Lightweight Aggregates in High Performance Concrete. *Constr. Build. Mater.* **2008**, *22*, 2393–2399. [[CrossRef](#)]
9. Arslan, H.; Baykal, G. Utilization of Fly Ash as Engineering Pellet Aggregates. *Environ. Geol.* **2006**, *50*, 761–770. [[CrossRef](#)]
10. Kockal, N.U.; Ozturan, T. Durability of Lightweight Concretes with Lightweight Fly Ash Aggregates. *Constr. Build. Mater.* **2011**, *25*, 1430–1438. [[CrossRef](#)]
11. Li, D.; Xu, Z.; Luo, Z.; Pan, Z.; Cheng, L. The Activation and Hydration of Glassy Cementitious Materials. *Cem. Concr. Res.* **2002**, *32*, 1145–1152. [[CrossRef](#)]
12. Baykal, G.; Döven, A.G. Utilization of Fly Ash by Pelletization Process; Theory, Application Areas and Research Results. *Resour. Conserv. Recycl.* **2000**, *30*, 59–77. [[CrossRef](#)]
13. Kockal, N.U.; Ozturan, T. Effects of Lightweight Fly Ash Aggregate Properties on the Behavior of Lightweight Concretes. *J. Hazard. Mater.* **2010**, *179*, 954–965. [[CrossRef](#)]
14. Keulen, A.; Van Zomeren, A.; Harpe, P.; Aarnink, W.; Simons, H.A.E.; Brouwers, H.J.H. High Performance of Treated and Washed MSWI Bottom Ash Granulates as Natural Aggregate Replacement within Earth-Moist Concrete. *Waste Manag.* **2016**, *49*, 83–95. [[CrossRef](#)] [[PubMed](#)]
15. Bravo, M.; De Brito, J.; Pontes, J.; Evangelista, L. Durability Performance of Concrete with Recycled Aggregates from Construction and Demolition Waste Plants. *Constr. Build. Mater.* **2015**, *77*, 357–369. [[CrossRef](#)]
16. Limbachiya, M.; Meddah, M.S.; Ouchagour, Y. Use of Recycled Concrete Aggregate in Fly-Ash Concrete. *Constr. Build. Mater.* **2012**, *27*, 439–449. [[CrossRef](#)]
17. Loffy, A.; Al-Fayez, M. Performance Evaluation of Structural Concrete Using Controlled Quality Coarse and Fine Recycled Concrete Aggregate. *Cem. Concr. Compos.* **2015**, *61*, 36–43. [[CrossRef](#)]
18. Poon, C.S.; Kou, S.C.; Lam, L. Influence of Recycled Aggregate on Slump and Bleeding of Fresh Concrete. *Mater. Struct.* **2007**, *40*, 981–988. [[CrossRef](#)]
19. Liu, J.; Li, Z.; Zhang, W.; Jin, H.; Xing, F.; Tang, L. The Impact of Cold-Bonded Artificial Lightweight Aggregates Produced by Municipal Solid Waste Incineration Bottom Ash (MSWIBA) Replace Natural Aggregates on the Mechanical, Microscopic and Environmental Properties, Durability of Sustainable Concrete. *J. Clean. Prod.* **2022**, *337*, 130479. [[CrossRef](#)]

20. Kwek, S.Y.; Awang, H. Utilisation of Recycled Silt from Water Treatment and Palm Oil Fuel Ash as Geopolymer Artificial Lightweight Aggregate. *Sustainability* **2021**, *13*, 6091. [[CrossRef](#)]
21. Ibrahim, M.A.; Atmaca, N. Cold Bonded and Low Temperature Sintered Artificial Aggregate Production by Using Waste Materials. *Period. Polytech. Civ. Eng.* **2022**, 1–11. [[CrossRef](#)]
22. Wei, Y.L.; Cheng, S.H.; Chen, W.J.; Lu, Y.H.; Chen, K.; Wu, P.C. Influence of Various Sodium Salt Species on Formation Mechanism of Lightweight Aggregates Made from Coal Fly Ash-Based Material. *Constr. Build. Mater.* **2020**, *239*, 117890. [[CrossRef](#)]
23. Sahoo, S.; Selvaraju, A.K.; Suriya Prakash, S. Mechanical Characterization of Structural Lightweight Aggregate Concrete Made with Sintered Fly Ash Aggregates and Synthetic Fibres. *Cem. Concr. Compos.* **2020**, *113*, 103712. [[CrossRef](#)]
24. Nadesan, M.S.; Dinakar, P. Structural Concrete Using Sintered Flyash Lightweight Aggregate: A Review. *Constr. Build. Mater.* **2017**, *154*, 928–944. [[CrossRef](#)]
25. Balapour, M. *Conversion of Waste Coal Combustion Ash to Value-Added Construction Lightweight Aggregates Through a Holistic Thermodynamics-Guided Manufacturing Framework*; Drexel University: Philadelphia, PA, USA, 2021.
26. Senneca, O.; Cortese, L.; Di Martino, R.; Fabbicino, M.; Ferraro, A.; Race, M.; Scopino, A. Mechanisms Affecting the Delayed Efficiency of Cement Based Stabilization/Solidification Processes. *J. Clean. Prod.* **2020**, *261*, 121230. [[CrossRef](#)]
27. Ferraro, A.; Colangelo, F.; Farina, I.; Race, M.; Cioffi, R.; Cheeseman, C.; Fabbicino, M. Cold-Bonding Process for Treatment and Reuse of Waste Materials: Technical Designs and Applications of Pelletized Products. *Crit. Rev. Environ. Sci. Technol.* **2021**, *51*, 2197–2231. [[CrossRef](#)]
28. Gomathi, P.; Sivakumar, A. Accelerated Curing Effects on the Mechanical Performance of Cold Bonded and Sintered Fly Ash Aggregate Concrete. *Constr. Build. Mater.* **2015**, *77*, 276–287. [[CrossRef](#)]
29. Colangelo, F.; Messina, F.; Di Palma, L.; Cioffi, R. Recycling of Non-Metallic Automotive Shredder Residues and Coal Fly-Ash in Cold-Bonded Aggregates for Sustainable Concrete. *Compos. Part B Eng.* **2017**, *116*, 46–52. [[CrossRef](#)]
30. Tajra, F.; Elrahman, M.A.; Stephan, D. The Production and Properties of Cold-Bonded Aggregate and Its Applications in Concrete: A Review. *Constr. Build. Mater.* **2019**, *225*, 29–43. [[CrossRef](#)]
31. Kang, M.C.; Yoo, D.Y.; Gupta, R. Machine Learning-Based Prediction for Compressive and Flexural Strengths of Steel Fiber-Reinforced Concrete. *Constr. Build. Mater.* **2021**, *266*, 121117. [[CrossRef](#)]
32. Colangelo, F.; Cioffi, R. Use of Cement Kiln Dust, Blast Furnace Slag and Marble Sludge in the Manufacture of Sustainable Artificial Aggregates by Means of Cold Bonding Pelletization. *Materials* **2013**, *6*, 3139–3159. [[CrossRef](#)] [[PubMed](#)]
33. Özkan, H.; Kabay, N.; Miyan, N. Properties of Cold-Bonded and Sintered Aggregate Using Washing Aggregate Sludge and Their Incorporation in Concrete: A Promising Material. *Sustainability* **2022**, *14*, 4205. [[CrossRef](#)]
34. Dabhade, A.N.; Chaudari, S.R.; Gajbhaye, A.R. Effect of Fly Ash on Recycle Coarse Aggregate Concrete. *Int. J. Civ. Eng. Res.* **2014**, *2278*, 3652.
35. Faraj, R.H.; Sherwani, A.F.H.; Jafer, L.H.; Ibrahim, D.F. Rheological Behavior and Fresh Properties of Self-Compacting High Strength Concrete Containing Recycled PP Particles with Fly Ash and Silica Fume Blended. *J. Build. Eng.* **2021**, *34*, 101667. [[CrossRef](#)]
36. Faraj, R.H.; Hama Ali, H.F.; Sherwani, A.F.H.; Hassan, B.R.; Karim, H. Use of Recycled Plastic in Self-Compacting Concrete: A Comprehensive Review on Fresh and Mechanical Properties. *J. Build. Eng.* **2020**, *30*, 101283. [[CrossRef](#)]
37. Faraj, R.H.; Sherwani, A.F.H.; Daraei, A. Mechanical, Fracture and Durability Properties of Self-Compacting High Strength Concrete Containing Recycled Polypropylene Plastic Particles. *J. Build. Eng.* **2019**, *25*, 100808. [[CrossRef](#)]
38. Glavind, M.; Munch-Petersen, C. 'Green' Concrete in Denmark. *Struct. Concr.* **2000**, *1*, 19–25. [[CrossRef](#)]
39. Li, Z.; Ding, Z.; Zhang, Y. *Proceedings of the International Workshop on Sustainable Development and Concrete Technology*; Center for Transportation Research and Education Iowa State University: Beijing, China, 2004; pp. 55–76.
40. Danish, A.; Mosaberpanah, M.A. Formation Mechanism and Applications of Cenospheres: A Review. *J. Mater. Sci.* **2020**, *55*, 4539–4557. [[CrossRef](#)]
41. Cui, H.Z.; Lo, T.Y.; Memon, S.A.; Xu, W. Effect of Lightweight Aggregates on the Mechanical Properties and Brittleness of Lightweight Aggregate Concrete. *Constr. Build. Mater.* **2012**, *35*, 149–158. [[CrossRef](#)]
42. Ranjbar, N.; Kuenzel, C. Cenospheres: A Review. *Fuel* **2017**, *207*, 1–12. [[CrossRef](#)]
43. Patel, S.K.; Satpathy, H.P.; Nayak, A.N.; Mohanty, C.R. Utilization of Fly Ash Cenosphere for Production of Sustainable Lightweight Concrete. *J. Inst. Eng. Ser. A* **2020**, *101*, 179–194. [[CrossRef](#)]
44. McBride, S.P.; Shukla, A.; Bose, A. Processing and Characterization of a Lightweight Concrete Using Cenospheres. *J. Mater. Sci.* **2002**, *37*, 4217–4225. [[CrossRef](#)]
45. Nadesan, M.S.; Dinakar, P. Influence of Type of Binder on High-Performance Sintered Fly Ash Lightweight Aggregate Concrete. *Constr. Build. Mater.* **2018**, *176*, 665–675. [[CrossRef](#)]
46. RILEM, D.R. Draft Recommendation: "Determination of the Fracture Energy of Mortar and Concrete by Means of Three-Point Bend Tests on Notched Beams". *Mater. Struct.* **1985**, *18*, 484.
47. Balendran, R.V.; Zhou, F.P.; Nadeem, A.; Leung, A.Y.T. Influence of Steel Fibres on Strength and Ductility of Normal and Lightweight High Strength Concrete. *Build. Environ.* **2002**, *37*, 1361–1367. [[CrossRef](#)]
48. Hillerborg, A. The Theoretical Basis of a Method to Determine the Fracture Energy G_F of Concrete. *Mater. Struct.* **1985**, *18*, 291–296. [[CrossRef](#)]

49. RILEM, R.C. Recommendations for the Testing and Use of Constructions Materials Bond Test for Reinforcement Steel. *Pull-Out Test* **1996**, 3. [[CrossRef](#)]
50. İpek, S.; Ayodele, O.A.; Mermerdaş, K. Influence of Artificial Aggregate on Mechanical Properties, Fracture Parameters and Bond Strength of Concretes. *Constr. Build. Mater.* **2020**, 238, 117756. [[CrossRef](#)]

Article

Object Detection for Construction Waste Based on an Improved YOLOv5 Model

Qinghui Zhou *, Haoshi Liu, Yuhang Qiu and Wuchao Zheng

School of Mechanical-Electronic and Vehicle Engineering, Beijing University of Civil Engineering and Architecture, Beijing 100044, China

* Correspondence: zhouqinghui@bucea.edu.cn

Abstract: An object detection method based on an improved YOLOv5 model was proposed to enhance the accuracy of sorting construction waste. A construction waste image sample set was established by collecting construction waste images on site. These construction waste images were preprocessed using the random brightness method. A YOLOv5 object detection model was improved in terms of the convolutional block attention module (CBAM), simplified SPPF (SimSPPF) and multi-scale detection. Then, the improved YOLOv5 model was trained, validated and tested using the established construction waste image dataset and compared with other conventional models such as Faster-RCNN, YOLOv3, YOLOv4, and YOLOv7. The results show that: based on the improved YOLOv5 model, the mean average precision (mAP) on the test dataset can reach 0.9480. The overall performance of this model is better than that of other conventional models in object detection, which verifies the accuracy and availability of the proposed method.

Keywords: construction waste; computer vision; deep learning; YOLOv5; waste sorting

1. Introduction

The rapid rise in construction activities has produced a large amount of construction waste with the global increase in population and urbanization [1]. According to a literature review and survey, construction waste accounts for more than 25% of the world's waste [2]. In China, the average recovery rate of construction waste is approximately 5%. Additionally, the annual construction waste level is about 1.55 billion tons to 2.4 billion tons [3], accounting for nearly 30–40% of urban waste, causing many environmental issues [4].

Due to the lack of proper recovery schemes and effective disposal technologies, construction waste without any treatment will be transported to the suburban landfill, causing land-use threats [5]. However, some materials are potentially valuable in construction and easily reused/recycled, including concrete, stone masonry, bricks, etc. These sustainable materials should be sorted out and turned into recycled aggregates that can be used in new building projects after crushing and separation, thus reducing the need to mine and process virgin materials. Therefore, reducing, reusing, and recycling construction waste has become an important and essential issue.

Currently, the traditional method of sorting construction waste is mixing, crushing and screening by means of mechanical operation, while preselecting, rejecting and diverting by manual work. However, there are problems of low recycling purity and low efficiency of manual work and especially serious harm to health in dusty and noisy environments. Increasingly, computer vision (CV), robotics, and other-artificial intelligent technologies are being used for construction waste sorting [6]. Usually, a robot for sorting construction waste is used to finely sort a large number of objects before mixing and crushing. Smart technologies can improve the reuse and recycling of construction waste. For example, the company ZenRobotics began to manufacture robots that used artificial intelligence and other recognition technologies to identify and sort household, industrial, and construction and demolition waste in 2007 [7]. Other well-known commercial robots have also been

Citation: Zhou, Q.; Liu, H.; Qiu, Y.; Zheng, W. Object Detection for Construction Waste Based on an Improved YOLOv5 Model. *Sustainability* **2023**, *15*, 681. <https://doi.org/10.3390/su15010681>

Academic Editors: Carlos Morón Fernández and Daniel Ferrández Vega

Received: 1 December 2022
Revised: 23 December 2022
Accepted: 28 December 2022
Published: 30 December 2022



Copyright: © 2022 by the authors. Licensee MDPI, Basel, Switzerland. This article is an open access article distributed under the terms and conditions of the Creative Commons Attribution (CC BY) license (<https://creativecommons.org/licenses/by/4.0/>).

tried for use in the waste management industry, such as Sadako [8], SamurAI [9], and AMP Robotics [10]. The majority of the existing systems capitalize on the agility of robots to rapidly transfer recyclables from a conveyor belt to a bin [11]. However, many factors affect the accuracy and efficiency of sorting construction waste. In a real work environment, the stacking of construction waste on the conveyor belt, the irregular shapes, and the small-sized objects lead to errors in detection. Measures should be taken to improve the accuracy of object detection.

Machine learning can improve the efficiency and accuracy of sorting construction waste. With sufficient data, a CV model can identify different waste materials by machine learning. Previous research has found that CV performed well in construction waste recycling. Several algorithms for CV have been used to identify and classify waste, but inter occlusion and small object detection were not fully considered. Convolutional neural network (CNN) is an algorithm that has become the standard in image classification and object recognition. Therefore, several model developments based on CNN have emerged. For example, Adedeji and Wang (2019) [12] employed such a technique, which extracted features learned by the ResNet-50, and performed waste classification with SVM. Chen et al. (2021) [13] developed a hybrid model that integrated visual features extracted by a DenseNet-169 network and physical features such as weight and depth collected by other sensors. These methods improve the accuracy of sorting waste, but still do not consider the inter occlusion and small object detection. Yang et al. (2021) [14] adopted a "ResNeXt + k-NN" structure. Lau Hiu Hoong et al. (2020) [15] improved the performance of sorting construction waste through the residual network. Chen et al. (2017) [16] employed Fast R-CNN to detect and locate waste objects on conveyor belts, which demonstrated a false negative rate (FNR) of 3% and a false positive rate (FPR) of 9%. Awe et al. (2017) [17], Wang et al. (2019) [18], and Nowakowski and Pamula (2020) [19] applied Faster R-CNN for the detection of residential and municipal waste, construction and demolition waste, and electronic waste, respectively. Ku et al. (2021) [6] proposed a deep learning method for grab detection based on R-CNN. Zhou et al. [20] selected the RepVGG residual network as the basic feature network based on the Faster-RCNN algorithm to retain more information of small-sized objects. Li et al. [21] built an RGB detection platform and used color cameras and laser line scanning sensors to collect RGB images to detect construction waste. Lin et al. [22] proposed a CVGGNet model based on knowledge transfer together with data enhancement and periodic-learning-rate technology to classify construction waste. From the above-mentioned studies, the applications of CV in waste sorting had been specifically focused on. The existing object detection algorithms were mainly improved from different perspectives: multi-scale feature fusion, data augmentation, training algorithm, and context-based detection.

In order to enhance the accuracy rate of object detection, the YOLO model has been used to identify and classify waste, such as YOLOv3 [23], YOLOv4 [24] and YOLOv5. The YOLO model uses multiple lower sampling layers, and the target features learned from the network are not exhaustive so the detection effect will be improved [25]. Liu et al. [26] improved the network structure and multi-scale detection based on the YOLOv3 algorithm. The mAP value could reach 91.96%. Chen et al. [27] designed a waste robot with a YOLOv4 model that can identify beverage bottles, cans, wastepaper, and banana peels in an unobstructed environment. Yuan et al. [28] proposed an improved algorithm based on YOLOv5 for underwater waste detection. Gamma transform was added in the preprocessing stage to improve the gray and contrast of underwater images, and the CBAM attention mechanism was embedded in the YOLOv5 detection part to highlight object features and suppress secondary information, thus improving the accuracy of detection. Therefore, YOLO algorithms have also been used for waste sorting. Similarly, YOLO algorithms were also improved from the following different perspectives: CBAM attention mechanism, multi-scale feature learning, data augmentation, and training strategy.

It is well known that small object detection and inter-occlusion are still challenging problems in computer vision. Currently, with the increasing need for recycling onsite

construction waste, a higher velocity of the conveyor belt and more stacking of waste will lead to difficulty in finely sorting, which is probably one of the most critical problems in construction waste management. Under the conditions of inter occlusion and small object detection, the accuracy of the CV may decrease [29].

Therefore, there are two problems in sorting construction waste: one is inter-object occlusion, i.e., multiple objects are overlaid on each other, occluding one another. The other problem is small-object detection. Hence, in order to solve these problems and further improve the accuracy of classification and detection of construction waste, an improved YOLOv5 model was proposed by applying the CBAM attention mechanism and SimSPPF module, adding a shallow detection layer to detect small construction waste objects and inter-occlusion and increasing the fourth scale feature fusion to the feature fusion part correspondingly. Additionally, a dataset was established, and a data enhancement method was used to expand the diversity of training samples.

2. Materials and Methods

2.1. YOLOv5 Architecture

Any robotic sorting system needs to accurately categorize recyclables from various waste material type. It is important for the system to develop an effective model. With the recent developments in deep learning, the YOLO family of models provides a scalable means for categorizing recyclables into various classes. Construction waste can be roughly split into 4 classes: brick, wood, stone and plastic, according to the material. Considering the accuracy and efficiency in object detection, the YOLOv5 model was chosen, which consists of three main architectural blocks: Backbone, Neck and Head, as shown in Figure 1.

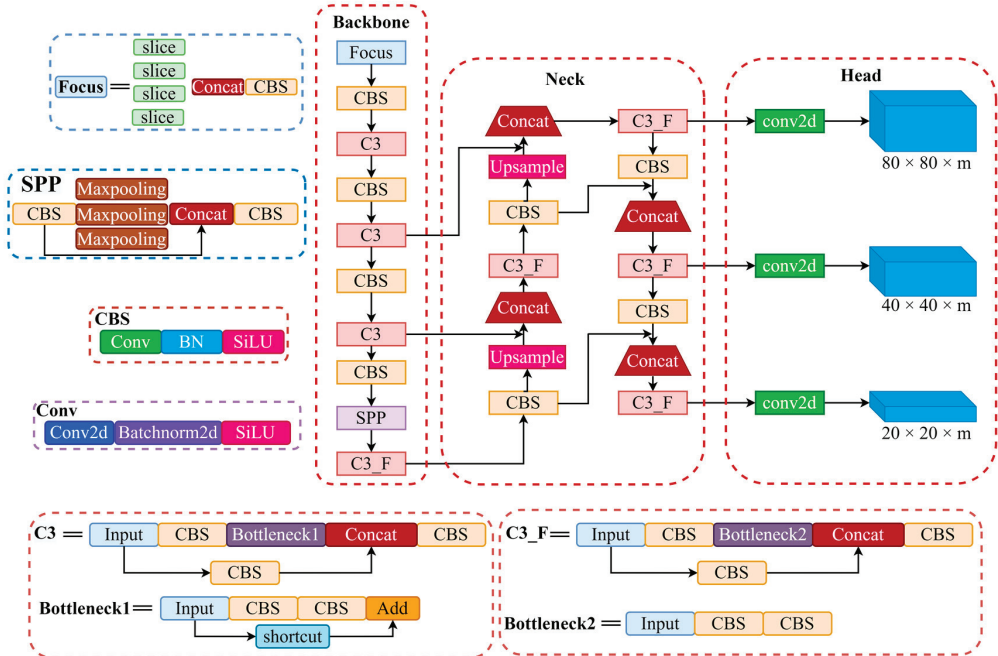


Figure 1. Architecture of YOLOv5 Model.

2.1.1. YOLOv5 Backbone

YOLOv5 Backbone employs CSPDarknet as the backbone for feature extraction from images consisting of cross-stage partial networks. The focus module, which rapidly down-samples the images of the dataset, can pass the image information into the channel, while

ensuring that the image information is not missing, i.e., more fully extracting the image information features. The backbone layer uses C3, C3_F and Spatial Pyramid Pooling (SPP) modules. C3 and C3_F modules can improve the ability of feature extraction from images, simplify the YOLOv5 model and make the detection speed faster [30]. The SPP module can improve the scale invariance of the dataset image, effectively increase the receiving range of the backbone features, make it easier to converge the network, and enhance the accuracy [31].

2.1.2. YOLOv5 Neck

YOLOv5 Neck uses PANet to generate a feature pyramid network to perform aggregation on the features and pass it to Head for prediction. The bottleneck layer of YOLOv5 combines feature pyramid network (FPN) and path aggregation network (PAN) structures. Deep feature images have stronger semantic information and weaker location information, while shallow feature images have stronger location information and weaker semantic information. FPN can transfer semantic information from the deep feature image to the shallow feature image [32]. Conversely, PAN can transfer location information from the shallow feature layer to the deep feature layer [33]. The combination of FPN and PAN can aggregate parameters of different detection layers from different trunk layers, which greatly strengthens the feature fusion ability of the network [24].

2.1.3. YOLOv5 Head

YOLOv5 Head consists of layers that generate predictions from the anchor boxes for object detection. The head includes two parts: loss function and non-maximum suppression (NMS). In YOLOv5, the binary cross entropy loss function is used to calculate classification loss and confidence loss, while the complete Iou (CIoU) loss function is applied to calculate location loss (bounding box regression loss). All the losses add up to the total loss. The CIoU loss function fully considers three key geometric parameters: the overlap area, the distance from the center point, and the aspect ratio, thus improving the speed and accuracy of the regression of the prediction box [34]. The NMS is mainly used to remove redundant detection boxes and reserve the candidate box with the highest prediction probability as the final prediction box [35].

YOLOv5 is a family of compound-scaled object detection models trained on the COCO dataset [36]. YOLOv5 is the latest object detection model developed by Ultralytics, which offers open-source research into future object detection methods. An open-source network, such as the COCO dataset, was employed since it has been particularly successful at similar tasks: object segmentation, object detection and classification. However, any open-source dataset cannot be used in all circumstances due to the various classes of object. Once a class is varied, the model should be retrained according to a new dataset. Meanwhile, the model needs to be further optimized in the case of object occlusion and small-object detection.

2.2. Improved YOLOv5

The convolutional block attention module (CBAM) is added to the Backbone of the original YOLOv5 model, the feature fusion of the fourth scale is embedded in the Neck, and the shallow detection layer is employed in the Head, which will be of benefit in detecting the small objects and inter occlusion. The improved model architecture is shown in Figure 2.

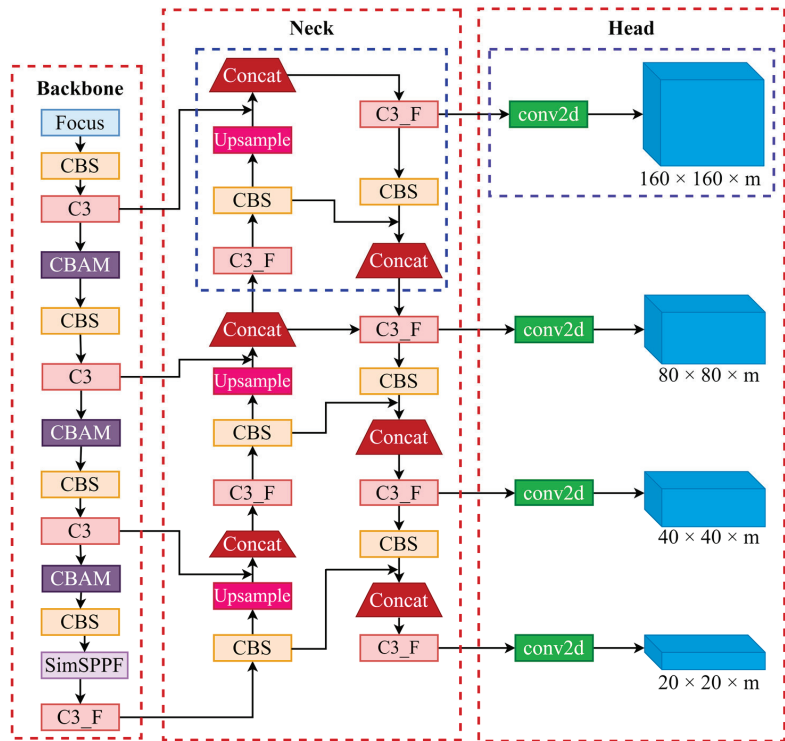


Figure 2. Architecture of the improved YOLOv5 Model.

2.2.1. CBAM-CSPDarknet53

Due to the problem of small objection with low pixels in the picture, it is easy for there to be missing information in construction waste sorting. The CBAM attention mechanism was added in the YOLOv5 backbone, named CBAM-CSPDarknet53. The CBAM attention mechanism module is mainly divided into a channel attention module and a spatial attention module [37]. The channel attention module pays more attention to the core information in the image of the dataset and can squeeze the spatial size, while the channel size remains uniform. The spatial attention module focuses on the position information of the object and can squeeze the channel size without modifying the spatial dimension. The structure of the CBAM attention mechanism module is shown in Figure 3.

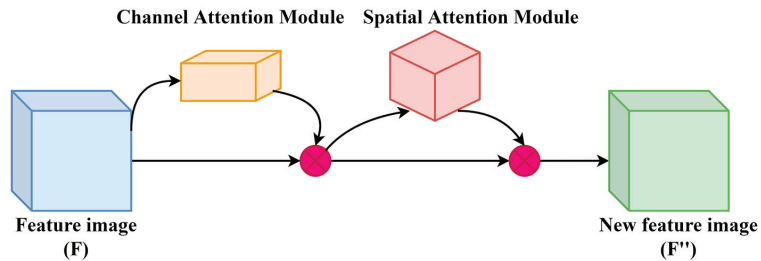


Figure 3. Structure of CBAM attention mechanism.

The structure of the channel attention module is described in Figure 4. The feature image $F (F \in R^{C \times H \times W})$ is processed by average pooling and maximum pooling, and then, the feature image size changes from $C \times H \times W$ to $C \times 1 \times 1$. Next, the new feature image

is sent to the Multi-Layer Perception (MLP) and the number of neurons in the first layer of the MLP is C/r , where r is the decline rate, and C is the number of neurons in the second layer of the MLP. Then, after processing by the Sigmoid function, the weight coefficient M_c will be obtained and calculated. The equation is shown in Equation (1).

$$M_c(F) = \sigma(W_1(W_0(F_{avg}^C)) + W_1(W_0(F_{max}^C))) \tag{1}$$

where: σ is the Sigmoid function; avg is global average pooling; max is the maximum pooling; $W_0 \in R^{C \times \frac{C}{r}}$; $W_1 \in R^{C \times \frac{C}{r}}$; F_{avg}^C is the global average pooled feature image of size $1 \times 1 \times C$; F_{max}^C is the largest pooled feature image with size $1 \times 1 \times C$.

Finally, the weight coefficient M_c is multiplied by the feature image F ($F \in R^{C \times H \times W}$). Therefore, the new feature image can be obtained.

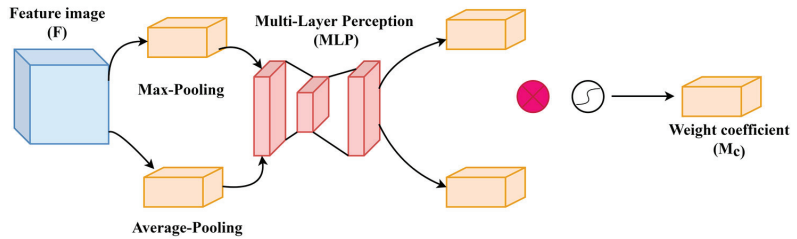


Figure 4. Structure of Channel Attention Module.

The structure of the spatial attention module is shown in Figure 5. The feature images of the new dataset obtained in the previous step are again processed by maximum pooling and average pooling, and then divided into two channels of size is $1 \times H \times W$. Then, the obtained tensors are stacked together by joining operations, and the weight coefficient M_s is obtained after convolution and Sigmoid function operations. The equation is shown in Equation (2).

$$M_s(F) = \sigma(f^{7 \times 7}([F_{avg}^S; F_{max}^S])) \tag{2}$$

where: σ is the Sigmoid function; avg is global average pooling; max is the maximum pooling; $f^{7 \times 7}$ is the convolution of 7×7 ; F_{avg}^S is the feature after the average pooling operation, and the size is $1 \times H \times W$; F_{max}^S is the feature after the maximum pooling operation, and the size is $1 \times H \times W$.

Finally, the calculated weight coefficient M_s is multiplied by the feature image F' which can obtain a new feature image F'' .

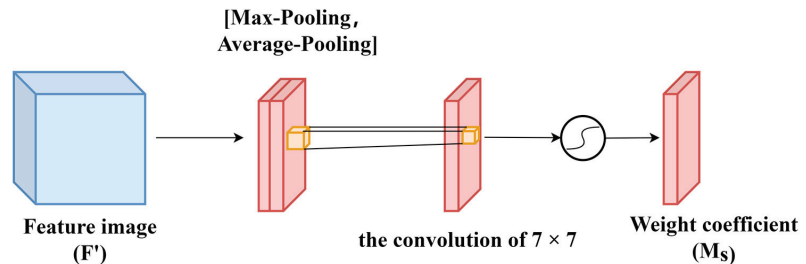


Figure 5. Structure of Spatial Attention Module.

2.2.2. SimSPPF (Simplified SPPF)

The SimSPPF module based on the maximum pooling layer at the same size is proposed to replace the SPP module in the original YOLOv5s model. The structure of the SimSPPF module is shown in Figure 6.

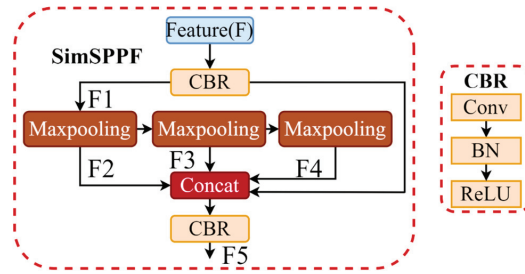


Figure 6. Structure of SimSPPF Module.

The SimSPPF module has a scale of 5×5 for the input feature images in the construction waste dataset. Because of the different maximum poolings in the three stages, channels should be connected for the output of the pooling layer. The equations are shown in Equations (3)–(7).

$$F1 = CBR(F) \quad (3)$$

$$F2 = Maxpooling(F1) \quad (4)$$

$$F3 = Maxpooling(F2) \quad (5)$$

$$F4 = Maxpooling(F3) \quad (6)$$

$$F5 = CBR([F; F2; F3; F4]) \quad (7)$$

The SimSPPF module can avoid the local feature loss of the construction waste dataset images, effectively reduce the residual parameter information, and retain the core texture features of construction waste dataset images. The calculation speed of the forward propagation of the SimSPPF module is faster than that of the SSP module. Meanwhile, after the SimSPPF module is embedded, the ability of the YOLOv5 model to extract image features can be improved greatly.

2.2.3. Multi-Scale Detection

In the process of sorting construction waste, small objects need to be detected. However, the original YOLOv5 model can only detect an 8×8 receptive field for an input image with a size of 640×640 . If the height or width of the detected object is less than 8 pixels in the dataset images, the image information features will be missing after convolution processing. In order to solve this problem, a special detection layer for small objects is added. This special detection layer is a 160×160 size output feature image, which can identify a receptive field size of more than 4×4 objects, basically meeting the detection requirements of sorting construction waste. Meanwhile, the three-scale feature fusion of the original YOLOv5 model was correspondingly increased to four-scale feature fusion, and a 160×160 feature detection layer was added. Therefore, the 80×80 feature detection layer was up-sampled twice. The twice up-sampled layer fused with the newly added 160×160 feature detection layer, which was used to detect small objects. The overall network structure of the improved YOLOv5 model is shown in Figure 7, where the dotted line in the Head denotes the increased detection of the fourth scale, and the dotted line in the Neck describes the corresponding increased part of the four-scale feature fusion.

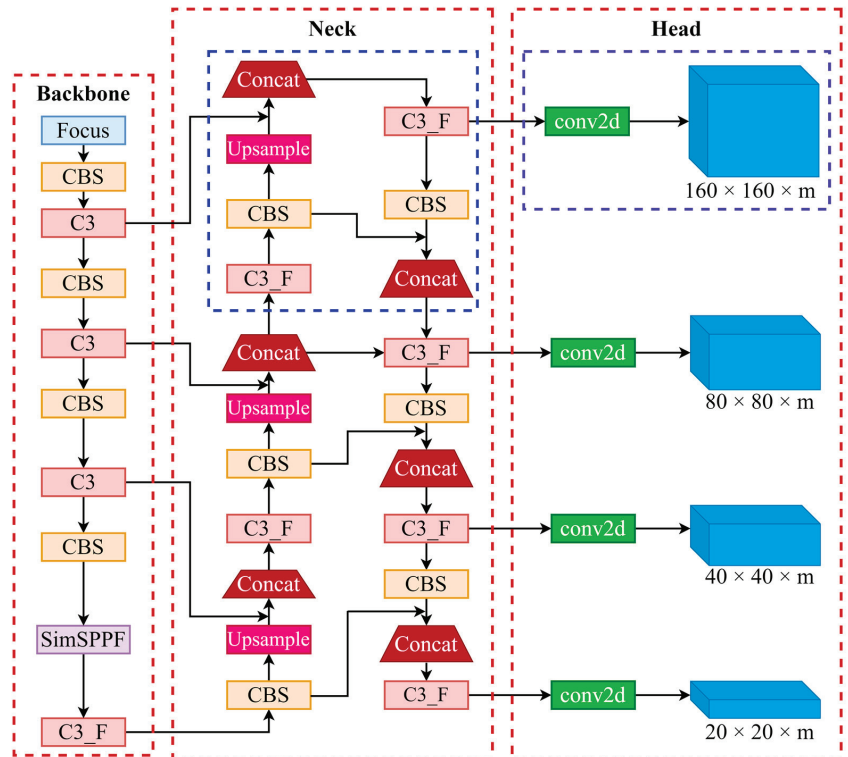


Figure 7. Structure of the Improved Multi-Scale Detection.

2.3. Dataset Construction and Evaluation Index

2.3.1. Dataset

To evaluate the improved YOLOv5 model, it was tested in the two datasets. One is the public dataset, PASCAL VOC [38], and the other is the self-built construction waste dataset. The PASCAL VOC dataset is a common object-detection dataset, which includes 4 categories and 20 subcategories. Here, the train + val parts of VOC2007 and VOC2012 are applied for the training set, which consists of 5011 training samples of VOC 2007 and 11,540 training samples of VOC2012. Additionally, the test part of the VOC2007 dataset is given as the test set, which consists of 4952 test samples.

A rich dataset including many construction waste images of different types should be implemented in sorting waste. Only two open-source datasets—TrashNet [39] and Taco [40]—are available, but they are not suitable for a robotic sorting system because the detected objects transferred on a conveyor belt would be irregular, dirty and piled up on one another. Developing a new dataset is the first important step. Thus, sample images were collected in the construction site, as shown in Figure 8. The dataset consisted of 3046 construction waste images divided into 4 classes: bricks, wood, stones, and plastics. To create a more effective dataset, further data enhancement processing should be carried out, such as image flipping, translation, rotation, cropping, scaling, adding noise and random occlusion operations [41], so as to effectively avoid the overfitting problem in the training and improve the robustness of the model. A graphical image annotation tool, Labeling, was used to label the image in the construction waste dataset. Finally, the dataset was divided into 3 subsets: the training set accounted for 80%, the verification set 10% and the test set 10%.



Figure 8. Construction waste image on site.

2.3.2. Model Performance Evaluation Index

Average precision (AP), $F1$ score ($F1$ -score) and mean average precision (mAP) were used as evaluation indicators to test the performance of the model. Average precision is a measure that combines recall and precision for ranked retrieval results. The recall rate reflects the ability to find positive samples, the precision expresses the ability to classify samples, and the AP shows the overall performance for object detection. The precision (P)–recall (R) curve can be plotted with the calculated P and R as the ordinate and abscissa, while the area under the curve is AP , and the mean value of AP is mAP . In addition, $F1$ -score is commonly used for multiple classification problems, which is considered the harmonic average of precision and recall. The equations are shown in Equations (8)–(12).

$$P = \frac{TP}{TP + FP} \quad (8)$$

$$R = \frac{TP}{TP + FN} \quad (9)$$

$$AP = \int_0^1 P \cdot RdR \quad (10)$$

$$mAP = \frac{1}{N} \sum_{i=1}^N AP_i \quad (11)$$

$$F1 = 2 \frac{P \cdot R}{P + R} \quad (12)$$

where: TP (true positive) is the number of positive samples correctly predicted as positive samples; FP is the number of negative samples wrongly predicted as positive; FN is the number of positive samples wrongly predicted as negative samples; N is the number of sample classes of dataset. Judgment of positive and negative samples was based on the threshold of the Intersection over Union (IoU) which is the area of overlap between the predicted segmentation and the ground truth divided by the area of union between the predicted segmentation and the ground truth. If the IoU is greater than the threshold, it is classified as a positive sample, and if the IoU is less than the threshold, it is a negative sample. When the IoU is 0.5, the average accuracy of the YOLOv5 model is expressed as $AP_{0.5}$, and the mean average accuracy is described as $mAP_{0.5}$.

2.3.3. Experimental Platform and Parameter Setting

The experimental configuration consists of the software environment of Pytorch1.8.0 and the hardware equipment of the CPU of Intel (R) Core (TM) i5 and GPU of NVIDIA GeForce RTX 3060 Ti with 16 GB memory and the Windows10 operation system, as shown in Table 1. During the training process of the YOLOv5 model, Adaptive Moment Estimation (Adam), an algorithm for stochastic optimization, is used - which only requires little memory. The momentum factor was set at 0.937 and the initial learning rate was 0.001.

The learning rate is adjusted by the cosine annealing method [42]. The weight attenuation coefficient, the Batch size, and the epoch times of training was set to 0, 16, and 300, respectively. The method of label smoothing was used to smooth the classification label of the image, which could help to avoid overfitting. The value of label smoothing was 0.01.

Table 1. Experimental platform configuration.

| Configuration Name | Parameter |
|-------------------------|---|
| Operation System | Win10 |
| GPU | NVIDIA GeForce RTX 3060 Ti |
| CPU | Intel (R) Core (TM) i5-10400F CPU @2.90 GHz |
| Memory | 16 G |
| Deep Learning Framework | Pytorch1.8.0 |

3. Results

3.1. Comparison of Experimental Results on a Public Dataset

In order to compare the performance of the improved model with that of the original YOLOv5 model, an experimental comparison was made on the PASCAL VOC dataset. The experimental results are shown in Table 2.

Table 2. Experimental results on PASCAL VOC dataset.

| Method | Training Dataset | Test Dataset | mAP |
|----------|------------------|--------------|--------|
| YOLOv5_Y | VOC07 + 12 | VOC-Test07 | 0.8620 |
| Ours | VOC07 + 12 | VOC-Test07 | 0.8731 |

The improved YOLOv5 model can increase the mAP by 1.11% and enhance the effect of objection detection.

3.2. Ablation Study

In order to compare the performance of the improved model with other different models, ablation studies were carried out. The label smoothing method was used to process the images in the training experiment. Evaluation was performed every 10 epochs of training. A total of 300 epochs were trained in the experiment. The experimental results are shown in Table 3.

Table 3. Ablation study results for model on self-built construction waste dataset.

| Method | AP | | | | mAP | F1 | | | |
|-----------|--------|--------|--------|---------|--------|-------|------|-------|---------|
| | Brick | Wood | Stone | Plastic | | Brick | Wood | Stone | Plastic |
| YOLOv5_Y | 0.8711 | 0.9138 | 0.9158 | 0.8959 | 0.8991 | 0.84 | 0.82 | 0.89 | 0.85 |
| YOLOv5_C | 0.9141 | 0.9572 | 0.9511 | 0.9581 | 0.9451 | 0.89 | 0.90 | 0.93 | 0.87 |
| YOLOv5_S | 0.9075 | 0.9565 | 0.9430 | 0.9447 | 0.9379 | 0.88 | 0.92 | 0.92 | 0.90 |
| YOLOv5_D | 0.9119 | 0.9581 | 0.9534 | 0.9605 | 0.9460 | 0.89 | 0.91 | 0.92 | 0.91 |
| YOLOv5_CS | 0.9132 | 0.9551 | 0.9506 | 0.9680 | 0.9467 | 0.89 | 0.92 | 0.94 | 0.90 |
| YOLOv5_CD | 0.9215 | 0.9485 | 0.9422 | 0.9545 | 0.9417 | 0.89 | 0.91 | 0.93 | 0.92 |
| YOLOv5_SD | 0.9095 | 0.9555 | 0.9412 | 0.9718 | 0.9445 | 0.88 | 0.93 | 0.93 | 0.92 |
| Ours | 0.9222 | 0.9659 | 0.9555 | 0.9485 | 0.9480 | 0.89 | 0.91 | 0.93 | 0.92 |

YOLOv5_Y, YOLOv5_C, YOLOv5_S, YOLOv5_D, YOLOv5_CS, YOLOv5_CD, and YOLOv5_SD represent the original YOLOv5 model, the model with CBAM, the model with the SimSPPF module, the model with improved multi-scale detection, the model with the CBAM and SimSPPF module, the model with CBAM and improved multi-scale detection, and the model with the SimSPPF module and improved multi-scale detection, respectively. Our study denotes the proposed YOLOv5 model, i.e., the model with all of the CBAM,

the SimSPPF module and improved multi-scale detection. Additionally, AP values of the four classes for the YOLOv5 original model are described in Figure 9 and for the improved YOLOv5 model in Figure 10.

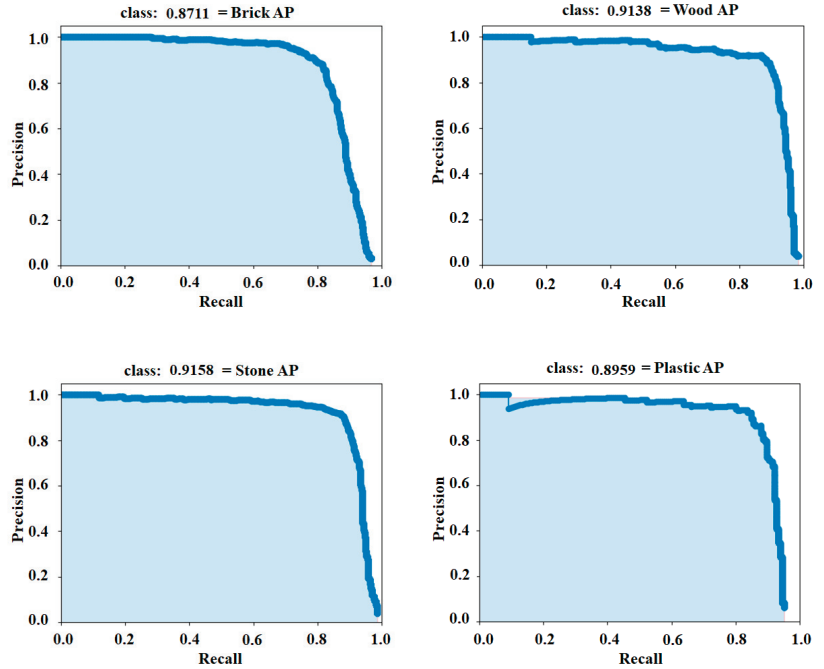


Figure 9. The AP Value of the Four Classes for YOLOv5 Original Model.

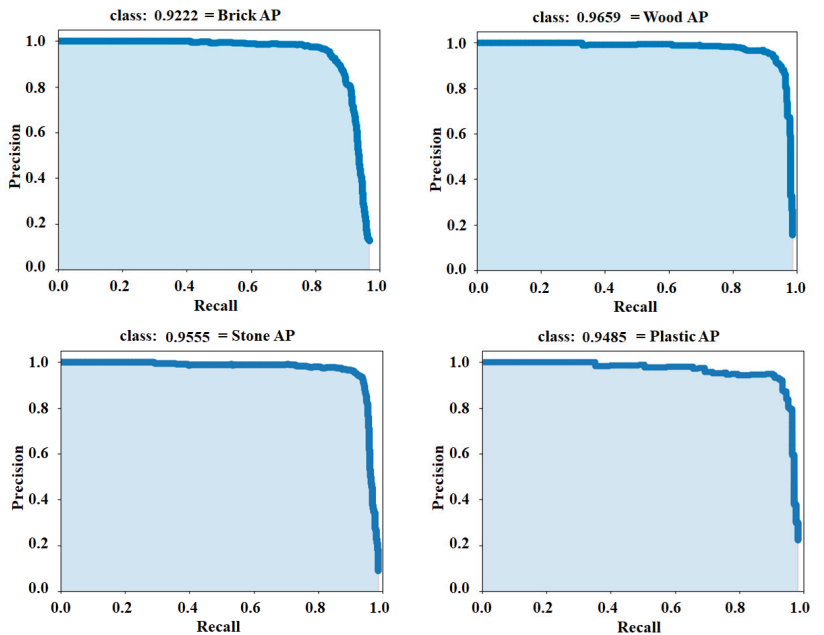


Figure 10. The AP Value of Four Types of objects for Our Improved Method.

It can be seen from Table 2 that the mAP of the original model of YOLOv5 on the construction waste dataset is the lowest, at only 0.8991. When CBAM was added, mAP can be improved by 4.6%, up to 0.9451, but with the replacement of the SPP module with the SimSPPF module, mAP could only be increased by 3.88%. Even so, the method of improvement of multi-scale detection can increase mAP by 4.69%. When both CBAM and the SimSPPF module were added, mAP increased by 4.76%. When increasing CBAM and improving multi-scale detection, mAP could be increased by 4.26%. With the addition of the SimSPPF module and the improvement of multi-scale detection, mAP was increased by 4.54%. However, in the experiment with our proposed method, i.e., when adding the CBAM, the SimSPPF module and improving multi-scale detection, mAP can be improved by 4.89%, the highest of all the different models.

Similarly, the F1-scores of brick, wood, stone and plastic of the original YOLOv5 model are 0.84, 0.82, 0.89 and 0.85, respectively, as shown in Table 2. However, in the proposed method, which adds all the CBAM and the SimSPPF module and improves multi-scale detection, the F1-scores of brick, wood, stone and plastic are 0.89, 0.91, 0.93 and 0.92, increasing by 5%, 9%, 4% and 7%, respectively. Therefore, the improved YOLOv5 model has a higher accuracy and better availability in objection detection, thereby improving the efficiency of sorting construction waste.

3.3. Contrast Experiment

To further verify the advantages and effectiveness of the improved YOLOv5 model on the construction waste dataset, a contrast experiment was also carried out. Comparing the improved model with other conventional models, such as YOLOv7, YOLOv5, YOLOv4, YOLOv3 and Faster-RCNN models, the loss indicator and mAP of every model in the training experiment and testing experiment are shown in Figure 11.

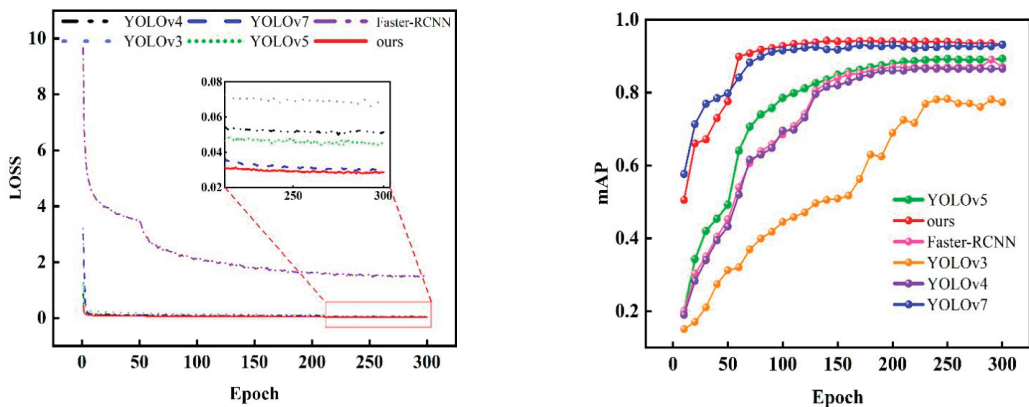


Figure 11. The Value of Loss and mAP of Different Models.

The loss of every model decreases rapidly in the first 20 epochs, which shows the training does not reach a stable state. If the training became stable, the loss in the curve would be flat rather than steep. When the training reaches a relatively stable state, the loss in our model is lower than that of other models. Meanwhile, the mAP value of every model increases rapidly at the first 60 epochs. Similarly, ours has the most obvious improvement among all the models. After 200 epochs of training, all models tend to be steadier, and the mAP of ours is significantly higher than that of other models.

The values of the evaluation indicators are also described in Table 4. Compared with YOLOv7, YOLOv5, YOLOv4, YOLOv3 and the Faster-RCNN model, the mAP value of our model increased by 2.15%, 4.89%, 8.24%, 16.12% and 7.78%, respectively. It shows that the improved YOLOv5 model can improve the accuracy to classify and detect construction waste.

Table 4. The Performance Contrast for Different Models.

| Method | AP | | | | mAP | F1 | | | |
|-------------|--------|--------|--------|---------|--------|-------|------|-------|---------|
| | Brick | Wood | Stone | Plastic | | Brick | Wood | Stone | Plastic |
| Ours | 0.9222 | 0.9659 | 0.9555 | 0.9485 | 0.9480 | 0.89 | 0.91 | 0.93 | 0.92 |
| YOLOv7 | 0.9006 | 0.9416 | 0.9250 | 0.9388 | 0.9265 | 0.88 | 0.93 | 0.91 | 0.92 |
| YOLOv5_Y | 0.8711 | 0.9138 | 0.9158 | 0.8959 | 0.8991 | 0.84 | 0.82 | 0.89 | 0.85 |
| YOLOv4 | 0.8063 | 0.8972 | 0.8809 | 0.8782 | 0.8656 | 0.74 | 0.85 | 0.85 | 0.84 |
| YOLOv3 | 0.7016 | 0.8157 | 0.8239 | 0.8058 | 0.7868 | 0.69 | 0.77 | 0.77 | 0.79 |
| Faster-RCNN | 0.7933 | 0.8967 | 0.8886 | 0.9021 | 0.8702 | 0.75 | 0.85 | 0.83 | 0.88 |

4. Conclusions

In construction waste sorting, inter-object occlusions and small-object detection are the two most important problems, affecting the effective performance of the construction waste detection system. In order to increase the accuracy of object detection, an improved YOLOv5 model is proposed for intelligent construction waste sorting and is trained by a dataset consisting of 3046 construction waste images of, for example, bricks, wood, stones, and plastics. The following conclusions can be drawn:

- (1) An improved YOLOv5 can be obtained through the fourth-scale feature fusion, shallow detection layer, CBAM and SimSPPF. The increase in CBAM and SimSPPF in the backbone layer of YOLOv5 can strengthen the characteristics of small objects and mutual occlusion and enhance the effect and accuracy of detection, thus improving the generalization ability and robustness of the model. The fourth-scale feature fusion is added to the feature fusion part in the Neck and a shallow detection layer is added to the Head, which can aid in the detection of small objects and inter-occlusion.
- (2) Compared with the conventional models of Faster-RCNN, YOLOv3, YOLOv4 and YOLOv7, the detection accuracy of the proposed model is higher, and its mAP can reach up to 0.9480, which verifies the accuracy and the availability of the improved YOLOv5 model.

Author Contributions: Project administration, Q.Z.; methodology, H.L.; Data collection, Y.Q. and W.Z. All authors have read and agreed to the published version of the manuscript.

Funding: This research was funded by the “Research Project of the Ministry of Housing and urban-rural Development of the People’s Republic of China, grant number 2022-K-079”.

Institutional Review Board Statement: Not applicable.

Informed Consent Statement: Not applicable.

Data Availability Statement: All data used in this research can be provided upon request.

Conflicts of Interest: The authors declare no conflict of interest.

References

1. Huang, B.; Gao, X.; Xu, X.; Song, J.; Geng, Y.; Sarkis, J.; Fishman, T.; Kua, H.; Nakatani, J. A life cycle thinking framework to mitigate the environmental impact of building materials. *One Earth* **2020**, *3*, 564–573. [CrossRef]
2. Teh, S.H.; Wiedmann, T.; Moore, S. Mixed-unit hybrid life cycle assessment applied to the recycling of construction materials. *J. Econ. Struct.* **2018**, *7*, 13. [CrossRef]
3. Duan, H.; Miller, T.R.; Liu, G.; Tam, V.W.Y. Construction debris becomes growing concern of growing cities. *Waste Manag.* **2019**, *83*, 1–5. [CrossRef] [PubMed]
4. Lei, J.; Huang, B.; Huang, Y. Life cycle thinking for sustainable development in the building industry. In *Life Cycle Sustainability Assessment for Decision-Making*; Elsevier: Amsterdam, The Netherlands, 2020; pp. 125–138.
5. Yu, B.; Wang, J.; Li, J.; Lu, W.; Li, C.Z.; Xu, X. Quantifying the potential of recycling demolition waste generated from urban renewal: A case study in Shenzhen, China. *J. Clean. Prod.* **2020**, *247*, 119127. [CrossRef]
6. Ku, Y.; Yang, J.; Fang, H.; Xiao, W.; Zhuang, J. Deep learning of grasping detection for a robot used in sorting construction and demolition waste. *J. Mater. Cycles Waste Manag.* **2021**, *23*, 84–95. [CrossRef]
7. Zen Robotics. Available online: <https://zenrobotics.com/> (accessed on 1 October 2022).

8. Sadako Technologies. Applications/Max-AI. Available online: <https://sadako.es/max-ai/> (accessed on 1 October 2022).
9. Machinex. SAMURAI-Recycling Sorting Robots. Available online: <https://www.machinexrecycling.com/products/samurai-sorting-robot/> (accessed on 1 September 2022).
10. AMP Robotics. Available online: <https://www.amrobotics.com/> (accessed on 1 October 2022).
11. Koskinopoulou, M.; Raptopoulos, F.; Papadopoulos, G.; Mavrakis, N.; Maniadakis, M. Robotic waste sorting technology: Toward a vision-based categorization system for the industrial robotic separation of recyclable waste. *IEEE Robot. Autom. Mag.* **2021**, *28*, 50–60. [[CrossRef](#)]
12. Adedeji, O.; Wang, Z. Intelligent waste classification system using deep learning convolutional neural network. *Procedia Manuf.* **2019**, *35*, 607–612. [[CrossRef](#)]
13. Chen, J.; Lu, W.; Xue, F. “Looking beneath the surface”: A visual-physical feature hybrid approach for unattended gauging of construction waste composition. *J. Environ. Manag.* **2021**, *286*, 112233. [[CrossRef](#)] [[PubMed](#)]
14. Yang, J.; Zeng, Z.; Wang, K.; Zou, H.; Xie, L. GarbageNet: A unified learning framework for robust garbage classification. *IEEE Trans. Artif. Intell.* **2021**, *2*, 372–380. [[CrossRef](#)]
15. Hoong, J.D.L.H.; Lux, J.; Mahieux, P.-Y.; Turcry, P.; Ait-Mokhtar, A. Determination of the composition of recycled aggregates using a deep learning-based image analysis. *Automat. Constr.* **2020**, *116*, 103204. [[CrossRef](#)]
16. Zhihong, C.; Hebin, Z.; Yanbo, W.; Binyan, L.; Yu, L. A vision-based robotic grasping system using deep learning for garbage sorting. In Proceedings of the 2017 36th Chinese Control Conference (CCC), Dalian, China, 26–28 July 2017; pp. 11223–11226.
17. Awe, O.; Mengistu, R.; Sreedhar, V. Smart trash net: Waste localization and classification. *arXiv 2017. preprint*. Available online: <http://cs229.stanford.edu/proj2017/final-reports/5226723.pdf> (accessed on 1 January 2022).
18. Wang, Z.; Li, H.; Zhang, X. Construction waste recycling robot for nails and screws: Computer vision technology and neural network approach. *Automat. Constr.* **2019**, *97*, 220–228. [[CrossRef](#)]
19. Nowakowski, P.; Pamuła, T. Application of deep learning object classifier to improve e-waste collection planning. *Waste Manag.* **2020**, *109*, 1–9. [[CrossRef](#)] [[PubMed](#)]
20. Zhou, H.; Zhao, L. Intelligent detection and classification of domestic waste based on improved faster-RCNN. *J. Fuyang Norm. Univ. Nat. Sci.* **2022**, *39*, 49–55.
21. Li, J.; Fang, H.; Fan, L.; Yang, J.; Ji, T.; Chen, Q. RGB-D fusion models for construction and demolition waste detection. *Waste Manag.* **2022**, *139*, 96–104. [[CrossRef](#)] [[PubMed](#)]
22. Lin, K.; Zhou, T.; Gao, X.; Li, Z.; Duan, H.; Wu, H.; Lu, G.; Zhao, Y. Deep convolutional neural networks for construction and demolition waste classification: VGGNet structures, cyclical learning rate, and knowledge transfer. *J. Environ. Manag.* **2022**, *318*, 115501. [[CrossRef](#)]
23. Redmon, J.; Farhadi, A. Yolov3: An incremental improvement. *arXiv 2018*, arXiv:1804.02767.
24. Bochkovskiy, A.; Wang, C.-Y.; Liao, H.-Y.M. Yolov4: Optimal speed and accuracy of object detection. *arXiv 2020*, arXiv:2004.10934.
25. Jiang, P.; Ergu, D.; Liu, F.; Cai, Y.; Ma, B. A Review of Yolo algorithm developments. *Procedia Comput. Sci.* **2022**, *199*, 1066–1073. [[CrossRef](#)]
26. Liu, W.; Peng, J.; Wu, B.; You, T. Improved YOLOv3 life article detection method for sorting. *Transducer Microsyst. Technol.* **2022**, *41*, 134–137.
27. Chen, Y.; Li, L.; Xie, H.; Lu, S.; Dong, J. Garbage sorting robot based on machine vision. *Instrum. Anal. Monit.* **2022**, *1*, 30–34.
28. Yuan, H.; Zang, T. Underwater garbage target detection based on the attention mechanism Ghosty-YOLOV5. *Environ. Eng.* **2022**, *9*, 1–14. Available online: <https://kns.cnki.net/kcms/detail/11.2097.X.20220913.1006.004.html> (accessed on 1 January 2022).
29. Wang, Z.; Li, H.; Yang, X. Vision-based robotic system for on-site construction and demolition waste sorting and recycling. *J. Build. Eng.* **2020**, *32*, 101769. [[CrossRef](#)]
30. Chen, L.; Cao, Y.; Huang, M.; Xie, X. Flame detection method based on improved YOLOv5. *Comput. Eng.* **2022**, *10*, 1–17. [[CrossRef](#)]
31. He, K.; Zhang, X.; Ren, S.; Sun, J. Spatial pyramid pooling in deep convolutional networks for visual recognition. *IEEE Trans. Pattern Anal. Mach. Intell.* **2015**, *37*, 1904–1916. [[CrossRef](#)]
32. Lin, T.-Y.; Dollár, P.; Girshick, R.; He, K.; Hariharan, B.; Belongie, S. Feature pyramid networks for object detection. In Proceedings of the IEEE Conference on Computer Vision and Pattern Recognition, Honolulu, HI, USA, 21–26 July 2017; pp. 2117–2125.
33. Liu, S.; Qi, L.; Qin, H.; Shi, J.; Jia, J. Path aggregation network for instance segmentation. In Proceedings of the IEEE Conference on Computer Vision and Pattern Recognition, Salt Lake City, UT, USA, 18–22 June 2018; pp. 8759–8768.
34. Jiang, D.; Jiang, Z.; Huang, Z.; Guo, C.; Li, B. Uav vehicle target detection algorithm based on Efficientnet. *Comput. Eng. Appl.* **2022**, *10*, 1–11. Available online: <https://kns.cnki.net/kcms/detail/11.2127.TP.20221027.0859.002.html> (accessed on 1 January 2022).
35. Su, S.; Chen, R.; Zhu, Y.; Jiang, B. Relocation non-maximum suppression algorithm. *Opt. Precis. Eng.* **2022**, *30*, 1620–1630.
36. Lin, T.-Y.; Maire, M.; Belongie, S.; Hays, J.; Perona, P.; Ramanan, D.; Dollár, P.; Zitnick, C.L. Microsoft coco: Common objects in context. In Proceedings of the European Conference on Computer Vision, Zurich, Switzerland, 8–11 September 2014; pp. 740–755.
37. Woo, S.; Park, J.; Lee, J.-Y.; Kweon, I.S. Cbam: Convolutional block attention module. In Proceedings of the European Conference on Computer Vision (ECCV), Munich, Germany, 8–14 September 2018; pp. 3–19.
38. Everingham, M.; van Gool, L.; Williams, C.K.I.; Winn, J.; Zisserman, A. The pascal visual object classes (voc) challenge. *Int. J. Comput. Vis.* **2010**, *88*, 303–338. [[CrossRef](#)]

39. Thung, G.; Yang, M. Classification of Trash for Recyclability Status. CS229 Project Report. 2016, pp. 1–6. Available online: <http://cs229.stanford.edu/proj2016/report/ThungYang-ClassificationOfTrashForRecyclabilityStatus-report.pdf> (accessed on 1 January 2022).
40. Proença, P.F.; Simões, P. Taco: Trash annotations in context for litter detection. *arXiv* **2020**, arXiv:2003.06975.
41. Zhao, X.; Zhang, Q.; Wang, W.; Xu, Z. Image detection method of combustible dust cloud. *China Saf. Sci. J.* **2020**, *30*, 8–13.
42. Qiu, Z.; Zhu, X.; Liao, C.; Shi, D.; Kuang, Y.; Li, Y.; Zhang, Y. Detection of bird species related to transmission line faults based on lightweight convolutional neural network. *IET Gener. Transm. Dis.* **2022**, *16*, 869–881. [[CrossRef](#)]

Disclaimer/Publisher’s Note: The statements, opinions and data contained in all publications are solely those of the individual author(s) and contributor(s) and not of MDPI and/or the editor(s). MDPI and/or the editor(s) disclaim responsibility for any injury to people or property resulting from any ideas, methods, instructions or products referred to in the content.

Ecological and Economic Assessment of the Reuse of Steel Halls in Terms of LCA

Piotr Sobierajewicz ¹, Janusz Adamczyk ^{2,*} and Robert Dylewski ³

¹ Faculty of Civil Engineering, Architecture and Environmental Engineering, Institute of Architecture and Urban Planning, University of Zielona Góra, ul. Licealna 9, 65-417 Zielona Góra, Poland

² Faculty of Economics and Management, Institute of Economics and Finance, University of Zielona Góra, ul. Licealna 9, 65-417 Zielona Góra, Poland

³ Faculty of Mathematics, Institute of Mathematics, Computer Science and Econometrics, University of Zielona Góra, ul. Licealna 9, 65-417 Zielona Góra, Poland

* Correspondence: j.adamczyk@wez.uz.zgora.pl

Abstract: In engineering practice, investment activities related to the construction of a building are still limited to the idea of a linear cradle to grave (C2G) economy. The aim of the study is to determine the ecological and economic benefits inherent in the reuse of structural elements of a hall building using the idea of a Cradle to Cradle (C2C) looped circular economy and Life Cycle Assessment (LCA). As a rule, a multiple circulation of materials from which model buildings are made was assumed through successive life cycles: creation, use, demolition and then further use of the elements. This approach is distinguished by minimizing negative impacts as a result of optimizing the mass of the structure—striving to relieve the environment, thus improving economic efficiency and leaving a positive ecological footprint. The assessment of cumulative ecological, economic and technical parameters (EET) methodology of generalized ecological indicator (WE) for quick and practical assessment of the ecological effect of multi-use steel halls, based on LCA, was proposed. The authors of the work attempted to assess the usefulness of such a structure with the example of four types of halls commonly used in the construction industry. The linear stream of C2G (cradle to grave) and then C2C (cradle to cradle) flows was calculated by introducing ecological parameters for comparative assessment. Finally, a methodology for calculating the ecological amortization of buildings (EAB) was proposed. The authors hope that the proposed integrated assessment of technical, economic and ecological parameters, which are components of the design process, will contribute to a new approach, the so-called fast-track pro-environmental project.

Keywords: LCA; reuse; steel halls; multiple assembly; sustainable construction; ecological and economic assessment

Citation: Sobierajewicz, P.; Adamczyk, J.; Dylewski, R. Ecological and Economic Assessment of the Reuse of Steel Halls in Terms of LCA. *Appl. Sci.* **2023**, *13*, 1597. <https://doi.org/10.3390/app13031597>

Academic Editors: Carlos Morón Fernández and Daniel Ferrández Vega

Received: 27 December 2022

Revised: 23 January 2023

Accepted: 24 January 2023

Published: 26 January 2023



Copyright: © 2023 by the authors. Licensee MDPI, Basel, Switzerland. This article is an open access article distributed under the terms and conditions of the Creative Commons Attribution (CC BY) license (<https://creativecommons.org/licenses/by/4.0/>).

1. Introduction

Limited natural resources increase the need for environmentally friendly production of material goods. The work focuses on the quantitative minimization of the waste stream in the design of production processes of hall-type buildings in order to eliminate or reduce, to the necessary minimum, the amount of solid and gaseous waste.

Waste management in accordance with the 3Rs hierarchy (Reduce-Reuse-Recycle) can be used in construction engineering to create a new approach to system design that can significantly reduce environmental impacts [1]. The article attempts to assess the economic and ecological second recycling in the 3Rs waste management hierarchy in accordance with a circular economy (CE) [2]. Equally important, in the context of the reuse of steel elements, is the design phase of the product, striving to optimize the weight of the structure as well as accompanying elements and energy consumption [3]. This approach is known as design for the environment (DFE) [4] and allows for the analysis of the object at all stages of its life cycle, including in the reconstruction (post-exploitation) phase. The 3Rs hierarchy

and the considered concept of the Indicative Environmental Assessment (EET) are part of the paradigm of sustainable development in the construction sector. The proposed methodology is aimed at using natural resources in such a state of equilibrium that they do not reach the point of exhaustion or non-renewal [5].

A lot of manufacturing companies, especially in Western Europe, which have introduced integrated Total Quality Environmental Management (TQEM) systems, are creating new concepts for environmentally oriented design. An important role in the process of preparing a pro-ecological construction investment is played by:

- optimization of technical solutions [6],
- impact assessment with a list of ecological effects [7],
- analysis of socio-economic effects (demand for a clean environment) [8],
- risk (feasibility) analysis [9].

The procedures presented are in line with the requirements set by the European Union [10]. The criterion of environmental effects is one of the basic criteria taken into account when granting co-financing from structural and investment funds. Thus, the problem of the impact of structures on the environment has an economic dimension [11], both in terms of macro- and microeconomics.

In the literature on the subject, a depreciation of structural steel reuse can be observed from the point of view of only an economic criterion. Cullen and Drewniok [12] found that the economic cost of large-scale reuse of steel is at least as high as that of new steel. They analyzed economic costs without considering ecological costs. Similar conclusions were reached by Tingley and Allwood [13], who showed that the reuse of building structures is about 25% more expensive, which is a significant barrier to reuse. At the same time, they demonstrated that it is necessary to study the reuse costs for a wider range of projects in order to have a larger evidence base for the costs of reusing steel.

For projects with low ecological values, the production entity generates pollution translated into costs, which are direct external effects [14]. External costs constitute an additional burden for the polluter and are equivalent to the lost component of the natural environment. This state can be called a kind of waste of capital. As a result, a dual mechanism of degradation arises: on the one hand, environmental degradation and, on the other hand, degradation of the economy through an increase in costs and production value.

It is assumed that the average period of depreciation of commercial or production buildings of the hall type is 39 years [15]. Reconstruction or demolition of existing hall facilities, often with a steel structure, results from the reorganization of the functional space (services, production) and adapting them to the current technical and environmental requirements.

In 2019, the construction sector absorbed more than half of the world's steel production. Allwood and Cullen [16] found that 14% of the world's steel produced is used in infrastructure and 42% in buildings. Steel used in construction, due to the need to reduce greenhouse gas emissions, should come primarily from previous building structures; however, as research [10,17,18] shows, the reuse of steel sections is at the level of 6%, compared to 93% recycled. Obviously, we can always ask a question whether the demolition of materials and their use will be the trend of the future [19]? However, an increasingly faster transition from a linear economy (LE) [20] with high waste to a circular economy (CE) [21] based on the reuse of materials and recycling [22] is to be expected. Creating a market for building elements with different actors (such as traders, investors, designers, contractors) can prove to be a key solution for multiplying the reuse of these building elements and reducing the environmental pressure of the construction sector [23].

Brief Description of Environmental Performance Assessment Methods

Reducing the environmental impact of processing and manufacturing activities, which consume large amounts of raw materials and energy inputs, is among the most important and difficult issues in the future. Effective measurement control and the introduction of new pro-ecological technologies will help reduce the pressure on the environment.

A major achievement in the construction sector is the use of procedures to minimize waste [24]. Benchmarking standard operating procedures have been used for many years to optimize production processes and services [25]. They are implemented in the form of a predetermined organizational chart, consisting of 4 phases, which include, among other things:

- 1/ planning and organization (adopting an environmental policy, setting goals),
- 2/ assessment (gathering data on processes and waste, creating variants of solutions),
- 3/ analysis of feasibility variants (technical and economic analysis),
- 4/ implementation (project implementation, implementation effectiveness assessment).

The construction sector generates around 35% of the waste mass of the 2502.9 million tons generated in the EU-28 (2016 Eurostat data). Minimizing the amount of generated waste is the goal of the new EU development programs until 2050 (the European Green Deal, Europe's new agenda for sustainable growth, 2019) [26] based on the circular economy [27,28].

In the case of construction, new paths are defined for the CE strategy [29], which refers to cleaner production (CP) management procedures and are introduced in EU countries despite many barriers [30]. The common LCA methodology [31] contained in the ISO 14040-44 guidelines is used to assess the environmental performance of products to minimize, reduce at source and recycle waste. ISO 14000 environmental management systems are implemented to produce environmental product declarations (EPDs) based on the ISO 14025 standard.

Other methods of environmental impact assessment are also noteworthy, such as:

- Eco-indicator method (Eco-indicator 99, ReCiPe) [32];
- ASEET method of integrated indicators of economic and ecological efficiency in architectural, socio-economic, ecological and technical space [33];
- Method of cumulative energy intensity indicators [34];
- Analysis of cumulative energy consumption and pollutant emissions over the full life cycle of the building [35];
- Method of valuation of ecological effects, which includes:
 - Ecological Accounting Units (EAU) [36];
 - Product Line Analysis (PLA) [37];
 - LCC (Life Cycle Costing) [38].

Using these methods, it is possible to study the impact of products, materials, services and entire industrial processes on the environment in product life cycles in accordance with the idea of a circular economy initiated in the late 1970s [2] and developed in various procedures and methodologies, e.g., M. Braungart and W. McDonough "Cradle to Cradle" [39–41]. In construction, it means a physical description of the behavior of industrial systems [42] when raw materials taken from the environment are introduced into the system and pollutants and waste are removed and recycled [43]. A modern approach to industrial ecosystems is characterized by minimizing inflows and outflows from the system by creating eco-industrial parks [44,45].

These environmental assessment methods potentially support the demand, especially for certified Ecolabel products [46,47]. They are a tool for calculating environmental costs, however, in the environments of designers and contractors. Despite the fact that highly developed countries, including the EU, have started to pursue the direction of the circular economy, among others, through green public procurement [48], the market expects science to develop coherent green executive procedures.

There is a lack of simple and quick methods of environmental assessment of buildings and available material databases [49] with ecological parameters on the market. The authors of the study attempted a simple ecological assessment at the stage of design and economic calculation with secondary use of the main structural elements of the building.

2. Purpose, Assumptions and Research Method

Figure 1 presents the methodological framework of the presented scientific approach to determine the ecological and economic benefits of reusing the structural elements of a steel hall building.

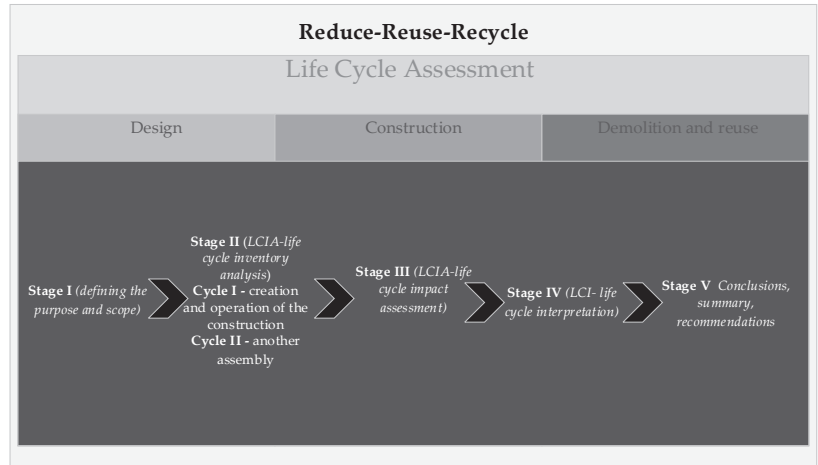


Figure 1. The methodological framework of the presented scientific approach to determining ecological and economic benefits.

2.1. Purpose of the Research

The aim of the study is to assess the ecological effects of the economic and technical aspects of steel halls in the process of their reuse. Conditions for multi-criteria environmental assessment have been introduced for the structure of hall-type buildings that are demolished and reassembled. Based on the generalized analysis [31], cumulative energy and material indicators were derived as total Q_i and partial cost equivalents (UK, UE) in three life phases: construction, demolition and reuse of hall buildings. The full life cycle assessment of steel halls (LCA) is based on methodological assumptions that enable the monitoring of the ecological effects of multiple-assembly buildings. Computational research models are the frame structures of steel halls [50]. The essence of the research is to reuse the existing building elements without the need to incur energy expenditure for their re-production. This approach is in line with the principles of the circular economy (CE) [39,40].

2.2. The Course of EET Assessment in LCA Methodology

The research was limited to analyzing the skeleton of steel halls subjected to the process of multiple assembly. A choice analysis (CA) of the most optimal ecological solution for steel halls was proposed according to the multi-criteria economic, ecological and technical assessment (EET) of cumulative indicators, taking into account the LCA methodological assumptions:

Stage I (defining the purpose and scope)—the purpose specified in point 2.1. The adopted methodological scope of EET:

Ecological—consisting of determining the ecological effects of a building object on the environment, included in the production processes of construction, use and demolition.

Technical—consisting of determining the optimal, with regard to the adopted ecological and economic criteria, technical variant of a building object or its part, e.g., construction, demonstrating the acceptable limits of discrepancy for the adopted optimal architectural and construction solution, resulting from insufficient consideration of ecological parameters.

Economical—consisting of determining the cost expenditure generated by the optimal variant of a multiple-assembly facility for the adopted technical and ecological assumptions.

The method proposed by the authors will make it possible to carry out an integrated indicative ETE assessment, taking into account the building's depreciation path and indicating the ecological profits that can be generated by hall-type buildings. Ecological depreciation is the reimbursement of the environmental costs incurred in constructing a building at LCA. The measure is the number of times the elements of the structure, housing or equipment are used.

Stage II (LCIA—life cycle inventory analysis):

Within the boundaries of the system, the flows of all materials, energy carriers and construction works used in the construction, use and demolition process were calculated based on the design assumptions of the steel hall models. Ecological costs were estimated for each of these flows.

Cycle I—creation and operation of the construction and operation of the building structure (hall design, cost estimates for selected model assumptions) determines the cumulative cost (Q^I) as the equivalent of all energy L/E (labor, equipment) and material processes M of the first assembly of the MASH structure.

Cycle II—another assembly (reconstruction or demolition project and erection of a new hall in a different place using the existing hall superstructure) determines the cumulative cost (Q^{II}) as the equivalent of all L/E and material M energy processes necessary for the second assembly of the MASH structure.

In the second phase of the hall structure's life, the following options are possible:

Option 1: change of function, but the superstructure of the hall remains in the same place; only the structure and the casing are renovated.

Option 2: change of function but the superstructure completely or partially dismantled and relocated while the foundations remain.

Option 3: the foundations and the superstructure of the hall are dismantled and moved to another location with the need for renovation.

This study focuses on option number 3.

Stage III (LCIA—life cycle impact assessment)—aggregation of data from cycle I and II of MASH life, presents the division of $Q_{I,II}$ cumulative total costs into partial ones as pro-environmental UE and environmentally degrading factors, UK. In the second phase of assembly (II life cycle), the accumulated energy is transferred to the next structure without the need to incur environmental and energy expenditures for the production of new steel elements. It was assumed that the ecological cost effectiveness contained in the repeated use of the main structure of the building translates indirectly into the reduction of the effects of environmental impacts resulting from the inventory of impacts in the LCA method.

Stage IV (LCI—life cycle interpretation) ecological assessment of the adopted structural solutions for multi-assembly steel halls (MASH). The research focused on the comparative analysis from stages II and III as an interpretation of the basic assessment of the environmental impacts of steel structure hall facilities.

Stage V Conclusions, summary, recommendations.

The idea of the method is in line with the development policy of the European Union [46] contained in "The European Green Deal" will transform the EU into a modern, resource-efficient and competitive economy, ensuring:

- no net emissions of greenhouse gases by 2050,
- economic growth decoupled from resource use,
- no person and no place left behind.

2.3. Main Criteria of the Ecological Evaluation of MASH

The criteria adopted for the EET assessment belong to stage II of LCA and result from the preparation of investment projects in the construction industry, starting from technical and economic assumptions, through the construction design and ending with implementation. Thus, the criteria represent the full life cycle of objects; they are divided into:

Location criteria: this refers to the necessity to adapt the functions of the areas for development to the natural conditions and not the other way around. The analysis shows the compensation indicators for the lost biologically active surface.

Criteria for the selection of design solutions: selection of the optimal static and material variant of the hall, enabling its disassembly and reassembly.

Cumulative design ETE criteria: determines the cumulative ecological and economic costs of the energy contained in work, equipment and materials for the primary and secondary MASH design.

Performance technology criteria related to the assembly and disassembly of the structure: It constitutes the share of the involved work of equipment, labor and auxiliary materials for the modern conditions of the investment implementation, e.g., Just in Time [47].

Reusability criteria: is the basis for a comparative analysis after the first period of operation. The analysis presents indicators that express the amount of energy and mass of structural elements to be reused, as well as material and energy treated as waste [34].

The aforementioned criteria create an interdependent chain of connections in the eco-industrial system (the sum of technological processes, energy and materials, starting from the construction of the object, demolition to subsequent use) [51]. This should be understood as a balancing system of inputs and outputs, the flow of energy and matter between the environment and the industrial system [51,52].

EU regulations apply to the selection of a work contractor or tenants of buildings, taking into account non-price criteria relating to environmental aspects [53].

3. Subject of the Research, Basic Assumptions

3.1. Stage I (Defining the Purpose and Scope)

The design and material assumptions in Sections 2.1 and 2.2 apply to selected model steel structures to test the EET method. Four static schemes of typical halls found in the investment market were adopted. The LCA path was analyzed on single-span structures in modular span variants ranging from 12.0 m to 48.0 m.

3.2. Stage II (LCIA-Life Cycle Inventory Analysis): Determination, Collection and Analysis of the Required Data

Physical and computational data (Materials and geometry).

The selection of the shape and dimensions of the halls adopted for the analysis was determined, assuming the typical solutions encountered in practice and the optimization work of steel frames [12,54]. The considered structural systems of halls consist of transverse flat frame structures connected with each other by bracing systems. In the analysis below, the transverse structural systems were examined, adopting, for their general stability, the buckling lengths that correspond to the node spacing of the longitudinal and transverse bracings of the halls [55]. This study did not analyze halls with a cooperating roofing made of a corrugated sheet (with the so-called diaphragm) as systems with an increased degree of difficulty in disassembly, which makes them less useful for the needs of multiple assembly. However, this does not prejudice the use of such solutions.

The following geometrical parameters of the bars and the design parameters of the hall nodes were adopted, which created the following flat static diagrams (Figure 2):

- "A" scheme—rigid frame;
- "B" scheme—frame with rigid columns on the support and articulation at the transom;
- "C" scheme—triple-joint frame;
- "D" scheme—rigid frame at the transom column nodes and articulated on the support.

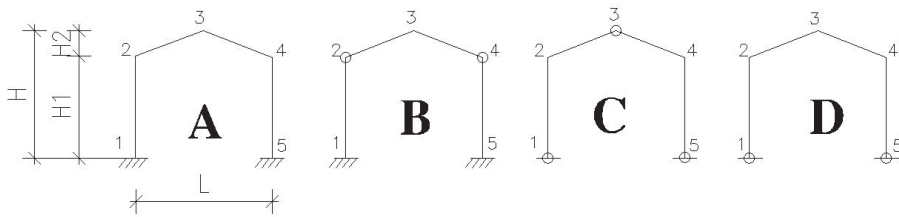


Figure 2. Research diagrams of steel halls.

Material data:

- Steel profiles of the hall cross system: HEA prismatic profiles,
- Type of structural steel: St3S (mullions, transoms, gusset plates, welds),
- Foundations: Concrete C16/20 (B-20), structural steel A-II.

Technical parameters for the adopted research models:

- Geometric—dimensions calculated in the axes of elements:
 - height $H = H1 + H2$ [m], ($H1 = 4.5$ m, $H2 = 1.5$ m).
 - frame spacing $S = 5.0$ m.
 - variable span, the same for each scheme, from $L = 12.0$ m to 48.0 m.
- Loads—equal for each scheme, i.e., wind, snow, roof loads, including purlins and bracings.
- Own weights—suitable for the structural scheme.
- Support compliance was presented as the intended relative displacement of support A with permissible values $dx = -2$ cm and $dy = 2$ cm (due to the disassembly conditions and the changeability of settlement during re-foundation).
- The following ground conditions and foundations were adopted:
 - foundation level $hp = 0.80$ m. p.p.t.,
 - soils with low bearing capacity ($Pd-Id = 0.3$, $\varphi = 15^\circ$, $\rho = 1.65$ t/m³),
 - strong soils ($Pav-Id = 0.60$, $\varphi = 31^\circ$, $\rho = 2.00$ t/m³).
- 1. Static calculations were made with the use of the ROBOT computer program. Dimensioning of the steel structure of the halls is based on [40,41].
- 2. Design of foundations according to [41,42],
- 3. The price of construction and assembly works—as the average values from I quarter 22', the following were adopted:
 - data for the steel skeleton (as of 03.2022) [43] (initially adopted to be produced with the material 12.76 euro/kg, assembly 1.5–3.5 euro/kg, material 8.50 euro/kg);
 - for reinforced concrete foundations (workmanship, material)—100.00 euro/m³, the execution with the material was initially adopted.
- 4. Other data according to technical standards and norms.

In the present study, it was assumed that the welds maintained the boundary conditions for individual frame nodes [56]. The welds were dimensioned for extreme cross-sectional forces at individual stages of structure operation, in accordance with [57,58], assuming the minimum weld mass [58–62] as the main optimization criterion. The indeforability of the substrate was assumed in the calculations. The welds were dimensioned for extreme nodal forces resulting from the load combinations adopted for the calculations.

- The dimensioning of the foundations was carried out on the basis of the standard [58,63,64]. C16/20 (B-20) concrete and A-I steel were adopted.
- Static and strength calculations were made using the computer program ROBOT Structural Analysis Professional 2019, ARCADIA BIM v.14.

Calculation of MASH construction costs:

The valuation of the structural elements of the halls, along with their assembly and disassembly for each of the stages of construction, was made on the basis of:

- Industry standards for the valuation of workshop works for steel structures,
- Cost Estimated Material Outlays (CEMO) for individual construction works, adopting the outlay costs (LME—labor, material, equipment) in IV qu. 2021. Calculations of material expenditure were carried out with the use of the NORMA computer program [65].

3.3. Stage III (LCIA)—Life Cycle Impact Assessment

Cycle I—construction of the MASH building/determination of cumulative QI cost equivalents

This stage was limited to the construction of a steel hall, while the costs of its use were omitted as secondary. Operating costs are variable and depend on the manner in which the structure is used (e.g., trade, production hall, etc.).

This is undoubtedly the most important stage of the selection analysis because it should define the optimal structural and ecological solution of the halls. The essence of this phase consists of the proper preparation of the object in terms of its secondary assembly and operation so that the energy accumulated in the mass of the structure is used to restore the lost ecological substance. The EET method was adopted to calculate the $Q_{k,l}^I$ equivalent energy and material costs in the first phase of the MASH structure for scheme “k” and span “l”.

$$Q_{k,l}^I = (\Sigma C_{si}^I + \Sigma C_{ri}^I + \Sigma C_{zi}^I + \Sigma CF_i^I + \Sigma RF_i^I + \Sigma W_i^I + \Sigma T_{wi}^I + \Sigma T_{mi}^I + \Sigma M_i^I + EP^I) / p \text{ [EURO/m}^2\text{]} \quad (1)$$

Construction cost in phase I of $Q_{k,l}^I$ includes the following components:

- $Q_{k,l}^I$ —total cumulative energy and material cost value of the construction of the MASH steel hall for the selected static scheme “k” and span “l”,
- $\Sigma C_{s,r,z}^I = \Sigma C_{si}^I + \Sigma C_{ri}^I + \Sigma C_{zi}^I$ —cost of producing the mass of MK structure elements (mullions, transoms, welds) calculated for the normative state of loads and displacements, taking into account the unit price of the mass for the i-th mullion, transom and weld,
- ΣCF_i^I (ΣRF_i^I)—cost of the total mass of foundations made (RF_i^I total mass of foundations removed after the first assembly), CF_i —mass of the i-th foundation,
- ΣW_i^I —total cost of producing i-th structural elements in the workshop,
- ΣT_i^I —total cost of transporting i-th structural elements in a specific process of the construction cycle:
- T_w —raw material transport to the workshop,
- T_m —transport of elements for assembly with the costs of operational storage,
- ΣM_i^I —cost equivalent of the assembly of the i-th load-bearing element of the hall,
- EP^I —cost equivalent of the biologically active surface lost. The analysis adopted the equivalent of development = area with the assimilation intensity of the grass surface,
- p—built-up area.

The summary of $Q_{k,l}^I$ values for schemes A, B, C and D and a span of up to 48 m is presented in Figure 3.

After cycle I of the hall construction work, the cumulative construction costs of MASH Q^I presented in Figure 3 reflect only the physical parameters of the adopted typological variants of the hall. At this stage, it is possible to conclude that the halls with rigid frames (scheme A) have the lowest economic cost-to-area ratios at the level of 400- 550 EUR/m² for spans of 12–30 m, which does not prejudice their selection, as the ecological impacts throughout their life cycle have not been taken into account.

Cycle II—dismantling and reassembly, the second stage of MASH’s work.

At this stage of the analysis, the $Q_{k,l}^{II}$ cumulative costs related to the relocation of the existing facility to another location were calculated.

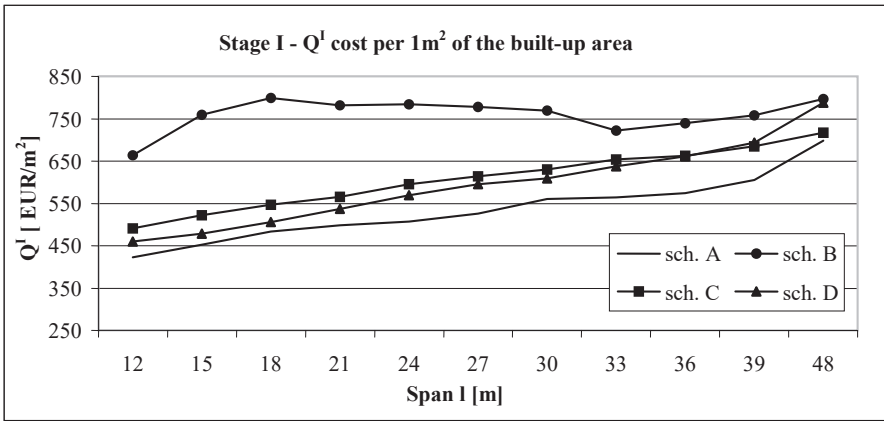


Figure 3. Cumulative Q^I cost per 1 m^2 of the built-up area.

Assembly errors (manufacturing imperfections) that may occur in support nodes have been taken into account. The change in the stress state of the structure optimized in stage I was examined in terms of achieving a minimum weight. The degree of stress of the structure after the second and subsequent assembly has a significant impact on the change (possible strengthening) of the nodal elements of the hall. Improper preparation of structural welds at the stage of construction may cause imperfections of geometrical contacts [66].

In the process of demolition, the structure is exposed to angle deformation α , β , γ and linear u , w and v of the plates in the assembly joints (Figure 4).

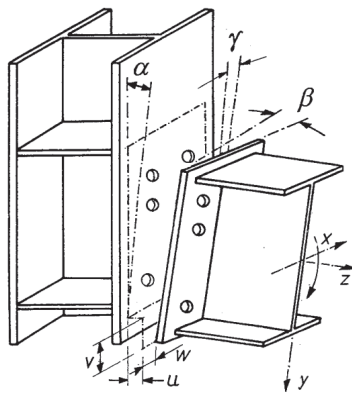


Figure 4. Scheme of imperfections of angular and linear butt contacts.

Therefore, it is necessary to test and carry out maintenance and measurement adaptation works in workshop conditions to adapt the object for reuse.

Including the criteria listed in chapter 3, the cumulative equivalent energy and material cost $Q^{II}_{k,l}$ was determined in the second life phase of the MASH structure for the scheme “k” and span “l”.

$$Q^{II}_{k,l} = (\Sigma \Delta C^{II}_{si} + \Sigma \Delta C^{II}_{ri} + \Sigma \Delta C^{II}_{zi} + \Sigma CF^{II}_i + \Sigma RF^{II}_i + \Sigma W^{II}_i + \Sigma T^{II}_{mi} + \Sigma M^{II}_i + \Sigma D^I_i + EP^{II}) / p \text{ [EURO/m}^2 \text{]} \quad (2)$$

Energy cost $Q^{II}_{k,l}$ includes the following components:

- $Q^{II}_{k,l}$ —cumulative equivalent energy and material cost in the second phase of MASH structure life for the selected scheme “k” and span “l”.

- $\Sigma CF^II_i (RF^II)$ —total mass cost of foundations made during secondary assembly (RF^II —total mass of foundations removed after subsequent assembly),
- $\Sigma \Delta C^II_{s,r,z} = \Sigma \Delta C^II_{si} + \Sigma \Delta C^II_{ri} + \Sigma \Delta C^II_{zi}$ —total cost of inspection and protection of the structure ΔMK resulting from the necessity to eliminate the stress of the structure due to assembly imperfections,
- ΣW^II_i —modification in the workshop or assembly of specific i -th structural elements,
- ΣT^II_{mi} —cost of transporting all elements of the hall for reassembly with the costs of operational storage,
- ΣM^II_i —cost of assembly of steel load-bearing elements of the hall in a new location,
- ΣD^I_i —cost of dismantling the steel load-bearing elements of the originally assembled hall,
- EP^II —cost equivalent of the biologically active area lost for the built-up area of the re-assembled hall,
- p —built-up area.

Figure 5 shows the cumulative LME cost (labor, material, equipment) of the structure in the second phase of its operation, i.e., reuse. The cost was summarized for an area of 1 m² of the MASH building area. From the estimated charts, it is possible to initially accept the hall solutions in schemes C and D due to the favorable price parameters. In particular, halls with a span of 12 m to 30 m should be distinguished. Their price threshold is at the level of 270–330 EUR/m² of the total value of $Q^II_{k,l}$ of the second assembly of MASH.

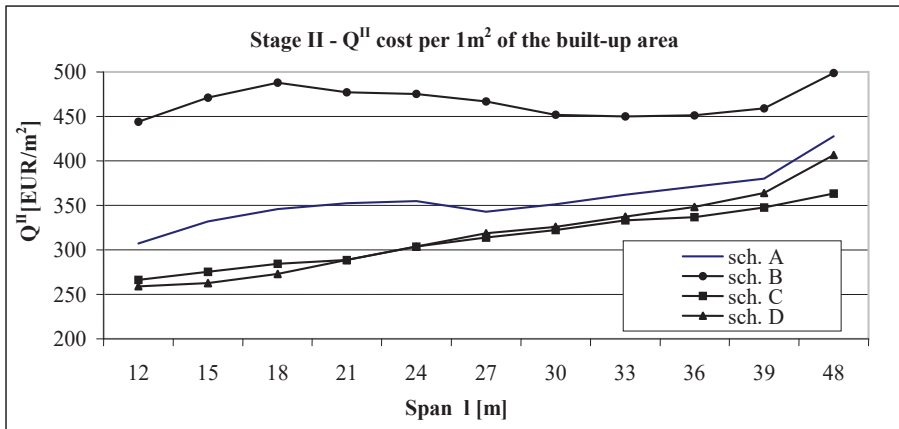


Figure 5. Cumulative cost Q^II of stage II per 1 m² of the built-up area.

3.4. STAGE IV (LCI—Life Cycle Interpretation)—Interpretation of Results

At each stage of the facility’s life (HSWM-BOMM), the EET analysis presents the distribution of the calculated values of the UE and UK sub-indices as shares of the $Q_{k,l}$ cumulative ecological cost. These are the components responsible for ecological losses and gains.

Interpretation of Cycle I results:

Stage of creating the MASH structure

The cumulative value of $Q^I_{k,l}$ (Equation (3)) includes the economic and ecological costs associated with the implementation and assembly of the UK^I structure as well as environmental regeneration and disposal of UE^I construction waste:

$$Q^I_{k,l} = (UE^I + UK^I)/p \text{ [EURO/m}^2\text{]} \tag{3}$$

UE^I —share of the ecological costs of environmental regeneration in the process of execution and operation of MASH,

UK^I—share of economic costs for the execution and assembly of the MASH facility structure (original hall structure cost).

The shares of UE^I and UK^I of the cost of building Q^I_{k,l} presented in Table 1 were examined in terms of environmental impacts in the I cycle of life of MASH and then in the II cycle of life, i.e., another assembly. Ecological costs of UE^I are considered necessary in the construction process, directly interfering with the biotic layer of the area on which the building stands. These include the components ΣRF^I_i + EP^I, which will be charged with construction costs in the first phase of life.

Table 1. Share of UE^I ecological (environmental) and UK^I economic costs.

| UE ^I | UK ^I |
|---|---|
| ΣRF ^I _i + EP ^I | ΣC ^I _{si} + ΣC ^I _{ri} + ΣC ^I _{zi} + ΣCF ^I _i + ΣW ^I _i + ΣT ^I _{wi} + ΣT ^I _{mi} + ΣM ^I _i |

Breaking down the cumulative costs of building the hall at UK^I and UE^I allows making an approximate selection of the MASH structure already in the first phase of construction work. It should be noted that the UK^I component contains energy and material elements that are the subject of reuse, e.g., ΣC^I_{si} + ΣC^I_{ri} + ΣC^I_{zi} components and energy lost components such as ΣW^I_i + ΣT^I_i + ΣM^I_i. In the approach to the environmental costs of multiple uses of MASH’s technological and operational elements and processes, this will be of significant importance. Referring to the share of UE^I regeneration costs, i.e., restoration of the biologically active surface, it seems right to include them in the pro-ecological costs, despite the destruction of the active layer of the biocenosis by foundation works and the zero state.

The total share of energy and material involved in the structure of the UK^I superstructure itself (part of the building above the ground) of the selected models of hall facilities in Figure 6 is an introduction to the environmental LCA comparative analysis.

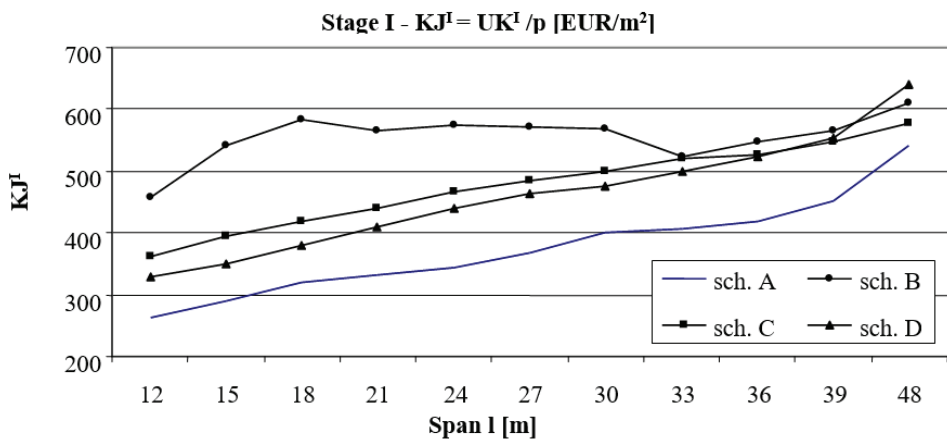


Figure 6. KJ^I unit cost of creating the UK^I structure per 1 m² of the built-up area [EURO/m²].

The structure of MASH in the first stage of construction, presented in Figures 3 and 6, confirms the initial correctness of the hall selection due to the total energy and material costs of KJ^I (Equation (4)) of all manufacturing processes for scheme A.

$$KJ^I = UK^I / p \text{ [EURO/m}^2\text{]} \tag{4}$$

where:

KJ^I—unit cost of construction creation, [EURO/m²],

UK^I —share of economic costs for the execution and assembly of the MASH facility structure (original hall structure cost), [EURO],

p —built-up area, [m²].

This proves the low impact of the economic costs of foundation work on the total Q^I accumulated costs. However, one should not forget about the costs of the ecological impacts generated by the construction of the MASH structure. The scope of these impacts is defined by the generalized ecological indicator WE_o^I (Figure 7) as the ratio of the ecological costs of the UE^I to the economic costs of the UK^I .

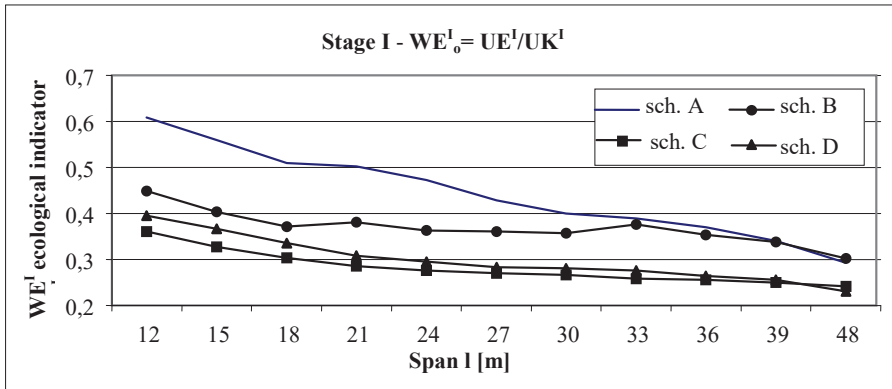


Figure 7. Ecological generalized WE_o^I index – cycle I of LCA.

Optimal solutions are contained between the schemes of construction C—with the lowest values of the WE_o^I index (Equation (5))—and scheme A, which shows the highest level.

$$WE_o^I = UE^I/UK^I \tag{5}$$

Figure 7 shows that the ecological profitability of construction solutions is the best for the range marked “from below” by schemes C and D—this impact is 37–23%, while for schemes A and B the values of ecological indicators for construction WE_o^I are the highest and amount to 61–30%. The higher the ecological indicators, the higher the environmental costs generated by the structure.

The presented WE_o^I index is a value enabling the initial selection of a structure because, as already mentioned, the cumulative $Q_{k,l}^I$ costs contain partial elements responsible for losses and ecological gains in the MASH construction process. Therefore, it is necessary to carry out a further analysis of the impact of these components on the selection of the optimal structure in the full life cycle and, therefore, in the subsequent assembly phases.

Interpretation of the results of Cycle II of the analysis—option 3 was adopted; therefore, it is the phase of demolition of the MASH building structure, including the foundations.

After calculating the cumulative cost of $Q_{k,l}^I$ (Equation (6)), similarly to the first stage, its distribution was examined into:

$$Q_{k,l}^{II} = (UE^{II} + UK^{II})/p \text{ [EURO/m}^2\text{]} \tag{6}$$

UE^{II} —ecological cost of compensation for the lost layer of biocenosis (regenerating the environment) in the process of the secondary assembly and operation of MASH,

UK^{II} —economic cost of reassembling the MASH structure elsewhere as a factor that degrades the environment with the use of elements from the first cycle of the facility’s operation.

The ratio of ecological to economic costs will be used to search for the optimal design solution from the point of view of the ecological impacts of MASH. The shares of the

individual components of Q^{II} are presented in the ecological generalized index of cycle II of the work of the WE^{II}_o structure.

$$WE^{II}_o = UE^{II}/UK^{II} \tag{7}$$

The table below shows the components UE^{II} and UK^{II} of the cumulative cost $Q^{II}_{k,l}$. Table 2 presents the ecological costs $\Sigma RF^{II}_i + EP^{II}$, necessary to regenerate the biologically active area (built-up area). The share of UE^{II} ecological (environmental) costs in the second phase is crucial in the LCA assessment of the hall structure. Generalized ecological indicators [$WE^{II}_{o,k,l}$] create a picture (Figure 8) of the impact of individual types of HSWM on ecological costs, included between the envelopes:

Table 2. Share of UE^{II} ecological and UK^{II} economic costs of LCA cycle II.

| UE^{II} | UK^{II} |
|------------------------------|---|
| $\Sigma RF^{II}_i + EP^{II}$ | $\Sigma \Delta C^{II}_{si} + \Sigma \Delta C^{II}_{ri} + \Sigma C^{II}_{zi} + \Sigma CF^{II}_i + \Sigma W^{II}_i + \Sigma T^{II}_{mi} + \Sigma M^{II}_i + \Sigma D^I_i$ |

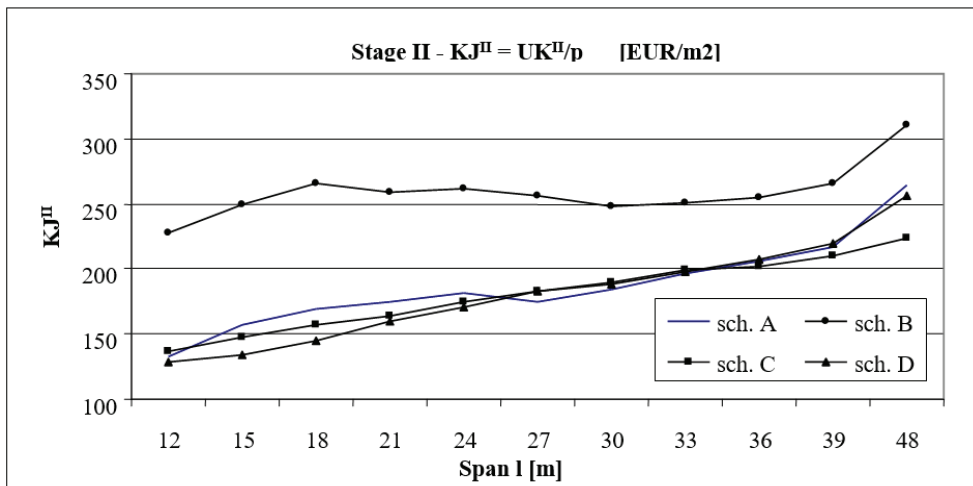


Figure 8. Generalized ecological indicator WE^{II}_o —cycle II.

- The lower envelope characterizes halls with the lowest ecological costs:
 - type B for $L = 12\text{--}13.5$ m, $WE^{II}_{o,k,l} = 0.95\text{--}1.1$
 - type C for $L = 13.5\text{--}39$ m, $WE^{II}_{o,k,l} = 0.85\text{--}0.65$
 - type D for $L = 39\text{--}48$ m, $WE^{II}_{o,k,l} = 0.65\text{--}0.55$
- The upper envelope characterizes the scheme with the highest ecological cost:
 - type A for $L = 12\text{--}48$ m, $WE^{II}_{o,k,l} = 1.35\text{--}0.65$.

Ecological indicators $WE^{II}_{o,k,l}$ of the structure are at the level of 0.55–0.65 for the largest spans of 39–48 m, which proves the lowest share of 35–45% of ecological costs in the entire investment.

The unit cost of construction is:

$$KJ^{II} = UK^{II}/p \text{ [EURO/m}^2\text{]} \tag{8}$$

where:

KJ^{II} —unit cost of construction creation, [EURO/m²]

UK^{II}—economic cost of reassembling the MASH structure elsewhere as a factor that degrades the environment with the use of elements from phase I of the facility’s operation, [EURO],

p—built-up area, [m²].

At the same time, in the second cycle of the hall structure’s life, the UK^{II} economic costs (as shown in Figure 9) are more than twice lower than the new structure and amount to approximately 130–180 EUR/m² for typical spans from 12–30 m, assuming the implementation of the investment on the *Just in time* basis [47].

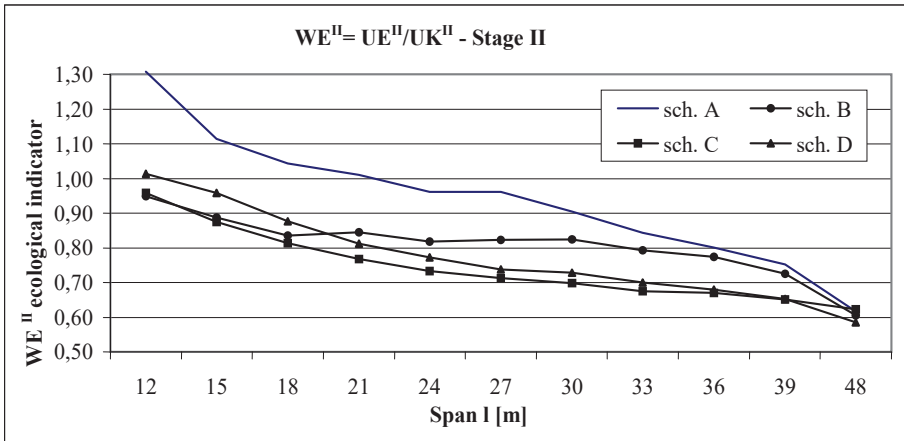


Figure 9. KJ^{II} unit cost of creating the UK^{II} structure per 1 m² of the built-up area [EURO/m²].

When analyzing stage II, it should be noted that the economic costs incurred to produce a “new” UK^{II} structure in the next phase of its life accelerate the total depreciation of the facility (Equation (9)) and are pro-environmental.

The depreciation ratio (W_a) would be:

$$W_a = 1 - KJ^I / (Q^I + Q^{II}) \tag{9}$$

The better the preparation of the UK^I structure to work in phase II, the lower the Q^{II} adaptation costs and the faster the environmental depreciation, i.e., W_a decreasing, and vice versa. Thus, the multiplicity of multiple installations (W_{km}) (Equation (10)) in order to recover environmental costs can be presented according to the formula:

$$W_{km} = (Q^I + Q^{II}) / KJ^I \tag{10}$$

According to the formula (Equation (10)), the lower the value of the assembly multiplication index W_{km} , the faster the path of ecological depreciation of the hall structure (this issue is the subject of further research). With each new phase of life (reuse), MASH halls reduce their ecological footprints and start generating ecological profits.

4. Stage V—Conclusions, Summary, Recommendations

The selection of the optimal ecological MASH solution was carried out taking into account the criteria listed in point 2.3. The criterion for reusing the structural elements of the facility is one of the most important. It characterizes objects with pro-ecological features. Adopting that the above-ground parts of the UK hall structure can be moved to another location and reassembled, their foundations remain on the ground and may constitute an obstacle to the redevelopment of the EU territory. Depending on the purpose of the land after the existing structure, the foundations, together with the development area, can be used, for example, as landscape elements or aggregates [67,68]. In most cases, however,

the existing foundations with the remaining elements of the technical infrastructure are removed because it is difficult to guarantee their use in newly erected facilities.

Referring to the results of the total cumulative costs $Q_I = 400\text{--}500$ EUR/m² from phase I of the construction work in relation to the costs of the secondary cycle $Q_{II} = 270\text{--}330$ EUR/m², this ratio is in favor of reusing the structure and is 67% for all analyzed types of halls. The important conclusions result from comparative studies of the optimal proportions between the construction costs of UK hall structures and the ecological costs of the UE related to restoring the original (initial) state of the environment.

The UK^{II} component of the next assembly of HSWM is a relatively constant parameter and ranges from 48–51% of the cost of a new investment, assuming the implementation of the investment on the Just in time basis [47,69], which was mentioned earlier.

Despite the pro-environmental action in the MASH implementation process, the WE^{II}_o indicators increased from 2.21 to 2.77 times compared to cycle I and will extend the depreciation period of multiple assembly facilities. At the same time, the cases of such halls are recommended for a repeat design cycle in the CE circulation loop in order to reduce UK ecological and UE economic costs.

WE^{II}_o indicators determine the impact of ecological costs on MASH's design solutions and constitute an approximate method but a reliable environmental assessment of the halls. The EET indicator assessment enables the elimination of incorrect technical solutions in the ecological and economic aspects already at the design stage. In the analyzed case, halls A and B, with a span of 21.0–36.0 m, have the most unfavorable WE^{II}_o indicators, higher on average by 14.3–28% than the others.

As previously mentioned, Tingley and Allwood [13] and Cullen and Drewniok [12] showed that the reuse of building structure elements is uneconomical. However, the integrated approach presented in the EET analysis proved the profitability of the secondary use of steel hall structures by as much as 67% compared to new construction.

Using the EET method, the technological, economic and ecological aspects included in the dimensioned execution processes were combined. Simple indicators for assessing the return on environmental outlays were derived, i.e., the W_a depreciation indicator and the subsequent assembly W_{km} index specifying the minimum reuse number of the hall structure to balance the environmental capital incurred for the original production of the facility. The presented approach, based on simple ecological indicators WE^I and WE^{II}, enables a quick analysis of the use of existing structures, which, in the era of limited raw material resources, are a good source of materials.

Reusing MASH elements is one aspect of the implementation of the construction sector sustainability paradigm [17]. It should be emphasized that the implementation of the reuse of MASH elements will require changes in the market from all participants in the investment process [19]. Starting from designers, through investors, traders, contractors, users and dismantling workers. This is important information for policymakers who should use a set of legal and financial instruments to lower the cost of reusing MASH structures.

The changes should also concern the creation of the MASH construction elements and the system of certification and trade in these elements [46], e.g., CE_R marking as an extension of the CE marking procedure has already been used for other products in the European Union.

However, due to widespread e-commerce, checking the availability of recycled MASH elements should not pose any major problems.

It is also important to change the perception of reusing MASH structural elements by the actors of the investment process. The common belief that only a "new" structural element will meet expectations regarding the safety of the structure should change.

The EET method can be dedicated to any steel structure, e.g., multi-span systems with any girders made of cylindrical profiles, openwork, plate girders or trusses; the same applies to columns.

The disadvantages of this method are the indirect assessment of ecological effects and the focus on material and economic gains in the life cycle of particular types of structures.

However, the method is open to parallel parameterization of effects and ecological impacts, with an indication of environmental hazards resulting from the adoption of a specific design solution.

Author Contributions: Conceptualization, P.S.; Methodology, P.S., R.D. and J.A.; Software, P.S.; Validation, P.S., R.D. and J.A.; Resources, P.S.; Data Curation, P.S.; Writing—Original Draft Preparation, P.S., J.A. and R.D.; Writing—Review & Editing, P.S., J.A. and R.D.; Visualization, P.S.; Supervision, P.S.; Project Administration, P.S. All authors have read and agreed to the published version of the manuscript.

Funding: This research received no external funding.

Institutional Review Board Statement: Not applicable.

Informed Consent Statement: Not applicable.

Data Availability Statement: Data available on request due to restrictions privacy.

Conflicts of Interest: The authors declare no conflict of interest.

Abbreviations

| | |
|---------------------|--|
| C2C— | Cradle to Cradle® is a trademark of McDonough Braungart Design, Chemistry, |
| C2G— | cradle to grave |
| CE— | circular economy |
| CEAP— | Circular Economy Action Plan |
| CEMO— | Cost Estimated Material Outlays |
| CP— | Cleaner Production |
| DFE— | design for the environment |
| EAB— | ecological amortization of buildings |
| EAU— | Ecological Accounting Units |
| EET— | assessment of cumulative ecological, economic and technical parameters |
| EPDs— | environmental product declarations |
| LCA— | life cycle assessment |
| LCI— | life cycle inventory |
| LCIA— | life cycle impact assessment |
| LE— | linear economy |
| LLC— | life cycle cost |
| LSF— | Light steel frame in building systems |
| MAO— | Multiple Assembly Objects |
| MASH— | multi-assembly steel halls |
| OSC— | Off-site construction, system for Off-Site Construction Projects |
| Q ^{I,II} — | determines the total cumulative cost of the hall after life cycle I and II |
| PLA— | Product Line Analysis |
| TQEM— | Total Quality Environmental Management |
| UE— | share of ecological costs of environmental regeneration in the process of execution and operation of MASH |
| UK— | share of economic costs for the execution and assembly of the MASH facility structure (original hall structure cost) |
| WE— | generalized ecological indicator |

References

1. Tam, V.W.Y.; Tam, C.M. Evaluations of existing waste recycling methods: A Hong Kong study. *Build. Environ.* **2006**, *41*, 1649–1660. [[CrossRef](#)]
2. Stahel, W.R. *The Circular Economy: A User's Guide*; Routledge: Oxfordshire, UK, 2019; ISBN 9780367200176.
3. Jelčić Rukavina, M.; Skejić, D.; Kralj, A.; Ščapec, T.; Milovanović, B. Development of Lightweight Steel Framed Construction Systems for Nearly-Zero Energy Buildings. *Buildings* **2022**, *12*, 929. [[CrossRef](#)]
4. Sun, J.; Han, B.; Ekwaro-Osire, S.; Zhang, H.-C. Design for Environment: Methodologies, Tools, and Implementation. *J. Integr. Des. Process Sci.* **2003**, *7*, 59–75.
5. Yilmaz, M.; Bakış, A. Sustainability in Construction Sector. *Procedia Soc. Behav. Sci.* **2015**, *195*, 2253–2262. [[CrossRef](#)]

6. Weerasuriya, A.U.; Zhang, X.; Wang, J.; Lu, B.; Tse, K.T.; Liu, C.-H. Performance evaluation of population-based metaheuristic algorithms and decision-making for multi-objective optimization of building design. *Build. Environ.* **2021**, *198*, 107855. [CrossRef]
7. Brachet, A.; Schioppa, N.; Clergeau, P. Biodiversity impact assessment of building's roofs based on Life Cycle Assessment methods. *Build. Environ.* **2019**, *158*, 133–144. [CrossRef]
8. McCollough, J. Determinants of a throwaway society—A sustainable consumption issue. *J. Socio-Econ.* **2012**, *41*, 110–117. [CrossRef]
9. Tesfamariam, S.; Goda, K. (Eds.) *Handbook of Seismic Risk Analysis and Management of Civil Infrastructure Systems*; Woodhead Publishing Limited: Sawston, UK, 2013. [CrossRef]
10. Girão Coelho, A.M.; Pimentel, R.; Ungureanu, V.; Hradil, P.; Kesti, J. *European Recommendations for Reuse of Steel Products in Single-Storey Buildings*, 1st ed.; ECCS—European Convention for Constructional Steelwork: Brussels, Belgium, 2020. Available online: https://www.steelconstruct.com/wp-content/uploads/PROGRESS_Design_guide_final-version.pdf (accessed on 3 May 2022).
11. Fiedor, B.; Czaja, S.; Graczyk, A.; Jakubczyk, Z. *Podstawy Ekonomii Środowiska i Zasobów Naturalnych (Fundamentals of Economics of the Environment and Natural Resources)*; Wyd. C.H. Beck: Warszawa, Poland, 2002. (In Polish)
12. Cullen, J.; Drewniak, M. *Structural Steel Reuse. Steel and the Circular Economy*; The Building Centre: London, UK, 2016. Available online: <https://steel-sci.com/assets/downloads/structural-steel-reuse/161130-bcsa-cullen%20002.pdf> (accessed on 3 May 2022).
13. Tingley, D.D.; Allwood, J. Reuse of structural steel: The opportunities and challenges. In Proceedings of the European Steel Environment & Energy Congress, Teeside University, Middlesbrough, UK, 15–17 September 2014.
14. Górka, K.; Poskropko, B.; Radecki, W. *Ochrona Środowiska*; PWE: Warszawa, Poland, 2001. (In Polish)
15. Bokhari, S.; Geltner, D. Characteristics of Depreciation in Commercial and Multi-Family Property: An Investment Perspective. *Real Estate Econ.* **2016**, *46*, 745–782. [CrossRef]
16. Allwood, J.; Cullen, J. *Sustainable Materials: With Both Eyes Open*; UIT Cambridge Ltd.: Cambridge, UK, 2012.
17. Tingley, D.D.; Davison, B. Design for deconstruction and material reuse. *Proc. Inst. Civ. Eng. Energy* **2011**, *164*, 195–204. [CrossRef]
18. Brown, D.G.; Pimentel, R.J.; Sansom, M.R. Structural Steel Reuse Assessment, Testing and Design Principles. 2019. Available online: https://steel-sci.com/assets/downloads/steel-reuse-event-8th-october-2019/SCI_P427.pdf (accessed on 5 May 2022).
19. Stephan, A.; Athanassiadis, A. Towards a more circular construction sector: Estimating and spatialising current and future non-structural material replacement flows to maintain urban building stocks. *Resour. Conserv. Recycl.* **2018**, *129*, 248–262. [CrossRef]
20. Foster, G. Circular economy strategies for adaptive reuse of cultural heritage buildings to reduce environmental impacts. *Resour. Conserv. Recycl.* **2020**, *152*, 104507. [CrossRef]
21. Upadhayay, S.; Alqassimi, O. A Study on Assessing a Business Viability for Transition to a Circular Economy. *Westcliff Int. J. Appl. Res.* **2020**, *4*, 78–94. [CrossRef]
22. Kirchherr, J.; Reike, D.; Hekkert, M. Conceptualizing the circular economy: An analysis of 114 definitions. *Resour. Conserv. Recycl.* **2017**, *127*, 221–232. [CrossRef]
23. Wu, H.; Zuo, J.; Zillante, G.; Wang, J.; Yuan, H. Status quo and future directions of construction and demolition waste research: A critical review. *J. Clean. Prod.* **2019**, *240*, 118163. [CrossRef]
24. Reisinger, J.; Kugler, S.; Kovacic, I.; Knoll, M. Parametric Optimization and Decision Support Model Framework for Life Cycle Cost Analysis and Life Cycle Assessment of Flexible Industrial Building Structures Integrating Production Planning. *Buildings* **2022**, *12*, 162. [CrossRef]
25. Sammut-Bonnici, T. *Wiley Encyclopedia of Management—Volume 12 Strategic Management*; John Wiley & Sons, Ltd.: New York, NY, USA, 2015.
26. European Commission. *Communication from the Commission to the European Parliament, the European Council, the Council, the European Economic and Social Committee and the Committee of the Regions the European Green Deal*, COM/2019/640; European Commission: Brussels, Belgium, 2019.
27. European Commission. *Communication from the Commission to the European Parliament, the Council, the European Economic and Social Committee and the Committee of the Regions a New Circular Economy Action Plan for a Cleaner and More Competitive Europe COM/2020/98 Final*; European Commission: Brussels, Belgium, 2020.
28. Geissdoerfer, M.; Savaget, P.; Bocken, N.M.; Hultink, E.J. The circular economy—A new sustainability paradigm? *J. Clean. Prod.* **2017**, *143*, 757–768. [CrossRef]
29. Ghaffar, S.H.; Burman, M.; Braimah, N. Pathways to circular construction: An integrated management of construction and demolition waste for resource recovery. *J. Clean. Prod.* **2020**, *244*, 118710. [CrossRef]
30. Vieira, L.C.; Amaral, F.G. Barriers and strategies applying Cleaner Production: A systematic review. *J. Clean. Prod.* **2016**, *113*, 5–16. [CrossRef]
31. Klöpffer, W.; Grahl, B. *Life Cycle Assessment (LCA): A Guide to Best Practice*; Wiley-VCH Verlag GmbH & Co. KGaA: Weinheim, Germany, 2014; 440p. [CrossRef]
32. Adamczyk, J.; Dylewski, R. Ecological and Economic Benefits of the “Medium” Level of the Building Thermo-Modernization: A Case Study in Poland. *Energies* **2020**, *13*, 4509. [CrossRef]
33. Sobierajewicz, P. *Kształtowanie Zabudowy Miejskiej o Zwiększonej Efektywności Ekologicznej i Energetycznej: Architektura, Rozwój, Społeczeństwo, Ekologia*; Oficyna Wydaw. Uniwersytetu Zielonogórskiego: Zielona Góra, Poland, 2013; p. 274.

34. Arvidsson, R.; Svanström, M. A framework for energy use indicators and their reporting in life cycle assessment. *Integr. Environ. Assess. Manag.* **2016**, *12*, 429–436. [CrossRef]
35. Hertwich, E.G.; Gibon, T.; Bouman, E.A.; Arvesen, A.; Suh, S.; Heath, G.A.; Bergesen, J.D.; Ramirez, A.; Vega, M.I.; Shi, L. Integrated life-cycle assessment of electricity-supply scenarios confirms global environmental benefit of low-carbon technologies. *Proc. Natl. Acad. Sci. USA* **2014**, *112*, 6277–6282. [CrossRef] [PubMed]
36. PAEC. *Final Report on Environmental Accounting and Reporting*; Parliament of Victoria: Melbourne, VIC, Australia, 2002. Available online: <http://www.parliament.vic.gov.au/papers/govpub/VPARL1999-2002No141.pdf> (accessed on 9 May 2022).
37. Sagarduy, G.; Bandinelli, S.; Lerchundi, R. Product-line Analysis: Do we go ahead? In Proceedings of the Software Product Lines: Economics, Architectures, and Implications, Workshop #15 at 22nd International Conference on Software Engineering (ICSE), Limerick, Ireland, 10 June 2000.
38. Sherif, Y.S.; Kolarik, W.J. Life Cycle Costing: Concept and Practice. *Omega* **1981**, *9*, 287–296. [CrossRef]
39. Braungart, M.; McDonough, W. *Cradle to Cradle: Remaking the Way We Make Things*; North Point Press: New York, NY, USA, 2002.
40. Kacprzak, M. *Chapter: Cradle to Cradle Marketplace, Biodegradable Waste Management in the Circular Economy*; John Wiley & Sons, Ltd.: Hoboken, NJ, USA, 2022; pp. 13–18. ISBN1 9781119679844. ISBN2 9781119679523. [CrossRef]
41. Diaz-Granados, J. *Encyclopedia of Sustainable Management*; Springer: Berlin/Heidelberg, Germany, 2021.
42. Jurkait, K.; Stiglmaier, J. Cradle-to-Cradle in Building Services. *IOP Conf. Ser. Earth Environ. Sci.* **2019**, *225*, 012013. [CrossRef]
43. Lowe, E.A.; Evans, L.K. Industrial ecology and industrial ecosystems. *J. Clean. Prod.* **1995**, *3*, 47–53. [CrossRef]
44. Sertyesilisik, B.; Sertyesilisik, E. Eco industrial Development: As a Way of Enhancing Sustainable Development. *J. Econ. Dev. Environ. People* **2016**, *5*, 6–27. [CrossRef]
45. Srinivasan, R.; Ingwersen, W.; Trucco, C.; Ries, R.; Campbell, D. Comparison of energy-based indicators used in life cycle assessment tools for buildings. *Build. Environ.* **2014**, *79*, 138–151. [CrossRef]
46. EU Ecolabel Home. Available online: https://ec.europa.eu/environment/topics/circular-economy/eu-ecolabel-home_en (accessed on 4 May 2022).
47. Pinto, J.L.Q.; Matias, J.C.O.; Pimentel, C.; Azevedo, S.G.; Govindan, K. *Just in Time Factory*; Springer: Berlin/Heidelberg, Germany, 2018. [CrossRef]
48. Public Procurement for a Circular Economy 2017. Available online: https://ec.europa.eu/environment/gpp/pdf/CP_European_Commission_Brochure_webversion_small.pdf (accessed on 12 November 2022).
49. Bilal, M.; Oyedele, L.O.; Akinade, O.O.; Ajayi, S.O.; Alaka, H.A.; Owolabi, H.A.; Qadir, J.; Pasha, M.; Bello, S.A. Big data architecture for construction waste analytics (CWA): A conceptual framework. *J. Build. Eng.* **2016**, *6*, 144–156. [CrossRef]
50. Konstrukcje Stalowe hal Wielkopowierzchniowych—Inżynier Budownictwa. Available online: <https://inzynierbudownictwa.pl/konstrukcje-stalowe-hal-wielkopowierzchniowych/> (accessed on 12 November 2022).
51. Kim, H.-W.; Dong, L.; Jung, S.; Park, H.-S. The Role of the Eco-Industrial Park (EIP) at the National Economy: An Input-Output Analysis on Korea. *Sustainability* **2018**, *10*, 4545. [CrossRef]
52. Life and the Circular Economy, European Commission, Environment Directorate General. 2017. Available online: <https://ec.europa.eu/environment/archives/life/publications/lifepublications/flippingbook/circulareconomy/HTML/files/assets/common/downloads/publication.pdf> (accessed on 15 May 2022).
53. Pozaccenowe Kryteria Oceny Ofert. *Poradnik z Katalogiem Dobrych Praktyk*; Urząd Zamówień Publicznych: Warszawa, Poland, 2020. (In Polish)
54. Gawęcki, A.; Garstecki, A.; Gawęcki, M. *Optymalizacja Systemu Lekkich hal Stalowych, Opracowanie, 6*; Instytut Podstawowych Problemów Techniki PAN: Warszawa, Poland, 1978. (In Polish)
55. Biegus, A. Projektowanie konstrukcji budowlanych według Eurokodów. *Builder* **2010**, *4*, 1–48. (In Polish)
56. Heinisuo, M.; Laine, V.; Lehtimäki, E. Enlargement of the component method into 3D. In Proceedings of the Nordic Steel Construction Conference (NSCC 2009), Malmö, Sweden, 2–4 September 2009; pp. 430–437.
57. *PN-EN 1993-1-1: 2006*; Eurokod 3: Projektowanie Konstrukcji Stalowych Część 1–1: Reguły Ogólne i Reguły dla Budynków. Polish Committee for Standardization: Warszawa, Poland, 2006.
58. *PN-EN 1993-1-8: 2006*; Eurokod 3: Projektowanie Konstrukcji Stalowych. Część 1–8: Projektowanie Węzłów. Polish Committee for Standardization: Warszawa, Poland, 2006.
59. Bogucki, W.; Żybertowicz, M. *Tablice do Projektowania Konstrukcji Metalowych*; Arkady: Warszawa, Poland, 2008. (In Polish)
60. Heller, H. *Bautechnische Tabellen Interaktiv—WINTAB RA 2.0 Rahmenformeln*; Ernst & Sohn: Berlin, Germany, 2001.
61. Kindmann, R.; Stracke, M. *Verbindungen im Stahl- und Verbundbau, 2. Auflage*; Ernst und Sohn: Berlin, Germany, 2009.
62. *PN-EN 1090-2+A1:2012*; Wykonanie Konstrukcji Stalowych i Aluminiowych—Część 2: Wymagania Techniczne Dotyczące Konstrukcji Stalowych. Polish Committee for Standardization: Warszawa, Poland, 2012.
63. *PN-EN 1997-1:2008*; Eurokod 7—Projektowanie Geotechniczne—Część 1: Zasady Ogólne. Polish Committee for Standardization: Warszawa, Poland, 2008.
64. *PN-EN 1992-1-1:2008*; Eurokod 2, Projektowanie Konstrukcji z Betonu, Część 1-1: Reguły Ogólne i Reguły dla Budynków. Polish Committee for Standardization: Warszawa, Poland, 2008.
65. SECOENBUD. Available online: www.sekocenbud.pl/produkty/wydawnictwa-sekocenbud/ (accessed on 20 April 2022).

66. Biegus, A. *Projektowanie Konstrukcji Stalowych Według Eurokodu 3, Materiały Dydaktyczne*; Politechnika Wroclawska WBLiW: Wroclaw, Poland, 2010. Available online: http://www.metale.pwr.wroc.pl/files/A.Biegus-Polaczenia_Srubowe.pdf (accessed on 25 April 2022).
67. Shah, R.A.; Pitroda, D.J. Recycling of Construction Materials for Sustainability. In Proceedings of the Conference: National Conference on Recent Trends in Engineering & Technology (NCRTEET), BVM Engineering College, Vallabh Vidyanagar, India, 13–14 May 2011.
68. Shinde, D.S.; Kadam, A.; Wadke, A.; Wani, A. A Study on Sustainable Construction Practices and Management. In Proceedings of the Conference: IOP Conference, Coimbatore, India, 12–13 February 2022.
69. Patel, V.; Solanki, J. Just in Time Concept Used in Construction Project. *Int. Res. J. Eng. Technol.* **2020**, *7*, 3298–3303.

Disclaimer/Publisher’s Note: The statements, opinions and data contained in all publications are solely those of the individual author(s) and contributor(s) and not of MDPI and/or the editor(s). MDPI and/or the editor(s) disclaim responsibility for any injury to people or property resulting from any ideas, methods, instructions or products referred to in the content.

Article

The Evolution of Research on C&D Waste and Sustainable Development of Resources: A Bibliometric Study

Li Wang ^{1,2,*}, Yanhong Lv ¹, Siyu Huang ³, Yu Liu ¹ and Xinrong Li ⁴¹ School of Architecture and Civil Engineering, Xihua University, Chengdu 610039, China² School of Management Science and Real Estate, Chongqing University, Chongqing 400030, China³ WMG (Warwick Manufacturing Group), University of Warwick, Coventry CV4 8UW, UK⁴ Department of Subject Information Service, Xihua Library, Chengdu 610039, China

* Correspondence: wangli@mail.xhu.edu.cn

Abstract: Construction and demolition (C&D) waste is steadily increasing as both urbanization and the construction industry advance. Therefore, numerous studies on C&D waste have been conducted. In this paper, the literature published in the field of C&D waste and sustainable development from 2002 to 2022 was utilized to examine the current state of research and potential future research hotspots via the bibliometric method. Herein, 3550 studies found in the literature were analyzed using Citespace and VOSviewer, two efficient visual analysis programs, for the annual quantitative distribution, contribution and cooperation of authors, influential and productive countries/regions and institutions, keyword co-occurrence analysis, literature co-citation analysis and identification of research frontiers. The findings show an exponential rise in publications on construction waste and sustainable resource development, while the research focus has clearly shifted from recycling and reduction of C&D waste to harmless and resourceful treatment in the last five years. The keywords “optimization”, “implementation” and “strategy” also indicate that more emphasis is being placed on the research of management method realization mechanisms, technological optimization schemes and policy strategies. The research results of this paper will help participants in the construction industry to grasp the current research hotspots and development trend in the field of C&D waste and the sustainable development of resources. It also plays a positive role in formulating relevant regulations and policies, reducing resource waste and construction project costs.

Keywords: construction and demolition waste; sustainable development; bibliometric study; visualization

Citation: Wang, L.; Lv, Y.; Huang, S.; Liu, Y.; Li, X. The Evolution of Research on C&D Waste and Sustainable Development of Resources: A Bibliometric Study. *Sustainability* **2023**, *15*, 9141. <https://doi.org/10.3390/su15129141>

Academic Editors: Carlos Morón Fernández, Daniel Ferrández Vega and Andres Seco Meneses

Received: 8 January 2023

Revised: 4 March 2023

Accepted: 29 May 2023

Published: 6 June 2023



Copyright: © 2023 by the authors. Licensee MDPI, Basel, Switzerland. This article is an open access article distributed under the terms and conditions of the Creative Commons Attribution (CC BY) license (<https://creativecommons.org/licenses/by/4.0/>).

1. Introduction

The reduction and recycling of construction and demolition (C&D) waste is crucial to human society and has a significant impact on sustainable development. Although C&D waste and sustainable development of the ecological environment were initially only the concern of local governments, they will eventually pose a threat to regional and global development [1]. With the rapid urbanization of the world, in order to resolve the serious conflict between increasing C&D waste and environmental protection, it is necessary to explore economically attractive sustainable solutions for the reduction and recycling of C&D waste [2]. The world is currently undergoing profound changes that have not occurred in a century; it is urgent to solve the problem of the large amount of waste produced by human construction activities and to develop research on the sustainability of resources.

C&D waste usually refers to construction waste, decoration waste and demolition waste generated during the construction, renovation and demolition phases of a project [3]. It is mainly composed of large amounts of inert materials (bricks, concrete, etc.), timber, asphalt, metals and plastic [4]. Economic, social, health and technical factors jointly affect the development direction of C&D waste research, and its key areas mainly include

recycling [5–8], reduction [9,10], environmental impact [11–13], and reduction of the environmental footprint of C&D waste [14,15].

Existing research results have shown that the process of recycling construction waste will be accelerated in some developing countries, while the trend of recycling construction waste in developed countries will gradually change [16]. Recently, the investigation of greenhouse emissions [17–19], carbon footprint [20,21], human factors [22,23] and waste treatment policies [24–26] in the research on recycling construction waste have developed rapidly. It is worth noting that human factors are more likely to appear in research related to construction waste, indicating that it is one of the important factors for the effective management of C&D waste. Li et al. further quantitatively studied the impact of construction waste reduction behavior based on the theory of planned behavior [27]. According to Udawtt, there were both technical and man-made obstacles to waste management in Australian construction projects, but the latter were more dominant [28]. Studies have shown that the development and progress of construction waste management is driven by social motivation and policies [25]. Therefore, the updating of laws and regulations on the treatment of construction waste can also reflect the change in research works on construction waste. Reducing construction waste has always been a hot topic in academia. Some scholars have explored effective methods from the perspectives of construction technology [29] and management methods [30]. With the increase in environmental damage, more and more research has been conducted on the environmental benefits of reduction management [31]. Recently, some scholars have studied the dynamic trend of construction waste by using visual analysis software [32]. The results show that extensive research has been conducted on construction waste reduction, system dynamics analysis and life cycle assessment over the past decade, while the circular economy, big data, building information modeling (BIM), environmental impact (carbon footprint), prefabricated buildings, human factors and logistics planning of construction waste transportation have been vigorously developed from 2019 to 2021. It can be seen that the effective management of C&D waste is related to the sustainability of resources, and then affects the ecological environment and economic development of the whole society [33,34]. Treatment methods are gradually developing towards the direction of resource sustainability, which mainly refers to developing the means of recycling and the reduction of construction waste to monitor and reduce harmful impacts on resources, including the comprehensive application of BIM technology [35–37], 3D printing technology [38,39] and other information technologies, as well as the circular economy and other management methods at various stages of the construction waste life cycle [40].

Since C&D waste has increased steeply and attracted the attention of the industry, many scholars have conducted hot spots and trends research on C&D waste or the sustainable development of resources. However, resource sustainability is closely linked to the development and progress of C&D waste management. Unfortunately, there is a gap in the discussion of the overall hotspots and trends in C&D waste and the sustainable development of resources. Therefore, this paper adopts a more reliable bibliometric analysis method to analyze 3550 publications collected from the Web of Science core collection, including annual quantitative distribution, author cooperation, influential and productive countries/regions and institutions, keyword co-occurrence analysis, literature co-citation analysis and identification of research frontiers, so as to further discover emerging technologies and theories for efficient resource utilization, improve the quality of engineering projects and reduce costs, and promote a virtuous cycle of resources in the construction industry. In the second section, the determination process of the research methods and data collection are expounded. The third section presents the analysis results, and accordingly, the results are further discussed in the fourth section. The research conclusions on C&D waste and the sustainable development of resources are shown in the fifth section.

2. Methods

2.1. Research Method

Knowing the hotspots, frontiers and status of a field can guide further research, and bibliometrics can achieve this [41]. Manual literature analysis [42] and scientometric analysis [43] are two methods commonly used in bibliometrics. In order to make the research results more accurate, scientometric analysis, which can visually present the quantitative analysis results, is adopted in this paper [44]. Citespace software developed by Professor Chen Chaomei [45], and VOSviewer, a scientific knowledge mapping software developed by professors Van Eck and Waltman [46] of Leiden University in the Netherlands, are both effective tools for visualization analysis. Many researchers have used Citespace and VOSviewer to research related fields. For example, Zheng et al. summarized the intellectual structure and evolution model of partnership research in the construction industry using Citespace [47]. Chellappa et al. analyzed the status of research on the safety of Indian construction workers through VOSviewer [48]. Therefore, Citespace and VOSviewer are selected in this paper to conduct author cooperation analysis, analysis of countries/territories and institutions, keyword co-occurrence and cluster analysis on the selected literature, in order to study the research status in the field of C&D waste and sustainable development.

2.2. Data Collection and Collation

Web of Science (WoS) and Scopus are the preferred databases for researchers conducting bibliometric analysis. Since the WoS database contains extensive literature in engineering, social science, medicine, management, philosophy and other disciplines, it is chosen as the database to select research data. The search terms in this study are “sustainability OR sustainable development” and “construction waste* OR C&D OR construction waste management OR demolition waste* OR decoration and renovation waste management”, and the literature language in the data was restricted to English at the same time. By comparing the search results of all databases and core collections of WoS, it is found that although the former published articles earlier (since 1994), the eight articles published between 1994 and 2001 are mainly early explorations on the sustainable development of construction waste and resources, with little impact on the identification of current hot spots and trends. Meanwhile, the literature in the core collection of WoS is groundbreaking and of high quality in terms of construction waste [49,50]; therefore, the original data of 3550 publications selected in this study are all from it, including research articles, review articles, proceedings papers, data papers and early access, and excluding editorial materials, letters and book reviews.

3. Results

3.1. Analysis of Publications

Quantitative distribution data for articles published on C&D waste and the sustainable development of resources are analyzed by Citespace, as shown in Figure 1. Among them, the countries with the highest number of publications are specially shown in stacked columns. The broken line in the figure represents the cumulative number of publications in the field, which reflects the development status of research results in this field from 2002 to 2022. It can be found by analyzing the broken line that the first article was published in 2002, and the number of published articles was less than 25 for six consecutive years, with slow growth. In 2016, the number of annual publications exceeded 100 for the first time, and academia became more and more interested in this field. In 2022, more than 700 articles were published, making the research more diversified. Thus, according to the above research results, the research progress since 2002 can be roughly divided into three parts: the exploration phase (2002–2007), the initial growth phase (2008–2015) and the rapid development phase (2016–2022).

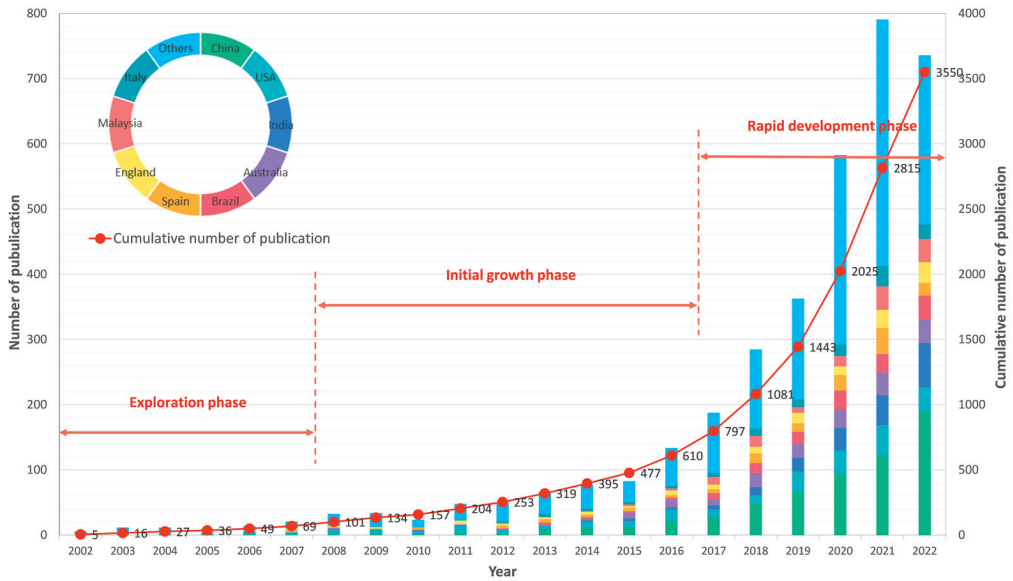


Figure 1. Statistical chart of literature publication.

At the same time, the stacked columns also presented the research status in the field of C&D waste and the sustainable development of resources among countries. It can be seen that China’s development in this field shows an exponential growth trend, while India and Brazil grew very slowly in the early stage, until they became active in 2018. Related research in the United States and Australia has developed steadily, while studies in Malaysia, Italy and other countries have shown fluctuating growth.

Table 1 lists the 10 most productive journals. The number of publications of *Journal of Cleaner Production* (11.414%) ranks first, which shows its high influential status, followed by *Sustainability* (8.012%), *Construction and Building Materials* (7.787%), *Materials* (2.952%) and *Resources Conservation and Recycling* (2.839%). Obviously, preservation of the environment, building materials, and sustainable development are the core themes of the top 10 most productive publications. This shows that researchers’ journal selection is relatively simple, and we can pay more attention to these journals to track the research frontiers and hot articles in the field of C&D waste and the sustainable development of resources.

Table 1. The proportion of published journals.

| NO. | Publication | Count | Proportion |
|-----|---|-------|------------|
| 1 | <i>Journal of Cleaner Production</i> | 406 | 11.414% |
| 2 | <i>Sustainability</i> | 285 | 8.012% |
| 3 | <i>Construction and Building Materials</i> | 277 | 7.787% |
| 4 | <i>Materials</i> | 105 | 2.952% |
| 5 | <i>Resources Conservation and Recycling</i> | 101 | 2.839% |
| 6 | <i>Journal of Building Engineering</i> | 67 | 1.884% |
| 7 | <i>Environmental Science and Pollution Research</i> | 61 | 1.715% |
| 8 | <i>Buildings</i> | 44 | 1.237% |
| 9 | <i>Waste Management</i> | 44 | 1.237% |
| 10 | <i>Journal of Materials in Civil Engineering</i> | 42 | 1.181% |

3.2. Co-Author Analysis

Co-author analysis can identify authors who have made significant contributions to this field, and their changes in research interests also reflect research trends to some extent. At the same time, the regional or global development of this field can be grasped in a timely manner by revealing the close relationship between them.

3.2.1. Co-Authorship Analysis

In this bibliometric study, 11,795 authors were included in the research on C&D waste and the sustainable development of resources. As shown in Figure 2, the network view and density view of 149 authors with more than 5 articles were drawn by VOSviewer. In the network view, a node represents an author, and its size is proportional to the number of articles by each author. The links between nodes intuitively demonstrate the cooperative relationship between authors. The thicker the line, the closer the connection between them. The distance between nodes indicates the affinity between them, and different colors represent different clusters of author collaboration. Accordingly, in the density view, the more nodes around a node, the brighter the color and the closer the cooperation.

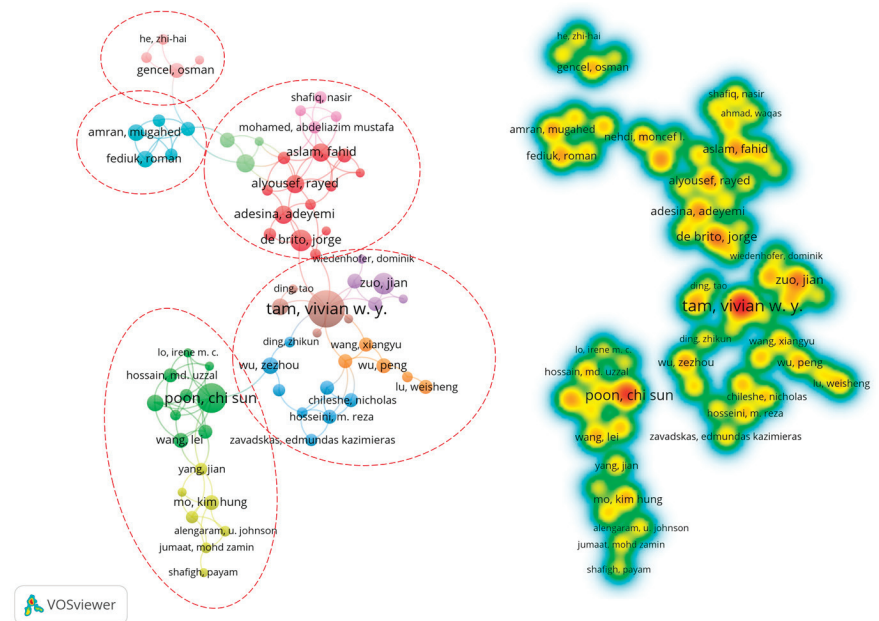


Figure 2. Co-author network.

As can be seen from Figure 2, 149 authors were labeled as 11 research clusters according to their degree of cooperation, and they can be roughly divided into five research communities. With Vivian W.Y. Tam, an author from the University of Western Sydney, as the central author, the most connected research community is formed with Jian Zuo from the University of South Australia and Xiangyu Wang from Curtin University, Australia, etc. They focused primarily on recycled aggregate concrete and sustainable performance assessment, while recent research has focused mainly on quality improvement of recycled concrete and lean construction management. Another closely connected research community consists of Chi Sun Poon, Lei Wang and Md Uzzal Hossain et al. They mainly worked on the environmental friendliness and sustainable management of recycled concrete products.

3.2.2. Co-Institution Analysis

To discover the important research organizations in the field of C&D waste and the sustainable development of resources, the collaborative network of institutions with more than 10 published articles is shown in Figure 3. In this part, 115 nodes represent 115 institutions, most of which are universities. The size of the node depends on the number of publications, and the degree of collaboration between the two institutions is indicated by the thickness of the lines. Colors of institutions represent the clusters to which they belong. As can be seen from Figure 3, Hong Kong Polytechnic University is the largest node, which is most closely related to the purple cluster and the blue cluster, such as Tongji University, Hong Kong University and City University of Hong Kong in the purple cluster, while in the blue cluster, the China Academy of Science and Shanghai Jiao Tong University are the main partners, indicating that there are close cooperations between top scientific research institutions and top universities in China. There are also orange clusters and red clusters with frequent cooperation. Malaysia Petroleum University is the central institution that maintains close cooperation with Chongqing University, Melbourne Institute of Technology, Milan Institute of Technology, Curtin University and Delft University of Technology, etc. It also shows that global institutions attach greater importance to the areas of C&D waste and the sustainable development of resources, and are actively expanding cooperation and exchange of research experiences.

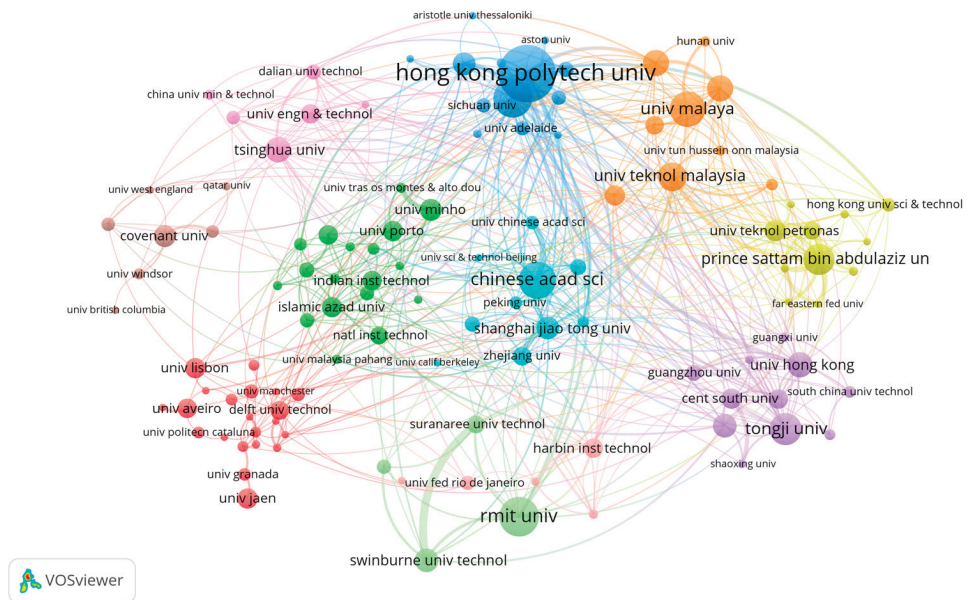


Figure 3. Co-institution network.

3.2.3. Co-Country Analysis

The research situation of countries/territories was analyzed using VOSviewer. A total of 117 countries/territories have contributed to this field, but only 69 countries/territories with more than or equal to 10 papers are presented in Figure 4. Similarly, the larger the node, the more articles the country or region has published, and the thicker the line, the more frequently the two countries/territories communicate. China is the most productive country ($n = 828$, 23.32%), followed by India ($n = 339$, 9.55%), Australia ($n = 299$, 8.42%), the United States ($n = 285$, 8.03%) and England ($n = 258$, 7.27%).

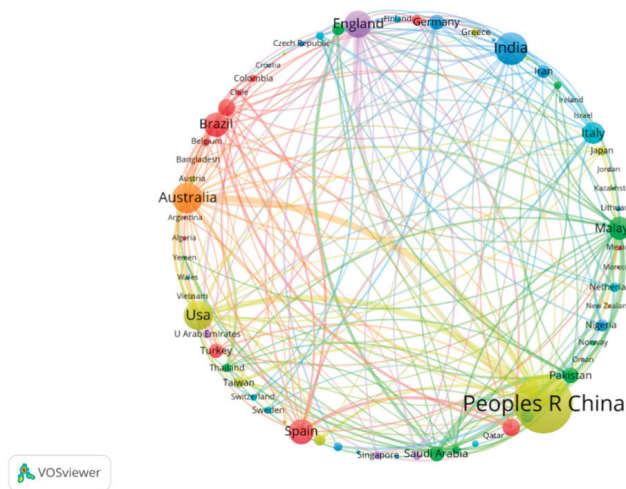


Figure 4. Co-country network.

With the development of the construction industry, countries pay more attention to construction waste. It can be observed that China, which publishes the most articles, has very frequent cooperation with Australia, the United States and England. These countries have many partners and have made rapid progress in C&D waste and the sustainable development of resources through global communication, cooperation and information sharing. As can be seen from Figure 1, despite India publishing research articles later than expected, the number of articles on construction waste has increased rapidly in recent years, indicating that India has gradually realized the importance of the sustainable development of construction resources.

Analyzing the research cooperation network among individuals, institutions and countries from the perspective of temporal evolution can better reveal the overall development trend of this field in recent years [51]. Starting from the year (2003) when the number of papers was more than 10, longitudinal change charts of nodes, links, and density are illustrated using Citespace. Among them, the time interval is set to 5 years, nodes represent authors, links represent cooperation among authors, and the density is the actual number of relationships in the network divided by the theoretical maximum coefficient. Figure 5 shows the results. Three line charts show changes in relevant parameters for individuals, institutions and countries, respectively. The horizontal axis represents time, the left side of the vertical axis represents the counts of nodes and links, while the right side represents density value.

It can be seen from Figure 5 that the blue line representing the number of authors continues to grow, indicating that new researchers (individuals, institutions, and nations) have joined and contributed to the field of C&D waste and sustainable development as a result of the current environmental deterioration, and the increase has gradually accelerated since 2018. Another set of green lines indicates a change in the number of links among researchers, which is also on the rise in general. Although the number of collaborations between individuals and institutions decreased slightly from 2003 to 2007, they all resumed their enthusiasm for cooperation in 2008 and continued to increase later, while cooperation between countries kept increasing throughout the period. The strength of the nodes' collaboration is shown by the purple line. According to Figure 5, research on C&D waste and sustainable development was still in its infancy between 2003 and 2017. Many new researchers were still in the exploratory phase and had not started active external communication, which led to a downward trend in the overall density line. With the continuous deepening of research, this field has achieved great results. Therefore,

researchers have engaged in active experience sharing and academic cooperation to seek new breakthroughs in the field, making the density curve rise again.

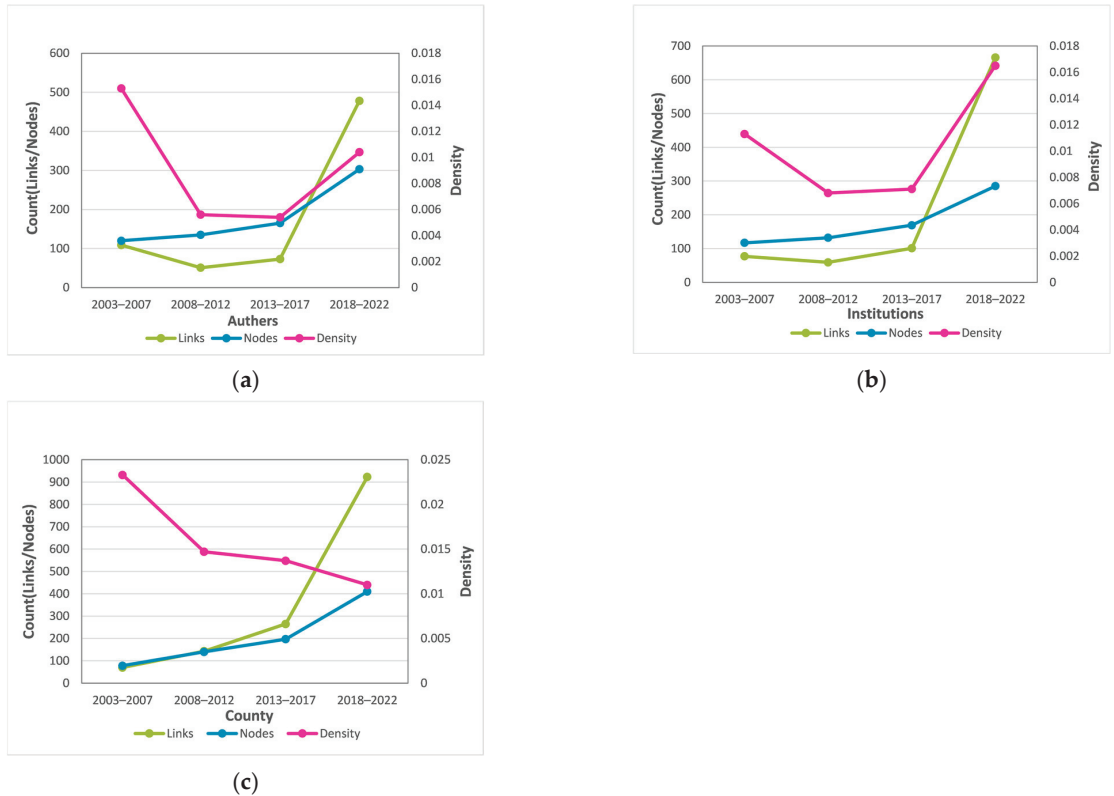


Figure 5. (a) Longitudinal analysis of co-author networks. (b) Longitudinal analysis of co-institution networks. (c) Longitudinal analysis of co-country networks.

3.3. Keywords Analysis

Keywords are concise summaries of the research content covered. We can identify the main hotspots and central trends in the field of C&D waste and the sustainable development of resources through bibliometric analysis.

3.3.1. Keywords Co-Occurrence Analysis

As shown in Figure 6, the co-occurrence network with 528 keywords that have a frequency of more than 10 was presented by VOSviewer. Each node represents a keyword, and the frequency of keywords is expressed by the size of the nodes. The thickness of the connection lines between nodes intuitively reflects the intensity of the connection between keywords. These keywords are mainly distributed in the first three clusters, respectively by three colors (red, green and blue).

Lu et al. established performance benchmarks for the management of construction waste in different project categories using big data technology to promote better management of construction waste [56]. Figure 6 also shows newer high-frequency keywords, such as “circular economy” ($n = 285$) and “microstructure” ($n = 151$). Studies have shown that about three quarters of the solid waste generated by the construction industry has residual value [57]. As awareness of sustainable development and resource management improved, many nations started exploring new models, and researchers gradually paid more attention to waste reduction, so as to minimize the negative impact of construction waste on the environment and further realize the sustainable development of resources. This also makes the circular economy model continue to attract the attention of researchers [58,59].

3.3.2. Keyword Evolution Analysis

In order to more intuitively understand the research work of C&D waste and sustainable development, the evolution of keywords in this field was analyzed using Citespace, as shown in Figures 7 and 8. The time axis in Figure 7 indicates the time point when the keyword first appeared. The red section in Figure 8 represents a sudden increase in interest in keywords during this period.

As can be seen, “emission” and “sustainable development” appeared the earliest, demonstrating that harmful gases produced by the construction industry, particularly CO₂, are responsible for the deterioration of the ecological environment. It is the gradual exposure of ecological and social issues that promote the sustainable development trend of the construction industry. Although the issue of emissions was brought up in 2002, little research has been carried out on it, and it has only recently become active. Some researchers have started to reduce CO₂ emissions by studying environmentally-friendly and cost-competitive geopolymers to gradually replace ordinary Portland concrete (OPC) that is energy-dependent and environmentally damaging [60]. There are also scholars who calculated the carbon emissions of geopolymer recycled aggregate concrete and studied its physical properties, such as slump and compressive strength, in order to prove its feasibility to replace OPC-based concretes [61]. From Figure 7, it is also clear that many keywords related to materials, such as “energy”, “concrete”, “cement”, and “aggregate”, occurred between 2004 and 2006. Among them, “energy” has the highest centrality (centrality = 0.13) and functions as a bridge. The energy consumption and pollution of the construction industry is enormous, so scholars have begun to pay attention to the environmental performance of the construction industry and its materials [62]. The keywords “environmental impact” and “design” appeared in 2006 and also reflect that researchers have gradually shifted their focus to other links besides the construction phase, in order to optimize the final disposal process of waste materials [63]. In the following years, most efforts were devoted to the development and performance optimization of various recycled materials. Since 2018, the emergence of “green concrete” and “circular economy” indicates that the construction industry has been guided by new theories, such as green building and the circular economy [64,65]. It is necessary to explore new and effective management models to promote resource utilization of construction waste and the sustainable development of construction resources.

With the development of C&D waste and the sustainable development of resources, although the introduction of new topics has slowed down after 2018, there are still many new opportunities and challenges. Combined with Figure 8, it can be seen that the keywords “optimization”, “implementation” and “strategy” have again received great attention from academia in the recent period (2019–2022). Their respective citation bursts also rank among the top three. Therefore, these keywords can be identified as recent hot topics in this field. Identifying and implementing standards for green building materials (GBM) and assessing their sustainability, breaking down barriers to promoting a circular economy (CE), integrating life cycle sustainability assessment (LCSA) into the design phase to optimize building performance, and designing waste minimization strategies are expected to be future research directions.

the research topic, and cluster 9 was repeated, so 4 clusters were manually deleted [66]). Modularity and silhouette values are 0.7877 and 0.8974, indicating the high reliability of the clustering structure. The result is shown in Figure 9 and Table 2.

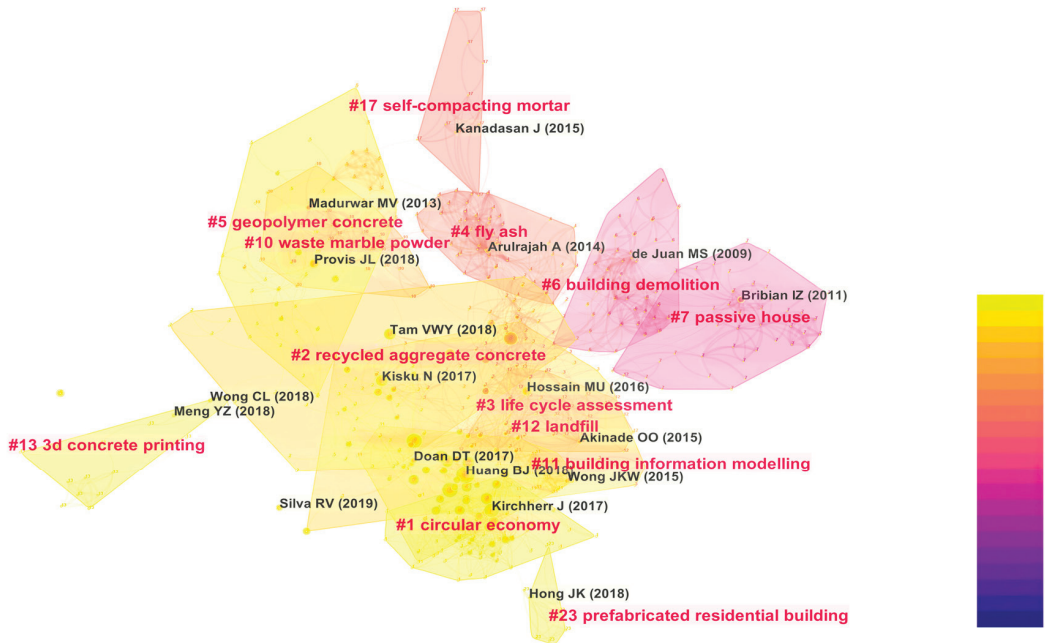


Figure 9. Cluster analysis of documents co-citation.

Table 2. Cluster information.

| Cluster ID | Cluster Label | Size | Mean Year |
|------------|------------------------------------|------|-----------|
| 1 | Circular economy | 84 | 2018 |
| 2 | Recycled aggregate concrete | 74 | 2015 |
| 3 | Life cycle assessment | 65 | 2015 |
| 4 | Fly ash | 54 | 2012 |
| 5 | Geopolymer concrete | 45 | 2017 |
| 6 | Building demolition | 44 | 2009 |
| 7 | Passive house | 42 | 2009 |
| 10 | Waste marble powder | 31 | 2014 |
| 11 | Building information modelling | 30 | 2017 |
| 12 | Landfill | 29 | 2013 |
| 13 | 3D concrete printing | 14 | 2018 |
| 17 | Self-compacting mortar | 13 | 2012 |
| 23 | Prefabricated residential building | 7 | 2018 |

In Table 2, the cluster size represents the number of co-cited references in the cluster. The larger the value, the more popular it is in a certain field. The average year can reflect the development trend of cluster. It can be seen from the results that there were many studies on the definition, classification and treatment of C&D waste in the early stages, and then the research direction turned to life cycle assessment and performance research of recycled aggregate concrete. In recent years, most scholars have begun to discuss the sustainable development of C&D waste based on some emerging theories, materials and technologies, such as the circular economy, geopolymer concrete, 3D printing technology

and prefabricated buildings, in order to further explore the sustainable development mode of C&D waste resources.

To further understand the recent development status of this research area, the three clusters with the highest average years are listed in Table 3. Meanwhile, the three most active cited articles and the three most active citing articles related to the cluster are listed in order to identify the intellectual bases and research frontiers in this field [67]. Details are discussed below.

Table 3. The three most active citing and cited papers in the latest three clusters.

| Cluster ID | Cited Publications | | Citing Publications | |
|------------|----------------------------------|------|--------------------------------------|------|
| | Author | Year | Author | Year |
| 1 | Kirchherr, Julian et al. [68] | 2017 | Norouzi, Masoud et al. [59] | 2021 |
| | Geissdoerfer, Martin et al. [69] | 2017 | Yu, Yifei et al. [71] | 2022 |
| | Mahpour, Amirreza [70] | 2018 | Rahla, Kamel Mohamed et al. [72] | 2021 |
| 13 | Wong, Chee Lum et al. [73] | 2018 | Ahmed, Ghafur H et al. [76] | 2022 |
| | Meng, Yazhi et al. [74] | 2018 | Sahin, Hatice Gizem et al. [77] | 2022 |
| | Habert, G. et al. [75] | 2018 | Qian, Hao et al. [78] | 2022 |
| 23 | Hong, Jingke et al. [79] | 2018 | Lopez-Guerrero, Rafael E et al. [82] | 2022 |
| | Teng, Yue et al. [80] | 2018 | Yuan, Mengqi et al. [83] | 2022 |
| | Hao, Jianli et al. [81] | 2020 | Zhang, Riqi et al. [84] | 2022 |

Cluster 1 is labeled “circular economy”, which has been a hot topic in the last five years. The three most active cited papers mainly focus on defining the circular economy and identifying obstacles to its implementation. Kirchherr et al. [68] summarized 114 definitions of CE and finally outlined the definition, which refers to an economic system that replaces the “end-of-life” of waste with reducing, reusing and recycling materials and recycling in the production/distribution and consumption process. Geissdoerfer et al. [69] provide conceptual clarity by illustrating similarities and differences between the terms “circular economy” and “sustainability” to improve the efficiency of the use of these approaches in research and practice. Mahpour [70], on the other hand, provided direction for further research by identifying barriers to the transition to CE in C&D waste management. Therefore, on the basis of intellectual bases, the three papers most actively cited are related to the promotion of CE. Norouzi et al. [59] further clarified the development process of CE through bibliometric analysis, and put forward future research topics, such as exploring the relationship between the smart city and CE, developing the business model of CE, etc. Yu et al. [71] found the lack of a decision-making framework in CE mainly from the perspective of policy formulation, and proposed a bi-directional policy-making mechanism based on two policy models. Rahla et al. [72] proposed strategies to promote the circular economy in three respects: resource management, architectural design methods, and digitalization of the construction industry.

Cluster 13, labeled “3D concrete printing”, reflects that researchers have recently paid particular attention to the combination of waste disposal with 3D printing technology. In the intellectual bases, Wong et al. [73] found that brick powder is the most practical form of recycled brick, but it can only be used sparingly as concrete aggregate because it cannot significantly improve concrete performance. Meng et al. [74] reviewed the published literature on the use of various wastes in the production of concrete blocks, demonstrating the good potential of incorporating C&D waste into concrete blocks as aggregates. Habert et al. [75] provided medium-term and long-term solutions to environmental problems in concrete production. In the most active citing papers, Ahmed et al. [76] reviewed the existing 3D concrete printing technology and studied the different application technologies for structural reinforcement. Sahin et al. [77] showed that the use of geopolymers, recycled aggregates and waste in the mix design of 3D printed concrete (3DPC) can contribute to the sustainability of 3DPC. Qian et al. [78] also suggested that using recycled products as 3D

concrete printing materials can reduce carbon emissions and technology costs, which have high economic and environmental benefits. In general, 3D concrete printing technology is worth promoting in the field of C&D waste and the sustainable development of resources.

Cluster 23 is labeled “Prefabricated Residential Building” (PRB), so the top three cited papers all focus on the topic of prefabricated buildings. Hong et al. [79] established a framework for cost performance analysis to investigate the basic cost composition of prefabricated buildings, and assess the impact of adopting prefabricated technologies on the total cost of actual construction projects. Teng et al. [80] systematically examined evidence of reducing building life cycle carbon through prefabricated technologies. It showed that prefabrication resulted in a 15.6% reduction in embodied carbon and a 3.2% reduction in operational carbon. Hao et al. [81] developed a BIM-based approach to evaluating carbon emission reduction of a prefabricated building project, which showed that prefabrication has less negative environmental impact compared to traditional building technology. In the three citing papers, Lopez-Guerrero et al. [82] considered that the sustainability of industrial building systems (IBS) had previously only been examined in terms of environmental aspects and through qualitative indicators. To fill the gap, IBS sustainability was assessed using quantitative and qualitative indicators based on economic, social and environmental aspects. Based on evolutionary game theory, Yuan et al. [83] discussed the evolutionary decision-making behavior and stabilization strategy of the government, real estate developers and homebuyers in the PRB industry. They also proposed a promotion mechanism to help China’s construction industry achieve orderly and sustainable development of the PRB. Zhang et al. [84] assessed the environmental impact of prefabricated building policies in Hong Kong SAR and Singapore by comparing these policies. This shows that researchers are beginning to notice the impact of prefabricated buildings on environmental benefits and sustainable development.

In general, Cluster 1 discusses the resourceful and sustainable treatment of construction waste from the perspective of circular economy management methods. Cluster 13 focuses on 3DCP technology for the reuse of construction waste. Cluster 23, on the other hand, focuses more on prefabricated building policies and regulations, and takes them as a new engine for reducing waste and carbon footprint and promoting resourceful utilization of construction waste.

4. Discussion

The research hotspots in the field of C&D waste and sustainable development of resource can be concluded based on the findings of keyword co-occurrence and cluster analysis. According to Figure 6, “performance”, “concrete”, “mechanical-properties”, “fly-ash”, “management”, “life-cycle assessment”, “circular economy” and “microstructure” have high frequency. At present, concrete is the material most often considered among recycled products. Geopolymer concrete, steel fiber recycled aggregate concrete, and other new types of recycled concrete are being developed. Research on the compressive strength, flexural strength, slump, durability and other mechanical properties of recycled concrete are also enduring topics in this field. In recent years, construction waste management methods have been developed and some achievements have been made. Academia has given the life cycle assessment (LCA) approach a lot of attention, showing that relevant research on reducing the environmental footprint is a hot topic in this area, as shown in Table 2. The application of LCA in the resource management of C&D waste places an emphasis on preventing the overall environmental impact of waste throughout the entire process. It changes the previous idea of focusing only on economic benefits or technological development, optimizes the specific steps of some promising technologies, and provides a new direction for the management of construction waste. There are also proposals to incorporate Life Cycle Sustainability Assessment (LCSA) into building design. In addition, the related research on CE and reduction has also become the focus in this field, so as to further improve the level of resourceful and harmless utilization of construction waste.

Combined with Figure 8 and Table 3, research frontiers in C&D waste and resource sustainability can be identified. Although the circular economy has been extensively promoted in recent years, many countries still face difficulties in implementing it due to a variety of problems. The development of 3D concrete printing technology conforms to the current trend of construction informatization. It can realize the recycling of resources when choosing construction waste as printing materials. Prefabricated buildings can make full use of their labor-saving and energy-saving advantages in the selection of prefabricated materials, production process and construction process, but the technical bottleneck of using construction waste in prefabricated buildings has always existed. Therefore, breaking the restriction of CE promotion and effective implementation, optimizing the performance of recycled products to meet the material selection standards of emerging technologies, such as 3D printing technology and prefabricated technology, using evolutionary game theory and other methods to study the behavior factors of various stakeholders and making policy suggestions to the government to encourage the use of the above management methods and technologies can be regarded as the current research frontiers.

Trends in C&D waste and sustainable development are summarized in Figures 7 and 8 and Table 2. The construction industry has contributed significantly to energy consumption and environmental damage while advancing economic development, such as resource shortages, greenhouse gas emissions, land loss, and other issues. The contradiction between them is becoming increasingly acute. As a result, many countries are gradually realizing that if construction waste continues to rise in line with the current situation, it will lead to huge losses. Therefore, the concept of resource sustainability is gradually integrated into construction waste considering the high residual value of construction waste. First, scholars started to develop and study recycled products to value construction waste and expand the market, such as recycled aggregate, recycled blocks and recycled bricks. After that, scholars began to emphasize the reduction in construction waste, and pay attention to the economic and environmental benefits of resource recovery to prove its sustainability, such as life cycle assessment, performance optimization of recycled products, the establishment of an environmental benefit assessment model, cost compensation model research, etc. BIM, GIS and big data technology are also constantly evolving. The circular economy and green building materials have been the focus of C&D waste and sustainable development in recent years, as the aim is to explore a new management model and fully integrate the idea of resource sustainability. In general, the evolution process can be summarized as recycling–reduction–sustainability. It is worth emphasizing that the stages in the evolution process is not completely separate from each other. For example, in the past five years, in addition to focusing on sustainability, reduction technologies such as 3D printing technology and prefabricated construction are constantly advancing.

Through the discussion of the above research hotspots, research frontiers and development trends, future research directions are also proposed:

1. Promoting innovation in recycling technology. Recycling construction waste is a key strategy for the sustainable development of resources in the future. More attention should continue to be paid to the pre-treatment and reproductive phases of construction waste. First, it can more effectively reduce waste generation at the source and lower the cost of construction projects, such as material costs, labor costs and management fees. Second, it may increase the secondary or multiple utilization potential of different types of construction waste and prolong their life, so as to improve the utilization rate of construction waste resources, which plays a role in saving resources, improving the environment and promoting the sustainable development of society.
2. Developing information technology for the reduction in construction waste. The development of construction waste reduction is the focus of scientific research. It is not only a scientific problem, but also a common concern of politics, economics and society. At present, some information technologies, such as BIM, GIS and big data, have made good achievements in predicting waste generation and reducing waste output. However, some newly developed technologies, such as 3D concrete printing

- and prefabricated construction, are still only used in projects with simple structure and small scale. How to combine existing mature information technologies or find new ones to solve the limitations of emerging technologies deserves further consideration.
3. More research on top-level design. The direction of development in the field of C&D waste and sustainability is also influenced by policy. Combined with research frontiers and hotspots, it is clear that current research focuses primarily on environmental benefits, such as carbon emissions and environmental footprints. Therefore, further improvement of relevant policies and regulations can enhance the environmental awareness of participants and provide impetus for the effective operation of the recycling industry chain. First, it is necessary to establish a comprehensive supervision system. BIM, GIM and other technologies can be fully used to supervise the whole process of the recycled products industry. Second, it is necessary to formulate effective incentive policies to promote the development of the construction waste industry. Financial support can be provided to recycling companies in the research and development of new materials and technologies.
 4. More investigation of different project stakeholders. As things stand, it is inefficient to promote the recycling of C&D waste only through government procurement and subsidies. The participation of contractors in the reduction in construction waste and the willingness of recycling companies to engage in the development of production materials and technology research is not strong. Therefore, establishing a behavior model to find the motivation to stimulate all stakeholders to actively participate in the resourceful disposal of construction waste can be taken as the future development direction in order to guide the market stakeholders' selection behavior of resourceful treatment and achieve higher economic, social and environmental benefits.

5. Conclusions

In this paper, 3550 publications related to C&D waste and the sustainable development of resources are visually analyzed using Citespace and VOSviewer, in order to identify research hotspots, research fronts, and development trends in this field. The conclusions are summarized as follows:

1. Research progress on C&D waste and the sustainable development of resources can be roughly divided into exploration phase (2002–2007), initial growth phase (2008–2015) and rapid development phase (2016–2022). China is the most active country in this field, while the United States, India, Australia, Brazil, Spain, the United Kingdom, Malaysia and Italy contribute a large number of publications. The *Journal of Cleaner Production*, *Sustainability*, *Construction and Building Materials*, *Materials*, and *Resource Conservation and Recycling* are the most productive journals, which is closely related to the impact of journals in the field of C&D waste and sustainable development.
2. Based on the author's contributions and collaboration, it seems that more and more scholars have begun to devote themselves to research in this field. However, most of them only communicate with members of small research groups. Among the most active institutions, they are also more inclined to cooperate with domestic universities and research institutes. At present, there is still relatively little global cooperation.
3. The results of keyword co-occurrence and cluster analysis indicate that research and development of recycled products, methods for reducing construction waste, and sustainable management modes have been current research hotspots. Among them, the circular economy, life cycle sustainability assessment, and the environmental benefits of recycled products have attracted much attention.
4. The identification of research trends shows that the evolution process in this field is summarized as recycling–reduction–sustainability, and future research directions are also proposed. On the one hand, strengthening the research and development of new technologies for waste recycling and reduction can optimize the process of C&D waste management, reduce the waste of resources and construction project costs. On the other hand, more discussion of top-level design and stakeholder behavior factors is

conductive to breaking the restriction on the circular economy and other management modes, changing the inherent thinking of stakeholders, so as to promote the green development of the construction industry and improve social benefits.

In addition, some constraints on bibliometrics methods have been found. (1) The data used in bibliometric analysis vary due to the different screening criteria of researchers. (2) Two types of visualization software may present different results. Therefore, this paper tries to use one kind of software to analyze a similar set of data. (3) The correlation between cited papers and citing papers may not be obvious in some clusters, and new technical methods should be adopted to minimize the occurrence of such problems.

Author Contributions: Conceptualization, L.W.; methodology, L.W.; validation, S.H., Y.L. (Yu Liu) and X.L.; data curation, S.H. and Y.L. (Yu Liu); writing—original draft preparation, L.W. and Y.L. (Yanhong Lv); writing—review and editing, S.H., Y.L. (Yu Liu) and X.L.; visualization, L.W. and Y.L. (Yanhong Lv); project administration, L.W. All authors have read and agreed to the published version of the manuscript.

Funding: This research was funded by 2022 Project of Development Research Center of Sichuan Old Revolutionary Base, Sichuan Provincial Key Research Base of Philosophy and Science, grant number SLQ2022SB-22.

Institutional Review Board Statement: Not applicable.

Informed Consent Statement: Not applicable.

Data Availability Statement: All relevant data generated and analyzed during this research were collected from the WoS database and are accessible with the help of the search query mentioned in the Methods section.

Conflicts of Interest: The authors declare no conflict of interest.

References

1. Pacheco-Torgal, F.; Jalali, S. Earth construction: Lessons from the past for future eco-efficient construction. *Constr. Build. Mater.* **2012**, *29*, 512–519. [[CrossRef](#)]
2. Vieira, C.S.; Pereira, P.M. Use of recycled construction and demolition materials in geotechnical applications: A review. *Resour. Conserv. Recycl.* **2015**, *103*, 192–204. [[CrossRef](#)]
3. Wu, Z.Z.; Yu, A.T.W.; Shen, L.Y.; Liu, G.W. Quantifying construction and demolition waste: An analytical review. *Waste Manag.* **2014**, *34*, 1683–1692. [[CrossRef](#)]
4. Wu, H.Y.; Duan, H.B.; Zheng, L.N.; Wang, J.Y.; Niu, Y.N.; Zhang, G.M. Demolition waste generation and recycling potentials in a rapidly developing flagship megacity of South China: Prospective scenarios and implications. *Constr. Build. Mater.* **2016**, *113*, 1007–1016. [[CrossRef](#)]
5. Rao, A.; Jha, K.N.; Misra, S. Use of aggregates from recycled construction and demolition waste in concrete. *Resour. Conserv. Recycl.* **2007**, *50*, 71–81. [[CrossRef](#)]
6. Siddique, R.; Khatib, J.; Kaur, I. Use of recycled plastic in concrete: A review. *Waste Manag.* **2008**, *28*, 1835–1852. [[CrossRef](#)]
7. Behera, M.; Bhattacharyya, S.K.; Minocha, A.K.; Deoliya, R.; Maiti, S. Recycled aggregate from C&D waste & its use in concrete—A breakthrough towards sustainability in construction sector: A review. *Constr. Build. Mater.* **2014**, *68*, 501–516.
8. Islam, R.; Nazifa, T.H.; Yuniarto, A.; Uddin, A.S.M.S.; Salmiati, S.; Shahid, S. An empirical study of construction and demolition waste generation and implication of recycling. *Waste Manag.* **2019**, *95*, 10–21. [[CrossRef](#)]
9. Esin, T.; Cosgun, N. A study conducted to reduce construction waste generation in Turkey. *Build. Environ.* **2007**, *42*, 1667–1674. [[CrossRef](#)]
10. Jaillon, L.; Poon, C.S.; Chiang, Y.H. Quantifying the waste reduction potential of using prefabrication in building construction in Hong Kong. *Waste Manag.* **2009**, *29*, 309–320. [[CrossRef](#)]
11. Ortiz, O.; Pasqualino, J.C.; Castells, F. Environmental performance of construction waste: Comparing three scenarios from a case study in Catalonia, Spain. *Waste Manag.* **2010**, *30*, 646–654. [[CrossRef](#)] [[PubMed](#)]
12. Yu, D.; Duan, H.; Song, Q.; Li, X.; Zhang, H.; Zhang, H.; Liu, Y.; Shen, W.; Wang, J. Characterizing the environmental impact of metals in construction and demolition waste. *Environ. Sci. Pollut. Res.* **2018**, *25*, 13823–13832. [[CrossRef](#)]
13. Chen, K.; Wang, J.; Yu, B.; Wu, H.; Zhang, J. Critical evaluation of construction and demolition waste and associated environmental impacts: A scientometric analysis. *J. Clean. Prod.* **2021**, *287*, 125071. [[CrossRef](#)]
14. Kucukvar, M.; Egilmez, G.; Tatari, O. Evaluating environmental impacts of alternative construction waste management approaches using supply-chain-linked life-cycle analysis. *Waste Manag. Res.* **2014**, *32*, 500–508. [[CrossRef](#)]

15. Marrero, M.; Puerto, M.; Rivero-Camacho, C.; Freire-Guerrero, A.; Solis-Guzman, J. Assessing the economic impact and ecological footprint of construction and demolition waste during the urbanization of rural land. *Resour. Conserv. Recycl.* **2017**, *117*, 160–174. [[CrossRef](#)]
16. Duan, H.; Miller, T.R.; Liu, G.; Tam, V.W.Y. Construction debris becomes growing concern of growing cities. *Waste Manag.* **2019**, *83*, 1–5. [[CrossRef](#)] [[PubMed](#)]
17. Wang, J.; Wu, H.; Duan, H.; Zillante, G.; Zuo, J.; Yuan, H. Combining life cycle assessment and Building Information Modelling to account for carbon emission of building demolition waste: A case study. *J. Clean. Prod.* **2018**, *172*, 3154–3166. [[CrossRef](#)]
18. Zhang, C.; Hu, M.; Dong, L.; Xiang, P.; Zhang, Q.; Wu, J.; Li, B.; Shi, S. Co-benefits of urban concrete recycling on the mitigation of greenhouse gas emissions and land use change: A case in Chongqing metropolis, China. *J. Clean. Prod.* **2018**, *201*, 481–498. [[CrossRef](#)]
19. Xu, J.; Shi, Y.; Xie, Y.; Zhao, S. A BIM-Based construction and demolition waste information management system for greenhouse gas quantification and reduction. *J. Clean. Prod.* **2019**, *229*, 308–324. [[CrossRef](#)]
20. Xiao, J.; Wang, C.; Ding, T.; Akbarnezhad, A. A recycled aggregate concrete high-rise building: Structural performance and embodied carbon footprint. *J. Clean. Prod.* **2018**, *199*, 868–881. [[CrossRef](#)]
21. Jimenez, L.F.; Dominguez, J.A.; Enrique Vega-Azamar, R. Carbon Footprint of Recycled Aggregate Concrete. *Adv. Civ. Eng.* **2018**, *2018*, 7949741. [[CrossRef](#)]
22. Li, J.; Zuo, J.; Cai, H.; Zillante, G. Construction waste reduction behavior of contractor employees: An extended theory of planned behavior model approach. *J. Clean. Prod.* **2018**, *172*, 1399–1408. [[CrossRef](#)]
23. Shen, H.; Peng, Y.; Guo, C. Analysis of the Evolution Game of Construction and Demolition Waste Recycling Behavior Based on Prospect Theory under Environmental Regulation. *Int. J. Environ. Res. Public Health* **2018**, *15*, 1518. [[CrossRef](#)] [[PubMed](#)]
24. Lu, W.; Tam, V.W.Y. Construction waste management policies and their effectiveness in Hong Kong: A longitudinal review. *Renew. Sust. Energ. Rev.* **2013**, *23*, 214–223. [[CrossRef](#)]
25. Ajayi, S.O.; Oyedele, L.O. Policy imperatives for diverting construction waste from landfill: Experts’ recommendations for UK policy expansion. *J. Clean. Prod.* **2017**, *147*, 57–65. [[CrossRef](#)]
26. Li, J.; Yao, Y.; Zuo, J.; Li, J. Key policies to the development of construction and demolition waste recycling industry in China. *Waste Manag.* **2020**, *108*, 137–143. [[CrossRef](#)]
27. Li, J.; Tam, V.W.Y.; Zuo, J.; Zhu, J. Designers’ attitude and behaviour towards construction waste minimization by design: A study in Shenzhen, China. *Resour. Conserv. Recycl.* **2015**, *105*, 29–35. [[CrossRef](#)]
28. Udawatta, N.; Zuo, J.; Chiveralls, K.; Zillante, G. Improving waste management in construction projects: An Australian study. *Resour. Conserv. Recycl.* **2015**, *101*, 73–83. [[CrossRef](#)]
29. Lachimpadi, S.K.; Pereira, J.J.; Taha, M.R.; Mokhtar, M. Construction waste minimisation comparing conventional and precast construction (Mixed System and IBS) methods in high-rise buildings: A Malaysia case study. *Resour. Conserv. Recycl.* **2012**, *68*, 96–103. [[CrossRef](#)]
30. Yuan, H.; Chini, A.R.; Lu, Y.; Shen, L. A dynamic model for assessing the effects of management strategies on the reduction of construction and demolition waste. *Waste Manag.* **2012**, *32*, 521–531. [[CrossRef](#)]
31. Ding, Z.; Yi, G.; Tam, V.W.Y.; Huang, T. A system dynamics-based environmental performance simulation of construction waste reduction management in China. *Waste Manag.* **2016**, *51*, 130–141. [[CrossRef](#)]
32. Li, Y.; Li, M.; Sang, P. A bibliometric review of studies on construction and demolition waste management by using CiteSpace. *Energy Build.* **2022**, *258*, 111822. [[CrossRef](#)]
33. Alsheyab, M.A.T. Recycling of construction and demolition waste and its impact on climate change and sustainable development. *Int. J. Environ. Sci. Technol.* **2022**, *19*, 2129–2138. [[CrossRef](#)]
34. Mostert, C.; Sameer, H.; Glanz, D.; Bringezu, S. Climate and resource footprint assessment and visualization of recycled concrete for circular economy. *Resour. Conserv. Recycl.* **2021**, *174*, 105767. [[CrossRef](#)]
35. Won, J.; Cheng, J.C.P.; Lee, G. Quantification of construction waste prevented by BIM-based design validation: Case studies in South Korea. *Waste Manag.* **2016**, *49*, 170–180. [[CrossRef](#)] [[PubMed](#)]
36. Won, J.; Cheng, J.C.P. Identifying potential opportunities of building information modeling for construction and demolition waste management and minimization. *Autom. Constr.* **2017**, *79*, 3–18. [[CrossRef](#)]
37. Akinade, O.O.; Oyedele, L.O.; Ajayi, S.O.; Bilal, M.; Alaka, H.A.; Owolabi, H.A.; Arawomo, O.O. Designing out construction waste using BIM technology: Stakeholders’ expectations for industry deployment. *J. Clean. Prod.* **2018**, *180*, 375–385. [[CrossRef](#)]
38. Zhang, J.; Wang, J.; Dong, S.; Yu, X.; Han, B. A review of the current progress and application of 3D printed concrete. *Compos. Pt. A-Appl. Sci. Manuf.* **2019**, *125*, 105533. [[CrossRef](#)]
39. Lin, A.; Tan, Y.K.; Wang, C.-H.; Kua, H.W.; Taylor, H. Utilization of waste materials in a novel mortar-polymer laminar composite to be applied in construction 3D-printing. *Compos. Struct.* **2020**, *253*, 112764. [[CrossRef](#)]
40. Hossain, M.U.; Ng, S.T. Influence of waste materials on buildings’ life cycle environmental impacts: Adopting resource recovery principle. *Resour. Conserv. Recycl.* **2019**, *142*, 10–23. [[CrossRef](#)]
41. Wang, M.-H.; Ho, Y.-S.; Fu, H.-Z. Global performance and development on sustainable city based on natural science and social science research: A bibliometric analysis. *Sci. Total Environ.* **2019**, *666*, 1245–1254. [[CrossRef](#)]
42. Lehtiranta, L. Risk perceptions and approaches in multi-organizations: A research review 2000–2012. *Int. J. Proj. Manag.* **2014**, *32*, 640–653. [[CrossRef](#)]

43. Oraee, M.; Hosseini, M.R.; Papadonikolaki, E.; Palliyaguru, R.; Arashpour, M. Collaboration in BIM-based construction networks: A bibliometric-qualitative literature review. *Int. J. Proj. Manag.* **2017**, *35*, 1288–1301. [[CrossRef](#)]
44. Hood, W.W.; Wilson, C.S. The Literature of Bibliometrics, Scientometrics, and Informetrics. *Scientometrics* **2001**, *52*, 291–314. [[CrossRef](#)]
45. Chen, C.M. CiteSpace II: Detecting and visualizing emerging trends and transient patterns in scientific literature. *J. Am. Soc. Inf. Sci. Technol.* **2006**, *57*, 359–377. [[CrossRef](#)]
46. van Eck, N.J.; Waltman, L. Software survey: VOSviewer, a computer program for bibliometric mapping. *Scientometrics* **2010**, *84*, 523–538. [[CrossRef](#)] [[PubMed](#)]
47. Zheng, C.; Ning, Y.; Yuan, J.; Zhao, X.; Zhang, Y. Partnering research within the construction industry (1990–2018): A scientometric review. *Int. J. Technol. Manag.* **2020**, *82*, 97–131. [[CrossRef](#)]
48. Chellappa, V.; Srivastava, V.; Salve, U.R. A systematic review of construction workers' health and safety research in India. *J. Eng. Des. Technol.* **2021**, *19*, 1488–1504. [[CrossRef](#)]
49. Mongeon, P.; Paul-Hus, A. The journal coverage of Web of Science and Scopus: A comparative analysis. *Scientometrics* **2016**, *106*, 213–228. [[CrossRef](#)]
50. Zhao, X.; Zuo, J.; Wu, G.; Huang, C. A bibliometric review of green building research 2000–2016. *Archit. Sci. Rev.* **2019**, *62*, 74–88. [[CrossRef](#)]
51. Xu, J.; Lu, W.; Xue, F.; Chen, K.; Ye, M.; Wang, J.; Chen, X. Cross-boundary collaboration in waste management research: A network analysis. *Environ. Impact Assess. Rev.* **2018**, *73*, 128–141. [[CrossRef](#)]
52. Thomas, C.; Setien, J.; Polanco, J.A.; Alaejos, P.; Sdnchez de Juan, M. Durability of recycled aggregate concrete. *Constr. Build. Mater.* **2013**, *40*, 1054–1065. [[CrossRef](#)]
53. Silva, R.V.; de Brito, J.; Dhir, R.K. Properties and composition of recycled aggregates from construction and demolition waste suitable for concrete production. *Constr. Build. Mater.* **2014**, *65*, 201–217. [[CrossRef](#)]
54. Aslani, F.; Ma, G.; Wan, D.L.Y.; Muselin, G. Development of high-performance self-compacting concrete using waste recycled concrete aggregates and rubber granules. *J. Clean. Prod.* **2018**, *182*, 553–566. [[CrossRef](#)]
55. Hossain, M.U.; Poon, C.S.; Lo, I.M.C.; Cheng, J.C.P. Comparative environmental evaluation of aggregate production from recycled waste materials and virgin sources by LCA. *Resour. Conserv. Recycl.* **2016**, *109*, 67–77. [[CrossRef](#)]
56. Lu, W.; Chen, X.; Peng, Y.; Shen, L. Benchmarking construction waste management performance using big data. *Resour. Conserv. Recycl.* **2015**, *105*, 49–58. [[CrossRef](#)]
57. Purchase, C.K.; Al Zulayq, D.M.; O'Brien, B.T.; Kowalewski, M.J.; Berenjian, A.; Tarighaleslami, A.H.; Seifan, M. Circular Economy of Construction and Demolition Waste: A Literature Review on Lessons, Challenges, and Benefits. *Materials* **2022**, *15*, 76. [[CrossRef](#)]
58. Diaz-Lopez, C.; Bonoli, A.; Martin-Morales, M.; Zamorano, M. Analysis of the Scientific Evolution of the Circular Economy Applied to Construction and Demolition Waste. *Sustainability* **2021**, *13*, 9416. [[CrossRef](#)]
59. Norouzi, M.; Chafer, M.; Cabeza, L.F.; Jimenez, L.; Boer, D. Circular economy in the building and construction sector: A scientific evolution analysis. *J. Build. Eng.* **2021**, *44*, 102704. [[CrossRef](#)]
60. Assi, L.; Carter, K.; Deaver, E.; Anay, R.; Ziehl, P. Sustainable concrete: Building a greener future. *J. Clean. Prod.* **2018**, *198*, 1641–1651. [[CrossRef](#)]
61. Xie, J.; Chen, W.; Wang, J.; Fang, C.; Zhang, B.; Liu, F. Coupling effects of recycled aggregate and GGBS/metakaolin on physicochemical properties of geopolymer concrete. *Constr. Build. Mater.* **2019**, *226*, 345–359. [[CrossRef](#)]
62. Horvath, A. Construction materials and the environment. *Annu. Rev. Environ. Resour.* **2004**, *29*, 181–204. [[CrossRef](#)]
63. Ortiz, O.; Castells, F.; Sonnemann, G. Sustainability in the construction industry: A review of recent developments based on LCA. *Constr. Build. Mater.* **2009**, *23*, 28–39. [[CrossRef](#)]
64. Kazmi, S.M.S.; Munir, M.J.; Wu, Y.-F. Application of waste tire rubber and recycled aggregates in concrete products: A new compression casting approach. *Resour. Conserv. Recycl.* **2021**, *167*, 105353. [[CrossRef](#)]
65. Ghisellini, P.; Ripa, M.; Ulgiati, S. Exploring environmental and economic costs and benefits of a circular economy approach to the construction and demolition sector: A literature review. *J. Clean. Prod.* **2018**, *178*, 618–643. [[CrossRef](#)]
66. Rousseeuw, P.J. Silhouettes: A graphical aid to the interpretation and validation of cluster analysis. *J. Comput. Appl. Math.* **1987**, *20*, 53–65. [[CrossRef](#)]
67. Chen, H.; Yang, Y.; Yang, Y.; Jiang, W.; Zhou, J. A bibliometric investigation of life cycle assessment research in the web of science databases. *Int. J. Life Cycle Assess.* **2014**, *19*, 1674–1685. [[CrossRef](#)]
68. Kirchherr, J.; Reike, D.; Hekkert, M. Conceptualizing the circular economy: An analysis of 114 definitions. *Resour. Conserv. Recycl.* **2017**, *127*, 221–232. [[CrossRef](#)]
69. Geissdoerfer, M.; Savaget, P.; Bocken, N.M.P.; Hultink, E.J. The Circular Economy A new sustainability paradigm? *J. Clean. Prod.* **2017**, *143*, 757–768. [[CrossRef](#)]
70. Mahpour, A. Prioritizing barriers to adopt circular economy in construction and demolition waste management. *Resour. Conserv. Recycl.* **2018**, *134*, 216–227. [[CrossRef](#)]
71. Yu, Y.; Junjan, V.; Yazan, D.M.; Iacob, M.-E. A systematic literature review on Circular Economy implementation in the construction industry: A policy-making perspective. *Resour. Conserv. Recycl.* **2022**, *183*, 106359. [[CrossRef](#)]

72. Rahla, K.M.; Mateus, R.; Braganca, L. Implementing Circular Economy Strategies in Buildings-From Theory to Practice. *Appl. Syst. Innov.* **2021**, *4*, 26. [[CrossRef](#)]
73. Wong, C.L.; Mo, K.H.; Yap, S.P.; Alengaram, U.J.; Ling, T.-C. Potential use of brick waste as alternate concrete-making materials: A review. *J. Clean. Prod.* **2018**, *195*, 226–239. [[CrossRef](#)]
74. Meng, Y.; Ling, T.-C.; Mo, K.H. Recycling of wastes for value-added applications in concrete blocks: An overview. *Resour. Conserv. Recycl.* **2018**, *138*, 298–312. [[CrossRef](#)]
75. Habert, G.; Miller, S.A.; John, V.M.; Provis, J.L.; Favier, A.; Horvath, A.; Scrivener, K.L. Environmental impacts and decarbonization strategies in the cement and concrete industries. *Nat. Rev. Earth Environ.* **2020**, *1*, 559–573. [[CrossRef](#)]
76. Ahmed, G.H.; Askandar, N.H.; Jumaa, G.B. A review of largescale 3DCP: Material characteristics, mix design, printing process, and reinforcement strategies. *Structures* **2022**, *43*, 508–532. [[CrossRef](#)]
77. Sahin, H.G.; Mardani-Aghabaglou, A. Assessment of materials, design parameters and some properties of 3D concrete a state-of-the-art review. *Constr. Build. Mater.* **2022**, *316*, 125865. [[CrossRef](#)]
78. Qian, H.; Hua, S.; Yue, H.; Feng, G.; Qian, L.; Jiang, W.; Zhang, L. Utilization of recycled construction powder in 3D concrete printable materials through particle packing optimization. *J. Build. Eng.* **2022**, *61*, 105236. [[CrossRef](#)]
79. Hong, J.; Shen, G.Q.; Li, Z.; Zhang, B.; Zhang, W. Barriers to promoting prefabricated construction in China: A cost-benefit analysis. *J. Clean. Prod.* **2018**, *172*, 649–660. [[CrossRef](#)]
80. Teng, Y.; Li, K.; Pan, W.; Ng, T. Reducing building life cycle carbon emissions through prefabrication: Evidence from and gaps in empirical studies. *Build. Environ.* **2018**, *132*, 125–136. [[CrossRef](#)]
81. Hao, J.L.; Cheng, B.; Lu, W.; Xu, J.; Wang, J.; Bu, W.; Guo, Z. Carbon emission reduction in prefabrication construction during materialization stage: A BIM-based life-cycle assessment approach. *Sci. Total Environ.* **2020**, *723*, 137870. [[CrossRef](#)]
82. Lopez-Guerrero, R.E.; Vera, S.; Carpio, M. A quantitative and qualitative evaluation of the sustainability of industrialised building systems: A bibliographic review and analysis of case studies. *Renew. Sust. Energ. Rev.* **2022**, *157*, 112034. [[CrossRef](#)]
83. Yuan, M.; Li, Z.; Li, X.; Li, L.; Zhang, S.; Luo, X. How to promote the sustainable development of prefabricated residential buildings in China: A tripartite evolutionary game analysis. *J. Clean. Prod.* **2022**, *349*, 131423. [[CrossRef](#)]
84. Zhang, R.; Xu, Y. The Air Quality Impact Evaluation of Modular Construction Practices in Hong Kong and Singapore. *Sustainability* **2022**, *14*, 1016. [[CrossRef](#)]

Disclaimer/Publisher’s Note: The statements, opinions and data contained in all publications are solely those of the individual author(s) and contributor(s) and not of MDPI and/or the editor(s). MDPI and/or the editor(s) disclaim responsibility for any injury to people or property resulting from any ideas, methods, instructions or products referred to in the content.

Article

A New Hybrid Monitoring Model for Displacement of the Concrete Dam

Chongshi Gu ^{1,*}, Xinran Cui ¹, Hao Gu ¹ and Meng Yang ^{2,3,*}¹ College of Water Conservancy and Hydropower Engineering, Hohai University, Nanjing 210098, China² Nanjing Hydraulic Research Institute, Nanjing 210029, China³ Research Center on Levee Safety and Disaster Prevention of Ministry of Water Resources, Zhengzhou 450003, China

* Correspondence: csgu@hhu.edu.cn (C.G.); ymym_059@126.com (M.Y.)

Abstract: For the structural health diagnostic of concrete dams, the mathematical monitoring model based on the measured deformation values is of great significance. The main purpose of this paper is to reconstruct the ageing component and the temperature component in the traditional Hydraulic-Seasonal-Time (HST) hybrid model by combining the measured values. On the one hand, a better mathematical model for the ageing displacement of concrete dams is proposed combined with the Burgers model to separate the instantaneous elastic hydraulic deformation and the hysteretic hydraulic deformation, and then it subsumes the latter into the ageing deformation to describe its reversible component. According to the Burgers model, the inverted elastic modulus of the Jinping-I concrete dam is 46.5 GPa, which is closer to the true value compared with the HST model. On the other hand, the kernel principal component analysis (KPCA) method is used to extract the principal components of the dam thermometers for replacing the period harmonic thermal factor. A multiple linear regression (MLR) model is established to fit the measured displacement of the concrete arch dam and to verify the accuracy of the proposed hybrid model. The results show that the proposed model reaches higher accuracy than the traditional HST hybrid model and is helpful to improve the interpretation of the separated displacement components of the concrete dams.

Keywords: ageing component; temperature component; HST model; concrete dam

Citation: Gu, C.; Cui, X.; Gu, H.; Yang, M. A New Hybrid Monitoring Model for Displacement of the Concrete Dam. *Sustainability* **2023**, *15*, 9609. <https://doi.org/10.3390/su15129609>

Academic Editor: José Ignacio Alvarez

Received: 15 December 2022

Revised: 9 January 2023

Accepted: 27 March 2023

Published: 15 June 2023



Copyright: © 2023 by the authors. Licensee MDPI, Basel, Switzerland. This article is an open access article distributed under the terms and conditions of the Creative Commons Attribution (CC BY) license (<https://creativecommons.org/licenses/by/4.0/>).

1. Introduction

Since the increasing requirement and utilization of water resources in China, a large amount of concrete dams have been constructed and contributed significantly to economic development [1,2]. The safety issues and the risks of dam failure are always unavoidable due to uncertainties in geology, hydrology, design, construction, and operational management. The dam failure, which resulted in major casualties, is a tragic lesson worldwide. Hence, dam safety has always been a high priority for governments and relevant authorities and has played an important role in preventing dam failures.

Displacement, stress, strain, and cracks [3–9] et al. are essential for dam health monitoring and operational instruction. As the most intuitive reflection of the integrity of concrete dams, displacement is frequently adopted for predicting the behaviour of the dam. Among the models that were used to fit and predict dam displacements, there are two main categories. The first one is based on deterministic functions, physical extrapolation methods, and multiple linear regression. For instance, statistical, deterministic, and hybrid models are the commonly used monitoring models in engineering. Chen et al. [10] adopted a semi-parametric statistical model, which has more imitative effect and explanatory than the parametric statistical model. Shang [11] analysed the key dam section of the roller compacted concrete (RCC) gravity dam with statistical modeling methods. Hu et al. [12] proposed a statistical hydrostatic-thermal-crack-time model to deal with the influential horizontal cracks in concrete arch dams. Another type is based on machine learning models.

Kang et al. [13] presented a dam health monitoring model based on kernel extreme learning machines. Chen et al. [14] combined the advantages of extreme learning machines and elastic networks for predicting dam deformation. Su et al. [15] used rough set theory and a support vector machine to build the early-warning models of dam safety. The monitoring models based on machine learning techniques; however, do not take the structural characteristics of the concrete dams into account. Furthermore, they lack direct mathematical expressions, causing them to only be useful for making predictions rather than providing a causal interpretation of dam deformation, such as statistical models [16].

The causes of ageing components in dams are complex, including cracking [17], alkali-aggregate reactions (AAR) [18], dissolution [19], etc. It can also be interpreted by the compression deformation of the rock foundation structure, as well as self-generated volume deformation and irreversible displacement due to cracks in the dam. Therefore, the ageing displacement is relatively difficult to give the mathematical expression directly according to the actual situation. Among a variety of HST-based models, the ageing component is expressed as the exponential function or the combination of the linear and logarithmic functions. However, the formation mechanism of the ageing displacement of the concrete dam caused by the theological properties of the dam material is extremely complicated. Therefore, the HST model based on a simple exponential function or a logarithmic function may not appropriately represent the relationships between the influencing factors and the dam displacement. The development law of the ageing component is studied and expressed as some function of time, which can then be separated in some way based on the relationship between the ageing displacement and the dam load to optimize the traditional HST model. For instance, Li et al. presented a hydrostatic-seasonal-state (HSS) model for rationally obtaining and accurately interpreting ageing displacement from total displacement monitoring data [20]. Hu and Wu [12] presented a statistical hydrostatic-thermal-crack-time model and applied it to assess the impact of the large-scale horizontal crack on the Chencun dam's downstream face. To explain the abnormal displacement behaviour of the Jinping-I arch dam, Wang et al. [21] introduced a hysteretic hydraulic component into the HST model, transforming the traditional HST model into an improved HHST model. The ageing component reflects a combination of reversible and irreversible deformation of the dam body and rock foundation. According to the changing pattern of the displacement and the periodic regulation of the reservoir water level for the concrete dams, Gu and Wu [22] concluded that a combination of the exponential and periodic harmonic functions, which are used for the irreversible and reversible ageing displacements [23], should be used to represent the ageing displacement according to the periodic regulation of the reservoir water level for most dams.

The temperature displacement component is the displacement due to temperature changes in the dam body and rock foundation of the dam; thermometer measurements of the dam body and rock foundation of the dam should be selected as a factor. The traditional hybrid model expressed the temperature component in the statistical mode and then was optimally fitted to the measured values. In recent years, the thermal components have been extracted or considered in dam displacement prediction by various methods [24]. Mata et al. conducted the Short Time Fourier Transform analysis of the residuals to determine the impact of the daily air temperature variation on the displacement of concrete dams [25]. Kang et al. considered that the temperature varies over time and substituted harmonic sinusoidal functions to the long-term air temperature for thermal effect simulation [26]. Chen et al. [27] adopted kernel principle component analysis (KPCA) to extract the temperature variables. Among a significant number of the thermometers buried in the dam sections, principal component extraction is an important process. Additionally, the KPCA method used in the paper (20) validates that it assists to reduce the dimensionality of the thermal measurement results by minimizing the loss of the original information.

The main idea of this paper is to propose a new hybrid model. For the extraction of the ageing component, a better mathematical model for the ageing displacement of concrete dams is proposed. For the temperature component, the KPCA method is used to extract

the inherent characteristics of the thermometer measurement data to substitute the periodic harmonic factors. Then, a multiple linear regression (MLR) model is developed to fit the measured displacement to validate the reasonableness of the extracted ageing component and temperature component. In this paper, the MLR model is established based on Matlab. The accuracy of the new hybrid model and the extracted components are compared with the components in the HST model. The displacement components of the concrete dam can be more easily understood with the help of the suggested model.

The research significance is for dam safety based on the monitoring model of displacement messages, which can fully reflect the recoverable creep component of the concrete and rock and accurately separate the ageing component from the total displacement.

2. Model Establishment

The factors influencing dam displacement can be broadly summarized as water level, temperature, and time. The traditional HST hybrid model can be generally interpreted as the following equation:

$$\delta = \delta_H + \delta_T + \delta_\theta = X\delta'_H + \sum_{i=1}^2 \left[b_{1i} \sin \frac{2\pi it}{365} + b_{2i} \cos \frac{2\pi it}{365} \right] + c_1\theta + c_2 \ln \theta, \quad (1)$$

where δ_H , δ_T , and δ_θ represent the hydraulic displacement component, temperature displacement component, and ageing displacement component, respectively; δ'_H is the FEM-calculated hydraulic component; X is the adjustment coefficient; H is the water depth of the upstream reservoir on the same monitoring day; t is the number of cumulative days since the initial monitoring day; θ is equal to $t/100$.

2.1. FEM-Calculated Elastic Hydraulic Component

In the traditional HST hybrid model, the ageing component only contains the irreversible component. The reversible ageing displacement follows the same evolution rule as the instantaneous hydraulic displacement due to the common causal factor of reservoir water pressure, these two types of displacements are separated into the hydraulic component in the paper [28]. In contrast to the instantaneous elastic modulus determined by the material properties, the inverted elastic modulus of dam body concrete provides a thorough reflection of the immediate and hysteretic elastic deformation ability through the analysis of the traditional HST hybrid model [3]. According to the theoretical derivation above, the hysteretic water pressure component is subsumed into the ageing component in this paper; therefore, only the elastic water pressure component needs to be calculated by the finite element method [29] as follows:

$$\delta_{He} = X\delta'_{He}, \quad (2)$$

$$E_0 = \frac{E'_0}{X}, \quad (3)$$

where δ_{He} is the actual water pressure component. δ'_{He} is the water pressure component value obtained from the elastic finite element calculation; X is the total water pressure component adjustment factor, and E_0 is the initial value of the instantaneous elastic modulus used in the calculation.

In the conventional elastic inversion method, the resulting modulus of elasticity of the dam concrete is a composite reflection of the instantaneous elastic deformation and viscoelastic hysteresis deformation. Therefore, a combined model of mechanical elements is required to separate the instantaneous elastic modulus and viscoelastic modulus when calculating the elastic hydrodynamic component. The Burgers model is a four-parameter fluid model that is commonly used to describe viscoelastic behaviour. It is a hybrid of the Maxwell and Kelvin–Voigt models. The Maxwell model is used to describe stress relaxation, but only in the case of irreversible flow. Although the Kelvin–Voigt model can represent creep, it cannot represent instantaneous deformation. It is not able to account for the stress

relaxation [28]. After the combination of these two models, the Burgers model can express both relaxation and creep effects after combining these two models [30]. Many researchers have used it extensively in recent years to describe the dynamic behaviour of viscoelastic materials [31,32]. Thus, it is used in this paper to calculate the instantaneous and hysteretic hydraulic displacements by the FEM and in the inversion analysis.

2.2. Mathematical Expression of the Ageing Displacement of the Concrete Dam Considering Viscoelastic Deformation

Dam structural properties primarily consist of three states: elasticity, viscoelasticity, and unstable failure [33]. The dam monitoring displacement consists of two components: an elastic component and a nonlinear component that fluctuates with load and time (commonly known as the time effect). The elastic displacement is influenced and calculated by the instantaneous elastic modulus. The actual ageing displacement is a process of increasing and decreasing around a certain base value, including irrecoverable and recoverable terms [34]. The factors that generally affect the ageing displacement include the material properties of the dam concrete, such as autogenous volume displacement, wet and dry displacement, plastic displacement, creep of concrete, the material properties of the dam base rock, and the creep of the dam structure. Creep deformation reflects an inherent property of the dam concrete and the rock. It consists of an irreversible viscoplastic component and a reversible viscoelastic (also known as hysteretic elastic) component. During a long period of creep displacement, the reversible viscoelastic component accounts for a significant portion of the total elastic displacement [35], which is influenced by the delayed elastic modulus separated by the Burgers model shown in Figure 1. On a macroscopic scale, the displacement is characterised by a high degree of variation at the beginning of the storage period, followed by a gradual stabilisation over time. However, laboratory tests on concrete and rock have shown that a portion of the creep displacement of concrete and rock recovers after the unloading lag. Part of the recovery is influenced by the size of the unloading lag, as well as the age of the concrete, as shown in Figure 2.

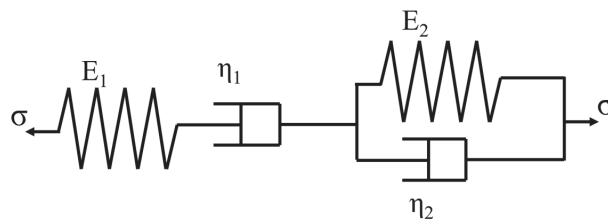


Figure 1. The Burgers model for dam concrete.

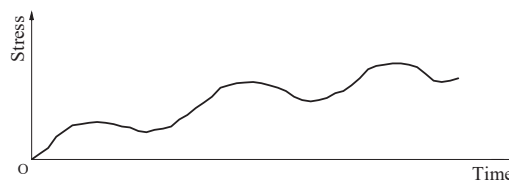


Figure 2. The radial displacement and the reservoir water level of the NO.9 dam section.

In the case of intermittent loading, the creep is a combination of increasing and decreasing curves. Because the water level in a reservoir is constantly changing, its effect on the dam can be seen as intermittent loading. As the water level is lowered, the dam and rock body thus undergo some non-linear recovery of creep with time, which can be linked to the delayed elastic moduli of the dam concrete. Therefore, it would not be accurate enough to describe the ageing displacement simply as a monotonically increasing function. A new model needs to be investigated to make the fit more accurate. As mentioned above,

the ageing displacement is caused by the creep of the concrete and rock foundation and the plastic deformation caused by the compression of fractures and joints in the concrete and rock base. Their effects are discussed separately as follows.

2.2.1. Creeping Law of Concrete

The total strain $\varepsilon(t)$ of concrete at age τ_1 , under the action of the external force $\sigma(\tau_1)$ can be expressed by the following equation [36]:

$$\varepsilon(t) = \frac{\sigma(\tau_1)}{E(\tau_1)} + \sigma(\tau_1)C(t, \tau_1), \tag{4}$$

where $C(t, \tau_1)$ is the creep degree of the concrete; $E(\tau_1)$ is the modulus of elasticity of concrete at age τ_1 .

In general, dams are old enough when they are built to hold water. According to the theory of elastic creep, the creep at load changes conforms to the principle of superposition, i.e., [37]:

$$\varepsilon_c(t) = \sigma(\tau_1)C(t, \tau_1) + \sum \Delta\sigma_i C(t, \tau_i), \tag{5}$$

where $\Delta\sigma_i$ is the stress increment at the moment τ_i .

The variation pattern of Equation (5) can be seen in Figure 2, which shows the effect of load history on strain.

2.2.2. Derivation of the Equation for the Creep Displacement of a Dam on a Rigid Foundation

Assume that the modulus of elasticity of the foundation $E_r \rightarrow \infty$. The dam is built on a rigid foundation, and the water pressure can be approximated as proportional loading; according to the theory of creep mechanics, the total displacement u at the top of the dam can be expressed as [38]:

$$u = u^e f(t), \tag{6}$$

where u^e is the elastic displacement under external load.

$f(t)$ can be expressed as follows [39]:

$$f(t) = 1 + E(t) \int_{\tau_1}^t \varphi(t, \tau) \xi(t, \tau, \tau_1) d\tau. \tag{7}$$

For a dam, its physical force is a constant and can be taken as $\varphi(t, \tau) = 1$. So, the above equation becomes

$$f(t) = 1 + E(t) \int_{\tau_1}^t \xi(t, \tau, \tau_1) d\tau. \tag{8}$$

After deducting the elastic displacement from Equation (6), we can obtain

$$\delta_\theta = u - u^e = u^e [f(t) - 1]. \tag{9}$$

Substitute Equation (8) into Equation (9) and give

$$\delta_\theta = u^e E(t) \int_{\tau_1}^t \xi(t, \tau, \tau_1) d\tau. \tag{10}$$

$\xi(t, \tau, \tau_1)$ in Equation (10) is the kernel of integration and using the conclusions of elastic creep theory, can be expressed as [40]:

$$\xi(t, \tau, \tau_1) = \sum_{i=1}^m C_i r_i e^{-r_i(t-\tau_1)} + \sum_{j=m+1}^p C_j r_j e^{-r_j(t-\tau_1)}. \tag{11}$$

Substitute $\zeta(t, \tau, \tau_1)$ into Equation (10) and give

$$\delta_\theta = u^e E(t) \sum_{i=1}^p C_j [1 - e^{-r_i(\tau_1-t)}]. \tag{12}$$

When taking $p = 1$, it can be expressed as

$$\delta_\theta = u^e E(t) C_1 [1 - e^{-r_1(\tau_1-t)}]. \tag{13}$$

It should be noted that in Equation (13), δ_θ is the creep displacement at time t when the water level is H (the water level at the age of the dam concrete at τ_1). In fact, the water level in the reservoir is constantly changing from time τ_1 to time t . Therefore, considering the water level change, the displacement expression at the moment t is

$$\delta_{\theta 1} = u^e E(t) C_1 [1 - e^{r_1(\tau_1-t)}] + E(t) \int_{\tau_1}^t [u^e(H, t) - u^e(H, \tau)] \cdot C_2 [1 - e^{r_2(\tau-t)}] d\tau, \tag{14}$$

where $u^e(H, t)$ and $u^e(H, \tau)$ are the elastic displacements of the dam crest due to the reservoir water pressure at moments t and τ .

The age of the dam concrete is generally large due to reservoir storage. Therefore, it can be assumed that $E(t)$ is a constant. Thus, $u^e, E(t)$, and C_1 are combined as C'_1 and $E(t)$ and C_2 are combined as C'_2 . τ_1 is the age of the concrete at the start of the monitored displacement. Therefore, $\tau - t$ can be replaced by $-t'$. t' indicates that the first day of the period starts at zero. In this way, Equation (14) can be rewritten as [38]

$$\delta_{\theta 1} = C'_1 [1 - e^{-r_1 t'}] + C'_2 \int_{\tau_1}^t [u^e(H, t) - u^e(H, \tau)] [1 - e^{r_2(\tau-t)}] d\tau. \tag{15}$$

2.2.3. Creep Displacement of Intact Rock Masses under External Loading

According to the Poynting–Thomso rheological model, the intrinsic structure of the rock is related to

$$\frac{d\sigma}{dt} + \frac{E_1\sigma}{\eta_1} = (E_1 + E_2) \frac{d\varepsilon}{dt} + \frac{E_1 E_2}{\eta_1} \varepsilon. \tag{16}$$

When $\sigma = \sigma_0 = \text{const}$ and $\varepsilon|_{t=0} = \frac{\sigma_0}{E_1 + E_2}$. The solution to the above equation is

$$\varepsilon = \frac{\sigma}{E_2} + \sigma \left(\frac{1}{E_1 + E_2} - \frac{1}{E_2} \right) e^{-\frac{E_1 E_2}{E_1 + E_2} \cdot \frac{t}{\eta_1}}. \tag{17}$$

The first term on the right-hand side of the above equation represents the instantaneous deformation and the second term is the creeping deformation. Therefore, the above equation can be rewritten as

$$\varepsilon = \frac{\sigma}{E_0} + \frac{\sigma}{E'} (1 - e^{-\frac{E'}{\eta} t}), \tag{18}$$

where E_0 is the instantaneous elastic modulus; E' is the delayed elastic modulus; η is the corresponding viscosity coefficients.

From the above equation, the creep deformation can be expressed as follows:

$$\varepsilon_p(t) = \frac{\sigma}{E'} (1 - e^{-\frac{E'}{\eta} t}). \tag{19}$$

The above equation indicates that when the stress is constant, the creep deformation varies with time as an exponential function, and after considering the integrated constants, the above equation is rewritten as

$$\varepsilon_p(t) = C_3(1 - e^{-r_3t}). \quad (20)$$

However, the water level in the reservoir is constantly changing and there is a certain amount of creep recovery in the rock mass as it is unloaded. Therefore, the total expression for the deformation of the foundation in the case of variable water level is

$$\varepsilon_p(t) = C_3(1 - e^{-r_3t}) + C_4 \int_{\tau_1}^t [G(H, t) - G(H, \tau)][1 - e^{r_3(\tau-t)}] d\tau, \quad (21)$$

where $G(H, \tau)$ is the effect of water level H on the function of creep deformation. It is generally difficult to obtain its expression, thus, it can be used instead of the water pressure displacement component.

2.2.4. The Effect of Fractures and Joints in a Rock Body under Water Pressure on the Ageing Displacement

Rock bodies where fissures and joints are present will gradually close under the weight of water, and weak inclusions will deform plastically. In general, this part of the deformation does not recover from unloading, it is a monotonically increasing function of time, and it is difficult to deduce physically an expression for this part of the deformation with time. However, based on its characteristics of rapid change in the early stages of water storage and gradual stabilisation, the solution of the first-order decay differential equation can be used to describe the whole process of this change.

Let C_5 be the final stable value of the displacement, displacement $\delta_{\theta 3}$ with time t , and the rate of gradual decay and deformation residual $C_5 - \delta_{\theta 3}$ is proportional to

$$\frac{d\delta_{\theta 3}}{dt} = r_5(C_5 - \delta_{\theta 3}). \quad (22)$$

Its solution can be expressed as

$$\delta_{\theta 3} = C_5(1 - e^{-r_5t}). \quad (23)$$

Combining Equations Equations (14), (21) and (23), it can be seen that the ageing displacement of the dam under the action of water pressure can be expressed as

$$\delta_{\theta} = C(1 - e^{-rt}) + C' \int_{\tau_1}^t [u^e(H, t) - u^e(H, \tau)][1 - e^{r'(\tau-t)}] d\tau. \quad (24)$$

When the reservoir level varies with the seasons, the elastic displacement $u^e(H, t)$ of the dam caused by the cyclic load, the water pressure, also varies in an approximate annual cycle. As mentioned above, the hysteretic elastic hydraulic deformation caused by the viscoelastic creep feature is divided into the ageing component. Therefore, a set of basic functions ($\cos \frac{2\pi t}{365}, \sin \frac{2\pi t}{365}, \cos \frac{4\pi t}{365}, \sin \frac{4\pi t}{365}, \dots, \cos \frac{2\pi mt}{365}, \sin \frac{2\pi mt}{365}$) is taken and their linear combination is used to express the term of the product function in Equation (24).

The decay term $1 - e^{r'(\tau-t)}$ in Equation (24) does not affect the periodicity of the product function. Clearly,

$$u^e(H, t) \leftrightarrow \sum_{i=1}^m [A_i \sin \frac{2\pi it}{365} + B_i \cos \frac{2\pi it}{365}]. \quad (25)$$

After replacing the original integral equation with the right-hand end of Equation (25), the resulting function is still a periodic function based on the trigonometric system, i.e.,

$$\int_{\tau_1}^t \sum_{i=1}^m \left[A_i \sin \frac{2\pi it}{365} + B_i \cos \frac{2\pi it}{365} \right] dt = \sum_{i=1}^m \left[C_i \sin \frac{2\pi it}{365} + K_i \cos \frac{2\pi it}{365} \right], \quad (26)$$

where $C_i = \frac{365A_i}{2\pi i}$, $K_i = \frac{365B_i}{2\pi i}$.

The second term on the right side of the Equation (24) is replaced by a periodic function term that varies with time. At this point, the practical expression for the ageing displacement can be expressed as

$$\delta_{\theta}(t) = C(1 - e^{-rt}) + \sum_{i=1}^2 (C_i \sin \frac{2\pi it}{365} + K_i \cos \frac{2\pi it}{365}). \quad (27)$$

Using Equation (27) in combination with the measured data of the ageing displacement, the multiple linear regression method can be used to estimate the coefficient C , r , C_i , and K_i .

The Equation (27) contains the creep recovery part of the water level component, which makes the inversion obtained in the process of calculating the water level component and the elastic modulus shall be the instantaneous elastic modulus. In the HST model, the modulus of elasticity of the dam concrete obtained by the elastic inversion method is a composite reflection of the instantaneous elastic deformation and the deformation after viscoelasticity. Therefore, the viscoelastic inversion method must be used to separate the instantaneous elastic modulus from the viscoelastic modulus.

2.3. Temperature Kernel Principal Components Analysis

As a result, the temperature component is assumed to follow an annual cycle and is formulated in a predefined periodic harmonic factor, which may not accurately represent the thermal displacement effect of concrete dams [41]. For dams with buried thermometers, kernel principal components analysis has the advantage of better performance when extracting the feature and reducing the dimensionality of the thermometer measurement data [42]. Based on the principal component analysis (PCA) method, the KPCA method maps the input space into a high-dimensional feature space through nonlinear mapping, which makes the PCA able to perform in Hilbert space. The nonlinear problem can then be solved in high-dimensional space. Consider a set of n thermometer measurement data $X = [x_1, x_2, \dots, x_n]$, and then standardize it as follows:

$$\tilde{x}_i = \frac{x_i - A_i}{S_i}, A_i = \frac{1}{n} \sum_{i=1}^n x_i, S_i = \sqrt{\frac{1}{n-1} \sum_{i=1}^n (x_i - A_i)^2}, \quad (28)$$

where A_i is the mean value of the thermometer measurement data, and S_i is the standard deviation of the thermometer measurement data.

After the standardization, use the mapping function $\phi(\cdot)$ to map x_i ($i = 1, 2, \dots, n$) to the high-dimensional feature space ψ ($\phi: \mathbb{R}^m \rightarrow \psi$). As a result, the dot set corresponding to the original thermometer measurement data can be written as $\Phi = \{\phi(x_i)\} (i = 1, 2, \dots, n)$. In the high-dimensional feature space, the initial input data of the thermometers satisfies the equation shown as follows:

$$\sum_{i=1}^n \phi(x_i) = 0. \quad (29)$$

Furthermore, the feature space covariance matrix C is computed as follows:

$$C = \frac{1}{n} \sum_{i=1}^n \phi(x_i)^T \phi(x_i) = \frac{1}{n} \Phi^T \Phi. \quad (30)$$

The characteristic equation of the covariance matrix can thus be expressed as follows:

$$\lambda \bar{\zeta}_i = \mathbf{C} \bar{\zeta}_i, \quad (31)$$

where λ denotes the eigenvalue of the covariance matrix \mathbf{C} ; $\bar{\zeta}_i$ is the eigenvector λ , corresponding to the eigenvalue.

The nonlinear mapping function $\phi(\cdot)$ is implicit, it is difficult to calculate the covariance matrix \mathbf{C} directly, so a kernel matrix \mathbf{K} is introduced. As shown below, the kernel matrix \mathbf{K} should meet the Mercer condition:

$$\mathbf{K} = \phi(x_i) \cdot \phi(x_i)^T. \quad (32)$$

The characteristic equation of the kernel matrix \mathbf{K} is expressed as follows:

$$\bar{\lambda}_i \alpha_i = \mathbf{K} \alpha_i, \quad (33)$$

where $\bar{\lambda}_i = n \lambda_i$ has the meaning of the eigenvalue of the kernel matrix \mathbf{K} .

To normalize the eigenvectors α_i , the following condition must be met [43]:

$$1 = \sum_{i=1}^n \alpha_i \alpha_i^k \mathbf{K} = \lambda_k (\alpha^k \cdot \alpha^k). \quad (34)$$

Following that, the covariance matrix \mathbf{C} and the kernel matrix \mathbf{K} are entered into the characteristic equation of the kernel matrix \mathbf{K} . In addition, the eigenvector $\bar{\zeta}_i$ of the covariance matrix \mathbf{C} can be introduced by the nonlinear function $\phi(x_i)$, which can be obtained as follows:

$$\bar{\zeta}_i = \sum_{i=1}^n \alpha_i^k \phi(x_i), \quad (35)$$

where α_i^k is the i -th coefficient associated with $\bar{\zeta}_i$.

The eigenvalues $\bar{\lambda}_i$ of the kernel matrix \mathbf{K} are ordered in descending order as follows:

$$\bar{\lambda}_1 \geq \bar{\lambda}_2 \geq \dots \geq \bar{\lambda}_s \geq \dots \geq \bar{\lambda}_n > 0. \quad (36)$$

The proportion of the information contained in the i th and the first k principal components in the total amount of the information (contribution rate l_i and cumulative contribution rate Q) of these eigenvalues are calculated in the following equations:

$$\left\{ \begin{array}{l} l_i = \frac{\bar{\lambda}_i}{\sum_{i=1}^n \bar{\lambda}_i} \\ Q = \frac{\sum_{i=1}^s \bar{\lambda}_i}{\sum_{i=1}^n \bar{\lambda}_i} \end{array} \right\}. \quad (37)$$

When the cumulative contribution rate Q of the cumulative s th eigenvalue exceeds 85%, the information corresponding to these eigenvalues is thought to be adequate to convey the information of the original input thermometer measurement data.

Finally, the kernel PCs $P_i(x)$ of the mapped input thermometer measurement data $\phi(x_i)$ in the feature space employed to the eigenvalue $\bar{\zeta}_i$ is the i th principal component, as presented in Equation (38):

$$P_i(x) = \bar{\zeta}_i \phi(x_i) = \sum_{i=1}^n \alpha_i^k \phi(x_i) \phi(x_i)^T = \sum_{i=1}^n \alpha_i^k \mathbf{K}. \quad (38)$$

The matrix $\mathbf{P} = \{P_1(x), P_2(x), \dots, P_s(x)\}$ is made up of the kernel PCs, which are the temperature principal component matrices obtained after reducing the dimensionality of the original input thermometer measurement data set. It retains enough information

from the original data. After the KPCA process, the redundant information in the original thermometer measurement data is removed, resulting in a robust temperature database for developing a data-driven model.

3. Mathematical Expression of the New Hybrid Model

The water pressure, temperature, and ageing components are used as independent variables to perform an MLR with the measured displacement components. As mentioned above, the elastic hydraulic component and the hysteretic hydraulic component are separated from the original hydraulic component in the HST model by the Burgers model. In this paper, the hysteretic hydraulic component was subsumed into the ageing component. As for the temperature component, it can be determined by the KPCA method through the thermometers embedded in the dam and the foundation. The mathematical expression of the new hybrid model can be expressed as follows:

$$\delta = \delta_{He} + \delta_T + \delta_\theta = X\delta_{He}^t + \sum_{i=1}^n b_i T_{PCi} + C(1 - e^{-rt}) + \sum_{j=1}^2 (C_j \sin \frac{2\pi jt}{365} + K_j \cos \frac{2\pi jt}{365}) \quad (39)$$

where X is the adjustment coefficient of the elastic hydraulic component and the FEM-calculated elastic hydraulic component; n is the total number of the principal components; T_{PCi} is the principal components extracted from the thermometers by the KPCA method; b_i , C , C_j , and K_j are all coefficients.

4. Case Study

Jinping-I super-high arch dam is the highest concrete arch dam in the world. The dam has a crest elevation of 1885.0 m and a maximum dam height of 305.0 m. Jinping Grade I Hydropower Station started to store water from the lower gate of the right bank diversion hole on 30 November 2012, to 1800 m on 18 July 2013, and to the normal water level of 1880 m on 24 August 2014. After August 2014, the reservoir level is in an annual cycle and can be divided into four main stages in the following order: (1) a rising period from mid-to-late June to mid-July and mid-September each year; (2) a stable period of high-water level at 1880 m, lasting for 97 to 167 d; (3) a falling period from late-December to early-April till early-June each year; (4) a stable period of low water level at 1800 m, lasting for half a month to two months. (4) 1800 m low water level stabilisation period, lasting from half a month to 2 months. Figure 3 depicts the displacement of the PL9-1 plumb-line monitoring point and the water reservoir changing trend from 1 October 2013 to 31 December 2018 for a continuous time period. According to the reservoir water level changes, the reservoir water level change process was divided into four stages. Figure 4 shows the water level segmentation interval during a year, and Figure 5 represents the simulation of the scenario of the Jinping-I super-high arch dam.

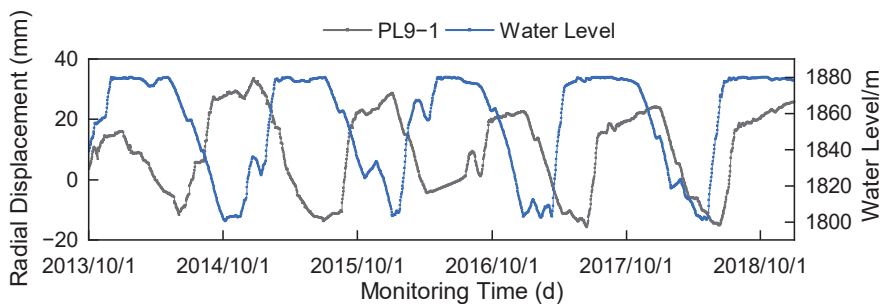


Figure 3. The radial displacement and the reservoir water level of the NO.9 dam section.

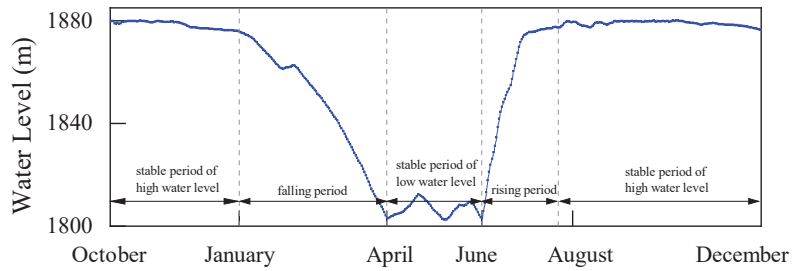


Figure 4. The water level segmentation interval diagram.



Figure 5. The simulation of the scenario and the of Jinping-I super-high arch dam.

5. Results and Accuracy of the Proposed Model

5.1. A Better Mathematical Model for the Ageing Displacement of Concrete Dams

To calculate the hydraulic displacement component by the FEM, a three-dimensional FEM model is established using ABAQUS, as shown in Figure 6. The instantaneous elastic modulus of the dam concrete is determined to be 38 GPa, which is an elastic inversion value conducted according to the measured dam displacement during the initial rising period of the upstream reservoir water level, rising from 1800.41 m to 1880 m [44]. The parameters of the foundation rocks are determined by their designed values. The instantaneous elastic modulus E_1 and delayed elastic modulus E_2 in the Burgers model are determined to be 46.5 GPa and 130.5 GPa. The corresponding viscosity coefficients are 376.2 GPa.d and 20,074.5 GPa.d, respectively. During the simulation period, there are a total of 32 incremental steps in the FEM simulation, with each step resulting in a 5 m change in water level. Figure 7 shows the relationship between the elastic FEM-calculated radial displacement and the upstream reservoir water depth for PL9-1.

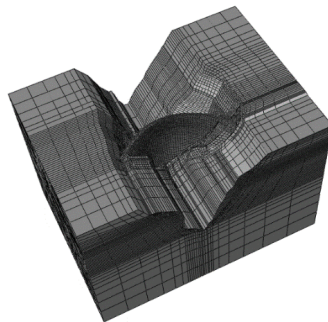


Figure 6. FEM model of the Jinping-I super-high arch dam.

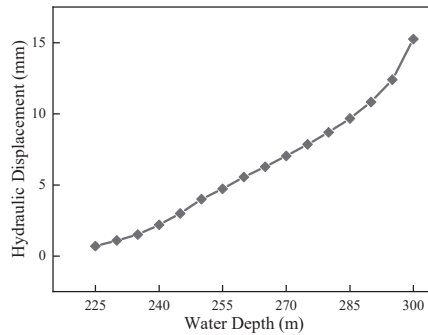


Figure 7. Relationship between the elastic FEM-calculated radial displacement and the upstream reservoir water depth for PL9-1.

5.2. Calculation of Temperature Displacement by KPCA Method

A large number of thermometers are embedded in the dam body. From the mechanical point of view, the thermometer measurement data of the concrete and rock foundation of the dam should be selected as the temperature factor. The principal component analysis (PCA) method was used in the previous studies [45,46] to analyse and separate the temperature measurement principal component. Its linear technique, on the other hand, has difficulty reducing large amounts of temperature variables to new uncorrelated variables while minimizing the loss of original information. In this paper, the principal components of thermometers are extracted by the KPCA method. As a result, the temperature components can be fitted more precisely. The advantages of using the measured temperatures of the concrete dam have been mentioned and testified by several articles [47–49]. In order to improve the KPCA's high performance on feature extraction and dimensionality reduction of input temperature dataset, the comparison process with PCA is necessarily proposed. The PCA method is based on the assumption that there was a linear hyperplane. The KPCA method is kernel-based, and the mapping performed by the KPCA method highly relies on the choice of the kernel function. Possible choices for the kernel function are the Linear kernel, Gaussian kernel, Polynomial kernel, Sigmoid kernel, and Laplacian kernel [50,51]. Table 1 shows the performance of the KPCA models based on different kernel functions. According to the results, the KPCA method with the Linear kernel, Polynomial kernel, and Sigmoid kernel achieves nearly the same accuracy rate and maximum contribution rate as the first kernel PC. In contrast, the Gaussian kernel and Laplacian kernel approach the low maximum contribution rate of the first kernel PC. As a result, the Polynomial kernel is chosen to replace the linear projection process. Figure 8 depicts the comparison of the two methods in the extraction result. It can conclude that after using the KPCA method with the polynomial kernel, two PCs are extracted. These two PCs can explain approximately 93.65% of the information in the original temperature dataset. They are considered to represent the thermal effect. The PC1, which has the maximum contribution proportion among all the principal components, explains 73.31% of the information in the original temperature dataset. In contrast, after using the PCA method, four PCs are extracted, and the PC1 explains only 46.87% of the information. As a result of using the KPCA method, a small number of principal components from the thermometers can be extracted and used for the temperature component as follows:

$$\delta_T = \sum_{i=1}^2 b_i T_{PCi}, \quad (40)$$

where T_{PCi} is the i th extracted temperature principal component; b_i is the coefficient of the principal component.

Table 1. The performance of the KPCA models based on different kernel functions.

| Kernel Type | Accuracy Rate (%) | Maximum Contribution Rate of the First Kernel PC PC ₁ (%) |
|-------------------|-------------------|--|
| Linear kernel | 97.04 | 82.00 |
| Polynomial kernel | 98.32 | 81.72 |
| Gaussian kernel | 95.85 | 50.84 |
| Polynomial kernel | 97.63 | 82.40 |
| Gaussian kernel | 94.67 | 51.65 |

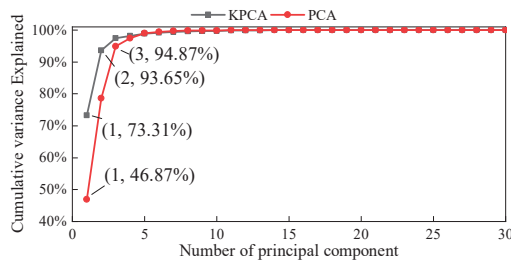


Figure 8. The comparison of the PCA method and the KPCA method in the extraction result.

5.3. Fitting and Predicting Accuracy of the Proposed Hybrid Model

To test the accuracy of the new hybrid model, the long monitoring data from 1 October 2013 to 31 December 2018 were divided into the training set, and the predicting set [52]. The first 1560 data in the dataset are used as the training set and the last 354 data are used as the predicting set. The coefficients of the Equation (39) are calculated and shown in Table 2. For the Jinping-I super high arch dam, the design and inversion values of the instantaneous elastic modulus of the dam concrete are 38.0 GPa and 38.5 GPa, respectively. As a result, the elastic hydraulic displacement calculated by FEM should be multiplied by the coefficient X of 0.98 (38.0/38.5).

Table 2. Coefficients of the new hybrid model for PL9-1.

| Coefficient | X | b ₁ | b ₂ | C | C ₁ | C ₂ | K ₁ | K ₂ |
|-------------|------|----------------|----------------|----------|----------------|----------------|----------------|----------------|
| Values | 0.98 | −0.8089 | −0.1356 | −17.1222 | −0.9430 | 0.7931 | 3.2374 | 0.6715 |

The model results are tested and compared using several estimation criteria, including the mean absolute error MAE, the mean squared error MSE and the determination coefficient R². The criteria mentioned above can be calculated as follows:

$$MAE = \frac{1}{N} \sum_{i=1}^N |\hat{y}_i - y_i|, \tag{41}$$

$$RMSE = \sqrt{\frac{1}{N} \sum_{i=1}^N [\hat{y}_i - y_i]^2}, \tag{42}$$

$$R^2 = \frac{\left[\sum_{i=1}^N (\hat{y}_i - \bar{\hat{y}})(y_i - \bar{y}) \right]^2}{\sum_{i=1}^N [\hat{y}_i - \bar{\hat{y}}]^2 \sum_{i=1}^N [y_i - \bar{y}]^2}, \tag{43}$$

where N is the number of observations; \hat{y} is the predicted displacement value of the model; y is the measured displacement of the concrete dam; $\bar{\hat{y}}$ and \bar{y} are the mean value of predicted and measured displacement, respectively. The estimation criteria MAE, MSE, and R² are displayed in Table 3, respectively for the HST model and the proposed hybrid model.

Table 3. The regression model performance comparison of the proposed model and the HST model.

| Model | Fitting | | | Predicting | | |
|----------------|---------|--------|----------------|------------|--------|----------------|
| | MAE | MSE | R ² | MAE | MSE | R ² |
| Proposed model | 1.6886 | 4.8333 | 0.9746 | 0.5062 | 0.3404 | 0.9902 |
| HST model | 1.7164 | 4.8737 | 0.9743 | 1.2798 | 2.2055 | 0.9898 |

As can be seen in Table 3, the two models realize the satisfactory performance that the correlation coefficients in the training set and predicting set are both higher than 0.95. The new hybrid model reaches deduced error and higher correlation coefficient than the HST model. It is reasonable to conclude that the model developed in this paper has both a clear physical meaning and a high fitting accuracy. As shown in Figure 9, the more significant error occurs when the measured value changes more violently, that is, when the water level changes more violently. However, the new hybrid model provides better stability in the fitting process compared to the HST model when the water level changes drastically.

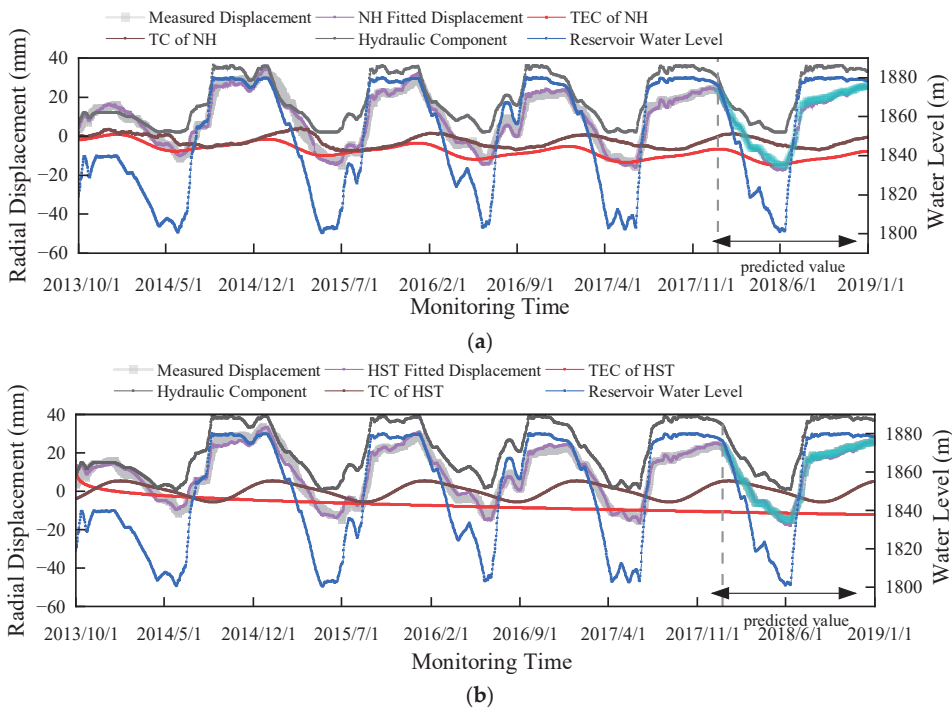


Figure 9. Fitted process lines for measurement point PL9-1 in the NO.9 dam section: (a): The new hybrid model; (b) The HST hybrid model. Abbreviation: NH: new hybrid model; HST: hydraulic-seasonal-time model; HC: hydraulic component; AC: ageing component; TC: temperature component.

The variation laws and values of the thermal displacement obtained by the new hybrid model and the HST model are displayed in Figure 10. The line temperature component (TC) of HST and the line TC of the new hybrid model (NH) are the ambient temperature of the dam and the internal temperature displacement of the dam, respectively, which both follow a periodic pattern. The internal temperature displacement of the dam has a slight lag relative to the ambient temperature displacement of the dam, in line with the law that the internal temperature of concrete has a phase difference relative to the ambient temperature. This phenomenon has the following possible explanations. The

external ambient temperature at any given moment affects the change of its temperature field by means of heat conduction inside the dam concrete, and it takes some time for this heat conduction process to be finally completed. At the same time, the continuous change of external temperature causes the internal heat exchange of the dam body, i.e., when the heat input to the dam body in the current period has not yet been transferred to the deep concrete, the heat input to the dam body in the latter period has already begun to affect the layers of concrete, and so is the next. The slow and continuous heat transfer inside the dam body inevitably leads to the superposition of the influence of the external ambient temperature on the internal temperature field of the dam body at different times, thus causing a lag in the internal temperature field of the dam body relative to the external temperature.

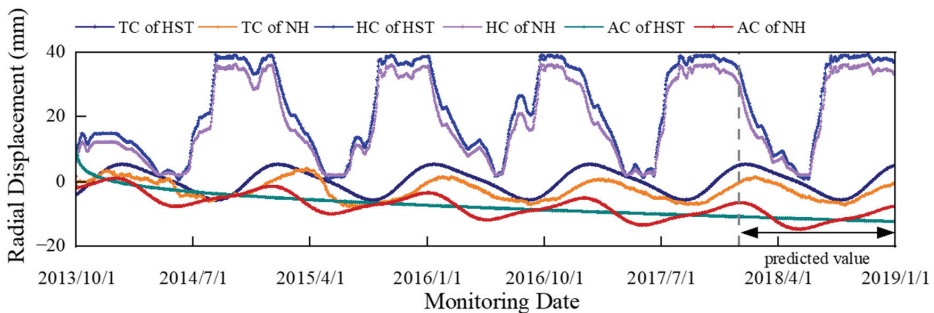


Figure 10. Radial displacement of hydraulic, thermal and ageing components separated by the HST hybrid model and the new hybrid model. Abbreviation: NH: new hybrid model; HST: hydraulic-seasonal-time model; HC: hydraulic component; AC: ageing component; TC: temperature component.

The ageing displacement separated by the model is a combination of increasing and decreasing curves, containing reversible ageing displacement that varies with the main load of the dam in addition to irreversible trend ageing displacement, and the change in ageing displacement slightly lags behind the change in reservoir level at this stage, in line with the hysteresis effect of viscoelastic deformation. In comparison, the ageing component is expressed as $c_1\theta + c_2\ln\theta$ in the HST model, which only contains irreversible deformations. The instantaneous and hysteretic elastic hydraulic deformations are owned to the hydraulic component, which will result in larger hydraulic displacement in the HST model, as can be seen in Figure 10. While the hydraulic displacement, which is determined by the evolution of reservoir water level, has an annual evolution law comparable to the reversible ageing displacement in the new hybrid model. Thus, the development trend of the ageing displacement can be better reflected in the new hybrid model. It contains both reversible and irreversible components.

6. Conclusions and Discussion

In this paper, we proposed a new hybrid model for a concrete dam in which the temperature displacement and the ageing displacement of the traditional hybrid model are improved, and the validity and interpretability of the model accuracy of this paper can be confirmed through example validation according to the smaller predicting MSE (0.3404) and larger R^2 (0.9902), whereas in the traditional HST hybrid model they are 2.2055 and 0.9898, respectively. The following conclusions are drawn:

- (1) The principal component factors are extracted using kernel principal component analysis in conjunction with measured thermometer information in the concrete dam body, which can better reflect the influence of temperature variations inside the concrete dam body on its displacement compared with the traditional HST hybrid model.
- (2) The Burgers model was used to determine the instantaneous elasticity modulus and viscoelastic modulus of the dam; thus the hysteretic hydraulic elastic displacement in

the original hybrid model can be subsumed into the ageing displacement component, while the period factor was added to the ageing displacement to fit this component. Thus, a better mathematical model for the ageing displacement of concrete dams was established. It can fully reflect the recoverable creep component of the concrete and rock and accurately separate the ageing component from the total displacement.

However, some problems also should be pointed out. Firstly, the effectiveness of the proposed model is only validated in the experimental conditions. It needs to be applied in the actual engineering programs to verify the practicability. Moreover, the time range of the ageing deformation selected in this paper is only from 2013 to 2018, but the ageing deformation of the dam, especially in the stability period, will last for a long time. The change of water level component, temperature component, and ageing component for a longer time need to be discussed.

Author Contributions: Conceptualization, M.Y. and C.G.; methodology, X.C.; software, H.G.; validation, M.Y., X.C., H.G. and C.G.; formal analysis, M.Y.; investigation, X.C.; resources, H.G.; data curation, C.G.; writing—original draft preparation, M.Y. and X.C.; writing—review and editing, M.Y., X.C., H.G. and C.G. All authors have read and agreed to the published version of the manuscript.

Funding: This work was supported by the China Postdoctoral Science Foundation (Grant No. 2022M721668, 2021M701044); Central Public-Interest Scientific Institution Basal Research Fund, NHRI (Y423006, Y423004); the National Natural Science Foundation of China (51739008, U2243223, 51739003, 51779086 and 52079046); Science and technology projects managed by the headquarter of State Grid Corporation (5108-202218280A-2-417-XG); the Fundamental Research Funds for the Central Universities of Hohai (Grant No. B230201011); the Open Fund of Research Center on Levee Safety Disaster Prevention of Ministry of Water Resources under Grant (LSDP202204); Water Conservancy Science and Technology Project of Jiangsu (Grant No. 2022024); the National Natural Science Foundation for Young Scientists of China (Grant No. 51909173); Open fund of the National Dam Safety Research Center (Grant No. CX2020B02); The Fundamental Research Funds for the Central Universities (B210202017); the Jiangsu young science and technological talents support project (TJ-2022-076); the Open Fund of National Dam Safety Research Center (CX2020B02) and the Anhui Natural Science Foundation grant number (Grant No. 2208085US17).

Institutional Review Board Statement: Not applicable.

Informed Consent Statement: Not applicable.

Data Availability Statement: The data presented in this study are available on request from the corresponding author. The data are not publicly available due to project confidentiality.

Conflicts of Interest: The authors declare that there are no conflict of interest.

References

1. Liu, Y.Z.; Li, J.T.; Chen, W.F.; Zhang, G.X.; Tan, Y.S. Optimization study on super-high arch dam temperature control standard and measure. In Proceedings of the 4th International Workshop on Renewable Energy and Development (IWRED), Sanya, China, 24–26 April 2020; *Electr Network*. Volume 510.
2. Zhang, C.; Ali, A.; Sun, L. Investigation on low-cost friction-based isolation systems for masonry building structures: Experimental and numerical studies. *Eng. Struct.* **2021**, *243*, 112645. [[CrossRef](#)]
3. Wang, S.; Xu, C.; Gu, C.; Su, H.; Wu, B. Hydraulic-seasonal-time-based state space model for displacement monitoring of high concrete dams. *Trans. Inst. Meas. Control.* **2021**, *43*, 3347–3359. [[CrossRef](#)]
4. Huang, H.; Li, M.; Yuan, Y.; Bai, H. Experimental Research on the Seismic Performance of Precast Concrete Frame with Replaceable Artificial Controllable Plastic Hinges. *J. Struct. Eng.* **2023**, *149*, 04022222. [[CrossRef](#)]
5. Zhang, Z.; Liang, G.; Niu, Q.; Wang, F.; Chen, J.; Zhao, B.; Ke, L. A Wiener degradation process with drift-based approach of determining target reliability index of concrete structures. *Qual. Reliab. Eng. Int.* **2022**, *38*, 3710–3725. [[CrossRef](#)]
6. Huang, H.; Li, M.; Yuan, Y.; Bai, H. Theoretical analysis on the lateral drift of precast concrete frame with replaceable artificial controllable plastic hinges. *J. Build. Eng.* **2022**, *62*, 105386. [[CrossRef](#)]
7. Gu, M.; Cai, X.; Fu, Q.; Li, H.; Wang, X.; Mao, B. Numerical Analysis of Passive Piles under Surcharge Load in Extensively Deep Soft Soil. *Buildings* **2022**, *12*, 1988. [[CrossRef](#)]
8. Deng, E.-F.; Zhang, Z.; Zhang, C.-X.; Tang, Y.; Wang, W.; Du, Z.-J.; Gao, J.-P. Experimental study on flexural behavior of UHPC wet joint in prefabricated multi-girder bridge. *Eng. Struct.* **2023**, *275*, 115314. [[CrossRef](#)]

9. Cheng, Y.; Fu, L.-Y. Nonlinear seismic inversion by physics-informed Caianiello convolutional neural networks for overpressure prediction of source rocks in the offshore Xihu depression, East China. *J. Pet. Sci. Eng.* **2022**, *215*, 110654. [\[CrossRef\]](#)
10. Chen, J.H.; Gu, C.S. Study on Semi-parametric Statistical Model of Safety Supervision of Concrete Dam. *Disaster Adv.* **2013**, *6*, 16–24.
11. Shang, C. Statistical analysis of deformation monitoring data of a RCC gravity dam. *J. Water Resour. Water Eng.* **2017**, *28*, 205–211.
12. Hu, J.; Wu, S. Statistical modeling for deformation analysis of concrete arch dams with influential horizontal cracks. *Struct. Health Monit.* **2019**, *18*, 546–562. [\[CrossRef\]](#)
13. Kang, F.; Liu, X.; Li, J. Temperature effect modeling in structural health monitoring of concrete dams using kernel extreme learning machines. *Struct. Health Monit.* **2020**, *19*, 987–1002. [\[CrossRef\]](#)
14. Chen, Y.; Xiao, G.; Hu, M.; Huang, J. Dam deformation prediction based on extreme learning machine and elastic network. *Sci. Surv. Mapp.* **2020**, *45*, 20.
15. Su, H.; Wen, Z.; Wu, Z. An Early-warning Model of Dam Safety Based on SVM Theory. *J. Basic Sci. Eng.* **2009**, *17*, 40–48.
16. Salazar, F.; Toledo, M.; Oñate, E.; Suárez, B. Interpretation of dam deformation and leakage with boosted regression trees. *Eng. Struct.* **2016**, *119*, 230–251. [\[CrossRef\]](#)
17. Campos, A.; López, C.M.; Blanco, A.; Aguado, A. Structural Diagnosis of a Concrete Dam with Cracking and High Nonrecoverable Displacements. *J. Perform. Constr. Facil.* **2016**, *30*, 04016021. [\[CrossRef\]](#)
18. Lamea, M.; Mirzabozorg, H. Simulating Structural Responses of a Generic AAR-Affected Arch Dam Considering Seismic Loading. *Sci. Iran* **2018**, *25*, 2926–2937. [\[CrossRef\]](#)
19. Wang, S.; Xu, C.; Gu, H.; Zhu, P.; Liu, H.; Xu, B. An Approach for Quantifying the Influence of Seepage Dissolution on Seismic Performance of Concrete Dams. *Comput. Model. Eng. Sci.* **2022**, *131*, 97–117. [\[CrossRef\]](#)
20. Li, F.; Wang, Z.; Liu, G.; Fu, C.; Wang, J. Hydrostatic seasonal state model for monitoring data analysis of concrete dams. *Struct. Infrastruct. Eng.* **2015**, *11*, 1616–1631. [\[CrossRef\]](#)
21. Wang, S.; Xu, Y.; Gu, C.; Bao, T.; Xia, Q.; Hu, K. Hysteretic effect considered monitoring model for interpreting abnormal deformation behavior of arch dams: A case study. *Struct. Control. Health Monit.* **2019**, *26*, e2417. [\[CrossRef\]](#)
22. Gu, C.S.; Wu, Z.R. Safety Monitoring of Dams and Dam Foundations: Theories & Methods and Their Application. 2006. Available online: <https://www.scopus.com/inward/record.uri?eid=2-s2.0-85119970332&partnerID=40&md5=b759974ac898b3b32a5e01140f7cd34f> (accessed on 14 December 2022).
23. Hu, J.; Ma, F. Zoned deformation prediction model for super high arch dams using hierarchical clustering and panel data. *Eng. Comput.* **2020**, *37*, 2999–3021. [\[CrossRef\]](#)
24. Tatin, M.; Briffaut, M.; Dufour, F.; Simon, A.; Fabre, J.-P. Thermal displacements of concrete dams: Accounting for water temperature in statistical models. *Eng. Struct.* **2015**, *91*, 26–39. [\[CrossRef\]](#)
25. Mata, J.; de Castro, A.T.; da Costa, J.S. Time–frequency analysis for concrete dam safety control: Correlation between the daily variation of structural response and air temperature. *Eng. Struct.* **2013**, *48*, 658–665. [\[CrossRef\]](#)
26. Kang, F.; Li, J.; Zhao, S.; Wang, Y. Structural health monitoring of concrete dams using long-term air temperature for thermal effect simulation. *Eng. Struct.* **2019**, *180*, 642–653. [\[CrossRef\]](#)
27. Chen, S.; Gu, C.; Lin, C.; Zhao, E.; Song, J. Safety Monitoring Model of a Super-High Concrete Dam by Using RBF Neural Network Coupled with Kernel Principal Component Analysis. *Math. Probl. Eng.* **2018**, *2018*, 1712653. [\[CrossRef\]](#)
28. Zhang, J.; Richards, C.M. Parameter identification of analytical and experimental rubber isolators represented by Maxwell models. *Mech. Syst. Signal Process.* **2007**, *21*, 2814–2832. [\[CrossRef\]](#)
29. Pelosi, G. The finite-element method, part 1: R. L. Courant. *IEEE Antennas Propag. Mag.* **2007**, *49*, 180–182. [\[CrossRef\]](#)
30. Ren, S.; Zhao, G.; Zhang, S. Elastic–Viscoelastic Composite Structures Analysis with an Improved Burgers Model. *J. Vib. Acoust.* **2018**, *140*, 031006. [\[CrossRef\]](#)
31. Xiong, L.; Yang, L.; Zhang, Y. Non-stationary Burgers model for rock. *J. Cent. South Univ.* **2010**, *41*, 679–684.
32. Zhang, S.; Sheng, D.; An, W.; Liu, B.; Qi, R.; Cheng, J. Nonlinear Visco-Elastic-Plastic Analysis of Rubber Asphalt Composites Based on Improved Burgers Model. *Chin. Q. Mech.* **2021**, *42*, 528–537.
33. Huang, Y.; Wan, Z. Study on Viscoelastic Deformation Monitoring Index of an RCC Gravity Dam in an Alpine Region Using Orthogonal Test Design. *Math. Probl. Eng.* **2018**, *2018*, 8743505. [\[CrossRef\]](#)
34. Hu, Y.; Gu, C.; Meng, Z.; Shao, C. Improve the Model Stability of Dam’s Displacement Prediction Using a Numerical-Statistical Combined Model. *IEEE Access* **2020**, *8*, 147482–147493. [\[CrossRef\]](#)
35. Ranaivomanana, N.; Multon, S.; Turatsinze, A. Basic creep of concrete under compression, tension and bending. *Constr. Build. Mater.* **2013**, *38*, 173–180. [\[CrossRef\]](#)
36. Mei, S.; Wang, Y.; Zou, R.; Long, Y.; Zhang, J. Creep of concrete-filled steel tube considering creep-recovery of the concrete core. *Adv. Struct. Eng.* **2020**, *23*, 997–1009. [\[CrossRef\]](#)
37. Ju, Y.-W.; Li, K.-F.; Han, J.-G. Experimental and theoretical research on tensile creep of early-age concrete. *Eng. Mech.* **2009**, *26*, 43–49.
38. Gu, C.S.; Zhao, E.F. *Theory and Method of dam Safety Monitoring*; Hohai University Press: Nanjing, China, 2019.
39. Yang, C.; Chen, M.; Zhang, M.; Li, Q.; Fang, W.; Wen, Q. Research on the creep of concrete filled steel tubular columns based on the generalized kelvin chain. *Eng. Mech.* **2022**, *39*, 200–207.

40. Yakubovskiy, Y.E.; Kolosov, V.I.; Donkova, I.A.; Kruglov, S.O. Creep mathematical model on the example of early age concrete. *IOP Conf. Ser. Mater. Sci. Eng.* **2020**, *972*, 012054. [[CrossRef](#)]
41. Sun, K.; Wu, Z.D.; Wu, Y.Y.; Wu, Y.Z. Research on fault diagnosis of altimeter based on KPCA-BN. *J. Ordnance Equip. Eng.* **2020**, *41*, 95–99.
42. Li, X.; Zhang, L.; Khan, F.; Han, Z. A data-driven corrosion prediction model to support digitization of subsea operations. *Process. Saf. Environ. Prot.* **2021**, *153*, 413–421. [[CrossRef](#)]
43. Su, H.; Wen, Z.; Ren, J. A kernel principal component analysis-based approach for determining the spatial warning domain of dam safety. *Soft Comput.* **2020**, *24*, 14921–14931. [[CrossRef](#)]
44. Wang, S.; Xu, C.; Su, H. Back analysis of viscoelastic working behavior for Jinping-I Arch Dam. *Adv. Sci. Technol. Water Resour.* **2020**, *40*, 62–69.
45. Li, Y.; Bao, T.; Shu, X.; Chen, Z.; Gao, Z.; Zhang, K. A Hybrid Model Integrating Principal Component Analysis, Fuzzy C-Means, and Gaussian Process Regression for Dam Deformation Prediction. *Arab. J. Sci. Eng.* **2021**, *46*, 4293–4306. [[CrossRef](#)]
46. Ren, L.; Song, C.; Wu, W.; Guo, M.; Zhou, X. Reservoir effects on the variations of the water temperature in the upper Yellow River, China, using principal component analysis. *J. Environ. Manag.* **2020**, *262*, 110339. [[CrossRef](#)]
47. Su, H.; Li, J.; Hu, J.; Wen, Z. Analysis and Back-Analysis for Temperature Field of Concrete Arch Dam During Construction Period Based on Temperature Data Measured by DTS. *IEEE Sens. J.* **2013**, *13*, 1403–1412. [[CrossRef](#)]
48. Yang, M.; Su, H. A study for optical fiber multi-direction strain monitoring technology. *Optik* **2017**, *144*, 324–333. [[CrossRef](#)]
49. Xu, B.; Liu, B.; Zheng, D.; Chen, L.; Wu, C. Analysis method of thermal dam deformation. *Sci. China Technol. Sci.* **2012**, *55*, 1765–1772. [[CrossRef](#)]
50. Yang, M.; Su, H.; Wen, Z. An approach of evaluation and mechanism study on the high and steep rock slope in water conservancy project. *Comput. Concr.* **2017**, *19*, 527–535. [[CrossRef](#)]
51. Halim, H.; Isa, S.M.; Mulyono, S. Comparative analysis of PCA and KPCA on paddy growth stages classification. In Proceedings of the IEEE Region 10 Symposium (TENSYP), Sanur, Indonesia, 9–11 May 2016; pp. 167–172.
52. Shao, C.; Zheng, S.; Gu, C.; Hu, Y.; Qin, X. A novel outlier detection method for monitoring data in dam engineering. *Expert Syst. Appl.* **2022**, *193*, 116476. [[CrossRef](#)]

Disclaimer/Publisher’s Note: The statements, opinions and data contained in all publications are solely those of the individual author(s) and contributor(s) and not of MDPI and/or the editor(s). MDPI and/or the editor(s) disclaim responsibility for any injury to people or property resulting from any ideas, methods, instructions or products referred to in the content.

MDPI
St. Alban-Anlage 66
4052 Basel
Switzerland
www.mdpi.com

MDPI Books Editorial Office
E-mail: books@mdpi.com
www.mdpi.com/books



Disclaimer/Publisher's Note: The statements, opinions and data contained in all publications are solely those of the individual author(s) and contributor(s) and not of MDPI and/or the editor(s). MDPI and/or the editor(s) disclaim responsibility for any injury to people or property resulting from any ideas, methods, instructions or products referred to in the content.



Academic Open
Access Publishing

[mdpi.com](https://www.mdpi.com)

ISBN 978-3-0365-8305-1